MONTANA STATE UNIVERSITY

Turbulence structure in smooth and rough pipes
by Ralph Edward Powe

A thesis submitted to the Graduate Faculty in partial fulfillment of the requirements of the degree of DOCTOR OF PHILOSOPHY in Aerospace and Mechanical Engineering
Montana State University
© Copyright by Ralph Edward Powe (1970)

Abstract:
This thesis presents the results of an experimental and analytical investigation of turbulent flow in circular pipes having both smooth and rough walls. The analytical portion of the study includes the development of applicable forms of the governing conservation equations of mass, momentum, and energy. The rough-walled pipes require the inclusion of temporal mean radial and angular velocities in these equations, and the random shape distribution of the roughness elements suggests a spatial averaging process. Development of the governing equations in this manner yielded the controlling parameters in the turbulent flow process, and an experimental investigation was devised to study these, as well as other, parameters of interest. This investigation was conducted for flow in one smooth and two rough pipes having relative roughness of about 0.005 and 0.04. All experimental data were obtained at a Reynolds number of about 165,000, and for this case, flow in the hydraulically smooth, transition, and fully rough regimes was obtained for the relative roughnesses of 0, 0.005,. and 0.04 respectively. Although much of this smooth pipe information is currently available, all experimental measurements, utilizing hot-wire anemometry techniques, were first conducted in the smooth pipe to validate the apparatus and procedures, and excellent results were obtained. Quantities measured included mean and fluctuating velocities, friction factors, second and third order velocity correlations, fluctuating velocity energy spectra, autocorrelation functions, Eulerian and spatial turbulence scales, and mean and turbulence energy terms. Rough pipe measurements indicate a definite change in flow structure, and this is especially predominate in the energy quantities and turbulence scales. This structural change appears to be due largely to the fact that the roughness elements occupy the region where the three-dimensional streaky structure originates for smooth pipe flow.

TURBULENCE STRUCTURE IN SMOOTH AND ROUGH PIPES

by

RALPH ELWARD POWE

A thesis submitted to the Graduate Faculty in partial fulfillment of the requirements of the degree

of

DOCTOR OF PHILOSOPHY

in

Aerospace and Mechanical Engineering

Approved:

E. N. Bishop
Head, Major Department

Harry W. Townes
Chairman, Examining Committee

R. Goering
Graduate Dean

MONTANA STATE UNIVERSITY
Bozeman, Montana

December, 1970

ACKNOWLEDGMENT

The author wishes to express his sincere appreciation to Dr. H. W. Townes, under whose guidance this investigation was accomplished. The assistance of Mr. John L. Gow in soldering the hot-wires is most deeply appreciated. The writer is especially appreciative of the patience of his wife and children, who have given up their portion of his time during the past several years.

The apparatus and instrumentation utilized in the experimental portion of this investigation was obtained with funds received from the Atomic Energy Commission through Research Contract AT (45-1)-1954. Maintenance for the equipment and computer time was furnished by the Aerospace and Mechanical Engineering Department of Montana State University. During the course of this investigation the author was supported by research and teaching assistantships from the Aerospace and Mechanical Engineering and the Civil Engineering and Engineering Mechanics Departments of Montana State University, an NSF Traineeship, and a Marjorie Roy Rothermel Memorial Scholarship from the Woman's Auxiliary to the American Society of Mechanical Engineers.

TABLE OF CONTENTS

	Page
VITA	ii
ACKNOWLEDGMENT	iii
LIST OF TABLES	viii
LIST OF FIGURES	ix
NOMENCLATURE	xxvi
ABSTRACT	xxxi
I. INTRODUCTION	1
II. LITERATURE REVIEW	5
Mean Velocity Profiles in Smooth Pipes	5
Flow Resistance and Roughness Characterization	20
Mean Velocity Profiles in Rough Pipes	31
Velocity Fluctuations	36
Fluctuating Velocity Correlations	43
Eddy Diffusivity For Momentum	49
Spectral Analysis	53
Autocorrelations	64
Turbulence Scales	67
Pressure Field	70
Turbulence Structure	73
III. CURRENT PROBLEM	80

Page

IV. ANALYTICAL CONSIDERATIONS 82

Momentum and Continuity Relations 82

Energy Relations 91

Spectral Analysis 99

V. EXPERIMENTAL SYSTEM 101

Wind Tunnel 101

Pressure Measurements 105

Roughness Characterization 109

Electronic Equipment 111

Longitudinal Mean and Fluctuating Velocity Measurements . 114

Second Order Velocity Correlation Measurements 119

Third Order Velocity Correlation Measurements 125

Dissipation Function Measurements 131

Energy Spectra Measurements 137

Data Reduction 145

VI. SMOOTH PIPE RESULTS 150

Mean Velocity and Flow Resistance 150

Fluctuating Velocities 156

Fluctuating Velocity Correlations 169

Dissipation Function 188

Page

Energy Relations 203

Energy Spectra 220

Autocorrelation Functions 246

Turbulence Scales 253

VII. RESULTS FOR SMALL ROUGHNESS 267

Mean Velocity and Flow Resistance 267

Fluctuating Velocities 269

Fluctuating Velocity Correlations 279

Dissipation Function 295

Energy Relations 308

Energy Spectra 324

Autocorrelation Functions 345

Turbulence Scales 355

VIII. RESULTS FOR LARGE ROUGHNESS 371

Mean Velocity and Flow Resistance 371

Fluctuating Velocities 373

Fluctuating Velocity Correlations 385

Dissipation Function 398

Energy Relations 409

Energy Spectra 421

Autocorrelation Functions 447

Page

Turbulence Scales 453

IX. COMPARISON OF SMOOTH AND ROUGH PIPE RESULTS 464

Mean Velocity and Flow Resistance 464

Fluctuating Velocities 465

Fluctuating Velocity Correlations 467

Dissipation Function 470

Energy Relations 471

Energy Spectra 474

Autocorrelation Functions 476

Turbulence Scales 477

X. CONCLUSION AND RECOMMENDATIONS 482

APPENDIX I. Hot-Wire Sensitivity For an Arbitrary Orientation . 494

APPENDIX II. Equipment List 499

APPENDIX III. Determination of Wave Analyzer Effective Bandwidths . 502

APPENDIX IV. Calibration of Analog to Digital Conversion System . 504

APPENDIX V. Computer Programs for Data Reduction 506

SELECTED BIBLIOGRAPHY 518

LIST OF TABLES

Table		Page
1.	Logarithmic Velocity Profile Equations For Smooth Pipes . .	10
2.	Wave Analyzer Operating Ranges	141
3.	Hot-Wire Sensitivity For Specific Orientations	498

LIST OF FIGURES

Figure		Page
1.	Schematic Representation of Wind Tunnel	102
2.	Schematic Representation of Pressure Measurement System	107
3.	Schematic Diagram of Circuitry for Measuring Longitudinal Mean and Fluctuating Velocity Components	116
4.	Schematic Diagram of Circuitry for Second Order Correlation Measurements	123
5.	Schematic Diagram of Electronic Circuitry for Third Order Correlation Measurements	127
6.	Schematic Diagram of Electronic Circuitry for Operation of Spatial Correlation Probes	134
7.	Schematic Diagram of Electrical System Utilized for Obtaining $E_1(n)$ Spectrum Function	142
8.	Schematic Diagram of Electrical System Utilized for Obtaining $E_2(n)$ and $E_3(n)$ Spectrum Functions	143
9.	Flow Resistance Characterization for Smooth Pipe	151
10.	Mean Velocity Profile For Center Portion of Smooth Pipe	153
11.	Wall Region Mean Velocity Profile For Smooth Pipe	154
12.	RMS Values of Fluctuating Velocities in Center Portion of Smooth Pipe	157
13.	RMS Values of Fluctuating Velocities Near Wall of Smooth Pipe	158
14.	Turbulence Intensities For Smooth Pipe	160
15.	Smooth Pipe Anisotropy Ratios	162
16.	Turbulence Kinetic Energy For Central Region of Smooth Pipe	164

Figure Page

17. Turbulence Kinetic Energy For Wall Region of Smooth Pipe . 165

18. Radial Pressure Variation For Central Region of Smooth Pipe 167

19. Radial Pressure Variation For Wall Region of Smooth Pipe . 168

20. Cross Correlation Between Longitudinal and Radial Fluctuating Velocities For Central Portion of Smooth Pipe . . 170

21. Cross Correlation Between Longitudinal and Radial Fluctuating Velocities For Wall Region of Smooth Pipe 171

22. Correlation Coefficient ψ_{12} for Longitudinal and Radial Fluctuating Velocities in Smooth Pipe 173

23. Ratio of Turbulence Shear Stress to Turbulence Kinetic Energy for Smooth Pipe 174

24. Eddy Diffusivity For Momentum in Central Region of Smooth Pipe 176

25. Eddy Diffusivity For Momentum in Wall Region of Smooth Pipe 177

26. Cross Correlation Between Longitudinal and Angular Fluctuating Velocities For Central Region of Smooth Pipe 179

27. Cross Correlation Between Longitudinal and Angular Fluctuating Velocities for Wall Region of Smooth Pipe 180

28. Radial Variation of Third Order $\overline{u_1^2 u_2}$ Correlation For Central Region of Smooth Pipe 181

29. Radial Variation of Third Order $\overline{u_1^2 u_2}$ Correlation For Wall Region of Smooth Pipe 182

30. Correlation Coefficient For Third Order $\overline{u_1^2 u_2}$ Correlation in Smooth Pipe 183

Figure Page

31. Radial Variation of Third Order $\overline{u_2^3}$ Correlation For Central Region of Smooth Pipe 185

32. Radial Variation of Third Order $\overline{u_2^3}$ Correlation For Wall Region of Smooth Pipe 186

33. Correlation Coefficient For Third Order $\overline{u_2^3}$ Correlation in Smooth Pipe 187

34. Dissipation Terms For Turbulent Core of Smooth Pipe 189

35. Dissipation Terms For Turbulent Core of Smooth Pipe 190

36. Dissipation Terms For Turbulent Core of Smooth Pipe 191

37. Dissipation Terms For Wall Region of Smooth Pipe 192

38. Dissipation Terms For Wall Region of Smooth Pipe 193

39. Dissipation Terms For Wall Region of Smooth Pipe 194

40. Dissipation Terms For Wall Region of Smooth Pipe 195

41. Dimensionless Dissipation Function For Central Region of Smooth Pipe 198

42. Dimensionless Dissipation Function For Wall Region of Smooth Pipe 199

43. Isotropic Dissipation Function For Turbulent Core of Smooth Pipe 201

44. Isotropic Dissipation Function Near Wall of Smooth Pipe . . 202

45. Lin's Condition For Applicability of Taylor's Hypothesis in Core Region of Smooth Pipe 204

46. Lin's Condition For Applicability of Taylor's Hypothesis in Wall Region of Smooth Pipe 205

47. Availability of Mean Energy In Turbulent Core of Smooth Pipe Due to Longitudinal Pressure Drop 206

Figure Page

48. Conversion of Mean Energy to Turbulence Energy in Turbulent Core of Smooth Pipe 207

49. Direct Viscous Dissipation of Mean Energy in Turbulent Core of Smooth Pipe 208

50. Availability of Mean Energy Due to Longitudinal Pressure Drop Near Wall of Smooth Pipe 210

51. Conversion of Mean Energy to Turbulence Energy Near Wall of Smooth Pipe 211

52. Direct Viscous Dissipation of Mean Energy Near Wall of Smooth Pipe 212

53. Gradient Diffusion of Turbulence Kinetic Energy in Central Region of Smooth Pipe 215

54. Gradient Diffusion of Turbulence Kinetic Energy in Wall Region of Smooth Pipe 216

55. Convective Diffusion of Total Turbulence Energy in Central Region of Smooth Pipe 218

56. Convective Diffusion of Total Turbulence Energy in Wall Region of Smooth Pipe 219

57. Frequency Domain Energy Spectra For u_1 Fluctuating Velocity in Smooth Pipe 222

58. Contour Map of u_1 Energy Spectra for Smooth Pipe 223

59. Inertial Subrange of Eddy Sizes for u_1 Fluctuations in Smooth Pipe 225

60. Production Subrange of Eddy Sizes for u_1 Fluctuations in Smooth Pipe 226

61. Viscous Subrange of Eddy Sizes For u_1 Fluctuations in Smooth Pipe 227

62. u_1 Spectra for Smooth Pipe Normalized as Proposed by

Figure Page

Robertson et al [47] 229

63. u_1 Spectra for Smooth Pipe Normalized as Proposed by Goma and Gelhar [30] 230

64. Frequency Domain Energy Spectra for u_2 Fluctuating Velocity in Smooth Pipe 231

65. Contour Map of u_2 Energy Spectra for Smooth Pipe 232

66. Inertial Subrange of Eddy Sizes for u_2 Fluctuations in Smooth Pipe 235

67. Production Subrange of Eddy Sizes for u_2 Fluctuations in Smooth Pipe 236

68. Viscous Subrange of Eddy Sizes for u_2 Fluctuations in Smooth Pipe 237

69. u_2 Spectra for Smooth Pipe Normalized as Proposed by Robertson et al [47] 238

70. u_2 Spectra for Smooth Pipe Normalized as Proposed by Goma and Gelhar [30] 239

71. Frequency Domain Energy Spectra for u_3 Fluctuations in Smooth Pipe 240

72. Contour Map of u_3 Energy Spectra for Smooth Pipe 241

73. Inertial Subrange of Eddy Sizes for u_3 Fluctuations in Smooth Pipe 243

74. Production Subrange of Eddy Sizes for u_3 Fluctuations in Smooth Pipe 244

75. Viscous Subrange of Eddy Sizes for u_3 Fluctuations in Smooth Pipe 245

76. u_3 Spectra for Smooth Pipe Normalized as Proposed by Robertson et al [47] 247

Figure Page

77. u_3 Spectra for Smooth Pipe Normalized as Proposed by Goma and Gelhar [30] 248

78. Autocorrelation Function for u_1 Fluctuating Velocity in Smooth Pipe 249

79. Autocorrelation Function for u_2 Fluctuating Velocity in Smooth Pipe 250

80. Autocorrelation Function for u_3 Fluctuating Velocity in Smooth Pipe 251

81. Eulerian Micro Scales for Central Region of Smooth Pipe . . 254

82. Eulerian Micro Scales for Wall Region of Smooth Pipe . . . 255

83. Eulerian Macro Scale for u_1 Fluctuating Velocity in Central Region of Smooth Pipe 256

84. Eulerian Macro Scale for u_2 Fluctuating Velocity in Central Region of Smooth Pipe 257

85. Eulerian Macro Scale for u_3 Fluctuating Velocity in Central Region of Smooth Pipe 258

86. Eulerian Macro Scale for u_1 Fluctuating Velocity in Wall Region of Smooth Pipe 260

87. Eulerian Macro Scale for u_2 Fluctuating Velocity in Wall Region of Smooth Pipe 261

88. Eulerian Macro Scale for u_3 Fluctuating Velocity in Wall Region of Smooth Pipe 262

89. Spatial Micro Scales for Central Region of Smooth Pipe . . 263

90. Spatial Micro Scales for Wall Region of Smooth Pipe 264

91. Spatial Macro Scales for Smooth Pipe 266

92. Flow Resistance Characterization for Small Roughness . . . 268

Figure Page

93. Longitudinal Mean Velocity Profile for Central Region of Pipe With Small Roughness Elements 270

94. Longitudinal Mean Velocity Profile for Wall Region of Pipe With Small Roughness Elements 271

95. Fluctuating Velocities in Central Region of Pipe With Small Roughness Elements 273

96. Fluctuating Velocities for Wall Region of Pipe With Small Roughness Elements 274

97. Turbulence Intensities in Pipe With Small Roughness Elements 275

98. Anisotropy Ratios for Flow in Pipe With Small Roughness Elements 276

99. Turbulence Kinetic Energy for Flow in Pipe With Small Roughness Elements 278

100. Radial Pressure Variation in Central Region of Pipe With Small Roughness Elements 280

101. Radial Pressure Variation Near Wall of Pipe With Small Roughness Elements 281

102. Second Order $\overline{u_1 u_2}$ Cross Correlation for Flow in Pipe With Small Roughness Elements 282

103. Variation of ψ_{12} Correlation Coefficient for Pipe With Small Roughness Elements 284

104. Turbulence Shear Stress to Kinetic Energy Ratio for Pipe With Small Roughness Elements 285

105. Spatial $\overline{\hat{U}_1 \hat{U}_2}$ Correlation for Pipe With Small Roughness Elements 287

106. Eddy Diffusivity for Momentum in Central Region of Pipe With Small Roughness Elements 289

Figure Page

107. Eddy Diffusivity for Momentum in Wall Region of Pipe With Small Roughness Elements 290

108. Second Order $\overline{u_1 u_3}$ Correlation for Turbulent Core of Pipe With Small Roughness Elements 291

109. Second Order $\overline{u_1 u_3}$ Correlation Near Wall of Pipe With Small Roughness Elements 292

110. Third Order $\overline{u_1^2 u_2}$ Correlation for Central Region of Pipe With Small Roughness Elements 293

111. Third Order $\overline{u_1^2 u_2}$ Correlation for Wall Region of Pipe With Small Roughness Elements 294

112. Correlation Coefficient for $\overline{u_1^2 u_2}$ in Pipe With Small Roughness Elements 296

113. Third Order $\overline{u_2^3}$ Correlation for Central Portion of Pipe With Small Roughness Elements 297

114. Third Order $\overline{u_2^3}$ Correlation Near Wall of Pipe With Small Roughness Elements 298

115. Correlation Coefficient for $\overline{u_2^3}$ in Tube With Small Roughness Elements 299

116. Dissipation Terms for Central Region of Tube With Small Roughness Elements. 300

117. Dissipation Terms for Central Region of Tube With Small Roughness Elements 302

118. Dissipation Terms for Wall Region of Tube With Small Roughness Elements 303

119. Dissipation Terms for Wall Region of Tube With Small Roughness Elements 304

120. Dissipation Function in Central Region of Tube With Small Roughness Elements 306

Figure Page

121. Dissipation Function Near Wall of Tube With Small Roughness Elements 307

122. Lin's Condition for Applicability of Taylor's Hypothesis in Turbulent Core of Tube With Small Roughness Elements 309

123. Lin's Condition for Applicability of Taylor's Hypothesis Near Wall of Tube With Small Roughness Elements . . . 310

124. Mean Energy Terms for Central Region of Tube With Small Roughness Elements 312

125. Direct Viscous Dissipation of Mean Energy in Turbulent Core of Tube With Small Roughness Elements 313

126. Roughness and Turbulence Energy Production Near Wall of Tube With Small Roughness Elements 315

127. Availability of Mean Energy Near Wall of Tube With Small Roughness Elements 316

128. Direct Viscous Dissipation of Mean Energy Near Wall of Tube With Small Roughness Elements 317

129. Gradient Diffusion of Turbulence Kinetic Energy in Central Region of Tube With Small Roughness Elements 319

130. Gradient Diffusion of Turbulence Kinetic Energy in Wall Region of Tube With Small Roughness Elements 320

131. Convective Diffusion of Turbulence Energy in Central Region of Tube With Small Roughness Elements 322

132. Convective Diffusion of Turbulence Energy Near Wall of Tube With Small Roughness Elements 323

133. Frequency Domain Energy Spectra for u_1 Fluctuations in Tube With Small Roughness Elements 325

134. Wave Number Space Energy Spectra for u_1 Fluctuations in

Figure Page

Tube With Small Roughness Elements 326

135. Inertial Subrange of Eddy Sizes for u_1 Fluctuations in Tube With Small Roughness Elements 328

136. Production Subrange of Eddy Sizes for u_1 Fluctuations in Tube with Small Roughness Elements 329

137. Viscous Subrange of Eddy Sizes for u_1 Fluctuations in Tube With Small Roughness Elements 330

138. u_1 Spectra for Pipe With Small Roughness Elements Normalized as Suggested by Robertson et al [47] 332

139. u_1 Spectra for Pipe With Small Roughness Elements Normalized as Suggested by Goma and Gelhar [30] 333

140. Frequency Domain Energy Spectra of u_2 Fluctuating Velocity in Pipe With Small Roughness Elements 334

141. Wave Number Space Energy Spectra of u_2 Fluctuating Velocity in Pipe With Small Roughness Elements 335

142. Inertial Subrange of Eddy Sizes for u_2 Velocity Fluctuations in Pipe With Small Roughness Elements 337

143. Production Subrange of Eddy Sizes for u_2 Velocity Fluctuations in Pipe With Small Roughness Elements . 338

144. Viscous Subrange of Eddy Sizes for u_2 Velocity Fluctuations in Pipe With Small Roughness Elements 339

145. u_2 Spectra for Pipe With Small Roughness Elements Normalized as Proposed by Robertson et al [47] 341

146. u_2 Spectra for Pipe With Small Roughness Elements Normalized as Proposed by Goma and Gehlar [30] 342

147. Frequency Domain Energy Spectra for u_3 Fluctuating Velocity in Pipe With Small Roughness Elements 343

148. Wave Number Space Energy Spectra for u_3 Fluctuating

Figure Page

Velocity in Pipe With Small Roughness Elements . . . 344

149. Inertial Subrange of Eddy Sizes for u_3 Velocity Fluctuations in Pipe With Small Roughness Elements 346

150. Production Subrange of Eddy Sizes for u_3 Velocity Fluctuations in Pipe With Small Roughness Elements . 347

151. Viscous Subrange of Eddy Sizes for u_3 Velocity Fluctuations in Pipe With Small Roughness Elements 348

152. u_3 Spectra for Flow in Pipe With Small Roughness Elements Normalized as Suggested by Robertson et al [47] . . . 349

153. u_3 Spectra for Flow in Pipe With Small Roughness Elements Normalized as Suggested by Goma and Gelhar [30] . . . 350

154. Autocorrelation Function for u_1 Velocity Fluctuations in Pipe With Small Roughness Elements 351

155. Autocorrelation Function for u_2 Velocity Fluctuations in Pipe With Small Roughness Elements 352

156. Autocorrelation Function for u_3 Fluctuating Velocity in Pipe With Small Roughness Elements 353

157. Eulerian Micro Scales in Central Region of Pipe With Small Roughness Elements 356

158. Eulerian Micro Scales in Wall Region of Pipe With Small Roughness Elements 357

159. Eulerian Macro Scale in x_1 Direction For Central Region of Pipe With Small Roughness Elements 359

160. Eulerian Macro Scale in x_2 Direction For Central Region of Pipe With Small Roughness Elements 360

161. Eulerian Macro Scale in x_3 Direction for Central Region of Pipe With Small Roughness Elements 361

162. Eulerian Macro Scale in x_1 Direction for Wall Region of

Figure Page

Pipe With Small Roughness Elements 362

163. Eulerian Macro Scale in x_2 Direction for Wall Region of Pipe With Small Roughness Elements 363

164. Eulerian Macro Scale in x_3 Direction in Wall Region of Pipe With Small Roughness Elements 364

165. Spatial Micro Scales for Central Region of Tube With Small Roughness Elements 366

166. Spatial Micro Scales for Wall Region of Pipe With Small Roughness Elements 367

167. Spatial Macro Scale in x_1 Direction for Pipe With Small Roughness Elements 368

168. Spatial Macro Scales in x_2 and x_3 Directions for Tube With Small Roughness Elements 369

169. Flow Resistance Characterization for Large Roughness . . . 372

170. Longitudinal Mean Velocity Profile in Central Region of Pipe With Large Roughness Elements 374

171. Longitudinal Mean Velocity Profile in Wall Region of Pipe With Large Roughness Elements 375

172. RMS Values of Fluctuating Velocities in Pipe With Large Roughness Elements 377

173. Turbulence Intensities in Central Region of Pipe With Large Roughness Elements 378

174. Turbulence Intensities in Wall Region of Pipe With Large Roughness Elements 379

175. Anisotropy Ratios for Pipe With Large Roughness Elements . 381

176. Turbulence Kinetic Energy in Pipe With Large Roughness Elements 382

Figure Page

177. Radial Pressure Variation in Pipe With Large Roughness Elements 384

178. Second Order $\overline{u_1 u_2}$ Cross Correlation in Pipe With Large Roughness Elements 386

179. Variation of ψ_{12} Correlation Coefficient for Pipe With Large Roughness Elements 387

180. Turbulence Shear Stress to Kinetic Energy Ratio for Pipe With Large Roughness Elements 388

181. Spatial $\overline{\hat{U}_1 \hat{U}_2}$ Correlation for Pipe With Large Roughness Elements 390

182. Eddy Diffusivity for Momentum in Central Region of Pipe With Large Roughness Elements 391

183. Eddy Diffusivity for Momentum in Wall Region of Pipe With Large Roughness Elements 392

184. Second Order $\overline{u_1 u_3}$ Cross Correlation for Pipe With Large Roughness Elements 394

185. Third Order $\overline{u_1^2 u_2}$ Correlation for Central Region of Pipe With Large Roughness Elements 395

186. Third Order $\overline{u_1^2 u_2}$ Correlation for Wall Region of Pipe With Large Roughness Elements 396

187. Correlation Coefficient for $\overline{u_1^2 u_2}$ in Pipe With Large Roughness Elements 397

188. Third Order $\overline{u_2^3}$ Correlation for Central Region of Pipe With Large Roughness Elements 399

189. Third Order $\overline{u_2^3}$ Correlation Near Wall of Pipe With Large Roughness Elements 400

190. Correlation Coefficient for $\overline{u_2^3}$ in Pipe With Large Roughness Elements 401

Figure Page

191. Dissipation Terms for Central Region of Pipe With Large Roughness Elements 402

192. Dissipation Terms for Central Region of Pipe With Large Roughness Elements 403

193. Dissipation Terms for Central Region of Pipe With Large Roughness Elements 404

194. Dissipation Terms for Wall Region of Pipe With Large Roughness Elements 405

195. Dissipation Terms for Wall Region of Pipe With Large Roughness Elements 406

196. Dissipation Function For Pipe With Large Roughness Elements 408

197. Lin's Condition for Applicability of Taylor's Hypothesis in Pipe With Large Roughness Elements 410

198. Availability of Mean Energy in Central Region of Pipe With Large Roughness Elements 412

199. Viscous Dissipation of Mean Energy in Central Region of Pipe With Large Roughness Elements 413

200. Mean Energy Conversion Terms for Pipe With Large Roughness Elements 414

201. Availability of Mean Energy Near Wall of Pipe With Large Roughness Elements 415

202. Viscous Dissipation of Mean Energy Near Wall of Pipe With Large Roughness Elements 416

203. Gradient Diffusion of Turbulence Kinetic Energy in Central Region of Pipe With Large Roughness Elements 419

204. Gradient Diffusion of Turbulence Kinetic Energy Near Wall of Pipe With Large Roughness Elements 420

Figure Page

205. Convective Diffusion of Turbulence Energy in Central Region of Pipe With Large Roughness Elements 422

206. Convective Diffusion of Turbulence Energy in Wall Region of Pipe With Large Roughness Elements 423

207. Frequency Domain Energy Spectra for u_1 Fluctuations in Pipe With Large Roughness Elements 424

208. Wave Number Space Energy Spectra for u_1 Fluctuations in Pipe With Large Roughness Elements 425

209. Inertial Subrange of Eddy Sizes for u_1 Fluctuations in Pipe With Large Roughness Elements 427

210. Production Subrange of Eddy Sizes For u_1 Fluctuations in Pipe With Large Roughness Elements 428

211. Viscous Subrange of Eddy Sizes for u_1 Fluctuations in Pipe With Large Roughness Elements 429

212. u_1 Spectra for Pipe With Large Roughness Elements Normalized as Proposed by Robertson et al [47] 431

213. u_1 Spectra for Pipe With Large Roughness Elements Normalized as Proposed by Goma and Gelhar [30] 432

214. Frequency Domain Energy Spectra for u_2 Fluctuating Velocity in Pipe With Large Roughness Elements . . . 433

215. Wave Number Space Energy Spectra for u_2 Fluctuations in Pipe With Large Roughness Elements 434

216. Inertial Subrange of Eddy Sizes for u_2 Fluctuations in Pipe With Large Roughness Elements 436

217. Production Subrange of Eddy Sizes for u_2 Fluctuations in Pipe With Large Roughness Elements 437

218. Viscous Subrange of Eddy Sizes for u_2 Fluctuations in Pipe With Large Roughness Elements 438

Figure Page

219. u_2 Spectra for Pipe With Large Roughness Elements Normalized as Proposed by Robertson et al [47] 440

220. u_2 Spectra for Pipe With Large Roughness Elements Normalized as Proposed by Goma and Gelhar [30] 441

221. Frequency Domain Energy Spectra for u_3 Fluctuating Velocity in Pipe With Large Roughness Elements 442

222. Wave Number Space Energy Spectra for u_3 Fluctuating Velocity in Pipe With Large Roughness Elements . . . 443

223. Inertial Subrange of Eddy Sizes for u_3 Velocity Fluctuations in Pipe With Large Roughness Elements . 444

224. Production Subrange of Eddy Sizes for u_3 Velocity Fluctuations in Pipe With Large Roughness Elements . 445

225. Viscous Subrange of Eddy Sizes for u_3 Velocity Fluctuations in Pipe With Large Roughness Elements 446

226. u_3 Spectra for Flow in Pipe With Large Roughness Elements Normalized as Suggested by Robertson et al [47] . . . 448

227. u_3 Spectra for Flow in Pipe With Large Roughness Elements Normalized as Suggested by Goma and Gelhar [30] . . . 449

228. Autocorrelation Function for u_1 Velocity Fluctuations in Pipe With Large Roughness Elements 450

229. Autocorrelation Function for u_2 Velocity Fluctuations in Pipe With Large Roughness Elements 451

230. Autocorrelation Function for u_3 Velocity Fluctuations in Pipe With Large Roughness Elements 452

231. Eulerian Micro Scales in Pipe With Large Roughness Elements 454

232. Eulerian Macro Scale in x_1 Direction for Pipe With Large Roughness Elements 456

Figure Page

233. Eulerian Macro Scales in x_2 and x_3 Directions for Pipe With Large Roughness Elements 457

234. Spatial Micro Scales in x_1 and x_3 Directions for Pipe With Large Roughness Elements 458

235. Spatial Micro Scale in x_2 Direction for Pipe With Large Roughness Elements 459

236. Spatial Macro Scale in x_1 Direction for Pipe With Large Roughness Elements 461

237. Spatial Macro Scale in x_2 Direction for Pipe With Large Roughness Elements 462

238. Spatial Macro Scale in x_3 Direction for Pipe With Large Roughness Elements 463

239. Sketch of Hot-Wire at an Arbitrary Orientation With Respect to the Mean Velocity 495

NOMENCLATURE

Symbol	Description
a	Empirical exponent in power law velocity profile, equation (2.50)
A, B, C, K	Constants
dB	Decibel output of wave analyzer
e	Voltage
e_{avg}	Average value of a rectified voltage
e_{ref}	Reference voltage setting on wave analyzer
$E_i(n)$	Frequency domain energy spectrum function for velocity u_i (ft^2/sec)
$E_i(k_1)$	Wave number space energy spectrum function for velocity u_i (ft^3/sec^2)
F	Any dependent variable
F_i	Momentum term for x_i direction defined by equation (4.18)
h_i	Scale factor for x_i direction defined by equation (4.17)
I	Electrical current
$\vec{i}_i$	Unit vector in x_i direction
$\vec{i}_p$	Unit vector parallel to hot-wire
k_1	Wave number (ft^{-1})
k_s	Nikuradse's equivalent sand diameter

Symbol	Description
L	Prandtl's mixing length
m,n	Circular frequency (sec^{-1})
Δn	Bandwidth
P	Instantaneous pressure
p	Fluctuating pressure
q^2	Instantaneous turbulence kinetic energy, $(u_1^2+u_2^2+u_3^2)/2$
r	Electrical resistance
R	Pipe radius or half-width of rectangular channel
Re	Reynolds number, $2R\overline{U}_{avg}/v$
S	Strouhal number, nv/u^{*2}
s	Ratio of shear stress at wall to shear stress at wall in laminar flow with same maximum velocity, $Ru^{*2}/2v\overline{U}_{max}$
T_i	Eulerian macro scale of turbulence in x_i direction, defined by equation (2.89)
t, t'	Time
U_i	Instantaneous velocity in x_i direction
u_i	Fluctuating velocity component in x_i direction
u_i'	RMS value of fluctuating velocity component in x_i direction
u^+	Dimensionless longitudinal mean velocity, $\overline{U}_1/u^*$
u^*	Shear velocity $\sqrt{\tau_0/\rho}$

Symbol	Description
$\overline{U}_{avg}$	Bulk fluid velocity, $\frac{1}{\pi R^2}\int_0^R 2\pi x_2\,\overline{U}_1 dx_2$
$\overline{U}_{max}$	Maximum value of $\overline{U}_1$ ($\overline{U}_1$ at $x_2 = 0$)
u^+_{max}	Maximum value of u^+, $\overline{U}_{max}/u^*$
u^+_{avg}	Average value of u^+ over pipe cross-section, $\overline{U}_{avg}/u^*$
u_d	Velocity defect, $(\overline{U}_{max} - \overline{U}_1)/u^*$
ν	Fluid kinematic viscosity
V	Velocity normal to hot-wire
W	Turbulence dissipation function, equation (4.25)
x_i	Cylindrical coordinate system component
y	Distance from solid surface measured normal to surface
y^+	Dimensionless distance from solid surface yu^*/ν

Greek Letters

α_i	Spatial micro scale of turbulence in x_i direction, defined by equation (2.91)
β	Pipe factor, $\overline{U}_{avg}/\overline{U}_{max}$
γ_i	Eulerian micro scale of turbulence in x_i direction, defined by equation (2.87)
Γ	Fraction of u_2 velocity sensed by hot-wire

Symbol	Description
δ^*	Displacement thickness, $\int_0^R (1 - \overline{U}_1/\overline{U}_{max})dy$
Δ	Empirical constant in Nikuradse's rough pipe velocity profile expression, equation (2.46)
ε	Mean roughness height
ε^+	Roughness Reynolds number, $\varepsilon u^*/v$
ε_n	Eddy diffusivity for momentum
ζ	Hot-wire orientation angle, Figure 239
η	Displacement in x_2 direction
κ	Fraction of mean velocity sensed by hot-wire
λ	Friction factor, $8(u^*/\overline{U}_{avg})^2$
Λ_i	Spatial macro scale of turbulence in x_i direction, defined by equation (2.93)
ξ	Dummy cylindrical coordinate system component
ρ	Fluid density
σ	Hot-wire orientation angle, Figure 239
τ	Shear stress
τ_ℓ	Viscous Shear Stress
τ_t	Turbulence shear stress
ϕ_i	Autocorrelation function for velocity u_i
χ	Convective diffusion of turbulence energy

Symbol	Description
ψ_{ij}	Cross Correlation Coefficient, $\overline{u_i u_j}/u_i' u_j'$
ω	Empirical constant in Pai's velocity profile expression, equation (2.30)
Ω	Fraction of u_3 velocity sensed by hot-wire

Subscripts

1	Indicates longitudinal direction
2	Indicates radial direction
3	Indicates angular direction
0	Denotes conditions at solid boundary
c	Denotes conditions at center of pipe or channel
PRIME	Denotes Root-Mean-Square (RMS) Value
OVERBAR	Denotes Time Average
^	Denotes spatial average
$\rightharpoonup$	Denotes Vector Quantity

ABSTRACT

This thesis presents the results of an experimental and analytical investigation of turbulent flow in circular pipes having both smooth and rough walls. The analytical portion of the study includes the development of applicable forms of the governing conservation equations of mass, momentum, and energy. The rough-walled pipes require the inclusion of temporal mean radial and angular velocities in these equations, and the random shape distribution of the roughness elements suggests a spatial averaging process. Development of the governing equations in this manner yielded the controlling parameters in the turbulent flow process, and an experimental investigation was devised to study these, as well as other, parameters of interest. This investigation was conducted for flow in one smooth and two rough pipes having relative roughness of about 0.005 and 0.04. All experimental data were obtained at a Reynolds number of about 165,000, and for this case, flow in the hydraulically smooth, transition, and fully rough regimes was obtained for the relative roughnesses of 0, 0.005, and 0.04 respectively. Although much of this smooth pipe information is currently available, all experimental measurements, utilizing hot-wire anemometry techniques, were first conducted in the smooth pipe to validate the apparatus and procedures, and excellent results were obtained. Quantities measured included mean and fluctuating velocities, friction factors, second and third order velocity correlations, fluctuating velocity energy spectra, autocorrelation functions, Eulerian and spatial turbulence scales, and mean and turbulence energy terms. Rough pipe measurements indicate a definite change in flow structure, and this is especially predominate in the energy quantities and turbulence scales. This structural change appears to be due largely to the fact that the roughness elements occupy the region where the three-dimensional streaky structure originates for smooth pipe flow.

CHAPTER I

INTRODUCTION

The determination of the nature of turbulent flow near smooth and rough boundaries has been an important unsolved problem in the areas of heat transfer and fluid mechanics for many decades, and much more information is required before this problem can be fully resolved. With the advent of nuclear reactors the use of rough surfaces to increase heat transfer rates has gained considerable importance. It has been demonstrated by Dipprey [1][1] that under certain flow conditions, and for certain ranges of Prandtl and Reynolds numbers, this increase in heat transfer more than offsets the increased pumping power required because of the surface roughness. Before heat exchangers can be designed effectively to take advantage of this increase in heat transfer, more must be known about the mechanism of turbulent flow over rough surfaces. Also, due to an aging process, most commercial pipes gradually experience an increase in surface roughness. Again the structure of turbulent flow must be better understood before the changes in flow rate and heat transfer caused by this increase in roughness can be predicted. In addition, the

---

[1]Numbers in brackets refer to references listed in the selected bibliography.

mechanism of turbulent flow is of considerable importance in flow over such objects as aerofoils and ship hulls and in noise problems created by turbulent pressure fluctuations.

In laminar flow, surface roughness has no effect on the structure of fluid motion, so long as the surface contour is not changed appreciably by the addition of the roughness, while in turbulent fluid motion the structure of the flow is intimately associated with the nature of the solid surface. Although a great deal of empirical data is available concerning turbulent flow over a smooth boundary, the flow mechanism is still not fully understood, and this problem cannot be satisfactorily handled analytically. While several studies have recently appeared concerning turbulent flow over rough surfaces, they have been concentrated mainly in the areas of flow resistance and mean velocity measurements. Thus, a great deal more information is needed before any explanation of the structure of turbulent flow near rough boundaries can be attempted.

The purpose of the present study will be to experimentally investigate turbulent flow in rough pipes. The roughness elements will consist of sand particles, sifted and scaled with U. S. standard seives to obtain uniformity and glued to the pipe wall. Although an almost infinite number of types of roughness elements could be utilized, the sand roughness was chosen because of its rather random

shape distribution and because velocity profile and flow resistance data have previously been obtained for this case by Nikuradse [2], among others. In most applications the roughness of a surface is related to an equivalent sand diameter, with the aid of Nikuradse's [2] flow resistance data, for evaluation of the flow parameters. Dipprey [1] has also shown that the closely-packed sand grain type roughness yields more efficient heat transfer, under the previously mentioned conditions, than does a smooth pipe, whereas many other types of roughness do not show this increase in heat transfer efficiency.

In order to place this investigation in proper perspective, it should be noted, as pointed out by Kline [3, 4], that the study of turbulent flow can effectively be broken down into two separate areas. The first of these deals with the study of the statistical properties of turbulence, which attempt to define the basic flow mechanism. Although such statistical information is, in many cases, directly useful to the engineering profession, it more commonly serves as a raw material for the second area of study. In this second area an attempt is made to convert the statistical information into improved correlation and predictive procedures for the physical processes of interest such as heat transfer, momentum transfer, mass transfer, drag, etc. The current investigation will be concerned

with a combination of these two areas of study.

CHAPTER II

LITERATURE REVIEW

Mean Velocity Profiles in Smooth Pipes

The study of the field of turbulence began with the classical experiments of Osborne Reynolds which were presented to the Royal Society in London in 1883 and which are summarized by Shepherd [5]. Since that time a vast number of studies in this area have appeared in the literature, so no attempt is made in this section to give a complete review of the literature in the field of turbulent fluid flow. Instead, only those references which are applicable to the current problem will be discussed, and for more detailed surveys of the earlier work in the general area of turbulence the interested reader may consult Bakhmeteff [6], Goldstein [7, 8], Hinze [9], Kuethe [10], Schlichting [11], and Townsend [12].

The governing equations for any fluid flow process are the conservation equations of mass, momentum, and energy. However, turbulent flow is defined by random three-dimensional motions superimposed on the average flow, thus making it impractical to apply the governing equations directly to a turbulent fluid stream. The fact that the turbulent motions are random led Osborne Reynolds (see Schlichting [11]) to attempt a statistical description of the flow

field. This was accomplished by writing the instantaneous velocity at a given point in the flow field, and in a given coordinate direction, as the sum of a time averaged or temporal mean value and a fluctuating component. The time averaged value of the fluctuating component is then identically equal to zero. The foregoing expressions for the instantaneous velocities in the three coordinate directions are then introduced into the governing conservation equations, and these equations are time averaged. Although the resulting equations do indicate measurable quantities which are important in turbulent flow, they have not led to success analytically because of the fact that more unknowns than equations are present. Thus, in order to treat turbulence it has been found necessary to resort to semi-empirical methods which are usually called phenomenological theories.

Probably the best known of the phenomenological theories is Prandtl's mixing length theory which is fully discussed by Kays [13]. Prandtl's mixing length theory consists basically of the assumption that a fluid particle maintains its identity over a distance L in the y direction, where L is called the mixing length. In other words, no x_1 momentum exchange occurs with the particle until it has traversed a distance L in the y direction, and at this point a complete x_1 momentum exchange occurs by viscous interaction. With this assumption and the additional assumption that L is simply proportional to the

distance from the wall

$$L = K\,y \quad , \tag{2.1}$$

Prandtl was able to develop an expression for the shear stress in terms of the velocity gradient,

$$\tau/\rho = K^2\,y^2 \left(\frac{d\,\overline{U}_1}{dy}\right)^2 \quad . \tag{2.2}$$

At this point Prandtl introduced the far-reaching assumption that the shear stress is constant throughout the pipe and equal to the wall shear τ_0. Thus

$$\tau_0/\rho = K^2\,y^2 \left(\frac{d\,\overline{U}_1}{dy}\right)^2 \quad , \tag{2.3}$$

or introducing the dimensionless variables u^+ and y^+,

$$\frac{du^+}{dy^+} = \frac{1}{Ky^+} \quad . \tag{2.4}$$

Integrating equation (2.4), an expression is obtained for the velocity distribution

$$u^+ = \frac{1}{K}\,\ell n\,(y^+) + C \quad , \tag{2.5}$$

where the constants K and C are to be determined by experiment.

Obviously equation (2.5) does not satisfy the boundary conditions at either the wall or the pipe center line. At the wall this equation yields a negative infinite value of u^+, whereas this value must actually be zero, and at the center line a non-zero velocity gradient results from the equation in contrast with physical reality. An attempt can be made to correct this situation at the wall by recognizing that

$$u^+ = y^+ \tag{2.6}$$

at $y^+ = 0$ and assuming that this relationship remains valid for small distances from the wall. Implicitly included in this argument is the assumption that a thin layer, in which the viscous stresses are predominant, exists near the wall. If such a viscous layer exists near the wall, then a buffer layer in which both viscous and turbulent stresses are significant is supposed to exist between this viscous layer and the turbulent core. In this region it is usually assumed that a logarithmic equation must apply,

$$u^+ = A \ln (y^+) + B \quad . \tag{2.7}$$

Equations (2.5), (2.6), and (2.7) have been extensively studied

by many investigators for flow in smooth pipes, and the equations are normally considered to be valid over the following regions of the pipe:

$$u^+ = y^+ \qquad \text{for } y^+ \leq 5 \quad , \tag{2.8}$$

$$u^+ = A \ln (y^+) + B \qquad \text{for } 5 \leq y^+ \leq 30 \quad , \tag{2.9}$$

$$u^+ = \frac{1}{K} \ln (y^+) + C \qquad \text{for } y^+ \geq 30 \quad . \tag{2.10}$$

Having selected the ranges over which each of the equations is valid, the requirement of continuity of u^+ fixes the values of A and B in terms of K and C. In other words, if continuity of u^+ is required, equation (2.9) becomes

$$u^+ = \left[\frac{1.896}{K} + \frac{C}{1.792} - 2.790\right] \cdot [\ln (y^+) - 3.401]$$

$$+ \frac{3.401}{K} + C \quad , \qquad \text{for } 5 \leq y^+ \leq 30 \quad . \tag{2.11}$$

The results of the major investigations in which a relation such as (2.10) has been determined are summarized in Table 1. With the exception of the region near the center of the pipe, the available experimental data do indicate that the logarithmic velocity profile equations are nearly universal, although evidence of a slight Reynolds

number dependence of K and C has been presented by Coantic [21], Corcoran, Opfell, and Sage [22], Page, Schlinger, Breaux, and Sage [23], Quarmby [24], and Rothfus and Monrad [25]. Tennekes [26] has outlined the approach which might be taken in obtaining a second order theory of turbulent flow to account for these Reynolds number variations. Rothfus and Monrad [25] attempt to compensate for this Reynolds number effect by plotting $u^+\beta$ versus y^+/β where β is the pipe factor $\overline{U}_{avg}/\overline{U}_{max}$. The

Investigator	Reference	$\frac{1}{K}$	C	A	-B
Deissler	[14]	2.78	3.80	4.60	2.39
Gow	[15]	2.75	4.55	4.96	2.98
Hughes and Brigthton	[16]	2.44	4.90	4.57	2.35
Laufer	[17]	2.91	5.50	5.80	4.32
Longwell	[18]	2.71	3.50	4.30	1.91
Mower	[19]	2.53	5.23	4.93	2.92
Nikuradse	[2]	2.50	5.50	5.00	3.05
Ross	[20]	2.43	5.60	4.94	2.94
Skinner	[17]	2.71	6.00	5.70	4.16
Wattendorf	[17]	2.68	4.00	4.52	2.27

Table 1. Logarithmic Velocity Profile Equations for Smooth Pipes

resulting plot appears to also represent a straight line in the turbulent core,

$$\beta u^+ = A_1 + B_1 \ln (y^+/\beta) \qquad \text{for } y^+ \geq 30 \quad . \tag{2.12}$$

If it is again assumed that a viscous sublayer, in which the velocity is given by equation (2.8), exists near the wall and that a logarithmic equation applies in the buffer zone, then this equation, because of continuity of u^+, must be given by

$$u^+ = 5.0 + [A_1 - 5.0 + B_1 \ln (30/\beta)] \frac{\ln (y^+/5)}{\ln(6)} \quad . \tag{2.13}$$

The empirical constants A_1 and B_1 in equation (2.12) have not been determined experimentally.

Equation (2.10) has also been modified by Kays [13] so that the boundary condition at the center line is satisfied,

$$u^+ = A_2 + B_2 \ln \left[\frac{1.5\ y^+(1 + x_2/R)}{1 + 2(x_2/R)^2}\right] \qquad \text{for } y^+ \geq 30 \quad . \tag{2.14}$$

Kays suggests letting A_2 and B_2 take on the value of C and 1/K, respectively, from equation (2.10) in the absence of better information, and then applying equation (2.14) in conjunction with equations (2.8)

and (2.9) since the x_2/R term approaches unity at $y^+ = 30$. However, if A_2 and B_2 are determined experimentally, and if equation (2.8) is considered to be valid, then the velocities in the buffer layer can be calculated from

$$u^+ = 5.0 + \left\{ A_2 - 5.0 + B_2 \ln \left[\frac{30y_c^+(y_c^+ - 15.0)}{(y_c^+ - 10.0)(y_c^+ - 30.0)} \right] \right\} \frac{\ln(y^+/5)}{\ln(6)} \tag{2.15}$$

where y_c^+ is the value of y^+ at the pipe center line.

An equation which is valid through the viscous sublayer and the transition zone has been proposed by Dunn (see Longwell [18]). This equation is given by

$$u^+ = A_3 \tanh (y^+/A_3) \quad , \text{ for } y^+ \geq y_a^+ \quad , \tag{2.16}$$

and has the distinct advantage of yielding continuity in the velocity gradient, as well as the velocity, at $y^+ = y_a^+$ when used with any of the foregoing logarithmic equations for the turbulent core, i.e., equations (2.10), (2.12), or (2.14). In using this form of the equation, the values of A_3 and y_a^+ are fixed by an experimental determination of the coefficients in the appropriate equation utilized

in the turbulent core.

In order to reduce the number of constants which had to be determined empirically with equation (2.10), Prandtl (see Schlichting [11]) by introducing the boundary condition of maximum velocity at the pipe center line, found C to be given by

$$C = u^+_{max} - \frac{1}{K} \ln (y^+_C) \quad , \tag{2.17}$$

and the velocity profile equation becomes

$$\frac{\overline{U}_{max} - \overline{U}_1}{u^*} = \frac{1}{K} \ln (R/y) \quad . \tag{2.18}$$

The term on the left hand side of this equation is normally called the velocity defect, u_d. As would be expected, this equation has also been found to exhibit a fairly universal behavior with K = 0.4, except for points near the wall.

Another logarithmic velocity profile has been derived by von Karman (see Schlichting [11]) by assuming that Prandtl's mixing length can be expressed as

$$L = K \left| \frac{d\overline{U}_1/dy}{d^2\overline{U}_1/dy^2} \right| \quad . \tag{2.19}$$

This assumption results in a second velocity defect equation

$$u_d = -\frac{1}{K}\left[\ln\left(1 - \sqrt{x_2/R}\right) + \sqrt{x_2/R}\right] \qquad (2.20)$$

This equation also shows good agreement with experimental results, except near the pipe wall, although the value of K obtained using this equation is usually slightly different from that obtained with equations (2.10) or (2.18) (0.36 rather than 0.4).

Actually, it is possible to derive a velocity defect equation from each of the foregoing logarithmic equations. Although such equations have not been extensively utilized, they will be presented here for reference purposes. Consider first equation (2.12). The velocity defect corresponding to this equation is

$$u_d = (B_1/\beta)\ \ln(R/y) \qquad (2.21)$$

Also, the defect equation corresponding to equation (2.14) will be

$$u_d = B_2\ \ln\left[\frac{1 + 2(x_2/R)^2}{1 - (x_2/R)^2}\right] \qquad (2.22)$$

A third phenomenological theory has been proposed by Taylor [27] who introduced a vorticity transport hypothesis rather than the

previously employed momentum concept. This hypothesis resulted in the same expression for the turbulent shear stress as obtained from von Karman's similarity hypothesis, but Taylor was able to satisfy all boundary conditions at the pipe center line with the equation

$$u_d = \frac{\sqrt{2}}{K} \sin^{-1} [\sqrt{y/R} - \sqrt{yx_2} / R] \quad . \tag{2.23}$$

This velocity defect equation, however, still does not satisfy the boundary condition at the pipe wall.

Several additional forms of velocity defect equations have also been derived using various mixing length arguments. Typical of these are the equations of Wang [28] and Williamson [29]. Both Wang and Williamson deduced expressions for the mixing length from available experimental data and then employed Prandtl's mixing length theory to derive expressions for the velocity profile. The resulting expression given by Williamson is

$$u_d = -\frac{1}{K} \left\{ \ln (y/R) + \sum_{n=1}^{\infty} C_n [1 - (y/R)^n] \right\} \quad , \tag{2.24}$$

and that given by Wang is

$$u_d = 2.5 \left[\ln \left(\frac{1 + \sqrt{x_2/R}}{1 - \sqrt{x_2/R}} \right) - 2 \tan^{-1} (\sqrt{x_2/R}) \right.$$

$$- 5.72 \ln \left(\frac{x_2/R + 1.75 \sqrt{x_2/R} + 1.53}{x_2/R - 1.75 \sqrt{x_2/R} - 1.53} \right)$$

$$\left. + 1.14 \tan^{-1} \left(\frac{1.75 \sqrt{x_2/R}}{1.53 - x_2/R} \right) \right] \quad . \qquad (2.25)$$

Williamson found the value of K to be 0.38 and calculated the values of the first seven coefficients in the summation. As with previous defect equations, neither equation (2.24) nor equation (2.25) satisfies the boundary condition at the wall, and although both represent experimental data in the turbulent core better than do the equations of Prandtl and von Karman, they have not been extensively employed due to their algebraic complexity.

In addition to equation (2.24), Williamson [29] also derived a velocity defect equation, which is valid near the pipe wall, by modifying equation (2.8) to fit experimental data. The resulting equation is given by

$$u_d = 28.6 - \mathrm{Re} \sqrt{\lambda/32} \, (y/R) \quad , \qquad (2.26)$$

where Re is the Reynolds number, and λ is the friction factor which will be discussed in the following section.

All of the preceding expressions for the mean velocity profile have in common the fact that they can be derived from an assumed analytical expression for the mixing length L, as shown by Goma and Gelhar [30]. This indicates the wide usefulness of Prandtl's mixing length concept even though it is not completely realistic physically.

A number of purely empirical equations have also been proposed to represent the temporal mean velocity profile in smooth tubes. As an example of these, Schlichting [11] found that Nikuradse's data could be successfully represented by the equation

$$\frac{\overline{U}_1}{\overline{U}_{max}} = (y/R)^{1/n} \tag{2.27}$$

if the exponent n is permitted to increase slightly with increasing Reynolds number.

Recently several equations have been proposed which give y^+ as a function of u^+ rather than u^+ as a function of y^+. By considering u^+ to simply approach y^+, instead of becoming equal to y^+, as y^+ approaches zero, Deissler [14] developed an expression which agrees well with experimental data through the viscous sublayer and the

buffer zone,

$$y^+ = \sqrt{\frac{\pi}{2m}} \exp\left(m\, u^{+2}/2\right) \operatorname{erf}\left(u^+ \sqrt{m/2}\right) \quad , \tag{2.28}$$

where he determined m to be 0.0119 from experimental data. Another equation giving y^+ as a function of u^+ was developed by Spalding and is presented by Brand and Persen [31],

$$y^+ = u^+ A \left[\exp(K\, u^+) - 1.0 - K\, u^+ - \frac{1}{2!} (K\, u^+)^2 - \frac{1}{3!} (K\, u^+)^3 - \frac{1}{4!} (K\, u^+)^4 \right] \quad , \tag{2.29}$$

where K and A were determined by Spalding to be 0.4 and 0.1108 respectively. Although this equation does not give a zero velocity gradient at the pipe center line, Brand and Persen [31] indicate good agreement with experimental data over the remainder of the pipe.

Pai [32,33] has obtained an expression for the mean velocity profile from a direct consideration of the Navier-Stokes equations by employing the Reynolds transformations. The resulting equation for pipe flow is given by

$$\frac{\overline{U}_1}{\overline{U}_{max}} = 1 + \frac{\ddot{s} - \ddot{\omega}}{\omega - 1}\left(\frac{x_2}{R}\right)^2 + \frac{1 - \ddot{s}}{\omega - 1}\left(\frac{x_2}{R}\right)^{2\omega} \quad , \qquad (2.30)$$

where $\ddot{s}$ is the ratio of the shear stress at the wall in the turbulent flow to the corresponding shear stress at the wall for a laminar flow with the same maximum velocity, and ω must be determined from experimental data. This equation is said by Pai to be valid for laminar, transitional, or turbulent flow. Knudsen and Katz [34] indicate excellent agreement of this equation with Nikuradse's data at a given Reynolds number. Brodkey [35] indicates a Reynolds number dependence of the parameter ω which is given by

$$\omega = -0.617 + 0.008211\ (Re)^{0.786} \quad . \qquad (2.31)$$

Before the true worth of equation (2.30) can be established, however, more comparisons are needed with actual velocity measurements.

In addition to the foregoing methods, the integral equations of a boundary layer are also employed for turbulence calculations in many cases. This technique is not expected, however, to yield new information regarding the structure of a turbulent flow field but simply the gross parameters of the turbulence. Reviews of results obtained utilizing this method are presented by Dorfman [36], Okabe

[37], and Schlichting [11].

Several sets of experimental data concerning the temporal mean velocity profile in smooth tubes are available for verification of the foregoing equations and for comparison with any equations which might be proposed in the future. Typical of the investigations producing such data are those of Bakewell [38], Clark [39], Deissler [14], Gow [15], Laufer [40, 41], Reynolds, McEligot, and Davenport [42], and Schraub [43].

Flow Resistance and Roughness Characterization

Since turbulent flow has not been handled satisfactorily analytically, it is necessary to treat the resistance to flow empirically, as was the case with the mean velocity profile. In order to satisfy Reynolds' law of similarity, the flow resistance is normally related to a parameter λ called the friction factor and defined by

$$\lambda = \frac{8\tau_0}{\rho \overline{U}_{avg}^2} = 8\,(u^*/\overline{U}_{avg})^2 \quad . \tag{2.32}$$

The shear stress at the wall, τ_0, appearing in this equation can be related to the pressure drop along the pipe by a simple momentum balance which yields

$$\tau_0 = -\frac{R}{2}\frac{\partial \overline{P}}{\partial x_1} \quad . \tag{2.33}$$

The first empirical equation relating the friction factor to the Reynolds number, and hence the bulk velocity $\overline{U}_{avg}$, was given by Blasius (see Schlichting [11]) after an examination of the available experimental data. This equation is

$$\lambda = 0.3164\ (\mathrm{Re})^{-0.25} \quad , \tag{2.34}$$

and is valid in smooth pipes for Reynolds numbers less than 100,000. It is interesting to note that Schlichting [11] shows that the power law for the mean velocity profile, equation (2.27) can be derived directly from equation (2.34), and this fact indicates that equation (2.27), with a constant value of the exponent n, should be valid for Reynolds numbers below 100,000. The validity of this statement has been verified by Nikuradse [2] who took n equal to seven.

A second relationship between the friction factor and Reynolds number for a smooth pipe was derived by Prandtl (see Schlichting [11]) utilizing both his velocity defect and logarithmic equations, (2.5) and (2.18). Schlichting [11] modified the coefficients in these equations to agree with Nikuradse's data and presents the final form

of the equation as

$$\lambda^{-0.5} = 2 \log (\mathrm{Re} \sqrt{\lambda}) - 0.8 \quad . \tag{2.35}$$

Utilizing his similarity hypothesis, von Karman (see Knudsen and Katz [34]) derived an expression,

$$\lambda^{-0.5} = 2.03 \log (\mathrm{Re} \sqrt{\lambda}) - 0.911 \quad , \tag{2.36}$$

which has the same form as equation (2.35) but differs slightly in the numerical values of the constants. A similar equation has also been derived by Williamson [29] from an extension of Prandtl's mixing length theory,

$$\lambda^{-0.5} = 2.106 \log (\mathrm{Re} \sqrt{\lambda}) - 1.270 \quad , \tag{2.37}$$

and Rothfus, Monrad, and Senecal [44] have obtained an empirical equation of this form,

$$\lambda^{-0.5} = 2.035 \log (\mathrm{Re} \sqrt{\lambda}) - 0.8 \quad . \tag{2.38}$$

The numerical values of λ predicted by all the foregoing equations

are nearly identical, however.

Although equations (2.35) through (2.38) predict the more recent experimental data on friction factors in smooth tubes with a high degree of accuracy, they are somewhat inconvenient to use because they cannot be solved explicitly for λ. For this reason, a purely empirical equation, presented by Longwell [18], giving λ as an explicit function of Reynolds number is widely used. This equation,

$$\lambda = 0.0056 + 0.5\ (\mathrm{Re})^{-0.32} \quad , \tag{2.39}$$

is valid for Reynolds numbers between 10^3 and 3×10^6.

From his direct consideration of the momentum equations, as described in the previous section, Pai [23] was also able to obtain an expression for the friction factor. This expression is given by

$$\lambda = \frac{128\ (\omega + 1)^2\ s^2}{y_c^{+2}\ (\omega + s)^2} \quad , \tag{2.40}$$

where as previously stated, ω is a parameter which must be determined from experimental velocity profile data in the turbulent core of the tube. Equation (2.40) has not been compared with experimental data.

So far, only the flow resistance of smooth tubes has been considered. This resistance is entirely due to viscous drag on the

pipe wall and is therefore dependent only on the Reynolds number. As the wall becomes rough, the resistance mechanism may change significantly, and these changes may be briefly described in the following manner.

For roughness heights which are small enough so that the roughness elements are completely contained within the viscous sublayer, the resistance is still entirely due to viscous drag, and the flow behaves as if the pipe were smooth. On the other extreme, if the roughness elements extend completely into the turbulent core, the flow resistance is due primarily to form drag on the elements, and hence the friction factor is a function only of the relative roughness ε/R. For roughness heights intermediate to these two extremes, the flow resistance is caused by a combination of viscous drag and form drag, thereby yielding a friction factor dependent both on Reynolds number and relative roughness. Schlichting [11] breaks the roughness effects on the flow down into three regimes:

(1) hydraulically smooth, $\lambda = \lambda(\mathrm{Re})$, $0 \leq \varepsilon^+ \leq 5$; (2.41a)

(2) transition, $\lambda = \lambda(\mathrm{Re}, \varepsilon/R)$, $5 \leq \varepsilon^+ \leq 70$; (2.41b)

(3) fully rough, $\lambda = \lambda(\varepsilon/R)$, $\varepsilon^+ \geq 70$; (2.41c)

where ε^+ is a roughness Reynolds number defined by

$$\varepsilon^+ = \varepsilon\, u^*/\nu \quad . \tag{2.42}$$

Of course, the description of the resistance mechanism given in the preceding paragraph will hold true rigorously only for a high concentration (surface area occupied by roughness elements/total surface area) of roughness elements of a relatively uniform height. This type of roughness is probably obtained strictly only with artificial roughness elements such as sand grains. More natural roughness in pipes will be composed of elements of different sizes, and thus all elements will not simultaneously be included in the same layer of the flow (viscous sublayer, buffer zone, or turbulent core). Also, if the roughness elements are larger than some characteristic length in the flow direction, it would be expected that the flow would not separate as readily from the elements, and a viscous resistance would thereby tend to be maintained. Such an effect would occur with what might be termed a "wavy" surface. These various types of roughness will be discussed in the following paragraphs.

First, consider the artifical type of sand roughness. Comprehensive tests on the flow resistance for this type have

previously been performed by Nikuradse [2]. Nikuradse obtained the sand grains which were to be used as roughness elements by sifting between standard screen sizes, and thus the roughness elements were of a rather uniform height and exhibited a high degree of angularity, thereby yielding a somewhat random shape distribution. The flow resistance due to the sand grains can be described in the following manner. For low Reynolds numbers, all of the elements will be contained within the viscous sublayer, as explained previously, and the pipe will behave as if it were smooth, with the friction factor decreasing with increasing Ryenolds number. When the Reynolds number is increased to some particular value, depending upon the relative roughness, essentially all of the roughness elements will protrude into the buffer layer, and the resistance will be due to a combination of form and viscous drag. This leads to a slight increase in the friction factor over that which would be obtained in a smooth tube. As the Reynolds number is again increased, the roughness elements protrude more into the buffer layer, leading to further increases in the friction factor. When the Reynolds number becomes large enough so that the elements extend completely into the turbulent core, the friction factor becomes independent of the Reynolds number and dependent only upon the relative roughness ε/R.

Even though the sand roughness is rather artifical, it is found

that almost all other types of roughness behave in the same manner in fully rough flow, though some deviations do occur in the transition region. It has become common practice to express the roughness of a pipe of unknown roughness in terms of an equivalent sand roughness. This can be accomplished by measuring the friction factor for flow in the fully rough regime and then determining the equivalent sand roughness which would yield this same friction factor. This equivalent sand roughness is normally denoted by k_s.

Several equations relating the friction factor to the equivalent relative roughness are available for simplifying the process of determining k_s. Utilizing his similarity principle, von Karman (see Schlichting [11]) derived the relation

$$\frac{1}{\lambda} = [1.68 - 2 \log (k_s/R)]^2 \quad . \tag{2.43}$$

Nikuradse [2] modified the constant term in this relationship slightly to fit his experimental data and obtained

$$\frac{1}{\lambda} = [1.74 - 2 \log (k_s/R)]^2 \quad . \tag{2.44}$$

Utilizing this equation, measurement of the friction factor in the fully rough regime then allows calculation of the equivalent sand

roughness.

The resistance mechanism just described for flow in sand roughened pipes tends also to be verified by several recent investigations including those of Dipprey and Sabersky [45], Gow [15], and Robertson, Burkhart, and Martin [46, 47].

The behavior of the friction factor in commercially rough pipe is essentially identical to that of a sand roughened pipe except in the transition regime. This exception is due to the fact that the roughness elements in a naturally rough pipe will not be of a uniform height as are the sand particles discussed previously. Although all of these elements will be contained within the viscous sublayer at a sufficiently low Reynolds number, they will not all begin to protrude beyond the viscous sublayer at the same value of the Reynolds number. Thus, transition from the hydraulically smooth regime to the fully rough regime will take place in a continuous monotone decreasing fashion for this type of roughness. This behavior in the transition regime is also exhibited by some types of uniform roughness. However, the reason for such behavior with a uniform roughness has not been clearly established.

Extensive measurements of the friction factor in commercial pipes have been carried out by Moody [48], and the resultant friction factor plot now appears in most texts on fluid mechanics. The

roughness of the pipes utilized in this study was referenced to an equivalent sand diameter. Schlichting [11] presents an equation, developed by Colebrook and White, which can be utilized for predicting the friction factor in commercially rough pipes throughout all three flow regimes,

$$\lambda^{-0.5} = 1.74 - 2 \log \left(k_s/R + \frac{18.7}{Re\sqrt{\lambda}} \right) \quad . \tag{2.45}$$

Another type of densely packed roughness element which has been recently studied in pipe flow by Goma and Gelhar [30] is that of spherical beads. They utilized 0.125 inch diameter beads in a 10 inch diameter pipe and obtained an equivalent roughness, k_s, of about 0.08 inches. This indicates that the spherical elements behave more "smoothly" than would sand particles of the same characteristic dimension. However, the behavior of the friction factor in the transition region was characteristic of that obtained in sand roughened pipes.

It is interesting to note that some physically measurable geometrical significance has been indicated for the equivalent roughness k_s in an open channel flow investigation by Brown and Chu [49]. Two different types of roughness elements were utilized, and the elements were closely packed in each case. Using several sizes

of both crushed limestone and cubical concrete roughness elements, they found that the equivalent roughness is related to the root-mean-square (rms) height of the surface protrusions and that this relationship is not dependent on the element size or geometry as long as the elements are densely packed in a random manner. This indicates a possibility of treating the actual rms height as a roughness parameter instead of the equivalent roughness, and possible methods for accomplishing this type of measurement are indicated by Wallach [50], Whitehouse and Archard [51], and Williamson, Pullen, and Hunt [52].

It should also be noted that the use of an equivalent roughness as a characteristic parameter is not completely unquestioned. Morris [53] suggests that perhaps a more appropriate parameter would be the longitudinal distance between roughness crests, and Rand [54] suggests the use of both dimensions. However, for closely packed, randomly shaped elements, such as sand grains, these two dimensions will be the same order of magnitude, and thus a separate effect would not be anticipated.

The flow resistance and roughness characterization phenomena associated with several additional types of elements have been investigated, and the earlier such studies are reviewed by Knudsen and Katz [34] and Schlichting [11]. Elements investigated more recently include wire screens by Scottron and Power [55]; square

cavities by Perry and Joubert [56], Townes [57], and Townes and Sabersky [58]; and single hemispheres by Seban and Caldwell [59]. In addition, a method for predicting the flow resistance, from geometrical information, caused by low concentrations of regularly spaced elements of many different shapes has recently been proposed by Roberson [60] and Roberson and Chen [61].

A final point should be made regarding Nikuradse's equivalent roughness, k_s. Recent investigations have shown, even for sand grain type roughness elements, that k_s should be regarded as simply an arbitrary scale for the universal representation of roughness and not a measure of the actual element size. Gow [15] showed good agreement between ε and k_s for $R/\varepsilon = 208$, but for $R/\varepsilon = 26.4$, k_s was found to be about 2.3 times as large as ε. Robertson, Burkhart, and Martin [47] found k_s to be about 1.3 times as large as ε for $R/\varepsilon = 86$. Similar results have been obtained for other types of elements. This discussion should be kept in mind in experimental investigations where an attempt is being made to obtain a particular value of k_s.

Mean Velocity Profile in Rough Pipes

Though phenomenological theories were utilized for the development of velocity profile expressions for smooth tubes, such theories are practically nonexistent for rough tubes, and empirical relations

must be sought. Nikuradse [2] was able to correlate his experimental measurements of the velocity profile in the turbulent core by modifying Prandtl's logarithmic equation, equation (2.10), to obtain

$$u^+ = \frac{1}{K} \ln (y/k_s) + \Delta \quad , \tag{2.46}$$

where the value of Δ depends upon whether the flow is in the hydraulically smooth, transition, or fully rough regime. In the fully rough regime, Nikuradse [2] found that Δ is constant and approximately equal to 8.5. For the hydraulically smooth regime the value of Δ can be obtained by comparing equation (2.46) with equation (2.10). This yields

$$\Delta = C + \frac{1}{K} \ln (k_s^+) \quad . \tag{2.47}$$

Nikuradse [2] also shows values of Δ for flows in the transition regime but presents no mathematical relationship for this region. More recently, equation (2.46) has been verified for open channel flow in the fully rough regime by Brown and Chu [49].

Schlichting [11] shows that a velocity defect equation can also be derived from equation (2.46). Applying the boundary condition at the center of the pipe,

$$\Delta = u^{+}_{max} - \frac{1}{K} \ln (R/k_s) \tag{2.48}$$

is obtained. Thus equation (2.46) can be written

$$u_d = \frac{1}{K} \ln (R/y) \quad , \tag{2.49}$$

and this is identical to the velocity defect equation utilized for smooth pipes. This form of equation (2.46) has been experimentally verified by several authors including Nikuradse [2] for flow in sand roughened pipes, and by Larras [62], for open channel flow.

Nikuradse [2] showed that an equation of the form

$$\overline{U}_1/\overline{U}_{max} = (y/R)^{1/a} \tag{2.50}$$

also applies to rough pipes if the exponent is allowed to vary with roughness and Reynolds number. Migay [63] states that taking

$$a = \lambda^{-0.5} \tag{2.51}$$

results in equation (2.50) being valid for both smooth and rough pipes.

A second equation which is valid for the velocity distribution

in both smooth and rough tubes is developed by Knudsen and Katz [34]. Integrating equation (2.10) over the tube cross section, the average velocity for flow in a smooth tube is found to be

$$u^+_{avg} = \frac{1}{K} \ln (y^+_c) + C - 1.5/K \quad . \tag{2.52}$$

Subtracting equation (2.52) from equation (2.10) then yields

$$\frac{\overline{U}_1 - \overline{U}_{avg}}{u^*} = \frac{1}{K} [\ln (y/R) + 1.5] \quad . \tag{2.53}$$

Similarly, integrating equation (2.46) to find the average velocity in rough pipes yields

$$u^+_{avg} = \frac{1}{K} \ln (R/k_s) + \Delta - 1.5/K \quad , \tag{2.54}$$

and subtracting this expression from equation (2.46) yields

$$\frac{\overline{U}_1 - \overline{U}_{avg}}{u^*} = \frac{1}{K} [\ln (y/R) + 1.5] \quad , \tag{2.55}$$

which is identical to equation (2.53) for smooth pipes. Thus equation (2.53) is valid for flow in both smooth and rough pipes in the

turbulent core. Knudsen and Katz's [34] analysis can easily be extended to yield an expression for the constant K by applying the boundary condition in the center of the pipe. The result is

$$K = \frac{1.5u^*}{\overline{U}_{max} - \overline{U}_{avg}} \quad . \tag{2.56}$$

Introducing equation (2.56) into equation (2.53) then results in a velocity parameter which should be universal for all degrees of roughness and all Reynolds numbers. The resulting expression is

$$\frac{\overline{U}_{max} - \overline{U}_1}{\overline{U}_{max} - \overline{U}_{avg}} = -\frac{2}{3} \ln (y/R) \quad . \tag{2.57}$$

Recently, velocity profile data for flow in rough pipes has been obtained by Gow [15] using a sand roughness, by Robertson, Burkhart, and Martin [47] using a sand roughness and a natural roughness, and by Goma and Gelhar [30] using spherical roughness elements. In addition, Logan and Jones [64] have obtained such profiles downstream of an abrupt increase in surface roughness. Although Logan and Jones' profiles were not obtained in the fully developed flow regime, it is interesting to note that Marris [65] interprets their velocity measurements to indicate a possible spiral flow down the pipe in this

transition length.

Thus far, only the velocity profile within the turbulent core has been considered. In rough pipe flow, the velocity profile in the viscous sublayer and the buffer zone is almost completely intractable, since at least a portion of these layers is below the top of the roughness elements. Several authors, e.g., Perry and Joubert [56] and Goma and Gelhar [30], suggest fitting a straight line to u^+ versus log (y/k_s) data in the turbulent core and considering the pipe wall to be at the value of y/k_s where u^+ becomes zero on this line. However, this method cannot readily be extrapolated to areas where experimental data are not available. Also, it might be expected that the viscous sublayer hypothesis would apply from the top of the roughness elements to the turbulent core. However, evidence against this occurrence has been presented by Townes [57] for square cavity type elements and by Brown and Chu [49] for crushed limestone and cubical concrete elements.

Velocity Fluctuations

In the first section of this chapter it was stated that the instantaneous turbulent velocities are usually expressed as the sum of a temporal mean and a fluctuating component, and the temporal mean component has previously been considered. Attention is now directed

to the fluctuating components. In the statistical theory of turbulence, such components are usually expressed quantitatively by giving their root-mean-square value. For purposes of the following discussion, let u_1, u_2, and u_3 represent the fluctuating velocity components in the longitudinal, radial, and angular directions respectively, and let u_1', u_2', and u_3' denote corresponding rms values.

Laufer [41], during his turbulence studies for flow in a smooth pipe, measured the variation of all three of these components across the pipe diameter at two different values of the Reynolds number. By normalizing these rms velocities with the shear velocity he found, at the pipe center line, that

$$\frac{u_1'}{u^*} = \frac{u_2'}{u^*} = \frac{u_3'}{u^*} \simeq 0.8 \tag{2.58}$$

for both Reynolds numbers. As y/R decreases below a value of unity, the three quantities all increase--u_1'/u^* at the highest rate and u_2'/u^* at the lowest. For $y/R \gtrsim 0.5$, however, no Reynolds number dependence is indicated on any of the three parameters, but for $y/R \lesssim 0.5$, the higher Reynolds number generally yields larger values of u_i'/u^* $(i = 1, 2, 3)$. The three values all decrease very rapidly to zero at the pipe wall, thereby satisfying the no-slip condition. In analyzing Laufer's data, Hinze [9] shows that for both Reynolds

numbers, u_1'/u^* attains a maximum value at about $y^+ = 15$, which is not too far removed from the edge of the viscous sublayer. Also, by normalizing the rms velocities with the local temporal mean value in the longitudinal direction, he shows that $u_2'/\overline{U}_1$ and $u_3'/\overline{U}_1$ approach zero as y^+ approaches zero while $u_1'/\overline{U}_1$ approaches a nonzero value of 0.3. This indicates that u_1' does not approach zero at a faster rate than does $\overline{U}_1$, thereby tending to refute the older concept of a laminar layer near the wall.

Since the work of Laufer, Pai [33] has shown that the only requirement of the Reynolds equations regarding center line isotropy is that $u_2' = u_3'$. This result is confirmed by the experimental results of Clark [39], Gow [15], and Robertson, Martin, and Burkhart [46], who all show u_2' and u_3' as being equal at the pipe center line while u_1' has a slightly higher value.

A significant extension to the work of Laufer has recently been published by Clark [39] utilizing a two-dimensional channel rather than a pipe. He showed that the ratio $u_1'/\overline{U}_1$ is independent of Reynolds number for $y/R > 0.2$ and becomes equal to 0.4 for $y^+ < 7$. For positions between $y^+ = 7$ and $y/R = 0.2$, $u_1'/\overline{U}_1$ is dependent upon the Reynolds number. The ratio u_1'/u^* was found to attain a maximum value of about 3.14, for Reynolds numbers between 10^4 and 10^5, at $y^+ = 14$, which agrees well with Hinze's [9] analysis of Laufer's

data. In the central portion of the flow field, $y/R > 0.2$, u_2' and u_3', when normalized with the maximum velocity in the channel, appear to be only slightly dependent on Reynolds number, though a definite Reynolds number dependency is noted for $y/R < 0.2$. In contrast with Hinze's analysis, $u_2'/\overline{U}_1$ and $u_3'/\overline{U}_1$, approach, rather than zero, 0.1 and 0.16 respectively as y^+ approaches zero.

As in the previously described studies, Robertson and Martin [66] found that u_1'/u^* is independent of Reynolds number at the pipe center line. Based on this fact, they showed that $(u_1'/\overline{U}_1)_c$ could be related to Reynolds number in the following manner:

$$(u_1'/\overline{U}_1)_c = (Re/2)^{-0.084} \quad . \tag{2.59}$$

In a later publication [46] they find that u_1'/u^* has a universal value of 0.78 at the pipe center line and 1.7 at $y/R = 0.1$. The anisotropy ratio u_2'/u_1' is shown by them to increase, in an approximately linear fashion, from a value of 0.6 at $y/R = 0.1$ to about 0.9 at $y/R = 1.0$. In constrast, an approximately constant value of this ratio, about 0.3, has been indicated by Smutek [67] at all values of y/R for flow in open channels.

Several additional groups of experimental data have been obtained concerning the rms value of the longitudinal fluctuating velocity

component in smooth pipe flow, and although essentially in agreement with the preceding discussion, they should be noted as being available. These include the investigations of Bakewell [68], Logan and Jones [64], McQuivey and Richardson [69], and van Thinh [70, 71].

Much less data are available concerning the fluctuating velocities for flow in rough pipes. Robertson et al [46, 47, 66] have studied turbulent flow in one sand-roughened pipe and another of natural roughness. Flow resistance studies on the sand roughened pipe [47] indicated an equivalent relative roughness of $k_s/R = 0.016$, although this value decreased slightly over a long period of time to about 0.0145, probably due to the dislodging of some of the sand grains or the collection of dust particles in the spaces between them. The natural roughness yielded an equivalent relative roughness of 0.0015. Although a great deal of scatter is apparent in their results, they do seem to indicate that the values of u_1' and u_2', when normalized with u^*, behave in essentially the manner found for flow in smooth pipes. The Reynolds number range investigated for the sand roughened pipe was limited to about 25,000 to 62,000 and that for the natural roughness was limited to 22,000 to 156,000.

Logan and Jones [64] have studied the longitudinal fluctuating component following an abrupt change from a smooth to a rough surface, and a portion of their results are near the fully developed

flow region in the rough pipe. Although they did not specify the equivalent relative roughness, they utilized sand grains yielding $\varepsilon/R = 0.018$. Their results indicate that an increase in roughness leads to an increase in $u_1'/\overline{U}_1$, over the entire cross-section of the pipe. These results tend to be confirmed in open channel flow by McQuivey and Richardson [69] utilizing lead shot roughness elements yielding $\varepsilon/R = 0.067$. They indicate that $u_1'/\overline{U}_1$ is approximately 50% greater near the wall for a rough surface than for a smooth surface and about 20% greater near the free surface. The ratio $u_2'/\overline{U}_1$ is said to be about 10% greater for the rough surface throughout the flow field. For flow over a smooth boundary $u_2'/\overline{U}_1$ was found to be about 50% as large as $u_1'/\overline{U}_1$, while for rough surface flow $u_2'/\overline{U}_1$ is shown to be approximately 60% of $u_1'/\overline{U}_1$. As in the previous cases, no Reynolds number influence was observed on either $u_1'/\overline{U}_1$ or $u_2'/\overline{U}_1$ for the rough surface. In contrast, Smutek [67], utilizing an open channel with $\varepsilon/R = 0.010$, indicates a definite increase in $u_1'/\overline{U}_1$ as Reynolds number increases.

A more thorough investigation of the fluctuating velocities in sand roughened pipes has recently been conducted by Gow [15] utilizing equivalent relative roughnesses, k_s/R, of 0.0047 and 0.0885. In agreement with Robertson <u>et al</u> [46, 47, 66], he found essential agreement between the values of u_1'/u^*, u_2'/u^*, and u_3'/u^* measured in

rough pipes and those measured in smooth pipes. The theoretical supposition by Pai [33] that $u_2' = u_3'$ at the pipe center line was confirmed for rough pipes, and as in the case of smooth pipes u_1' was found to be larger than u_2' and u_3' at the center line. For Reynolds numbers between 30,000 and 480,000, little Reynolds number dependence was observed for any of the fluctuating quantities when normalized with shear velocity, except that the maximum value of u_1'/u^* appeared to increase as Reynolds number increased. Also, as the Reynolds number increased the value of y/R where this maximum occurred appeared to decrease, becoming nearly equal to k_s/R at the higher Reynolds numbers.

Finally, a turbulence investigation in rough pipe flow utilizing spherical type roughness elements with $k_s/R = 0.016$ has been conducted by Goma and Gelhar [30]. They found significant increases in u_1' and u_2' over smooth tube results when normalized with $\overline{U}_1$ but, as in previous cases, found little difference between smooth and rough tube results, except near the wall, when the rms velocities were normalized with u^*. The anisotropy ratio u_2'/u_1' was also found to be in general agreement with smooth tube results. However, the limiting value near the wall was found to be 0.6, in contrast with about 0.25 for smooth tubes. The value of u_2'/u_1' at the center line of the pipe was also slightly lower than in the case of smooth tubes.

Fluctuating Velocity Correlations

In addition to u_1', u_2', and u_3', other quantities which are of importance in the statistical description of turbulence include the temporal mean values of the various products of u_1, u_2, and u_3, called cross correlations. As shown, e.g., by Hinze [9] and Lin [72], the second order cross correlations $\overline{u_1\ u_2}$, $\overline{u_1\ u_3}$, and $\overline{u_2\ u_3}$ (overbar denotes time average) can be interpreted as turbulent shear stresses, called Reynolds stresses, which act in addition to the viscous shear stresses. However, the only one of these terms which appears in the momentum equation for fully developed axisymmetric flow in a smooth circular pipe is $\overline{u_1\ u_2}$, and thus, most previous investigations have concentrated on measurement of this quantity.

The measurements of Reichardt, utilizing a smooth rectangular channel, and Klebanoff, utilizing a smooth flat plate, are summarized by Schlichting [11]. Reichardt found an almost linear variation in $\overline{u_1\ u_2}$ from zero at the center of the channel to $y/R = 0.1$, where $\overline{u_1\ u_2}$ dropped rapidly to zero. He also shows values of the correlation coefficient,

$$\psi_{12} = \frac{\overline{u_1\ u_2}}{u_1'\ u_2'} \quad ,$$

which increase rapidly from a value of zero at the center line and

become essentially constant at 0.45 for $y/R < 0.3$. Klebanoff found that $\overline{u_1 u_2}/\overline{U}^2_{max}$ increases from a value of zero at the edge of the boundary layer, where it also has essentially a zero slope, to a nearly constant value of about 10^{-3} in the vicinity of the wall.

Extensive measurements of the $\overline{u_1 u_2}$ Reynolds stress were accomplished by Laufer [41] for flow in a smooth circular pipe. He found that $\overline{u_1 u_2}/u^{*2}$ is essentially independent of Reynolds number for $y/R > 0.1$. The variation is nearly linear from $\overline{u_1 u_2}/u^{*2} = 0$ at $y/R = 1$ to a maximum value of $\overline{u_1 u_2}/u^{*2}$ which is slightly less than unity in the region $0 < y/R < 0.1$. Once this maximum value is attained, $\overline{u_1 u_2}/u^{*2}$ decreases rapidly to zero. Values of the correlation coefficient ψ_{12} are seen to be essentially independent of Reynolds number for $y/R > 0.5$, and for $y/R < 0.5$, an increase in Reynolds number yields a decrease in ψ_{12}, except possibly for the region in close proximity to the wall.

In a reanalysis of Laufer's data, Hinze [9], shows a plot of the $\overline{u_1 u_2}$ correlation normalized with the turbulent kinetic energy,

$$\overline{q^2} = \sum_{i=1}^{3} \overline{u_i^2}/2 \quad . \tag{2.61}$$

This plot shows $\overline{u_1 u_2}/\overline{q^2}$ to increase in an approximately linear fashion from zero at $y/R = 1.0$ to a value of about 0.26 at $y/R \simeq 0.7$.

The $\overline{u_1 u_2}/\overline{q^2}$ term then remains constant for $0.2 < y/R < 0.7$, and at $y/R = 0.2$, it begins to decrease.

Almost simultaneously, Pai [33] and Laufer [41] both derived an expression, from the momentum equations, relating the $\overline{u_1 u_2}$ Reynolds stress to the mean velocity gradient. This expression is given by

$$\frac{\overline{u_1 u_2}}{u^{*2}} = \frac{\nu}{u^{*2}} \frac{d\overline{U}_1}{dx_2} + \frac{x_2}{R} \quad . \tag{2.62}$$

Utilizing his mean velocity data, Laufer predicted values of $\overline{u_1 u_2}/u^{*2}$ from this equation and found excellent agreement with his measured values. Pai integrated equation (2.62) to find an expression for the mean velocity, thereby obtaining equation (2.30) described previously. Introducing equation (2.30) into equation (2.62), Pai obtained the following equation for $\overline{u_1 u_2}/u^{*2}$:

$$\frac{\overline{u_1 u_2}}{u^{*2}} = \frac{\omega(s - 1)}{s(\omega - 1)} \left(\frac{x_2}{R}\right) [1 - (x_2/R)^{2\omega - 2}] \quad , \tag{2.63}$$

where ω is an empirical constant to be determined from velocity profile data in the turbulent core of the pipe. Although Laufer's data were not available to Pai, he utilized Nikuradse's data at a particular Reynolds number to obtain numerical values for ω and s,

and the resulting curve is in very close agreement with the semi-empirical curve of Laufer for values of y/R where $\overline{u_1 u_2}/u^{*2}$ is independent of Reynolds number.

Robertson, Burkhart, and Martin [47] have also obtained $\overline{u_1 u_2}$ measurements for flow in a smooth pipe and compare them with the semi-empirical curve denoted by equation (2.62). A first glance at their data indicates substantial deviations from this curve and a definite Reynolds number variation over the entire pipe cross-section. However, closer inspection of their data reveals a nonzero value of the $\overline{u_1 u_2}$ correlation at the pipe center line, and this is a boundary condition on $\overline{u_1 u_2}$ which can be satisfied by equipment calibration procedures. It appears that, had $\overline{u_1 u_2}$ been adjusted to zero at the pipe center line, reasonable agreement with the semi-empirical curve would have been obtained.

Additional data on the $\overline{u_1 u_2}$ correlation for smooth pipe flow are available from the study of Logan and Jones [64]. They show a linear increase in $\overline{u_1 u_2}/\overline{U}^2_{max}$ from zero at the pipe center line to about 10^{-3} near the wall, which is the same value obtained by Klebanoff for a flat plate.

The theoretical results of Ohji [73] should also be noted at this point. From a statistical analysis of the turbulence quantities in the neighborhood of a smooth wall he shows that $\overline{u_1 u_2}$ should be of

order y^4 as y approaches zero and that the correlation coefficient ψ_{12} should be of order y. No experimental evidence has been obtained to support these results, however, and Ohji states that his theoretical evidence is by no means conclusive. Also, based on incompressibility and boundary conditions, Phillips [74] argues that $\overline{u_1 u_2}$ should be of order y^{+3} as a solid boundary is approached, so there is a definite need for experimental data concerning the $\overline{u_1 u_2}$ correlation near the wall.

The recent investigation of Gow [15] included measurements of both the $\overline{u_1 u_2}$ and $\overline{u_1 u_3}$ Reynolds stresses for flow in smooth pipes. Although it can be argued theoretically that, for fully-developed axisymmetric turbulent flow, the $\overline{u_1 u_3}$ correlation should be zero, this fact had not been demonstrated experimentally before Gow's investigation. His investigation did indicate a zero value of $\overline{u_1 u_3}$ across the entire cross-section. The $\overline{u_1 u_2}$ Reynolds stress is shown plotted as $\overline{u_1 u_2}/u^{*2}$ versus y/R, and good agreement with the semi-empirical equation, equation (2.62), is noted.

No experimental measurements of the $\overline{u_2 u_3}$ Reynolds stress for flow in smooth pipes have been published.

A very limited amount of information is available regarding the Reynolds stresses for flow in rough pipes. Gow [15] again measured both the $\overline{u_1 u_2}$ and $\overline{u_1 u_3}$ correlations for flow in two sand roughened pipes, $k_s/R = 0.0047$ and $k_s/R = 0.0885$. His $\overline{u_1 u_2}$ data are normalized

with u^{*2} and indicate, in the hydraulically smooth flow regime, an approach to smooth tube results and essential agreement with equation (2.62). For a fixed relative roughness and at a given position in the pipe, this dimensionless correlation is seen to decrease as Reynolds number, and hence k_s^+, increases. The $\overline{u_1 u_3}$ correlation is also shown to deviate from its smooth pipe behavior by assuming a nonzero value as the flow approaches the fully rough regime. Although zero values are indicated for $y/R > 0.5$, nonzero values are observed for $y/R < 0.5$.

Robertson, Burkhart, and Martin [47] also measured the $\overline{u_1 u_2}$ correlation in both their sand roughened and naturally rough pipes. However, due to the difficulties encountered in measuring $\overline{u_1 u_2}$ in the smooth pipe, they consider these data to be unreliable. Even so an examination of the data seems to indicate that their values of $\overline{u_1 u_2}/u^{*2}$ would also be below the curve predicted by equation (2.62) if a zero value of $\overline{u_1 u_2}/u^{*2}$ had been obtained at the pipe center line.

Goma and Gelhar [30], utilizing the spherical roughness elements, measured $\overline{u_1 u_2}/u^{*2}$ at three values of the Reynolds number, two yielding flows in the transition regime and one yielding flow in the fully rough regime. It would be expected, from the work of Gow [15], that the values of $\overline{u_1 u_2}/u^{*2}$ obtained at the latter Reynolds number would be somewhat less than values predicted from equation (2.62).

However, values of this Reynolds stress obtained at all three Reynolds numbers are essentially in agreement with this curve. More data on this correlation are needed before the reason for this descrepancy can be discerned.

As in the case of smooth pipes, the $\overline{u_2\ u_3}$ cross correlation has not been measured experimentally for flow in rough pipes. In view of the fact that the $\overline{u_1\ u_3}$ correlation was found by Gow [15] to be nonzero in rough pipes, though both $\overline{u_1\ u_3}$ and $\overline{u_2\ u_3}$ have theoretically been supposed to vanish, the determination of $\overline{u_2\ u_3}$ experimentally becomes of increased importance.

In addition to the second order cross correlations just discussed, third and higher order correlations are also important in the statistical theory of turbulence, but experimental data regarding such correlations are very limited. Laufer [41], utilizing a smooth pipe, has conducted measurements of the third order correlations which appear in the turbulence energy equation, and these will discussed in the final section of this chapter. No measurements of the higher order cross correlations have been attempted for flow in a rough pipe.

Eddy Diffusivity for Momentum

The main problem in the phenomenological theories of turbulent fluid motion described earlier in this chapter has been to establish

some relationship, empirically or by hypothesis, between the temporal mean values of the velocity components and the Reynolds stresses produced by the velocity fluctuations. One of the first to attempt this was Boussinesq (see Schlichting [11]) who wrote the total shear stress in a turbulent flow field as

$$\tau = \tau_\ell + \tau_t \quad , \tag{2.64}$$

where τ_ℓ is the viscous contribution given by

$$\tau_\ell = \rho \nu \frac{d\overline{U}_1}{dy} \quad , \tag{2.65}$$

and τ_t is the turbulent contribution defined as

$$\tau_t = \rho \, \overline{u_1 \, u_2} \tag{2.66}$$

Boussinesq defined an apparent kinematic, or eddy, viscosity ε_n so that an expression analogous to (2.65) could be written for the turbulent contribution,

$$\tau_t = \rho \, \varepsilon_n \frac{d\overline{U}_1}{dy} \quad . \tag{2.67}$$

Equating (2.66) and (2.67), an expression for the eddy viscosity is obtained,

$$\varepsilon_n = \frac{\overline{u_1 \; u_2}}{d\overline{U}_1/dy} \quad . \tag{2.68}$$

Equation (2.68) then gives a relationship between the $\overline{u_1 \; u_2}$ correlation and the mean velocity gradient in terms of ε_n. However, ε_n is not a property of the fluid as is v but instead will, in general, vary from point to point in the flow field. Also, the preceding analysis has tacitly assumed that ε_n is a scalar quantity, but Hinze [9] shows that ε_n should actually be treated as a second order tensor. Nevertheless, the use of ε_n, as defined by equation (2.68), has become widespread. In fact, Kays [13] utilizing the concept of the local heat transfer coefficient, and Biot [75], utilizing the variational trailing function concept, show that most convective heat transfer theories for turbulent flow are based upon first finding an expression for ε_n and then determining how ε_n is related to an apparent thermal conductivity. Thus a knowledge of the behavior of ε_n is of definite importance.

In order to facilitate measurements of ε_n, equation (2.68) is usually replaced by another expression. Combining equation (2.65) and (2.67), the total shear stress in turbulent flow is given by

$$\tau = \rho \ (\nu + \varepsilon_n) \ \frac{d\overline{U}_1}{dy} \quad . \tag{2.69}$$

Also, a simple momentum balance for pipe flow shows that

$$\tau = \tau_0 \ x_2 \ / \ R \quad . \tag{2.70}$$

Equating (2.69) and (2.70), an expression can be obtained for ε_n,

$$\frac{\varepsilon_n}{Ru^*} = \frac{1 - y^+/y_c^+}{y_c^+(du^+/dy^+)} - \frac{1}{y_c^+} \quad . \tag{2.71}$$

This expression contains only the mean velocity gradient, for which experimental data are available. Actually, any of the equations for the mean velocity given in the preceding sections of this chapter can be utilized in conjunction with equation (2.71) to yield expressions for the eddy viscosity. Reviews of such expressions are given by Longwell [18] and Spalding [76].

In analyzing Laufer's data at a Reynolds number of 500,000, Hinze [9] shows ε_n/Ru^* to increase in an approximately linear fashion from zero at $y/R = 0$. A maximum value of about 0.075 is attained at $y/R \simeq 0.35$, and for $y/R > 0.5$, ε_n/Ru^* is essentially constant at a value of approximately 0.07. These general trends are in agreement

with those shown by Reynolds et al [42] and Page et al [23]. Explicit data for ε_n for flow in rough tubes have not been presented in the literature.

Spectral Analysis

One statistical approach to turbulent motion, presented by Hinze [9] and Lin [72] e.g., is summarized in the following paragraphs.

Turbulence can be considered to consist of the superposition of ever-samller periodic motions. But, such periodic motions involve the occurrence of gradients in the velocity distribution, and these gradients correspond to a vortex motion. The extent of the vortices is then determined by the periodicity. Thus, turbulence can be considered to consist of the superposition of ever-smaller eddies. Of course, both upper and lower size limits for these eddies will exist. The upper size limit, which corresponds to a minimum frequency of the turbulent motion, would be expected to be controlled mainly by the size of the apparatus under consideration, whereas the lower size limit, which corresponds to a maximum frequency of the turbulent motion, will be determined by viscosity effects in the flow field. This can be explained in the following fashion. The smaller the size of an eddy, the greater will be the velocity gradient within the eddy, and an increase in the velocity gradient leads to an increase

in the viscous shear stress which tends to counteract the eddying motion.

Each of the various size eddies occurring in a turbulent flow field will posses a certain kinetic energy, which is determined by the intensity of the velocity fluctuation at the corresponding frequency. An important question in the statistical theory of turbulence is then the manner in which this kinetic energy is distributed among the frequencies which are present. Such a distribution is termed an energy spectrum.

The energy spectrum function, $E_i(n)$, is defined by Dryden [77] in the following manner. Considering a flow field that is homogeneous with respect to time, the contribution to $\overline{u_i^2}$ of the frequencies between n and n + dn will be

$$E_i(n)\ dn \quad . \tag{2.72}$$

The mean squared value of u_i will then be given by

$$\overline{u_i^2} = \int_0^\infty E_i(n)\ dn \quad . \tag{2.73}$$

In many cases, it is more convenient to consider the spatial spectrum of turbulence rather than the Taylor time spectrum as just

defined. For this purpose a wave number is defined as

$$k_1 = n/\overline{U}_1 \quad . \tag{2.74}$$

The spatial energy spectrum function is then given by

$$E_i(k_1) = \overline{U}_1 \, E_i(n) \quad , \tag{2.75}$$

and the mean squared value of u_i becomes

$$\overline{u_i^2} = \int_0^\infty E_i(k_1) \, dk_1 \quad . \tag{2.76}$$

If it is assumed that Taylor's hypothesis as stated by Hinze [9],

$$\frac{\partial}{\partial t} = - \overline{U}_1 \frac{\partial}{\partial x_1} \quad , \tag{2.77}$$

applies then the wave number k_1 is interpreted by Brodkey [35] as being roughly an inverse eddy size, the idea being that a large eddy takes longer to sweep past a given point in the flow field. Actually, Taylor [78] shows that this hypothesis applies approximately only if the intensity satisfies

$$\frac{u_1'}{\bar{U}_1} << 1, \tag{2.78a}$$

and Lin [79] gives an additional condition for a shear flow,

$$\bar{U}_1^2 \overline{\left(\frac{\partial u_1}{\partial x_1}\right)^2} >> \overline{u_2^2} \left(\frac{d\bar{U}_1}{dx_2}\right)^2 . \tag{2.78b}$$

Thus this hypothesis would not be expected to apply in close proximity to a solid wall where large intensities are usually observed. Kline [3] also points out that near the wall some of the longest time scales may be due to turbulent bursts from the wall, and Kline, Reynolds, Schraub, and Runstadler [80] show that these bursts may begin with very small eddies. Also, the spectrum function $E_i(k_1)$ does not give a complete picture of the energy distribution in a turbulent flow field since it is simply a one-dimensional cut of what is actually a three-dimensional wave number space. As pointed out by Laufer [41], however, present methods and equipment permit measurement of the time spectrum only, thereby yielding the one-dimensional section of the three dimensional wave number space.

A great deal of information can still be gleaned from data regarding both the time spectra and the wave number spectra even though measurement capability is somewhat limited. As will be pointed

out in the next few sections, information regarding autocorrelation functions and micro and macro scales of turbulence can be deduced from the time spectra. As stated by Pao [81], energy can be considered to be transferred, in the spatial spectrum, from smaller to larger wave numbers where it is eventually dissipated by viscous effects. Utilizing this idea, Kolmogorov [82] postulated that when the Reynolds number is large enough for the energy containing eddies (small wave numbers) to be much larger than the viscous dissipation eddies (large wave numbers), the small eddies will be statistically isotropic and independent of the structure of the large eddies. He also postulated that there exists a subrange of eddy sizes, called the inertial subrange, in which viscous dissipation is negligible, and the dominant process is the transfer of energy by inertia forces. Karman and Lin [83] then show that if such an inertial subrange exists, the spectrum functions $E_i(k_1)$ must be proportional to $k_1^{-5/3}$.

Tchen [84] further shows that there may be regions in which $E_i(k_1)$ is proportional to k_1^{-1} or k_1^{-7}. He shows that if the production of turbulent energy is larger than the transfer of turbulent energy, the k_1^{-1} law, rather than $k_1^{-5/3}$, will be obtained in the inertial subrange, and that the k_1^{-1} law normally applies to slightly larger eddies than does the $k_1^{-5/3}$ law. In fact, it is possible that both laws will apply over different wave number ranges for the same energy

spectrum. Tchen [84] further shows that in the viscous subrange (size of eddies responsible for viscous dissipation), the spectrum functions $E_i(k_1)$ should be proportional to k_1^{-7}.

Of course the three foregoing laws have been demonstrated only for isotropic turbulence and will not necessarily apply if anisotropy prevails, and it is not necessary for them to apply anywhere within even an isotropic flow field. However, they may certainly prove useful in interpreting experimental results from anisotropic turbulence. Also, Lumley [85] has estimated the effects on spectrum measurements of anisotropy and due to the fact that the convection velocity of some of the eddies may differ from the mean velocity. He estimates that under extreme circumstances these effects will not exceed 30%.

Measurements of the energy spectra functions for flow in smooth tubes have been carried out by Bakewell [38], Clark [39], Coantic [86], Laufer [41], and Wills [87]. Laufer [41] presents measurements of $E_1(k_1)$, $E_2(k_1)$, and $E_3(k_1)$ for a Reynolds number of 500,000 at $y/R = 0.074$, 0.691, and 1.0. Except for the position closest to the wall, the $E_1(k_1)$ spectra exhibit similar behavior over a wide range of wave numbers. In fact, he found these spectra to vary as $k_1^{-5/3}$ over a considerable range of values of k_1, although this range varied with position in the pipe. It is thus concluded that, over this range of wave numbers, energy is transferred from smaller to larger

wave numbers without being significantly influenced by viscous dissipation or by turbulence production. In the case of the spectra obtained very near the wall, Laufer found a wave number range where $E_1(k_1)$ varies nearly as k_1^{-1}, thus following one of the types of behavior predicted by Tchen [84].

The $E_2(k_1)$ and $E_3(k_1)$ spectra were found by Laufer to exhibit significantly different behavior than that just described for $E_1(k_1)$. Neither of these spectra were found to obey the $k_1^{-5/3}$ law, and a significant energy deficiency was observed at low wave numbers. This indicates that the higher wave numbers receive a significant portion of their energy from means other than the usual transport mechanism from small to large wave numbers. Also, Hinze [9] shows that for isotropic turbulence $E_2(k_1)$ and $E_3(k_1)$ can be calculated from

$$E_j(k_1) = \frac{1}{2}\left[E_1(k_1) - k_1 \frac{\partial E_1(k_1)}{\partial k_1}\right] \qquad \text{for } j = 2,\ 3. \quad (2.79)$$

Laufer [41] applied this equation to calculate $E_2(k_1)$, and the results of this calculation do not agree with the experimental measurements. This indicates a lack of isotropy, even at the center of the pipe, as was shown by Gow's [15] turbulence intensity results.

In general, the results found by Clark [39] tend to confirm the trends reported by Laufer [41]. However, Clark found no energy

deficiency at low wave numbers in the $E_2(k_1)$ or $E_3(k_1)$ spectra. Instead, he found these spectra to asymptotically approach a constant value at low wave numbers. By plotting $E_1(k_1)\ \overline{U}_1/(y\ u^{*2})$ versus $k_1 y$, Clark found that, at a particular value of y^+, $E_i(k_1)$ is independent of Reynolds number at large values of $n\ y/\overline{U}_1$. He also found that these coordinates collapsed $E_1(k_1)$, $E_2(k_1)$, and $E_3(k_1)$ into a single curve at large values of $k_1 y$ and at a given value of y^+. This indicates isotropy of the viscous dissipation eddies as suggested by Kolmogorov [82].

The measurements of Bakewell [38], Coantic [86], and Wills [87] were directed toward the region designated as the viscous sublayer. In the investigations of both Bakewell and Wills, the energy spectra $E_1(n)$ were obtained by taking Fourier transforms of measured autocorrelation functions, as will be discussed in the following section. However, the autocorrelation function is usually measured by two spatially separated hot-wire probes, and Hinze [9] notes that these measurements are susceptible to some inaccuracies for small probe separation distances. This, of course, does not negate the value of spectrum functions obtained from autocorrelation functions, but Hinze's point should be kept in mind.

Bakewell [38] shows plots of $E_1(n)$ versus n for y^+ values ranging from 1.25 to 4.0. The general shape of each of these curves

is essentially the same as that obtained by Laufer [41]. The spectra obtained by Bakewell at $y^+ = 10$ and $y^+ = 20$ are of nearly the same magnitude and are of higher magnitudes than the spectra obtained for both smaller and larger values of y^+. However, one distinct feature is noted in these spectra; for all values of y^+, $E_1(n)$ appears to acquire a nearly constant value, though different for each y^+, at frequencies slightly greater than 100 sec^{-1}. Then $E_1(n)$ again increases for $n < 100$ sec^{-1}. In addition, Bakewell found that the spectra which he acquired for all values of y^+ could be reduced to a single curve by plotting $E_1(n)/(y^2 n)$ versus the Strouhal number

$$S = \frac{nv}{u^{*2}} \quad . \tag{2.80}$$

No attempt was made to transform the time spectra into wave number spectra because of the high turbulence intensities near the wall.

Wills [87] shows the $E_1(n)$ spectrum plotted as $\overline{U}_{max}\, E_1(n)/\delta^*$ versus $n\delta^*/\overline{U}_{max}$ for $y^+ = 4$ and $y^+ = 12$, where δ^* is the displacement thickness given by

$$\delta^* = \int_0^R (1 - \overline{U}_1/\overline{U}_{max})\, dy \quad . \tag{2.81}$$

It is seen that both curves reduce almost to the same curve in this

coordinate system. This curve again appears to asymptotically approach a constant value at low frequencies. In addition to the high turbulence intensity restriction, Wills indicates that an additional restriction on the use of Taylor's hypothesis, equation (2.77), near the wall is the fact that the turbulence is convected much faster than the local mean velocity in this region. This tends to prohibit the use of the wave number space.

Coantic's [86] results are plotted in the form of $E_1(n)$ versus n for several values of y^+. As in previous cases, he shows that $E_1(n)$ has a maximum magnitude for values of y^+ between 10 and 20.

Energy spectra results for flow in rough tubes, or near any type of rough surface, are extremely limited. Robertson et al [46, 47, 66] have made such measurements of $E_1(n)$ at the center line of a sand roughened pipe at two Reynolds numbers, both in the transition flow regime. Each of these curves are similar in shape to those obtained by Laufer [41], though higher in magnitude, and tend to display the $k_1^{-5/3}$ law over an intermediate range of wave numbers. Results were also obtained at the center line of a naturally rough pipe for several Reynolds numbers in the transition regime, and also at several positions throughout the pipe at one Reynolds number. The center line results were compatible with those obtained in the sand roughened pipe, and measurements close to the wall indicated a significant increase

in magnitude over smooth tube results and a complete absence of the $k_1^{-5/3}$ law. Robertson et al attempt to obtain a universal plot of energy spectra by utilizing $E_1(n)\ \overline{U}_1/(\overline{u_1^2}\ \Lambda_1)$ versus $n\ \Lambda_1/\overline{U}_1$ coordinates, where Λ_1 is the macro scale of turbulence which will be discussed in a later section of this chapter. Measurements taken at the center of both pipes are plotted on these coordinates, and the data appear to approach a single curve except for low Reynolds numbers.

Utilizing a pipe roughened with spherical beads, Goma and Gelhar [30] have measured the energy spectra at several locations in the pipe for a Reynolds number slightly in the fully rough flow region. Their data are presented as $E_i(n)\ \overline{U}_1/(2R\ \overline{u_1^2})$ versus $2nR/\overline{U}_1$. These coordinates become identical to those of Robertson et al [46, 47, 66] if the macro scale of turbulence is equal to the pipe diameter. A fairly universal behavior is indicated in the foregoing coordinate system, though some systematic variations do occur. Probably the most noticeable of these is a substantial decrease in magnitude, over that obtained at the center line, of the spectra near the wall for low values of $2nR/\overline{U}_1$. At high values of $2nR/\overline{U}_1$ the wall spectra were found to surpass the center line spectra in magnitude. The above statements apply to both the $E_1(n)$ and $E_2(n)$ spectra, which were the only ones measured. Significant decreases in both of these spectra were observed at the lowest frequencies measured, but this is probably

due to experimental errors rather than indicating any energy deficiency at these frequencies.

In addition to the preceding measurements, McQuivey and Richardson [69] have obtained energy spectra, $E_1(n)$, in open channel flow for both smooth and rough boundaries. They found, in both cases, the major energy content at low frequencies. The inertial subrange was exhibited over a much smaller range of frequencies on the rough than on the smooth boundary. Although the energy content at low frequencies was approximately the same for the two cases, the energy content at higher frequencies was much larger for the rough than for the smooth boundary. Also, the k_1^{-7} law, as predicted by Tchen [84], was more closely approached on the rough than on the smooth boundary. It should be noted that the foregoing comparisons are qualitative in nature only, since the Reynolds number utilized in the rough boundary study was approximately 1.75 times as great as that utilized in the smooth boundary study.

Autocorrelations

In a previous section the correlation between the fluctuating velocities in two orthogonal directions at a given point in the flow field was discussed. The correlation between the values of a fluctuating velocity in a given direction and at a given point in

the flow field but at different instants of time will be considered in this section. Such a correlation,

$$\overline{u_i(t')\, u_i(t' - t)} \tag{2.82}$$

where the averaging is carried out with respect to t', is termed an Eulerian correlation or autocorrelation. It is normal to deal with a dimensionless form of this correlation called the correlation coefficient and defined by

$$\phi_i(t) = \frac{\overline{u_i(t')\, u_i(t' - t)}}{\overline{u_i^2}} \quad . \tag{2.83}$$

It can be shown (see Hinze [9] e.g.) that the correlation coefficient $\phi_i(t)$ is simply the Fourier cosine transform of the energy spectrum function $E_i(n)$. Care must be applied, however, in utilizing spectrum measurements to obtain autocorrelations since spectrum measurements are usually most accurate in the higher frequency range.

An inspection of equation (2.83) reveals that

$$\phi_i(0) = 1 \tag{2.84}$$

and that

$$\phi_i(\infty) = 0 \quad . \tag{2.85}$$

In fact, $\phi_i(t)$ must always lie within the range

$$-1 \leq \phi_i(t) \leq 1 \quad . \tag{2.86}$$

Hinze [9] shows that near $t = 0$, $\phi_i(t)$ must be parabolic in shape, and this parabola is known as the osculating parabola.

Measurements of the autocorrelation function $\phi_1(t)$ made by Favre et al in an isotropic flow field are presented by Hinze [9]. These measurements indicate a rather rapid decrease in $\phi_1(t)$ as t becomes larger than zero. $\phi_1(t)$ then approaches zero in an oscillatory manner.

Bakewell [68] has obtained measurements of the autocorrelation function $\phi_1(t)$ in the viscous sublayer of a smooth pipe. His data indicate a less rapid decline in $\phi_1(t)$, and a consequent broadening of this autocorrelation function, as the wall is approached. This effect is interpreted as being due to the increasingly dominant role of low frequencies near the wall.

No information is available regarding the autocorrelation functions for flow near rough surfaces.

Turbulence Scales

Several types of micro and macro scales are defined for a turbulent flow field. By expanding the autocorrelation coefficient in a Taylor series about $t = 0$, the equation for the osculating parabola results:

$$\phi_i(t) = 1 - (t/\gamma_i)^2 \quad . \tag{2.87}$$

Here γ_i is a measure of the most rapid changes that occur in the fluctuations of u_i and is called the Eulerian micro scale. Hinze [9] demonstrates that, if Taylor's hypothesis is applied, γ_i can be written as

$$\frac{1}{\gamma_i^2} = \frac{1}{2\overline{u_i^2}} \int_0^\infty n^2 E_i(n)\, dn \quad . \tag{2.88}$$

On the other hand, a rough measure of the longest connection time in the behavior of $u_i(t)$ is termed the Eulerian macro scale and is defined by

$$T_i = \int_0^\infty \phi_i(t)\, dt \quad . \tag{2.89}$$

Applying Taylor's hypothesis to this equation, as shown by Hinze [9],

yields

$$T_i = \frac{1}{4\,\overline{u_i^2}} \lim_{n \to 0} E_i(n) \quad . \tag{2.90}$$

In addition to the foregoing Eulerian time scales, spatial scales are also defined. A spatial micro scale, which may be considered a measure of the average dimension of the smallest eddies (i.e., those mainly responsible for viscous dissipation), may be defined as

$$\frac{1}{\alpha_i^2} = \frac{1}{2\,\overline{u_i^2}} \overline{\left(\frac{\partial u_i}{\partial x_1}\right)^2} \quad . \tag{2.91}$$

If it is assumed that Taylor's hypothesis, equation (2.77), applies, then equation (2.91) becomes

$$\alpha_i = \overline{U}_1 \, \gamma_i \quad . \tag{2.92}$$

A measure of the longest connection distance between the velocities at two points in the flow field is given by

$$\Lambda_i = \int_0^\infty \frac{\overline{u_i(x_1)\; u_i(x_1+\xi)}}{\overline{u_i^2}} \, d\xi \quad , \tag{2.93}$$

where Λ_i is a spatial macro scale of turbulence. As before, if Taylor's hypothesis applies, equation (2.93) becomes

$$\Lambda_i = \overline{U}_1 \, T_i \quad . \tag{2.94}$$

Measurements of Λ_i and α_i in a smooth rectangular channel have been conducted by Laufer [40]. He found Λ_1 to be approximately 0.8R while Λ_2 and Λ_3 were both equal to about R/4. No large variations in any of these spatial macro scales were observed across the turbulent core. On the other hand, the α_i showed increases with distance from the wall, all reaching maximum values of about 0.1R. These measurements are interpreted by Hinze [9] to indicate, in the turbulent core, the existence of large eddies elongated in the axial direction.

Bakewell [68] presents measurements of γ_1 obtained in the viscous sublayer of a smooth tube by curve-fitting measured values of the autocorrelation function to obtain the osculating parabola and then applying equation (2.87). His measurements show an increase in γ_1 with y^+ at small distances from the wall. γ_1 reaches a maximum value of about 16 ms at a y^+ value of about 5 and then begins to decrease rather rapidly. At $y^+ = 40$, which is as far as Bakewell's measurements extend, γ_1 appears to be approaching a constant value of

about 6 ms.

Robertson et al [46, 47, 66] have conducted measurements of α_1 and Λ_1 in a smooth pipe, a sand roughened pipe, and a naturally rough pipe. In general the values of Λ_1 are seen to be rather constant in the turbulent core and to decrease near the wall. However, a decrease in Λ_1 was observed near the center of the smooth pipe, and there was a marked Reynolds number dependence at this point, in disagreement with Laufer's [40] measurements. Their measurements of the micro scale in the smooth and sand roughened pipes were also in disaccord with Laufer's [40] channel results, being much lower in magnitude. The α_1 data obtained from the naturally rough pipe show somewhat the same trend as Laufer's results, however.

McQuivey and Richardson [69] present experimental measurements of α_1 and Λ_1 for flow in open channels with both smooth and rough surfaces. They find both scales to attain maximum values at y/R of approximately 0.45. For Reynolds numbers between 6,000 and 12,000 the Λ_1/R values at this point are around 0.12 to 0.15. They were not able to determine the scale difference over the smooth and rough boundaries due to the wide variations in Reynolds numbers utilized in the two tests.

Pressure Field

The pressure field occuring in a turbulent flow has not been

considered prior to this point. However, pressure fluctuations, as well as velocity fluctuations, can have an effect on the sturcture of a turbulent shear flow. In addition, interactions between the turbulent pressure and velocity fields, as exemplified by the pressure-velocity cross correlation term appearing in the energy equation, are important in studying the details of a turbulent flow.

On the other hand, it should be remembered that the independent importance of the pressure field stems from an incapability to handle turbulence theoretically. The velocity and pressure fields are not independent quantities; both are dependent variables of the turbulence problem, and a solution for the velocity automatically yields a solution for the pressure. This fact is demonstrated by Townsend [12] for cartesian coordinates by taking the divergence of the momentum equations, before time averaging, and applying the continuity equation to obtain

$$\sum_{i=1}^{3} \sum_{j=1}^{3} \frac{\partial^2 (U_i U_j)}{\partial x_i \partial x_j} = -\sum_{i=1}^{3} \frac{\partial^2 P}{\partial x_i^2} \quad . \tag{2.95}$$

Time averaging equation (2.95) yields an expression for the temporal mean pressure

$$-\sum_{i=1}^{3} \frac{\partial^2 \overline{P}}{\partial x_i^2} = \sum_{i=1}^{3} \sum_{j=1}^{3} \frac{\partial^2}{\partial x_i \partial x_j} (\overline{U}_i \overline{U}_j + \overline{u_i u_j}) \quad , \tag{2.96}$$

and subtracting (2.96) from (2.95) yields a relationship for the fluctuating pressure,

$$-\sum_{i=1}^{3} \frac{\partial P}{\partial x_i^2} = \sum_{i=1}^{3} \sum_{j=1}^{3} \frac{\partial^2}{\partial x_i \partial x_j} (\overline{U}_i u_j + \overline{U}_j u_i - \overline{u_i u_j}$$

$$+ u_i u_j) \quad . \tag{2.97}$$

Thus a solution for the velocity field would yield expressions for the pressure field, but such a solution has thus far eluded investigators in this area making it necessary to study both pressure and velocity fields in an attempt to gain a more complete understanding of the turbulence phenomena.

Investigations of turbulent pressure fields have recently been conducted by Corcos [88], Willmarth and Wooldridge [89], and Wills [90]. These investigators have obtained for pressure fields most of the types of statistical information previously discussed for velocity fields. A comprehensive review of the results of the foregoing studies will not be given here since the current interest is mainly in the velocity field, but some of the major results should be

noted. Corcos [88] found the region $y^+ \leq 100$ to be essentially free of pressure sources, thereby enabling specification of the pressure in terms of its boundary value. This also indicates that the velocity field, while dependent upon the turbulent pressures in this region, is unable to affect them appreciably. Willmarth and Wooldridge [89] found that the ratio of the rms value of the wall pressure on a rough surface to that on a smooth surface is substantially greater than the ratio of the respective wall shear stresses.

In his study of turbulent flow in a smooth pipe, Laufer [41] was able to obtain values of all terms appearing in the turbulent energy equation except the $\overline{pu_2}$ correlation gradient in the radial direction, which he then calculated from the experimental measurements. Although this term was found to be very small, making numerical determinations somewhat inaccurate, a null value was indicated at the pipe center line while a sharp maximum has reached near a y^+ value of 10.

Turbulence Structure

In this section an attempt will be made to summarize the material in the previous sections and to briefly present an up to date description of the structure of turbulent pipe flow. This discussion will necessarily be limited to smooth pipes due to the lack of information

available regarding rough pipes. Also, a great deal of the information regarding the flow structure near the wall will be deduced from experiments on turbulent boundary layers over flat plates. Although a great deal of similarity is known to exist near the solid boundary for pipe flow and boundary layer flow, this similarity diminishes at sufficient distances from the wall. In a turbulent boundary layer, the flow intermittently changes from laminar to turbulent at large distances from the wall, and this intermittency phenomenon does not occur in turbulent pipe flow. Also, there is a convective transport of momentum normal to the solid surface in the boundary layer flow which does not exist in pipe flow. These differences are pointed out by Hughes and Brighton [16].

One of the first investigations concerning turbulent pipe flow from which somewhat detailed information regarding the structure of the flow can be obtained is that of Laufer [41]. He was able to determine all terms appearing in the turbulent energy equation. These measurements, as corrected by Townsend [12] for the large gradients near the wall, indicate maximum values for the kinetic energy of the turbulence, its dissipation, and its production at a y^+ value in the neighborhood of ten. Over the major portion of the pipe the production and dissipation are nearly equal, so the turbulence is essentially in energy equilibrium. At the center of the pipe the

production vanishes, however, while the dissipation does not. This loss is compensated for by a diffusion of kinetic energy from the wall region, and the loss of kinetic energy in the wall region is accounted for by a diffusion of pressure energy to this area from the turbulent core.

Hinze [9] notes that at the point where the production of turbulence reaches a maximum, u_1' is rather large while u_2' and u_3' are relatively small. This indicates that turbulent kinetic energy produced by the shearing action of the mean flow goes mostly in favor of the u_1' component. Although a part of this energy is transferred to the turbulent core, most is immediately dissipated. Townsend [12] shows that this behavior may be explained by considering the turbulence near the wall to be composed both of small attached eddies with a fixed orientation and of detached free eddies. These free eddies, while diffusing toward the turbulent core, decay and dissipate energy. Nevertheless, they are still responsible for transporting kinetic energy to this region.

The energy spectral density measurements made by Laufer [41], for flow in a circular pipe, and by Clark [39], for flow in a rectangular channel, both show an increase in magnitude at higher frequencies as the wall is approached. This indicates small, high intensity eddies in this region, leading to large viscous dissipation.

These measurements also indicate the existence of large eddies, which are elongated in the axial direction, in the turbulent core. Both Clark [39] and Hinze [9], in interpreting Laufer's data, conclude that the small eddies, which are contained within the large eddies, become smaller as the wall is approached. This would imply that the large eddies are at least partially responsible for the diffusion of the small high intensity eddies toward the turbulent core. Hinze [9] notes that this also requires a transport of low intensity eddies toward the wall by the large eddies.

Though Laufer's [41] measurements yielded a qualitative description of the turbulence structure in pipe flow, they also strongly emphasized the importance of a knowledge of occurrences very near the wall. Clark's [39] study was undertaken to add knowledge in this area, but before considering his results it would be helpful to review other investigations which emerged in this time period.

As early as 1932, Fage and Townend (see Knudsen and Katz [34]) showed that turbulent fluctuations occur completely into the layer near the wall termed the viscous sublayer. Later, two schools of thought emerged concerning the role played by the viscous sublayer in the structure of turbulence. The first of these considered a passive sublayer which responds to a forcing motion produced by the outer flow. This view is exemplified by the works of Reynolds [91]

and Wills [87]. The second view, given by Einstein and Li [92], considered an active sublayer which generates its own structure and thus affects the flow away from the wall. This structure generation is taken to be due to an instability in the sublayer.

Recent investigations by Bakewell [38], Clark [39], Kline [4], Kline et al [80], and Schraub [43] have shown that neither of the foregoing viewpoints is entirely correct. Visual and quantitative studies [4, 43, 80] of turbulence near a smooth wall conducted at Stanford University have indicated the existence of a time dependent, three-dimensional, streaky structure from $y^+ = 0.1$ to $y^+ = 7$. No indication is given that a change in this structure occurs for $y^+ < 0.1$. This longitudinal streaky structure is apparently the result of low and high speed flow regions existing side by side. These streaks normally migrate slowly downstream and drift away from the wall at an extremely slow rate. An oscillation of the streak begins for y^+ between 8 and 12, and this oscillation is amplified as the streak moves farther from the wall. Termination of this oscillation occurs as a very abrupt breakup of the streak for y^+ between 10 and 30, and this fluid is then ejected into the outer flow region. The foregoing process is considered responsible for maintaining the turbulent flow.

Bakewell [38] reached a similar conclusion from a quantitative

study of the viscous sublayer. He concluded that the dominant phenomenon within this region is the process of vortex stretching of counter-rotating eddy pairs which are elongated in the longitudinal direction. This also suggests that the sublayer acts to maintain the turbulent flow field.

Having available the results of the foregoing investigations, Clark [39] was able to interpret the results of his channel flow study in terms of these three-dimensional streaks. He concluded that this streaky structure exists for $y^+ < 12$ and that the streak breakup occurs for $12 < y^+ < 70$. The region for $y^+ > 70$ is taken simply to be a manifestation of the processes occurring within the inner layers. If should be noted that, in view of the foregoing results, there does seem to be some justification for the three layer scheme previously proposed for the mean velocity profile from the phenomenological theories.

In contrast to the foregoing observations regarding the structure of turbulent flow in smooth pipes, virtually no information is available regarding the turbulence structure for flow in rough pipes. As noted by Kline et al [80], the turbulence mechanism for flow adjacent to rough surfaces may be entirely distinct from that for flow along smooth walls. It might be expected that the three-dimensional streaky structure will continue to exist for flow in the hydraulically

smooth regime, although some slight modifications may occur. However, data are not available for conjectures regarding the structure in the transition and fully rough regimes.

Some available data do indicate definite changes in the turbulence structure in rough pipes, but no suppositions regarding such changes have been supplied. Marris [65] has interpreted Logan and Jones' [64] data following an abrupt increase in surface roughness to indicate a spiral type mean flow, although such an interpretation cannot be rigorously supported. Gow [15] has observed substantial changes in the Reynolds stresses for flow in a rough pipe over those in a smooth pipe, indicating a definite change in structure, but the characteristics of this change have not been determined. Townes [57], in a study of turbulent flow over a two-dimensional square cavity type roughness element, found that in some cases fluid was actually removed from within the cavities by a phenomenon resembling the turbulent bursts described by Kline et al [80], but whether such a phenomenon is representative of the flow structure near three-dimensional roughness elements remains to be seen.

CHAPTER III

CURRENT PROBLEM

The physical importance of understanding the structure of turbulent flow over rough surfaces was pointed out in Chapter I, and in Chapter II the limited extent of current knowledge in this area was indicated. The purpose of the current study is to attempt to extend available information regarding flow over rough surfaces. The following approach is utilized in an effort to achieve this goal. First, the governing equations for the conservation of mass, momentum, and energy are examined in order to determine the quantities of importance in this problem. These quantities are then measured experimentally, using constant temperature hot-wire anemometry techniques, for flow in both smooth and rough pipes. Although some of this information is currently available for flow in smooth pipes, these measurements are repeated in order to insure that the experimental techniques and apparatus yield reliable results. In the current study, only the effect of variation in surface roughness is considered, and thus all measurements are made at a single Reynolds number, approximately 165,000. This value of the Reynolds number was selected to yield flow in the hydraulically smooth, transition, and fully rough regimes respectively for the three values of roughness utilized. This study is an extension of the investigations of Gow

[15] and that of Townes, Gow, Powe, and Weber [93].

As noted in Chapter II, Gow [15] found that the governing equations, subject to the assumptions normally applied for turbulent flow in smooth pipes, are not valid for flow in rough pipes. Thus, the governing equations are re-analyzed for flow in fough pipes.

A second type of analysis which has proven useful in previous investigations is also employed in the current study. This consists of a consideration of the energy spectra of the fluctuating velocity components in the three corrdinate directions. In addition to being directly useful in analyzing the flow structure, these measurements enable the calculation of additional quantities such as autocorrelation functions and turbulence scales.

In summary, this study should yield information regarding turbulent flow over rough surfaces which is currently unavailable in the literature. Such information should then produce clues regarding the structure of turbulent flow near rough surfaces and the manner in which this structure changes as the roughness is varied.

CHAPTER IV

ANALYTICAL CONSIDERATIONS

Momentum and Continuity Relations

The equations expressing the conservation of momentum for the Newtonian flow of a fluid at moderate pressures are the well-known Navier-Stokes equations. However, it is impractical to deal with these equations directly for turbulent flow since the fluid velocity consists of random fluctuations in the three coordinate directions. On the other hand, the fact that the velocity fluctuations are random suggests a statistical approach to the problem. This can be accomplished by considering the pressure and the velocity in each coordinate direction to consist of a mean and a fluctuating component. Although it might seem reasonable to also consider fluctuations in fluid density at this point, Hinze [9] shows that such fluctuations can be neglected for low mean velocities (less than about 200 fps for air) such as those to be considered in the experimental phase of this study.

Introduction of the mean and fluctuating components of pressure and velocity into the Navier-Stokes equations, and then time averaging these equations, results in the Reynolds equations for turbulent flow. Although no analytical solution to these equations has been possible since they possess a greater number of unknowns than equations, they

do serve to indicate measurable quantities of importance in the turbulent flow process. The Reynolds equations, as reduced for fully developed axisymmetric flow in smooth pipes, have been investigated experimentally by Laufer [41] and theoretically by Pai [33]. However, the recent investigation by Gow [15] has indicated that this form of the Reynolds equations may not be valid for turbulent flow in rough pipes. An attempt will thus be made in the current investigation to derive forms of the Reynolds equations which are valid for flow in rough pipes.

One of the assumptions made in reducing the Reynolds equations for flow in smooth pipes is that no mean velocity components occur in either the radial or angular directions, and this assumption is justified on the basis of continuity arguments. However, for flow in rough pipes, mean velocity components in the radial and angular directions must exist for flow around the roughness elements. Since the distance from the wall through which such effects may propagate cannot be definitely determined at this point, these mean velocity components must be retained. Thus, the following expressions will be utilized for the instantaneous pressure and velocities:

$$U_i = \overline{U}_i + u_i \quad , \tag{4.1a}$$

$$P = \overline{P} + p \quad . \tag{4.1b}$$

Now, for the incompressible flow of a constant property Newtonian fluid, the continuity equation, in cylindrical coordinates, is given by

$$\frac{\partial U_2}{\partial x_2} + \frac{U_2}{x_2} + \frac{1}{x_2}\frac{\partial U_3}{\partial x_3} + \frac{\partial U_1}{\partial x_1} = 0 \quad , \tag{4.2}$$

and the Navier-Stokes equations in the x_1, x_2, and x_3 directions, respectively, are given by

$$\frac{DU_1}{Dt} = -\frac{1}{\rho}\frac{\partial P}{\partial x_1} + v\,\nabla^2 U_1 \quad , \tag{4.3a}$$

$$\frac{DU_2}{Dt} - \frac{U_3^2}{x_2} = -\frac{1}{\rho}\frac{\partial P}{\partial x_2} + v\left[\nabla^2 U_2 - \frac{U_2}{x_2^2} - \frac{2}{x_2^2}\frac{\partial U_3}{\partial x_3}\right] \quad , \tag{4.3b}$$

$$\frac{DU_3}{Dt} + \frac{U_2 U_3}{x_2} = -\frac{1}{\rho x_2}\frac{\partial P}{\partial x_3} + v\left[\nabla^2 U_3 + \frac{2}{x_2^2}\frac{\partial U_2}{\partial x_3} + \frac{U_3}{x_2^2}\right] , \tag{4.3c}$$

where

$$\frac{D}{Dt} = \frac{\partial}{\partial t} + U_1\frac{\partial}{\partial x_1} + U_2\frac{\partial}{\partial x_2} + \frac{U_3}{x_2}\frac{\partial}{\partial x_3} \quad , \tag{4.4a}$$

$$\nabla^2 = \frac{\partial^2}{\partial x_1^2} + \frac{\partial^2}{\partial x_2^2} + \frac{1}{x_2}\frac{\partial}{\partial x_2} + \frac{1}{x_2^2}\frac{\partial^2}{\partial x_3^2} \quad . \tag{4.4b}$$

Multiplying the continuity equation by U_i and adding to the left hand side of the Navier-Stokes equation in the x_i direction yields

$$\frac{\partial U_1}{\partial t} + \frac{\partial (U_1^2)}{\partial x_1} + \frac{\partial (U_1 U_2)}{\partial x_2} + \frac{1}{x_2}\frac{\partial (U_1 U_3)}{\partial x_3} + \frac{U_1 U_2}{x_2}$$

$$= -\frac{1}{\rho}\frac{\partial P}{\partial x_1} + v\,\nabla^2 U_1 \quad , \tag{4.5a}$$

$$\frac{\partial U_2}{\partial t} + \frac{\partial (U_1 U_2)}{\partial x_1} + \frac{\partial (U_2^2)}{\partial x_2} + \frac{1}{x_2}\frac{\partial (U_2 U_3)}{\partial x_3} + \frac{U_2^2 - U_3^2}{x_2}$$

$$= -\frac{1}{\rho}\frac{\partial P}{\partial x_2} + v\left[\nabla^2 U_2 - \frac{U_2}{x_2^2} - \frac{2}{x_2^2}\frac{\partial U_3}{\partial x_3}\right] \quad , \tag{4.5b}$$

$$\frac{\partial U_3}{\partial t} + \frac{\partial (U_1 U_3)}{\partial x_1} + \frac{\partial (U_2 U_3)}{\partial x_2} + \frac{1}{x_2}\frac{\partial (U_3^2)}{\partial x_3} + \frac{2U_2 U_3}{x_2}$$

$$= -\frac{1}{\rho x_2}\frac{\partial P}{\partial x_3} + v\left[\nabla^2 U_3 + \frac{2}{x_2^2}\frac{\partial U_2}{\partial x_3} - \frac{U_3}{x_2^2}\right] \quad . \tag{4.5c}$$

Introducing the mean and fluctuating quantities, equations (4.1), and time averaging, equations (4.5) become

$$\frac{\partial}{\partial x_2}(\overline{U}_1\overline{U}_2 + \overline{u_1u_2}) + \frac{1}{x_2}\frac{\partial}{\partial x_3}(\overline{U}_1\overline{U}_3 + \overline{u_1u_3}) + \frac{\overline{U}_1\overline{U}_2 + \overline{u_1u_2}}{x_2}$$

$$= -\frac{1}{\rho}\frac{\partial \overline{P}}{\partial x_1} + \nu\,\nabla^2\,\overline{U}_1 \quad , \tag{4.6a}$$

$$\frac{\partial}{\partial x_2}(\overline{U}_2^2 + \overline{u_2^2}) + \frac{1}{x_2}\frac{\partial}{\partial x_3}(\overline{U}_2\overline{U}_3 + \overline{u_2u_3}) + \frac{\overline{U}_2^2 - \overline{U}_3^2 + \overline{u_2^2} - \overline{u_3^2}}{x_2}$$

$$= -\frac{1}{\rho}\frac{\partial \overline{P}}{\partial x_2} + \nu\left[\nabla^2\,\overline{U}_2 - \frac{\overline{U}_2}{x_2^2} - \frac{2}{x_2^2}\frac{\partial \overline{U}_3}{\partial x_3}\right] \quad , \tag{4.6b}$$

$$\frac{\partial}{\partial x_2}(\overline{U}_2\overline{U}_3 + \overline{u_2u_3}) + \frac{1}{x_2}\frac{\partial}{\partial x_3}(\overline{U}_3^2 + \overline{u_3^2}) + \frac{2}{x_2}(\overline{U}_2\overline{U}_3 + \overline{u_2u_3})$$

$$= -\frac{1}{\rho x_2}\frac{\partial \overline{P}}{\partial x_3} + \nu\left[\nabla^2\,\overline{U}_3 + \frac{2}{x_2^2}\frac{\partial \overline{U}_2}{\partial x_3} - \frac{\overline{U}_3}{x_2^2}\right] \quad . \tag{4.6c}$$

The reduction of the continuity equation, equation (4.2), under these same conditions shows that it must be satisfied separately by the mean and the fluctuating components.

Although equations (4.6) express the conservation of momentum for turbulent flow in rough pipes, a further simplification may be

expected if roughness elements of a fairly uniform height but with a random shape distribution are considered. An analogy with the statistical time averaging process for temporal velocity fluctuations suggests the possibility of a statistical space averaging process for spatial velocity fluctuations due to the presence of the roughness elements. Thus the spatial average, in the x_3 direction, of any variable F is defined as

$$\hat{F} = \frac{1}{2\pi} \int_0^{2\pi} F \, dx_3 \quad . \tag{4.7}$$

The spatially averaged mean velocity in the radial direction must then vanish to satisfy continuity, and no spatially averaged mean velocity component in the angular direction may exist in fully developed flow for the type of roughness under consideration. In addition, the fully developed flow restriction requires all spatially averaged velocity gradients in the x_1 direction to vanish. From equation (4.7), it may be seen that the gradient, in the x_3 direction, of any spatially averaged quantity must also be zero.

Utilizing the foregoing results and spatially averaging equations (4.6) yields the following relations:

$$\frac{d}{dx_2}\left(\overline{\hat{U}_1\hat{U}_2} + \overline{\hat{u}_1\hat{u}_2}\right) + \frac{\overline{\hat{U}_1\hat{U}_2} + \overline{\hat{u}_1\hat{u}_2}}{x_2}$$

$$= -\frac{1}{\rho}\frac{\partial\hat{\bar{P}}}{\partial x_1} + \frac{\nu}{x_2}\frac{d}{dx_2}\left(x_2\frac{d\hat{\bar{U}}_1}{dx_2}\right) \quad , \tag{4.8a}$$

$$\frac{d}{dx_2}\left(\hat{\bar{U}}_2^2 + \overline{\hat{u}_2^2}\right) + \frac{\hat{\bar{U}}_2^2 - \hat{\bar{U}}_3^2 + \overline{\hat{u}_2^2} - \overline{\hat{u}_3^2}}{x_2} = -\frac{1}{\rho}\frac{\partial\hat{\bar{P}}}{\partial x_2} \quad , \tag{4.8b}$$

$$\frac{d}{dx_2}\left(\overline{\hat{U}_2\hat{U}_3} + \overline{\hat{u}_2\hat{u}_3}\right) + \frac{2}{x_2}\left(\overline{\hat{U}_2\hat{U}_3} + \overline{\hat{u}_2\hat{u}_3}\right) = 0 \quad . \tag{4.8c}$$

The conservation of momentum for turbulent flow in a pipe having closely packed roughness elements of a fairly uniform height is thus expressed by equations (4.8). Some specific results can now be obtained from these equations. These results will be compared to smooth pipe results by taking $\bar{U}_2 = \bar{U}_3 = 0$.

First, equation (4.8) may be integrated to yield

$$\overline{\hat{U}_2\hat{U}_3} + \overline{\hat{u}_2\hat{u}_3} = c/x_2^2 \quad , \tag{4.9}$$

but all velocities vanish at $x_2 = R$, so c must also vanish. Therefore,

$$\overline{\hat{u}_2 u_3} = - \overline{\hat{U}_2 \hat{U}_3} \tag{4.10}$$

for all values of x_2. Thus, for a rough pipe, the $\overline{\hat{u}_2 u_3}$ correlation may have a nonzero value, while for smooth pipes it must vanish everywhere. This indicates physically the possibility of a transport of radial momentum through a plane normal to the angular axis in rough pipes.

At the pipe center line $\overline{\hat{U}_2^2}$ and $\overline{\hat{U}_3^2}$ would be expected to vanish, and in this case equation (4.8b) indicates that

$$\overline{\hat{u}_2^2} = \overline{\hat{u}_3^2} \quad \text{at} \quad x_2 = 0 \quad . \tag{4.11}$$

This result is also valid for flow in smooth pipes, since no mean velocity components appear, and has been verified experimentally by Laufer [41]. Also, integrating equation (4.8b) with respect to x_2 yields

$$\frac{\overline{\hat{P}}_0 - \overline{\hat{P}}}{\rho} = \overline{\hat{U}_2^2} + \overline{\hat{u}_2^2} + \int_R^{x_2} \frac{1}{\xi} \left(\overline{\hat{U}_2^2} - \overline{\hat{U}_3^2} + \overline{\hat{u}_2^2} - \overline{\hat{u}_3^2} \right) d\xi \quad , \tag{4.12}$$

an expression for the pressure variation in the radial direction. For flow in smooth pipes, Laufer [41] and Gow [15] have shown that

u_3' is greater than u_2' over the entire cross-section, so it may be deduced from equation (4.12) that the pressure on the solid wall will be greater than that within the fluid. This is in contrast with the results of Pai [33], but he apparently failed to account for the direction of integration.

By differentiating equation (4.8b) with respect to x_1 it can be shown that $\frac{\partial \hat{\bar{P}}}{\partial x_1}$ is a function only of x_1, and an examination of equation (4.8a) then reveals that $\frac{\partial \hat{\bar{P}}}{\partial x_1}$ must be a pure constant. Equation (4.8a) can thus be integrated to yield

$$\frac{\bar{U}_1\hat{\bar{U}}_2 + \overline{\hat{u}_1 u_2}}{u^{*2}} = \frac{x_2}{R} + \frac{\nu}{u^{*2}} \frac{d\hat{\bar{U}}_1}{dx_2} \quad , \tag{4.13}$$

where the pressure gradient has been replaced by the shear velocity. At the pipe center line, $\bar{U}_2$ must vanish so

$$\overline{\hat{u}_1 u_2} = 0 \quad \text{at} \quad x_2 = 0 \tag{4.14}$$

in agreement with smooth pipe results. Also, for a smooth pipe equation (4.13) enables the determination of the $\overline{u_1 u_2}$ correlation from mean velocity measurements only.

Equation (4.13) can now be integrated a second time to yield

$$\hat{\bar{U}}_1 = \frac{Ru^{*2}}{2v} \left[1 - (x_2/R)^2\right] + \int_R^{x_2} \frac{\overline{\hat{u}_1 u_2}}{v} \, d\xi$$

$$+ \int_R^{x_2} \frac{\hat{\bar{U}}_1 \bar{U}_2}{v} \, d\xi \quad . \tag{4.15}$$

For turbulent flow in smooth pipes the last term in this expression goes to zero, and equation (4.15) reduces to the relationship first obtained by Pai [33]. For smooth pipes, this equation produces the surprising result that the longitudinal mean velocity profile can be expressed as the linear sum of the laminar profile and a contribution due to the turbulence. Equation (4.15) indicates that the spatially averaged longitudinal mean velocity profile for turbulent flow in rough pipes can be expressed as the linear sum of the laminar profile, a contribution due to the turbulent flow itself, and a contribution due to the presence of the roughness elements.

Energy Relations

Since, in this investigation, no heat transfer is being considered, the applicable energy equations will simply express the conservation of mechanical energy, in analogy with the Bernoulli equation for laminar flow. In turbulent flow, however, two types of energy quantities must be considered--that of the mean flow and that of the

turbulent fluctuations. The approach taken in this section will be to first consider the turbulent energy balance and then to derive an expression for the conservation of energy in the mean flow.

In order to develop the energy balance for the turbulent motions, consider equation (4.3) which express the conservation of momentum. The momentum equation in the x_i direction can be rewritten as

$$\frac{\partial U_i}{\partial t} + \sum_{j=1}^{3} \frac{U_j}{h_j} \frac{\partial U_i}{\partial x_j} + F_i = -\frac{1}{\rho h_i} \frac{\partial P}{\partial x_i} + \nu \nabla^2 U_i \quad , \tag{4.16}$$

where

$$h_1 = h_2 = 1 \quad \text{and} \quad h_3 = x_2 \quad , \tag{4.17}$$

and

$$F_1 = 0 \tag{4.18a}$$

$$F_2 = -\frac{U_3^2}{x_2} + \frac{\nu}{x_2^2}\left(U_2 + 2\frac{\partial U_3}{\partial x_3}\right) \tag{4.18b}$$

$$F_3 = \frac{U_2 U_3}{x_2} + \frac{\nu}{x_2^2}\left(U_3 = 2\frac{\partial U_2}{\partial x_3}\right) \quad . \tag{4.18c}$$

Multiplying the continuity equation by U_i and adding to equation (4.16) yields

$$\frac{\partial U_i}{\partial t} + \sum_{j=1}^{3} \frac{1}{h_j} \frac{\partial (U_i U_j)}{\partial x_j} + F_i + \frac{U_i U_2}{x_2}$$

$$= - \frac{1}{\rho h_i} \frac{\partial P}{\partial x_i} + v \nabla^2 U_i \quad . \tag{4.19}$$

An instantaneous energy balance for each coordinate direction can now be obtained by multiplying equation (4.19) by U_i to obtain

$$\frac{\partial (U_i^2)}{\partial t} - U_i \frac{\partial U_i}{\partial t} + \sum_{j=1}^{3} \frac{1}{h_j} \frac{\partial (U_i^2 U_j)}{\partial x_j} - \sum_{j=1}^{3} \frac{U_i U_j}{h_j} \frac{\partial U_i}{\partial x_j}$$

$$+ U_i F_i + \frac{U_i^2 U_2}{x_2} = - \frac{U_i}{\rho h_i} \frac{\partial P}{\partial x_i} + v U_i \nabla^2 U_i \quad . \tag{4.20}$$

This equation can be simplified if equation (4.16) is multiplied by U_i and then added to equation (4.20). This yields

$$\frac{\partial (U_i^2)}{\partial t} + \sum_{j=1}^{3} \frac{1}{h_j} \frac{\partial (U_i^2 U_j)}{\partial x_j} + 2 U_i F_i + \frac{U_i^2 U_2}{x_2} = - \frac{2U_i}{\rho h_i} \frac{\partial P}{\partial x_i}$$

$$+ v \nabla^2 U_i^2 - \sum_{j=1}^{3} \frac{2v}{h_j^2} \left(\frac{\partial U_i}{\partial x_j} \right)^2 \quad . \tag{4.21}$$

Introducing the mean and fluctuating quantities given by equation (4.1) and time averaging, equation (4.21) becomes

$$\sum_{j=1}^{3} \frac{1}{h_j} \frac{\partial}{\partial x_j} \left[\overline{U}_i^2 \overline{U}_j + 2\overline{U}_i \overline{u_i u_j} + \overline{u_i^2} \overline{U}_j + \overline{u_i^2 u_j} \right]$$

$$+ 2\overline{U}_i \overline{F}_i + 2\overline{u_i F_i} + \frac{1}{x_2} \left[\overline{U}_i^2 \overline{U}_2 + 2\overline{U}_i \overline{u_i u_2} + \overline{u_i^2} \overline{U}_2 \right.$$

$$\left. + \overline{u_i^2 u_2} \right] = - \frac{2}{\rho h_i} \left[\overline{U}_i \frac{\partial \overline{P}}{\partial x_i} + \overline{u_i \frac{\partial P}{\partial x_i}} \right] + \nu \left[\nabla^2 \overline{U}_i^2 \right.$$

$$\left. + \nabla^2 \overline{u_i^2} \right] - \sum_{j=1}^{3} \frac{2\nu}{h_j^2} \left[\left(\frac{\partial \overline{U}_i}{\partial x_j} \right)^2 + \overline{\left(\frac{\partial u_i}{\partial x_j} \right)^2} \right] . \qquad (4.22)$$

The mean pressure gradient can now be eliminated from this equation by time averaging equation (4.19), then mulitplying it by $-2\overline{U}_i$, and adding the resulting equation to equation (4.22). This results in

$$\sum_{j=1}^{3} \frac{1}{h_j} \left[\overline{U}_i \overline{U}_j \frac{\partial \overline{U}_i}{\partial x_j} - \overline{U}_i \frac{\partial (\overline{U}_i \overline{U}_j)}{\partial x_j} + 2 \overline{u_i u_j} \frac{\partial \overline{U}_i}{\partial x_j} + \frac{\partial (\overline{u_i^2} \overline{U}_j)}{\partial x_j} \right.$$

$$\left. + \frac{\partial (\overline{u_i^2 u_j})}{\partial x_j} \right] + 2\overline{u_i F_i} - \frac{1}{x_2} \left[\overline{U}_2 (\overline{U}_2^2 - \overline{u_i^2}) - \overline{u_i^2 u_2} \right]$$

$$= - \frac{2\overline{\tilde{u}_i \frac{\partial P}{\partial x_i}}}{\rho h_i} + \nu \nabla^2 \overline{u_i^2} - \sum_{j=1}^{3} \frac{2\nu}{h_j^2} \overline{\left(\frac{\partial \tilde{u}_i}{\partial x_j} \right)^2} . \qquad (4.23)$$

The expression for the conservation of energy due to the turbulent fluctuations is then obtained by summing the three relationships indicated by equation (4.23). The expression for the conservation of energy thus becomes

$$\sum_{i=1}^{3} \sum_{j=1}^{3} \frac{1}{h_j} \left[\overline{u_i u_j} \frac{\partial \overline{U}_i}{\partial x_j} + \frac{1}{2} \frac{\partial (\overline{u_i^2}\, \overline{U}_j)}{\partial x_j} + \frac{1}{2} \frac{\partial (\overline{u_i^2 u_j})}{\partial x_j} \right]$$

$$+ \frac{3\overline{U}_3\, \overline{u_2 u_3} + \overline{U}_2\, \overline{u_3^2}}{x_2} + \frac{2v}{x_2^2} \left[\frac{\overline{u_2^2} + \overline{u_3^2}}{2} + \frac{\partial (\overline{u_2 u_3})}{\partial x_3} \right.$$

$$\left. - 2\, \overline{u_3 \frac{\partial u_2}{\partial x_3}} \right] + \frac{1}{x_2} [\overline{U}_2\, \overline{q^2} + \overline{u_2 q^2}]$$

$$= - \frac{1}{\rho} \sum_{i=1}^{3} \frac{1}{h_i} \frac{\partial (\overline{pu_i})}{\partial x_i} - \frac{\overline{pu_2}}{\rho x_2} + v\, \nabla^2\, q^2 - W \quad , \qquad (4.24)$$

where W is the dissipation function given by

$$W = \sum_{i=1}^{3} \sum_{j=1}^{3} \frac{v}{h_j^2} \overline{\left(\frac{\partial u_i}{\partial x_j} \right)^2} \quad , \qquad (4.25)$$

and q^2 is the turbulent kinetic energy.

As in the case of the momentum equation, a considerable simplification can be obtained by spatially averaging in the angular direction. This yields the equation

$$\sum_{i=1}^{3}\sum_{j=1}^{3}\frac{1}{h_j}\overline{u_i u_j}\frac{\partial\hat{\overline{U}}_i}{\partial x_j}+\frac{1}{x_2}\frac{d}{dx_2}\left[x_2\left(\hat{\overline{U}}_2\overline{\hat{q}^2}+\overline{\hat{u}_2\hat{q}^2}+\frac{\overline{\hat{p}\hat{u}_2}}{\rho}\right)\right]+\frac{3\hat{\overline{U}}_3\overline{\hat{u}_2\hat{u}_3}+\hat{\overline{U}}_2\overline{\hat{u}_3^2}}{x_2}+\frac{2\nu}{x_2^2}\left[\frac{\overline{\hat{u}_2^2}+\overline{\hat{u}_3^2}}{2}-2\,\overline{u_3\frac{\partial\hat{u}_2}{\partial x_3}}\right]=\frac{\nu}{x_2}\frac{d}{dx_2}\left[x_2\frac{d\overline{\hat{q}^2}}{dx_2}\right]-\hat{W}\quad. \tag{4.26}$$

This then is the equation expressing the conservation of energy due to the turbulent velocity fluctuations for flow in rough pipes.

For flow in smooth pipes equation (4.26) reduces to

$$\overline{u_1u_2}\frac{d\overline{U}_1}{dx_2}=-\frac{1}{x_2}\frac{d}{dx_2}\left[x_2\left(\overline{u_2q^2}+\frac{\overline{pu_2}}{\rho}\right)\right]-\frac{2\nu}{x_2^2}\left[\frac{\overline{u_2^2}+\overline{u_3^2}}{2}-2\,\overline{u_3\frac{\partial u_2}{\partial x_3}}\right]+\frac{\nu}{x_2}\frac{d}{dx_2}\left[x_2\frac{d\overline{q^2}}{dx_2}\right]-W\quad, \tag{4.27}$$

which has previously been obtained by Laufer [41]. Laufer showed that the ratio of the second term on the right hand side of this equation to any other term is of the order of the square of the ratio of the spatial micro scale to the pipe radius, and thus that this term is negligible. This same argument applies also to the energy equation for flow in rough pipes. Equation (4.27) can thus be

written as

$$\overline{u_1 u_2}\,\frac{d\overline{U}_1}{dx_2} = -\frac{1}{x_2}\frac{d}{dx_2}\left[x_2\left(\overline{u_2 q^2} + \frac{\overline{pu_2}}{\rho}\right)\right]$$

$$+\frac{\nu}{x_2}\frac{d}{dx_2}\left[x_2\frac{d\overline{q^2}}{dx_2}\right] - W \qquad . \qquad (4.28)$$

The left hand side of this equation represents the energy converted from the mean flow to the fluctuating flow by action of the turbulent shear stress. The first term on the right hand side of this equation represents the rate of energy change due to the transfer of both kinetic and potential energies by the velocity fluctuations in the x_2 direction and is normally referred to as the convective diffusion of total turbulence energy. The second term represents a gradient type diffusion of the turbulent kinetic energy, and the last term represents the direct dissipation of the turbulence energy by viscous effects.

Comparing equation (4.26) to (4.28) it can be seen that these two equations are very similar except that equation (4.26) contains several terms which do not appear in equation (4.28). With the exception of the first term in equation (4.26), these additional terms appear as spatial cross correlations between time averaged fluctuating velocities and mean velocities in the x_2 and x_3 coordinate

directions, and these terms would probably be expected to be relatively small, although this statement cannot be rigorously proven at this time. Also, the first term in equation (4.26) represents the conversion of energy from the mean motion to the fluctuating motion, and this would be expected to be due principally to the action of the $\overline{\hat{u}_1\hat{u}_2}$ shear stress on the longitudinal velocity gradient in the x_2 direction since $\overline{U}_2$ and $\overline{U}_3$ are expected to be small, as are gradients of $\overline{U}_1$ in the x_1 and x_3 coordinate directions. Thus, the energy equation for the turbulence energy in rough pipes will be written as

$$\overline{\hat{u}_1\hat{u}_2}\,\frac{d\overline{U}_1}{dx_2} + \chi - \frac{\nu}{x_2}\frac{d}{dx_2}\left[x_2\,\frac{d\overline{\hat{q}^2}}{x_2}\right] + W = 0 \quad . \qquad (4.29)$$

This equation will be utilized for flow in both smooth and rough pipes by taking χ to be the convective diffusion term in smooth pipes and the convective diffusion term plus the spatial correlation terms in rough pipes. The approach used in investigating this equation will be to experimentally measure all terms except χ and to then calculate this term. Also, some of the components of χ will be measured directly for flow in both smooth and rough pipes to determine roughness effects on them.

Now, the second type of energy balance to be considered is that for conservation of energy of the mean motion. This equation should

be formulated to include the first term in equation (4.29) which indicates the conversion of energy from the mean to the fluctuating flow. Such an equation can be developed simply by multiplying the integrated momentum equation in the longitudinal direction, equation (4.13), by the mean longitudinal velocity gradient in the x_2 direction. This yields

$$\frac{x_2}{R} \; u^{*2} \frac{d\hat{\bar{U}}_1}{dx_2} = \overline{u_1 \hat{u}_2} \frac{d\hat{\bar{U}}_1}{dx_2} + \overline{\hat{U}_1 \hat{U}_2} \frac{d\hat{\bar{U}}_1}{dx_2} - \nu \left(\frac{d\hat{\bar{U}}_1}{dx_2} \right)^2 \quad . \qquad (4.30)$$

This equation indicates that the energy available due to the pressure drop along the pipe is partly converted into turbulence energy by action of the $\overline{u_1 \hat{u}_2}$ shearing stress, partly converted into an energy associated with the presence of the roughness elements, and partly dissipated directly by viscous action. For flow in smooth pipes this equation becomes identical to the mean energy balance originally obtained by Laufer [41] since the $\overline{\hat{U}_1 \hat{U}_2}$ correlation vanishes.

Spectral Analysis

A slightly different approach to the analysis of turbulent flow than that taken in the previous section is an analysis of the kinetic energy of the turbulence fluctuations according to their distributions

over the various frequencies occurring in these fluctuations. Although this method is, in general, more useful in the study of isotropic turbulence than in the study of nonisotropic turbulence, it has been successfully utilized in several investigations of non-isotropic turbulence, including that of Laufer [41], to yield valuable information. The frequency spectra are also useful in that they can be transformed into wave number spectra to indicate eddy size distributions and in that various other quantities, including autocorrelation functions and spatial and temporal micro and macro scales, can be calculated from the frequency spectra.

A brief discussion of theoretical relationships regarding the analysis of energy spectra in smooth pipes has already been presented in the literature survey. Since this type of analysis is concerned with the frequency domain rather than a spatial domain, the theoretical relations for flow in smooth pipes will also be valid for flow in rough pipes. Thus, no new theoretical results will appear for flow in rough pipes, and the relationships presented in the literature review will not be repeated here. For more detailed theoretical analyses, the interested reader is referred to Bendat and Piersol [94], Blackman and Tukey [95], and Kozin [96].

CHAPTER V

EXPERIMENTAL SYSTEM

Wind Tunnel

The apparatus utilized for the experimental portion of this investigation consisted of a closed circuit wind tunnel which is illustrated schematically in Figure 1. Air was supplied by a centrifugal blower to the entrance section through an approximately two foot diameter flexible duct. The rectangular entrance section consisted of a baffle plate, a series of furnace filters to remove any dust or other foreign particles from the air, and a series of screens to dampen any large eddies from the flow. The cross-section of the entrance section was reduced to slightly above one foot square through a transition section in the form of a quarter sine wave. Transition from the square cross-section to the one foot diameter circular cross-section of the aluminum pipe was obtained through a short tapered sheet metal duct. A honeycomb section was also installed at the entrance to the aluminum pipe to further insure that no large eddies would propagate downstream.

Seventy feet of one foot diameter aluminum irrigation pipe preceded the test section in order to insure that the flow would be fully developed at the test section. The length to diameter ratio of approximately seventy is much greater than that usually considered

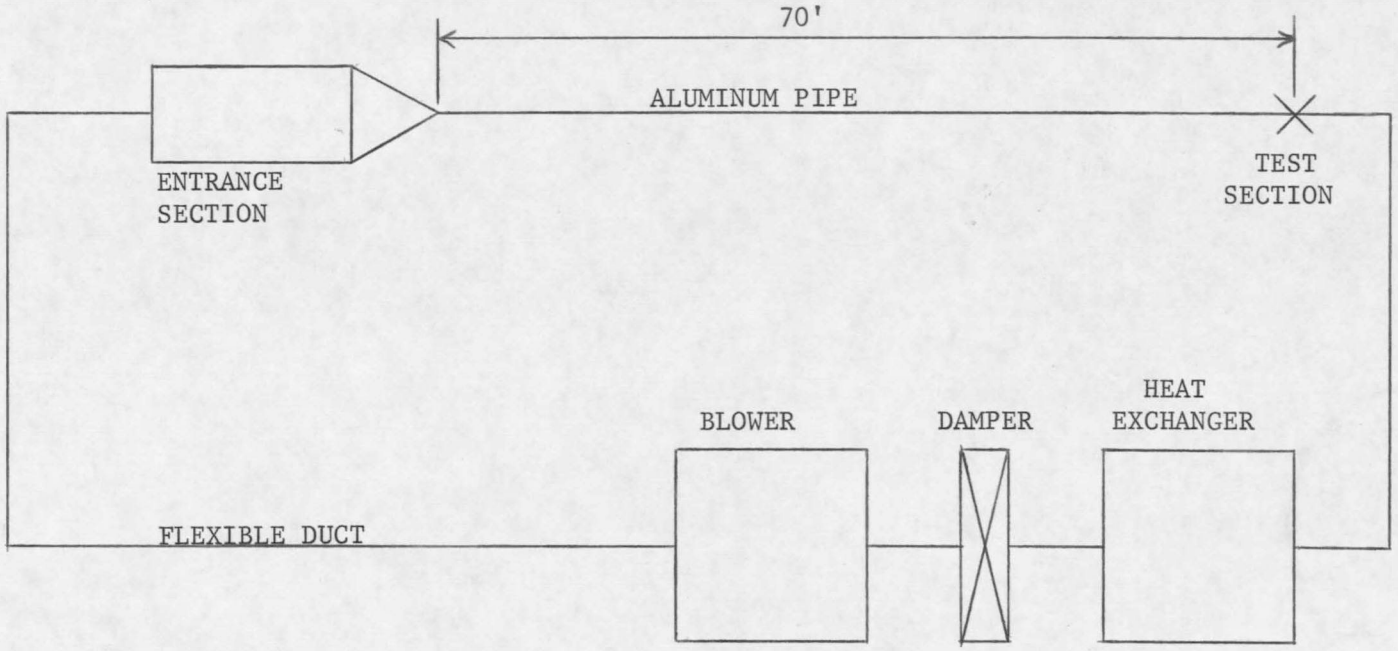

FIGURE 1. Schematic Representation of Wind Tunnel

necessary for the establishment of fully-developed flow, even in a smooth pipe with less suitable entrance conditions. For example, with good entry conditions, Laufer [41] found that a length to diameter ratio of about 19 was sufficient for a smooth pipe, and a much smaller entrance length would be expected for flow in a rough pipe than for flow in a smooth pipe.

Although the aluminum pipe was nominally one foot in diameter, careful measurments indicated an average diameter of 11.883 inches. Thus, the steel test section was machined to this dimension. A traversing mechanism for radial positioning of the probe was mounted on the test section. This mechanism consisted of a probe support holder mounted on two cylindrical rods which were positioned parallel to each other but normal to the test seciton. Motion of the holder on the rods was provided by ball-bearing guides. Twelve positioning rods, machined to lengths differing by precisely one inch, allowed location of a probe to within one inch of a desired position. A micrometer screw feed, having a one inch travel and mounted on the probe support holder, then enabled probe movements of less than 0.001 inches. In order to establish a reference for measuring probe location before each run the probe was moved toward a polished spot on the machined surface until the wire and its image appeared to coincide. This position was then considered to be at zero distance

from the wall. The probe support was free to rotate about an axis normal to the pipe axis, and determination of the angular rotation was made with a protractor attached to the support. Although the test section was normally mounted so that the linear probe movement was vertical, the entire test section could be rotated to allow probe movement in any other direction.

The test section was followed by another section of one-foot diameter aluminum pipe, which was approximately four feet long, to insure that downstream effects would not be felt at the test section. The air was then carried to a heat exchanger by a flexible duct. This heat exchanger consisted of a large rectangular box containing two automobile radiators through which water was circulated. This water flow rate was controlled by means of a throttling valve so that a constant air temperature at the test section was maintained during each run. Such a constant temperature was necessary to eliminate thermal effects on the hot-wire readings and to maintain constant fluid properties. The temperature was monitored by means of a mercury-in-glass thermometer located just downstream of the test section.

The heat exchanger was connected to a manual damper by means of a flexible duct. This manual damper was located on the inlet side of the blower and could be used to control the flow rate through the

system. Flexible ducts were utilized to establish a closed system because of the adverse effects of dust and other foreign particles on the response and calibration of the hot-wire probes.

Pressure Measurements

Two types of pressure measurements were required in this investigation. First, the average static pressure drop along the pipe was necessary for determination of the friction factor, and secondly, a dynamic pressure measurement was necessary for calibration of the hot-wire readings. A series of piezometer rings consisting of four wall taps each were located at various positions along the pipe, beginning at about fifty diameters downstream of the test section, for determination of the static pressure drop. The four wall taps comprising each piezometer ring were located ninety degrees apart and were connected to a single plastic tube which led to a taut diaphram differential pressure transducer. Pressure differences as small as 0.00005 mm Hg and as large as 2 mm Hg could be read with this transducer. Thus the pressure drop between two piezometer rings was read directly with this transducer and then divided by the distance between the piezometer rings to yield the pressure drop per unit length of pipe. This procedure was then repeated for numerous pairs of piezometer rings. Added validity was given to the assumption of

fully developed flow if each of these pressure drops per unit length was nearly the same, and this was found to be the case for all three pipes utilized. A final value for the pressure drop per unit length was obtained by arithmetically averaging the foregoing individual values. These pressure measurements were facilitated by means of the manifold system illustrated in Figure 2.

Although the differential pressure transducer was utilized as a null indicating device, in turbulent flow pressure fluctuations produce an unsteadiness in the meter reading, and this unsteadiness appears as fluctuations about the null reading. A more accurate determination of the null value can be obtained by feeding the electrical output of the pressure transducer into a filter to remove the fluctuating portion of the signal and then displaying the output of the filter on a digital DC voltmeter. This technique is also illustrated schematically in Figure 2.

The second type of pressure measurement required is the dynamic head for calibration purposes. As will be shown later, the hot-wire signal was electronically made linear with velocity, so only a single dynamic head measurement was required for calibration. The pipe center line was selected as the position for obtaining this measurement since the dynamic head will be largest in this location. A one-sixteenth inch diameter impact tube was located just downstream

NOTE: Equipment Abbreviations are Given in Appendix II

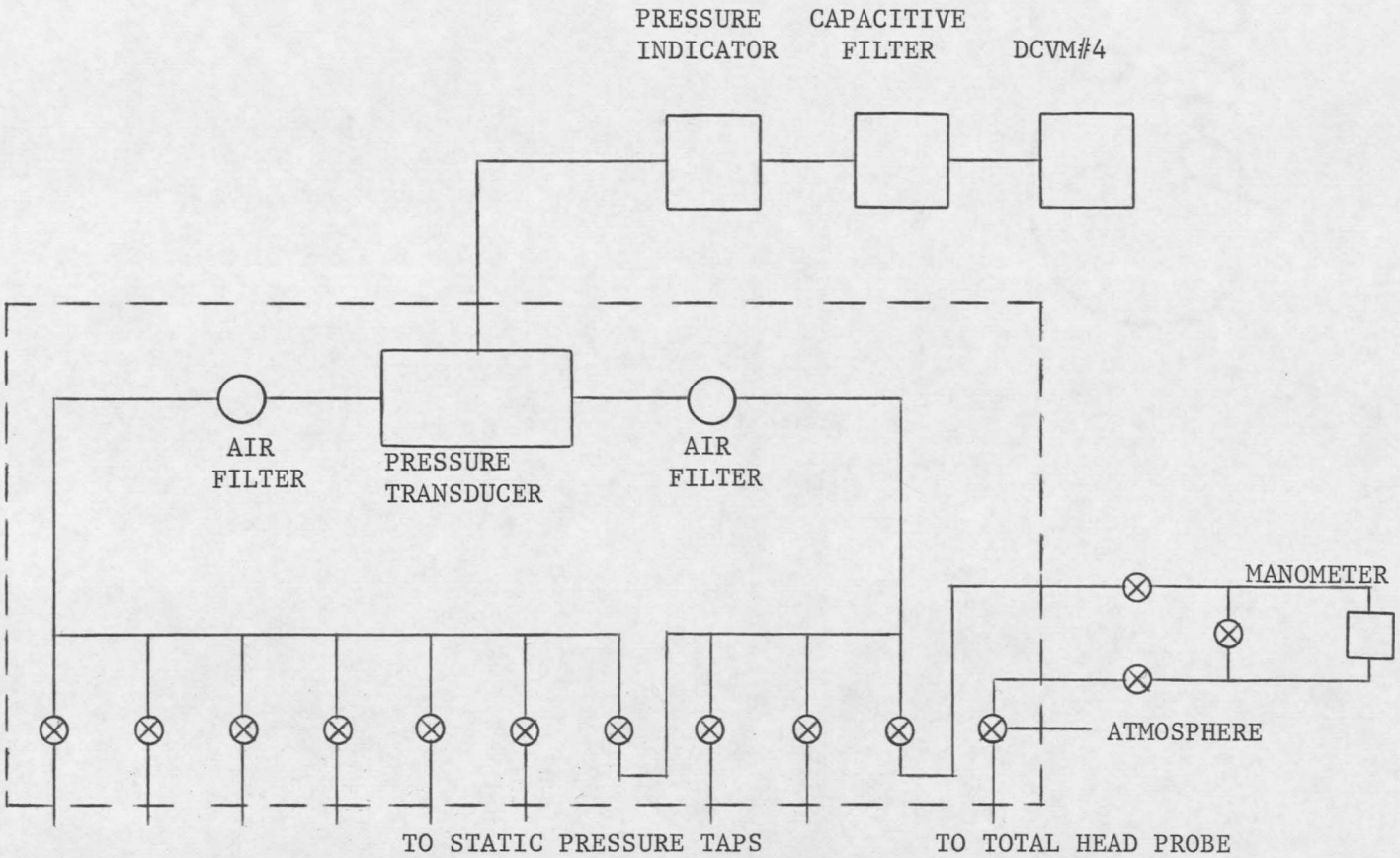

FIGURE 2. Schematic Representation of Pressure Measurement System

of the test section to measure the total pressure at the pipe center line. Since the dynamic pressure is simply the differential between total and static pressure, a static pressure measurement is also required at this location.

In laminar flow the static pressure is a constant at any given longitudinal position and could thus be measured at any radial position. However, this is not the case for turbulent flow as indicated by equation (4.12). Although this would seem to dictate that the static pressure should be measured at the pipe center line in turbulent flow, little information is currently available concerning static pressure measurements within a turbulent flow field. For instance, it is known that the fluctuating velocities have different effects on readings taken from different probes, but the magnitude of these effects is unknown. Thus it would be advantageous to be able to measure the static pressure on the pipe wall with a piezometer ring as described previously. The error involved, due to the radial pressure gradient, in following this procedure can be estimated for flow in smooth pipes from equation (4.12). This equation was applied both to the data of Laufer [41] and that of Gow [15], as well as to that of the current investigation as will be shown later. It was found that, for Reynolds numbers above about 50,000, the maximum error encountered in center line dynamic head readings because of

the radial pressure gradient is less than 0.5%. Thus, dynamic head readings were obtained by measuring the total pressure at the center line and the static pressure at the pipe wall. This reading was made using a water manometer which allowed readings from 0.001 to 20 inches of water.

To enable fluid property determination at the test section, the difference between the static pressure at the wall and atmosphere pressure was also determined with the aid of the water manometer. A barometer reading then allowed calculation of the actual static pressure at the test section. Corrections were applied to this value for the temperature of the water in the manometer and for the temperature of the mercury in the barometer.

Roughness Characterization

In the rough pipe studies, the entire seventy feet of aluminum pipe was replaced by one-foot diameter aluminum pipe with sand grains glued to its inner surface. These sand grains were obtained by sifting between two standard seive sizes, and the roughness size was taken to be the average mesh size of the two screens. Two different roughnesses were utilized; the smaller averaged 0.0286 inches, and the larger averaged 0.225 inches. As mentioned previously, these particular sizes allowed the study of the three flow regimes

(hydraulically smooth, transition, and fully rough) at a single Reynolds number. A water soluble glue was utilized for attaching the sand grains to the pipe wall in both cases. As will be shown later, friction factor measurements indicated that a uniform sand surface resulted in both cases.

As indicated in the literature review, most rough pipe studies are referenced to an equivalent sand diameter, k_s, by comparison with the friction factor curve obtained by Nikuradse [2]. Thus, the rough pipes utilized in this study will also be referenced to k_s in order to enhance comparison with both past and future studies. The method for making this comparison can be briefly described as follows. First, it was necessary to obtain a curve of friction factor versus Reynolds number for each pipe. However, in order to obtain either Reynolds number or friction factor, it is necessary to determine the bulk fluid velocity, $\overline{U}_{avg}$. This can be accomplished by employing equation (2.55) after making several velocity profile runs so that K can be experimentally determined. It should be remembered that this equation is valid for both smooth and rough pipes. Evaluating this equation at the pipe center line, only $\overline{U}_{max}$ and u^* need be determined in order to determine $\overline{U}_{avg}$. $\overline{U}_{max}$ can be evaluated directly from the dynamic head measurements at the pipe centerline, and u^* can be evaluated by employing data for pressure drop per unit length

with equation (2.33). These measurements, together with determination of fluid pressure and temperature, allow calculation of both the friction factor, equation (2.32), and the Reynolds number, Re. The equivalent sand diameter, k_s, can then be determined by employing equation (2.44) with the λ- Re data which lies in the fully developed flow regime. The results of this analysis will be presented in the following chapters.

Electronic Equipment

Constant temperature hot-wire anemometry equipment was utilized for all velocity measurements in the present investigation, and since the theory of operation of hot-wire anemometry equipment has become well known in recent years, only a brief description will be presented here. For more details the interested reader is referred to references [97, 98].

Basically, hot-wire anemometry is concerned with the determination of the convective heat transfer from a heated wire as fluid moves past the wire. If the fluid temperature and thermodynamic properties remain constant, then the convective heat transfer depends only on the fluid velocity and temperature difference between the wire and the fluid. In a constant temperature hot-wire anemometer, the heated wire is maintained at a constant temperature so that the

heat transfer depends only upon the fluid velocity. Maintenance of the wire at a constant temperature is accomplished by connecting the wire as one leg of a Wheatstone bridge curcuit. As the fluid velocity past the wire changes, a change in current passing through the wire is required to maintain the constant temperature, and this is accomplished by means of a feedback loop. The anemometer circuitry is arranged so that the output bridge voltage is proportional to the current through the hot-wire.

The form of the relationship between bridge voltage (wire current) and instantaneous velocity, normal to the wire, V, has been experimentally determined by King [99] to be

$$I^2 r = A + B V^{0.5} \quad , \tag{5.1}$$

where A and B are pure constants. The quantity A represents the intersection of the I^2r versus V calibration curve with the I^2r axis at zero velocity. Although this calibration curve becomes non-linear at very small velocities, it has been shown [97] that for most hot-wire applications, especially in air, A is very closely approximated by the power output at zero velocity, i.e., by the natural convection and conduction losses through the probe supports. Thus, A can be obtained by simply squaring the bridge voltage when the probe is

exposed to a zero velocity flow. Electronically this can be done by utilizing a linearizing circuit to first square the bridge voltage and then to subtract off the bridge voltage obtained in a zero flow situation. Squaring this signal then yields a voltage signal which is directly proportional to the velocity normal to the wire,

$$V = a\ e \quad . \tag{5.2}$$

The temporal mean value of this voltage (velocity) can then be determined by time averaging the signal and displaying it on a digital DC voltmeter, and the rms value of the fluctuating component can be determined by feeding the signal into an rms voltmeter.

It has been noted that the velocity V is the instantaneous fluid velocity normal to the probe, and thus velocity components in the three coordinate directions can be obtained by positioning the probe at different orientations in the flow field. An analysis for the sensitivity of the probe to the various components for an arbitrary orientation is presented in Appendix I.

The anemometer and linearizer circuits described in the foregoing paragraphs were utilized for all velocity measurements in the current investigation. Other instruments used for analyzing the signals from the linearizers will be discussed in the following sections,

and a complete list of equipment is given in Appendix II. It should be noted, however, that Thermo-Systems, Inc. anemometers, linearizers, and probe supports were utilized throughout the investigation. The probes themselves were 0.00015 inch diameter, copper coated tungsten having an active length of 0.05 inches.

Longitudinal Mean and Fluctuating Velocity Components

The analysis in Appendix II shows that the longitudinal mean and fluctuating velocity components can be conveniently measured by placing the hot-wire probe normal to the mean flow direction. In this case the voltage from the linearizer will be given by

$$e = K\ (\overline{U}_1 + u_1) \quad , \tag{5.3}$$

so that the time averaged value or DC component of e will be proportional to $\overline{U}_1$ while the AC component of e will be related to u_1 by the same constant of proportionality. Thus, $K\overline{U}_1$ can be obtained by feeding the signal e into a capacitive filter for time averaging and then displaying the output of this filter on a digital DC voltmeter. The quantity Ku_1' can be obtained by using e as an input to an rms voltmeter which first subtracts out the DC component, $K\overline{U}_1$, and then gives the rms value of the AC component. For convenience

and accuracy, an rms voltmeter having a DC output proportional to rms voltage was utilized, and the output of this voltmeter was displayed on a digital DC voltmeter. A schematic diagram of the instrumentation used for measuring the longitudinal mean and fluctuating components of velocity is shown in Figure 3. The oscilloscope shown in this figure was used for displaying the hot-wire signal so that the frequency response could be optimized using the method described in reference [100]. The signal was also monitored with the oscilloscope throughout each test run to enable the early detection of any malfunctions.

Before the voltage readings could be converted to velocities, it was necessary to determine the value of the constant K. This was accomplished experimentally as follows. First, a dynamic head measurement was made at the pipe center line as described previously, and $\overline{U}_{max}$ was calculated from this dynamic head measurement. Measurement of the DC value of e at the pipe center line then allowed calcuation of K from the equation

$$K = \overline{e} \; / \; \overline{U}_{max} \quad . \tag{5.4}$$

Since the hot-wire signal was electronically made linear with velocity, as described in the previous section, K was taken as constant over

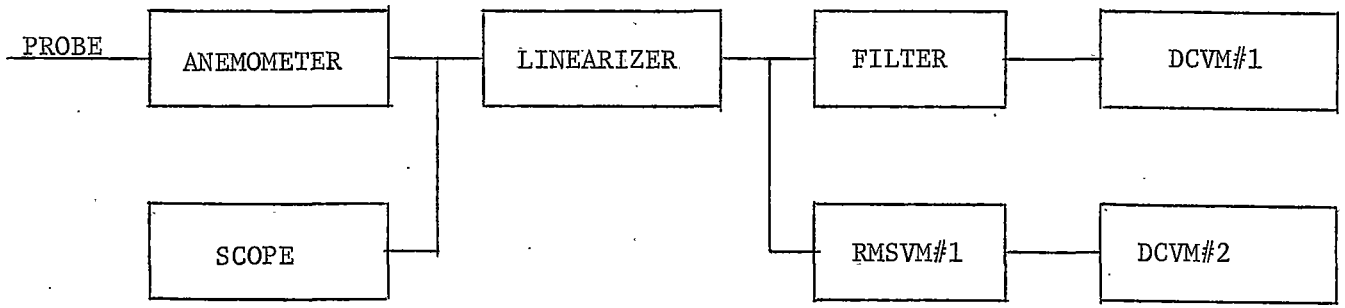

NOTE: Equipment Abbreviations are Given in Appendix II

FIGURE 3. Schematic Diagram of Circuitry for Measuring Longitudinal Mean and Fluctuating Velocity Components

the pipe cross-section. The mean and rms values of velocity at any radial position could thus be determined by dividing the respective voltage readings by K.

Although K was not a function of location in the pipe, it was found to vary slightly with time due to electronic drift and to small temperature changes in the test fluid. Thus, after measurements had been made at a few radial positions, the probe was returned to the pipe center line where the mean voltage was again read, and a new value of K was calculated. K was then taken to vary linearly with time between the two successive calibration points.

In the past, several corrections have been applied to velocity measurements obtained from hot-wire readings, and although most of these are at least partially accounted for by the calibration techniques described above, some deserve consideration at this point. The analysis of the hot-wire sensitivity in Appendix I neglected the higher order turbulence intensity terms in determining the velocity normal to the probe. This is certainly a valid assumption for small turbulence intensities, but at what point do the higher order terms gain significance? This is difficult, if not impossible, to estimate for a non-isotropic turbulence, but it is shown in reference [97] that for an isotropic turbulence with a normally correlated Gaussian distribution, the error in the mean velocity for a 20%

turbulence intensity ($u_1'/\overline{U}_1$) will be about 2% while that for a 50% turbulence intensity will be about 13%. Similar results would be expected for a non-isotropic flow field such as that currently under consideration. Thus, no correction will be attempted for the effect of turbulence intensity, but this discussion should be kept in mind if regions of large turbulence intensity are encountered.

A second type of possible error which should be considered is the possibility of a significant heat loss to the wall when the probe is in close proximity to this surface. An experimental investigation of this situation has been conducted by Wills [101]. He found that hot-wire readings could be corrected for this type of heat loss by subtraction of a constant from Reynolds number, based on wire diameter, to the 0.45 power. This new value is then used in place of the previous Reynolds number. The constant to be subtracted depends only upon the ratio of the wire diameter to the distance from the wall. This correction was applied to all hot-wire readings of the mean velocity in the current investigation. For the particular apparatus under consideration, it was found that this correction became non-zero only as the probe was positioned to within less than 0.02 inches of the wall.

Second Order Velocity Correlation Measurements

Several different types of second order velocity correlations are defined for turbulent pipe flow and will be considered in this section. These include cross correlations between velocity fluctuations in different coordinate directions, $\overline{u_1 u_2}$, $\overline{u_1 u_3}$, and $\overline{u_2 u_3}$, as well as mean squared values of the fluctuating velocities, $\overline{u_1^2}$, $\overline{u_2^2}$, and $\overline{u_3^2}$.

First consider the $\overline{u_1 u_2}$ correlation and the mean squared values $\overline{u_1^2}$ and $\overline{u_2^2}$. As shown in Appendix I, the voltage output of a wire oriented at $\sigma = 0°$ and $\zeta = -45°$ will be

$$e_A = K_A (u_1 + u_2) \quad , \tag{5.5}$$

and the voltage output of a wire oriented at $\sigma = 0°$ and $\zeta = 45°$ will be

$$e_B = K_B (u_1 - u_2) \quad . \tag{5.6}$$

An X-array probe having this wire orientation is available as a standard commercial item. Solving equation (5.5) and (5.6) for u_1 and u_2,

$$u_1 = \frac{e_A}{2K_A} + \frac{e_B}{2K_B} \quad , \tag{5.7a}$$

$$u_2 = \frac{e_A}{2K_A} + \frac{e_B}{2K_B} \quad , \tag{5.7b}$$

and the u_1u_2 cross correlation becomes

$$\overline{u_1u_2} = \frac{\overline{e_A^2}}{4K_A^2} - \frac{\overline{e_B^2}}{4K_B^2} \quad . \tag{5.8}$$

At the pipe center line, $\overline{u_1u_2}$ must vanish; however, this will occur only if the sensitivities of the two wires are indentical, i.e., if $K_A = K_B$. Since it is almost inconceivable to find two wires and electronic circuits with completely identical sensitivities, this condition can be accounted for experimentally by setting the X-array probe at the pipe center line and adjusting gain settings on the e_A and e_B circuits until $\overline{e_A^2}$ and $\overline{e_B^2}$ are equal. Equation (5.7) and (5.8), when time averaged, then become

$$\overline{u_1^2} = K^2 \, \overline{(e_A + e_B)^2} \quad , \tag{5.9a}$$

$$\overline{u_2^2} = K^2 \, \overline{(e_A - e_B)^2} \quad , \tag{5.9b}$$

$$\overline{u_1u_2} = K^2 \left(\overline{e_A^2} - \overline{e_B^2} \right) \quad . \tag{5.9c}$$

Thus, the $\overline{u_1 u_2}$ cross correlation can be obtained by determining the mean square values of e_A and e_B and then subtracting these two values. Similarly, $\overline{u_1^2}$ and $\overline{u_2^2}$ can be determined if some electronic means exists to add and subtract e_A and e_B. This can be accomplished through the use of a standard sum and difference circuit, called a correlator. For inputs e_A and e_B, the functions e_A, e_B, $e_A + e_B$, and $e_A - e_B$ are available at the output. Input attenuators on this circuit also provide a convenient means for setting the sensitivities of the two wires equal. This calibration procedure was repeated each time the probe was returned to the center line for a center line voltage reading. Also, the e_A and e_B signals presently under consideration should be purely AC signals, but it is known that the total signal from the hot-wire will consist of both a mean and a fluctuating component. However, this mean component is removed at the input to the correlator by operation of the correlator in the AC mode, thereby giving the desired result of a purely AC signal.

Before final determination of $\overline{u_1^2}$, $\overline{u_2^2}$, or $\overline{u_1 u_2}$ can be made, the constant K appearing in equations (5.9) must be obtained. This can be accomplished in the following manner. If the X-array probe is rotated through a 90° angle, both wires will be normal to the flow. Consider the upstream wire. Since this wire is normal to the flow, the voltage output from the linearizer will be

$$e = a\,(\overline{U}_1 + u_1) \quad , \tag{5.10}$$

so au_1' can be determined by simply reading the rms value of e as described in the previous section. The constant a can also be determined again by reading e and the dynamic head at the pipe center line, and thus $\overline{u_1^2}$ can be determined. Knowing $\overline{u_1^2}$ and having measured $\overline{(e_A + e_B)^2}$ when the wires were at an angle to the mean flow, K can be determined from equation (5.9a), and $\overline{u_2^2}$ and $\overline{u_1 u_2}$ can then be calculated from equations (5.9b) and (5.9c) respectively.

A schematic of the electronic circuitry utilized in obtaining these measurements is shown in Figure 4. Note that probe A in this figure represents the upstream wire when the probe is rotated so that the wires are normal to the flow. Also it should be pointed out that although complete mean velocity profiles and profiles of $\overline{u_1^2}$ were obtained with this probe, they would be expected to be slightly less accurate than the measurements described in the preceding section with the wire parallel to the solid surface. Thus, the measurements of $\overline{U}_1$ and $\overline{u_1^2}$ obtained with this probe were used for calibration purposes only, and the values of $\overline{U}_1$ and $\overline{u_1^2}$ presented later in the results of this study were obtained with a wire parallel to the solid boundary.

The schematic diagram shown in Figure 4 also applies to the

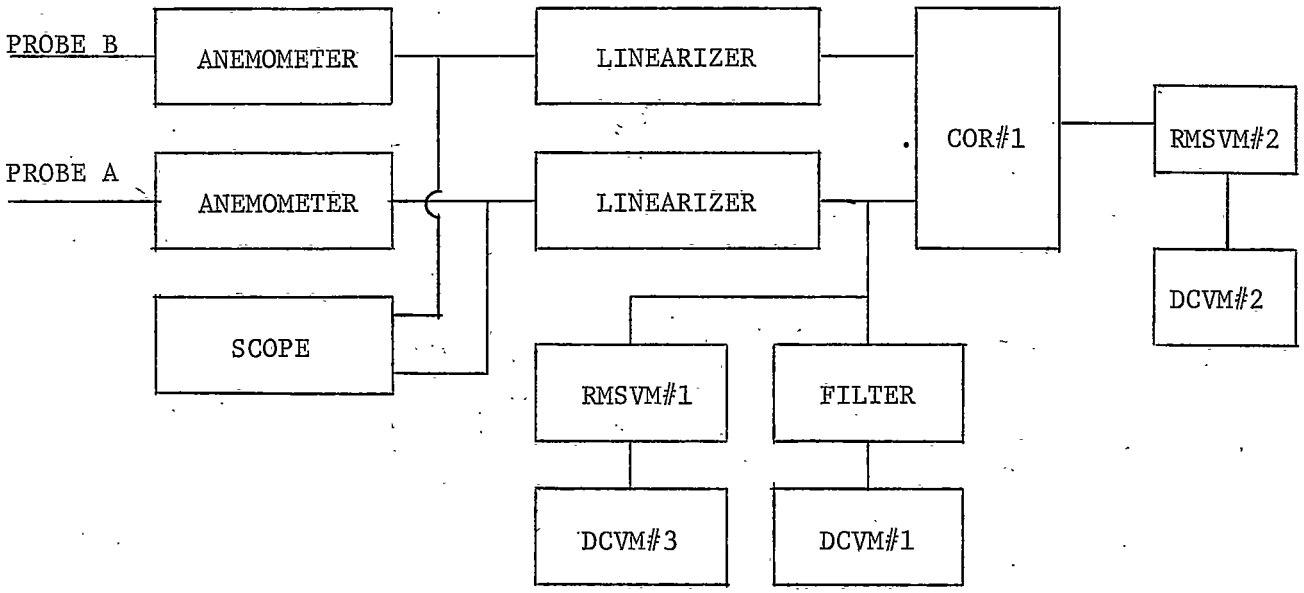

NOTE: Equipment Abbreviations are Given in Appendix II

FIGURE 4. Schematic Diagram of Circuitry for Second Order Correlation Measurements

measurement of the $\overline{u_1 u_3}$ correlation and $\overline{u_3^2}$ as do most of the foregoing comments, with a few minor exceptions. Again an X-array probe is utilized, and it can be seen from Appendix I that if one wire is oriented at $\sigma = 45°$ and $\zeta = 0°$ and the other wire is oriented at $\sigma = -45°$ and $\zeta = -90°$, equations (5.7) and (5.8) still apply if u_2 is replaced by u_3. The wire sensitivities can be set equal experimentally as before so that $\overline{u_1^2}$, $\overline{u_3^2}$, and $\overline{u_1 u_3}$ are given by equations (5.9), again replacing u_2 by u_3. To determine the constant K in this case the probe is rotated through a 45° angle rather than a 90° angle. Rotation is carried out in such a direction that the lower of the two wires is normal to the mean flow, thereby eliminating probe support interferences on this reading. Also, due to the fact that the two wires on this probe are separated by a small radial displacement, a correction, in the form of a linear interpolation between two successive readings, was applied to $\overline{e_A^2}$ and $\overline{e_B^2}$. For flow in the smooth pipe this correction tended to make the $\overline{u_1 u_3}$ correlation vanish over the entire cross-section of the pipe, thereby indicating its validity. The remainder of the previous remarks for the u_1-u_2 probe also apply to the u_1-u_3 probe.

The only remaining second order correlation term is the $\overline{u_2 u_3}$ cross correlation. Measurement of this term would require a combination of the two probes described previously. That is, four

hot-wires, four anemometers, and four linearizers would be required for simultaneous operation, and this would be a very difficult task from an experimental point of view, even if the necessary equipment were available. Fortunately, the $\overline{u_2u_3}$ correlation term does not appear in either the momentum or energy equations, and thus is not required in the investigation of these equations. Also, it was shown theoretically that this term is zero for flow in a smooth pipe, and it is, therefore, expected to be small for flow in rough pipes.

Several types of corrections have also been developed for application to the X-array type probes discussed in this section. For instance, Chapagne et al [102, 103, 104] and Friehe and Schwarz [105] have developed corrections for the cooling effect of velocity components parallel to the wire, and Uberoi and Kavansznay [106] have developed corrections for the effect of the nonzero size of the wire. However, since these terms are at least partially taken into account by the foregoing calibration procedures, no specific corrections were applied for these effects.

Third Order Velocity Correlation Measurements

The only governing equation which contains third order velocity correlation terms in this investigation is the energy equation, equation (4.29), and these terms appear implicitly in the convective

diffusion term χ. Although the technique used in investigating this equation will be to measure all terms except χ and then to calculate this quantity, it would certainly be useful to have some information regarding the variation with roughness of some of the terms comprising χ. For both smooth and rough pipes χ contains the third order correlation terms $\overline{u_2 q^2}$ which can be broken into three separate correlations, $\overline{u_1^2 u_2}$, $\overline{u_2^3}$, and $\overline{u_3^2 u_2}$. As shown in the previous section, the measurement of $\overline{u_2 u_3}$ is extremely difficult from an experimental point of view, and the same wire arrangement would also be required for measuring $\overline{u_3^2 u_2}$, thereby making its determination impractical also. However, the first two terms, $\overline{u_1^2 u_2}$ and $\overline{u_2^3}$, could be obtained with the available instrumentation, and a schematic diagram of the electronic circiutry utilized in these measurements is shown in Figure 5.

Consider first the $\overline{u_1^2 u_2}$ correlation. Using the u_1-u_2 X-array probe described in the previous section, the wire sensitivities can again be set equal experimentally so that u_1 and u_2 are given by

$$u_1 = K(e_A + e_B) \quad , \tag{5.11a}$$

$$u_2 = K(e_A - e_B) \quad . \tag{5.11b}$$

Thus, $\overline{u_1^2 u_2}$ can be written as

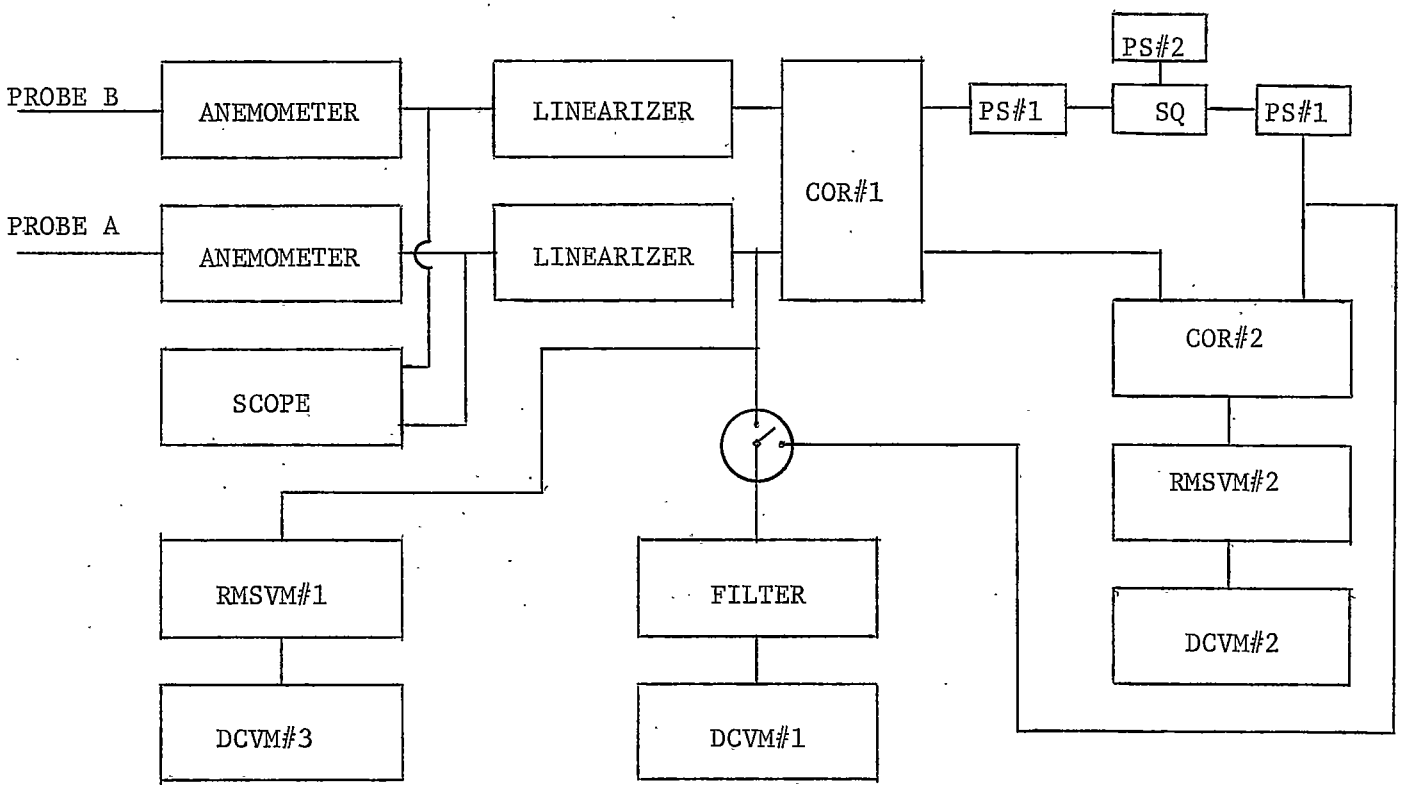

NOTE: Equipment Abbreviations are given in Appendix II

FIGURE 5. Schematic Diagram of Electronic Circuitry for Third Order Correlation Measurements

$$\overline{u_1^2 u_2} = \frac{K^3}{4} \left\{ \overline{[(e_A + e_B)^2 + (e_A - e_B)]^2} - \overline{[(e_A + e_B)^2 - (e_A - e_B)]^2} \right\} \quad . \tag{5.12}$$

The $\overline{u_1^2 u_2}$ correlation can then be obtained if the difference between e_A and e_B can be added to or subtracted from the square of the sum of e_A and e_B. This can be accomplished electronically by means of two correlators. Although not mentioned in the previous section, each correlator has two output terminals, at each of which e_A, e_B, $e_A + e_B$, and $e_A - e_B$ are available. Thus, e_A and e_B can be used as the input to the first correlator while $e_A - e_B$ is taken as one of the outputs. This output is fed directly into the A input of the second correlator. From the second output terminal of the first correlator, $e_A + e_B$ can be fed into a squaring circuit, and the output of this squaring circuit then becomes the B input to correlator number two. Reading the rms value of the output of correlator number two when it is set to add or subtract the inputs then yields the first and second terms in brackets from equation (5.12). These terms cannot be read directly, however. Although the input signals to the first correlator are purely AC signals, a DC component may be introduced by the squaring operation. This DC component can be read

directly on a digital DC voltmeter after the squaring operation. The true rms value of either of the terms in equation (5.12) is then the square root of the sum of the square of this DC component and the square of the rms reading from the output of the second correlator.

A slight problem encountered in utilizing the above technique is that, for a zero input voltage to either the first correlator or to the squaring circuit, the DC outputs of these instruments will not be identically zero, i.e., there will be a small DC offset. This can be subtracted out by placing a variable voltage DC power supply with a floating ground in series with these instruments and adjusting the power supply voltage to null the DC offset.

Calibration of this system was conducted in the following manner. First, a function generator set to yield a sine wave output was utilized to set all input and output gains on correlator number two equal to unity so that the DC component could be read prior to this correlator, and the correlator could be operated in the AC mode. The DC offset of correlator number one and the squaring circuit were nulled as described in the previous paragraph, and the two hot wires were given equal sensitivities by adjusting the input gains on the first correlator. The gain on the first output of correlator number one was set to unity. Since the output of the squaring circuit was only proportional to the actual square of the input signal, it was

necessary to eliminate this scale factor experimentally. This was accomplished by introducing a sine wave into either input of correlator number one and reading the rms value at output number one. The rms value of the square of this sine wave could then be calculated and the gain on output number two of the first correlator was adjusted to yield this desired value at the output of the squaring circuit.

In addition to measuring the quantities indicated by equation (5.12), $\overline{(e_A + e_B)^2}$ was also measured so that the procedure described in the previous section could be utilized for the determination of the constant K. The method described there was also utilized for determining the constant of proportionality between mean voltage and velocity. The entire calibration procedure given in the foregoing paragraph was repeated each time the probe was returned to the pipe center line for mean voltage measurement.

The $\overline{u_2^3}$ third order correlation can be determined in a manner completely analogous to that just described if it is recognized that $\overline{u_2^3}$ can be written, from equation (5.11b), as

$$\overline{u_2^3} = \frac{K^3}{4} \left\{ \overline{[(e_A - e_B)^2 + (e_A - e_B)]^2} - \overline{[(e_A - e_B)^2 - (e_A - e_B)]^2} \right\} \quad . \tag{5.13}$$

In fact, the only difference will be that the quantity being squared will be the difference between e_A and e_B rather than their sum.

Dissipation Function Measurements

Since several specialized techniques were required for determination of the terms appearing in the dissipation function, equation (4.25), a separate section is devoted to this term. First, it was indicated in the literature review that the quantities

$$\overline{\left(\frac{\partial u_i}{\partial x_1}\right)^2} \quad \text{for} \quad i = 1, 2, 3 \tag{5.14}$$

could be calculated from the spatial micro scale of turbulence by equation (2.91), and the determination of the spatial micro scale will be described in the energy spectra analysis. For the present, it is sufficient to realize that the quantities (5.14) can be determined experimentally.

Next, consider the term

$$\overline{\left(\frac{\partial u_1}{\partial x_2}\right)^2} \quad . \tag{5.15}$$

Hinze [9] has shown that this term is related to a spatial correlation

function by

$$\frac{\overline{u_1 u_1(\eta)}}{u_1' u_1'(\eta)} = 1 - \frac{1}{2\overline{u_1^2}} \overline{\left(\frac{\partial u_1}{\partial x_2}\right)^2} \eta^2 + \text{higher order terms} \quad (5.16)$$

where η is a small radial displacement. Laufer [41] neglected the higher order terms appearing in equation (5.16), and although one of these terms was considered by Townsend [12] in a reanalysis of Laufer's data, this term did not appreciably affect the results. Thus, the higher order terms appearing in equation (5.16) will be neglected in the current analysis. Now, realizing that $\overline{u_1^2}$ and $\overline{u_1^2(\eta)}$ will be nearly identical, equation (5.16) can be written as

$$\overline{\left(\frac{\partial u_1}{\partial x_2}\right)^2} = \frac{\overline{[u_1 - u_1(\eta)]^2}}{\eta^2} , \quad (5.17)$$

and this expression lends itself to experimental measurements much better than does equation (5.16).

The utilization of equation (5.17) for the determination of the quantity (5.15) requires the simultaneous measurement of the u_1 fluctuating velocity at two points separated by a small radial displacement, η. This was accomplished by purchasing a specially constructed probe consisting of two wires, each oriented at $\theta = 90°$

and $\zeta = 0°$. The electrical circuit illustrated schematically in Figure 6 was then used for operation of this probe. The correlator was used directly for determination of the difference between the two signals.

Calibration of this circuit was accomplished in the following manner. First, with the probe at the center line of the pipe the output gain on the B linearizer was set to the center of its range, and the output gain on the A linearizer was adjusted to give a mean voltage reading equal to that of the B linearizer. The A linearizer gain was then locked in position for the remainder of the run. Each time the probe was returned to the center line for voltage measurement, the B linearizer gain was adjusted, if necessary, to compensate for differences in drift between the two circuits. Using a known sine wave input from the function generator, the A input gain on the correlator was adjusted to unity, and the wires were experimentally given equal sensitivities by adjusting the B input gain until the rms voltage from probes A and B were equal. The output gain on the correlation was set to unity for the entire run. With the probe at any position other than the center line, the mean and rms voltage readings were then taken to be the averages of the readings from the two wires. Determination of the constant of proportionality between voltage and velocity followed exactly the same procedure

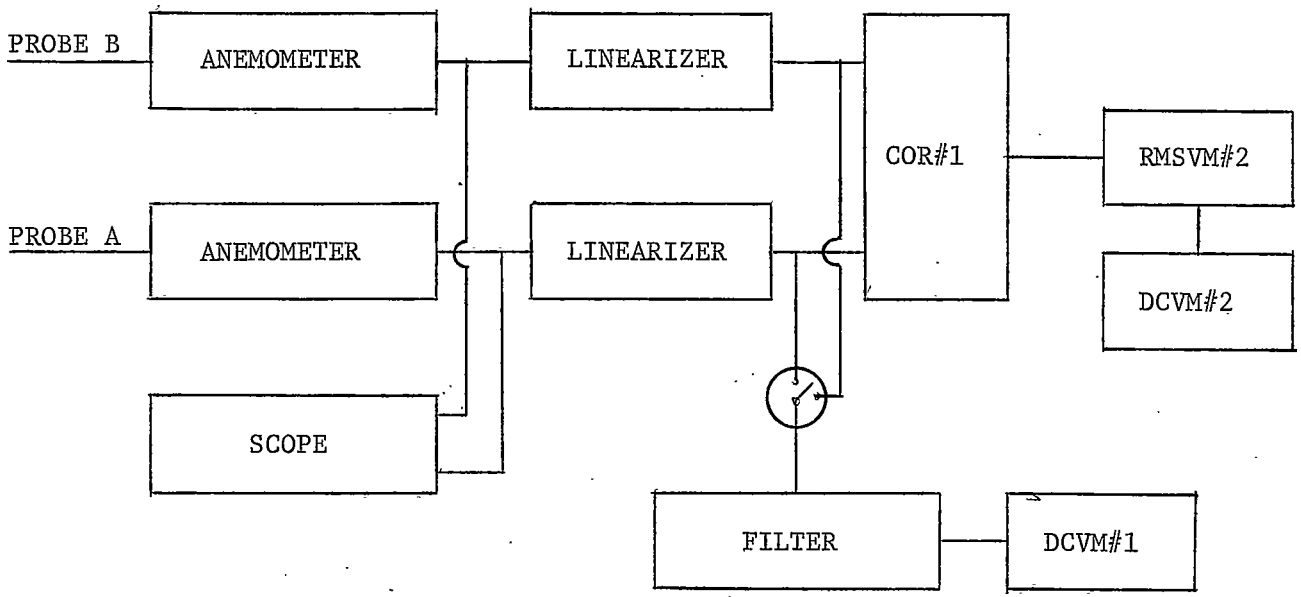

NOTE: Equipment Abbreviations are Given in Appendix II

FIGURE 6. Schematic Diagram of Electronic Circuitry for Operation of Spatial Correlation Probes

outlined in the section on mean velocity measurements.

Consider next the term

$$\frac{1}{x_2^2}\overline{\left(\frac{\partial u_1}{\partial x_3}\right)^2} \quad . \tag{5.18}$$

In a manner analogous to the previous development, this term can be expressed as

$$\frac{1}{x_2^2}\overline{\left(\frac{\partial u_1}{\partial x_3}\right)^2} = \frac{\overline{[u_1 - u_1(\xi)]^2}}{\xi^2} \quad . \tag{5.19}$$

where ξ is a small linear separation distance in the x_3 direction. The purchasing of a specially constructed probe consisting of two wires oriented at $\sigma = 0°$ and $\zeta = 90°$ allowed measurement of the quantity (5.18) using circuitry and calibration procedures identical to that just described.

The wire arrangements and electrical equipment required for the determination of the remaining terms in equation (4.25) make their measurement completely impractical. Thus, as in previous turbulence studies, e.g., that of Klebanoff [107] for a boundary layer and that of Laufer [41] for a smooth pipe, it is assumed that the mean square values of the derivatives with respect to a given coordinate direction separately satisfy the isotropic relations,

$$2\overline{\left(\frac{\partial u_2}{\partial x_2}\right)^2} = \overline{\left(\frac{\partial u_3}{\partial x_2}\right)^2} = \overline{\left(\frac{\partial u_1}{\partial x_2}\right)^2} \quad , \tag{5.20a}$$

$$\overline{\left(\frac{\partial u_2}{\partial x_3}\right)^2} = 2\overline{\left(\frac{\partial u_3}{\partial x_3}\right)^2} = \overline{\left(\frac{\partial u_1}{\partial x_3}\right)^2} \quad . \tag{5.20b}$$

This assumption allows the calculation of the remaining terms in equation (4.25) and thus the complete determination of the dissipation function.

It should be noted that in many previous turbulence studies, the dissipation function has been calculated by assuming isotropic relations between all terms. The resulting expression for W in this case is

$$W = 15\nu \overline{\left(\frac{\partial u_1}{\partial x_1}\right)^2} \quad . \tag{5.21}$$

Although an approximation has been made in the determination of W in the current analysis, the values obtained should be much more reliable than values obtained from equation (5.21). Comparisons will later be made between these two values in order to determine differences in magnitude.

Energy Spectra Measurements

As may be recalled from the literature review, the energy spectrum function $E_i(n)$ for the fluctuating velocity in the x_i direction is defined as the fraction of energy of $\overline{u_i^2}$ contained in a frequency range n to n + dn. Energy spectra for the fluctuating velocities in all three coordinate directions were obtained in the current investigation with the aid of a commercial wave analyzer sensitive to frequencies from about 10 Hz to 620KHz. Although bandwidths of 10 Hz, 100 Hz, 1000 Hz, and 3100 Hz were available on the instrument, only the first two of these were utilized, and calibration of the instrument indicated effective values of 6.2 Hz and 93.3 Hz rather than 10 Hz and 100 Hz. This calibration procedure is described in Appendix III.

The theory of operation of the wave analyzer may be briefly described in the following manner. Two outputs are taken from the instrument, the frequency n at the center of the bandwidth and the ratio of the average value of the rectified voltage appearing within the bandwidth to a reference voltage setting on the instrument. This ratio is indicated on a logarithmic scale in decibels. Thus, the dB output of the instrument is given by

$$dB = 10 \log \left[\frac{e^2_{avg}(n)}{e^2_{ref}} \right] , \qquad (5.22)$$

where $e_{avg}(n)$ represents the average value of the rectified signal appearing in the bandwidth centered on frequency n, and e_{ref} represents the reference voltage setting on the wave analyzer. Now, from equation (2.73) $\overline{u_i^2}$ can be written as

$$\overline{u_i^2} = \int_0^\infty E_i(n)\, dn = \int_0^\infty \frac{\overline{u_i^2(n)}}{\Delta n}\, dn \quad , \tag{5.23}$$

where $\overline{u_i^2(n)}$ is the mean squared value of u_i occurring in the bandwidth Δn centered at frequency n. Recalling that velocity is directly proportional to voltage, equation (5.23) can be rewritten as

$$\int_0^\infty \frac{1}{\Delta n} \frac{\overline{e_i^2(n)}}{\overline{e_i^2}}\, dn = 1 \quad , \tag{5.24}$$

or

$$\frac{e_{ref}^2}{\overline{e_i^2}} \int_0^\infty \frac{1}{\Delta n} \left[\frac{e_{avg}^2(n)}{e_{ref}^2}\right] \left[\frac{\overline{e_i^2(n)}}{e_{avg}^2(n)}\right] dn = 1 \quad . \tag{5.25}$$

Introducing equation (5.22)

$$\frac{e_{ref}^2}{\overline{e_i^2}} \int_0^\infty \frac{1}{\Delta n} \left[\frac{\overline{e_i^2(n)}}{e_{avg}^2(n)}\right] 10^{dB/10}\, dn = 1 \quad . \tag{5.26}$$

Before equation (5.26) can be utilized the ratio of the mean

squared to the rectified average value of e_i must be determined. This would be possible if something were known about the temporal distribution of e_i, and due to the random nature of turbulence, a Gaussian distribution might be suspected. Although this is not exactly the case, as has been shown by previous investigations, the deviation from a Gaussian is not expected to be substantial. Thus, such a distribution was assumed, and preliminary tests with the wave analyzer indicated that the left hand side of equation (5.26) was unity within $\pm 20\%$. This is well within the $\pm$ 40% deviation reported by Robertson et al [47] in their measurements of rough pipe energy spectra.

The deviations obtained from equation (5.26) can be significantly reduced, however, by relaxing the assumption of a Gaussian distribution. Instead, if the ratio of the mean squared to the rectified average value of e_i is only considered to be independent of frequency, as was the case with the Gaussian distribution, equation (5.26) can be rewritten as

$$\frac{e_{ref}^2}{\overline{e_i^2}} \; \frac{\overline{e_i^2(n)}}{e_{avg}^2(n)} = \left[\int_0^\infty \frac{1}{\Delta n} \; 10^{dB/10} \, dn \right]^{-1} . \qquad (5.27)$$

The right hand side of equation (5.27) can conveniently be evaluated by numerical integration of the experimental data, so the energy spectrum function can finally be evaluated from

$$E_i(n) = \frac{\overline{u_i^2}\ 10^{dB/10}}{\Delta n \int_0^\infty \frac{1}{\Delta n}\ 10^{dB/10} dn} \qquad (5.28)$$

The bandwidth Δn appearing in the integral is not cancelled because, in the experimental program, different bandwidths were utilized over different frequency ranges.

Two DC voltage outputs, proportional to frequency and dB respectively, were available from the wave analyzer, and this instrument had the capability of automatically sweeping through a desired frequency range. This made it convenient to feed the signals directly into a Hewlett Packard 2115A digital computer, through an analog to digital converter, for recording. This type of data acquisition system is described by Enochson [108], e.g. Calibration of the analog to digital conversion system, as described in Appendix IV, enabled the frequency and dB to be output directly from the computer.

In preliminary tests with the wave analyzer, it was found that large bandwidths or sweep rates did not yield reliable results for the very low frequencies, so three combinations of bandwidths and sweep rate were utilized to cover the necessary frequency range. These are tabulated in Table 2. Also, for frequencies less than 300 Hz it was found that the voltage signal proportional to frequency

n(min.) Hz	n(max.) Hz	Δn Hz	sweep rate Hz/sec
--	300	10	1
300	2000	100	10
2000	--	100	100

Table 2. Wave Analyzer Operating Ranges

was near zero, and therefore tended to be affected significantly by electronic noise. This problem was eliminated by plotting dB versus frequency directly with an X-Y plotter in this frequency range.

A schematic diagram of the electrical circuit utilized to obtain the $E_1(n)$ spectrum function is shown in Figure 7, and that used to obtain the $E_2(n)$ and $E_3(n)$ functions is shown in Figure 8. These circuits are identical to those utilized for obtaining $\overline{u_1^2}$, $\overline{u_2^2}$, and $\overline{u_3^2}$ except for the addition of the wave analyzer and the instrumentation for recording its outputs. Since the maximum input voltage to the analog to digital converter was one volt, while the outputs of the wave analyzer could reach about twenty volts, a simple resistive network was utilized to attenuate these signals so that they did not exceed a unit voltage. A variable speed pulse generator was utilized with the computer so that sampling rates from the analog to digital computer could be controlled by the source program. During actual

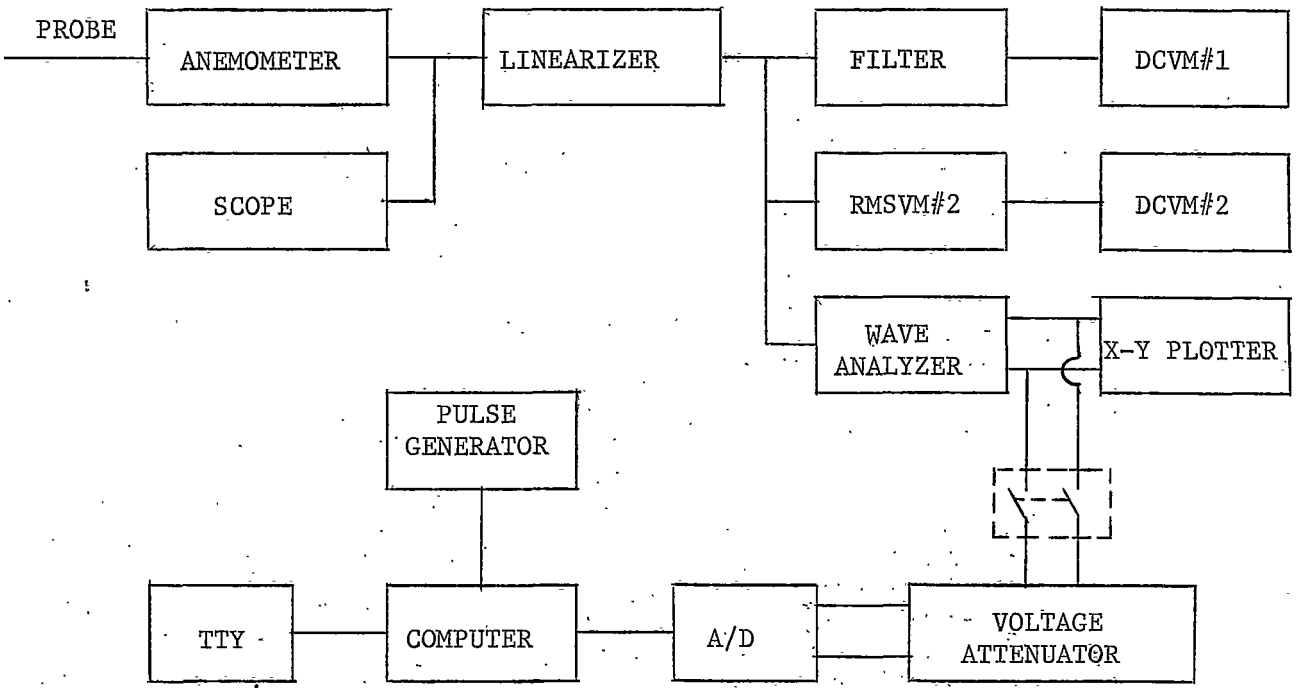

NOTE: Equipment Abbreviations are Given in Appendix II

FIGURE 7. Schematic Diagram of Electrical System Utilized For Obtaining $E_1(n)$ Spectrum Function

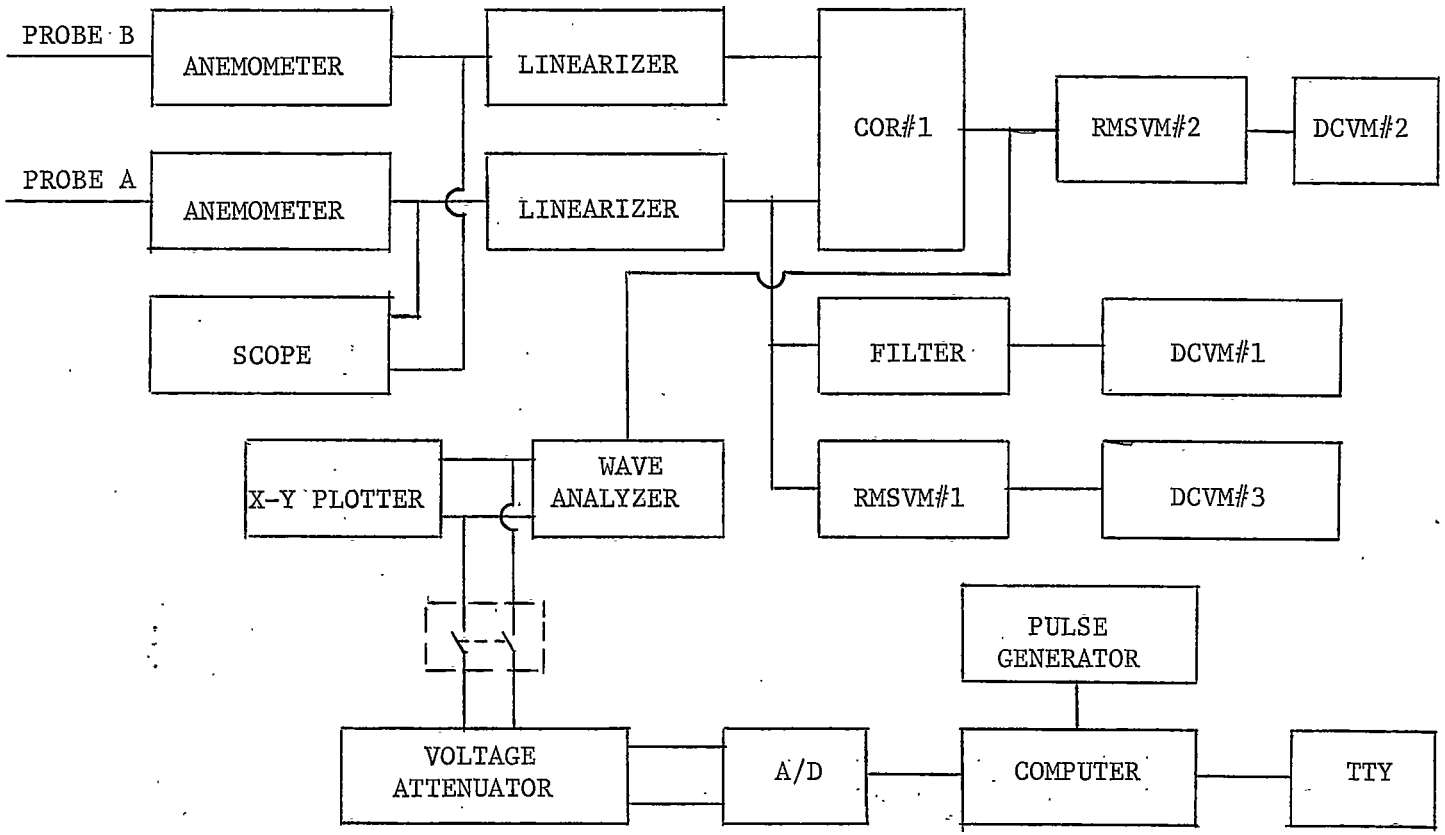

NOTE: Equipment Abbreviations are Given in Appendix II

FIGURE 8. Schematic Diagram of Electrical System Utilized for Obtaining $E_2(n)$ and $E_3(n)$ Spectrum Functions

data runs, control of the computer was exercised through a teletype located in the laboratory with the wind tunnel.

In addition to obtaining frequency domain and wave number domain information from the spectral analysis, autocorrelation functions and turbulence scales were also determined from these data. As stated previously, the autocorrelation function is simply the Fourier cosine transform of the spectrum function,

$$\phi_i(t) = \frac{1}{\overline{u_i^2}} \int_0^\infty E_i(n) \cos n t \, dn, \tag{5.29}$$

and can be obtained by numerical integration. The Eulerian turbulence scales can then be found by numerical integration of energy spectra and autocorrelation functions,

$$\frac{1}{\gamma_i^2} = \frac{1}{2\overline{u_i^2}} \int_0^\infty n^2 E_i(n) \, dn \quad , \tag{5.30}$$

$$T_i = \int_0^\infty \phi_i(t) \, dt \quad . \tag{5.31}$$

Next, spatial turbulence scales can be obtained by applying Taylor's hypothesis, equation (2.77), to the Eulerian scales,

$$\alpha_i = \overline{U}_1 \gamma_i \quad , \tag{5.32}$$

$$\Lambda_i = \overline{U}_1 T_i \quad , \tag{5.33}$$

Elements of the dissipation function, as discussed in the previous section, may finally be obtained from the spatial micro scale,

$$\overline{\left(\frac{\partial u_i}{\partial x_1}\right)^2} = \frac{2\overline{u_i^2}}{\alpha_i^2} \quad . \tag{5.34}$$

Data Reduction

The reduction of the experimental data in this investigation was accomplished through use of an XDS SIGMA 7 and a HP2116A digital computer. The HP2116A was programmed in BASIC for quick calculations, and the bulk of the data reduction was carried out using FORTRAN IVH on the XDS SIGMA 7 computer. A single program was written to determine the longitudinal mean and fluctuating velocities from the voltage data obtained in every experimental run. The corrections described previously for heat loss to the wall and electronic drift were applied in this program.

A subroutine, utilized together with the basic data reduction

program, was used for reduction of any auxiliary data such as the cross correlation data obtained with the X-array probes. Thus it was possible to utilize a single computer program to convert the many different types of voltage data obtained in this investigation to velocity data. This velocity data was recorded both on printed output and on punched cards. These punched cards could then be used as input data to a variety of additional programs for calculation of the quantities of interest. The output from these programs was again in the form of printed output and plots obtained through use of a numerically controlled CALCOMP X-Y plotter. These programs are described in more detail in Appendix V.

One source of difficulty in utilizing the punched card output directly was the fact that in many cases it was necessary to combine the data from two or more different types of runs in order to obtain a quantity of interest, and these data were usually not available at identical radial positions. Therefore, it was necessary to utilize some type of interpolation scheme to match the radial positions, and a linear interpolation was first attempted. Although this method of interpolation normally produced good results, its accuracy was found to be somewhat limited in certain cases.

A second source of difficulty stemmed from the fact that derivatives of measured quantities were required in some instances,

and as is usually the case, the direct numerical evaluation of these derivatives from the experimental data was found to yield unsatisfactory results.

These difficulties were alleviated by utilizing the method described by Powe and Smith [109] to first fit a series of curves to the experimental data, and then using the equations for these curves to reproduce the experimental data and intermediate points. Polynomials were normally used, and they were selected on the basis of how well they reproduced the experimental data rather than on the basis of being physically meaningful equations. As a result, polynomials from the first through the fifteenth order, in radial position, were commonly utilized.

Another source of difficulty was encountered in attempting to numerically evaluate the Fourier transforms encountered in reduction of the energy spectrum data. For instance, consider the integral

$$\int_0^\infty E_i(n) \cos n t \, dn \quad . \tag{5.35}$$

For a given value of t and at large frequencies, an experimental value of $E_i(n)$ will not be available for every cycle of the cosine function, and therefore, a direct numerical evaluation of this integral, using Simpson's rule e.g., will not be accurate. This problem can be eliminated in the following manner. Consider two

adjacent experimental values of the spectrum function, $E_i(m_j)$ and $E_i(m_{j+1})$, and assume a linear variation of $E_i(n)$ between frequencies m_j and m_{j+1}. Functionally, $E_i(n)$ can then be expressed, within this frequency range as

$$E_i(n) = E_i(m_j) + \frac{n - m_j}{m_{j+1} - m_j} \left[E_i(m_{j+1}) - E_i(m_j)\right] \quad , (5.36)$$

where $E_i(m_j)$ and $E_i(m_{j+1})$ are known experimental values. Utilizing this expression, the integral (5.35) can be written as

$$\int_0^\infty E_i(n) \cos n\,t\,dn = \sum_{j=1}^{N-1} \frac{1}{t} \left\{ \left[\left(1 + \frac{m_j}{m_{j+1} - m_j}\right) E_i(m_j) \right.\right.$$

$$\left. - \frac{m_j}{m_{j+1} - m_j} E_i(m_{j+1}) \right] \left[\sin(m_{j+1}t) - \sin(m_j t) \right.$$

$$+ \frac{1}{m_{j+1} - m_j} \left[E_i(m_{j+1}) - E_i(m_j)\right] \left[\frac{1}{t} \cos(m_{j+1}t) \right.$$

$$\left.\left. - \frac{1}{t} \cos(m_j t) + m_{j+1} \sin(m_{j+1}t) - m_j \sin(m_j t)\right] \right\} \quad , (5.37)$$

for t not equal to zero, N being the total number of experimental data points, and $E_i(n)$ equal to zero for all frequencies larger than N. Evaluation of the integral from equation (5.37) results in the

inclusion of all cycles of the cosine term and eliminates the previously described difficulty.

In previous investigations, energy spectrum data have usually been presented in the form of plots of the spectrum function versus frequency at a given radial position. Such a curve was plotted for several radii, thereby yielding a family of curves. In the current investigation, energy spectra were obtained in approximately thirty radial positions for the fluctuating velocities in all three coordinate directions, making it necessary to devise an alternative means of presenting these data. This was accomplished by obtaining contour maps of the spectrum functions, thereby allowing the data to be presented in a concise but meaningful form.

All of the final results of this investigation were obtained in the form of plots generated by a CALCOMP X-Y plotter controlled by the XDS SIGMA 7 computer. Printed output was also obtained as supporting information for these plots. These results will be presented in the following chapters. It should be noted that the solid lines appearing on the plots in these chapters represent the equations obtained by curve fitting the experimental data, unless otherwise indicated. All directly measured experimental data are also presented on these plots.

CHAPTER VI

SMOOTH PIPE RESULTS

Mean Velocity and Flow Resistance

In order to establish the fact that the smooth pipe did, in fact, yield flow in the hydraulically smooth regime, measurements were first made of friction factor versus Reynolds number over a wide range of Reynolds numbers. This was accomplished by utilizing Gow's [15] mean velocity data to determine values of K from equation (2.56). These calculations indicated that K was independent of Reynolds number and equal to approximately 0.336. Thus solving equation (2.56) for $\overline{U}_{avg}$,

$$\overline{U}_{avg} = \overline{U}_{max} - 1.5u^*/K \quad , \tag{6.1}$$

it is found that $\overline{U}_{avg}$ can be determined if the maximum mean velocity and the shear velocity are known, and these two quantities can be evaluated from dynamic and static pressure measurements. Therefore, a friction factor versus Reynolds number curve can be obtained solely from pressure measurements, and such data are presented in Figure 9. The solid line on this figure represents Prandtl's universal friction factor equation for turbulent flow in smooth tubes, equation (2.35), and the experimental data do indicate that the flow is in the hydraulically smooth regime over a wide range of Reynolds numbers.

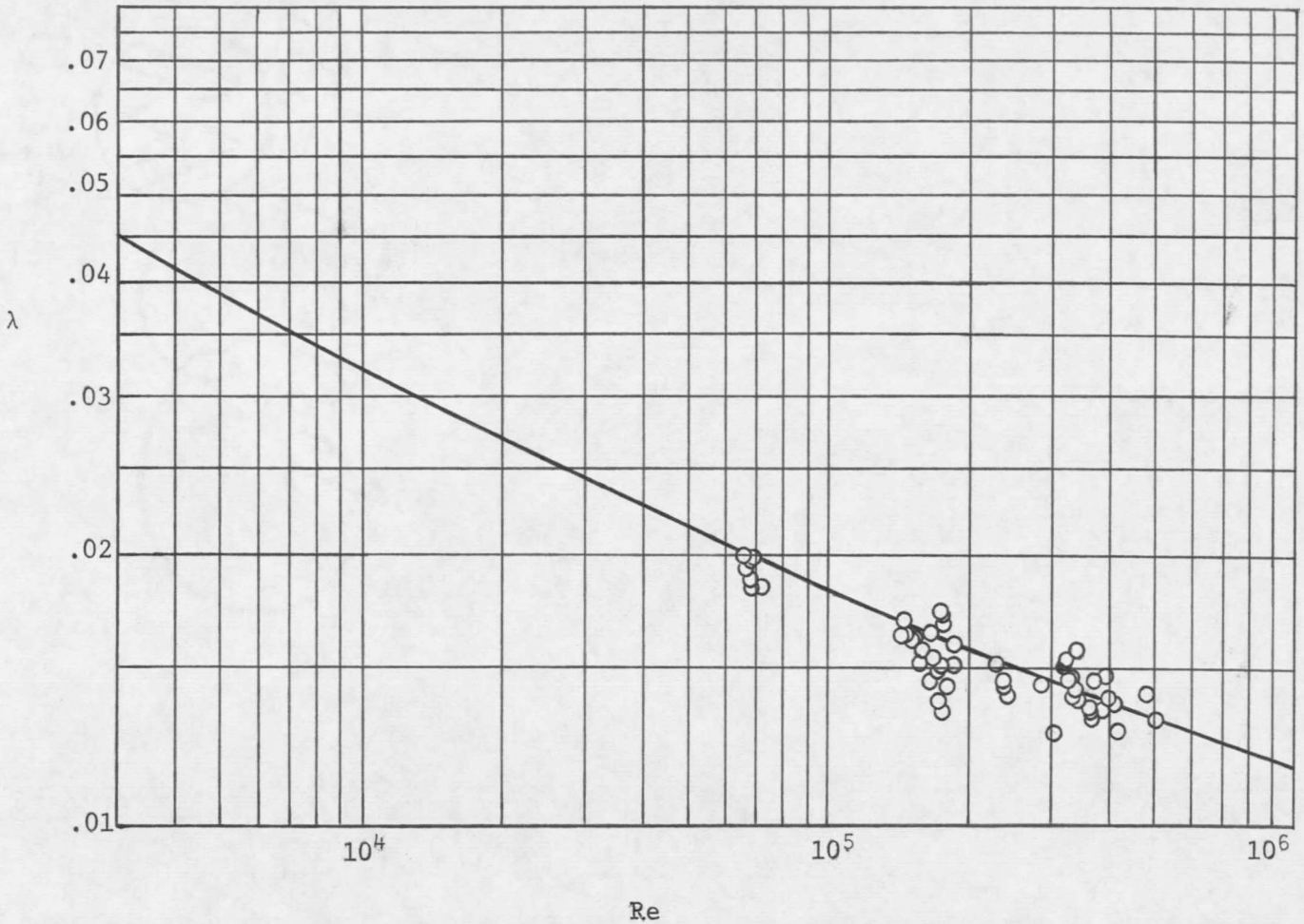

FIGURE 9. Flow Resistance Characterization for Smooth Pipe

Specifically, all measurements described in this section are made at a Reynolds number of 165,000 yielding a value of y^+ at the center line of 3510. Mean velocity measurements at the selected Reynolds number are shown in Figure 10 for the center portion of the pipe and in Figure 11 for the wall region. The dashed line in Figure 11 is the velocity gradient at the wall obtained by evaluating the integrated momentum equation, equation (4.13), at the solid boundary. This yields

$$\frac{d\overline{U}_1}{dx_2} = -\frac{u^{*2}}{\nu} \quad . \tag{6.2}$$

Thus, by employing equation (6.2) the velocity gradient at the wall can be predicted directly from measurements of the static pressure drop along the pipe and a check on the mean velocity measurements is obtained. The dashed line in Figure 11 shows excellent agreement with the mean velocity profile obtained with the hot-wire anemometer and corrected for the heat loss to the wall.

The solid line in Figures 10 and 11 represents values of the mean velocity predicted by the empirical equation obtained from a curve fit of the mean velocity data. Although the curve fitting procedures were not meant to generally yield physically significant equations, this particular equation appears to be general enough to warrant further consideration. It was obtained by modifying and

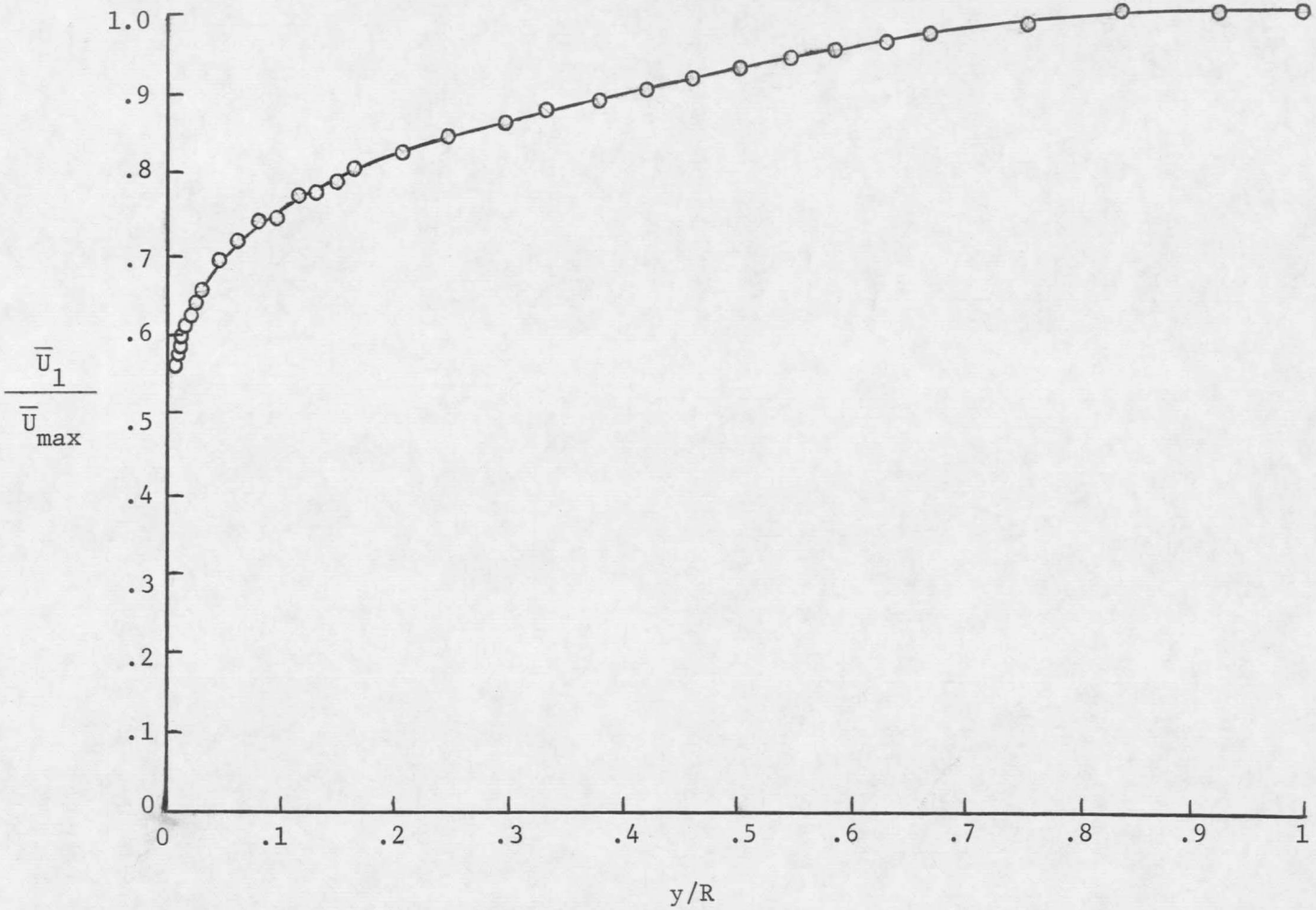

FIGURE 10. Mean Velocity Profile for Center Portion of Smooth Pipe

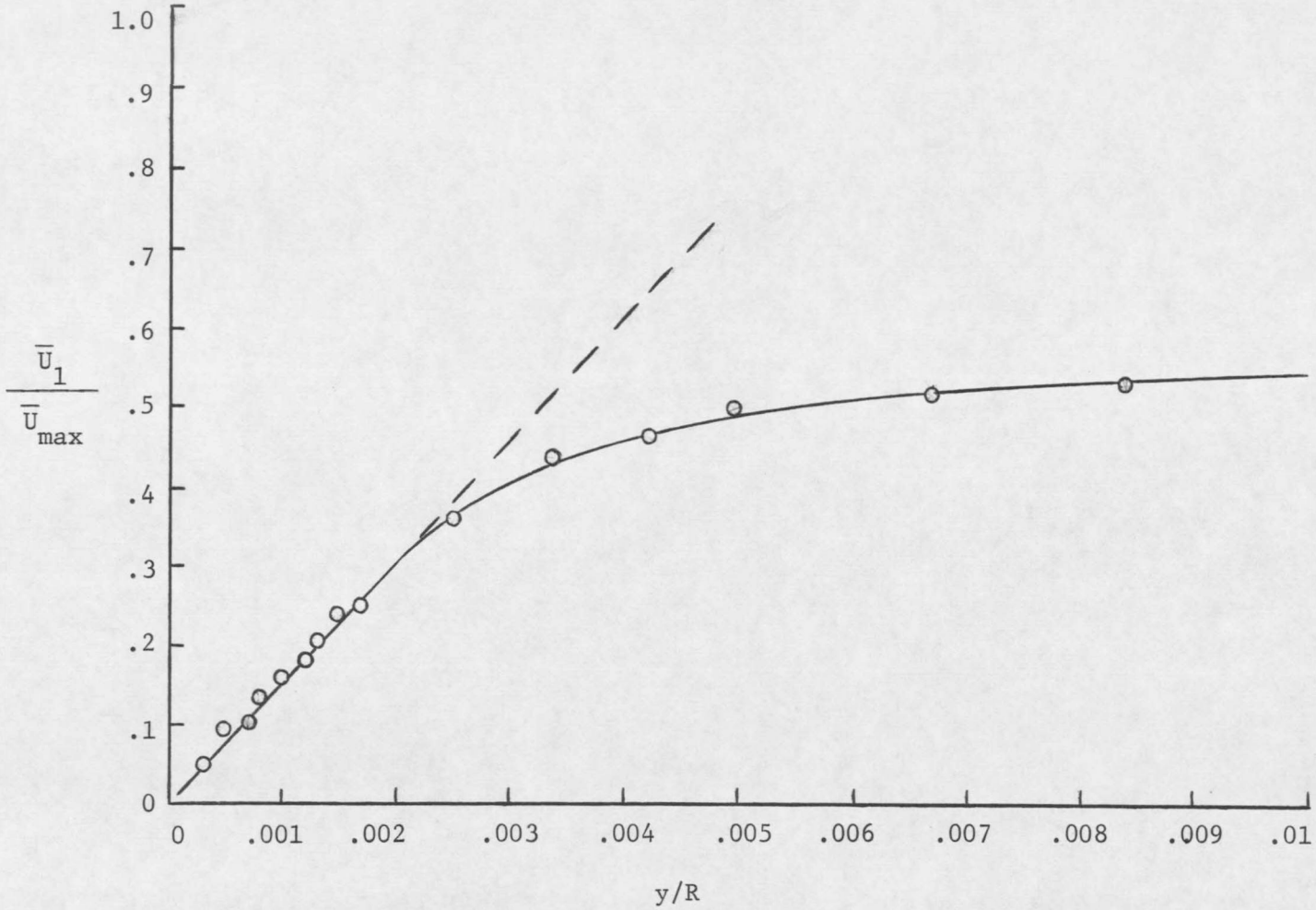

FIGURE 11. Wall Region Mean Velocity Profile for Smooth Pipe

combining two previously proposed relations for different regions of the pipe. Kays [13] has shown that equation (2.14) not only allows for a slight Reynolds number dependence but also yields a zero velocity gradient at the pipe center line in contrast with the standard logarithmic relation. Longwell [18] indicates that equation (2.16) satisfies the wall boundary conditions and yields continuity in the velocity and its gradient at y_a^+, the point where this equation is matched with a relationship for the center region of the pipe. During the course of the current investigation it was found that all boundary conditions, as well as the Reynolds equations, could be satisfied by a relationship of the form

$$u^+ = A_2 + B_2 \ln (Z) \text{ for } Z \geq Z_a \tag{6.3a}$$

$$u^+ = A_3 \tanh (Z/A_3) \text{ for } Z \leq Z_a \quad , \tag{6.3b}$$

where Z is defined by

$$Z = \frac{1.5\, y^+ (1 + x_2/R)}{1 + 2(x_2/R)^2} \quad . \tag{6.4}$$

Curve fitting Gow's [15] velocity profile data in the center region of the pipe ($y^+ > 30$) for Reynolds numbers between about 50,000 and

and 500,000 allowed the determination of A_2 and B_2 as 5.98 and 2.42, respectively. These values are in excellent agreement with the coefficients of the standard logarithmic equations listed in Table 1. Having values for A_2 and B_2, the constants A_3 and Z_a can be calculated from the requirement of continuity of u^+ and its gradient at Z_a. By this method A_3 and Z_a were determined to be 14.68 and 27.75 respectively. An error analysis for 25 velocity profile runs performed by Gow [15] in the given Reynolds number range revealed an average deviation from equations (6.3) of only 2.4%, while 98% of these data were within $\pm 10\%$ of the equation. Thus, equations (6.3) appear to represent universal velocity profile expressions and have the advantage over previously proposed relationships of satisfying all boundary conditions as well as the Reynolds equations.

Fluctuating Velocities

The rms values of the fluctuating velocities in the three coordinate directions are presented in Figure 12 for the central region of the pipe and in Figure 13 for the wall region. In contrast with Laufer's [41] results, Figure 12 indicates that isotropic flow is not attained at the pipe center line since the three fluctuating velocity components are not equal at that point. However, as required by equation (4.11), u_2' and u_3' are found to become equal when x_2

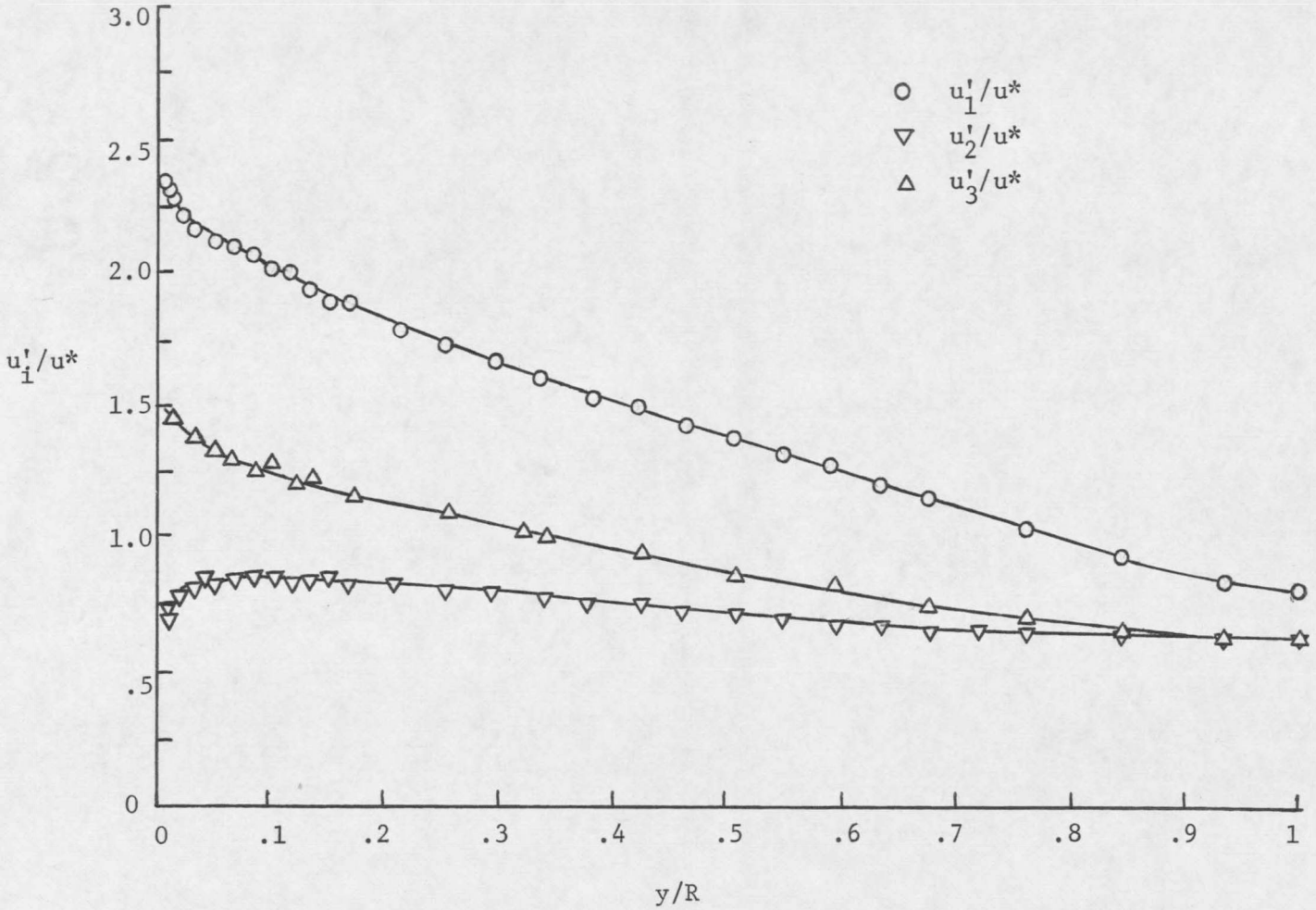

FIGURE 12. RMS Values of Fluctuating Velocities in Center Portion of Smooth Pipe

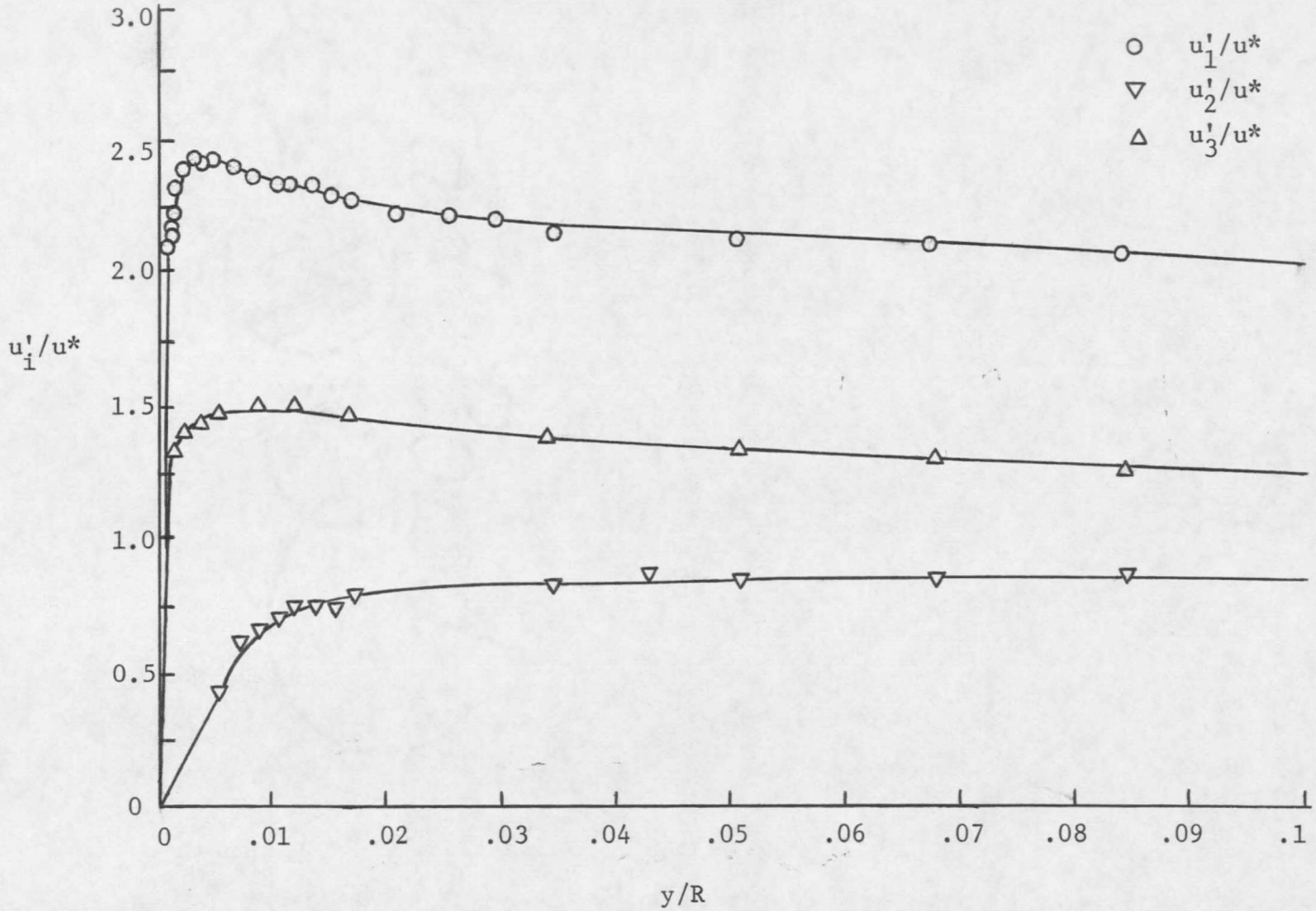

FIGURE 13. RMS Values of Fluctuating Velocities Near Wall of Smooth Pipe

vanishes. This finding is in agreement with the results of Clark [39], Gow [15], and Robertson et al [46] who all found u_2' and u_3' to be equal at the center line while u_1' had a slightly larger value. The magnitudes of the rms values of the fluctuating velocities, when normalized with the shear velocity, were found to be near 0.8 at the pipe center line in all the aforementioned investigations, and such magnitudes are also indicated in Figure 12. This figure shows that, for values of y/R less than unity, all the u_i' increase, u_1' at the fastest rate and u_2' at the slowest. A maximum value of u_1' was found to be attained at $y^+ = 14$ (y/R = 0.004), while maximum values of u_3' and u_2' were found at $y^+ = 28$ and $y^+ = 35$ respectively. The y^+ value of 14 for the maximum in u_1' is identical to the value discovered by Clark [39] and extremely close to the value of 15 given by Hinze [9] in his analysis of Laufer's [41] data.

It should be recalled that one of the assumptions made in utilizing the hot-wire anemometry equipment is that a small turbulence intensity exists. The intensities of the three fluctuating velocities in the current investigation are indicated in Figure 14, and it can been seen that all intensities remain less than about 20%, except possibly for points extremely near the wall. In view of the fact that it has been shown in reference [97] that a 20% turbulence intensity leads to an error of only about 2% in the mean velocity for an

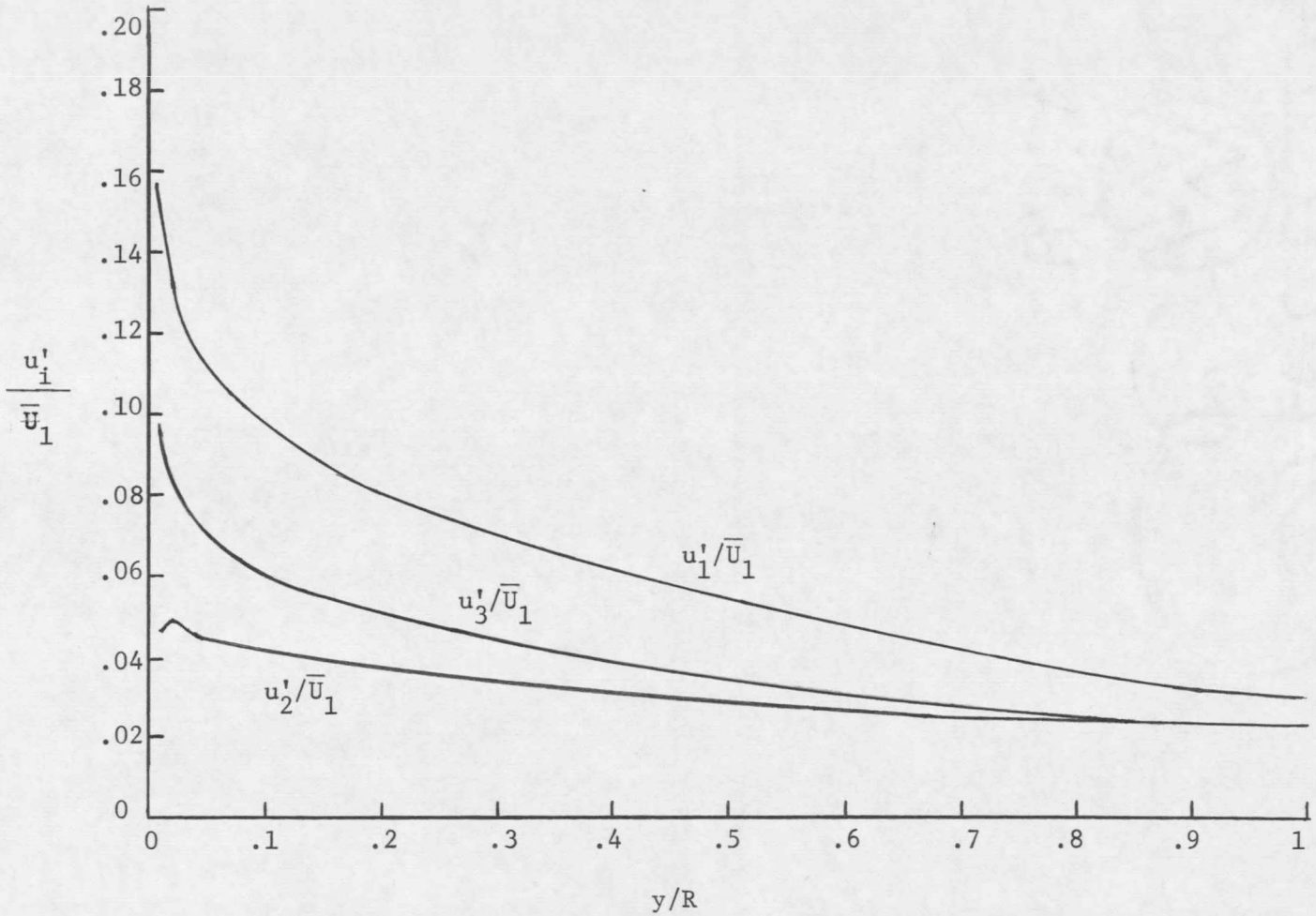

FIGURE 14. Turbulence Intensities for Smooth Pipe

isotropic turbulence with a normally correlated Gaussian distribution, the turbulence intensities indicated in Figure 14 are not expected to produce significant errors in the present results.

It has been indicated in the previous paragraphs that the flow in the smooth pipe was non-isotropic, but no quantitative measure of the degree of anisotropy has been given. One such measure is given by the ratios of the rms values of the fluctuating velocities in two different coordinate directions, called anisotropy ratios. For a perfectly isotropic flow, the anisotropy ratios would equal unity throughout the flow field, and therefore, the deviation of the anisotropy ratios from unity is an indication of the degree of anisotropy. Such results from the current investigation are indicated in Figure 15. In agreement with the investigation of Robertson et al [46], the anisotropy ratio u_2'/u_1' is seen to increase in an approximately linear fashion from y/R = 0.1 to y/R = 1.0. Numerical values of this ratio shown in Figure 15 are also in reasonable agreement with values obtained by Robertson et al [46]. They found values of 0.6 at y/R = 0.1 and 0.9 at y/R = 1.0, while values of 0.45 at y/R = 0.1 and 0.8 at y/R = 1.0 are indicated from the current results. The behavior of the two remaining ratios is somewhat similar to that just indicated for u_2'/u_1', i.e., their variation is approximately linear from y/R = 0.1 to y/R = 1.0. However, magnitude differences do occur in the three

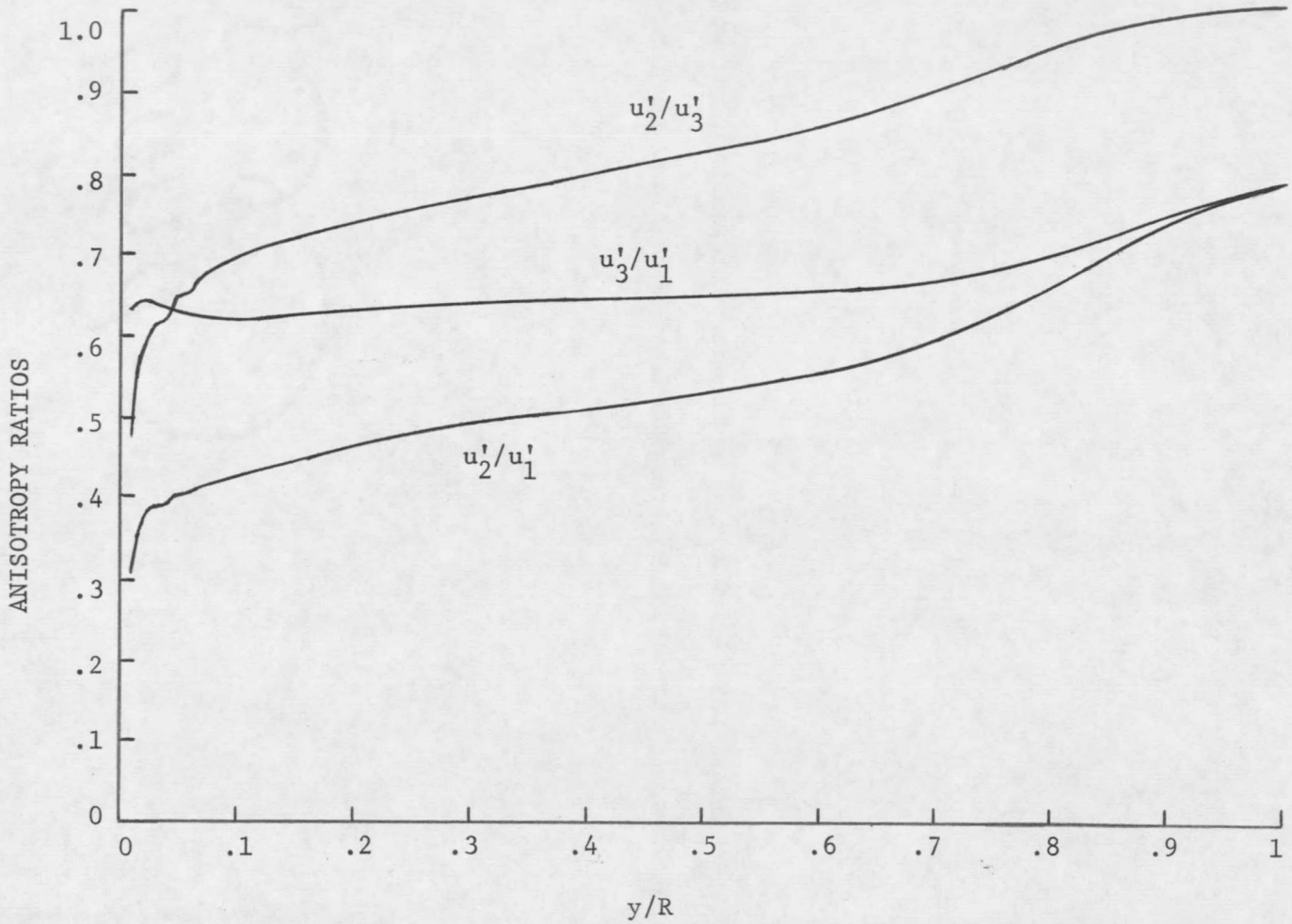

FIGURE 15. Smooth Pipe Anisotropy Ratios

ratios. At y/R = 0.1, u_3'/u_1' has a value of about 0.6, while u_2'/u_3' is approximately 0.7, and at the pipe center line u_3'/u_1' and u_2'/u_3' are 0.8 and 1.0 respectively. As expected, Figure 15 indicates a tendency toward isotropy by u_2' and u_3' at the pipe center line while u_1' prevents the flow from becoming completely isotropic. Substantial deviations from isotropic flow are indicated throughout the remainder of the pipe.

Measurement of the fluctuating velocities in the three coordinate directions allows the calculation of the turbulence kinetic energy, and this quantity will be of considerable importance in later considerations. Figures 16 and 17 indicate that this quantity, when normalized with the square of the shear velocity, has a value near unity at the pipe center line and then increases as x_2 increases. This rate of increase is very small near the center line but increases as x_2 increases. A maximum value of about 4.0 is acquired at a value of y/R of approximately 0.01, and $\overline{q^2}/u^{*2}$ then decreases rapidly to zero. These results are in very good agreement with Hinze's [9] analysis of Laufer's data, although Hinze indicates a maximum value of slightly greater than five. This is likely due to the Reynolds number difference between the two investigations since 165,000 was utilized in the current study while Hinze considered Laufer's results for a Reynolds number of 500,000.

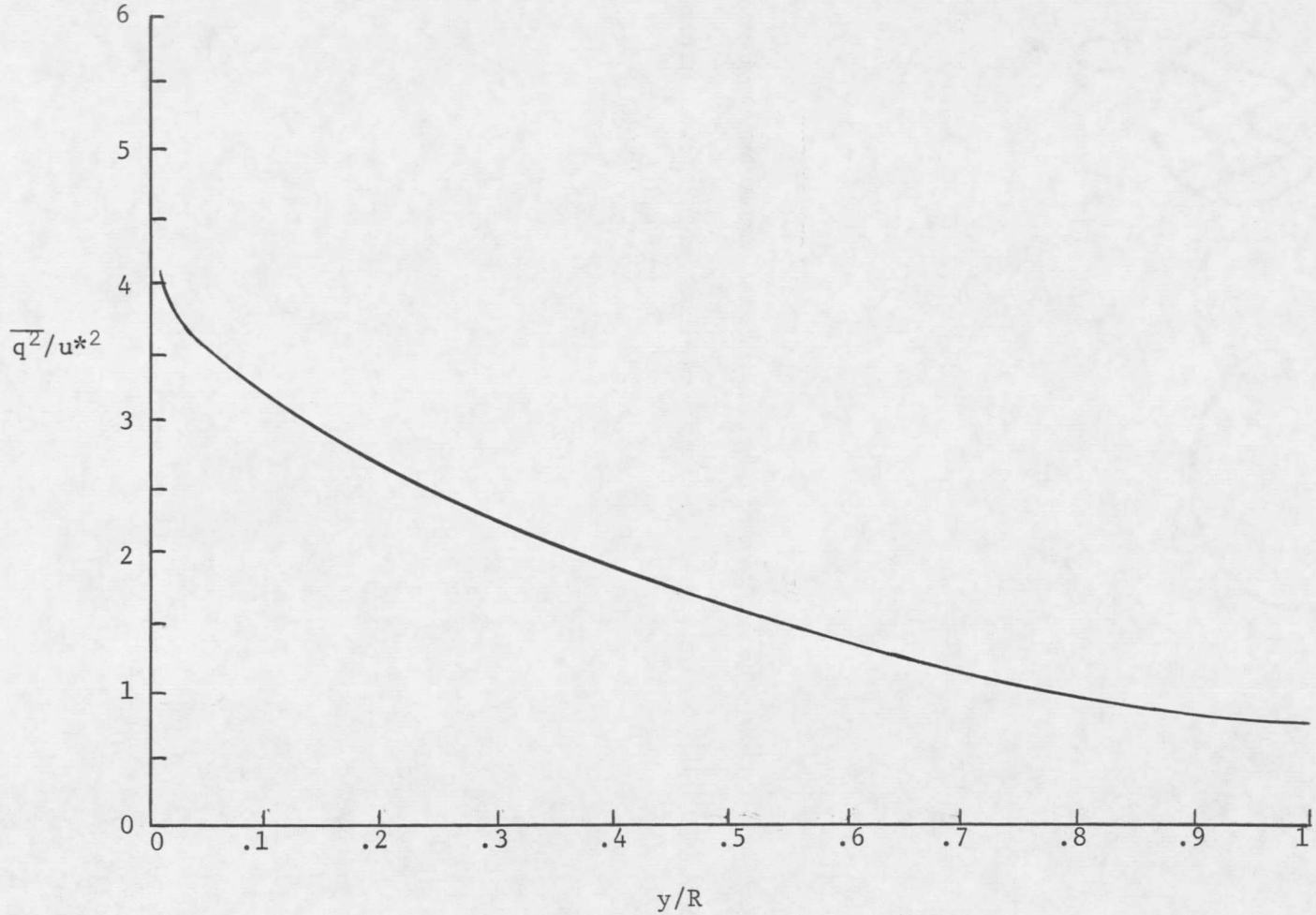

FIGURE 16. Turbulence Kinetic Energy for Central Region of Smooth Pipe

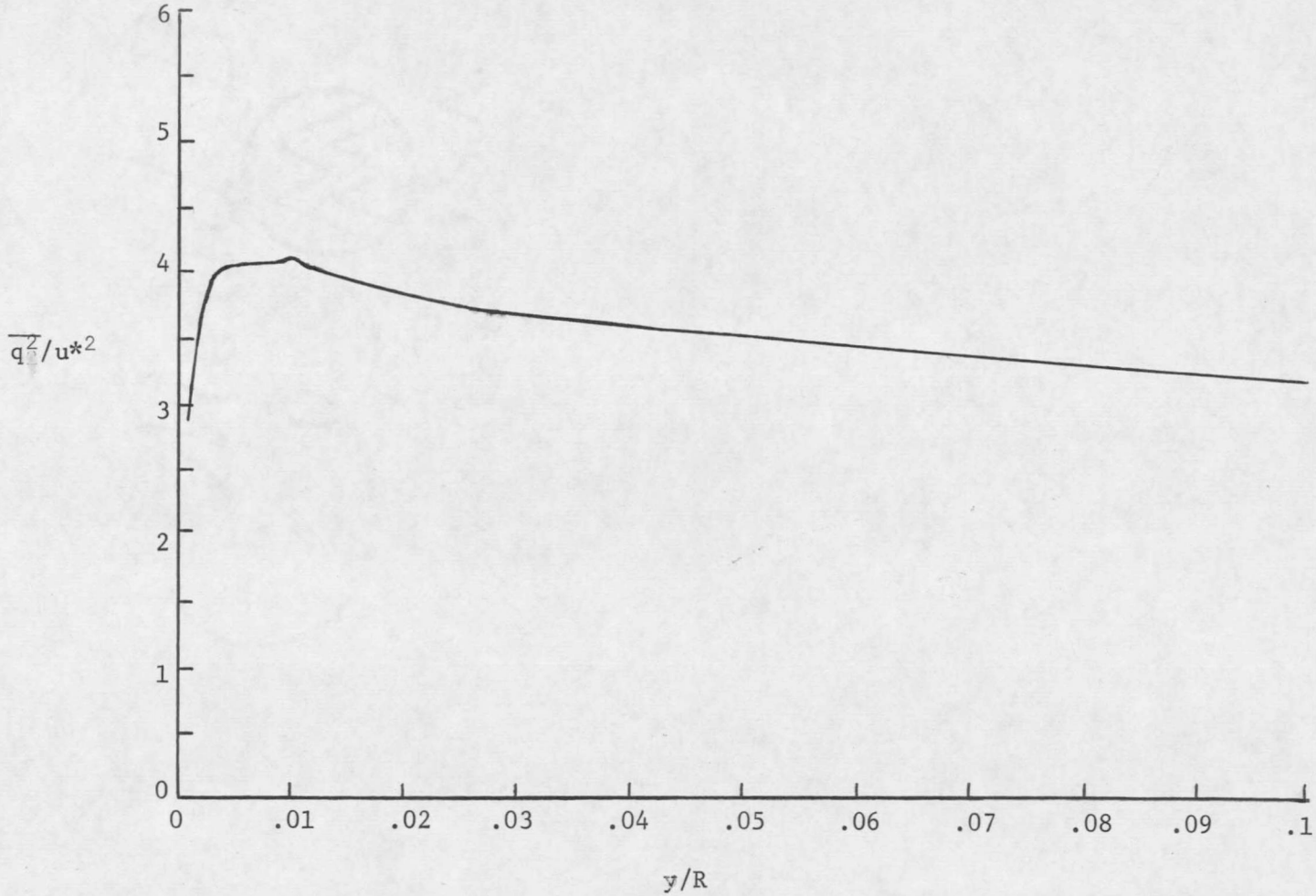

FIGURE 17. Turbulence Kinetic Energy for Wall Region of Smooth Pipe

A knowledge of the fluctuating velocities in the x_2 and x_3 coordinate directions also allows the prediction of the pressure variation in the radial direction from the integrated momentum relation, equation (4.12). The results of this numerical integration of the experimental data are shown in Figures 18 and 19. Figure 18 shows that the dimensionless pressure gradient $(\overline{P}_0 - \overline{P})/\rho u^{*2}$ has a value slightly less than unity at the pipe center line. This value remains nearly constant as x_2 is increased from zero to 0.9, although it does indicate a very slight decrease. At a value of y/R of approximately 0.1, this dimensionless pressure gradient begins a very rapid decrease to zero. However, Figure 19 indicates that this decrease does not occur in the expected manner; instead an inflection point exists at a y/R of about 0.005. Although this result might be somewhat questionable due to the close proximity of the solid surface, the possibility of an inflection point in the radial pressure profile should be kept in mind for possible significance. One very definite result which can be obtained from these calculations is a verification of the validity of measuring static pressure at the wall, rather than at the center line, for dynamic head determination. From Figure 18 it may be observed that $\overline{P}_0 - \overline{P}_c$ is approximately equal to ρu^{*2}. Thus, the error involved in calculating dynamic head from static pressure readings at the wall will be of the order of $2(u^*/\overline{U}_{max})^2$, and for

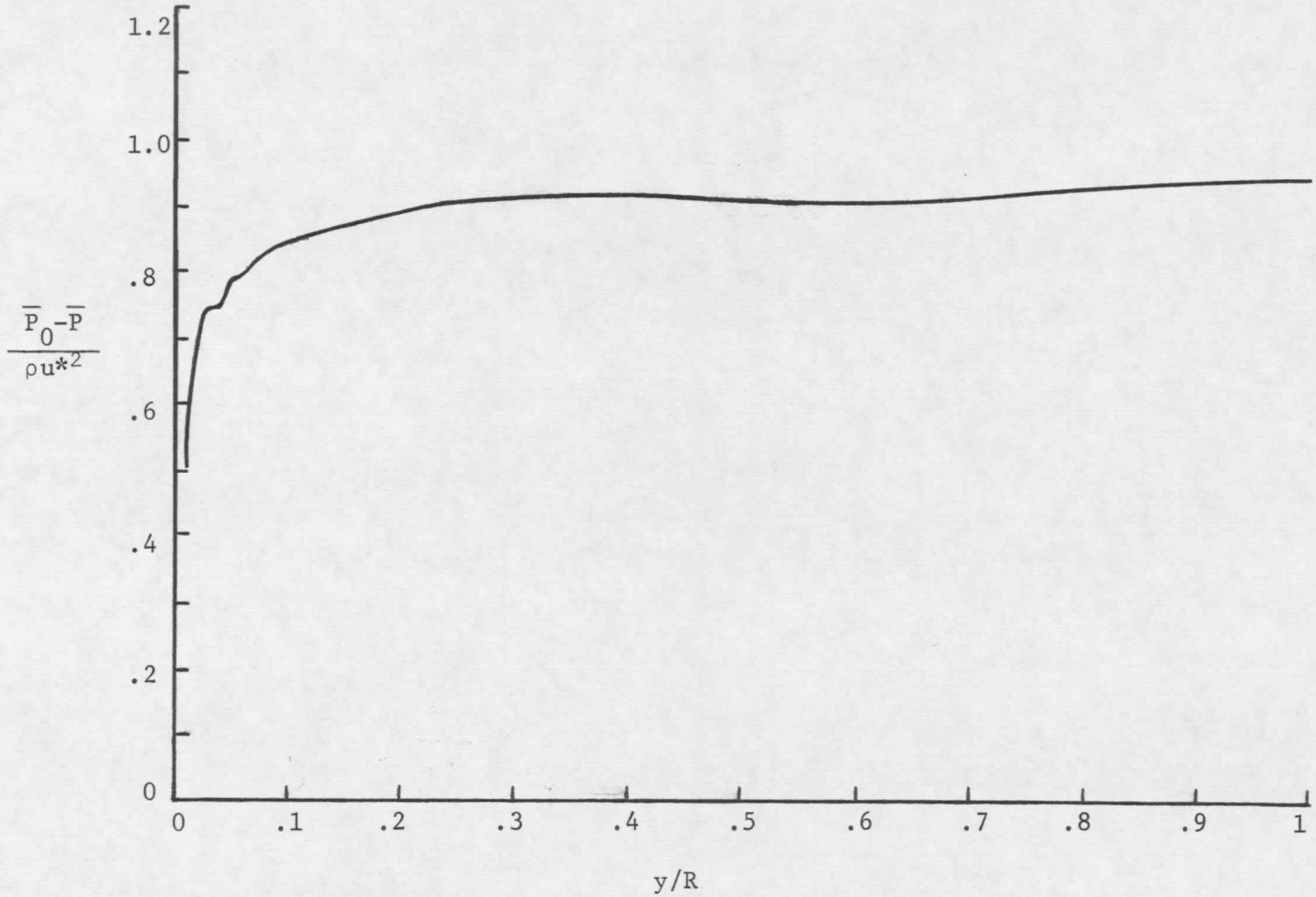

FIGURE 18. Radial Pressure Variation for Central Region of Smooth Pipe

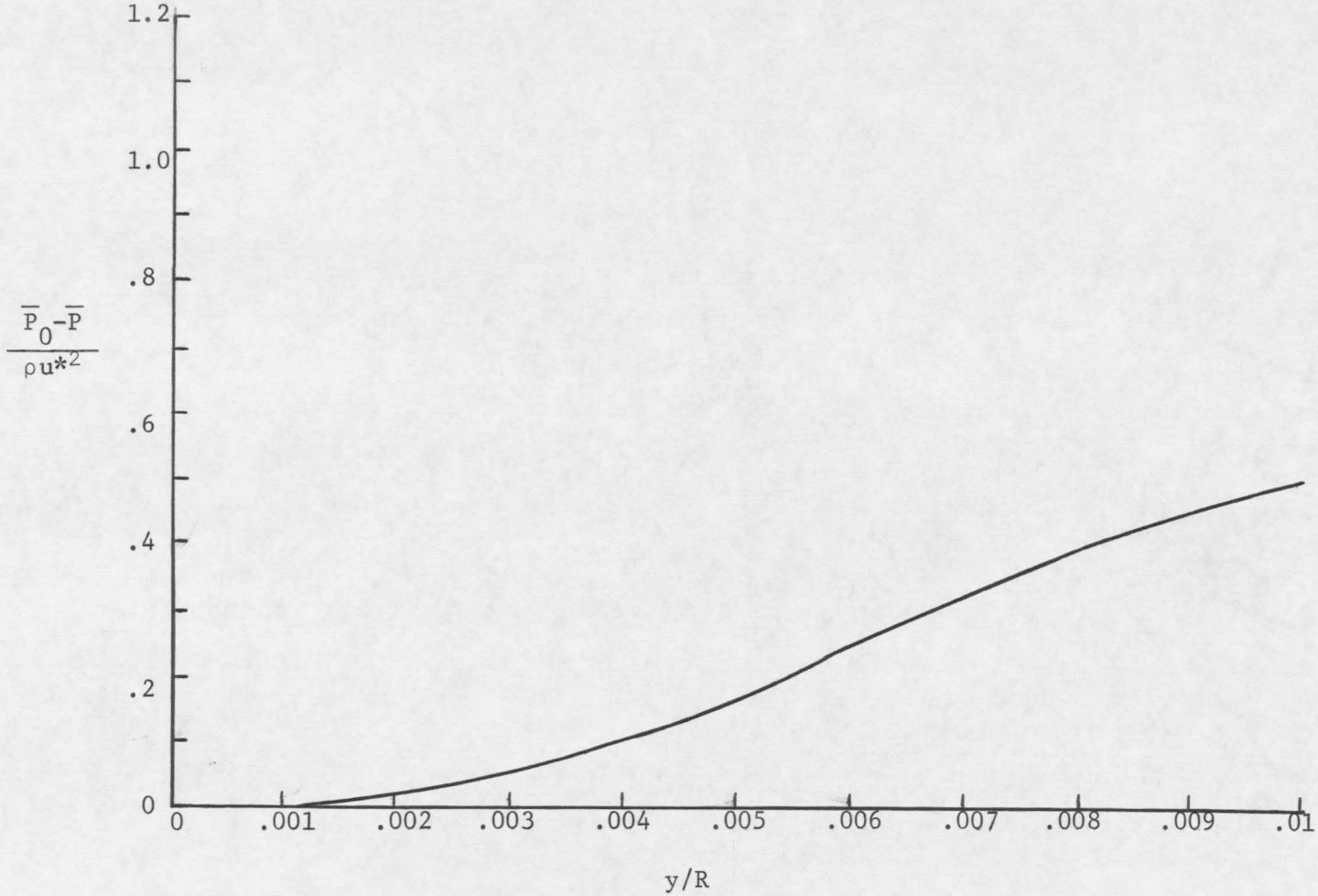

FIGURE 19. Radial Pressure Variation for Wall Region of Smooth Pipe

the Reynolds number considered in this investigation, this amounts to an error of only about 0.26%.

Fluctuating Velocity Correlations

As mentioned previously, both second and third order velocity correlations were considered in this investigation, and the second order will be considered prior to the third order. The second order $\overline{u_1 u_2}$ cross correlation, normalized with the square of the shear velocity, is presented in Figure 20 for the turbulent core and in Figure 21 for the wall region. The solid line in these figures is obtained from curve fitting the experimental data, and the dashed line is obtained by employing mean velocity data together with the momentum relationships given by equation (4.13). The experimental data presented in these figures show an approximately linear increase in the cross correlation from the center line to y/R less than 0.1. This correlation attains a maximum value slightly above 0.8 at $y/R \simeq 0.03$, and then begins a rapid decline to zero. A maximum deviation of about 6% may be observed very near the wall between the experimentally determined values of $\overline{u_1 u_2}/u^{*2}$ and values predicted from equation (4.13). First, some error may be involved in the numerical evaluation of equation (4.13). However, it is probably more likely that the major portion of the error occurs in the measurement of the cross correlation term

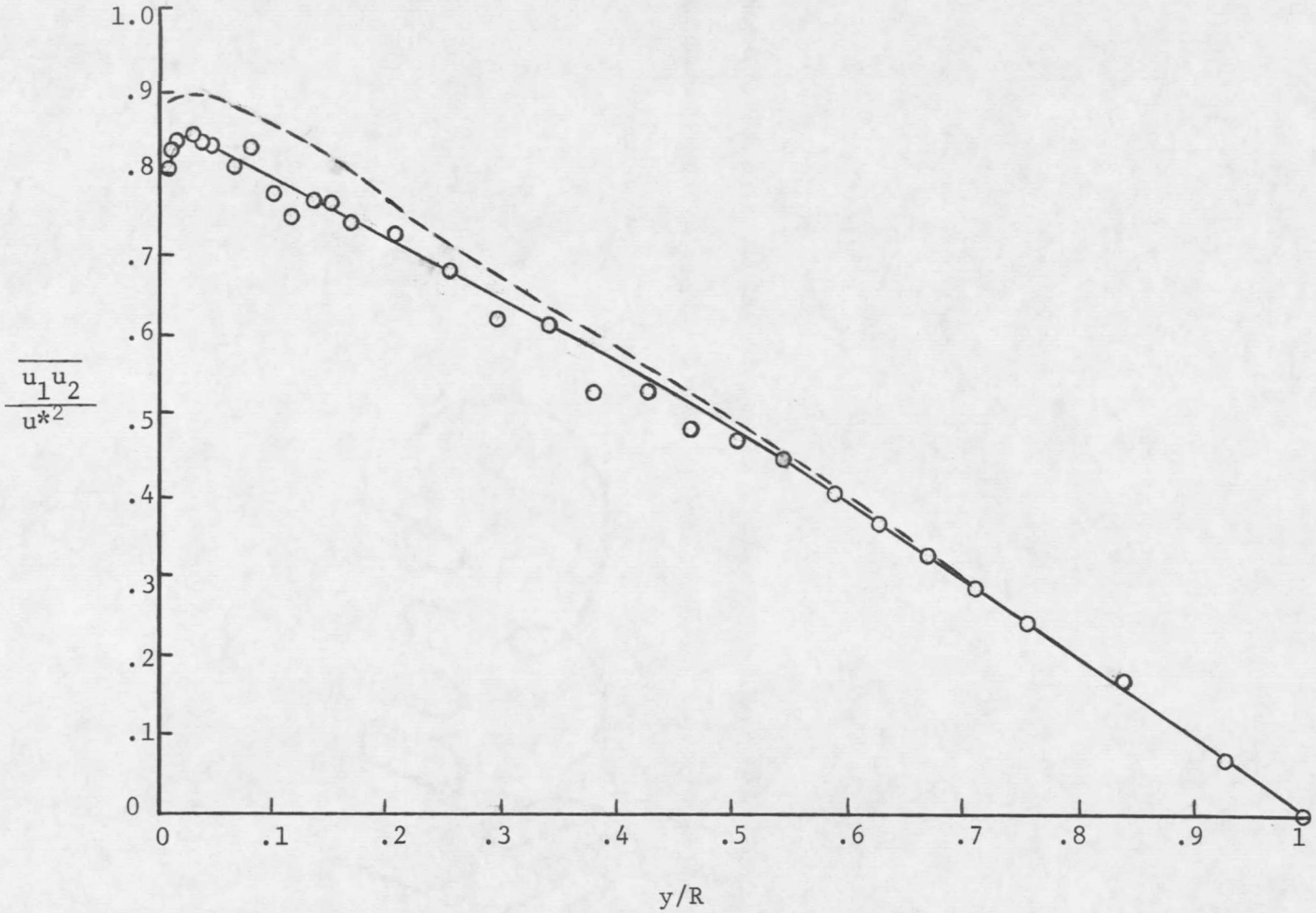

FIGURE 20. Cross Correlation Between Longitudinal and Radial Fluctuating Velocities for Central Region of Smooth Pipe

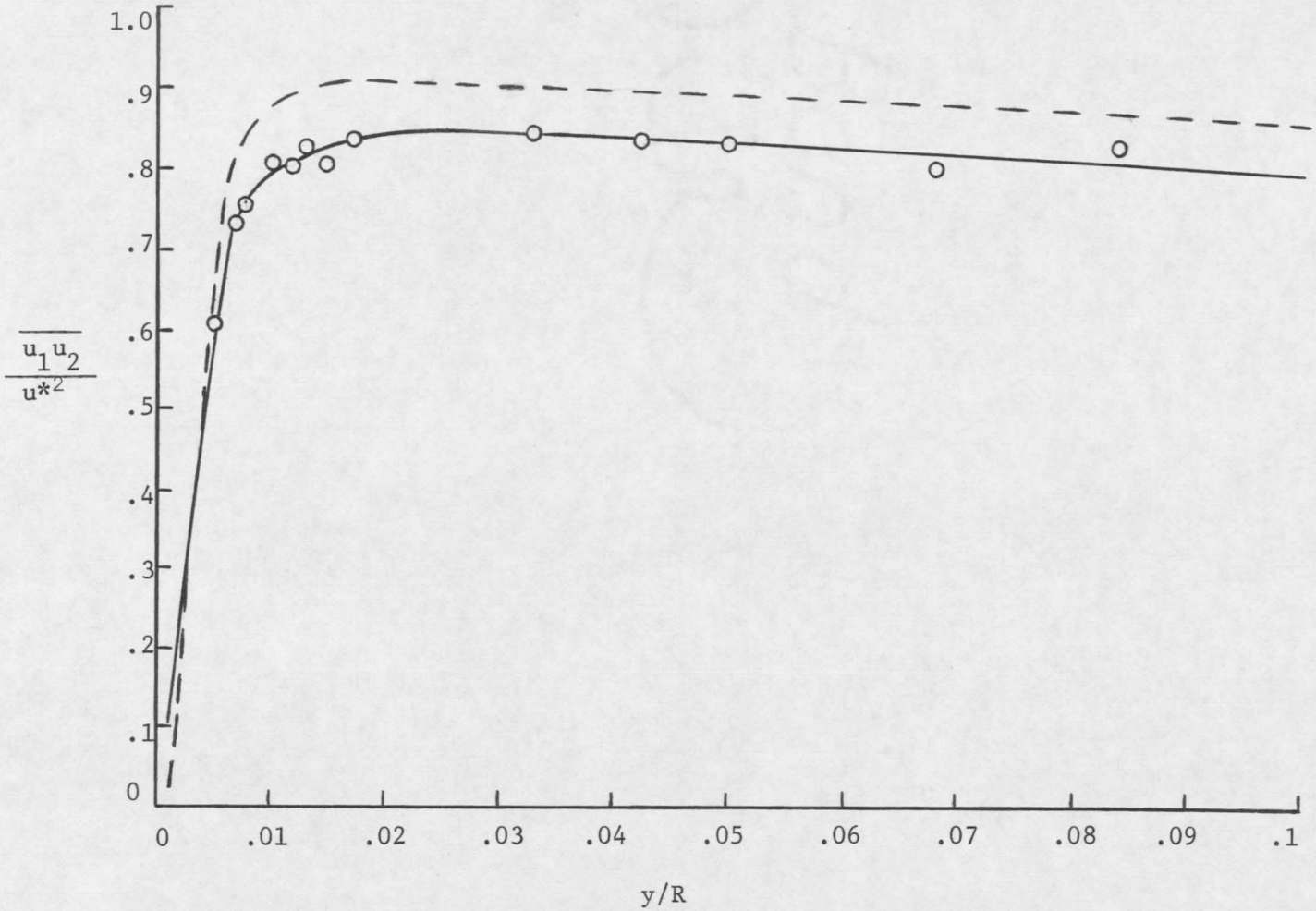

FIGURE 21. Cross Correlation Between Longitudinal and Radial Fluctuating Velocities for Wall Region of Smooth Pipe

in close proximity to the solid wall where large gradients in all velocity terms exist. Thus, the finite wire length has a certain effect on the readings at this point, as does the nonzero separation distance between the two wires. However, it is felt that this 6% maximum deviation is well within acceptable limits.

A second manner in which cross correlations between fluctuating velocities can be analyzed is in terms of the correlation coefficient ψ_{ij}. A plot of ψ_{12} versus y/R is presented in Figure 22. This curve shows a rapid increase in ψ_{12} from zero at the pipe centerline to about 0.48 at y/R = 0.5. For smaller values of y/R, ψ_{12} remains essentially constant. These results are in excellent agreement with Laufer's [41] pipe flow results and Reichardt's (see Schlichting [11]) rectangular channel results.

One of the assumptions implicit in von Karman's similarity hypothesis (see Schlichting [11]) is that the turbulence shear stress and kinetic energy distributions must be similar, i.e., the ratio of these two quantities must be constant. Hinze [9] also shows that if Prandtl's miximg length theory is valid a constant value of this ratio will again be obtained. From the data of the current investigation, Figure 23 shows that this ratio is, in fact, nearly constant over the major portion of the pipe at a value of about 0.26, although it does decline rapidly to a null value at the center

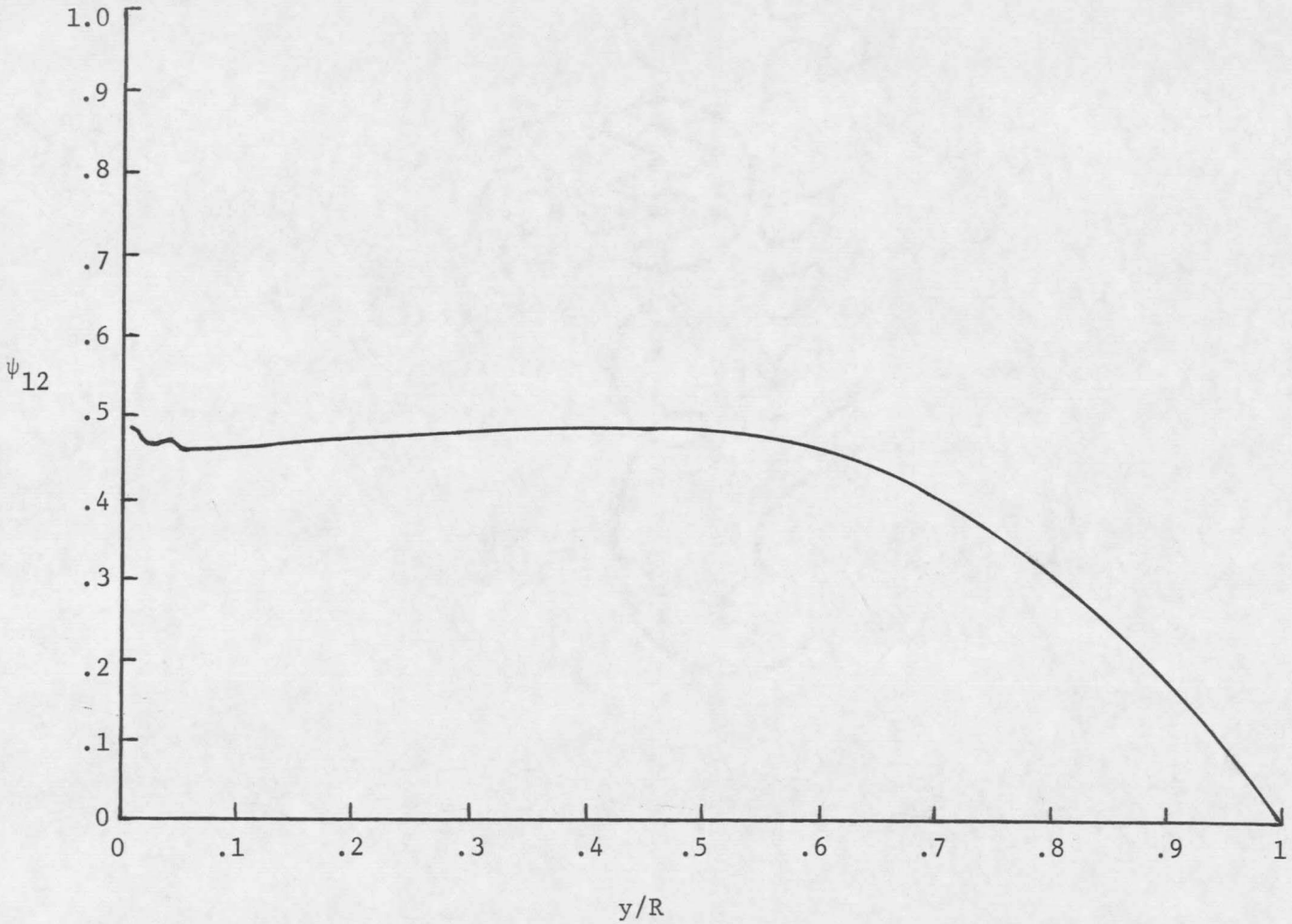

FIGURE 22. Correlation Coefficient ψ_{12} for Longitudinal and Radial Fluctuating Velocities in Smooth Pipe

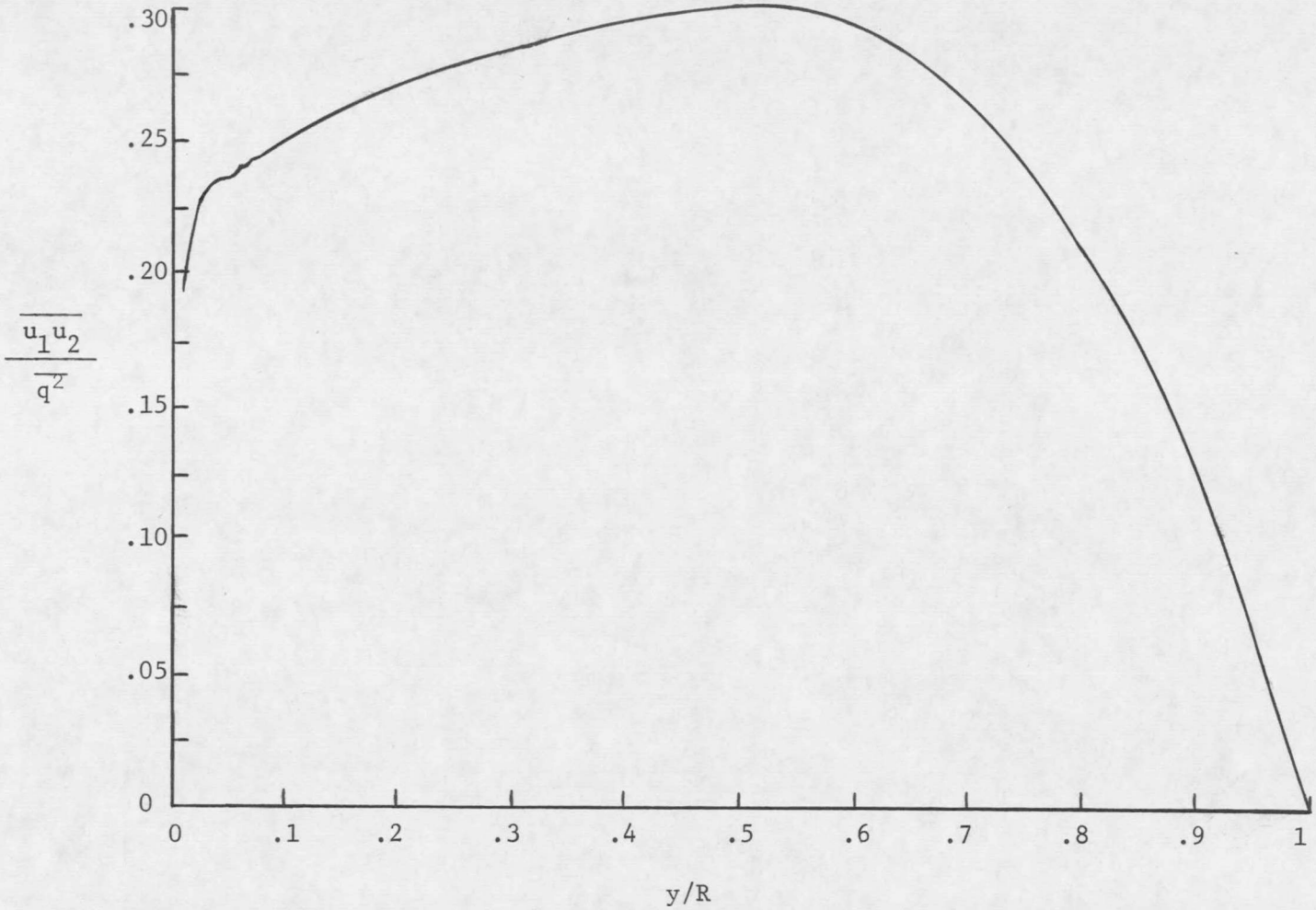

FIGURE 23. Ratio of Turbulence Shear Stress to Turbulence Kinetic Energy for Smooth Pipe

line of the pipe. This curve is in excellent qualitative agreement with Hinze's [9] analysis of Laufer's data, though the magnitudes do vary slightly, probably due to the difference in Reynolds number between the two investigations.

In many practical applications involving turbulent pipe flow, the quantity of interest is the eddy diffusivity for momentum, and this parameter can be calculated by utilizing experimental $\overline{u_1 u_2}$ cross correlation data and mean velocity data in conjunction with the definition of ε_n, equation (2.68). Such values of ε_n are indicated by the solid lines in Figures 24 and 25. From these figures, the eddy diffusivity for momentum is seen to be nearly constant over the central and major portion of the pipe. The constant value of $\varepsilon_n/Ru^* \simeq 0.06$ is in excellent agreement with values determined by Hinze [9] from the investigations of both Nunner and Laufer. Good agreement is also indicated near the wall where ε_n/Ru^* goes through an inflection point as it approaches zero. The solid line in Figures 24 and 25 is compared with the dashed line obtained by utilizing equation (2.71) which requires mean velocity data only. Thus, the solid line would be expected to lie slightly below the dashed line since experimental values of $\overline{u_1 u_2}$ were slightly less than those predicted from mean velocity data.

The second cross correlation term determined experimentally in

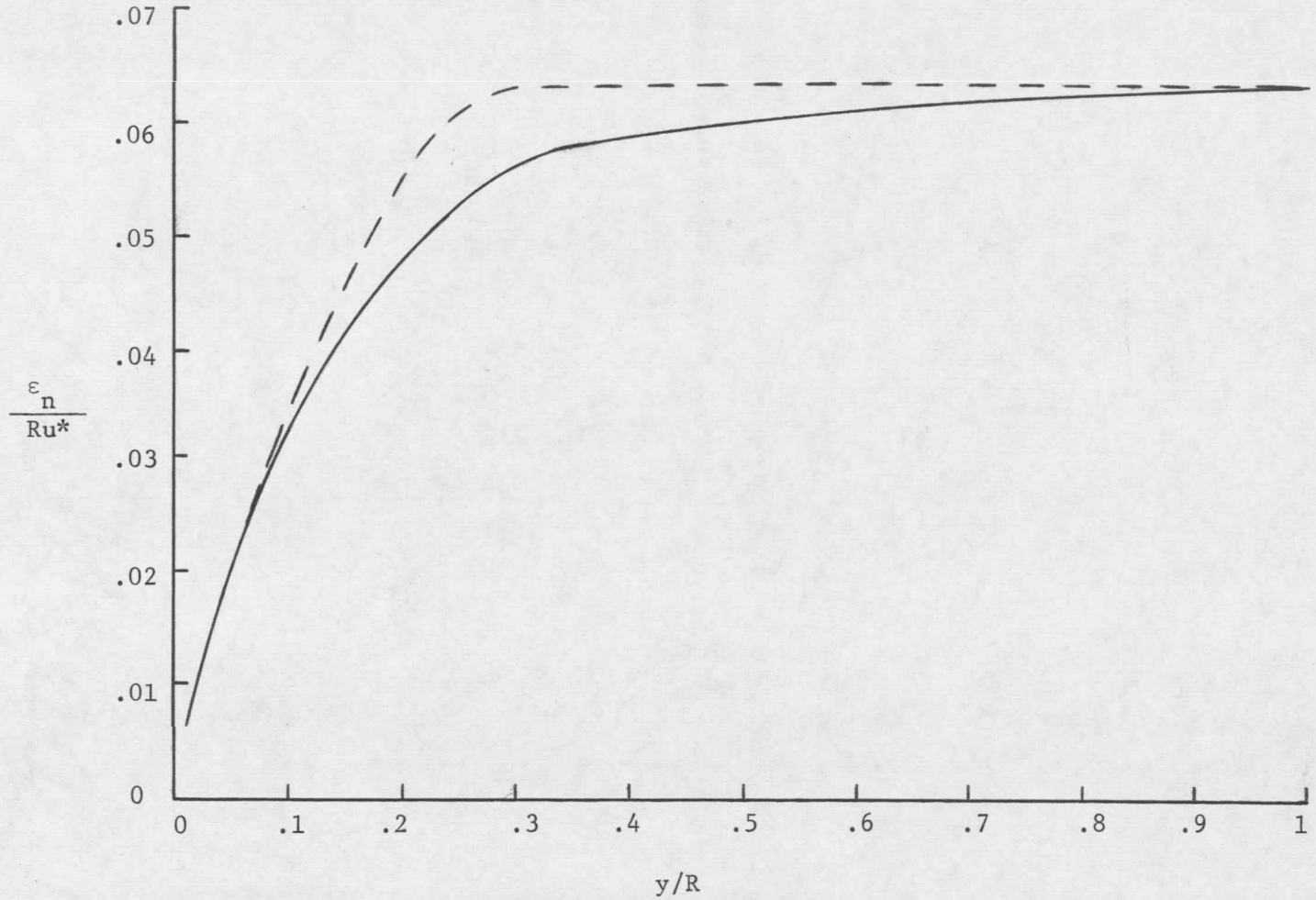

FIGURE 24. Eddy Diffusivity for Momentum in Central Region of Smooth Pipe

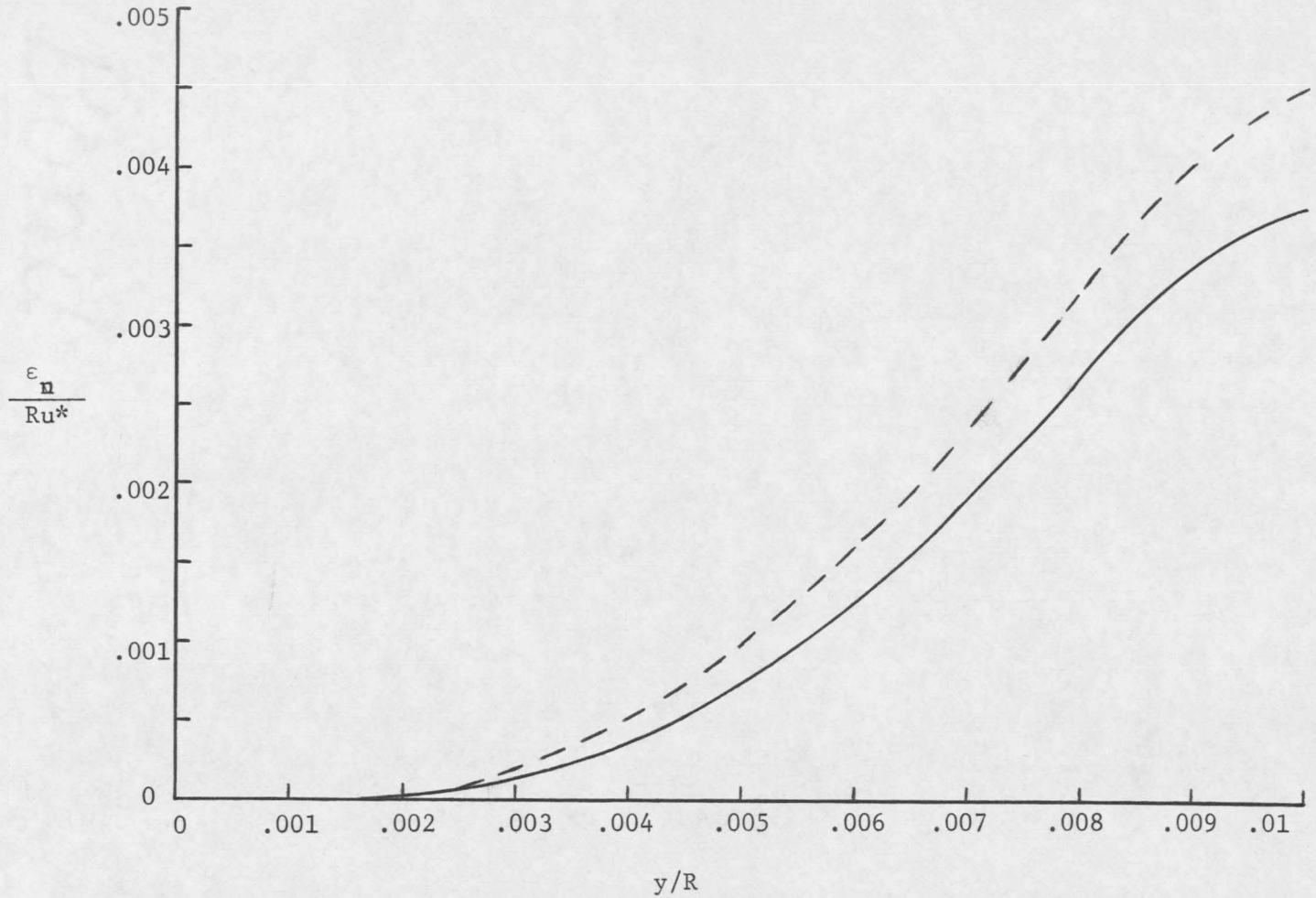

FIGURE 25. Eddy Diffusivity For Momentum in Wall Region of Smooth Pipe

the current investigation was the cross correlation between longitudinal and angular fluctuating velocities, $\overline{u_1 u_3}$. It should be recalled from the review of the literature that momentum arguments require that this term must vanish everywhere for flow in a smooth pipe, and this fact is verified experimentally by Figures 26 and 27. It should be noted that Gow's [15] data indicated slight deviations from zero, as did the current data in the initial stages of the investigation. However, it was found that the deviations in both the current investigation and that of Gow [15] could be accounted for by a correction due to the nonzero separation distance between the two wires used in making the $\overline{u_1 u_3}$ measurements. This correction has been described in the previous chapter.

Third order velocity correlation terms measured in this investigation included $\overline{u_1^2 u_2}$ and $\overline{u_2^3}$. The variation of $\overline{u_1^2 u_2}/u^{*2}$ with radial position is indicated in Figures 28 and 29. This correlation is seen to vanish at the wall and the pipe center line and to be negative at all intermediate points. A maximum magnitude of approximately 1.2 is attained for $y/R \simeq 0.2$. This result is in good agreement with those of Laufer [41] who also found the correlation to be negative and to attain a maximum magnitude of about 1.4 at $y/R \simeq 0.1$. Figure 30 indicates that the correlation coefficient corresponding to $\overline{u_1^2 u_2}$ is approximately constant at -0.5 for values

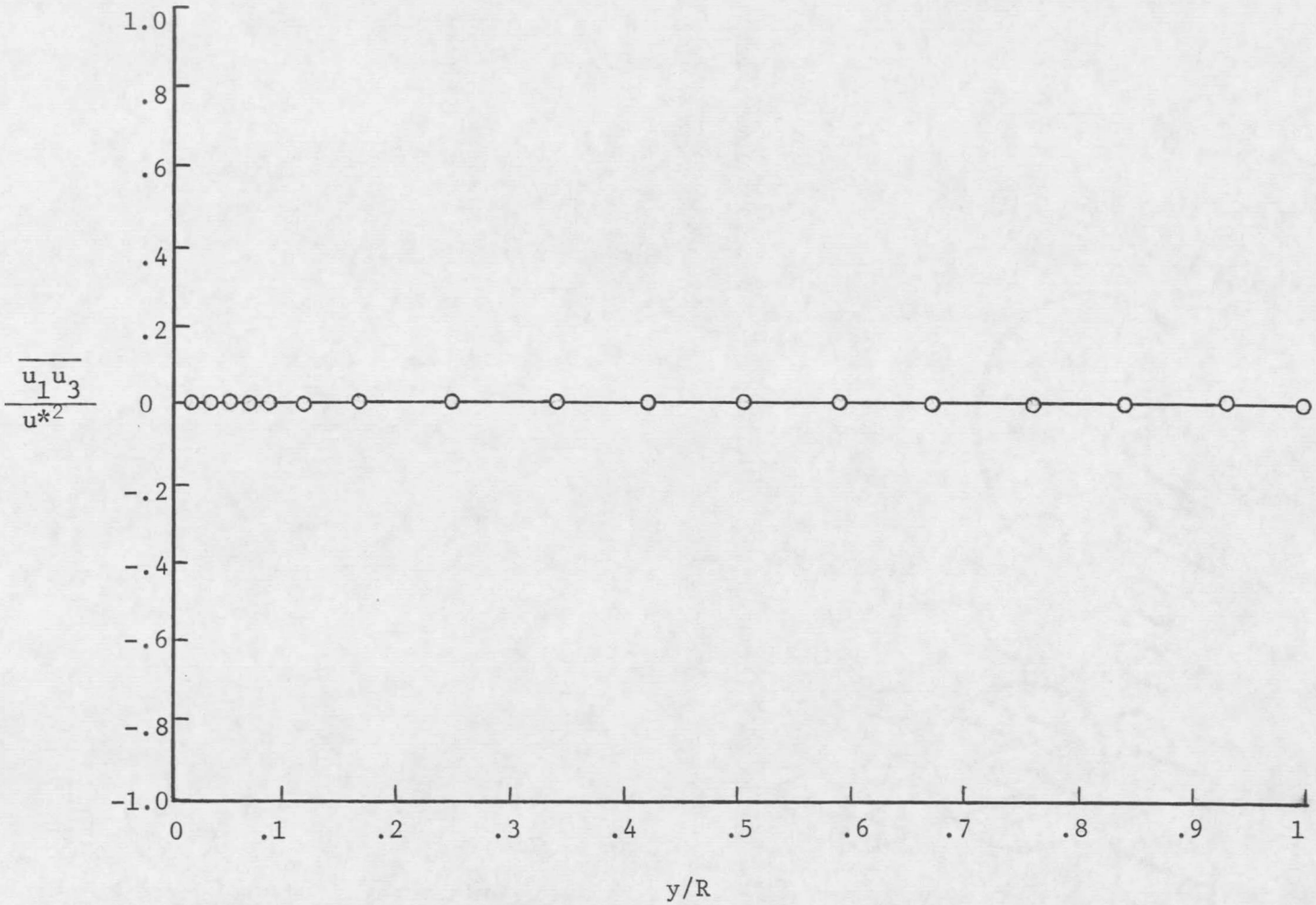

FIGURE 26. Cross Correlation Between Longitudinal and Angular Fluctuating Velocities for Central Region of Smooth Pipe

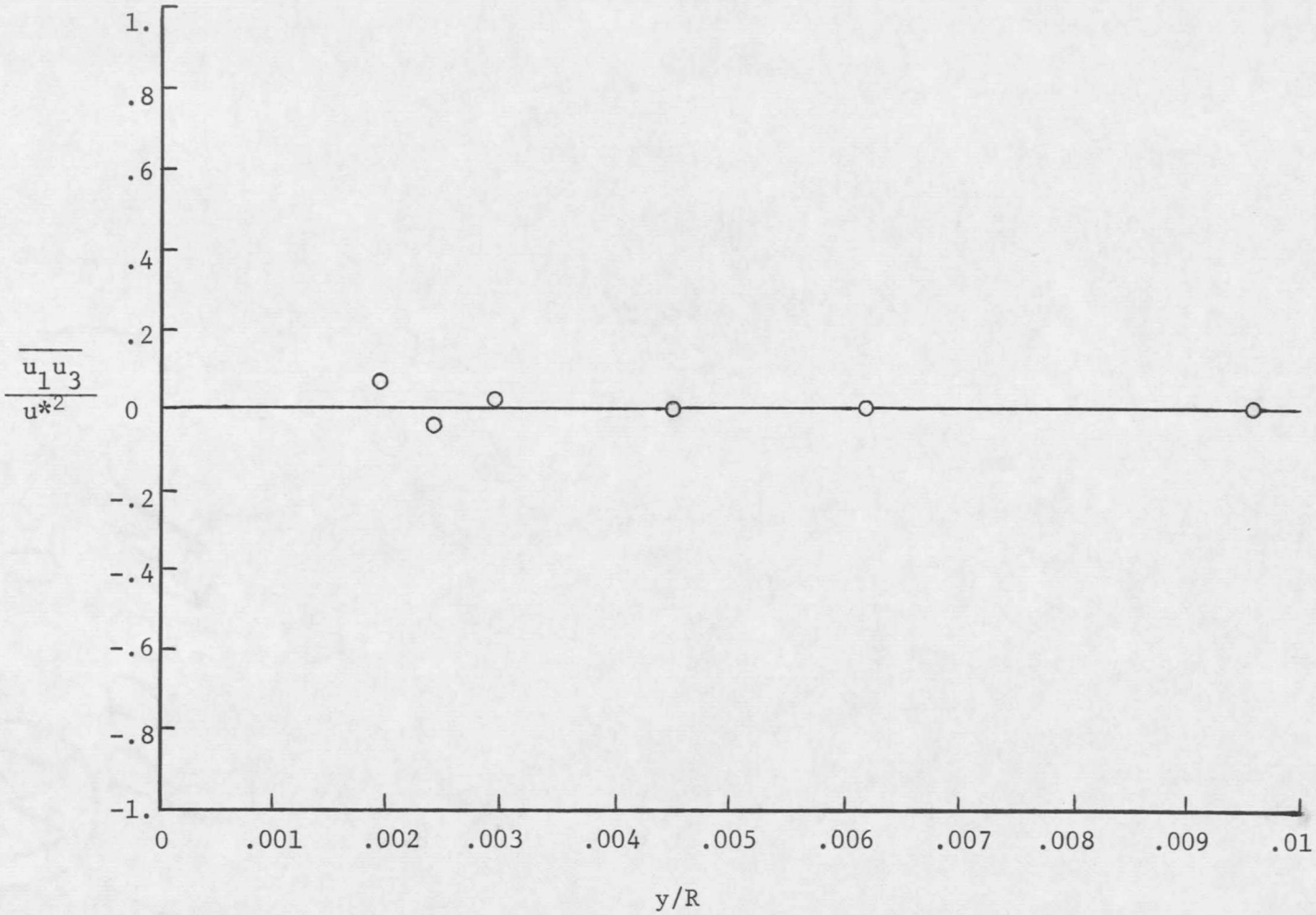

FIGURE 27. Cross Correlation Between Longitudinal and Angular Fluctuating Velocities for Wall Region of Smooth Pipe

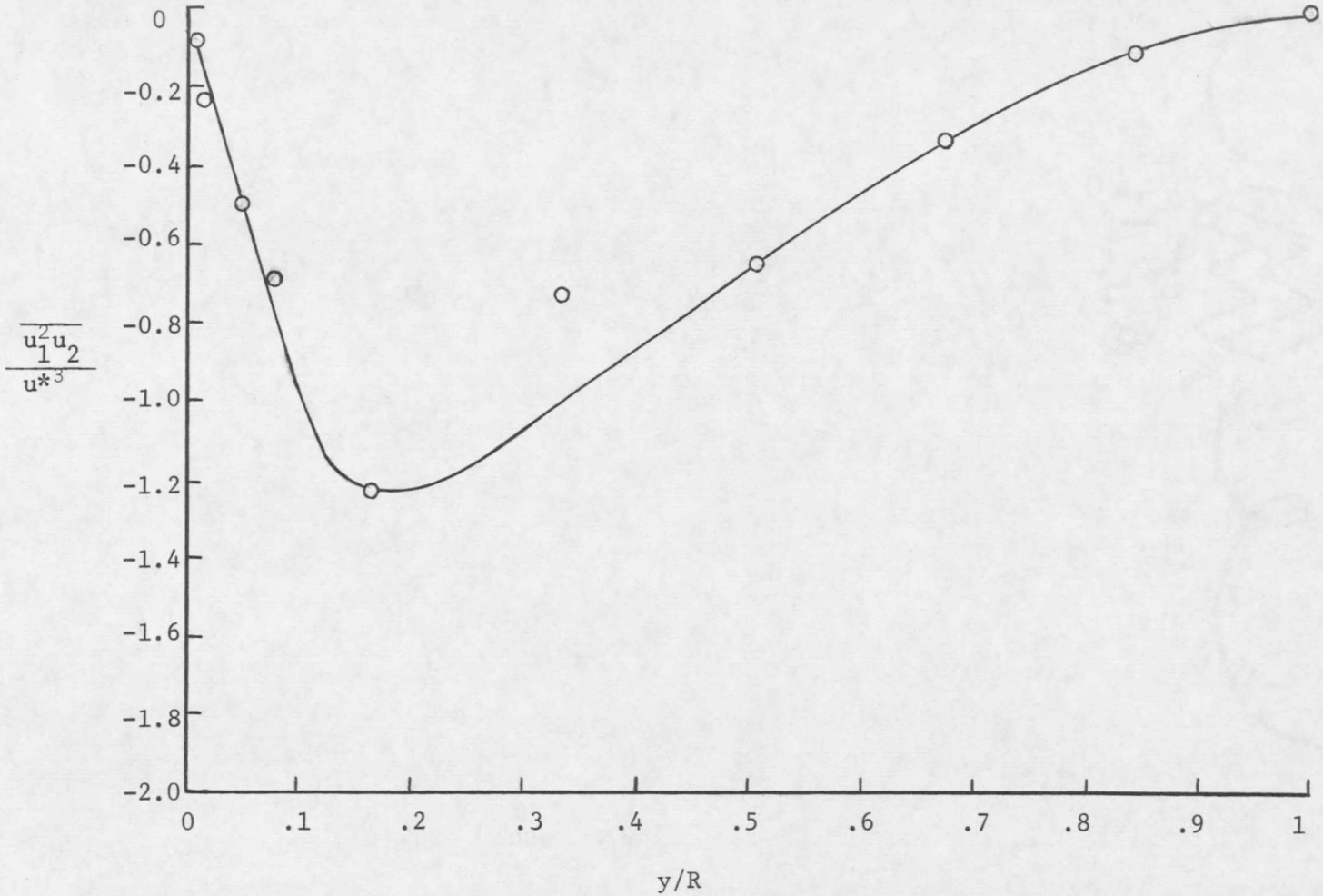

FIGURE 28. Radial Variation of Third Order $\overline{u_1^2 u_2}$ Correlation for Central Region of Smooth Pipe

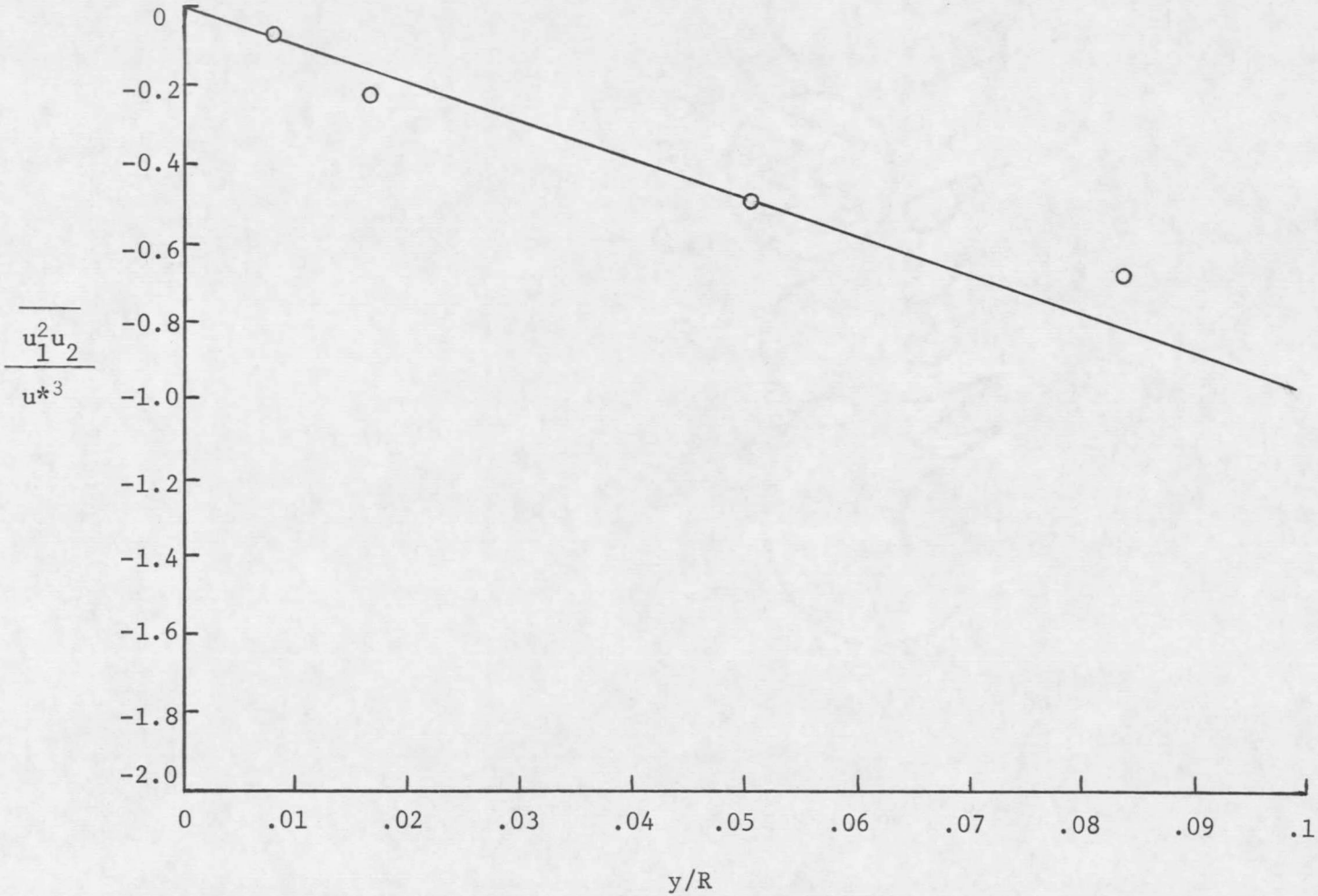

FIGURE 29. Radial Variation of Third Order $\overline{u_1^2 u_2}$ Correlation for Wall Region of Smooth Pipe

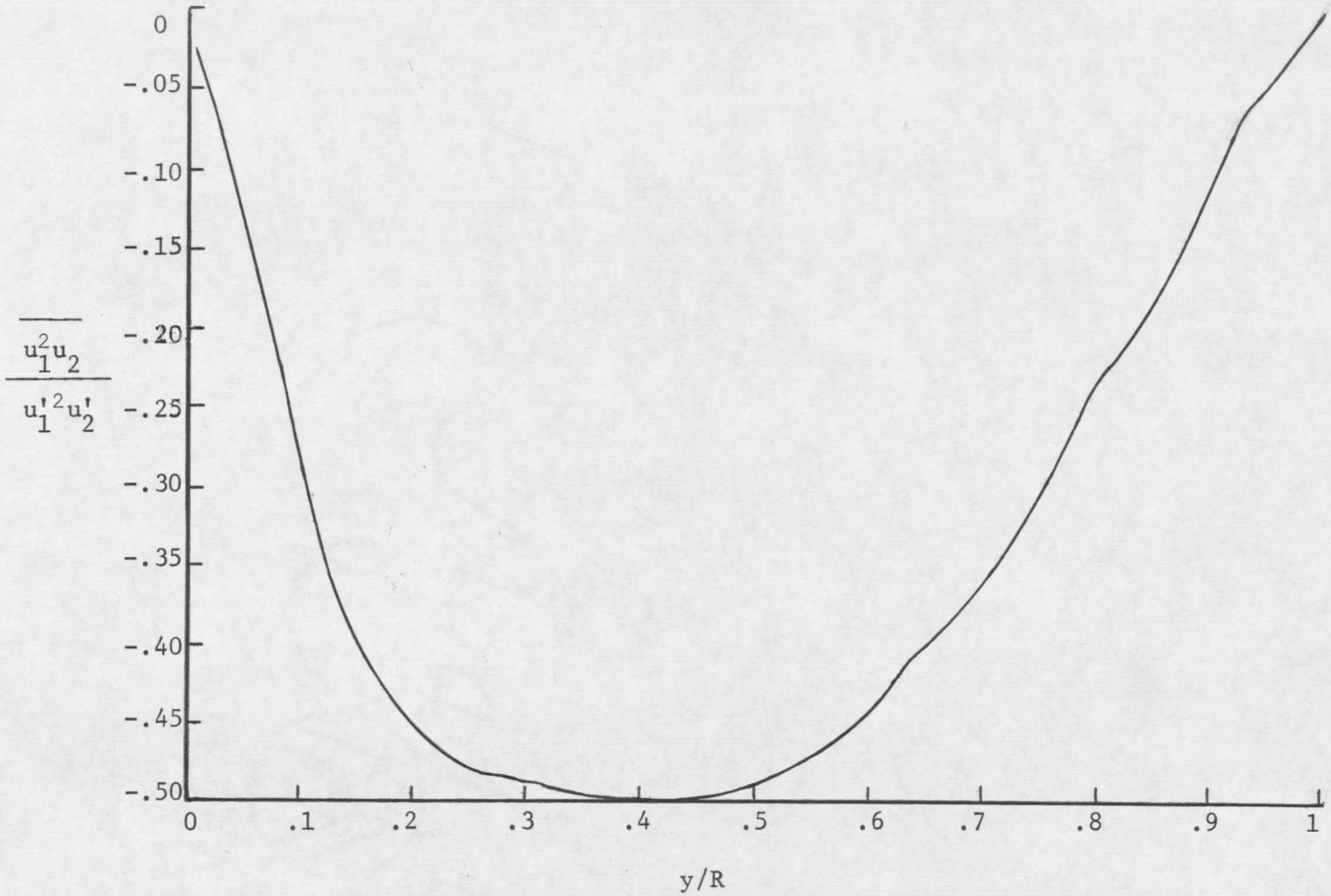

FIGURE 30. Correlation Coefficient for Third Order $\overline{u_1^2 u_2}$ Correlation in Smooth Pipe

of y/R between 0.3 and 0.5. For either larger or smaller values of y/R, this coefficient tends to zero in an approximately linear fashion.

In contrast with the $\overline{u_1^2 u_2}$ correlation, the $\overline{u_2^3}$ correlation is shown by Figures 31 and 32 to be positive throughout the flow field. At $y/R \approx 0.02$, $\overline{u_2^3}/u^{*3}$ acquires a maximum value of about 1.5 and then decreases to zero for smaller values of y/R. This correlation becomes equal to about 0.7 at the pipe center line. These results show a marked deviation from those of Laufer [41] who found $\overline{u_2^3}$ to be negative throughout the flow field. Although the reason for this discrepancy cannot be definitely discerned, Laufer did report difficulty with experimental measurement of the third order correlation terms, possibly due to a low frequency phase shift of his amplifiers, and this might partly explain the deviation. No other data regarding this correlation are available for comparison. The correlation coefficient corresponding to the third order $\overline{u_2^3}$ correlation is presented in Figure 33. This correlation coefficient is seen to be approximately constant at about 2.5 for $y/R > 0.5$ and then to decrease slightly to about 2.0 for y/R between 0.1 and 0.5. A rapid increase in the coefficient is observed for $y/R < 0.1$. Although a first impression might be that this correlation coefficient should not exceed unity, this can be readily disproved by consideration of

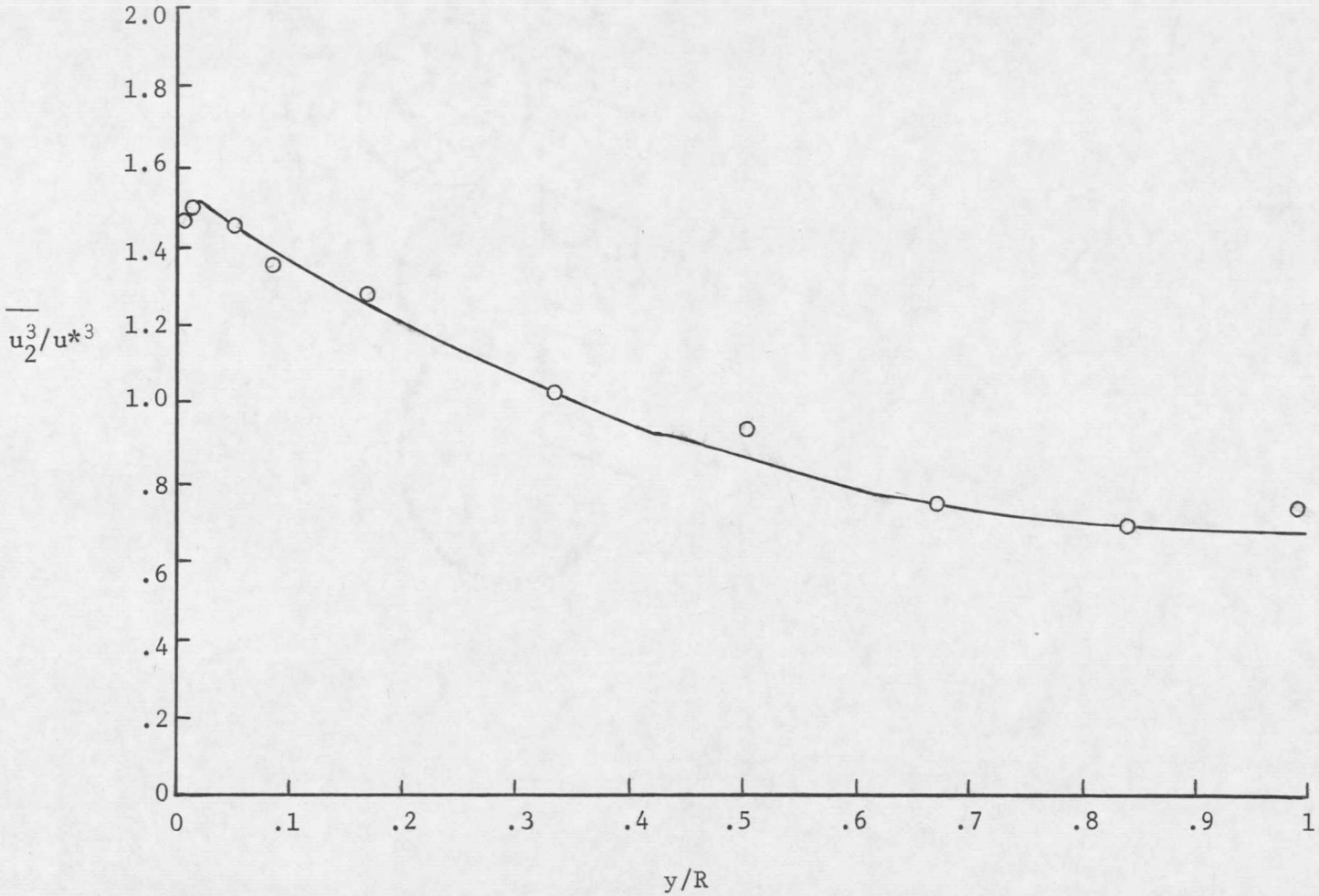

FIGURE 31. Radial Variation of Third Order $\overline{u_2^3}$ Correlation For Central Region of Smooth Pipe

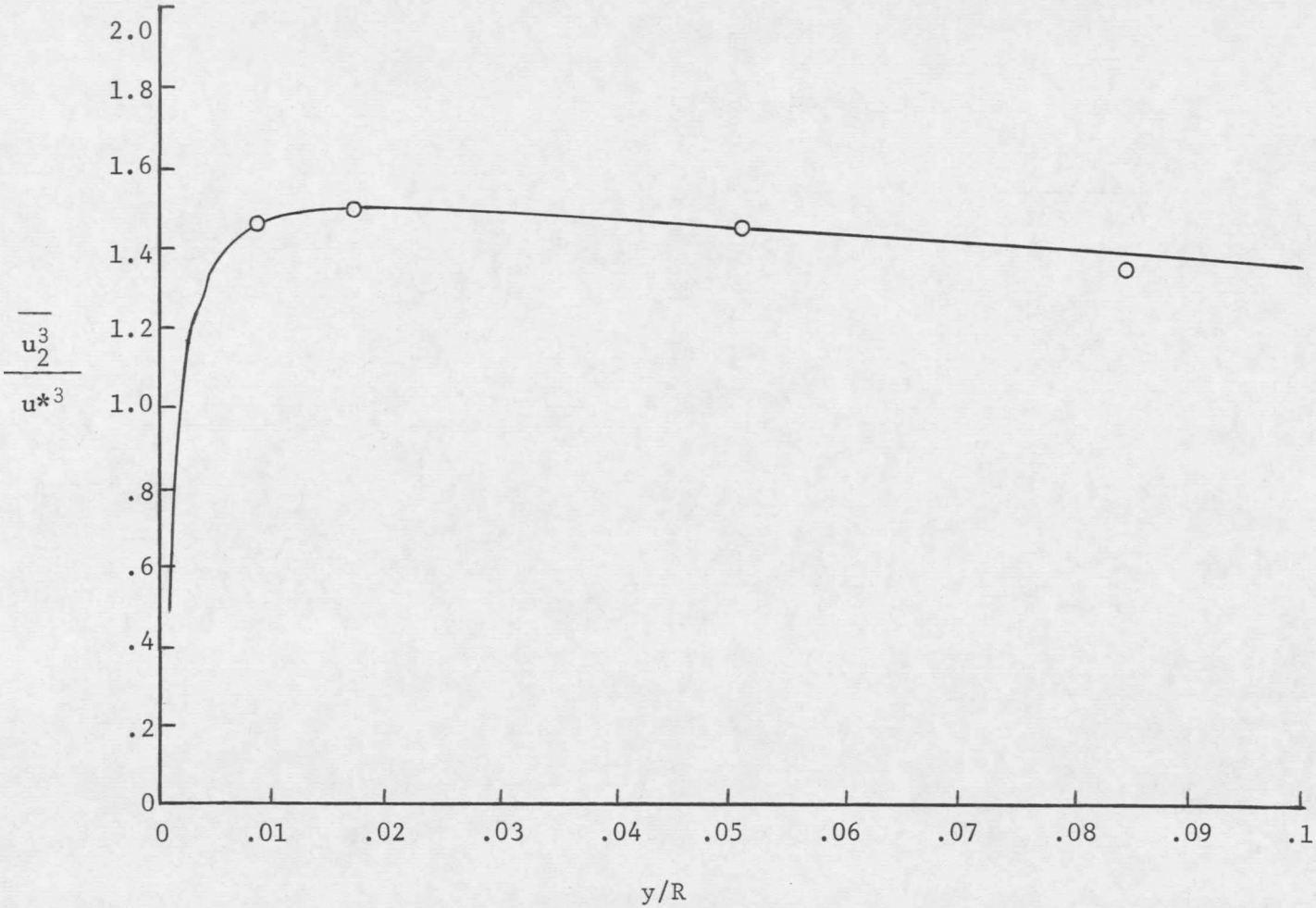

FIGURE 32. Radial Variation of Third Order $\overline{u_2^3}$ Correlation for Wall Region of Smooth Pipe

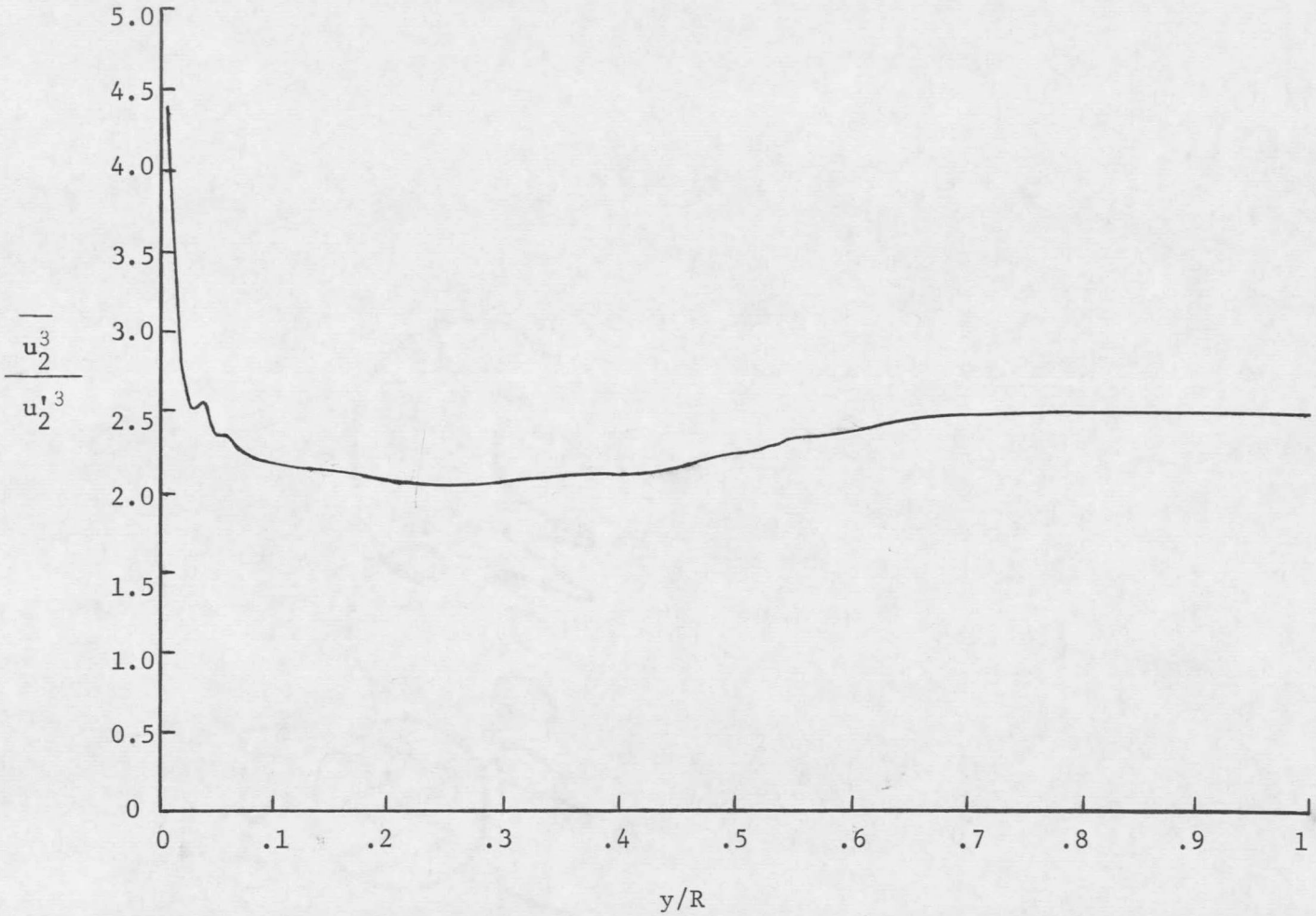

FIGURE 33. Correlation Coefficient for Third Order $\overline{u_2^3}$ Correlation in Smooth Pipe

a highly skewed wave form. Also it might be noted that Hinze [9] shows that the temporal mean value of the cube of any fluctuating velocity is null for an isotropic turbulence. Thus, $\overline{u_2^3}$ can be considered as a measure of the deviation from isotropy, and the foregoing results thereby indicate a lack of isotropy throughout the pipe. This is in agreement with the anisotropy ratios obtained in the previous section.

Dissipation Function

Utilizing the previously stated assumption that the mean square values of the derivatives of fluctuating velocities with respect to the x_2 and x_3 coordinate directions separately satisfy the isotropic relations, equations (5.20), measurement of the terms $\overline{\left(\frac{\partial u_1}{\partial x_i}\right)^2}$, for $i = 1, 2$, and $\overline{\left(\frac{\partial u_i}{\partial x_1}\right)^2}$, for $i = 1, 2, 3$, allows the complete determination of the dissipation function. Experimentally obtained values of these quantities in the turbulent core are presented in Figures 34, 35, and 36, and values in the wall region of the pipe are presented in Figures 37, 38, 39, and 40. The behavior of all of these parameters is somewhat similar, i.e., they all are relatively

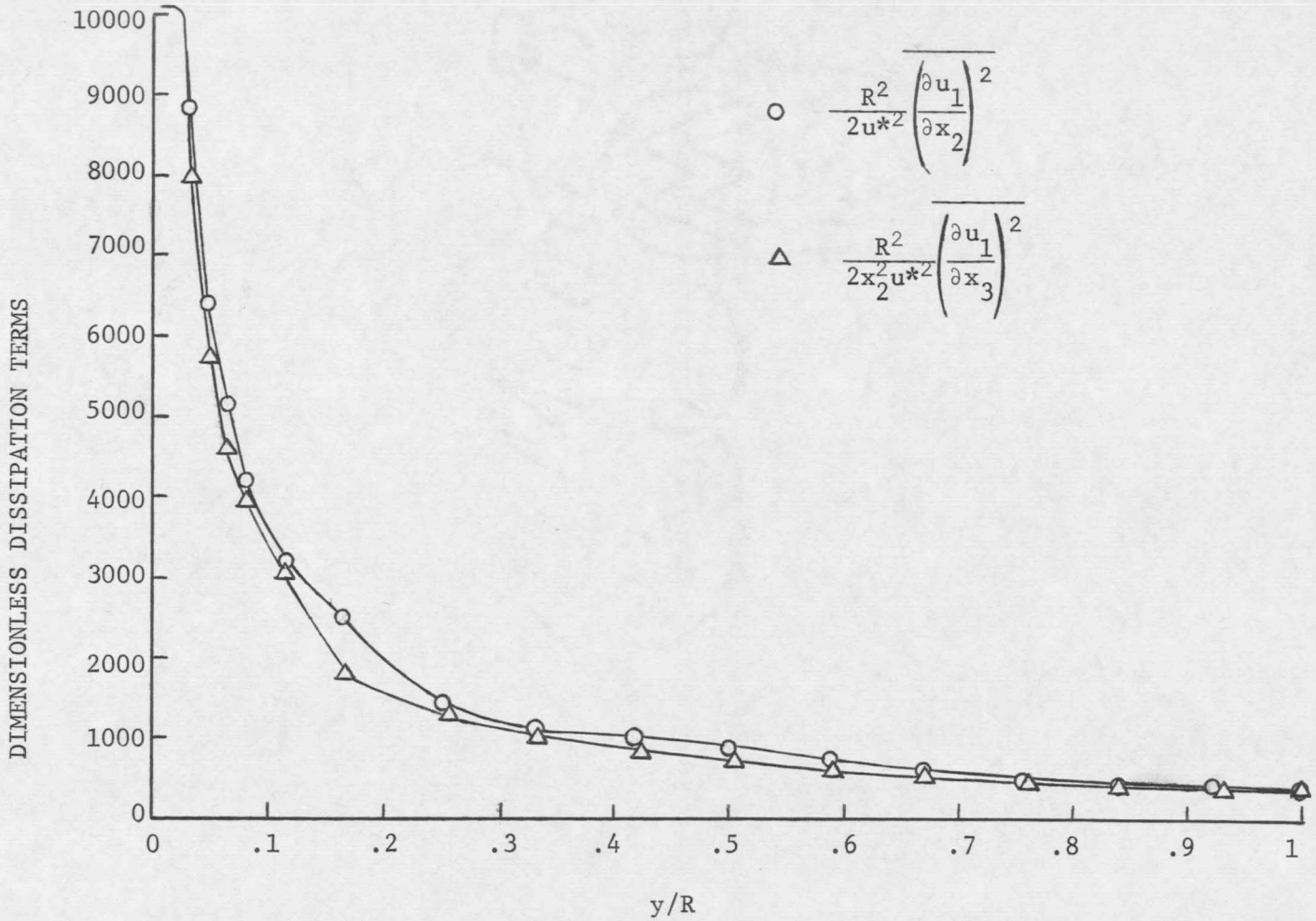

FIGURE 34. Dissipation Terms for Turbulent Core of Smooth Pipe

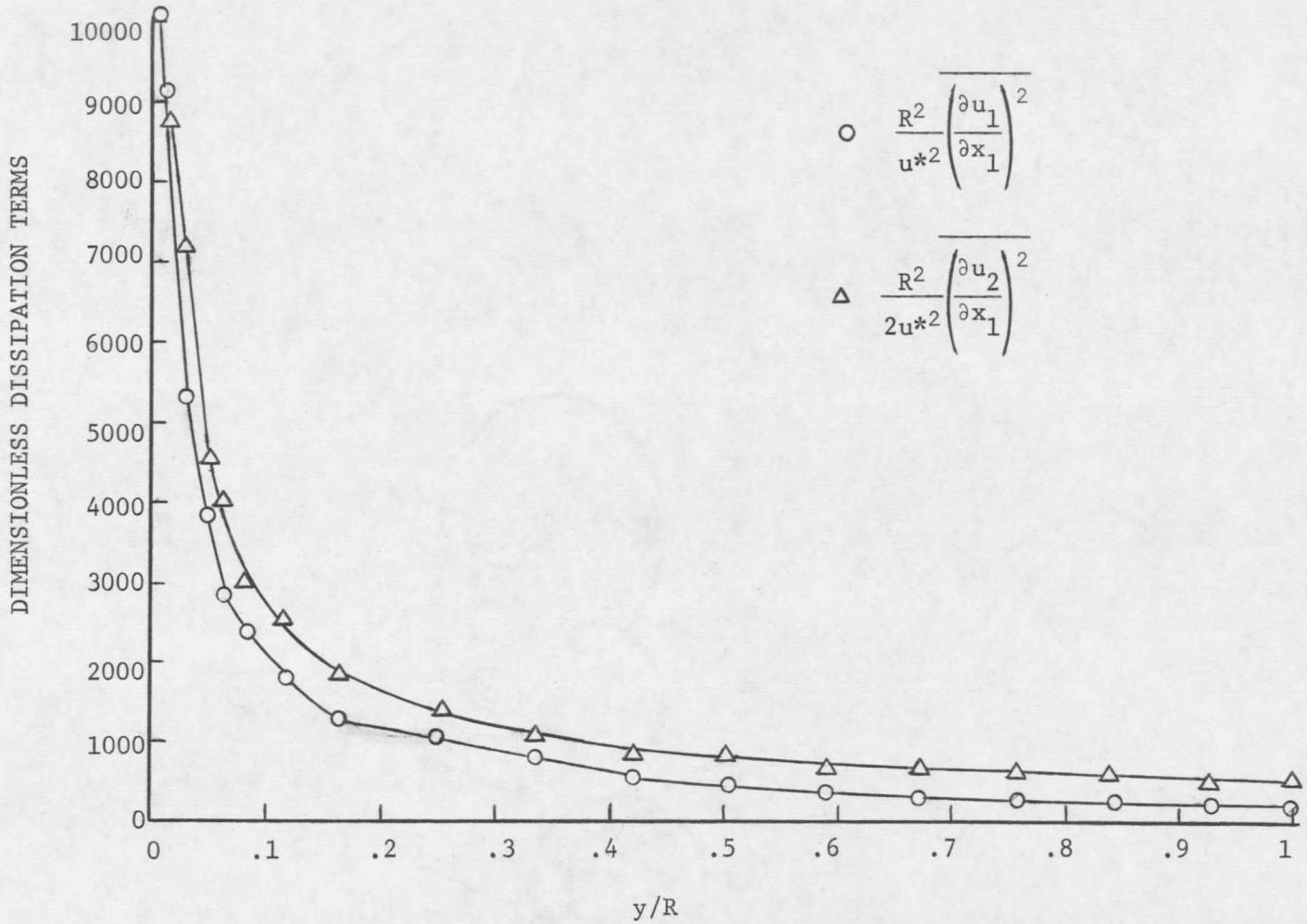

FIGURE 35. Dissipation Terms for Turbulent Core of Smooth Pipe

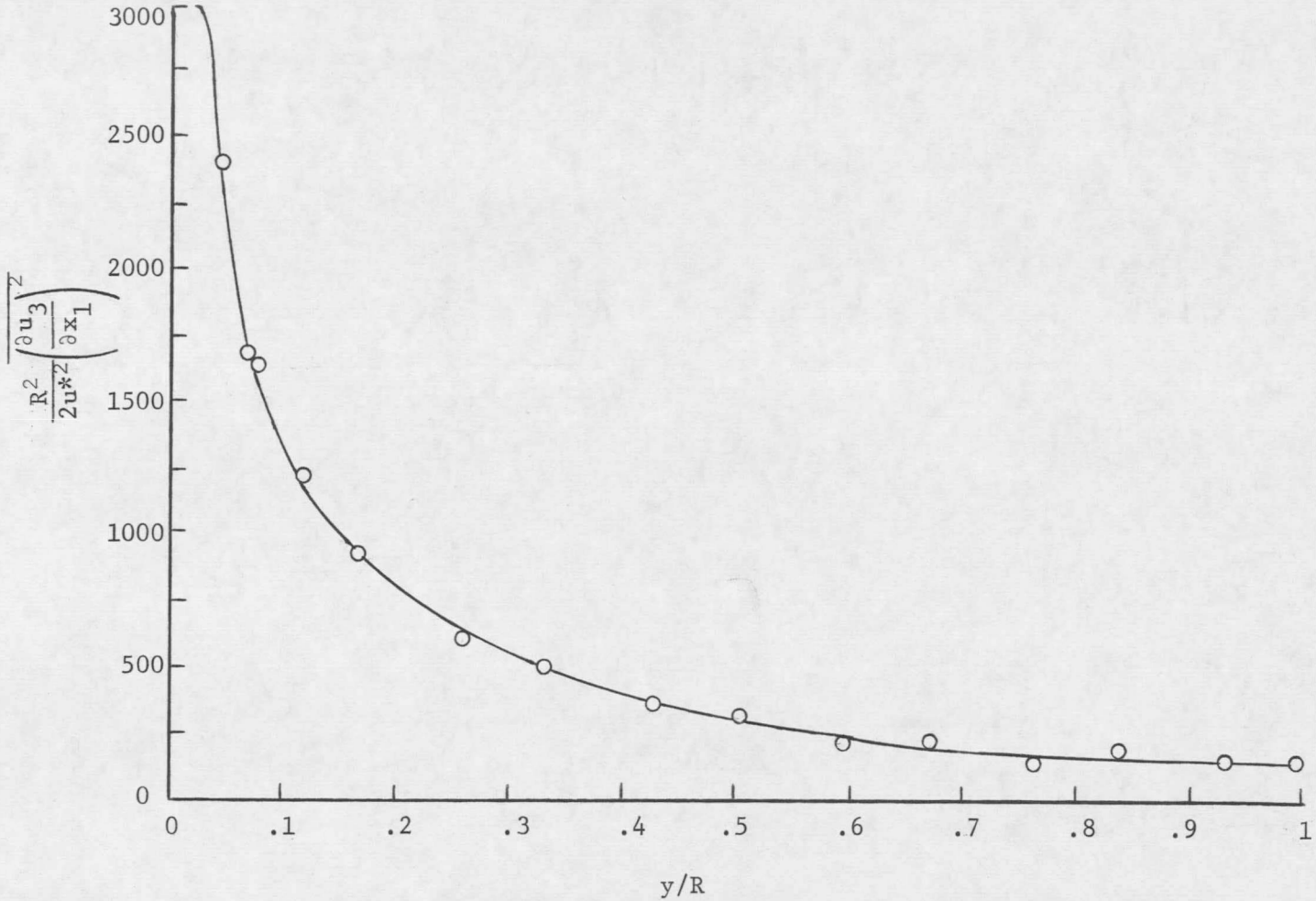

FIGURE 36. Dissipation Terms for Turbulent Core of Smooth Pipe

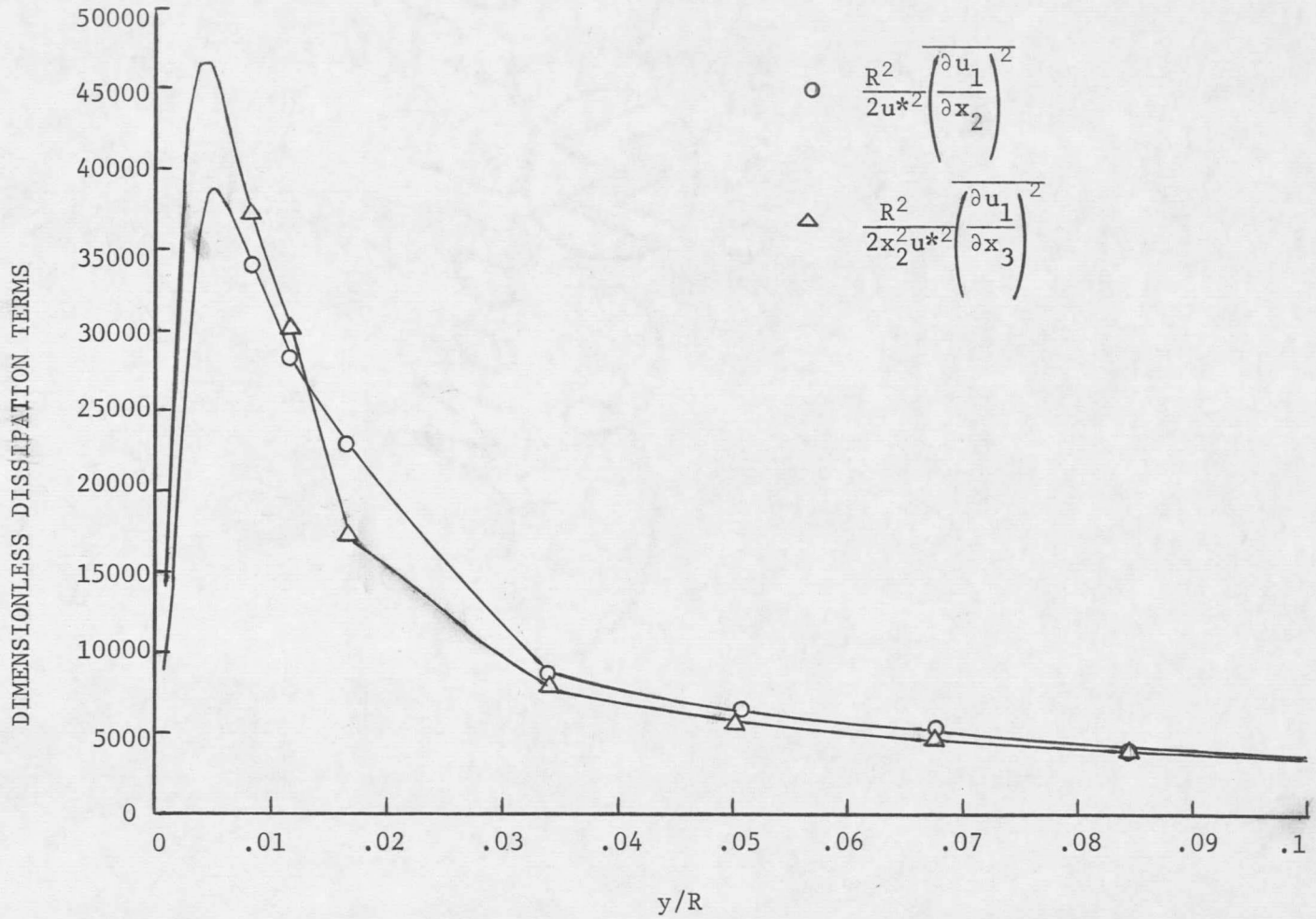

FIGURE 37. Dissipation Terms for Wall Region of Smooth Pipe

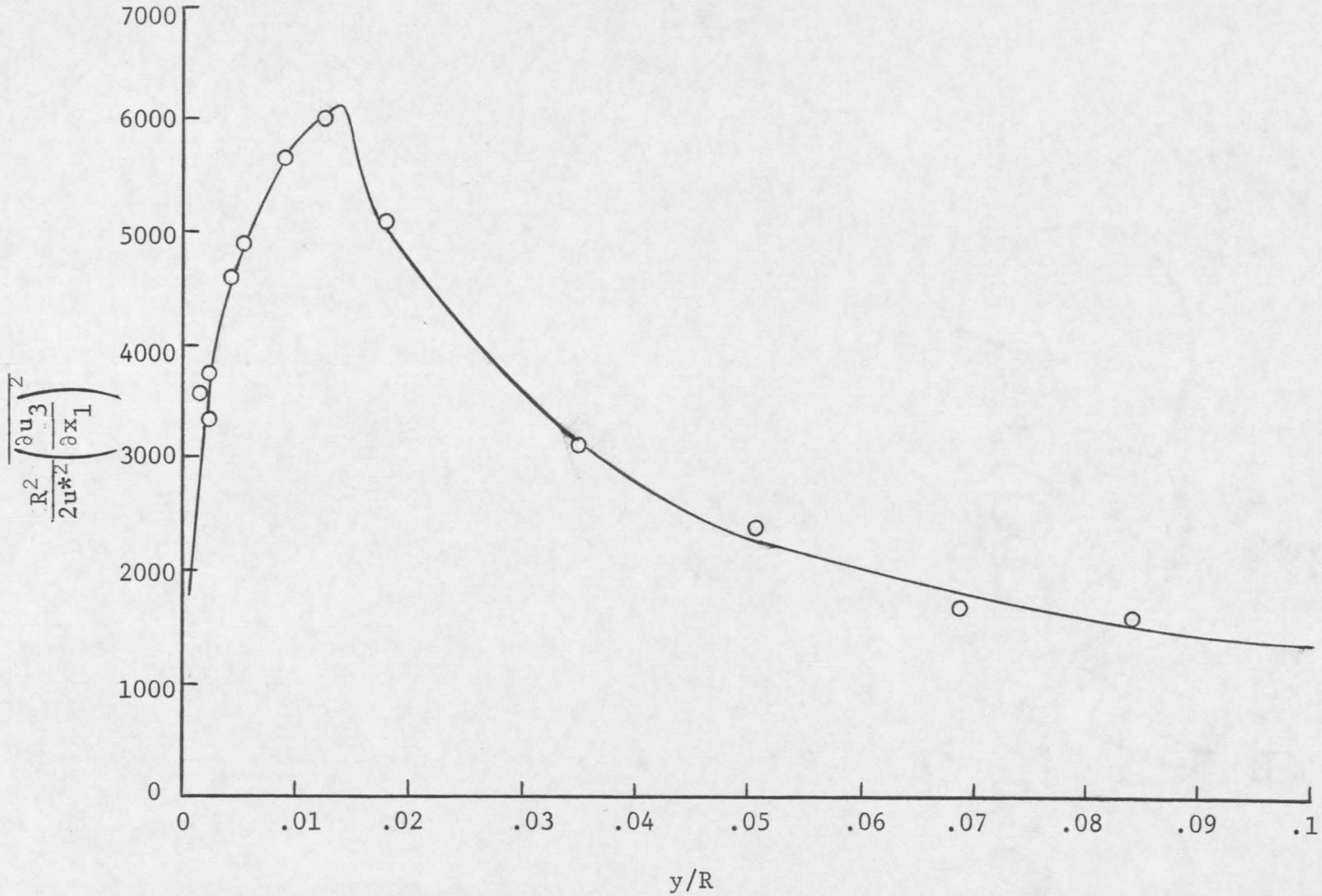

FIGURE 38. Dissipation Terms for Wall Region of Smooth Pipe

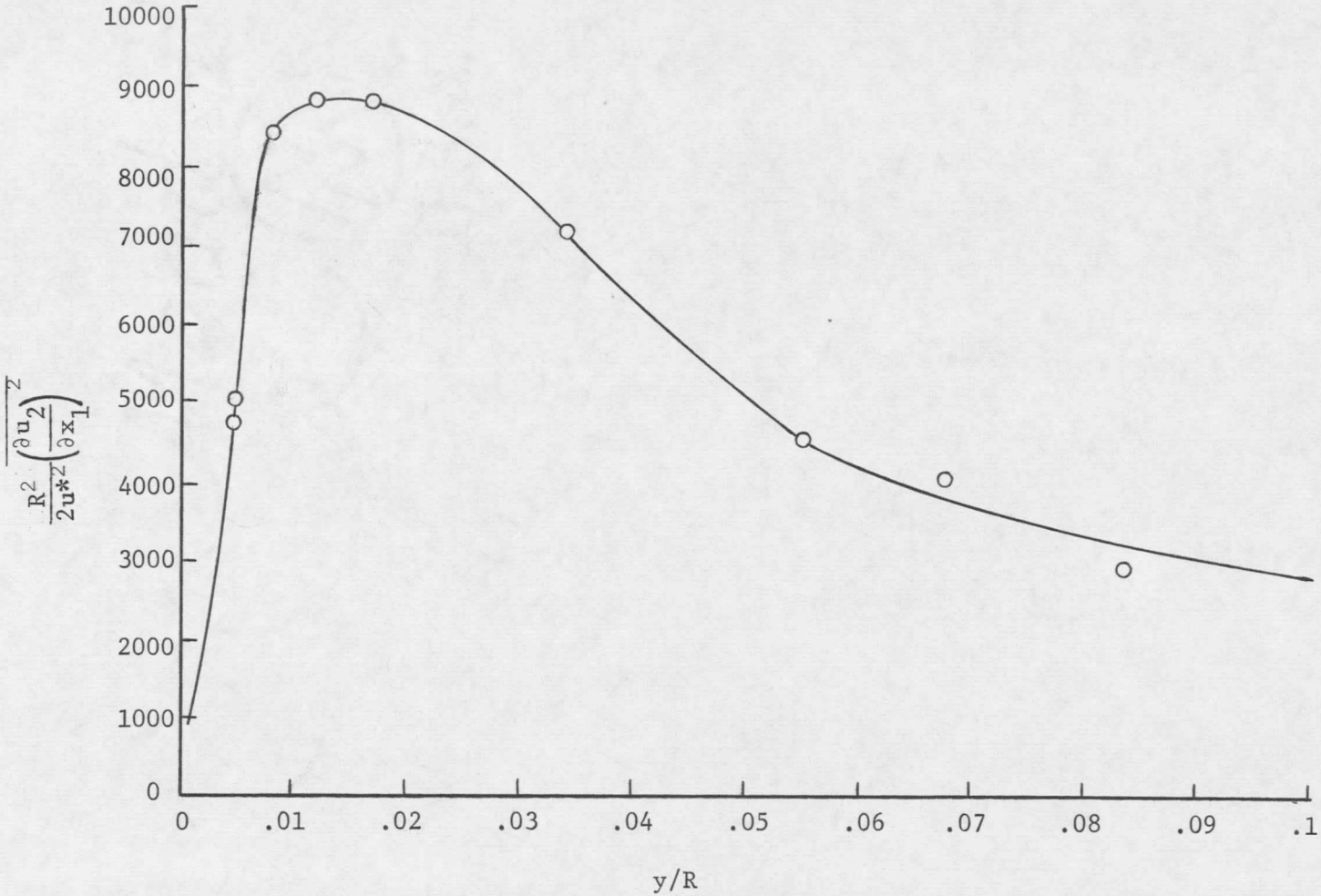

FIGURE 39. Dissipation Terms for Wall Region of Smooth Pipe

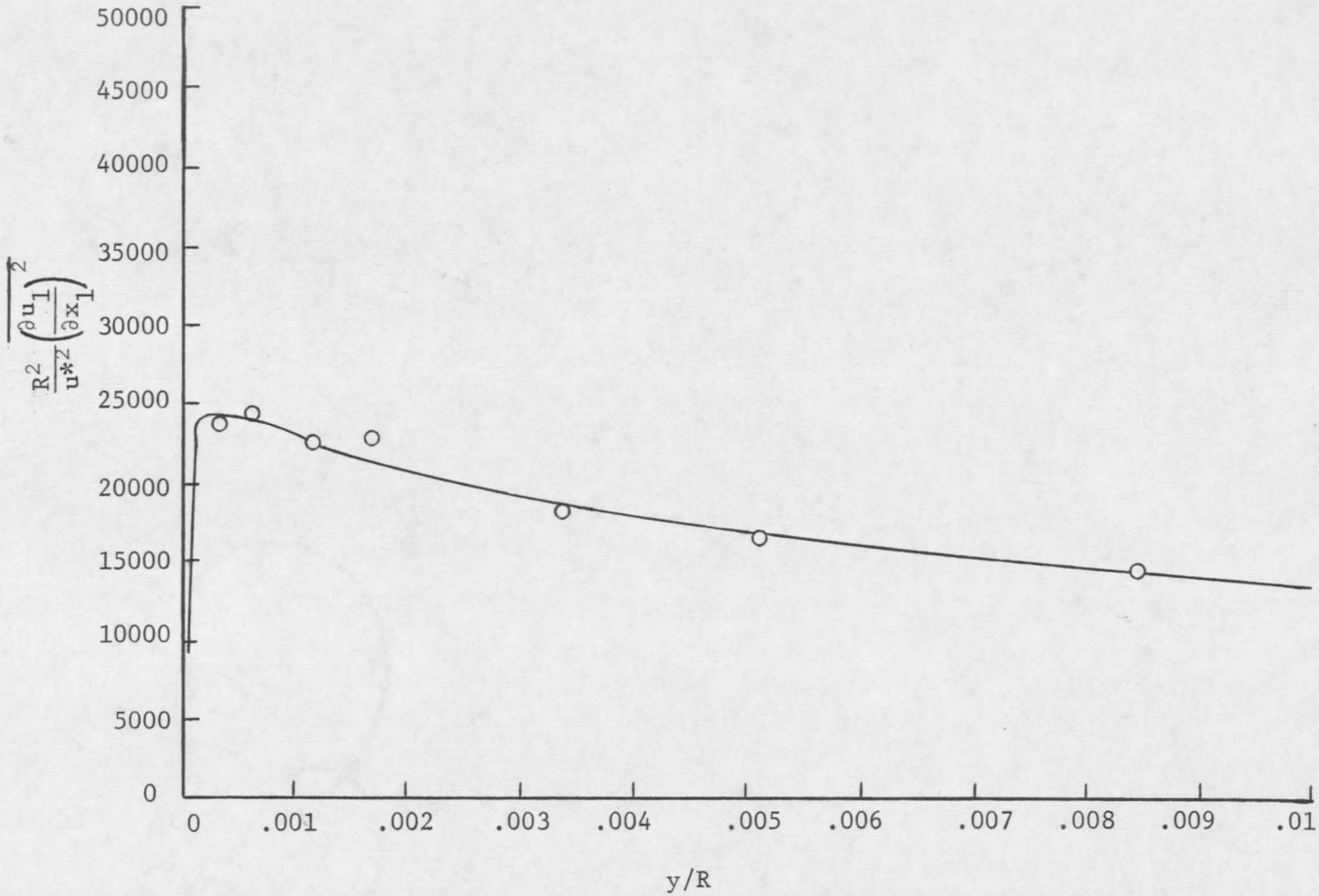

FIGURE 40. Dissipation Terms for Wall Region of Smooth Pipe

small at the pipe center line and have a small rate of magnitude change at this point. As the wall is approached, a sharp increase to a maximum value is noted, after which zero is approached rather rapidly. Some differences should be noted, however. Although the magnitudes of the values of these terms are all nearly equal at the center line, the maximum values are not equal, and these maxima are attained at different radial positions. The terms $\frac{R^2}{2u^{*2}} \overline{\left(\frac{\partial u_2}{\partial x_1}\right)^2}$ and $\frac{R^2}{2u^{*2}} \overline{\left(\frac{\partial u_3}{\partial x_1}\right)^2}$ both reach maximum values at a y/R of approximately 0.015, the former being about 9000 while the latter is near 6100. A decrease in distance from the wall and an accompanying increase in magnitude of the maximum values is noted for $\frac{R^2}{2u^{*2}} \overline{\left(\frac{\partial u_1}{\partial x_2}\right)^2}$ and $\frac{R^2}{2x_2^2 u^{*2}} \overline{\left(\frac{\partial u_1}{\partial x_3}\right)^2}$. At a y/R of approximately 0.005, maximum values of about 39,000 and 47,000, respectively are observed for the two terms. The extreme magnitude of 25,000 for $\frac{R^2}{2u^{*2}} \overline{\left(\frac{\partial u_1}{\partial x_1}\right)^2}$ occurs at a position much closer to the wall, $y/R \simeq 0.0001$.

The only other data available regarding the terms in the

dissipation function for fully developed turbulent flow in a smooth pipe appear to be those of Laufer [41], and a point by point comparison with his data is not possible since the two Reynolds numbers obtained by him were about a factor of three higher and three lower than that utilized in the current investigation. However, the shapes of the curves obtained in the current investigation are highly similar to those of Laufer's curves. Linear interpolation of Laufer's data for the two Reynolds numbers indicates good agreement with the current results, especially regarding center line magnitudes, maximum values, and the radial positions where these maximum values occur.

The foregoing experimental data can now be combined with the isotropic relations given by equations (5.20) for determination of the dissipation function itself, and a dimensionless form of this function is given in Figures 41 and 42. In similarity with the terms comprising W, vW/u^{*4} is very small at the center line and has a slow rate of increase at this point. Near a value of y/R of 0.03 a sharp increase is noted, and a maximum value of about 0.026 is reached at $y/R \simeq 0.005$. The dissipation function then decreases rapidly to zero. Thus, the dissipation is observed to become relatively large near the edge of the viscous sublayer as would be expected. These results again show good qualitative agreement with the values of the dissipation function determined experimentally by Laufer [41] if the

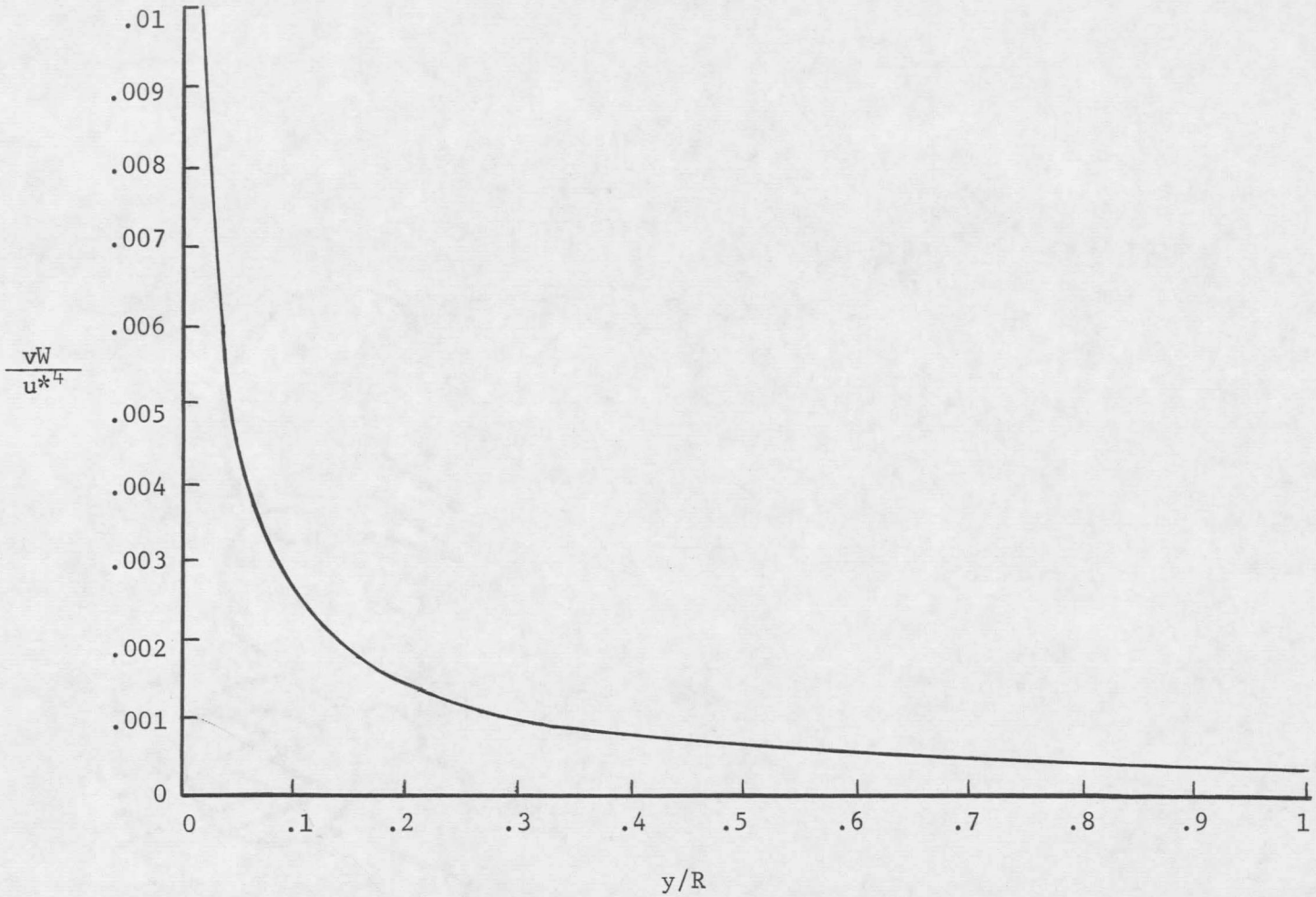

FIGURE 41. Dimensionless Dissipation Function for Central Region of Smooth Pipe

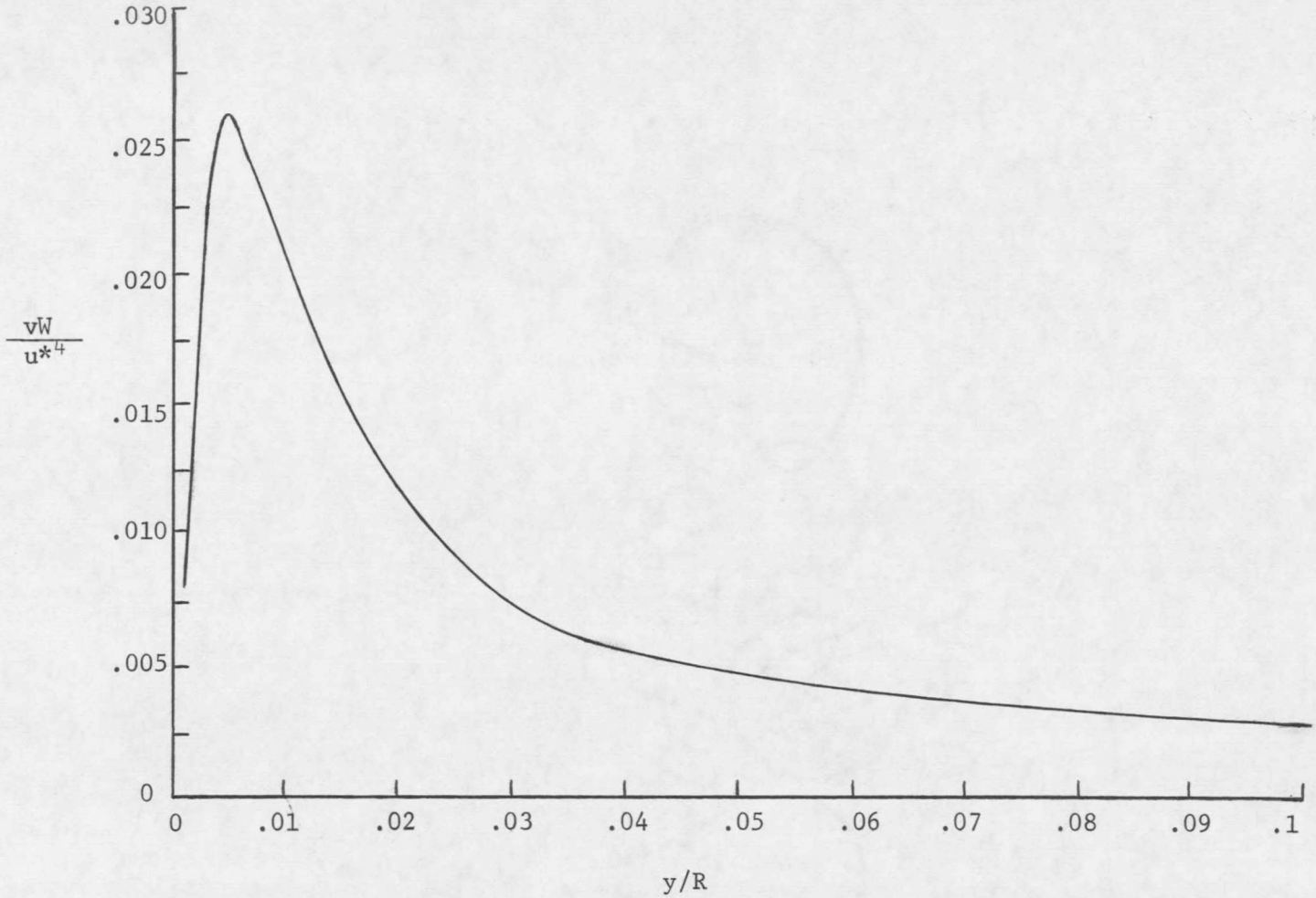

FIGURE 42. Dimensionless Dissipation Function For Wall Region of Smooth Pipe

Reynolds number difference between the two investigations is noted.

For comparison purposes, Figures 43 and 44 present the variation over the pipe cross section of the dissipation function calculated from equation (5.21) where complete isotropy between all terms is assumed. Of course, the experimental values of W obtained in the current investigation and presented in Figures 41 and 42 are not totally reliable because of the assumption of directional isotropy, but these values are expected to be much more reliable than those obtained with the assumption of complete isotropy. A comparison of Figures 43 and 44 with Figures 41 and 42 indicates reasonable agreement over the central and major portion of the pipe. However, large deviations begin to occur near the edge of the viscous sublayer where there is a sharp increase in the dissipation. The maximum value of the isotropic dissipation function occurs well within the viscous sublayer rather than near its edge. These results indicate that values of the dissipation function obtained in many previous investigations where complete isotropy was assumed are likely to be reliable in the central portion of the pipe where the dissipation is small, while such values may be somewhat unreliable near a solid surface where the dissipation is rather large.

At this point it should be noted that the measurement of one of the terms in the dissipation function, $\overline{\left(\frac{\partial u_1}{\partial x_1}\right)^2}$, allows a check on the

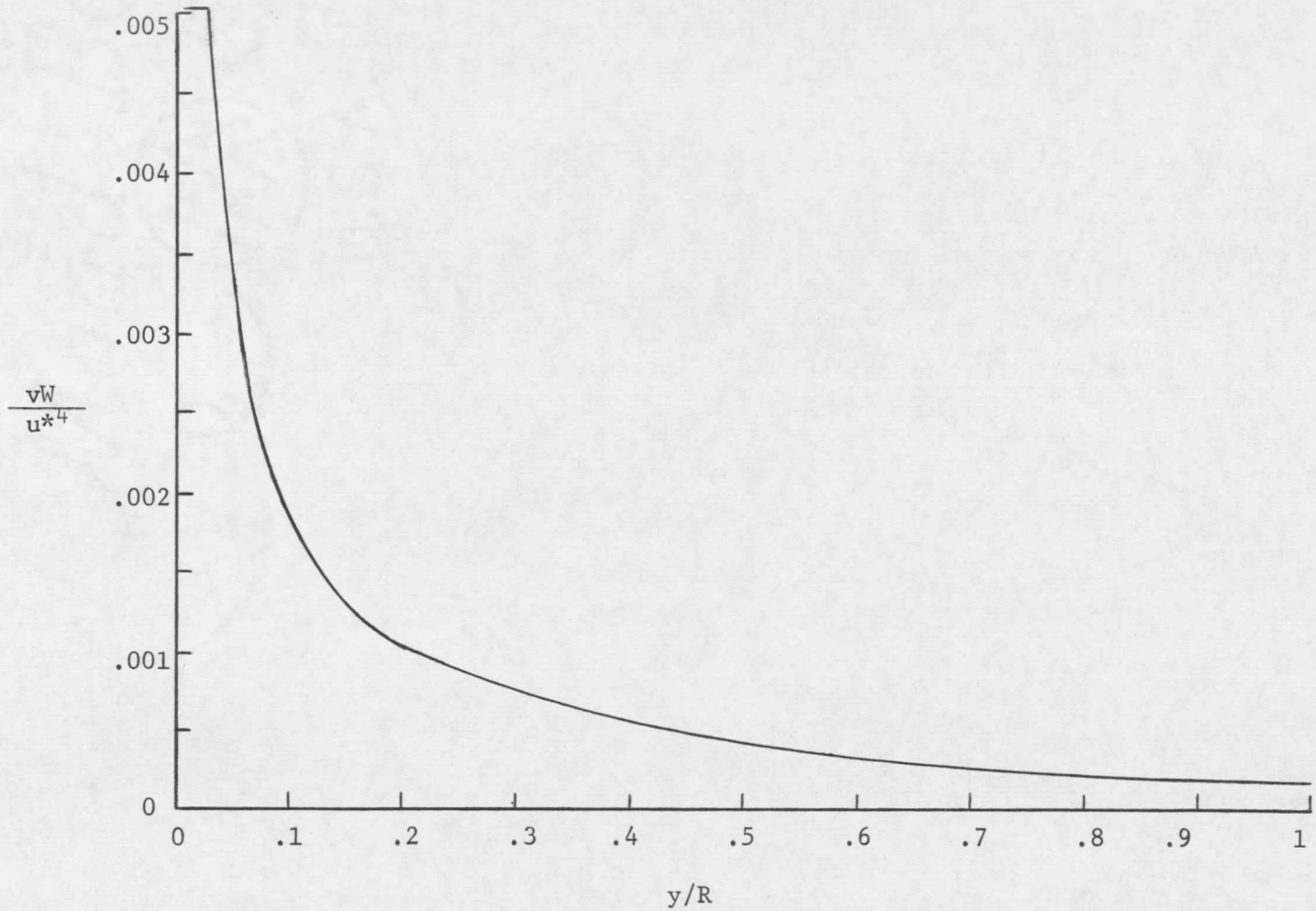

FIGURE 43. Isotropic Dissipation Function For Turbulent Core of Smooth Pipe

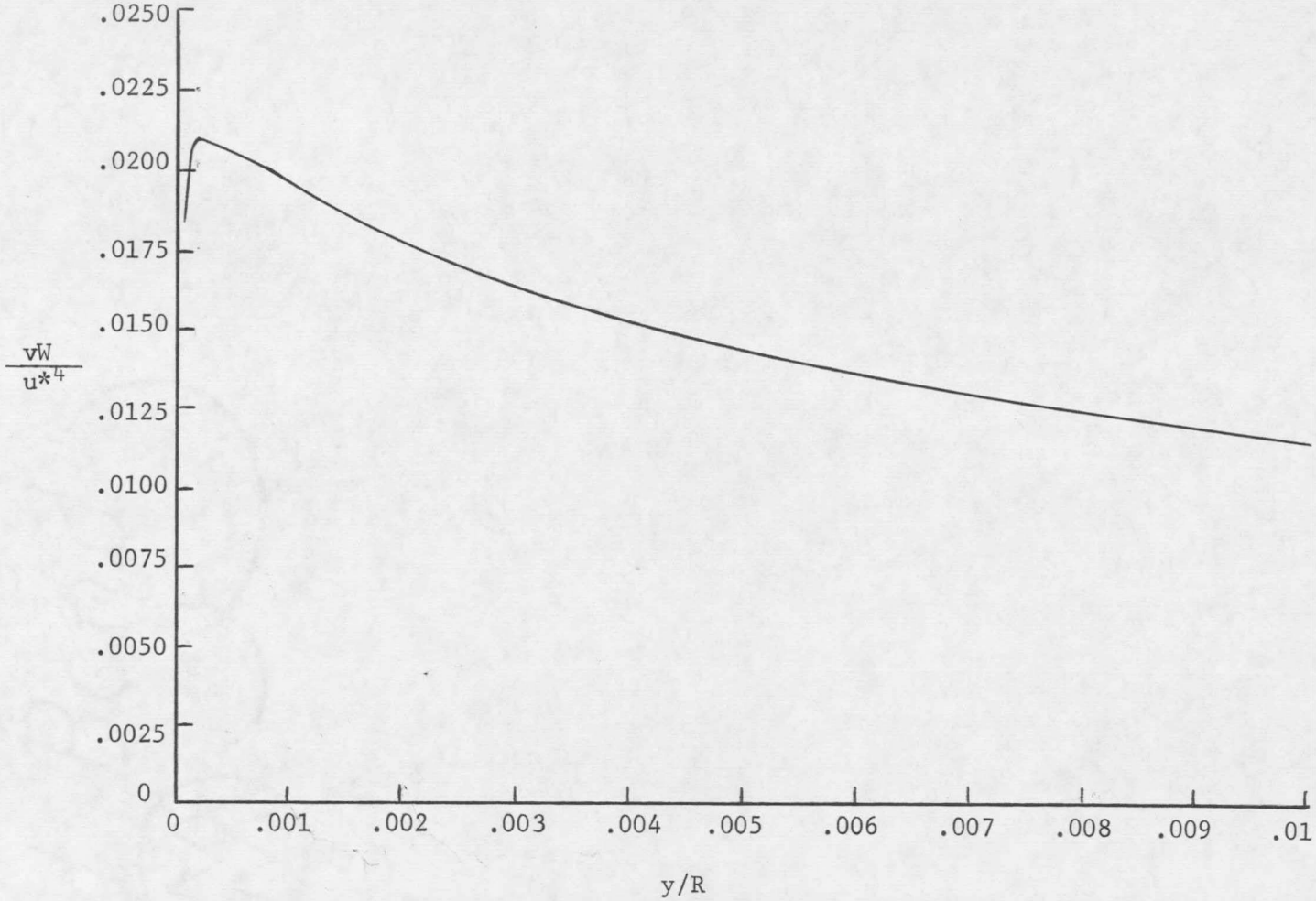

FIGURE 44. Isotropic Dissipation Function Near Wall in Smooth Pipe

validity of Taylor's hypothesis, equation (2.77), which is utilized in many of the calculations in this investigation. Lin [79] has shown that, in addition to possessing a small turbulence intensity, a shear flow must also satisfy the condition given by equation (2.78b) if Taylor's hypothesis is to apply. This condition is shown in Figures 45 and 46 to be satisfied with a high degree of accuracy throughout the flow field, except possibly for points extremely near the solid wall. Thus, Taylor's hypothesis is expected to be valid for flow in a smooth pipe with the possible exception of a very thin layer near the wall.

Energy Relations

Consider first the mean energy balance given by equation (4.30). For the smooth pipe, this equation indicates that the energy available due to the pressure drop along the pipe is partly converted into turbulence energy by action of the $\overline{u_1 u_2}$ shearing stress and partly directly dissipated by viscous action. The mean energy balance determined experimentally for the turbulent core of the pipe is indicated by Figures 47, 48, and 49. Figure 47 shows that only a relatively small amount of energy is available throughout the central portion of the pipe. This quantity vanishes at the center line and decreases to a value of -0.01 at $y/R \simeq 0.05$. The curve representing

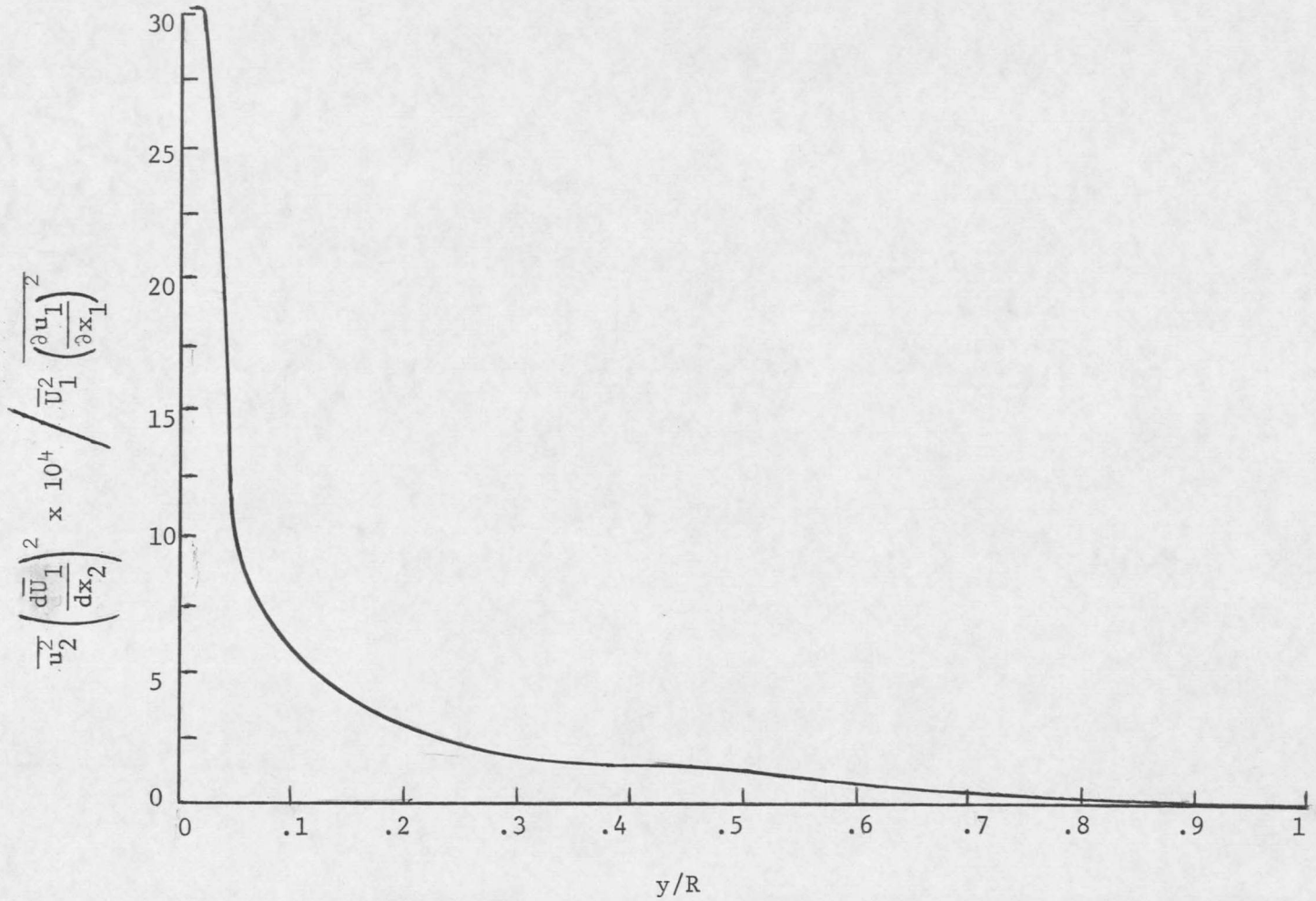

FIGURE 45. Lin's Condition for Applicability of Taylor's Hypothesis in Core Region of Smooth Pipe

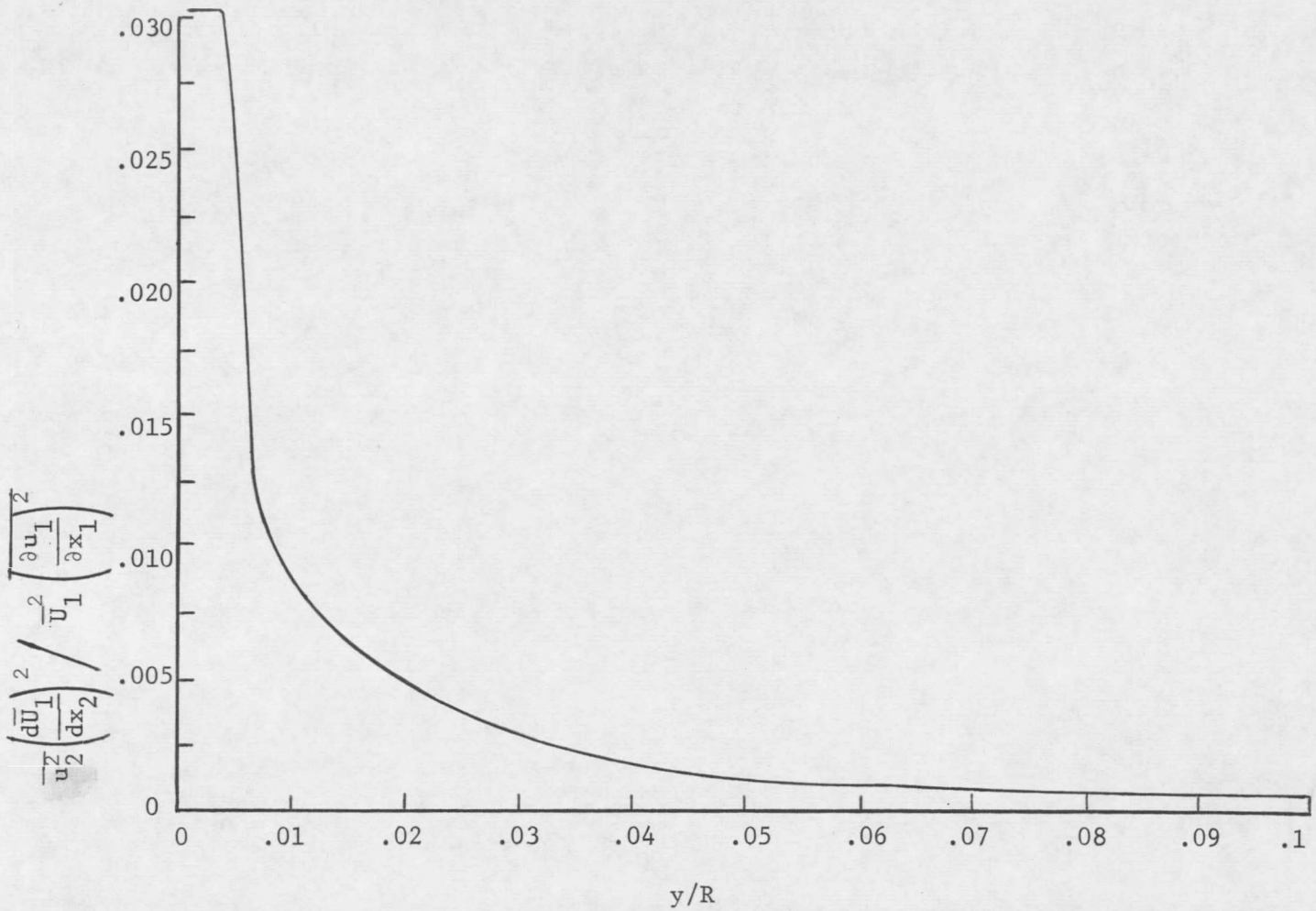

FIGURE 46. Lin's Condition for Applicability of Taylor's Hypothesis in Wall Region of Smooth Pipe

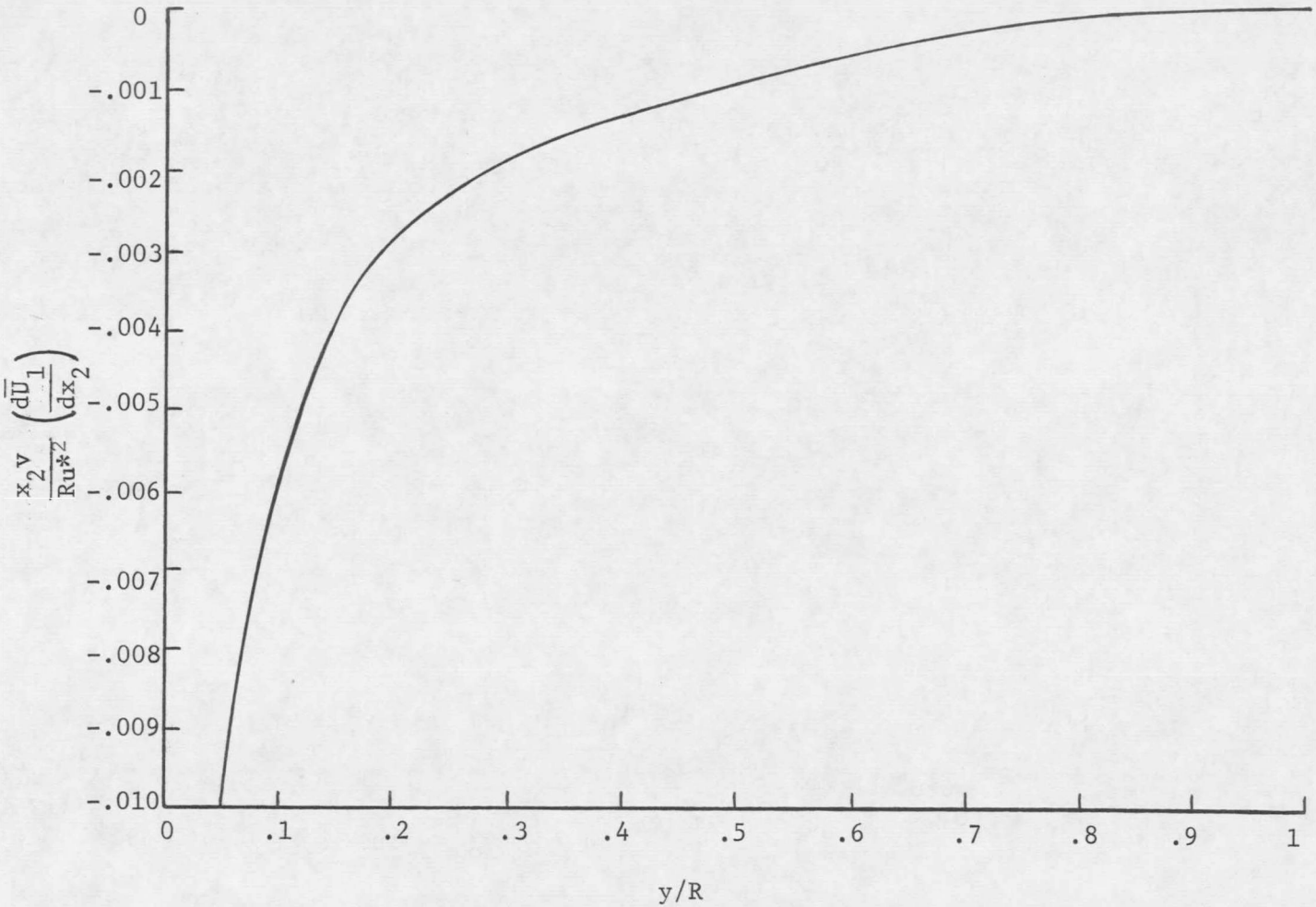

FIGURE 47. Availability of Mean Energy in Turbulent Core of Smooth Pipe Due to Longitudinal Pressure Drop

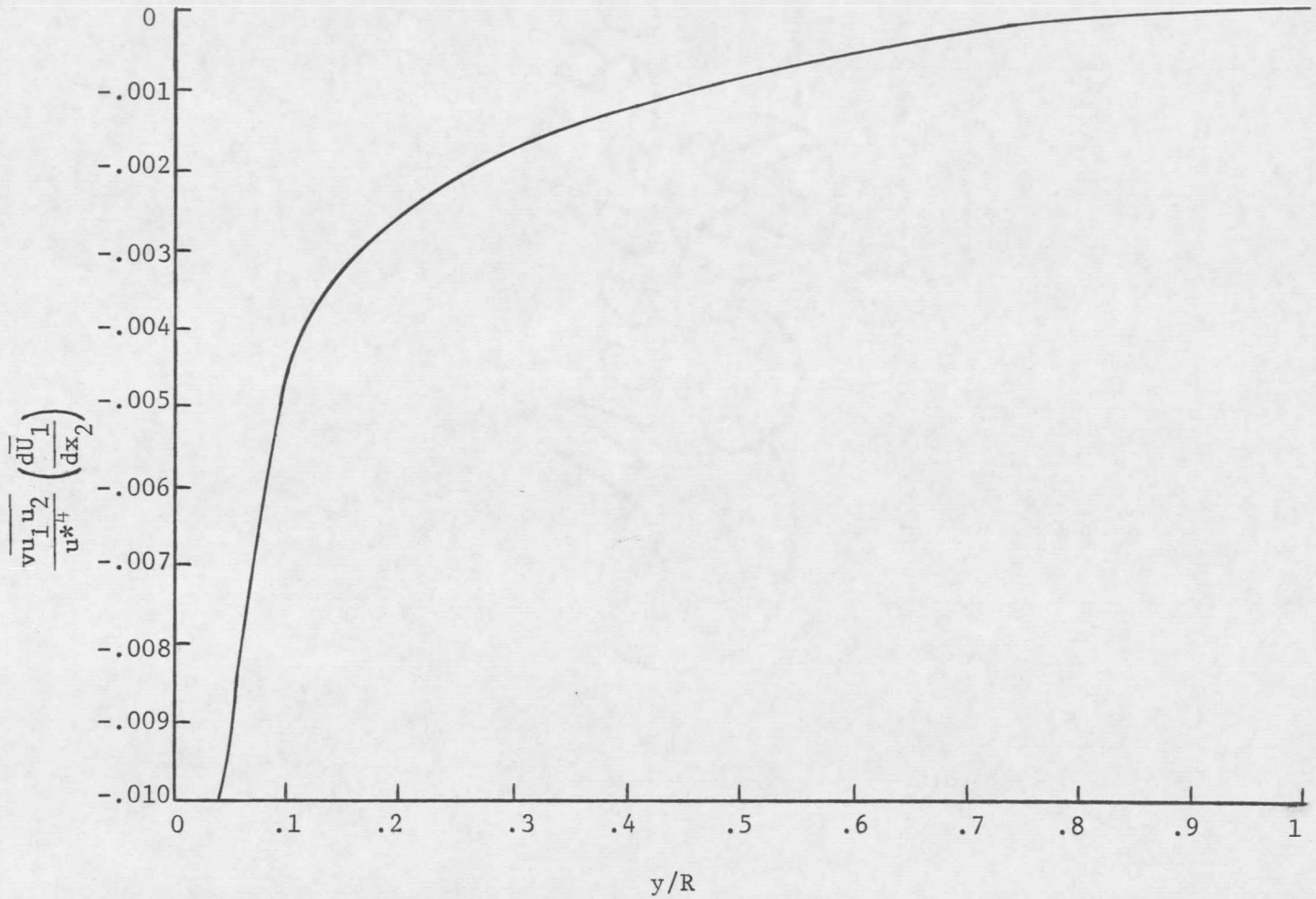

FIGURE 48. Conversion of Mean Energy to Turbulence Energy in Turbulent Core of Smooth Pipe

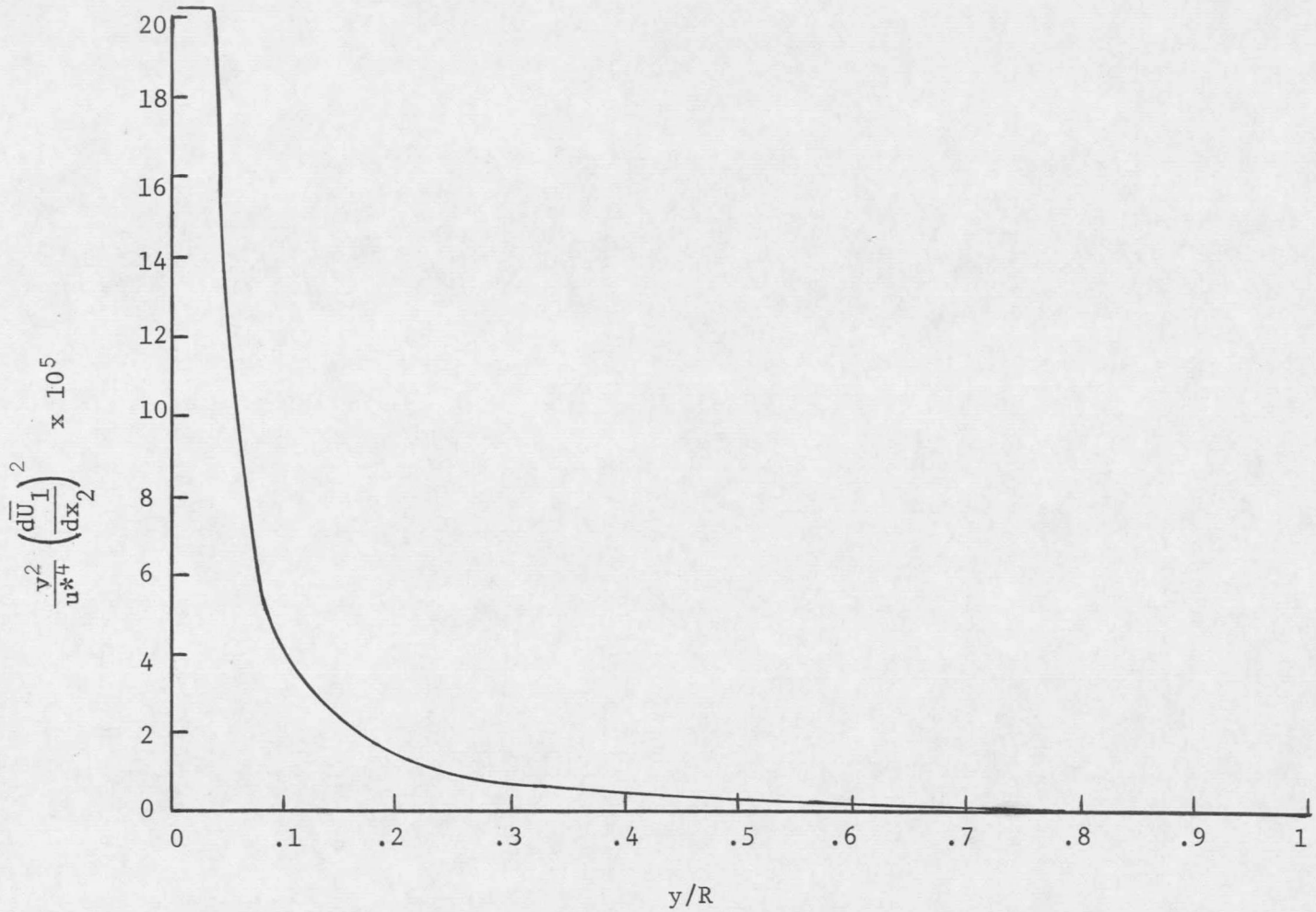

FIGURE 49. Direct Viscous Dissipation of Mean Energy in Turbulent Core of Smooth Pipe

the turbulence production and shown in Figure 48 is nearly identical to the curve representing the availability, thereby indicating that the major portion of the available energy in the central portion of the pipe is converted to turbulence energy with little direct viscous dissipation. This conclusion is confirmed by Figure 49 which shows the viscous dissipation to be negligible throughout this area of the pipe, although a marked increase is beginning to occur for y/R less than about 0.1.

The mean energy balance for that portion of the flow immediately adjacent to the pipe wall is presented in Figures 50, 51, and 52. The availability is shown by Figure 50 to remain small until a y/R of about 0.005 is reached. At this point the availability rapidly decreases until a value of -1.0 is attained at y/R ≈ 0.001. Figure 52 indicates that the direct viscous dissipation remains near a null value for values of y/R greater than about 0.005, and for smaller values it rapidly increases to a value of unity to balance the availability at the wall. Thus, as can be seen from Figure 51, for all values of y/R greater than about 0.005, the available mean energy is converted directly into turbulence energy. For y/R less than 0.005, there is a sharp increase in magnitude of the turbulence production, but this is accompanied by increases in both the available energy and the direct viscous dissipation. A maximum turbulence

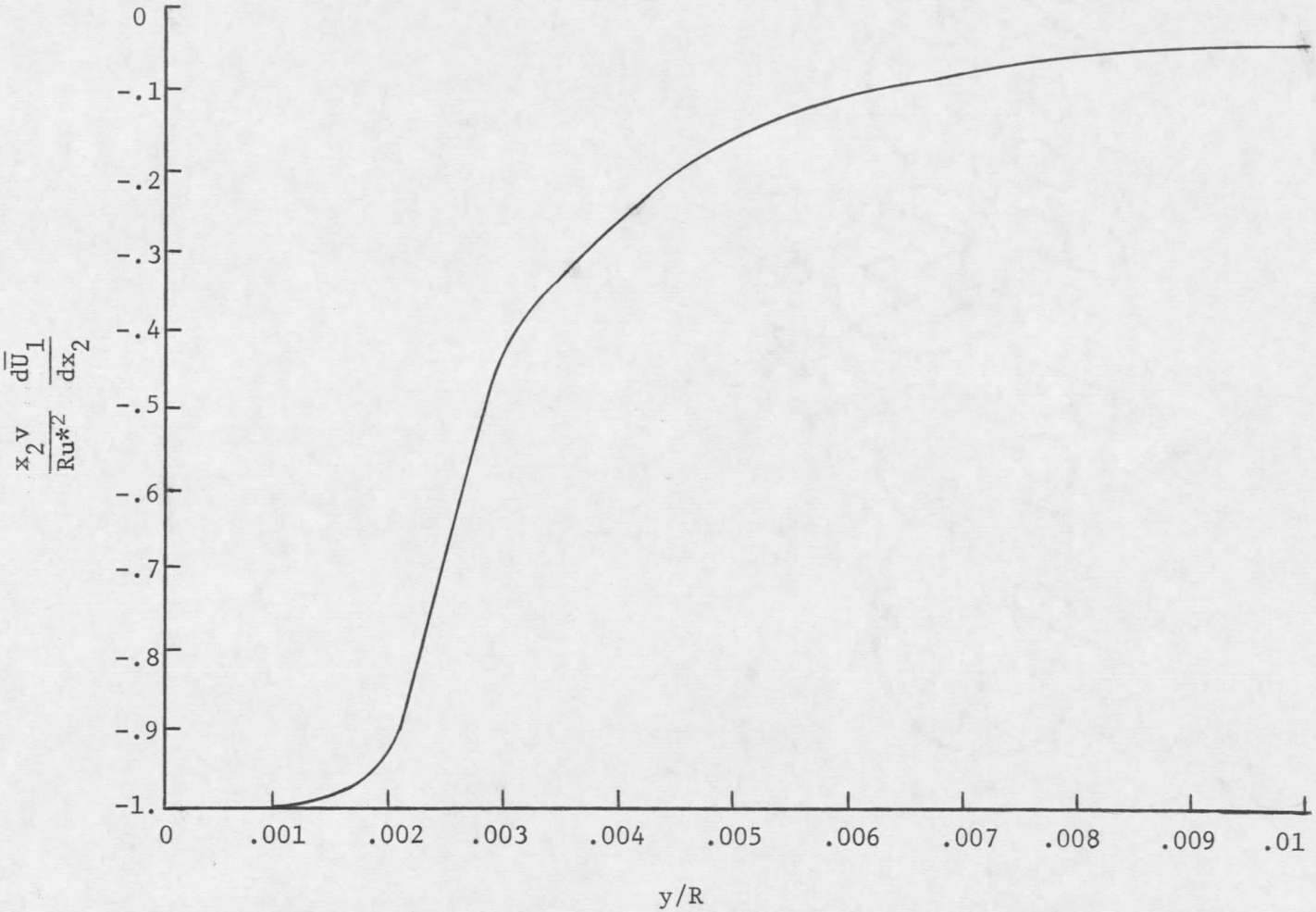

FIGURE 50. Availability of Mean Energy Due to Longitudinal Pressure Drop Near Wall of Smooth Pipe

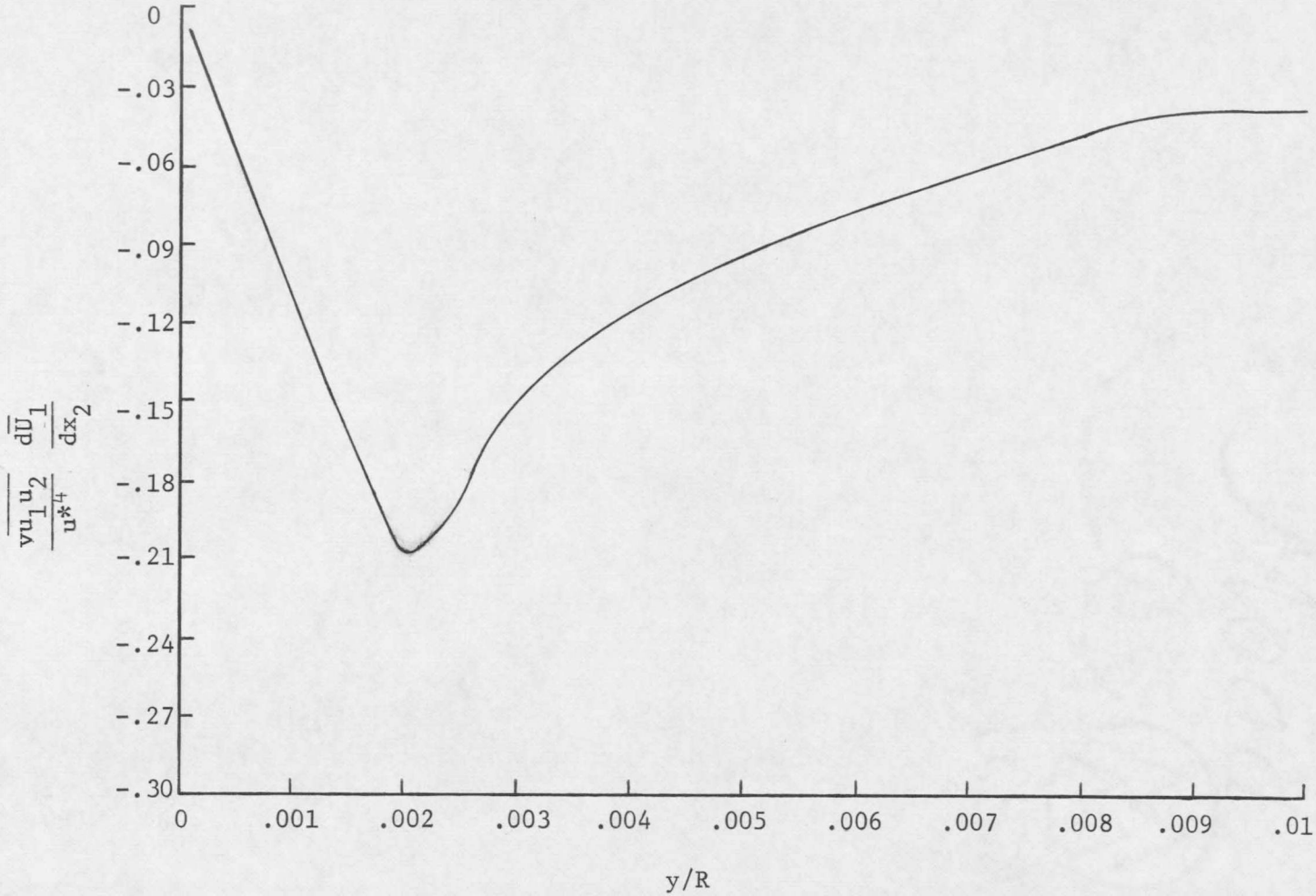

FIGURE 51. Conversion of Mean Energy to Turbulence Energy Near Wall of Smooth Pipe

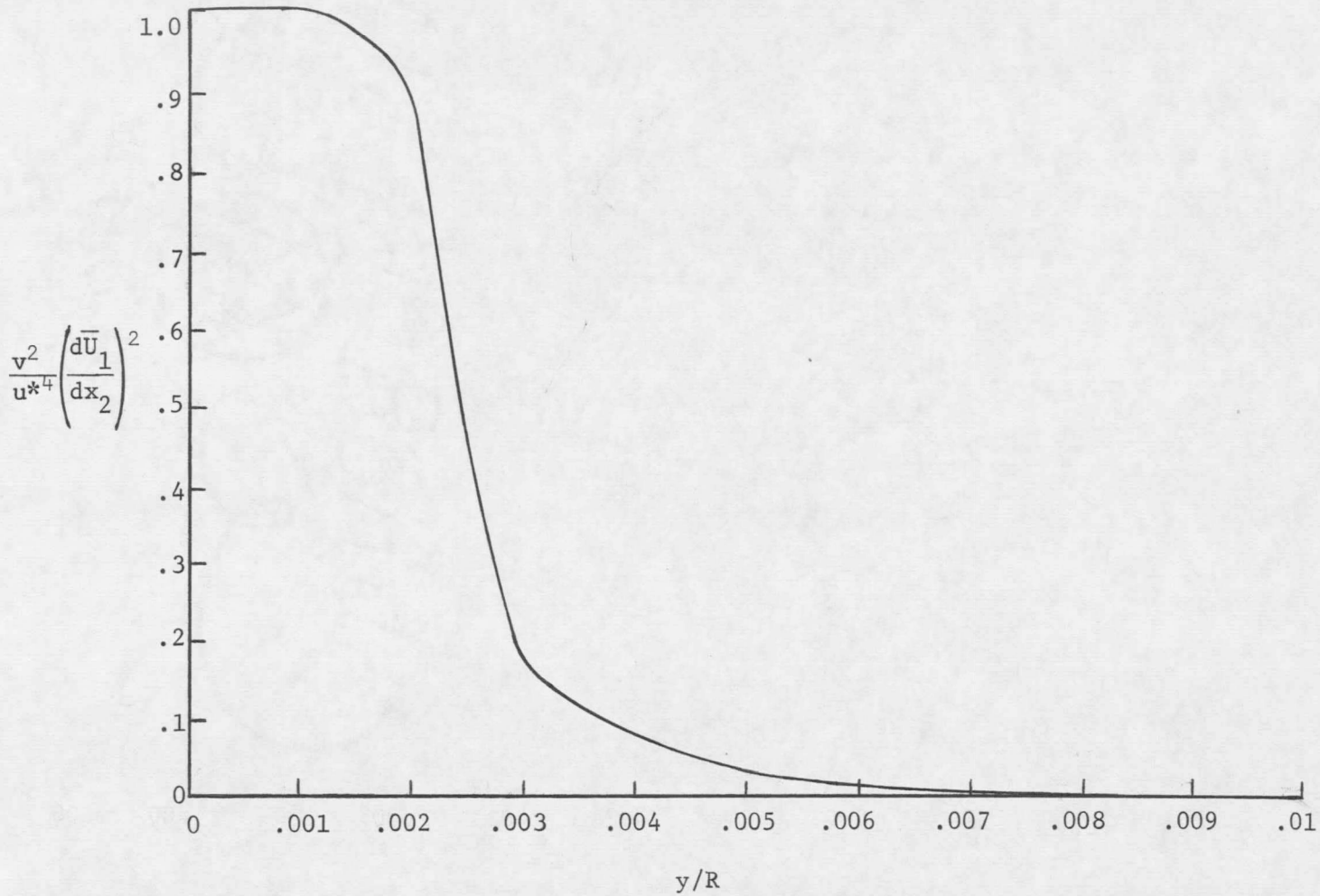

FIGURE 52. Direct Viscous Dissipation of Mean Energy Near Wall of Smooth Pipe

production is attained near $y/R = 0.0022$ ($y^+ = 8$), and the production then approaches zero in an approximately linear fashion. A comparison of Figures 51 and 52 indicates that the viscous dissipation and the turbulence production are approximately equal in magnitude at the point where the production is a maximum, and this is also the point where Kline et al [80] found the oscillations of the three dimensional streaky structure to begin. Also, Laufer [41] indicated no Reynolds number dependence in the terms appearing in the mean energy balance, and as a result, the data presented here are in excellent quantitative agreement with his data.

To summarize these results it should be noted that the bulk of the available energy is taken from the mean flow in a very narrow region immediately adjacent to the wall ($y^+ < 18$), and a large portion of this energy is directly dissipated by viscous action. However, a large portion of the total turbulence production also occurs within this same region. Thus, the importance, to a complete understanding of the turbulence phenomena, of a knowledge of occurrences within fluid layers very near the solid boundary is again emphasized.

Having established the amount of energy converted from the mean motion to turbulence energy, the expression for the turbulence energy balance, equation (4.29), will now be examined in order to determine the fate of this converted energy. The portion of this energy which

is dissipated by viscous effects was considered in the previous section, and the experimental results are shown in Figures 41 and 42. A comparison of the production and dissipation produces the interesting result that these two quantities nearly balance each other over the entire cross section, with two exceptions. Near the center of the pipe, the turbulence production vanishes while the dissipation maintains a nonzero value. This, of course, will have to be accounted for by a diffusion of turbulence energy into this area. Another slight difference occurs near the wall where the maximum value of the dissipation occurs at a somewhat larger value of y/R than does the maximum value of the production. It is interesting to note that these two maxima are nearly equal in magnitude, however.

Experimentally determined values of the gradient type diffusion of turbulence kinetic energy are indicated in dimensionless form in Figure 53 for the central region of the pipe and in Figure 54 for the wall region. This term is seen to be rather small over the entire cross section, as would be expected, although a pronounced maximum value is attained just outside the viscous sublayer ($y^+ \approx 70$) where the turbulence production is a maximum. From this point, the kinetic energy is diffused both toward the pipe wall and toward the center line. The resultant effect on the energy balance is a loss in energy for values of y/R between about 0.013 and 0.7 and a

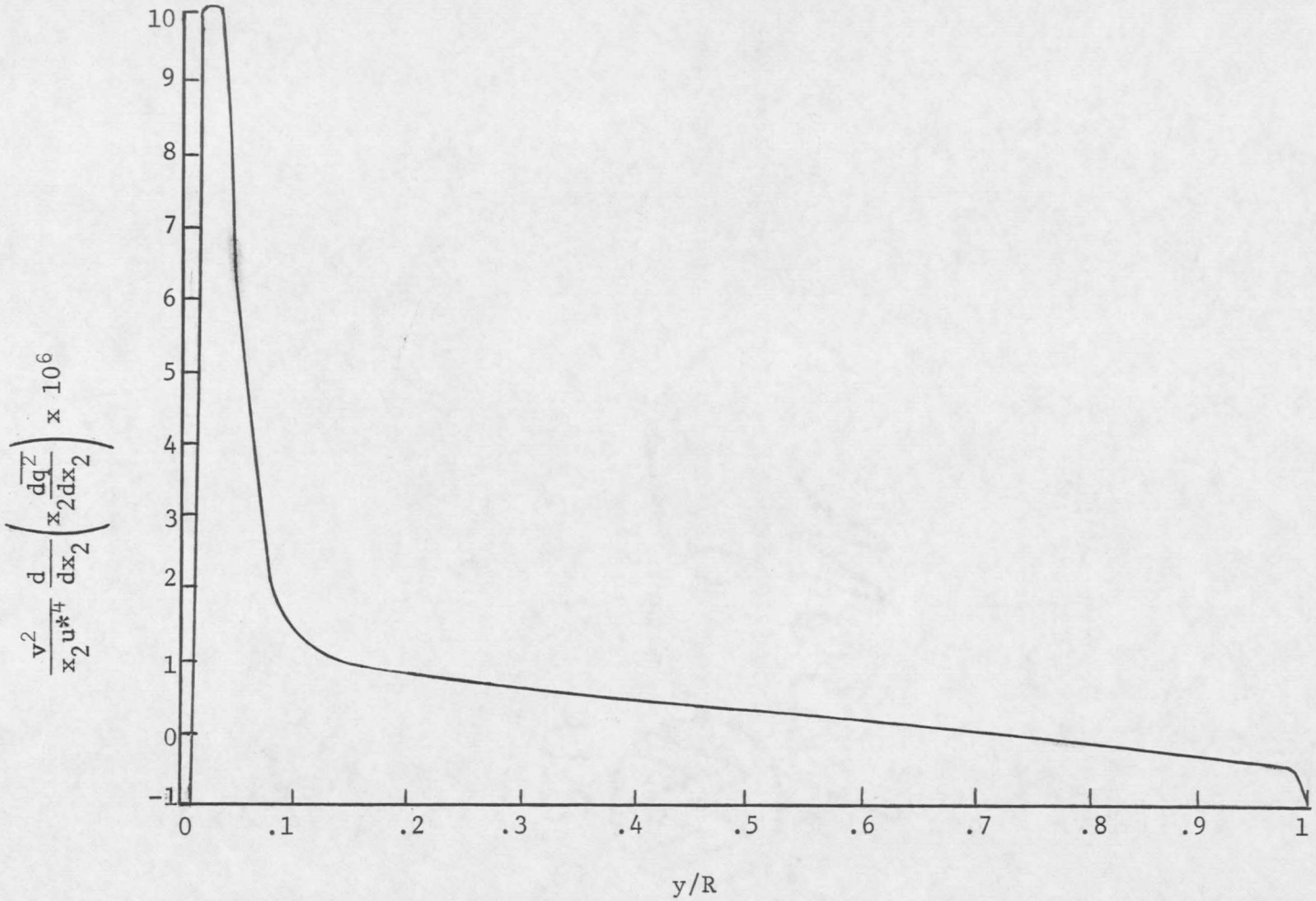

FIGURE 53. Gradient Diffusion of Turbulence Kinetic Energy in Central Region of Smooth Pipe

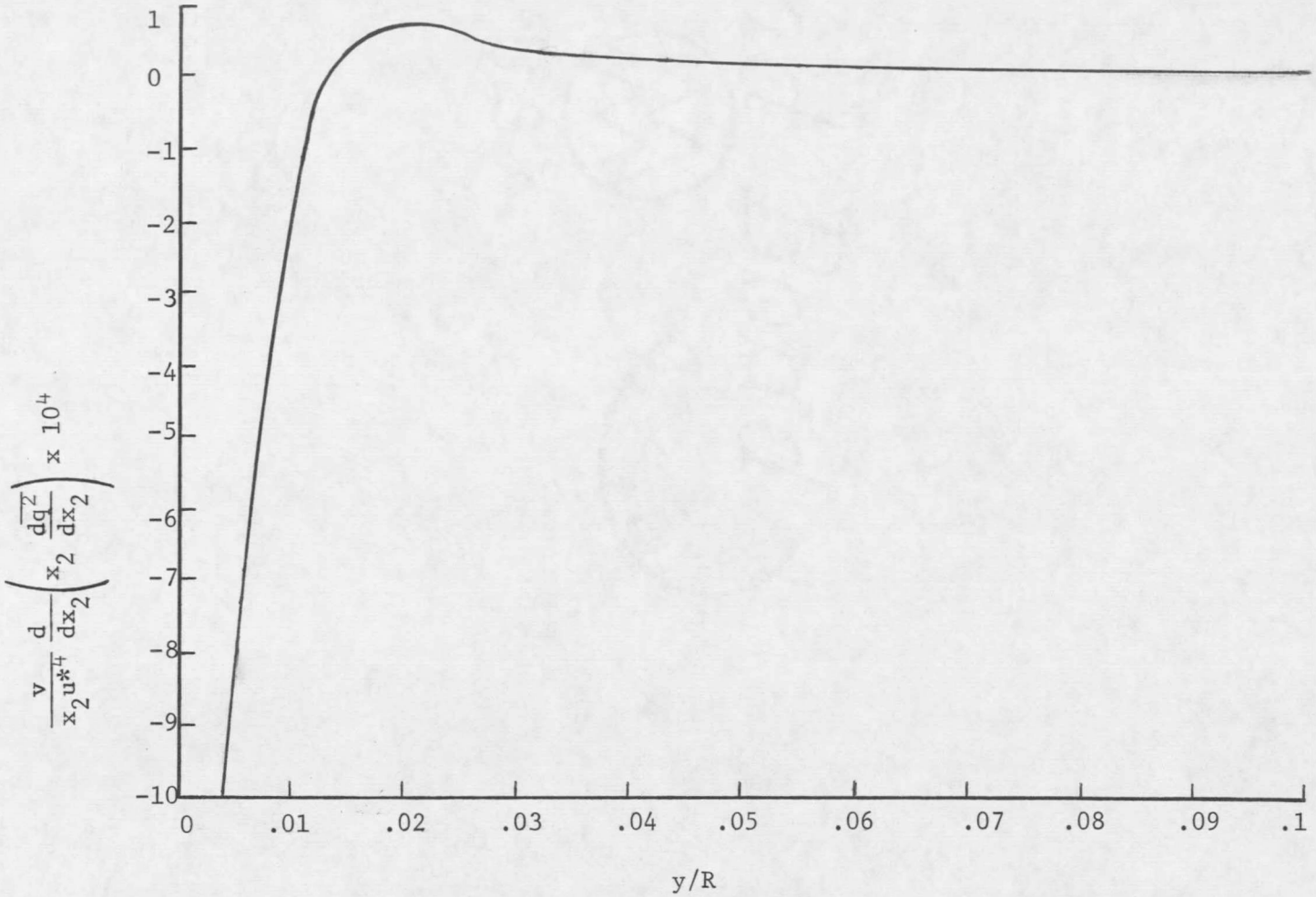

FIGURE 54. Gradient Diffusion of Turbulence Kinetic Energy in Wall Region of Smooth Pipe

gain in energy at the remaining radial positions. Thus the gradient type diffusion of kinetic energy at least partially accounts for the dissipation with lack of production at the pipe center line. It should be noted that the y^+ value of 70 is just outside the region where Kline et al [80] found the abrupt breakup of the three-dimensional streaks to occur.

All terms appearing in the turbulence energy balance have now been determined experimentally except the convective diffusion term χ, and this term may be calculated as the closing entry in equation (4.29). The results of this calculation are presented in Figures 55 and 56. As was the case with Laufer's [41] results, this term is seen to be somewhat larger throughout the pipe than was the gradient diffusion. A pronounced maximum occurs near $y^+ = 8$ which is identically the point where a maximum production of turbulence energy occurs. This results in a loss of energy for y/R less than about 0.7 and a gain of energy near the center line, thereby completing the compensation for dissipation without production in this area. Although a maximum value of the convective diffusion occurs at $y^+ = 8$, there still appears to be a loss of energy completely to the wall due to convective diffusion. This is thought to be a result of diffusion of pressure energy from the wall as reported by Laufer [41]. Such a loss would be expected, however, in order to balance the energy

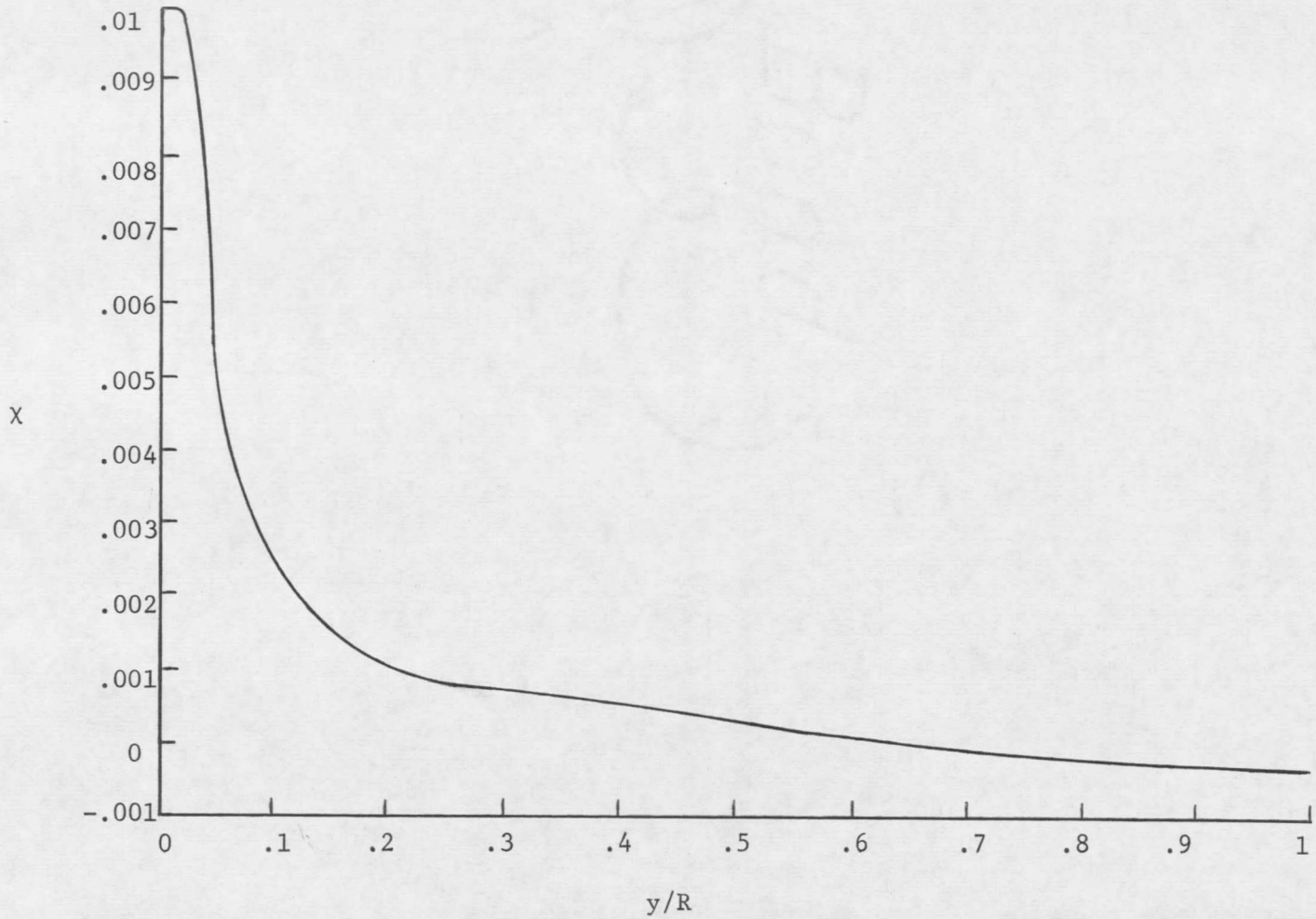

FIGURE 55. Convective Diffusion of Total Turbulence Energy in Central Region of Smooth Pipe

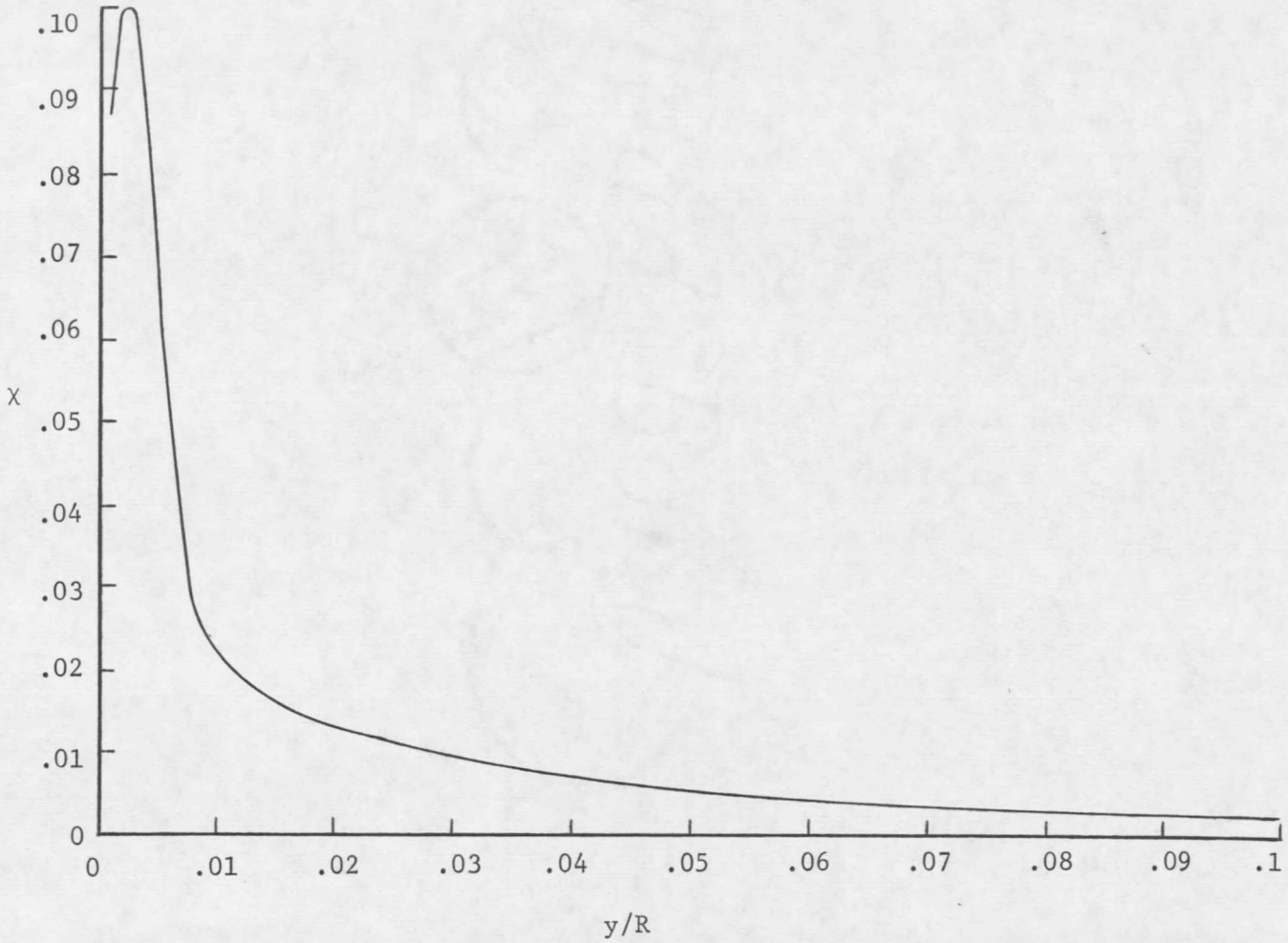

FIGURE 56. Convective Diffusion of Total Turbulence Energy in Wall Region of Smooth Pipe

gain from the gradient type diffusion.

Energy Spectra

In this discussion of the spectral analysis results, the commonly accpeted physical interpretation of the energy spectrum, as presented in the review of the literature, should be kept in mind. This interpretation may be briefly reviewed in the following manner. The dissipation of turbulence energy, in which viscosity plays an important role, is associated with small eddies corresponding to large wave numbers or frequencies. Kolmogorov [82] has postulated that such eddies will be statistically isotropic and independent of the structure of the large eddies, and Tchen [84] hypothesizes that $E_i(k_1)$ will be proportional to k_1^{-7} for this range of eddy sizes. On the other hand, both the production of turbulence energy by shear forces and the diffusion of turbulence energy are considered to be associated with low frequency velocity fluctuations corresponding to large eddies. Energy transfer in the frequency domain or the wave number space is then taken to be from low to high values of frequency or wave number. This is equivalent to a transfer of energy from large to small eddies. In fact, Kolmogorov [82] shows that a subrange of eddy sizes, where the dominant process is the transfer of energy by inertia forces with negligible dissipation and production, may exist,

and Karman and Lin [83] show that the spectrum function $E_i(k_1)$ will vary as $k_1^{-5/3}$ in this inertial subrange. Tchen [84] indicates that $E_i(k_1)$ will be proportional to k_1^{-1} in a subrange of eddy sizes where the dominant process is the inertial transfer of energy, dissipation is negligible, but the production is nonzero. The foregoing physical interpretation of energy spectra measurements has assumed the applicability of Taylor's hypothesis, and it should be remembered, as stated in the warning given by Kline [3], that this hypothesis may not be valid very near the wall, especially for the fluctuations normal to the longitudinal direction.

A contour map of the energy spectra of the u_1 fluctuating velocities is presented in Figure 57 for the frequency domain, and transformation to the wave number space is indicated by Figure 58. These figures indicate the normally expected variation of the energy spectrum at a given value of y/R, i.e, a relatively large value at small frequencies and a rather rapid decrease at large frequencies. Figure 58 indicates that for a given wave number there is a decrease in energy content of the dissipation eddies in moving from the wall to the center line of the pipe in agreement with the examination of the turbulence energy equation. Again for a constant wave number, the energy content of the eddies associated with production and diffusion is seen to indicate a rapid decline, at both the wall and

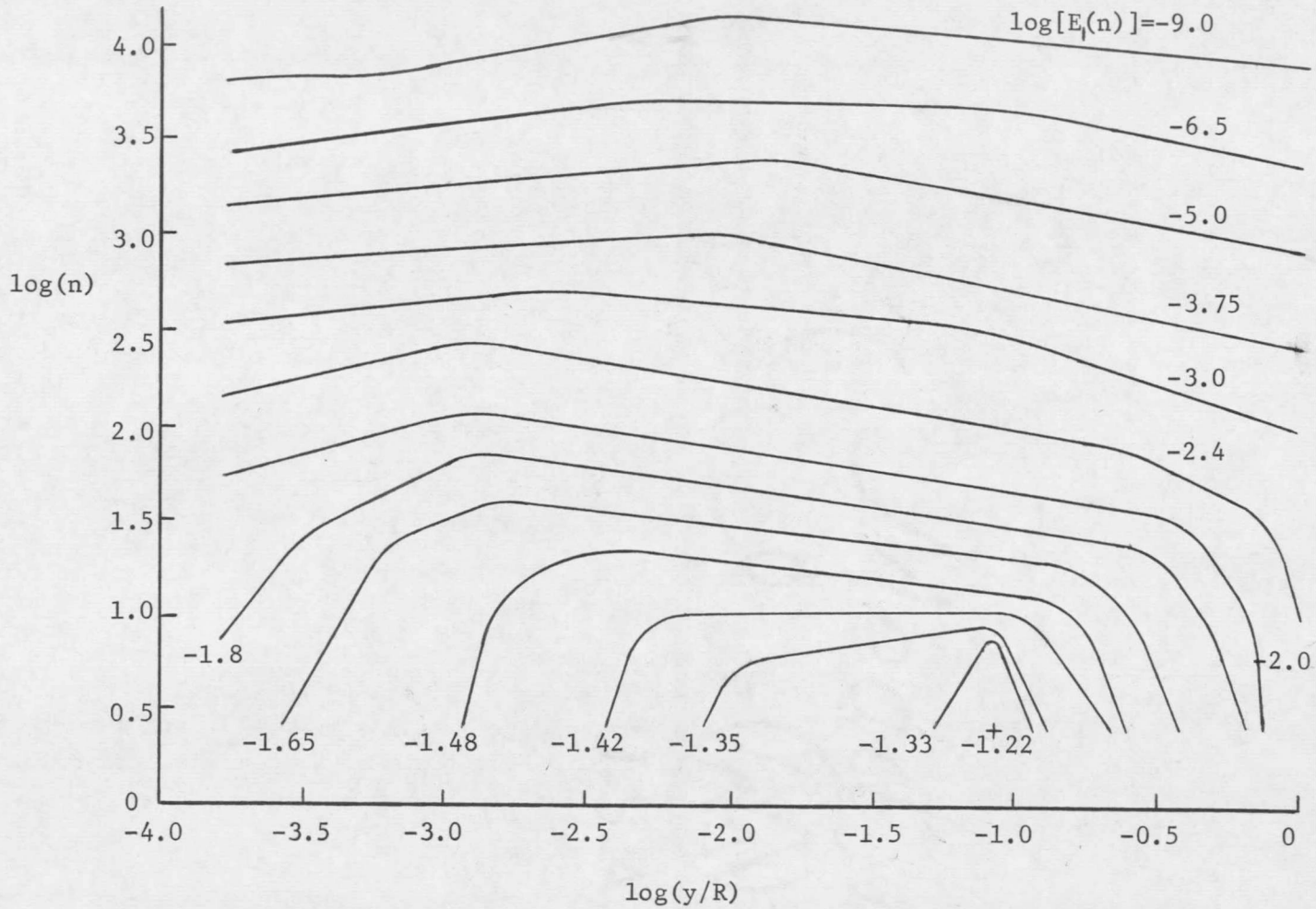

FIGURE 57. Frequency Domain Energy Spectra for u_1 Fluctuating Velocity in Smooth Pipe

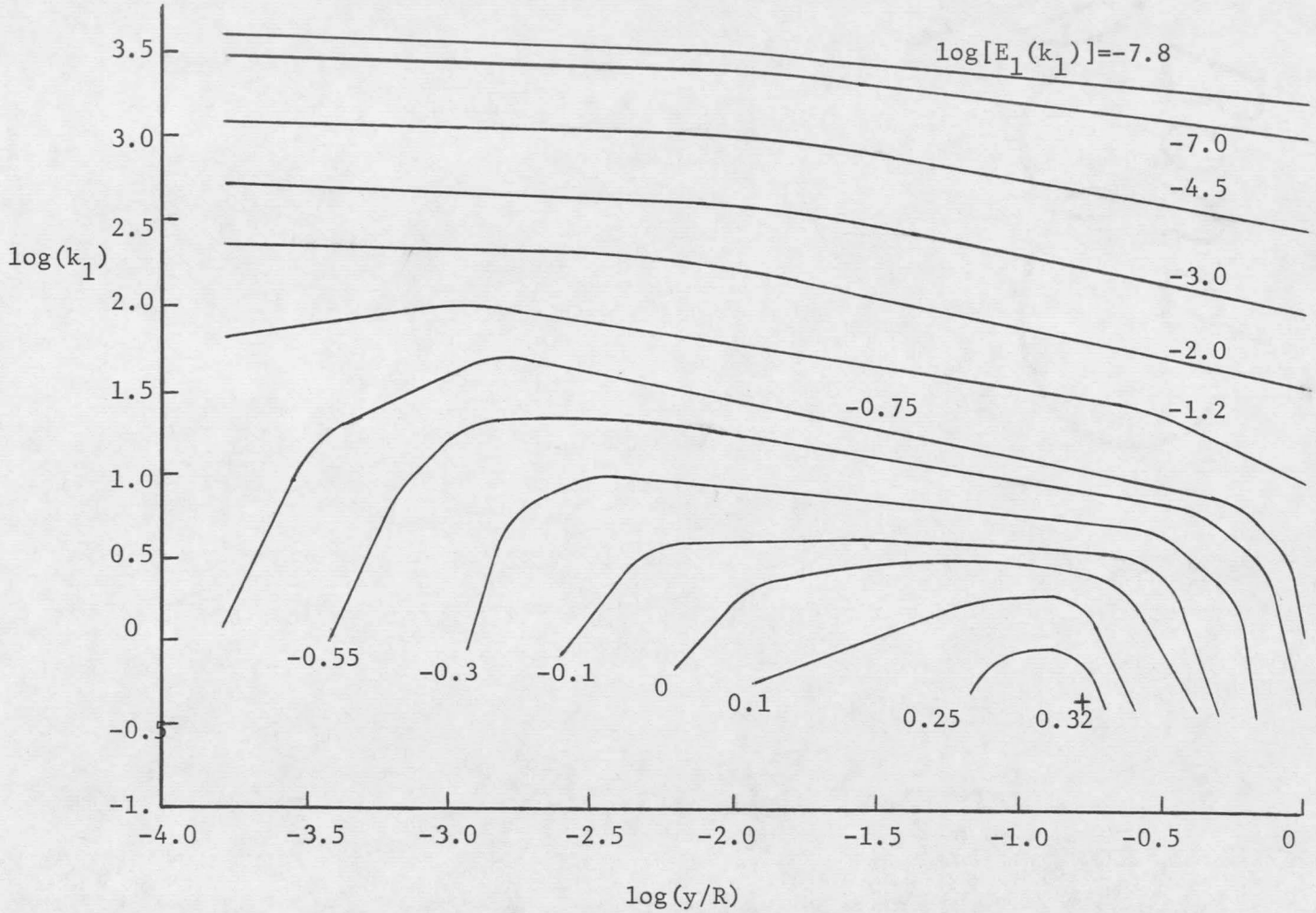

FIGURE 58. Contour Map of u_1 Energy Spectra for Smooth Pipe

the center line, from a maximum value at an intermediate radial position. The value of y/R where this maximum occurs is seen to vary from about 0.2 at the smallest wave numbers to around 0.001 for intermediate wave numbers. Such behavior would be expected since diffusion is relatively large in this region, as is the production of turbulence energy.

The possible existence of the various subranges of eddy sizes can be established by an examination of Figures 59, 60, and 61. Figure 59 shows the inertial subrange where the dominant process is the transfer of energy from smaller to larger wave numbers without significant production or dissipation. Such a subrange appears to be exhibited over a rather wide range of wave numbers over the entire pipe cross-section, and the wave numbers where this law applies decrease in moving from the wall to the center line. The production subrange is shown to indicate a similar behavior in Figure 60. A comparison of these two figures reveals that the production subrange does occur for slightly larger eddies than the inertial subrange, and this is exactly the behavior predicted by Tchen [84]. Within the range of variables examined experimentally in this investigation, an absence of any viscous subrange of eddy sizes is noted in Figure 61 for all values of y/R. The shape of the contours in this figure does indicate, however, that such a subrange will probably occur at

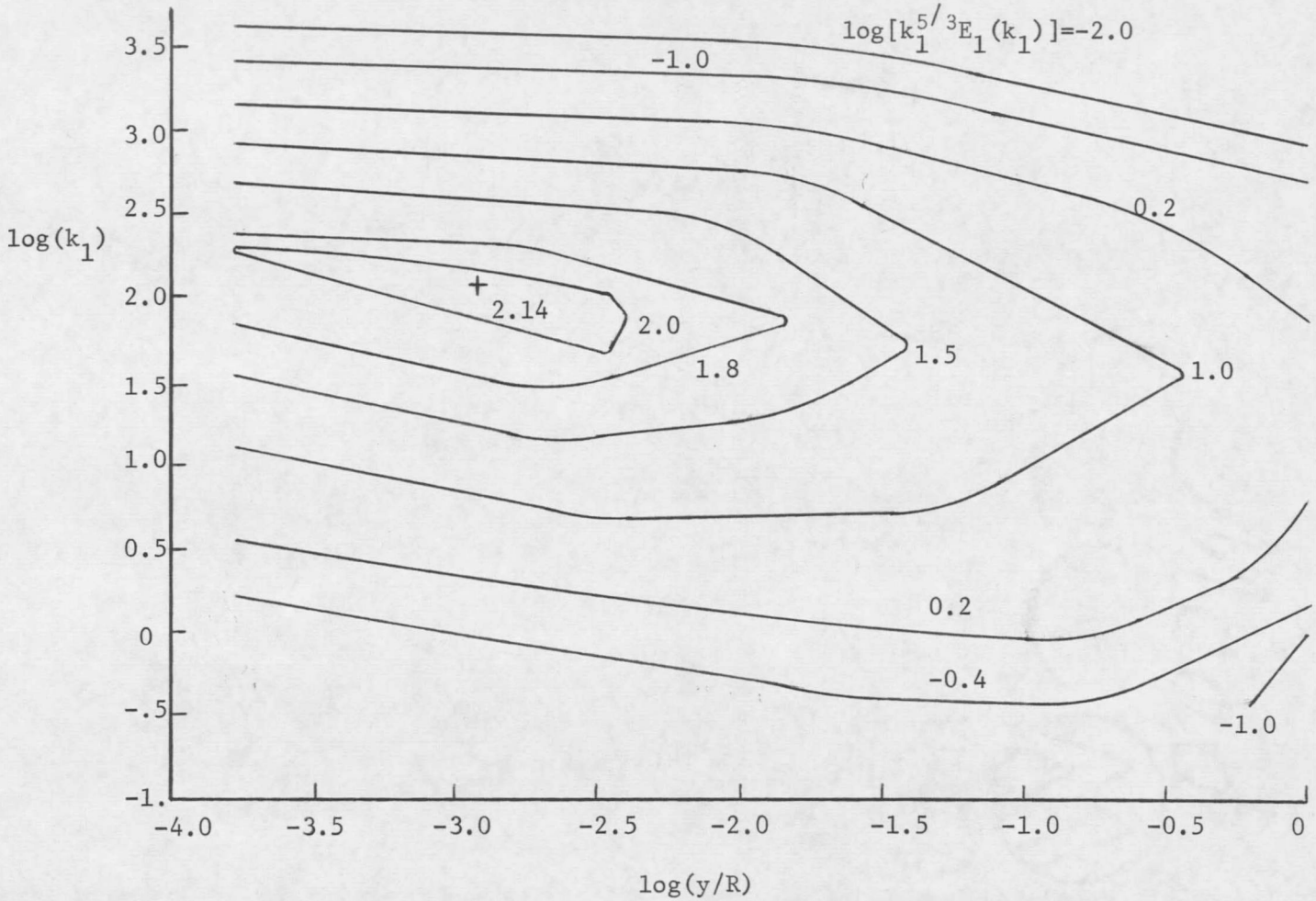

FIGURE 59. Inertial Subrange of Eddy Sizes for u_1 Fluctuations in Smooth Pipe

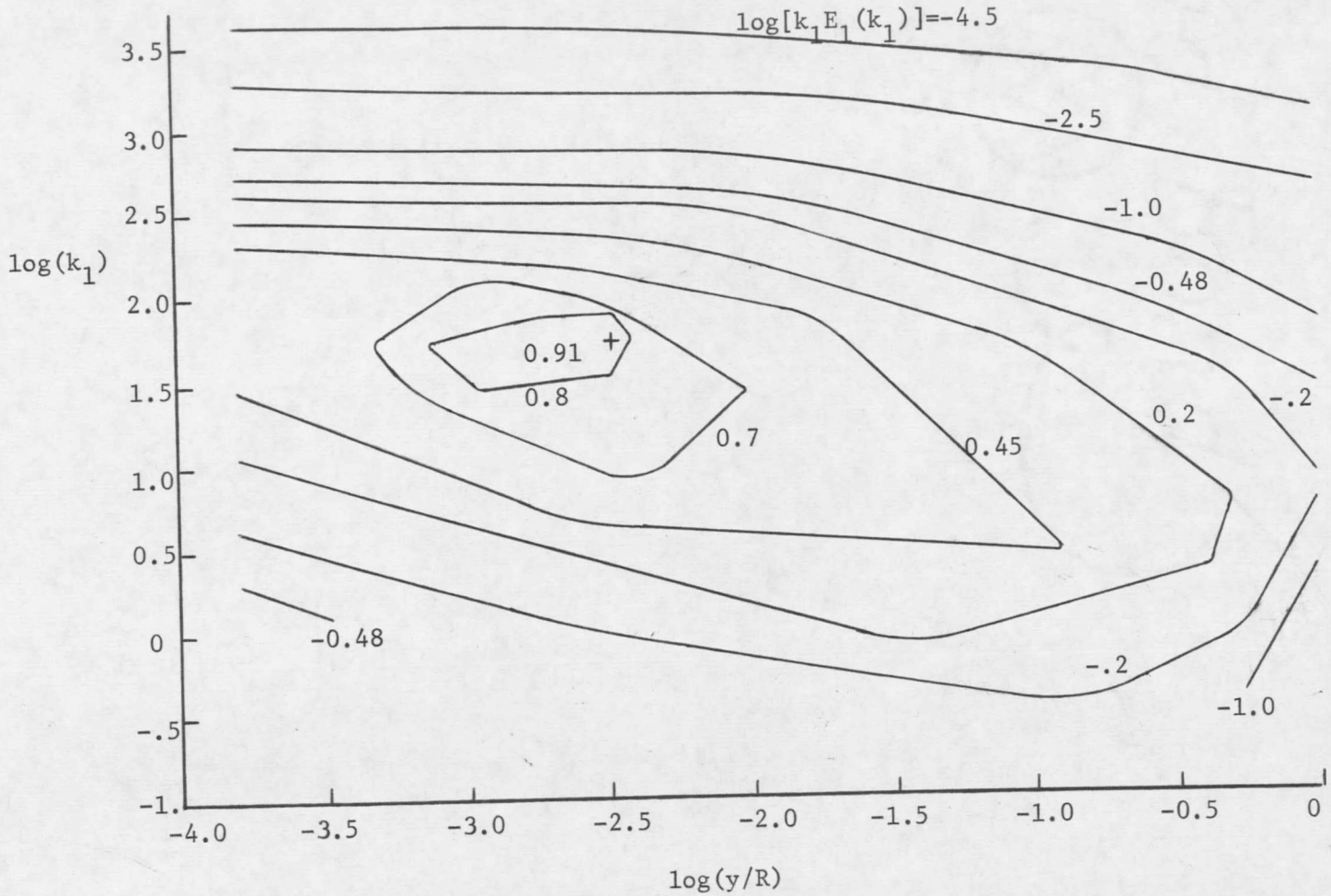

FIGURE 60. Production Subrange of Eddy Sizes For u_1 Fluctuations in Smooth Pipe

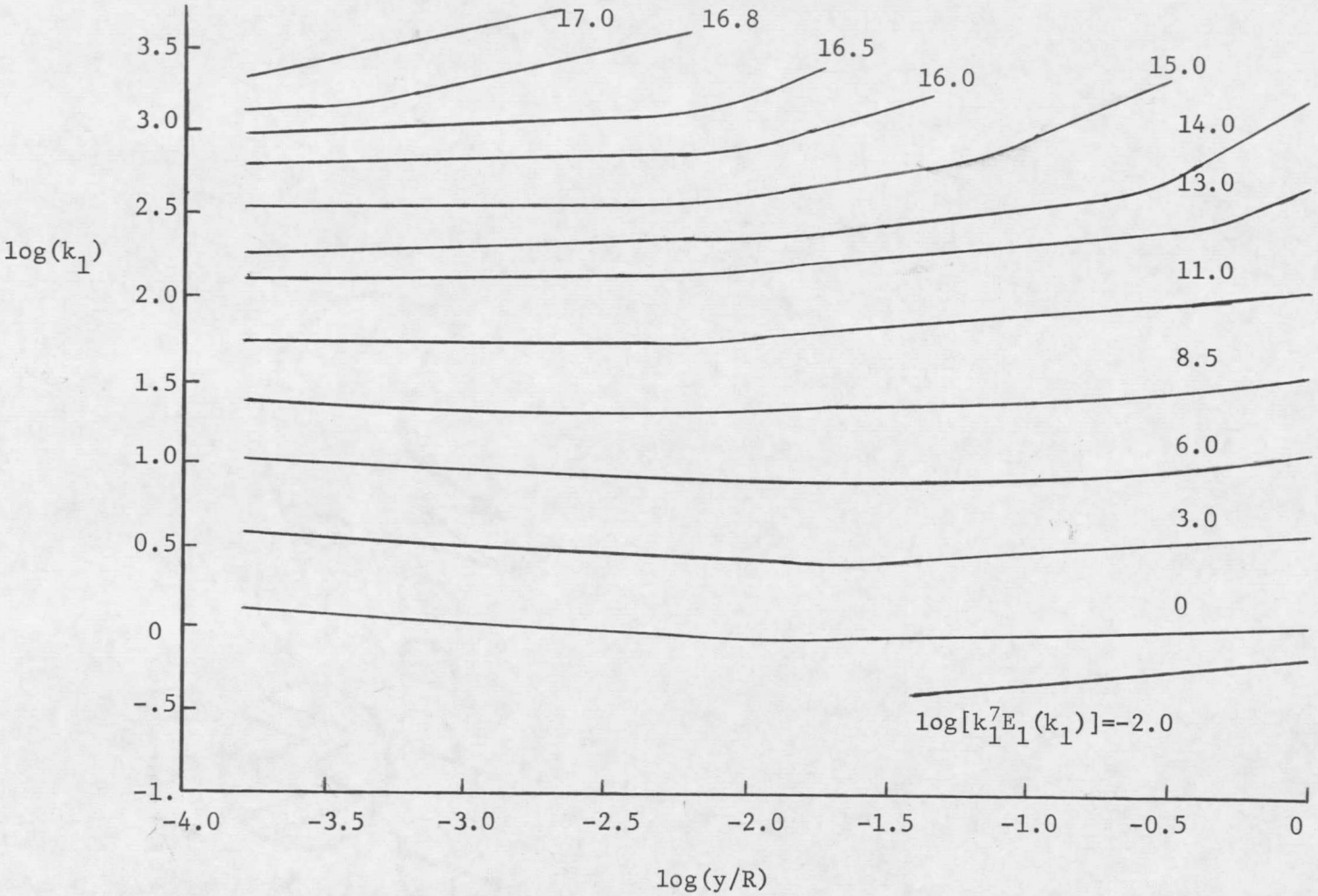

FIGURE 61. Viscous Subrange of Eddy Sizes For u_1 Fluctuations in Smooth Pipe

extremely large wave numbers.

The quantity of experimental data, regarding the spectrum function, which resulted from the present investigation enabled an accurate evaluation of previously proposed coordinate systems which tend to give the spectrum function a universal behavior, i.e., render it independent of radial position. The two such coordinate systems yielding the best results are shown in Figures 62 and 63. The coordinates proposed by Robertson et al [47] are shown to yield extremely good results over the entire pipe cross-section, with only slight variations occurring at the highest values of $n\Lambda_1/\overline{U}_1$. Figure 63 shows that the coordinates proposed by Goma and Gelhar [30] also yield fairly good results, the only exceptions being those previously noted by them. These are a decrease in magnitude of the spectrum function in moving from the center line to the wall at small values of $2nR/\overline{U}_1$, and an increase in magnitude as the wall is approached for large values of $2nR/\overline{U}_1$.

Energy spectra in the frequency domain and the wave number space for the velocity fluctuations in the x_2 coordinate direction are shown in Figures 64 and 65 respectively. As in the case of the E_1 spectra, a decrease in the energy content of the dissipation eddies may be observed in moving from the wall to the center line of the pipe at a constant frequency or wave number. Near the pipe wall

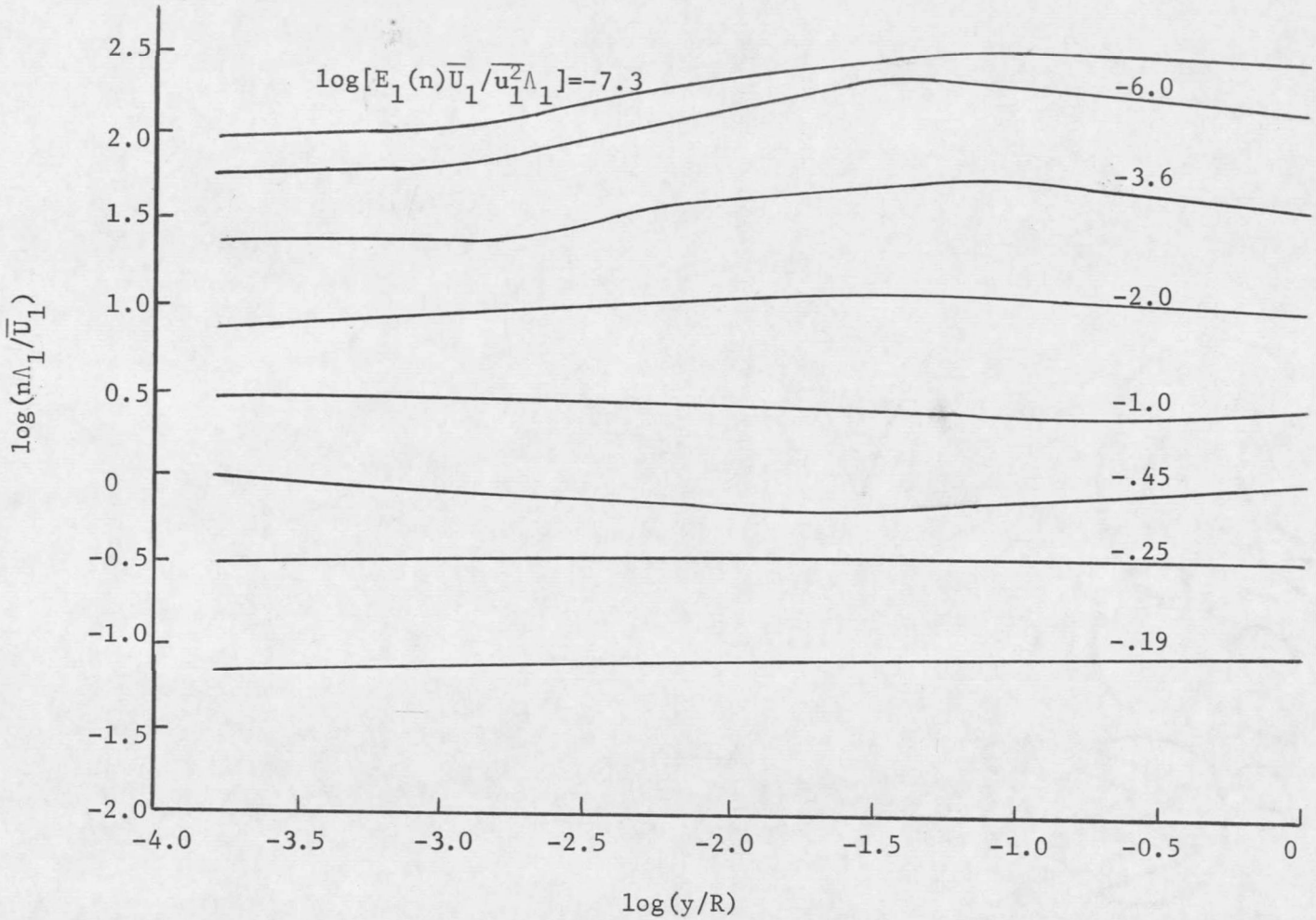

FIGURE 62. u_1 Spectra for Smooth Pipe Normalized as Proposed by Robertson et al [47]

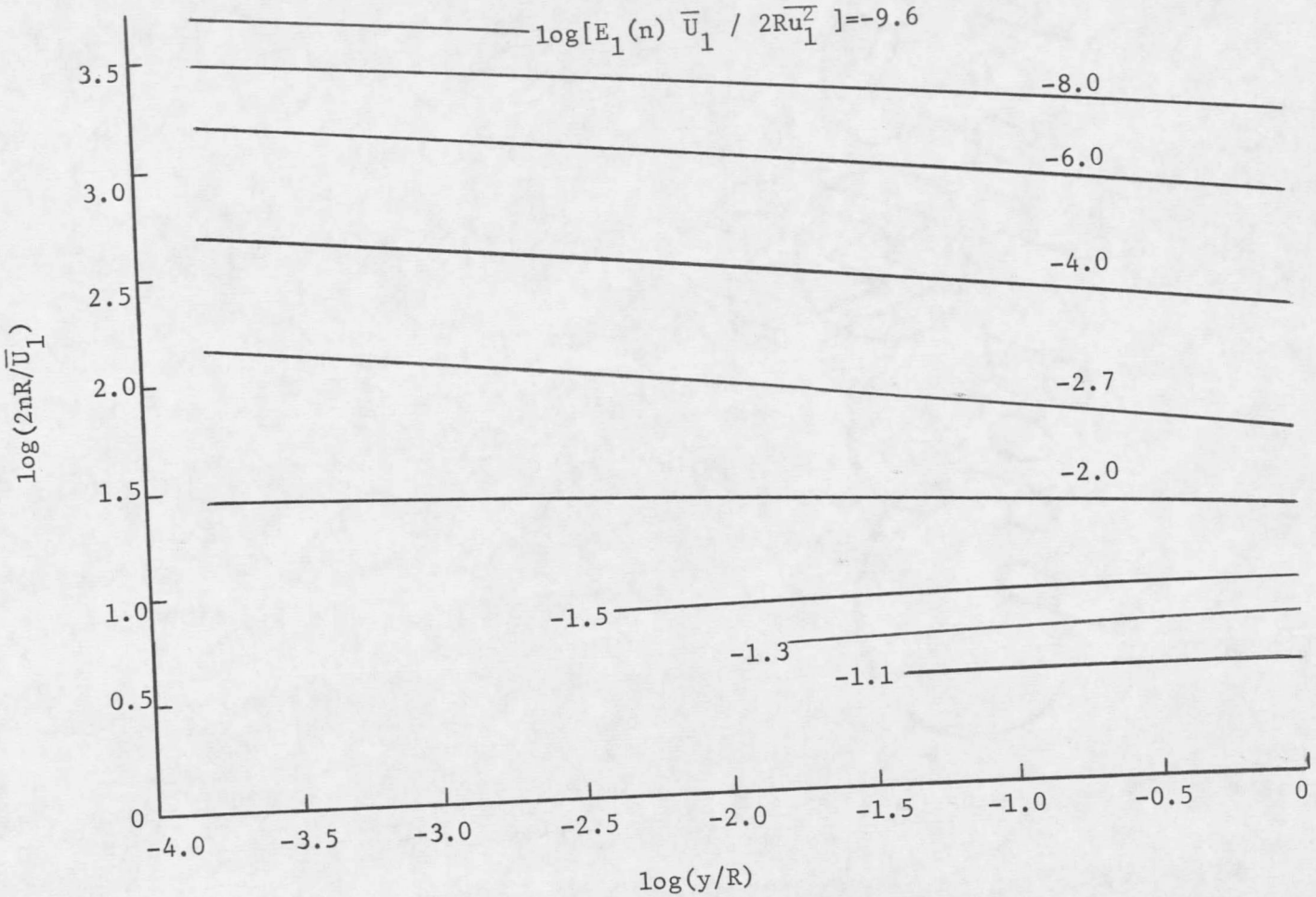

FIGURE 63. u_1 Spectra For Smooth Pipe Normalized as Proposed by Goma and Gelhar [30]

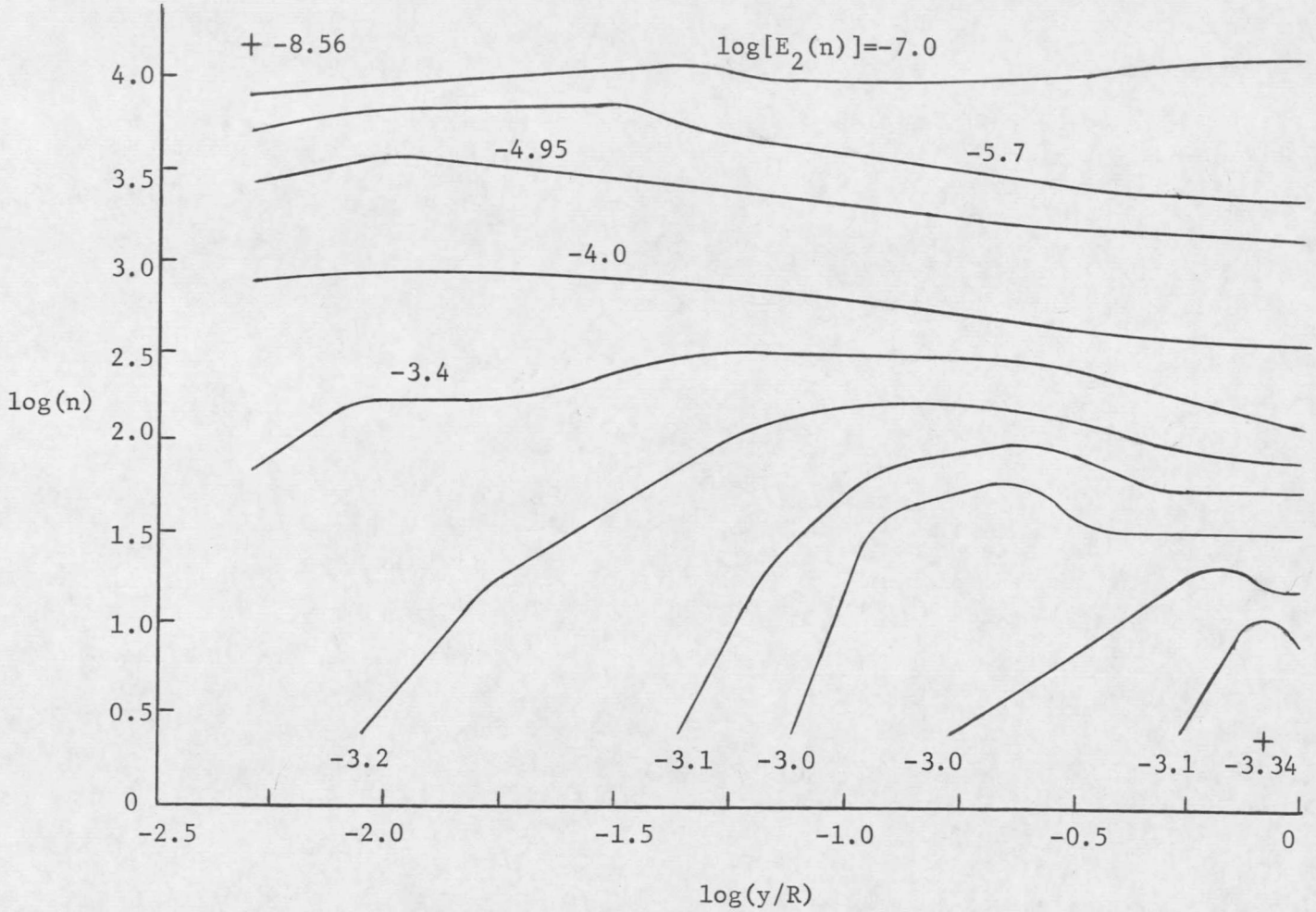

FIGURE 64. Frequency Domain Energy Spectra for u_2 Fluctuating Velocity in Smooth Pipe

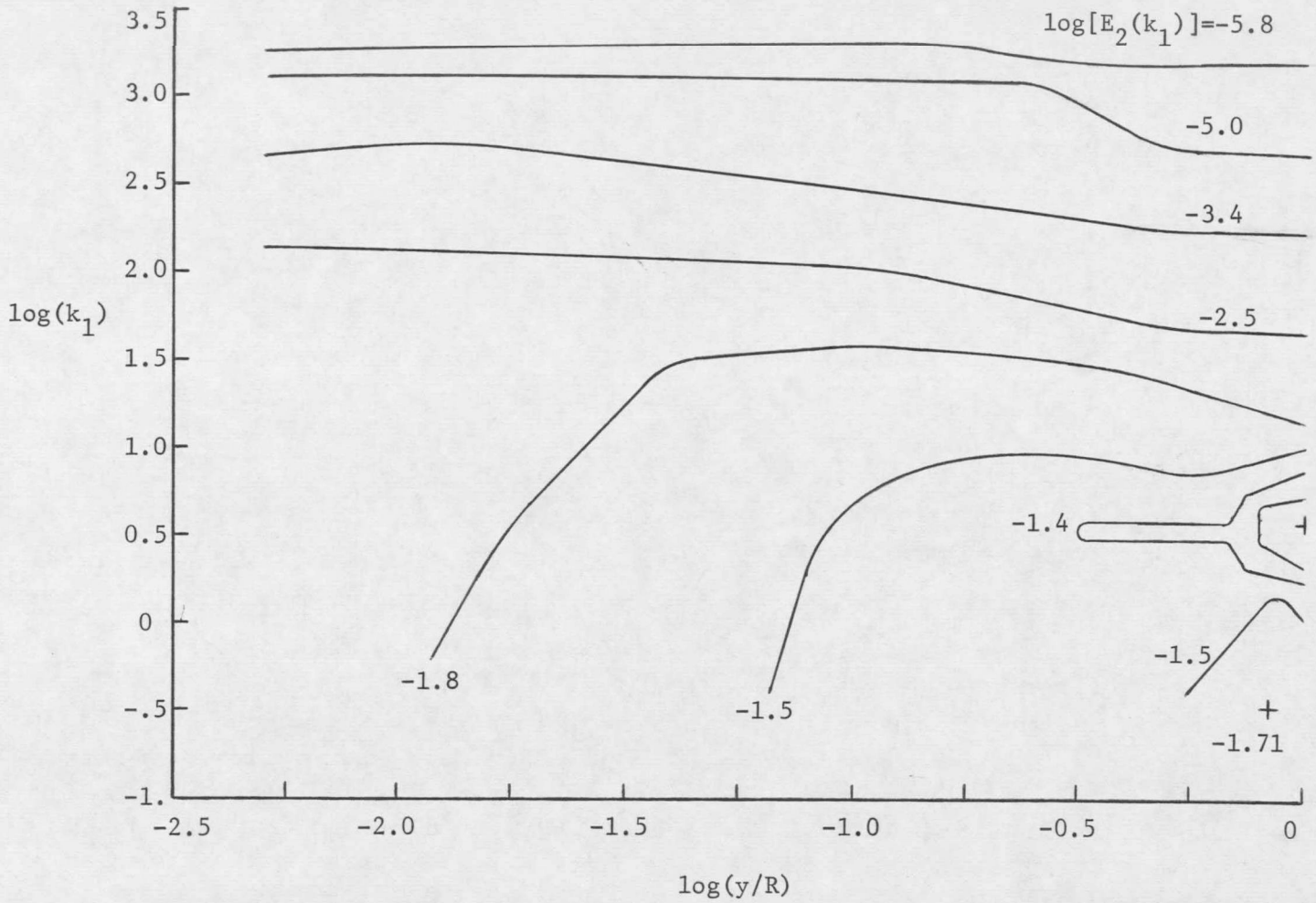

FIGURE 65. Contour Map of u_2 Energy Spectra for Smooth Pipe

the E_2 spectra are also similar to the E_1 spectra in that a sharp decline in energy content is noted as the wall is approached for low wave numbers. A significantly different behavior is indicated in the central region of the pipe, however, for the low wave numbers. Figure 65 shows that there is an energy deficiency at such wave numbers, and this result is in agreement with the findings of Laufer [41]. This indicates the occurrence of a very different process than the commonly accepted picture of energy transfer from lower to higher wave numbers. Since the gradient diffusion and the convective diffusion of kinetic energy, as well as the turbulence production, are considered to be very low frequency phenomena, while the dissipation is associated with high frequencies, the turbulence energy balance suggests that the energy deficiency in the E_2 spectra may possibly be due to the convective diffusion of pressure energy. If such energy were transferred from another of the fluctuating velocities, say u_1, in favor of the u_2 velocity, then the energy deficiency in Figure 65 could be explained. Such an explanation is plausible if Laufer's [41] hypothesis that the pressure energy term is associated with intermediate wave numbers is accepted. The generally smaller magnitude of the E_2 spectra than the E_1 spectra at a given wave number and a given value of y/R, as indicated by a comparison of Figures 65 and 58, would be expected due to the smaller magnitude of

$\overline{u_2^2}$ at any radial position.

The various subranges of eddy sizes for the E_2 spectra are examined by means of Figures 66, 67, and 68. As in the case of the E_1 spectra, the inertial and production subranges are seen to be exhibited over a fairly wide range of wave numbers throughout the pipe, and an increase in magnitude of the wave numbers where these subranges appear is observed as the wall is approached. Also, the production subrange again occurs for slightly larger eddies than does the inertial subrange. The viscous subrange does not appear in Figure 68, but its possible existence at very large wave numbers is indicated.

The dimensionless forms of the energy spectra suggested by Robertson et al [47] and by Goma and Gelhar [30] are shown plotted in Figures 69 and 70, respectively, for the u_2 velocity fluctuations. Neither of these coordinate systems render the E_2 spectra independent of y/R except for large wave numbers.

The variation of the E_3 function for the wave number space and for the frequency domain is indicated in Figures 71 and 72. The behavior of this function is seen to be similar to the E_2 spectra in most aspects. A very slight decrease in energy content of the viscous dissipation eddies may be observed in moving from the pipe wall to its center line at a constant wave number in Figure 72. An

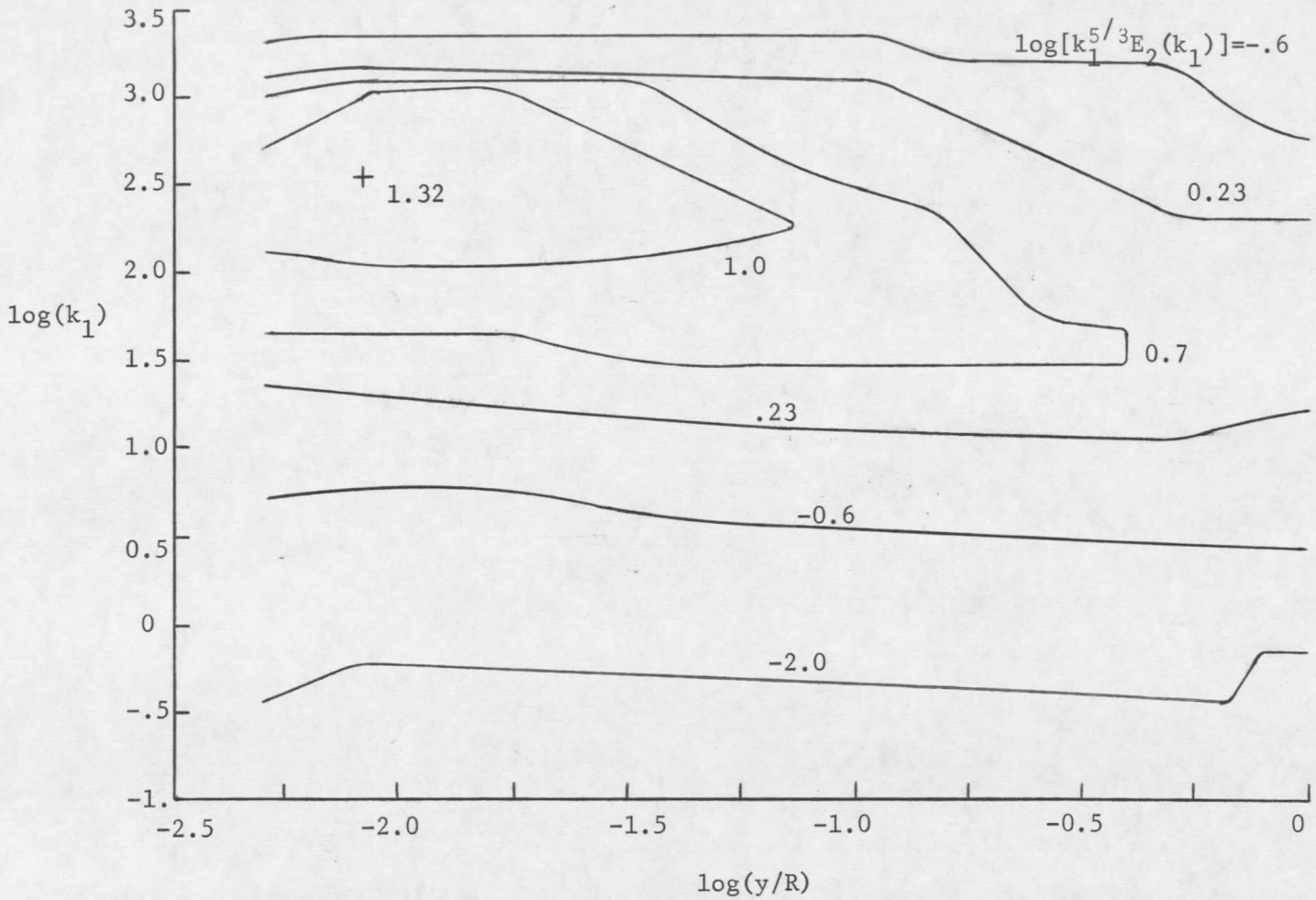

FIGURE 66. Inertial Subrange of Eddy Sizes For u_2 Fluctuations in Smooth Pipe

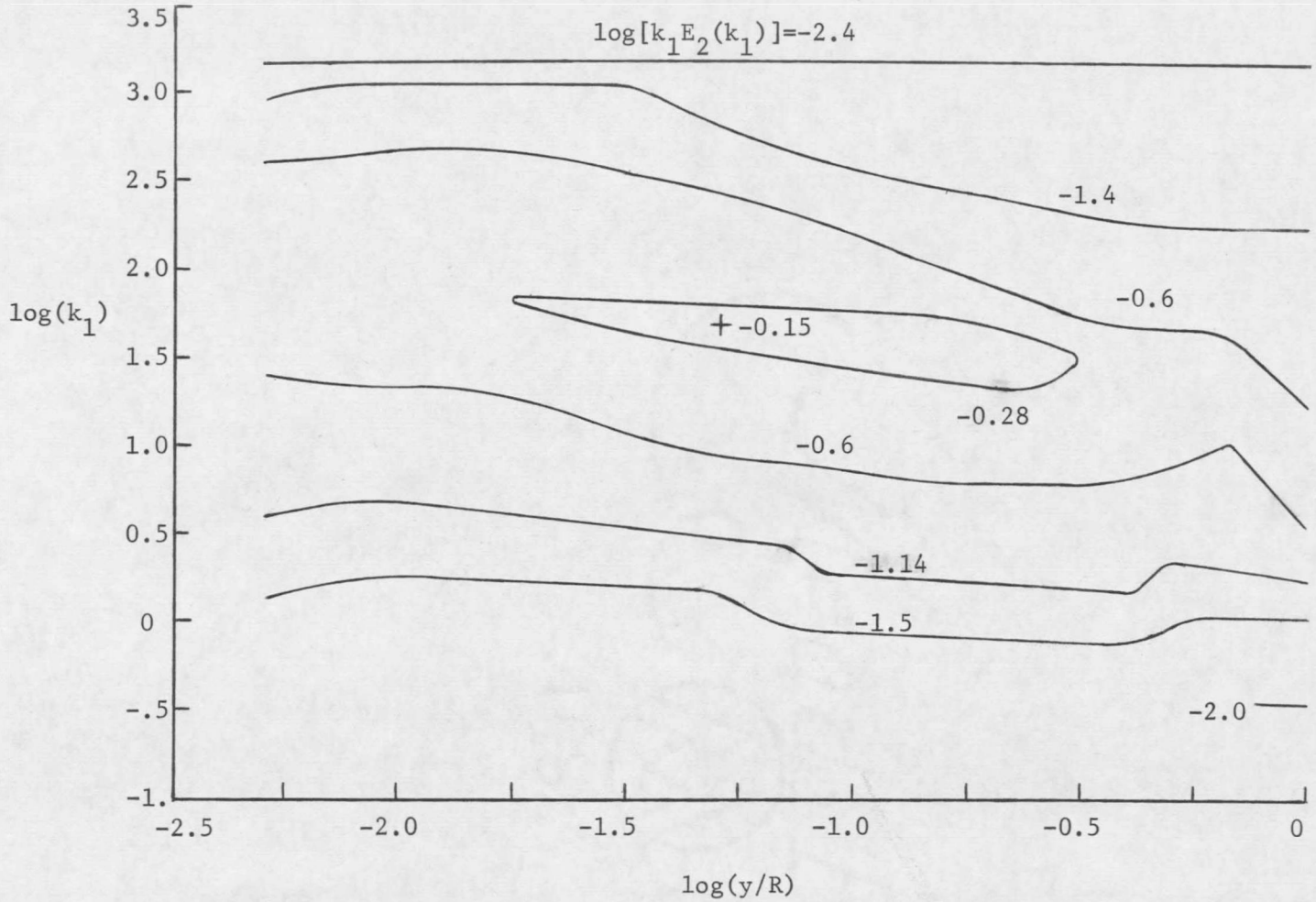

FIGURE 67. Production Subrange of Eddy Sizes for u_2 Fluctuations in Smooth Pipe

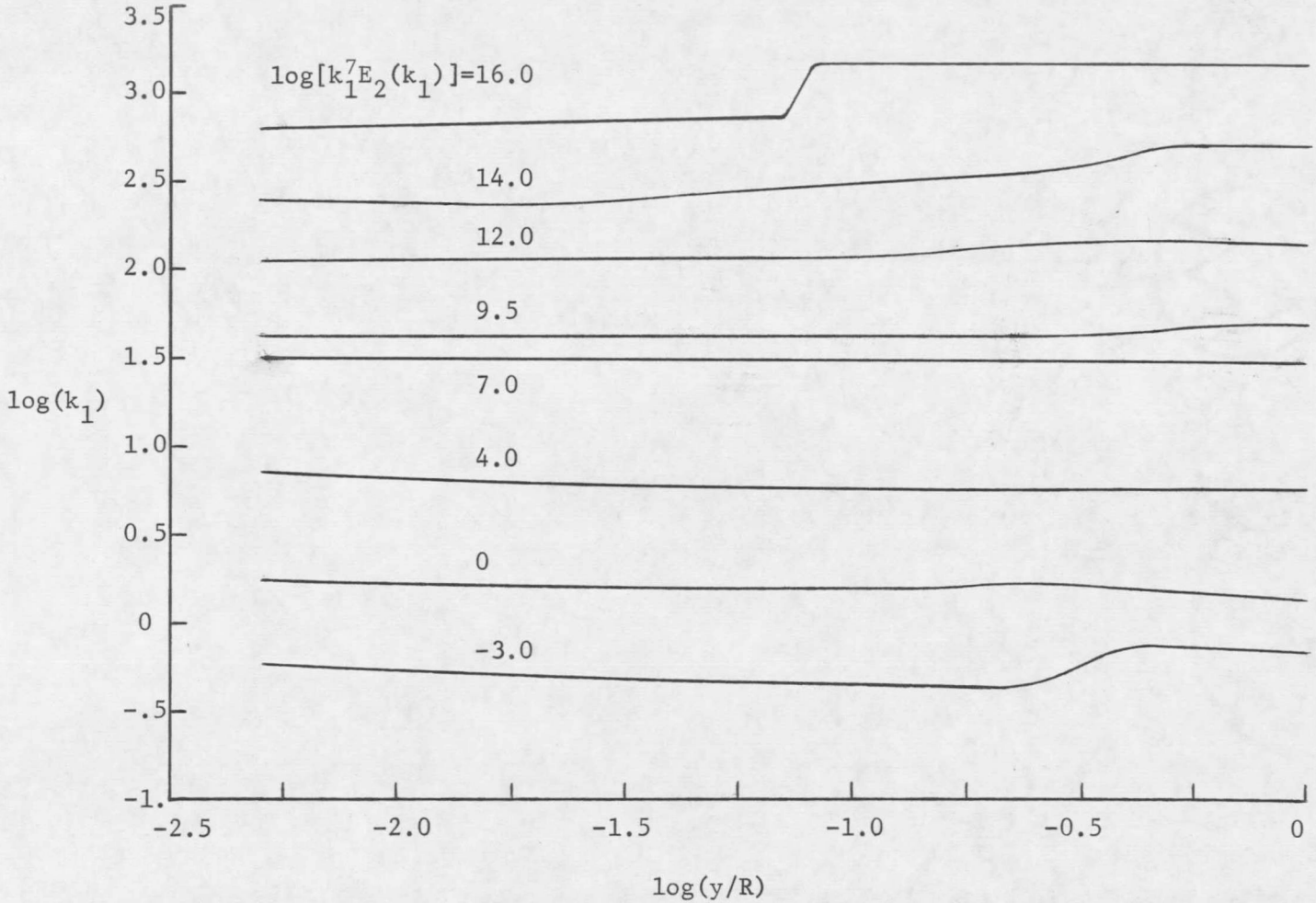

FIGURE 68. Viscous Subrange of Eddy Sizes For u_2 Fluctuations in Smooth Pipe

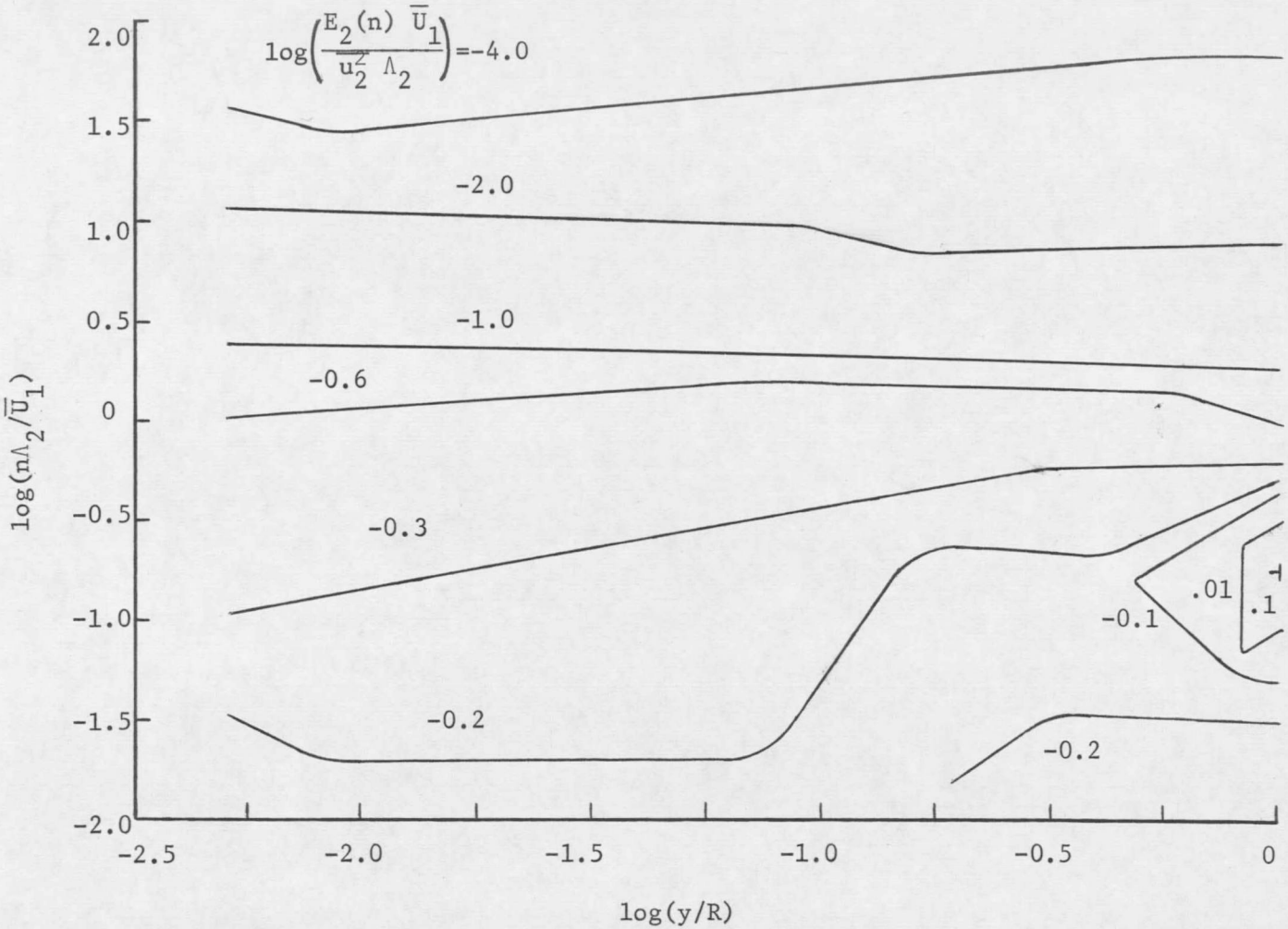

FIGURE 69. u_2 Spectra For Smooth Pipe Normalized as Proposed by Robertson et al [47]

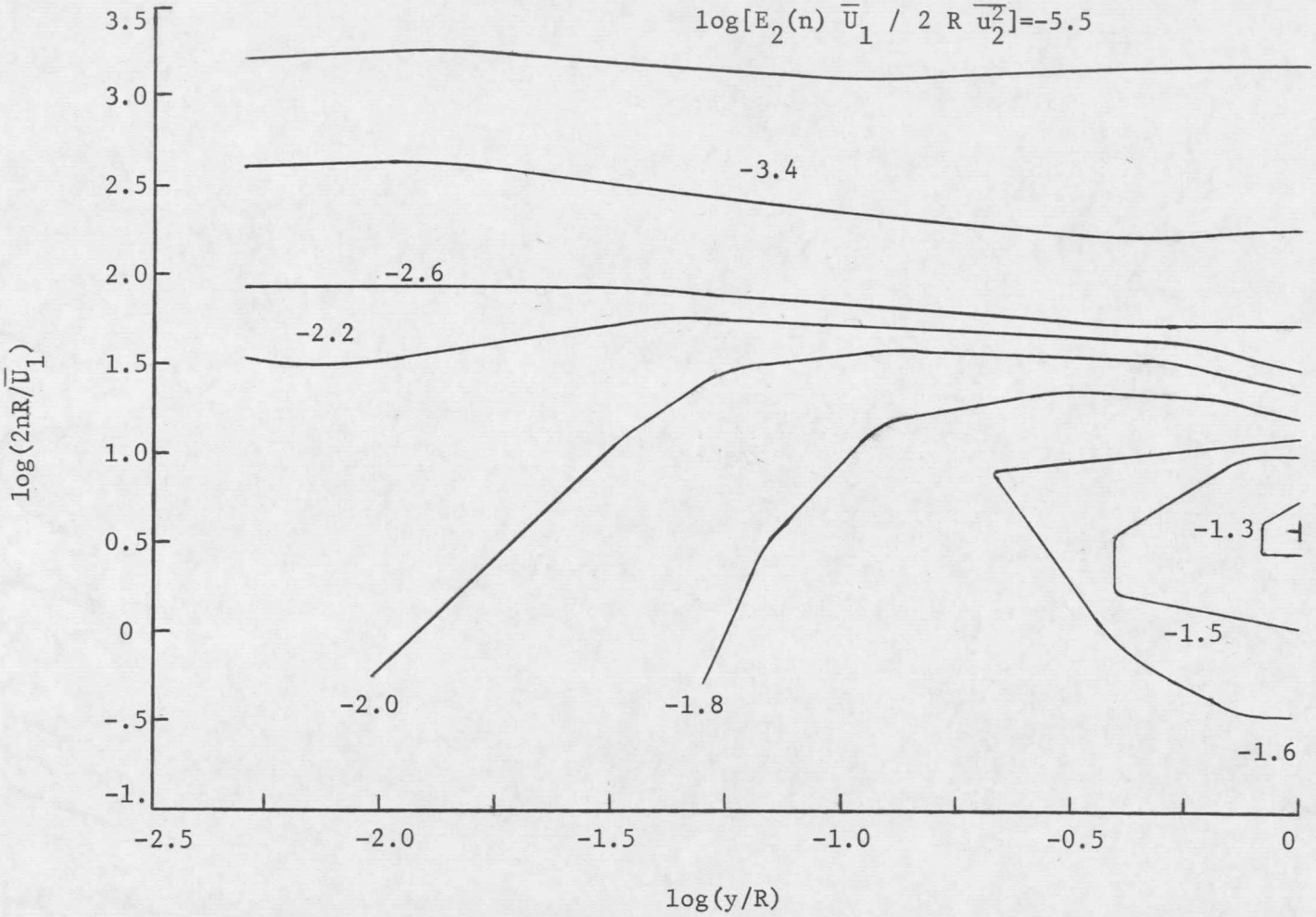

FIGURE 70. u_2 Spectra For Smooth Pipe Normalized as Proposed by Goma and Gelhar [30]

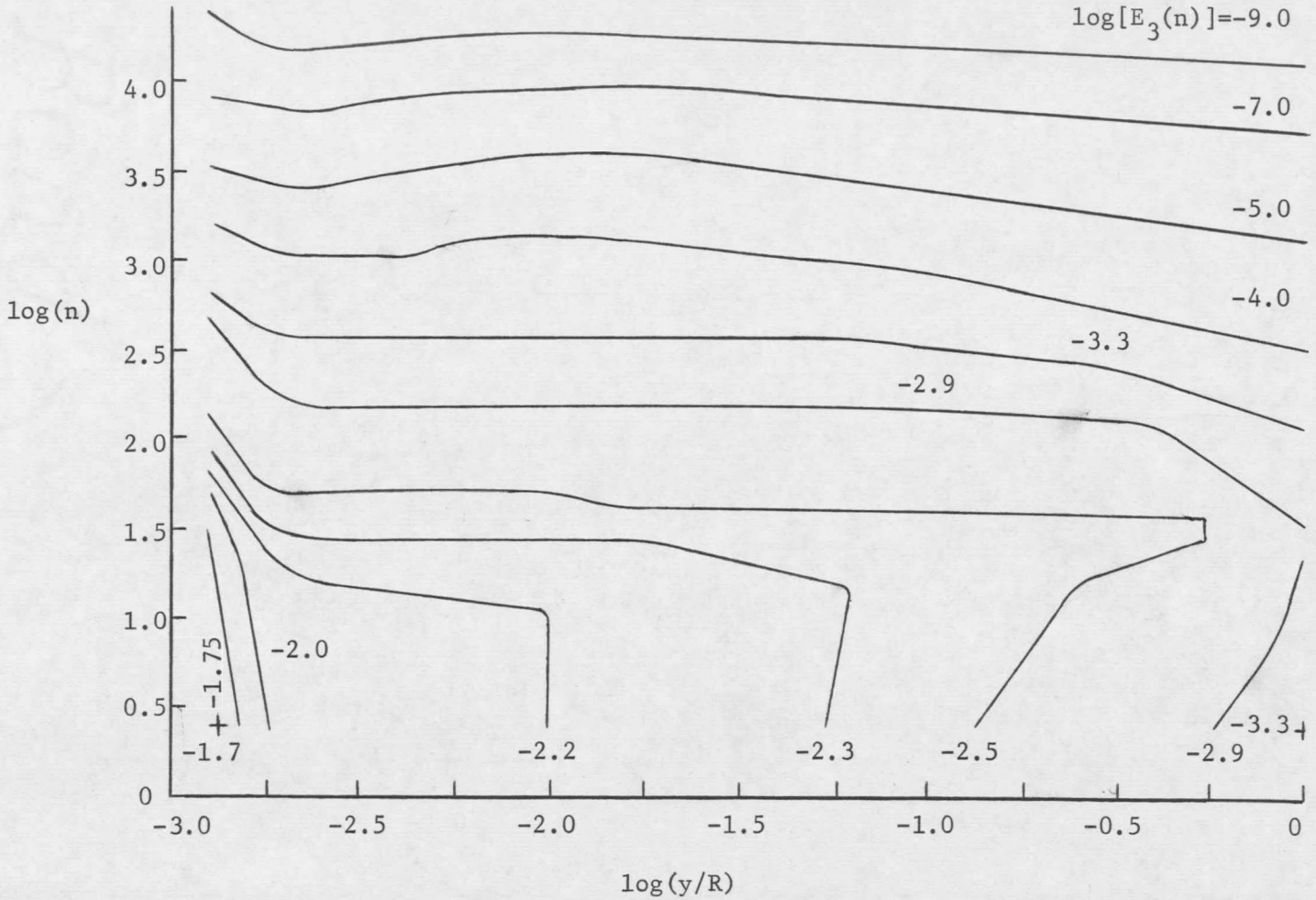

FIGURE 71. Frequency Domain Energy Spectra For u_3 Fluctuations in Smooth Pipe

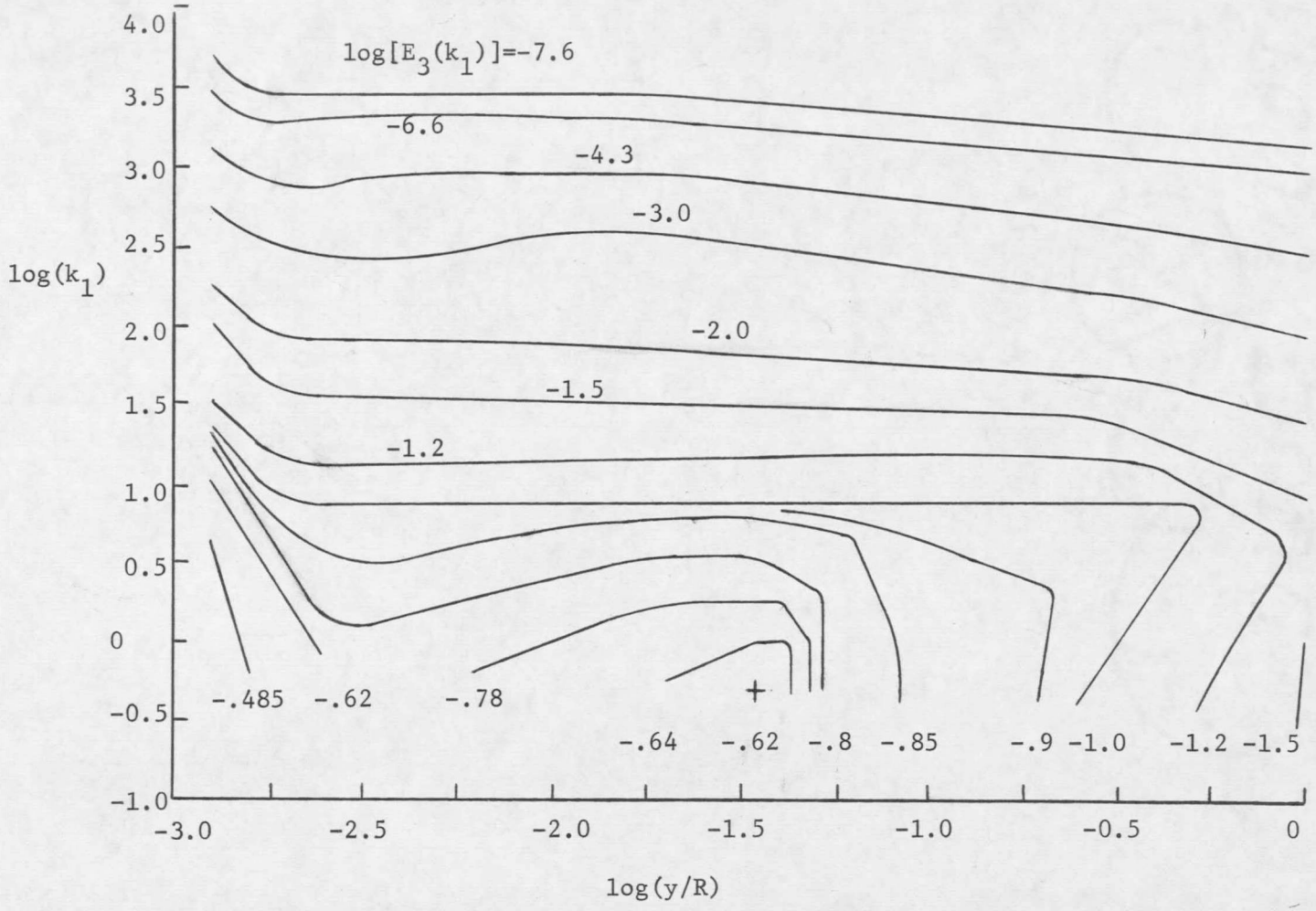

FIGURE 72. Contour Map of u_3 Energy Spectra for Smooth Pipe

energy deficiency is again observed near the pipe center line, and for an intermediate range of values of y/R, the E_3 spectra appear to be independent of wave number for the larger eddies. This indicates a possible transfer of energy from the u_1 fluctuating velocity to the u_3 fluctuating velocity by action of the fluctuating pressure. Again a pronounced decrease in energy content of the large eddies is noted near the edge of the viscous sublayer, but in contrast to previous cases, an increase in energy content may be observed for positions very close to the solid surface. This indicates that a significant portion of the production and diffusion of kinetic energy in this region may go in favor of the fluctuating velocity in the x_3 coordinate direction. A comparison of the magnitudes of the E_3 spectrum function in Figure 72 with those of the E_1 and E_2 functions, at a given value of y/R and a given wave number, indicates that E_3 lies between the other two functions. This would be expected since $\overline{u_3^2}$ is larger than $\overline{u_2^2}$ but smaller than $\overline{u_1^2}$.

The possibility of occurrence of the inertial, production, and viscous subranges of eddy sizes is examined in Figures 73, 74, and 75 respectively. As in the two previous cases, the inertial and production subranges occur throughout the pipe, and the wave numbers where they exist increase as the wall is approached. The production eddies are again larger than the inertial eddies. Figure 75

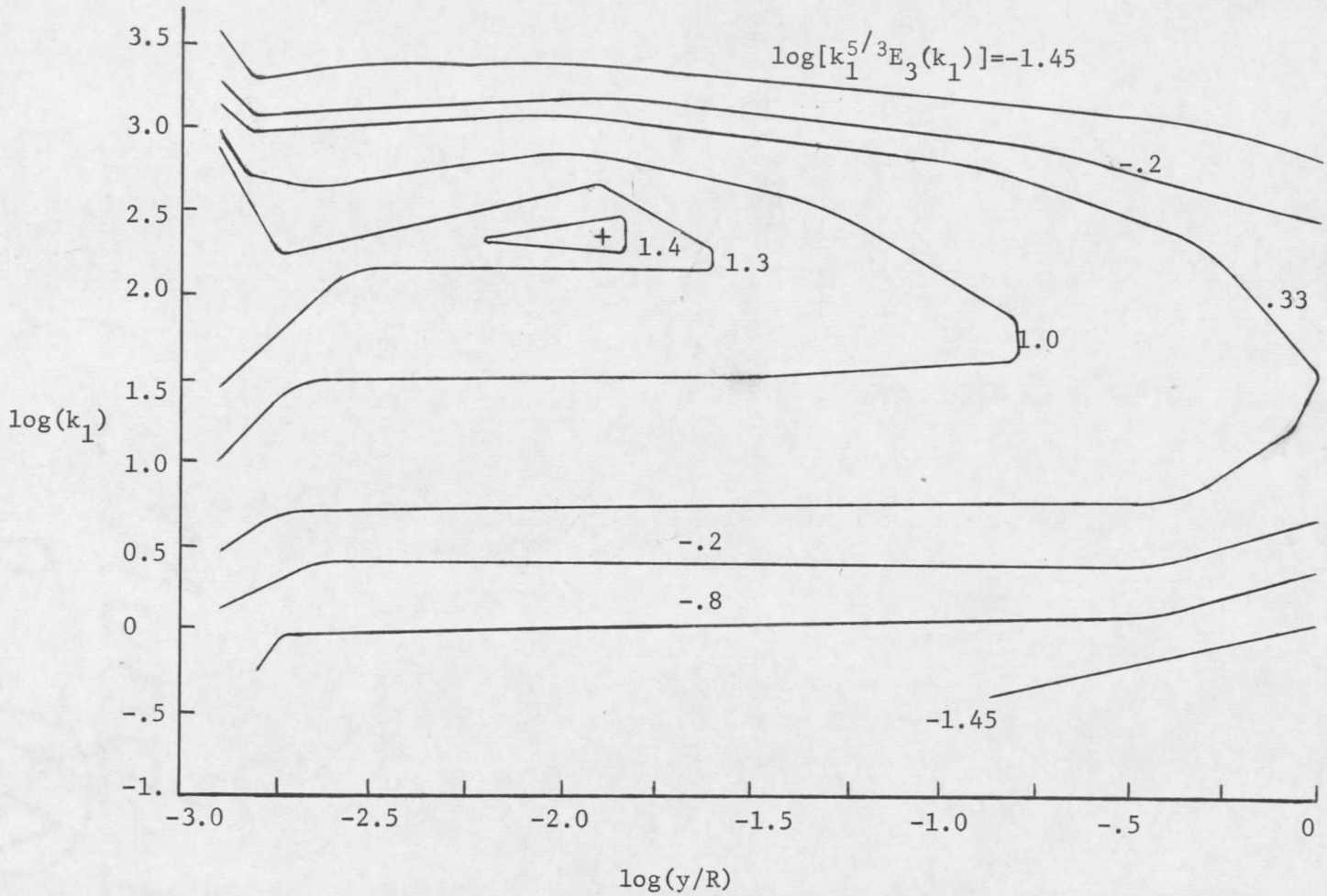

FIGURE 73. Inertial Subrange of Eddy Sizes for u_3 Fluctuations in Smooth Pipe

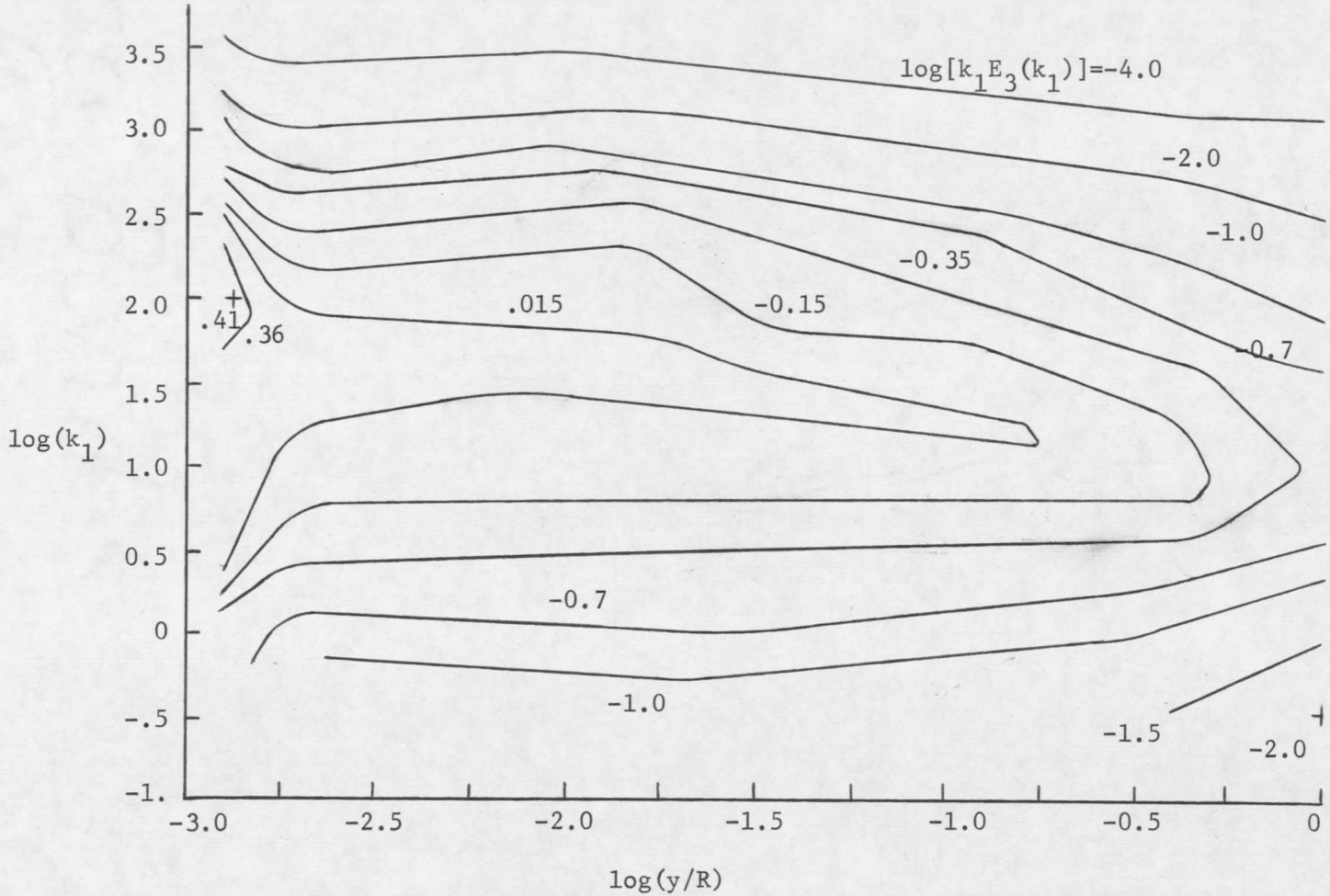

FIGURE 74. Production Subrange of Eddy Sizes For u_3 Fluctuations in Smooth Pipe

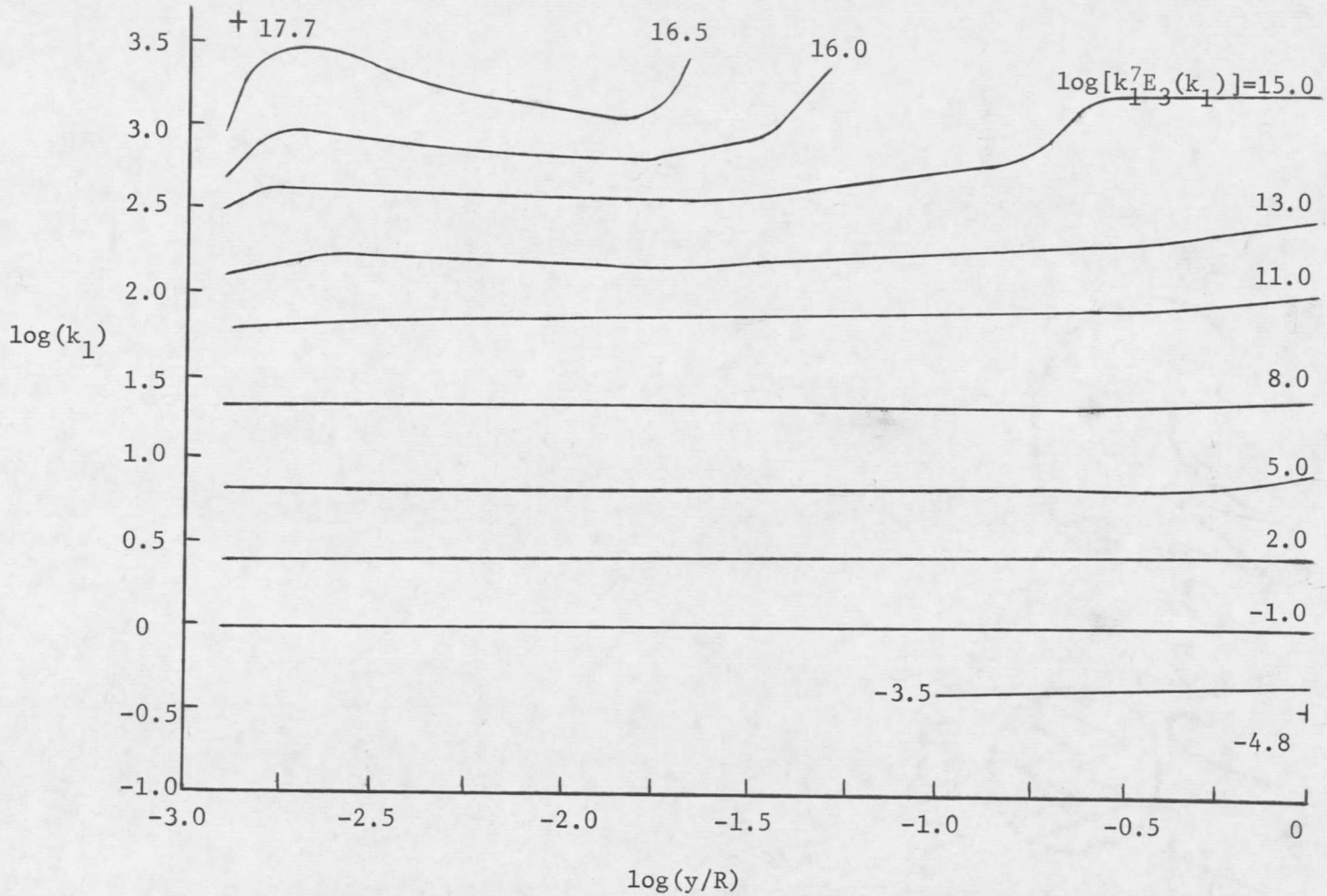

FIGURE 75. Viscous Subrange of Eddy Sizes For u_3 Fluctuations in Smooth Pipe

indicates the apparent occurrence of the viscous subrange at very large wave numbers, but it appears that the dissipation eddies for the u_3 fluctuating velocity are slightly larger than those for the u_1 and u_2 fluctuations.

The normalized forms of the E_3 spectra proposed by Robertson et al [47] and Goma and Gelhar [30] are presented in Figures 76 and 77 respectively. Both sets of coordinates appear to render the spectra virtually independent of radial position except for low values of the dimensionless frequency near the pipe center line. Thus, even though neither set of coordinates is completely universal, both yield good results for the E_1 and the E_3 spectra.

Autocorrelation Functions

Autocorrelation functions obtained by taking the Fourier cosine transform of the energy spectra are presented in Figures 78, 79, and 80 for the fluctuating velocities in the x_1, x_2 and x_3 coordinate directions respectively. These figures indicate a generally similar behavior for ϕ_1, ϕ_2, and ϕ_3 in that, for a particular value of time, they all acquire a minimum value near the edge of the viscous sublayer and then increase as either the wall or the center line is approached. This indicates that the curvature of ϕ_i with respect to time at $t = 0$ is smaller at the edge of the viscous sublayer

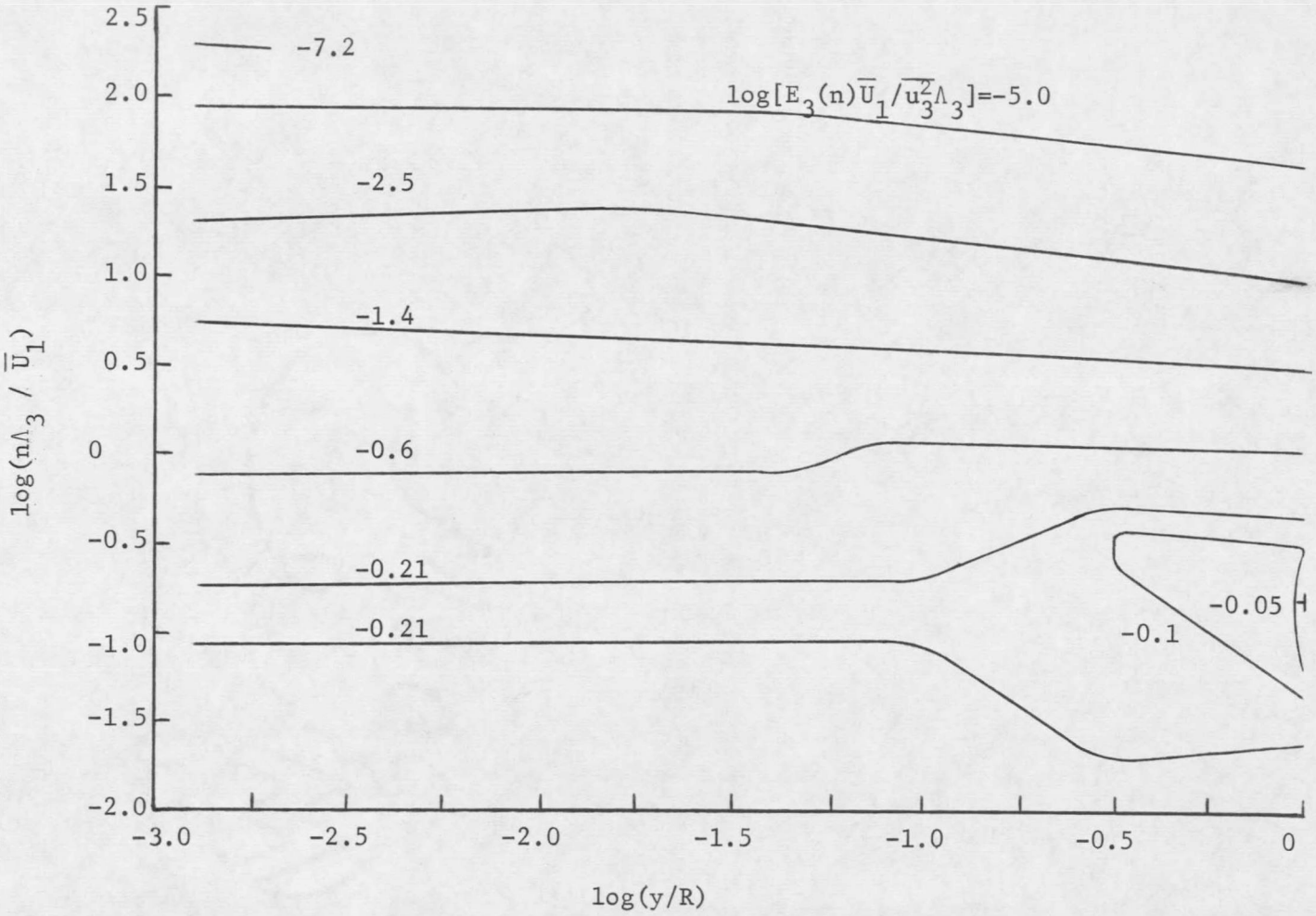

FIGURE 76. u_3 Spectra for Smooth Pipe Normalized as Proposed by Robertson et al [47]

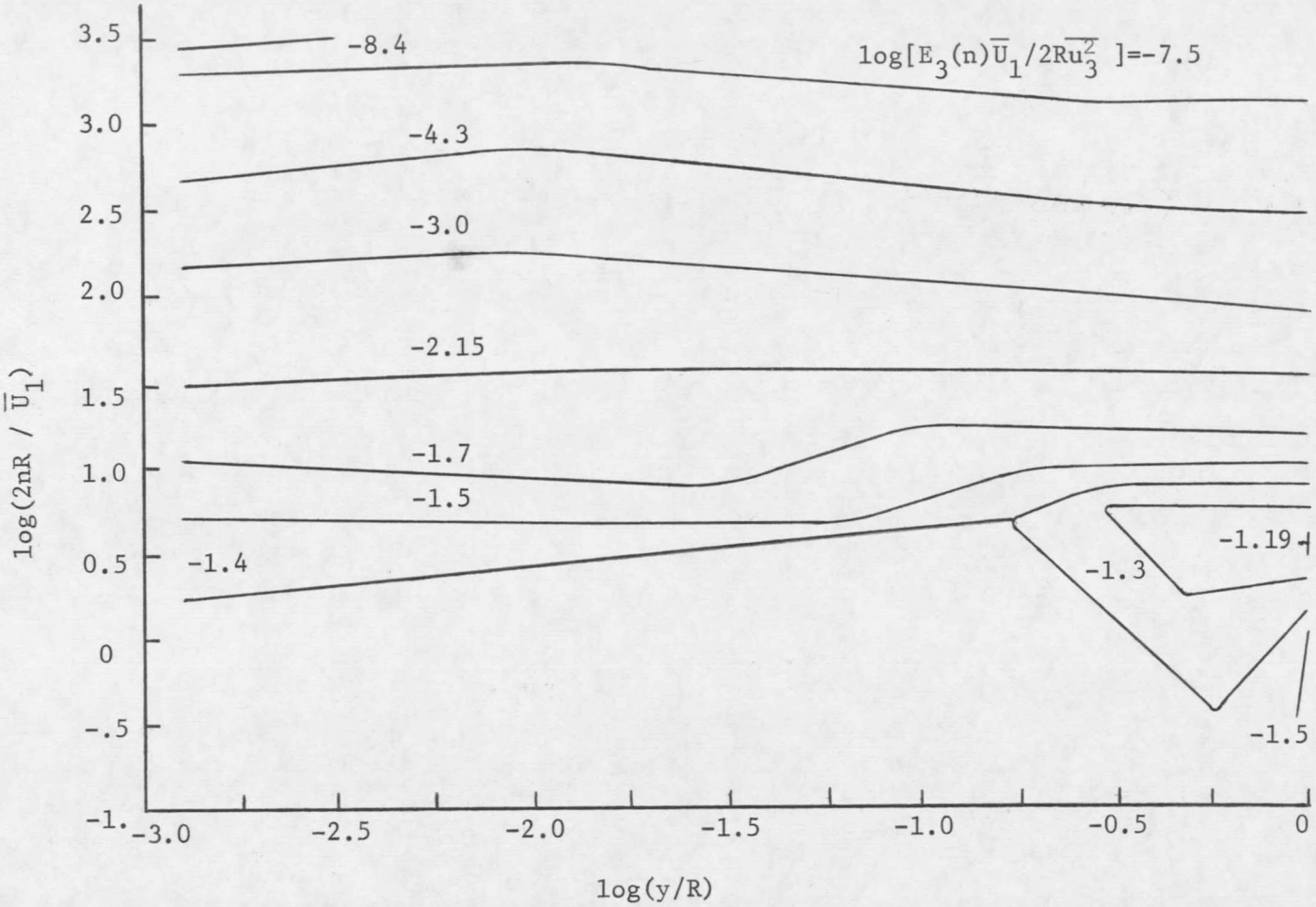

FIGURE 77. u_3 Spectra for Smooth Pipe Normalized as Proposed by Goma and Gelhar [30]

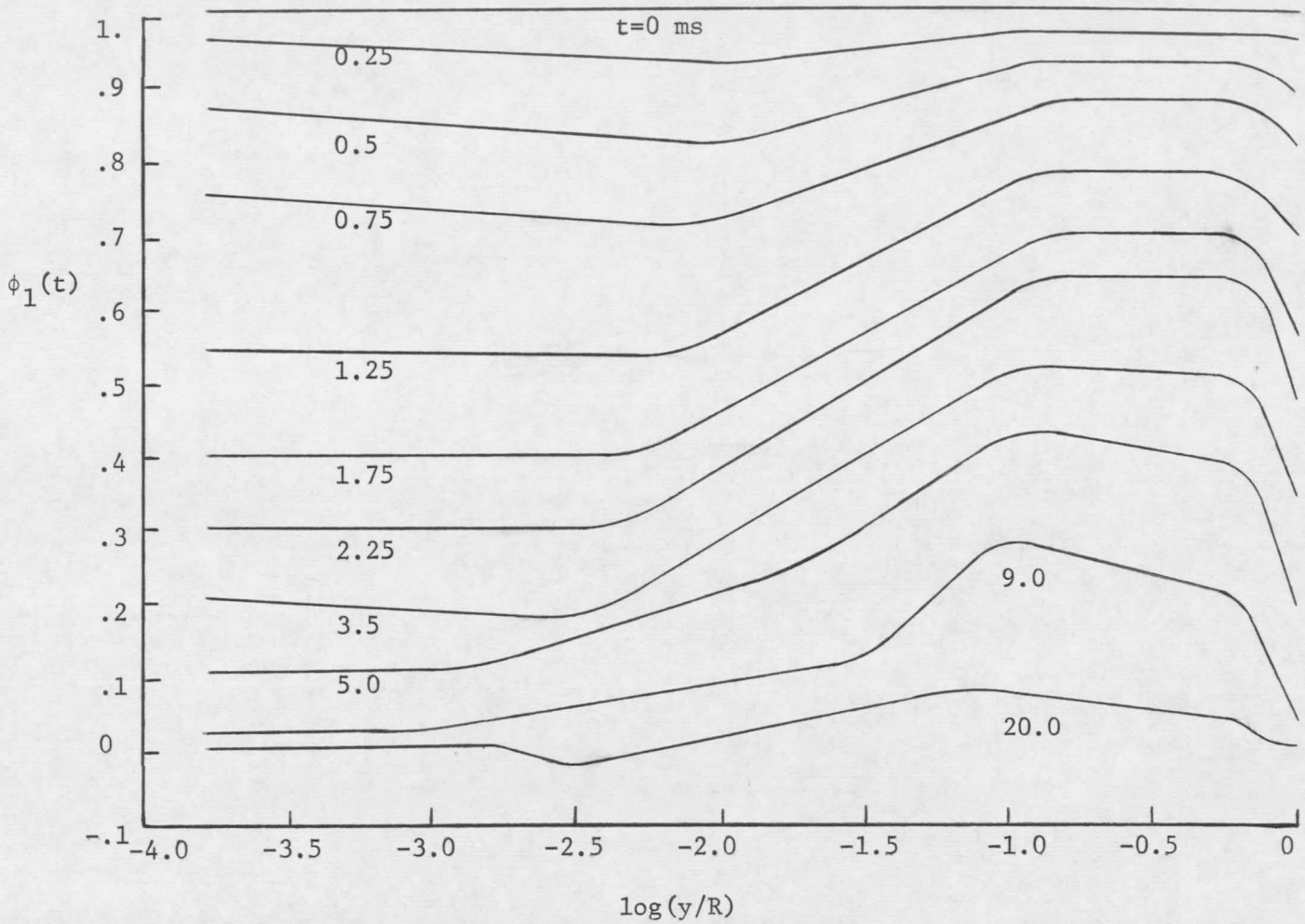

FIGURE 78. Autocorrelation Function for u_1 Fluctuating Velocity in Smooth Pipe

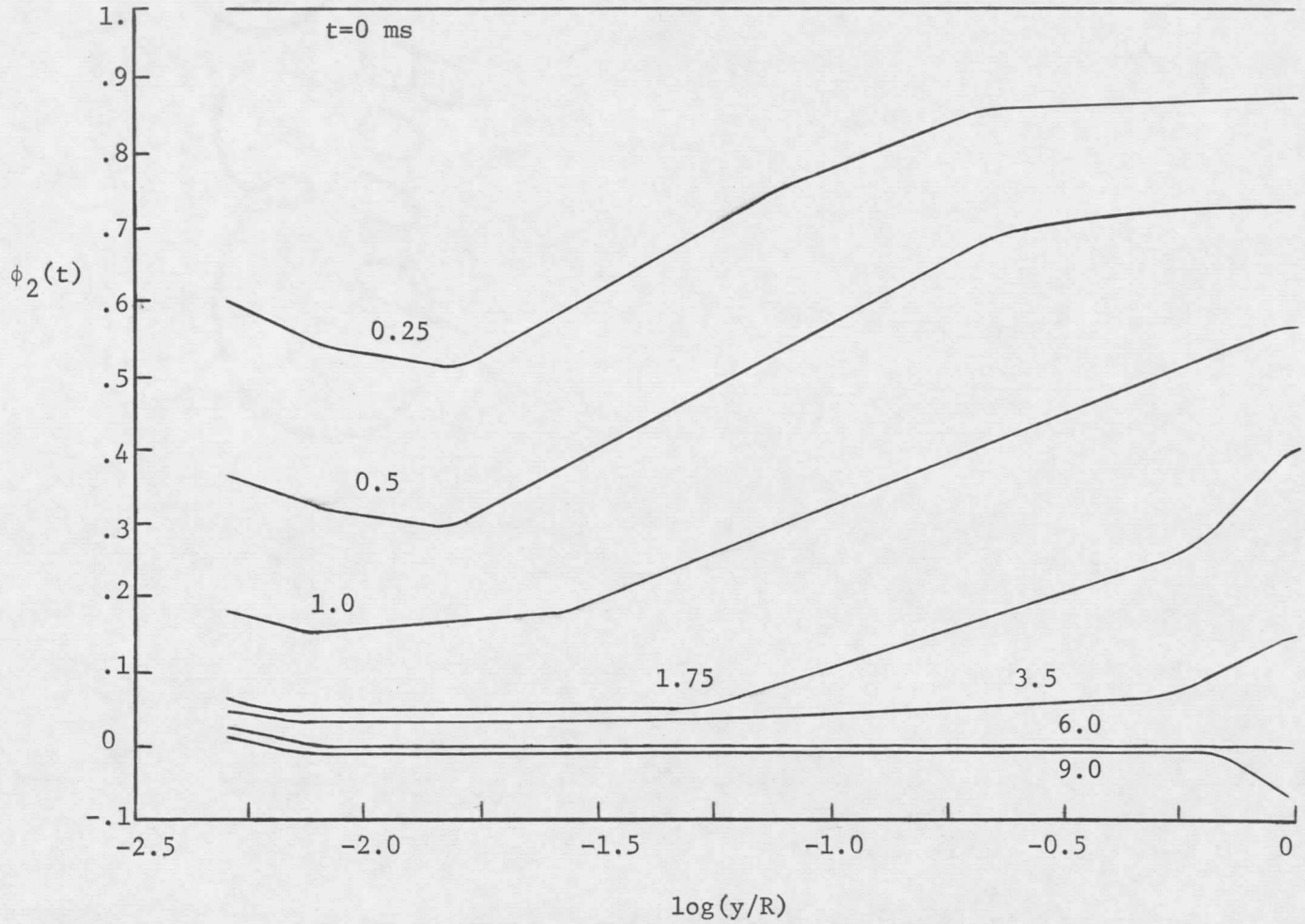

FIGURE 79. Autocorrelation Function for u_2 Fluctuating Velocity in Smooth Pipe

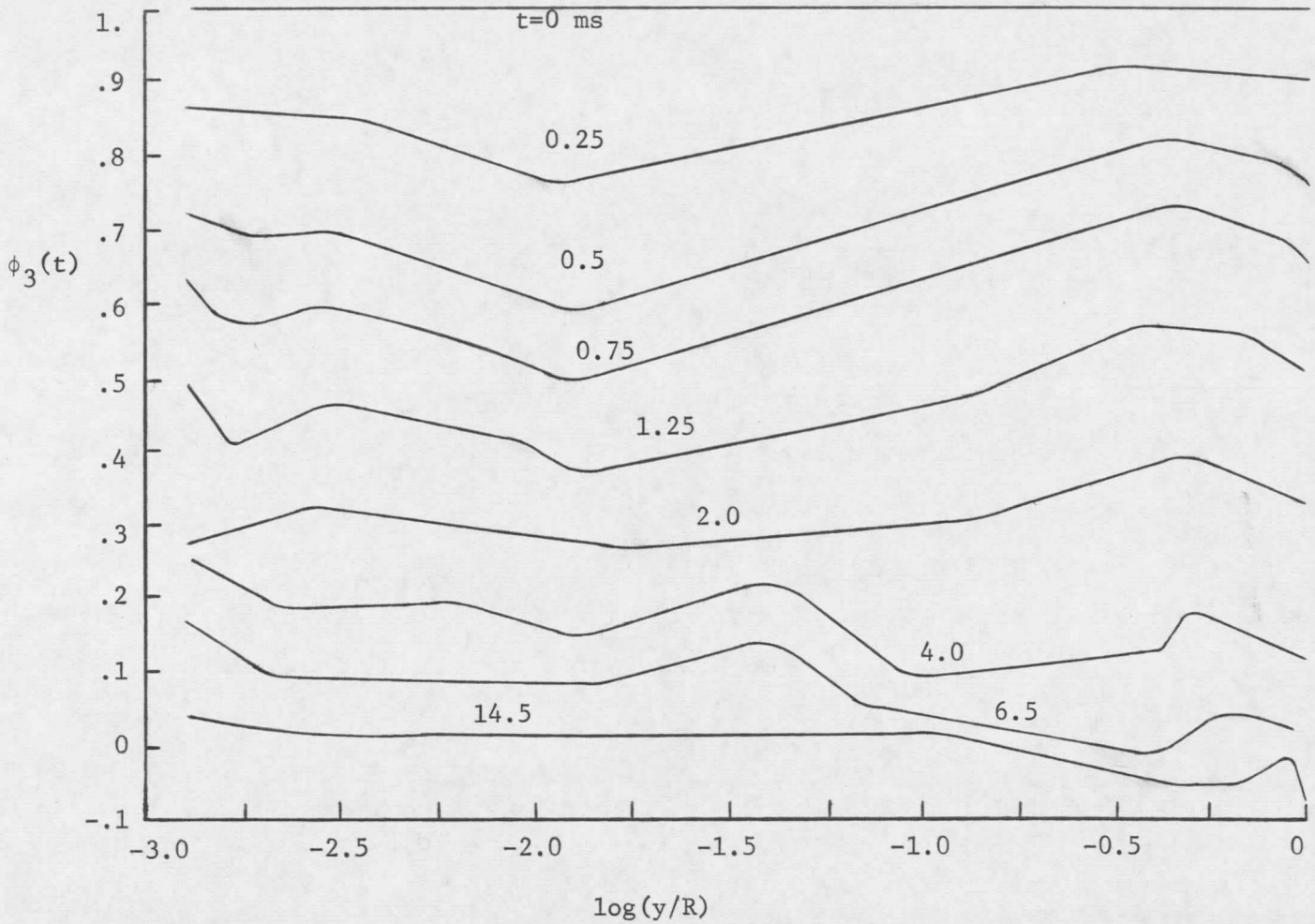

FIGURE 80. Autocorrelation Function for u_3 Fluctuating Velocity in Smooth Pipe

than at other radial positions. The resultant increasing curvature as the wall is approached is indicative of the increasingly dominant role of the low frequencies in this region. Bakewell [68], who also found this type of behavior for the autocorrelation functions in the wall region, points out that this type of variation is consistent with the intuitive notion that the depth of penetration of the viscous sublayer by high frequency velocity fluctuations should be much lower than that for low frequency fluctuations. On the other hand, the increase in curvature of the autocorrelation functions in moving from the edge of the viscous sublayer toward the center line is compatible with the spectral analysis where very large eddies were found to exist near the center of the pipe.

The behavior described in the foregoing paragraph applies to all three autocorrelation functions with only minor modifications. The increase in curvature of ϕ_1 in the wall region is not quite so pronounced as that of ϕ_2 or ϕ_3. This implies that high frequency u_1 velocity fluctuations penetrate further into the viscous sublayer than do those of u_2 or u_3 as might be expected. Also, very near the pipe center line, the curvature of ϕ_1 and ϕ_3 appears to decrease slightly while that of ϕ_2 continues to increase. This is indicative of a slight reduction of elongation of the eddies in the x_1 and x_3 directions, while the elongation in the x_2 direction continues to

increase.

Turbulence Scales

A measure of the most rapid changes which occur in the u_i fluctuations is the Eulerian micro scale γ_i, and experimentally determined values of this quantity are presented in Figure 81 for the central core of the pipe and in Figure 82 for the wall region. The curves for all three micro scales have a somewhat similar shape, i.e., they all increase slightly, in moving from the center line toward the wall, until a maximum value is attained in the vicinity of $y/R = 0.4$. These micro scales then decrease until a minimum value occurs just outside the viscous sublayer, and the values again show an increase. This increase is in accord with the autocorrelation results where it was observed that the high frequency eddies could not penetrate deeply into the viscous sublayer. Throughout the pipe, γ_1 is seen to be larger than γ_3 which, in turn, is larger than γ_2. This indicates the presence of higher frequency fluctuations in the u_2 velocity than in either u_1 or u_3.

The Eulerian macro scale of turbulence, which is a rough measure of the longest connection time in the behavior of the fluctuating velocities, is presented for the turbulent core of the pipe in Figures 83, 84, and 85 for velocity fluctuations in the three coordinate directions. Likewise, this same information for the wall region

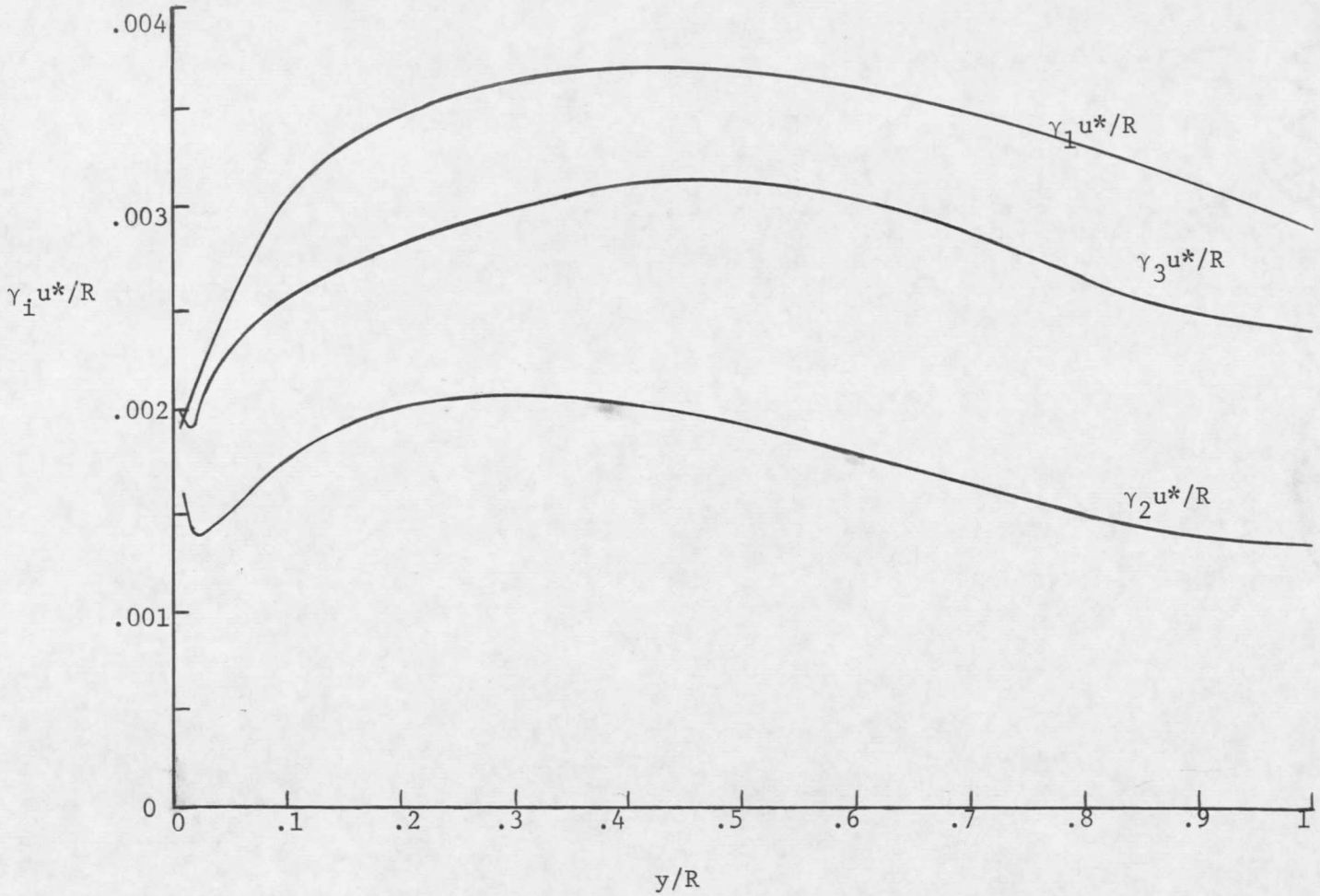

FIGURE 81. Eulerian Micro Scales for Central Region of Smooth Pipe

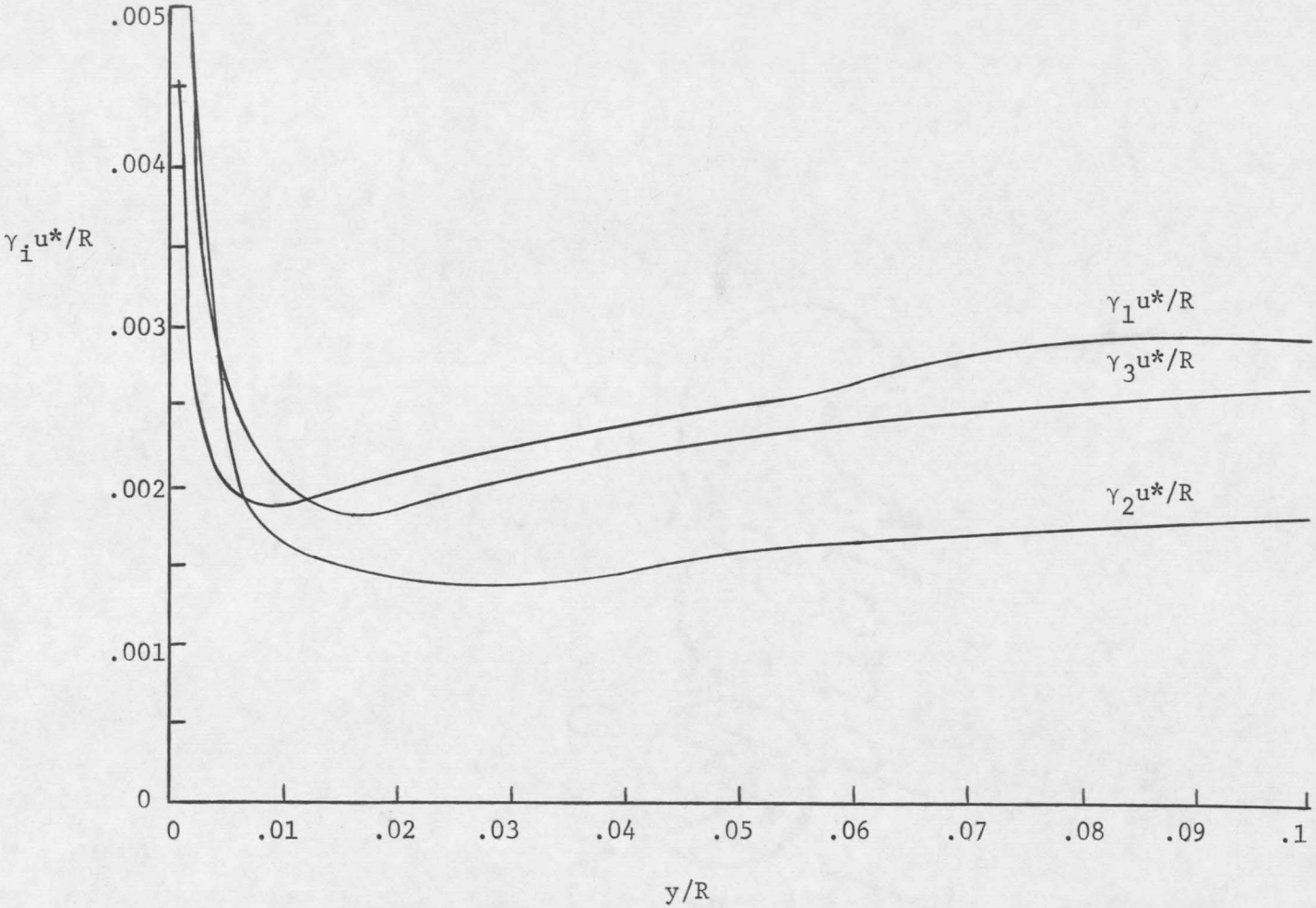

FIGURE 82. Eulerian Micro Scales for Wall Region of Smooth Pipe

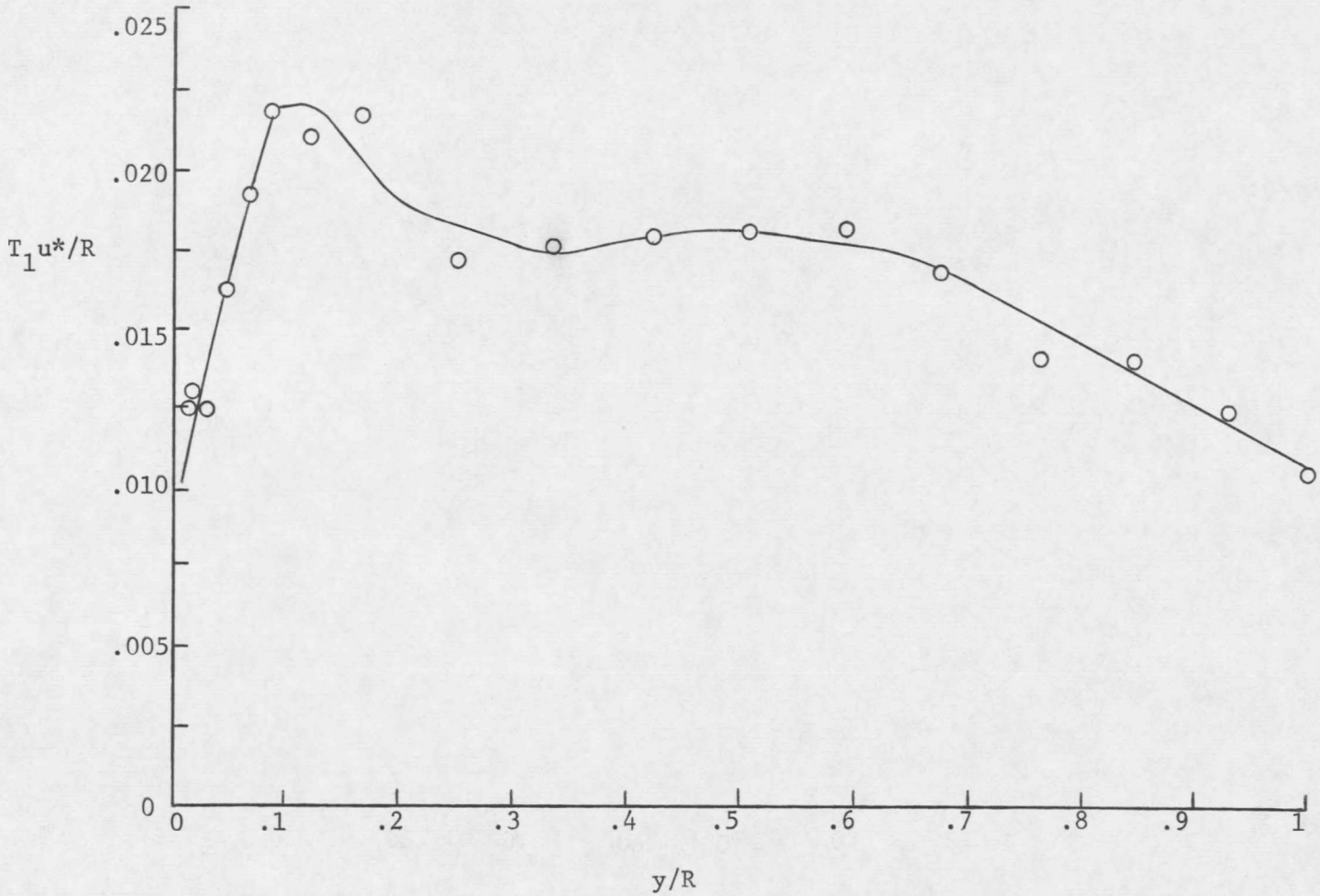

FIGURE 83. Eulerian Macro Scale For u_1 Fluctuating Velocity in Central Region of Smooth Pipe

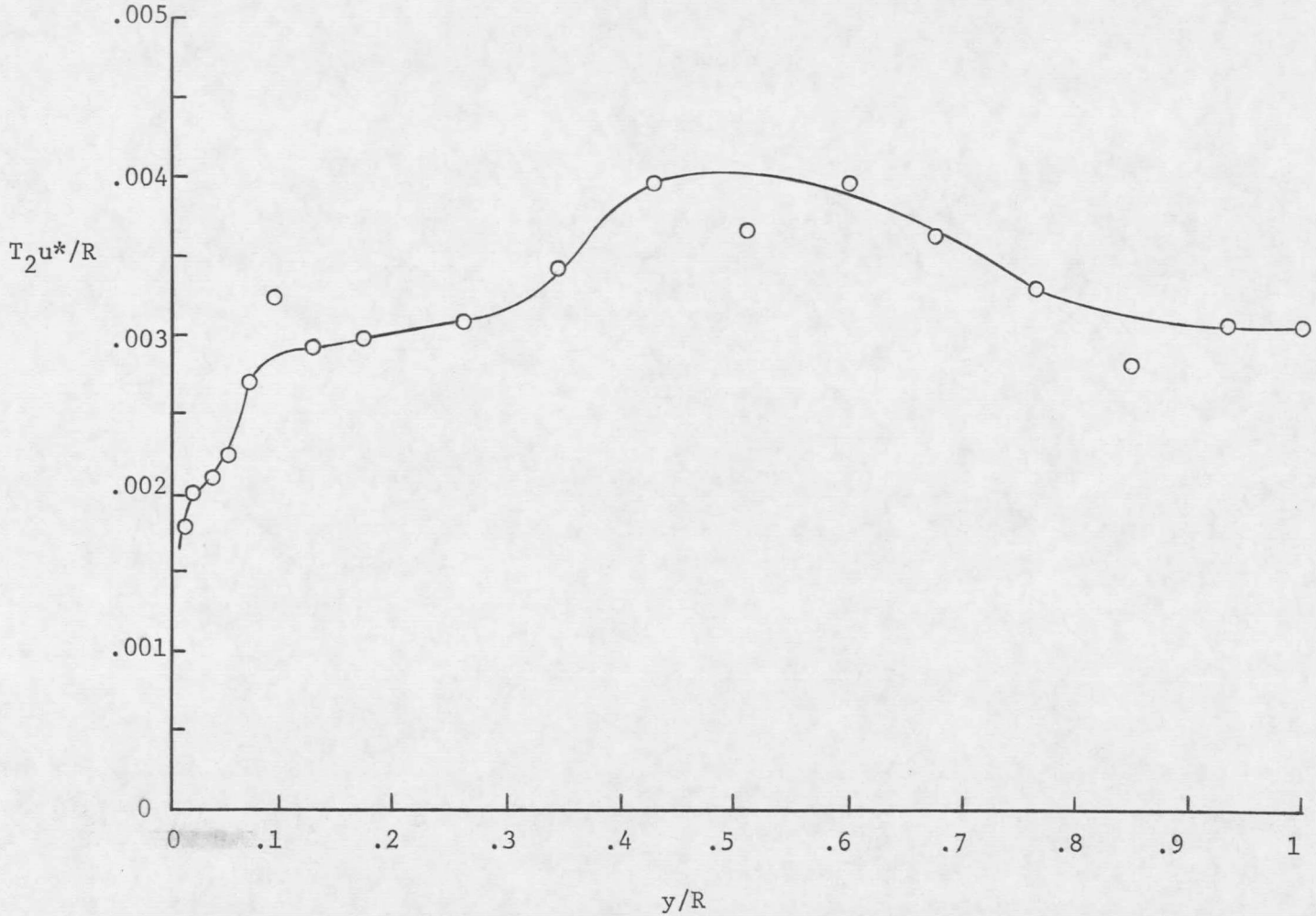

FIGURE 84. Eulerian Macro Scale for u_2 Fluctuating Velocity in Central Region of Smooth Pipe

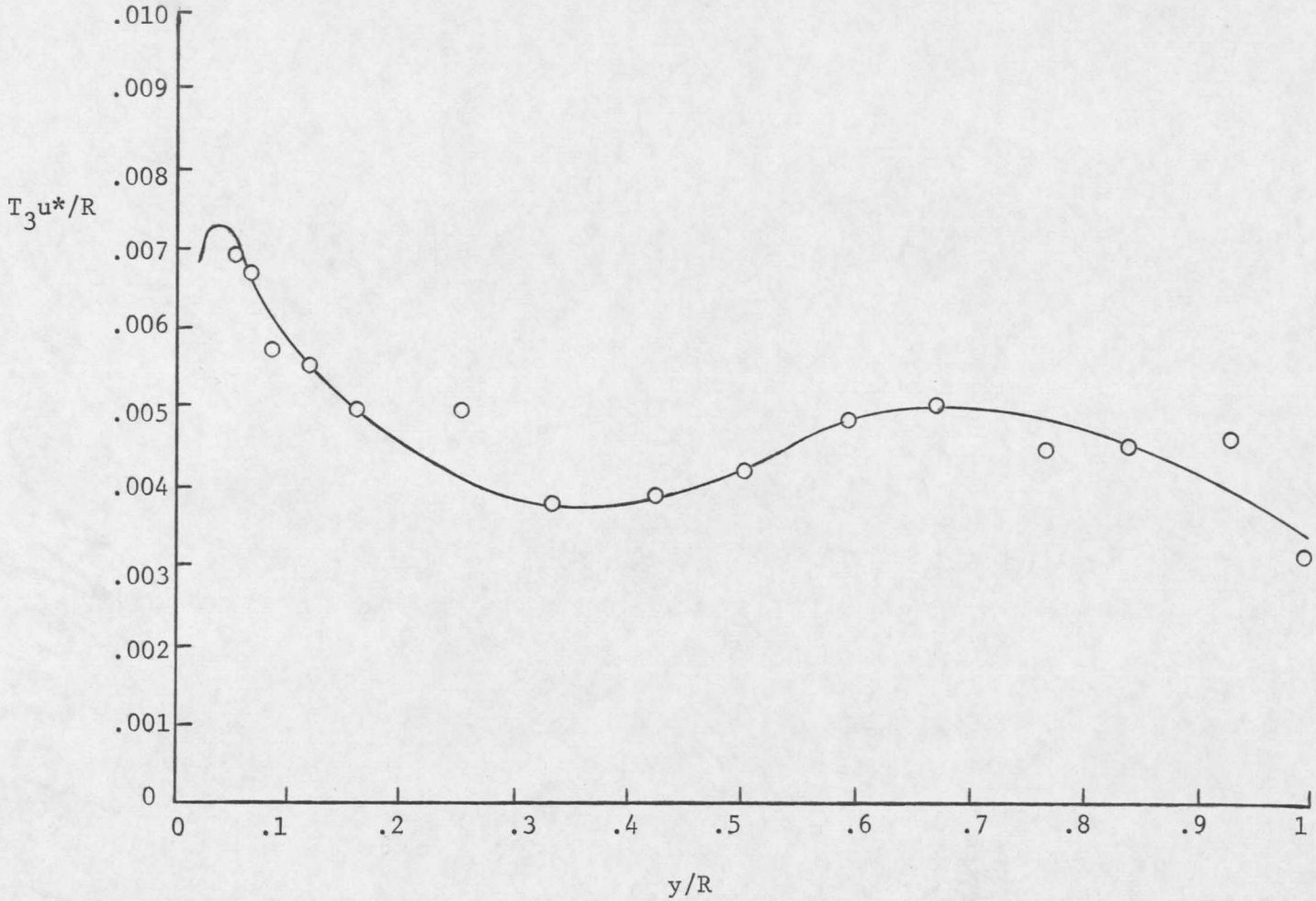

FIGURE 85. Eulerian Macro Scale For u_3 Fluctuating Velocity in Central Region of Smooth Pipe

of the pipe is presented in Figures 86, 87, and 88. These figures indicate that the Eulerian macro scale is fairly constant in the core region of the pipe for all three coordinate directions. However, near the wall increases are observed in T_2 and T_3 while T_1 decreases. This indicates the disappearance of some of the very low frequency components of u_1 at the same time that u_2 and u_3 are extended to lower frequencies. As in the case of the Eulerian micro scales, T_1 is observed to be of largest magnitude throughout the pipe, with the exception of the region very close to the wall, whereas T_2 is again of lowest magnitude. This is indicative of the occurrence of lower frequency velocity fluctuations in u_1 than in either of the other fluctuating velocities.

Transformation of the Eulerian micro scales into the spatial micro scales, with the aid of Taylor's hypothesis, is indicated in Figures 89 and 90. The spatial micro scales, which indicate the average dimensions of the smallest (viscous dissipation) eddies in the flow field, are seen to increase with distance from the wall to a maximum value near the mid radial position. A slight decrease then occurs in proceeding to the center line. This behavior is indicative of a decrease in the size of the viscous dissipation eddies as the wall is approached. Throughout the pipe, it is seen that these eddies are longest in the x_1 direction and shortest in

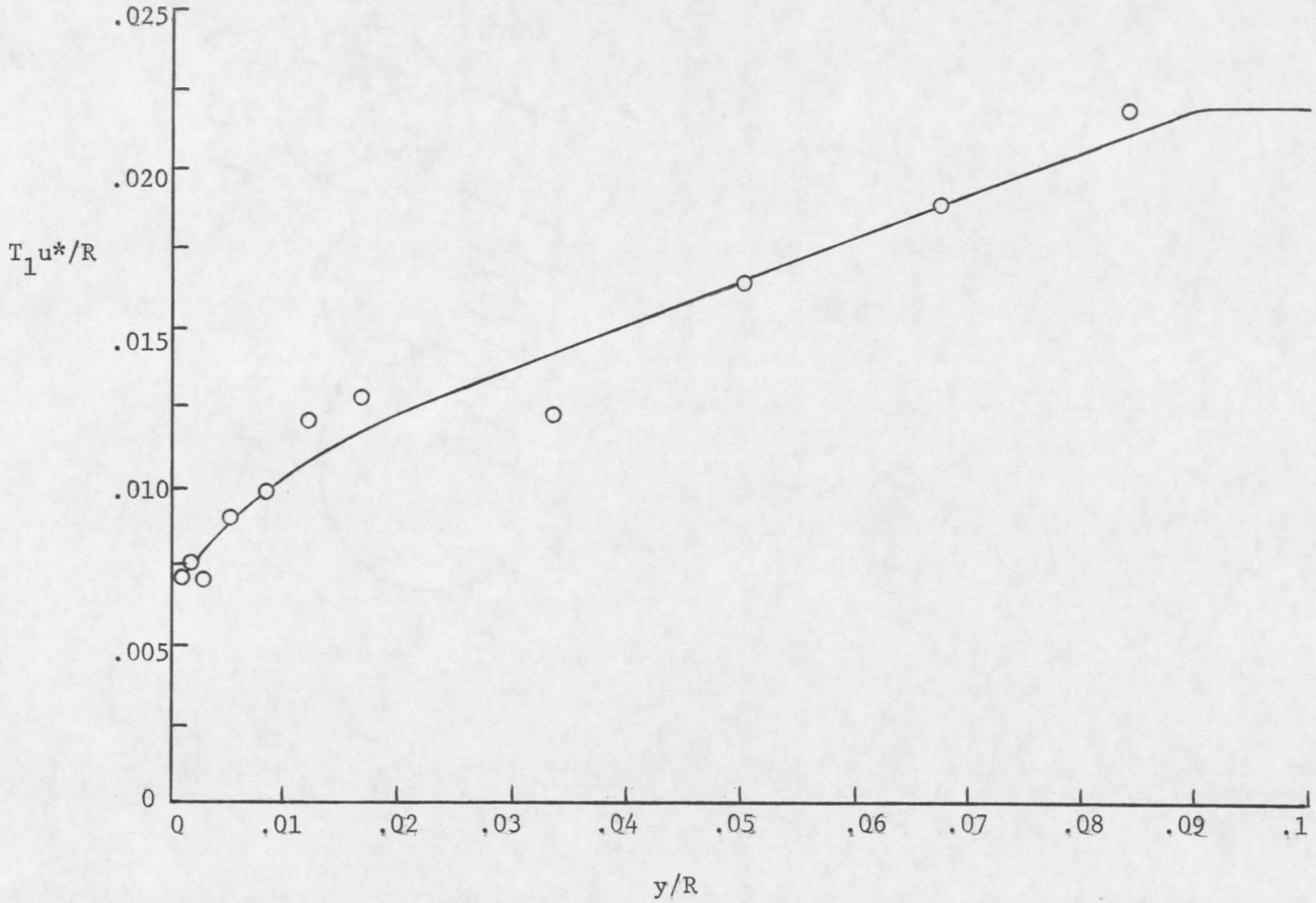

FIGURE 86. Eulerian Macro Scale For u_1 Fluctuating Velocity in Wall Region of Smooth Pipe

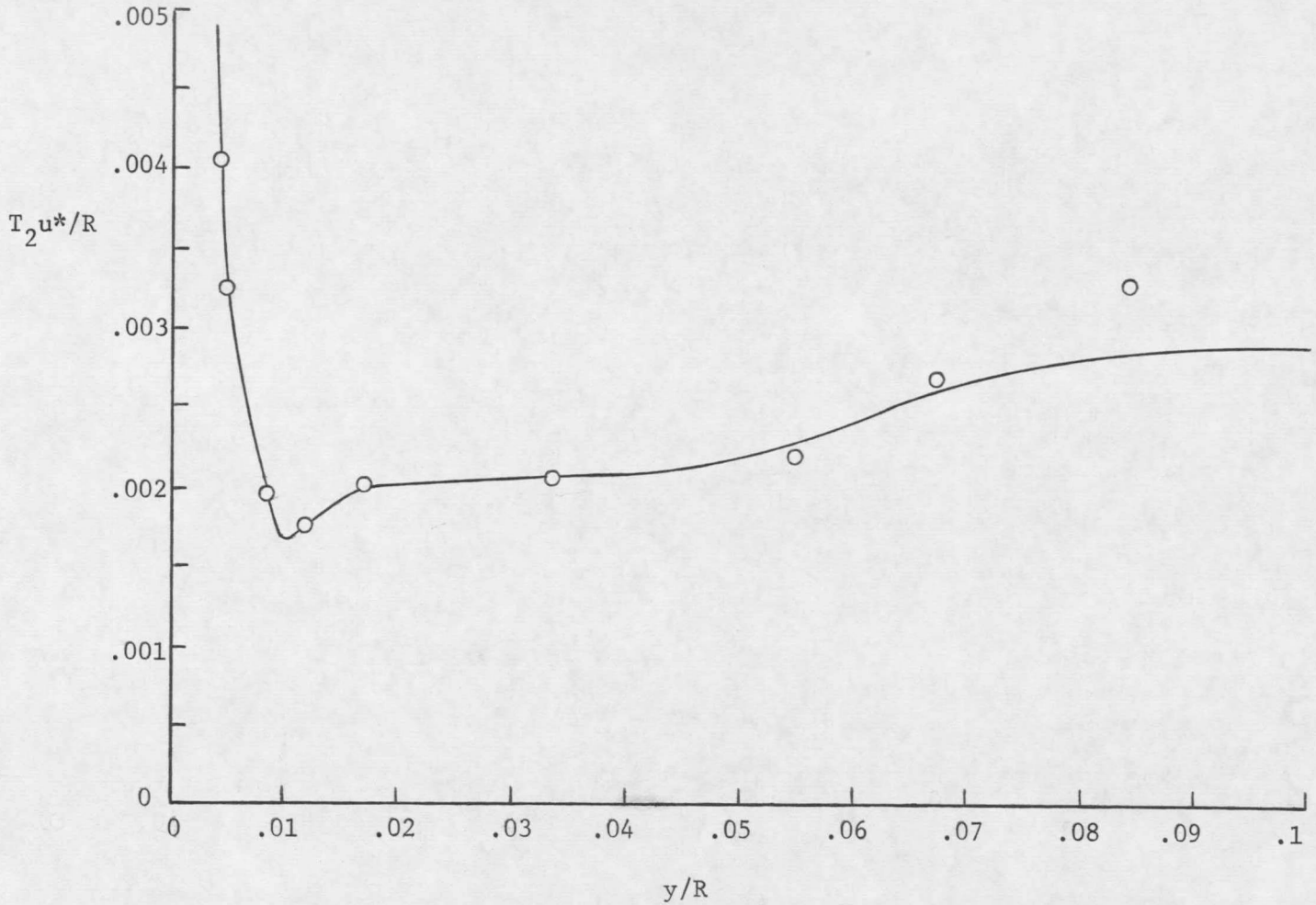

FIGURE 87. Eulerian Macro Scale For u_2 Fluctuating Velocity in Wall Region of Smooth Pipe

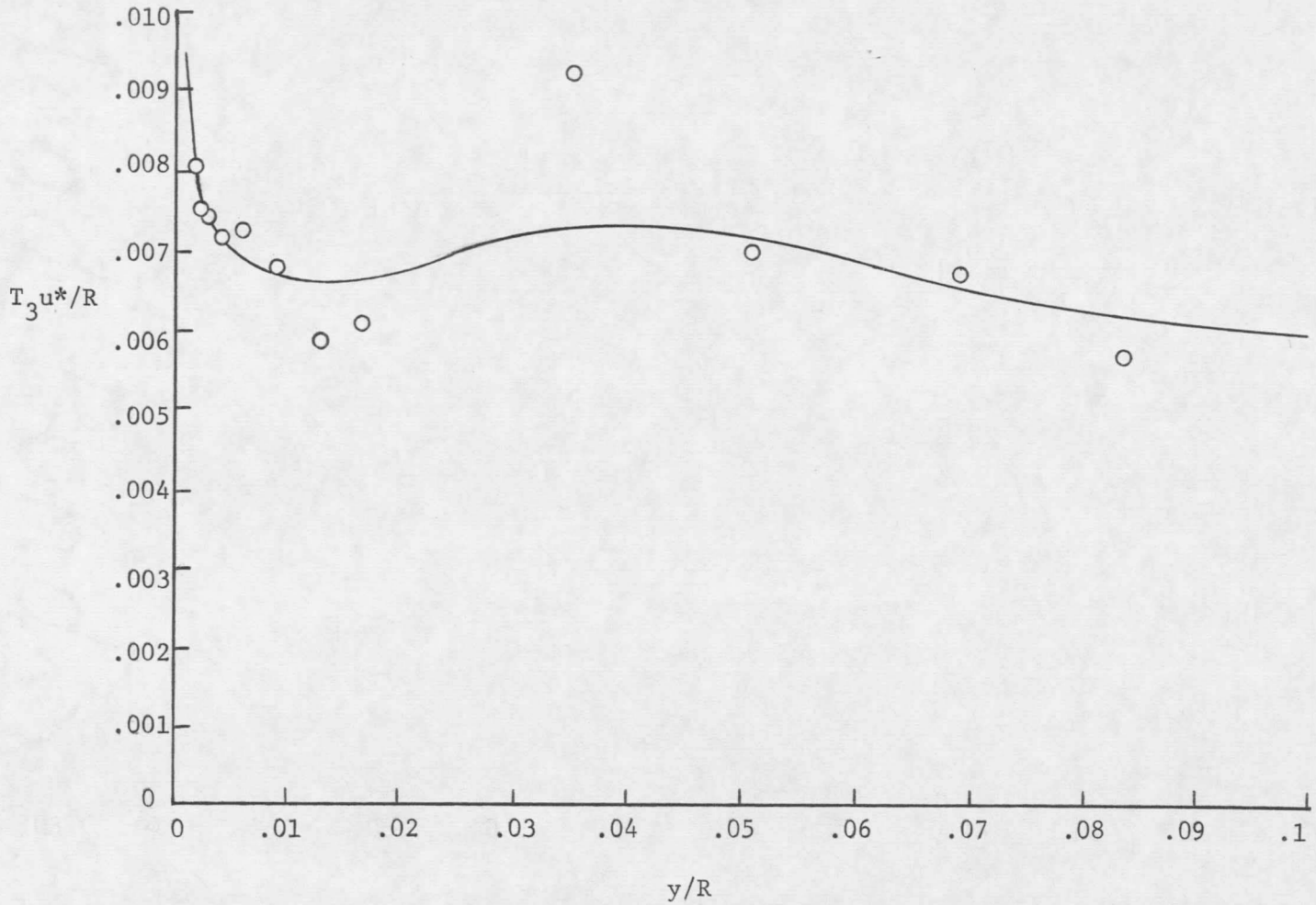

FIGURE 88. Eulerian Macro Scale for u_3 Fluctuating Velocity in Wall Region of Smooth Pipe

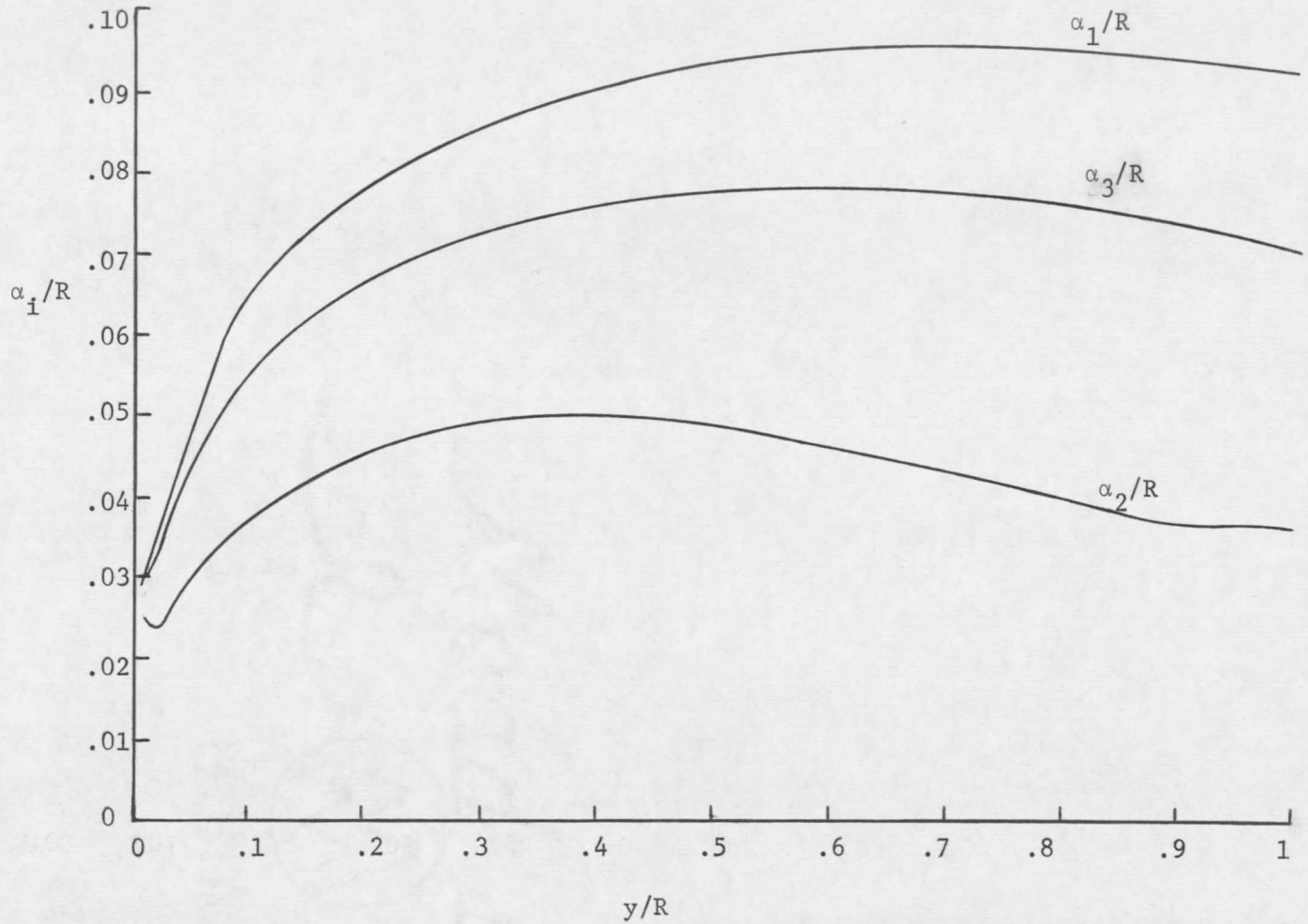

FIGURE 89. Spatial Micro Scales For Central Region of Smooth Pipe

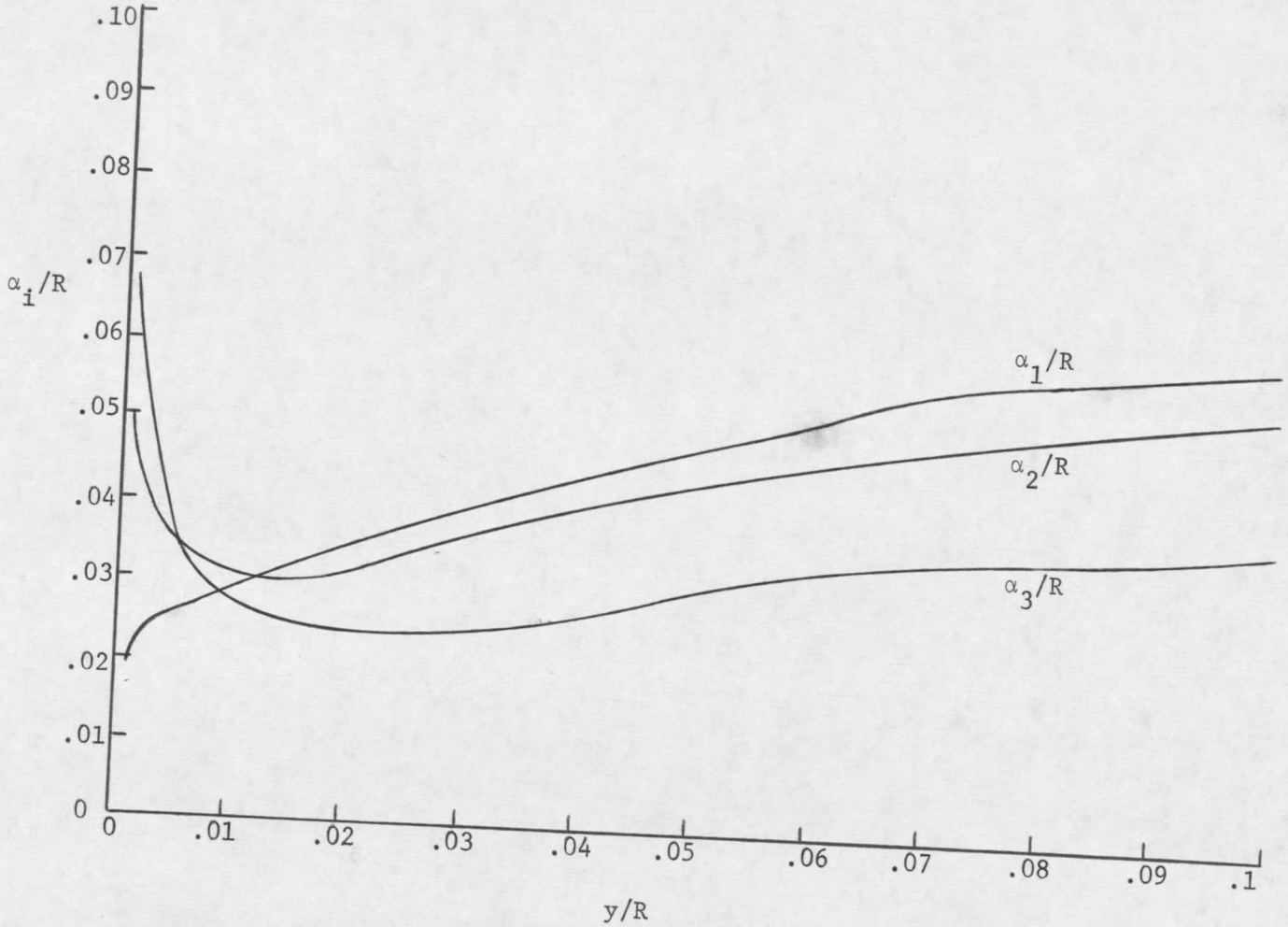

FIGURE 90. Spatial Micro Scales For Wall Region of Smooth Pipe

the x_2 direction. The magnitudes of the spatial micro scales are in good agreement with those obtained by Laufer [40], who found maximum values on the order of 0.1R for all three in his channel flow experiments.

Figure 91 shows the variation of the three spatial macro scales over the pipe radius. These macro scales, which are indicative of the longest connection distance between velocities at two points in the flow field or the size of the largest eddies, are seen to be relatively constant over the central and major portion of the flow field. One exception is a pronounced decrease in Λ_1 at the pipe center line. However, Λ_1 still remains larger than the other two scales throughout the pipe, and this implies the existence of large eddies which are elongated in the axial direction. In contrast with other turbulence scales, Λ_2 is seen to be larger than Λ_3 except near the pipe wall where the presence of the solid boundary is thought to suppress the extent of the large eddies in the x_2 direction. The magnitudes of Λ_1, Λ_2, and Λ_3 are considerably lower than the values found by Laufer [40] in his channel flow studies, and this finding is in agreement with the pipe flow experiments of Robertson _et al_ [47].

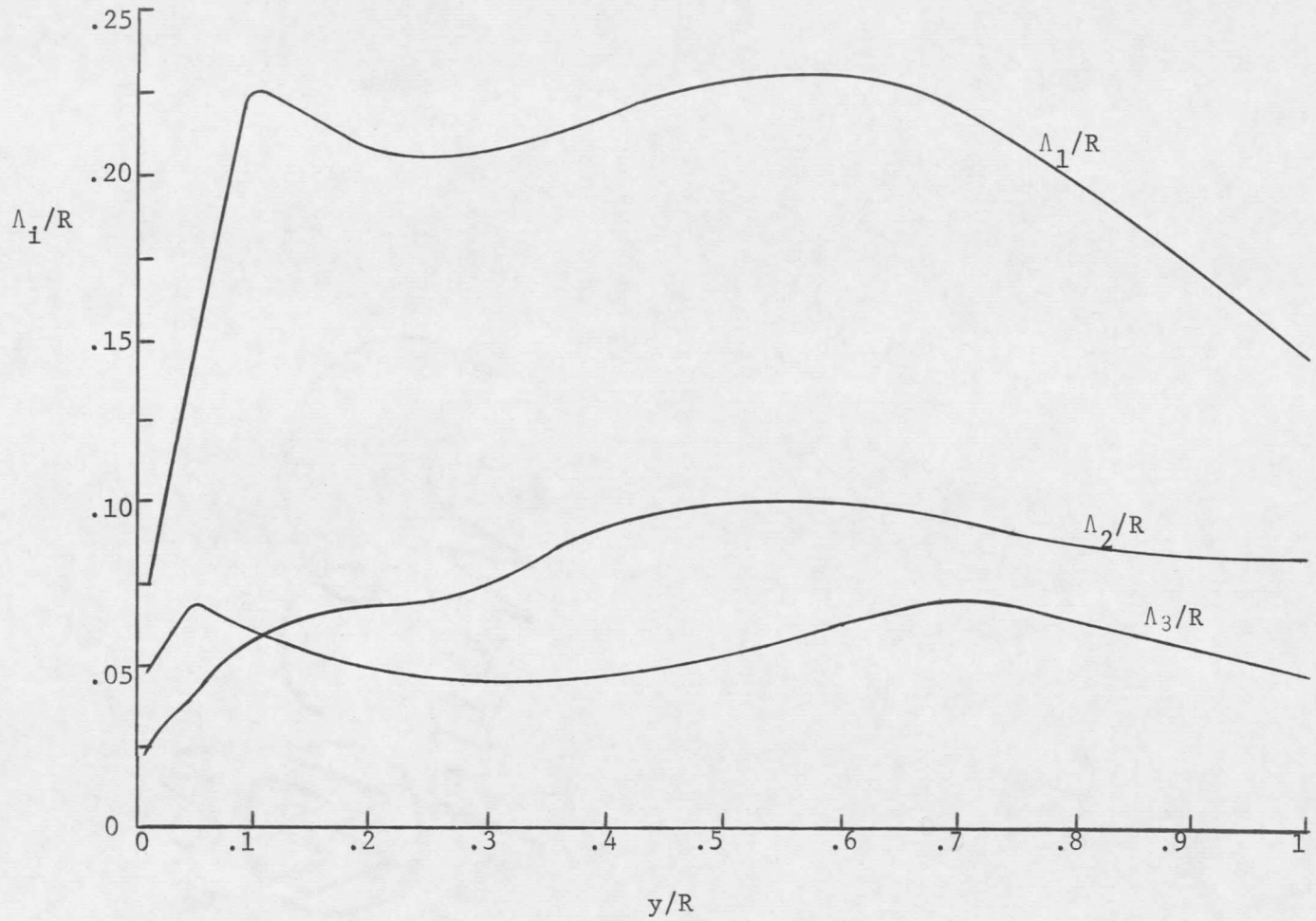

FIGURE 91. Spatial Macro Scales For Smooth Pipe

CHAPTER VII

RESULTS FOR SMALL ROUGHNESS

Mean Velocity and Flow Resistance

In order to establish the equivalent sand diameter of the roughness elements utilized in this pipe, measurements were first made of friction factor versus Reynolds number over a wide range of Reynolds numbers. As in the case of the smooth pipe, K was found to be independent of Reynolds number and equal to about 0.368 so that pressure measurements, together with equation (6.1), could be employed to generate the λ-Re curve. The results are shown in Figure 92 where the solid line again represents Prandtl's universal friction factor relationship for turbulent flow in smooth tubes, equation (2.35). The resultant friction factor curve indicates that the small roughness does yield flow in the hydraulically smooth regime for small Reynolds numbers, and the dip characteristic of a high density sand roughness is observed in the transition regime. For the higher Reynolds numbers obtained, the friction factor appears to be becoming independent of Reynolds number, thereby indicating an approach into the fully rough flow regime. The utilization of this high Reynolds number data with equation (2.44) allowed the determination of the equivalent sand diameter, k_s, as 0.0280 inches, in close agreement with the actual average roughness height of 0.0286 inches. All

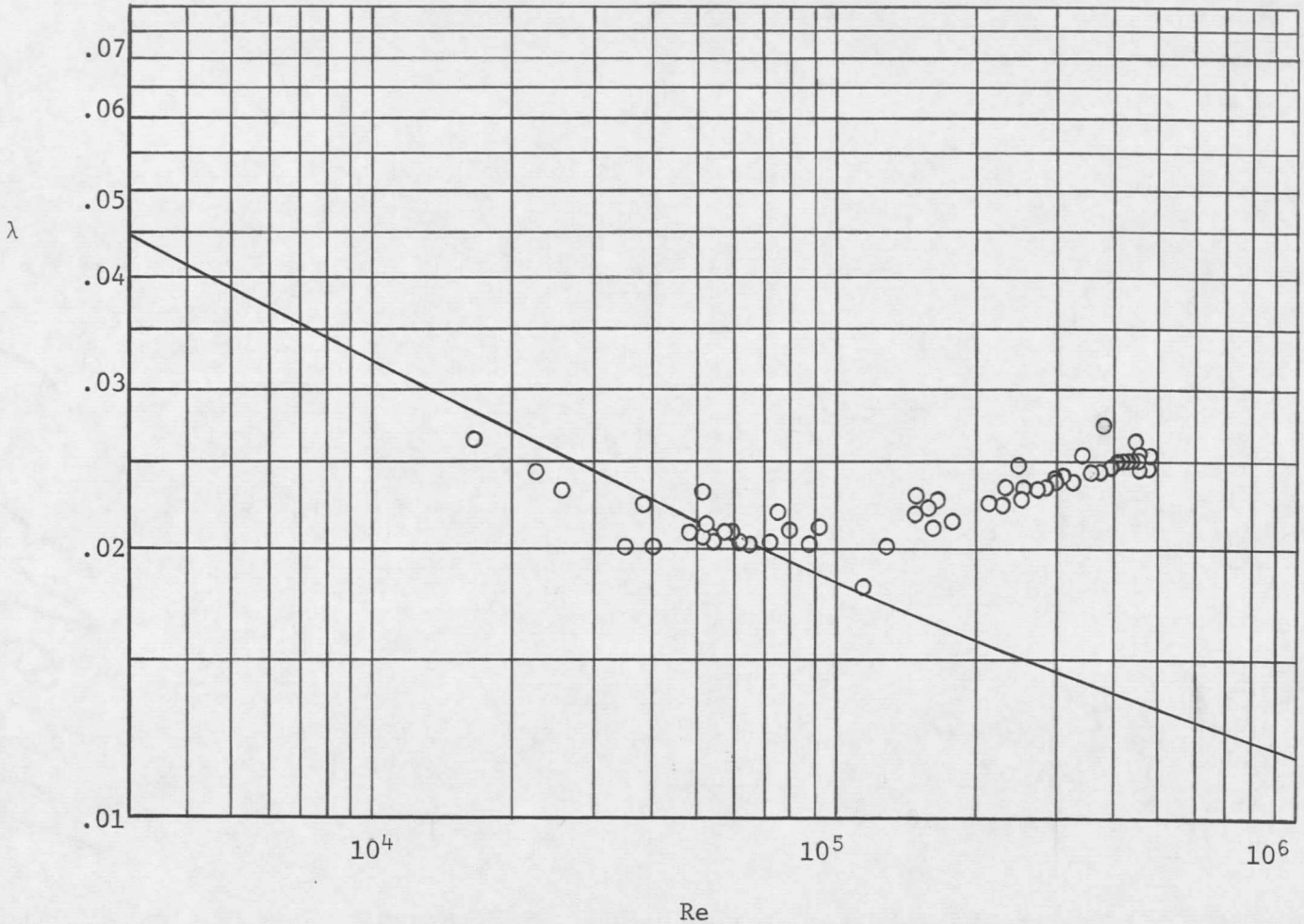

FIGURE 92. Flow Resistance Characterization for Small Roughness

experimental data obtained for this pipe were at a Reynolds number of 165,000 yielding a value of y^+ at the center line of 4220, and it may be noted from Figure 92 that this Reynolds number yields a friction factor near the bottom of the dip in the λ- Re curve.

Experimental measurements of the longitudinal mean velocity profile in the turbulent core of this pipe are presented in Figure 93, and such measurements for the wall region are shown in Figure 94. One feature of this profile deserves special notice. At a value of y/R near 0.002 a slight rise in the profile is noted, and this results in an apparent tendency toward a nonzero value of the velocity at the wall. This occurrence is not cause for concern regarding the validity of the experimental results, since data obtained below the mean height of the roughness elements ($y/R < 0.00482$) are not expected to be generally meaningful, but is simply thought to be indicative of an increased heat loss to the solid surface because of the presence of the roughness elements. In fact, this phenomenon has been observed in several previous smooth pipe investigations where no correction for heat loss to the wall was applied, e.g. that of Clark [39].

Fluctuating Velocities

The rms values of the fluctuating velocities in the three

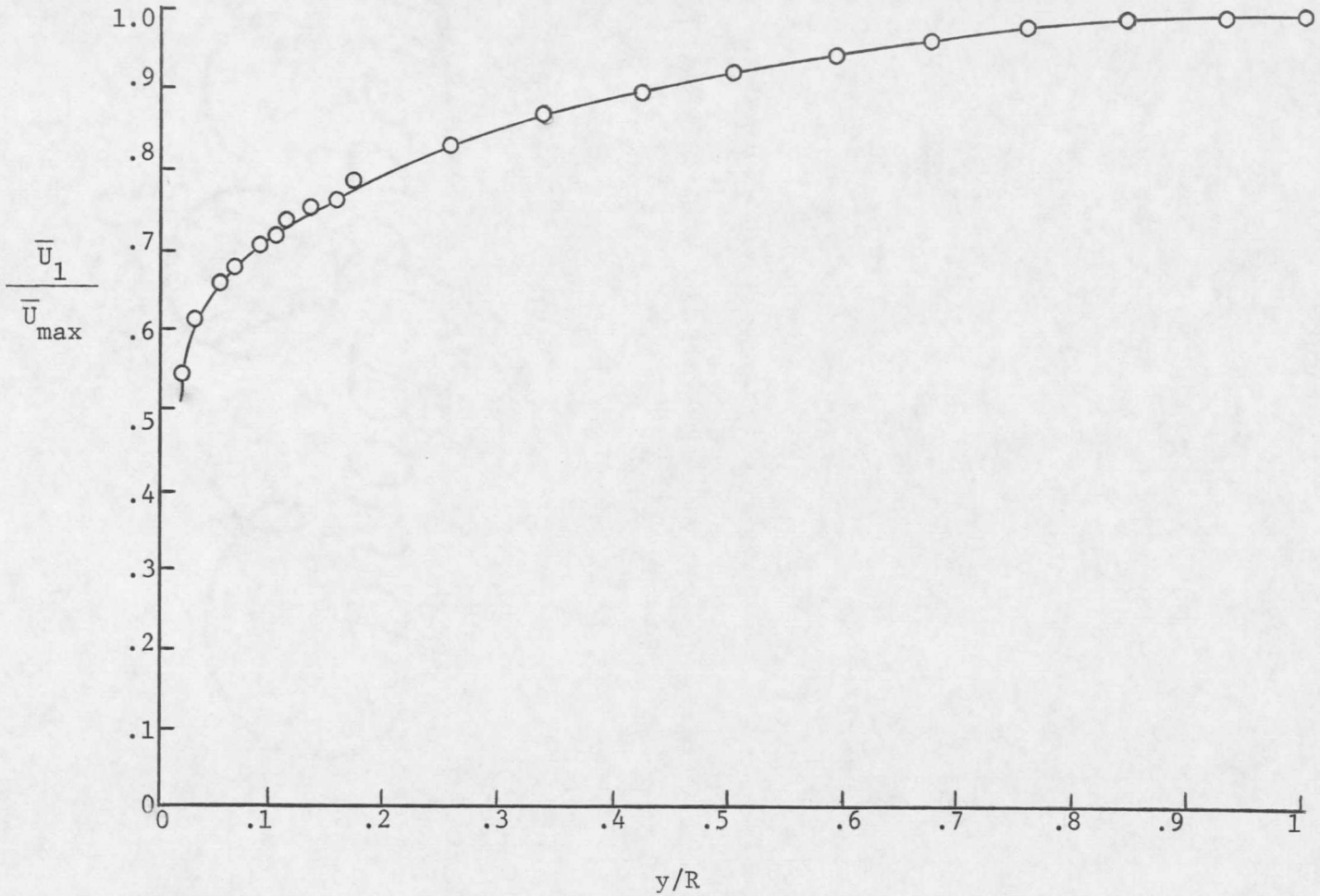

FIGURE 93. Longitudinal Mean Velocity Profile For Central Region of Pipe With Small Roughness Elements

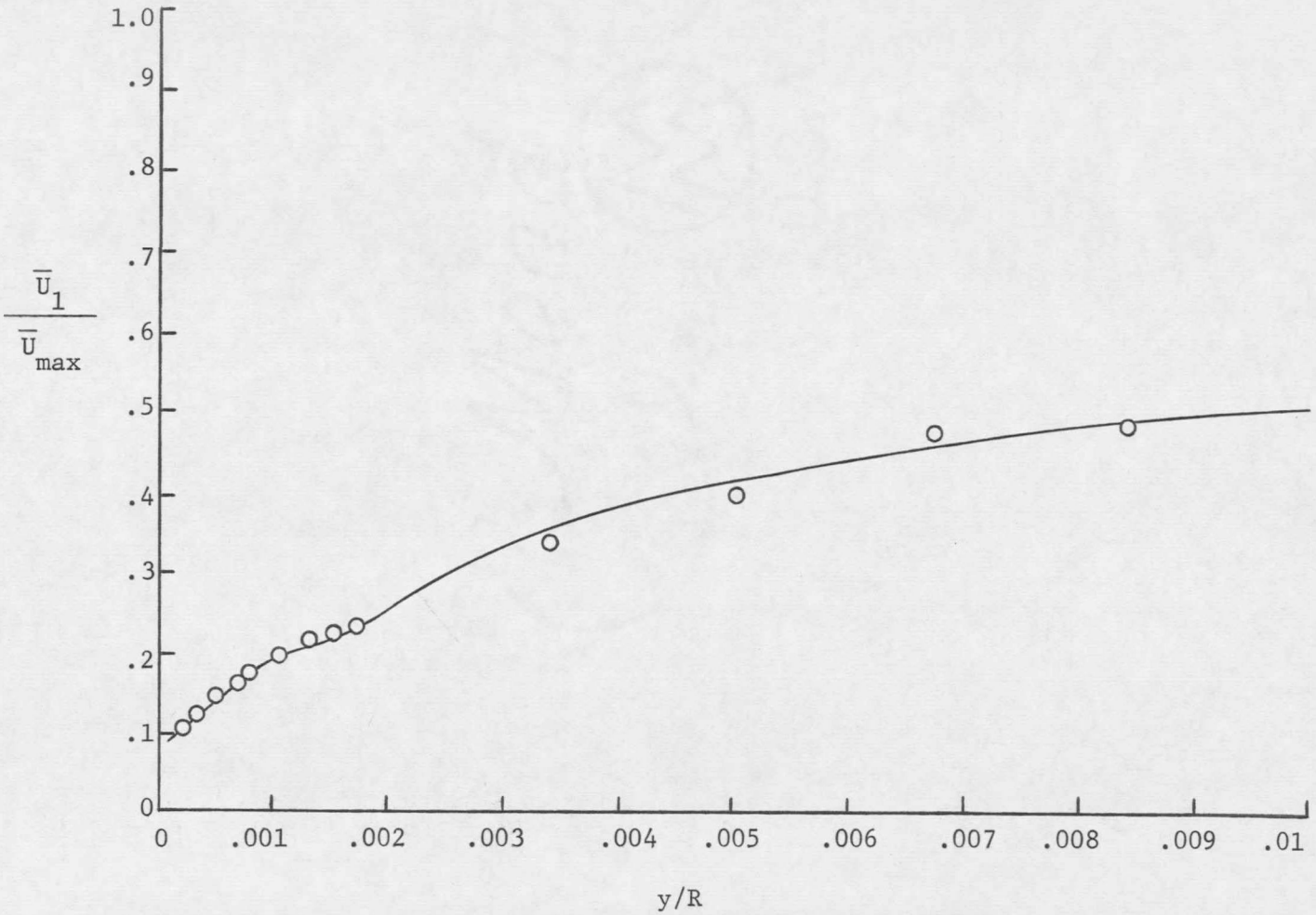

FIGURE 94. Longitudinal Mean Velocity Profile for Wall Region of Pipe With Small Roughness Elements

coordinate directions are presented in Figure 95 for the central region of the pipe and in Figure 96 for the wall region. As required by the momentum relation, equation (4.11), u_2' and u_3' are equal at the pipe center line, and u_1' has a somewhat larger magnitude. In moving from the center line toward the pipe wall, all three components are observed to increase, u_1' at the fastest rate and u_2' at the slowest. Maximum values of u_1' and u_3' were both found to be attained near $y/R = 0.05$ while a maximum in u_2' occurred around $y/R = 0.015$. This resulted in u_2' and u_3' becoming essentially equal for a short distance just beyond the mean height of the roughness elements.

As a check on the assumption of small turbulence intensities, the intensities of all three fluctuating velocity components are presented in Figure 97. The curves in this figure indicate intensities less than 20% in all cases, and in veiw of the discussion in reference [97], significant errors due to turbulence intensity magnitudes are not expected.

The degree of anisotropy prevailing in the pipe currently under consideration may be investigated by means of Figure 98 which shows the variation of the three anisotropy ratios over the pipe cross section. The ratios u_2'/u_1' and u_3'/u_1' are seen to be approximately constant near a value of 0.5 at most radial positions, although they increase to about 0.7 at the pipe center line. The ratio u_2'/u_3'

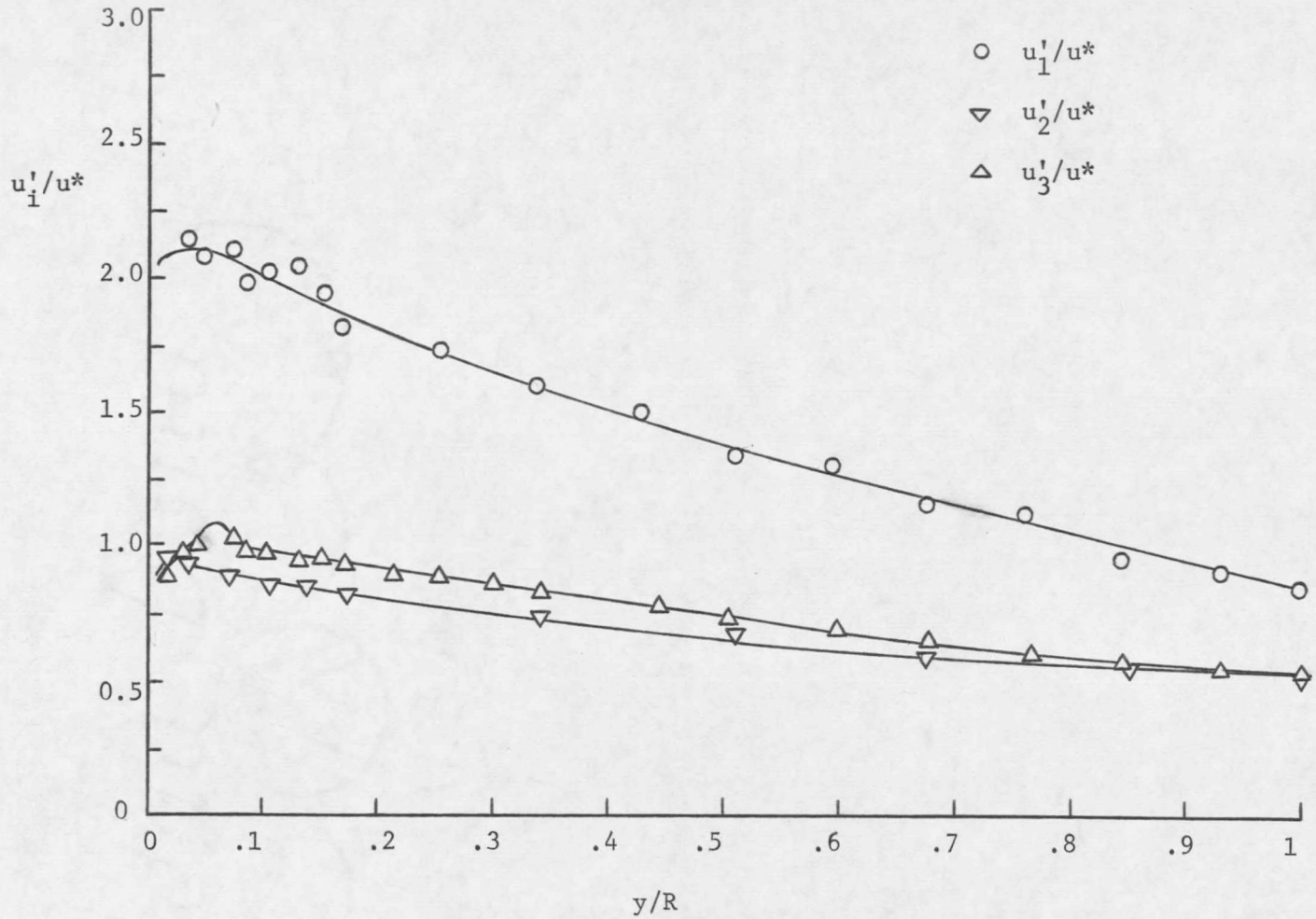

FIGURE 95. Fluctuating Velocities in Central Region of Pipe With Small Roughness Elements

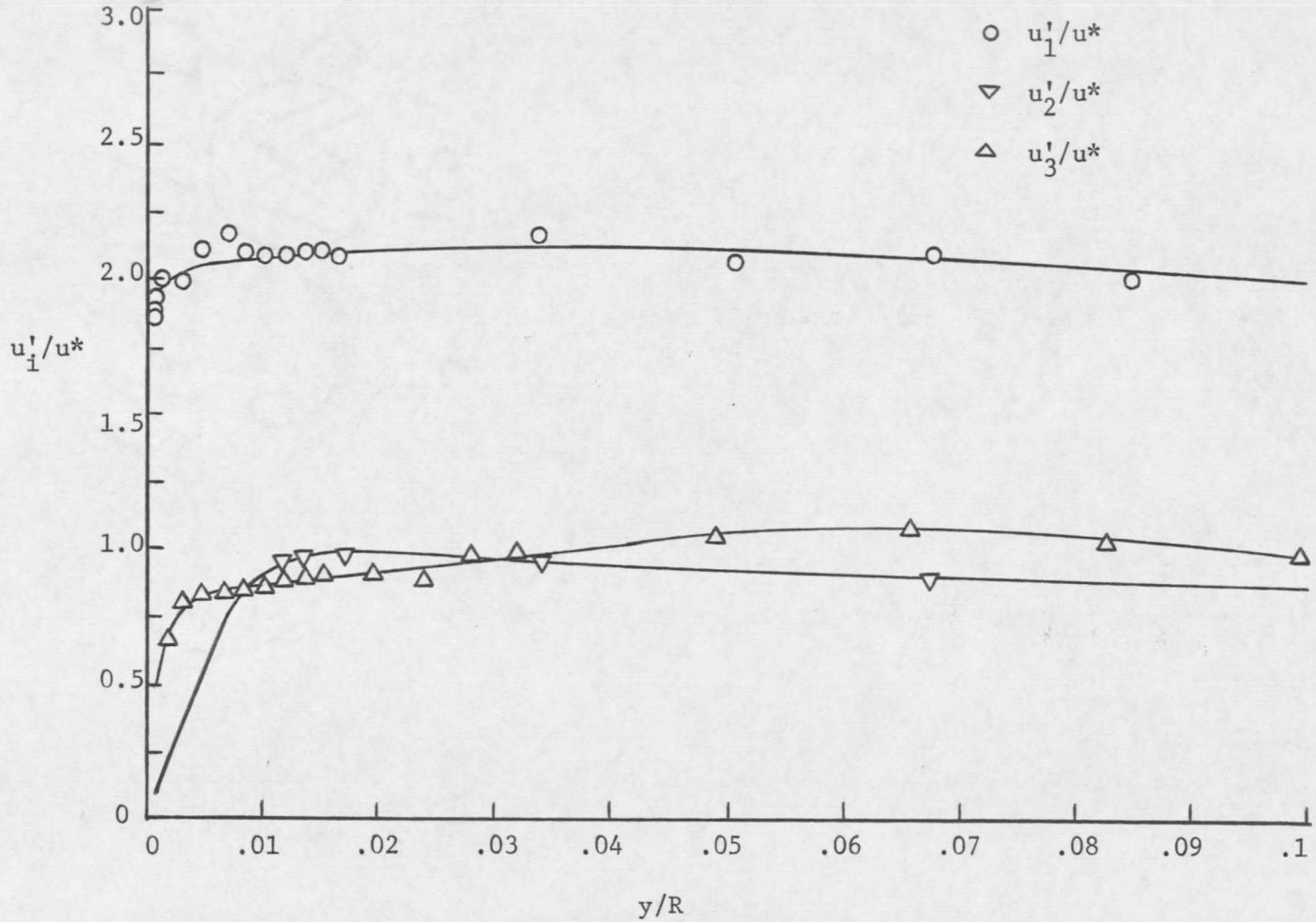

FIGURE 96. Fluctuating Velocities for Wall Region of Pipe With Small Roughness Elements

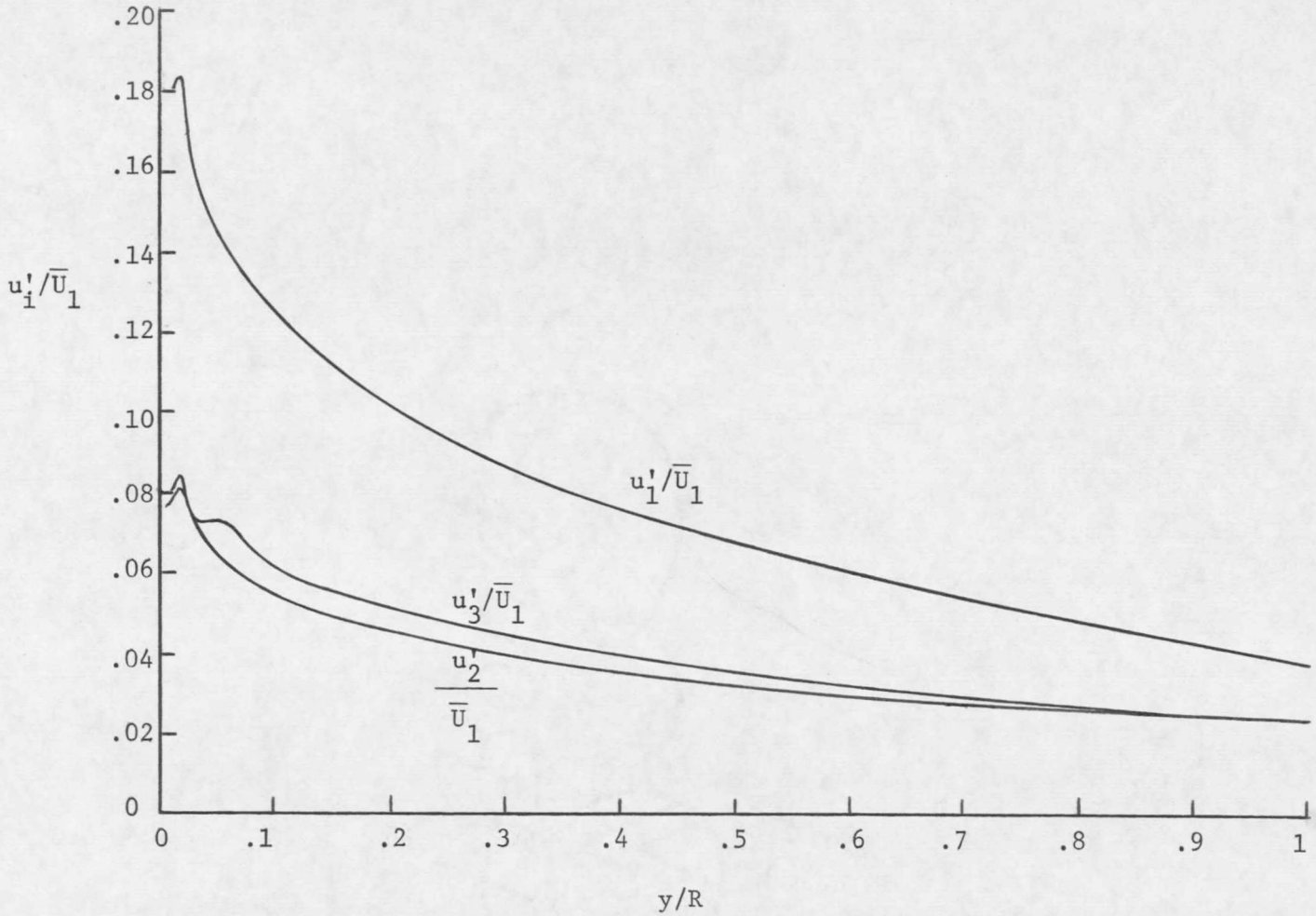

FIGURE 97. Turbulence Intensities in Pipe With Small Roughness Elements

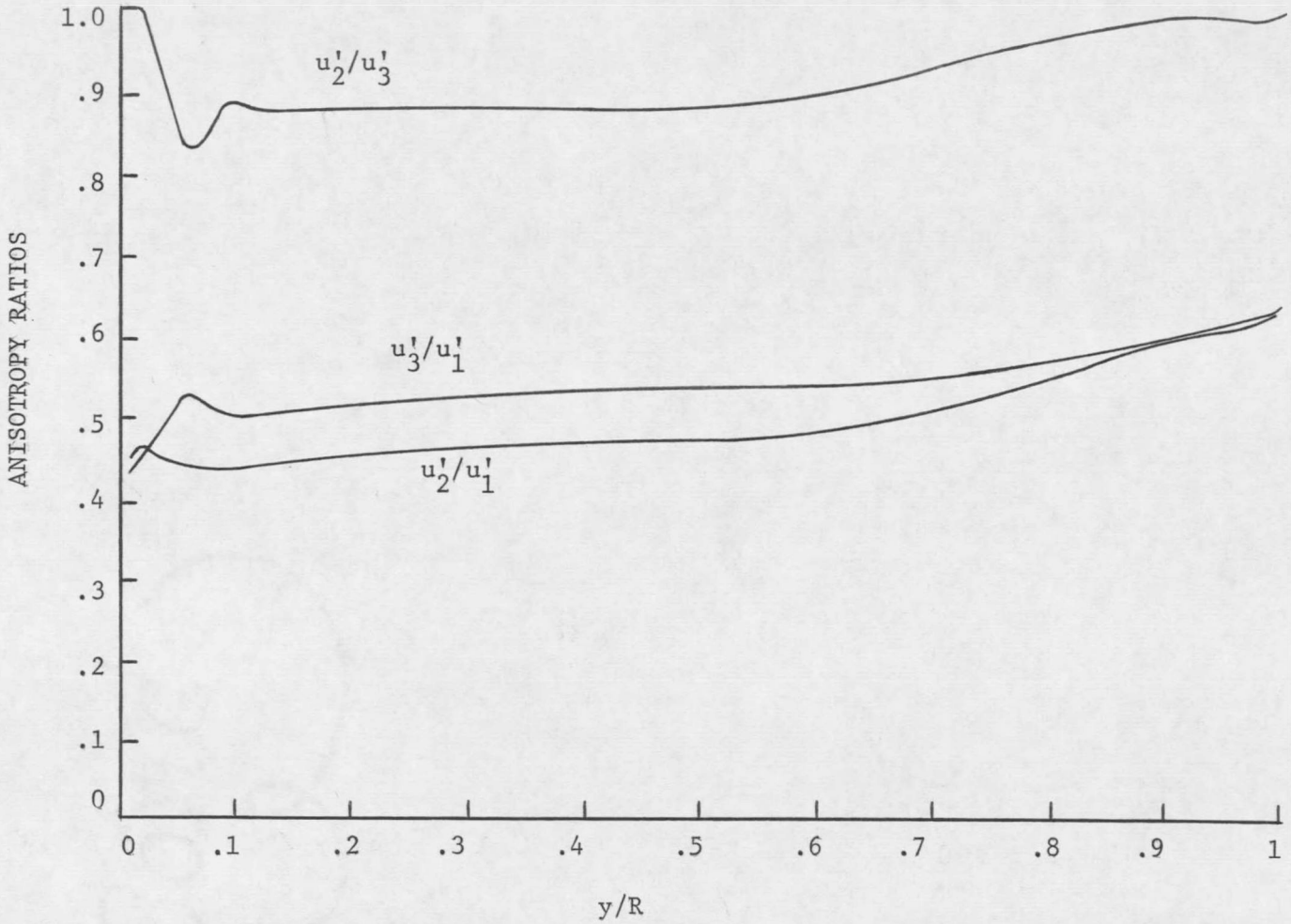

FIGURE 98. Anisotropy Ratios For Flow in Pipe With Small Roughness Elements

also remains nearly constant at about 0.9 through most of the pipe and increases to a value of 1.0 at both the wall and the center line. Thus, the u_2' and u_3' fluctuating velocities indicate a definite tendency toward isotropy for flow in the pipe with the small roughness elements, but the u_1' fluctuating velocity prevents the attainment of complete isotropy.

Having determined values of the fluctuating velocities in the three coordinate directions, the turbulence kinetic energy can now be calculated. This quantity is shown normalized with the square of the shear velocity in Figure 99. It can be seen that the normalized kinetic energy has a value near unity at the center line and then increases in moving toward the wall. This rate of increase is very small near the center line but increases with increasing radius. A maximum value of about 3.3 is acquired near a value of y/R of 0.06, and for y/R less than 0.01 the kinetic energy decreases rapidly to zero.

In contrast with the smooth pipe, a knowledge of the fluctuating velocities does not permit a rigorous calculation of the radial pressure variation in a rough pipe. It may be recalled that information regarding this pressure variation is needed to ascertain the validity of dynamic head calculations involving static pressure measurements at the pipe surface. However, this pressure variation

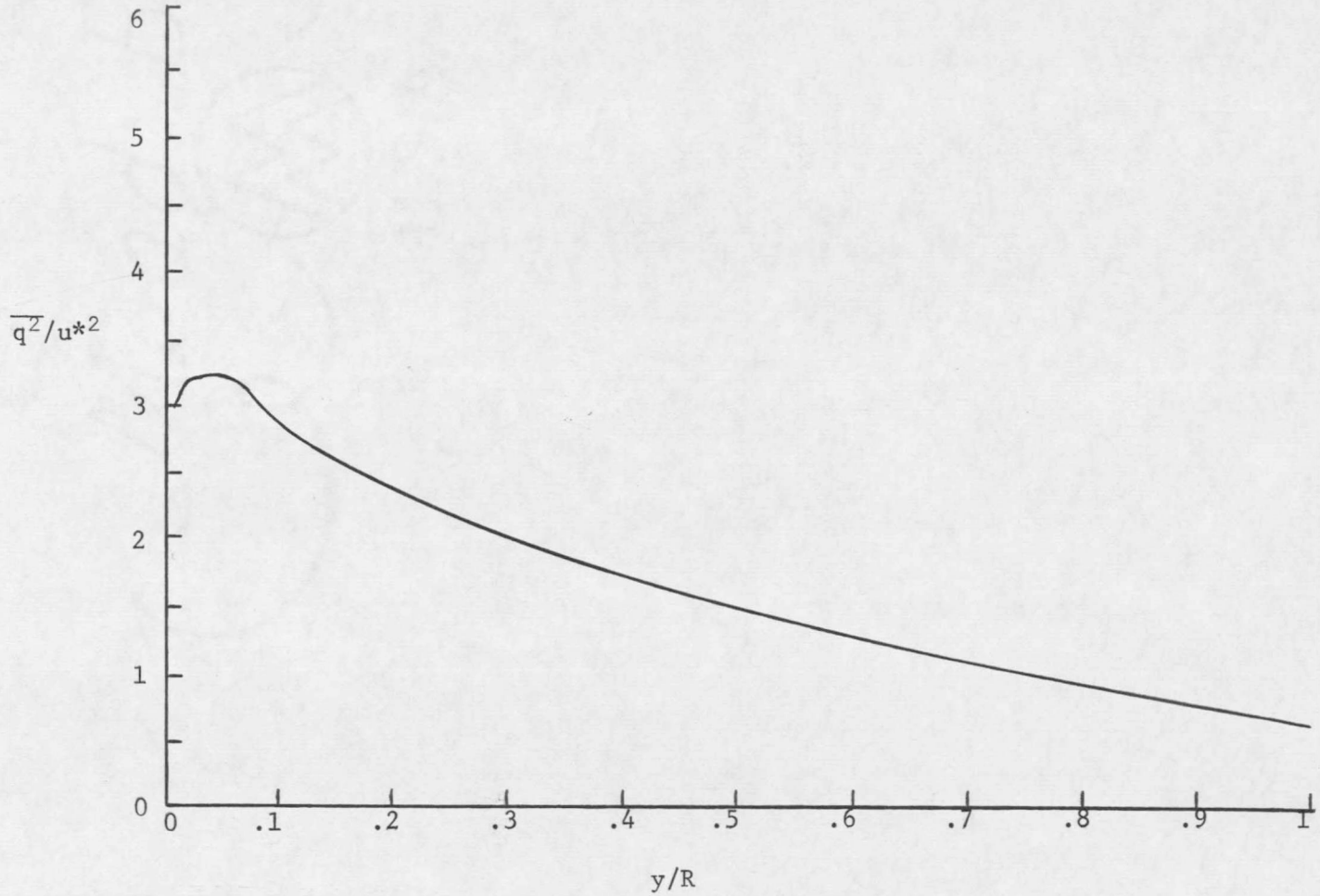

FIGURE 99. Turbulence Kinetic Energy For Flow in Pipe With Small Roughness Elements

may still be estimated from equation (4.12) if it is assumed that the spatially averaged mean velocities in the x_2 and x_3 coordinate directions yield only a negligible contribution to the pressure term. The results of calculations made using this assumption are shown in Figures 100 and 101. The dimensionless pressure term plotted in these figures is seen to remain constant at about 0.6 from the center line to the mid radial position, at which point it begins to increase. A sharp maximum value of unity is exhibited near $y/R \simeq 0.015$, and the dimensionless pressure then decreases to zero. As in the case of the smooth pipe, an inflection point in this profile is exhibited in the near wall region. From Figure 100 it may be observed that $\overline{P}_0 - \overline{P}_c$ is approximately equal to $\rho u^{*2}/2$. Thus, it is estimated that the error involved in calculating dynamic head from static pressure readings at the wall will be of the order of $(u^*/\overline{U}_{max})^2$, and in the current results this amounts to an error of only about 0.2%. Therefore, it is felt that measurement of the static pressure at the wall has been justified.

Fluctuating Velocity Correlations

The second order $\overline{u_1 u_2}$ cross correlation, normalized with the square of the shear velocity, is presented in Figure 102 for the pipe containing the small roughness elements. The variation in this

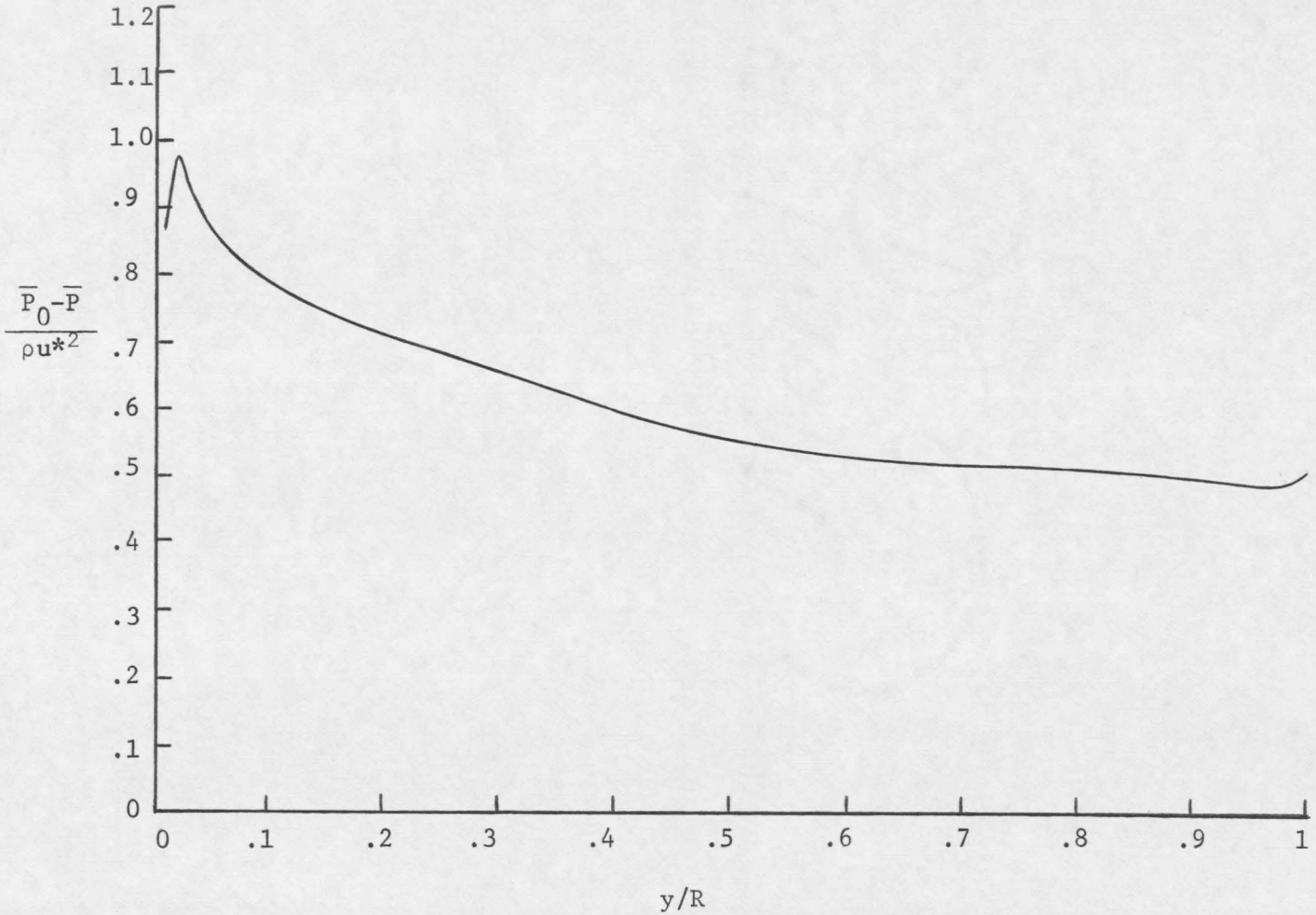

FIGURE 100. Radial Pressure Variation in Central Region of Pipe With Small Roughness Elements

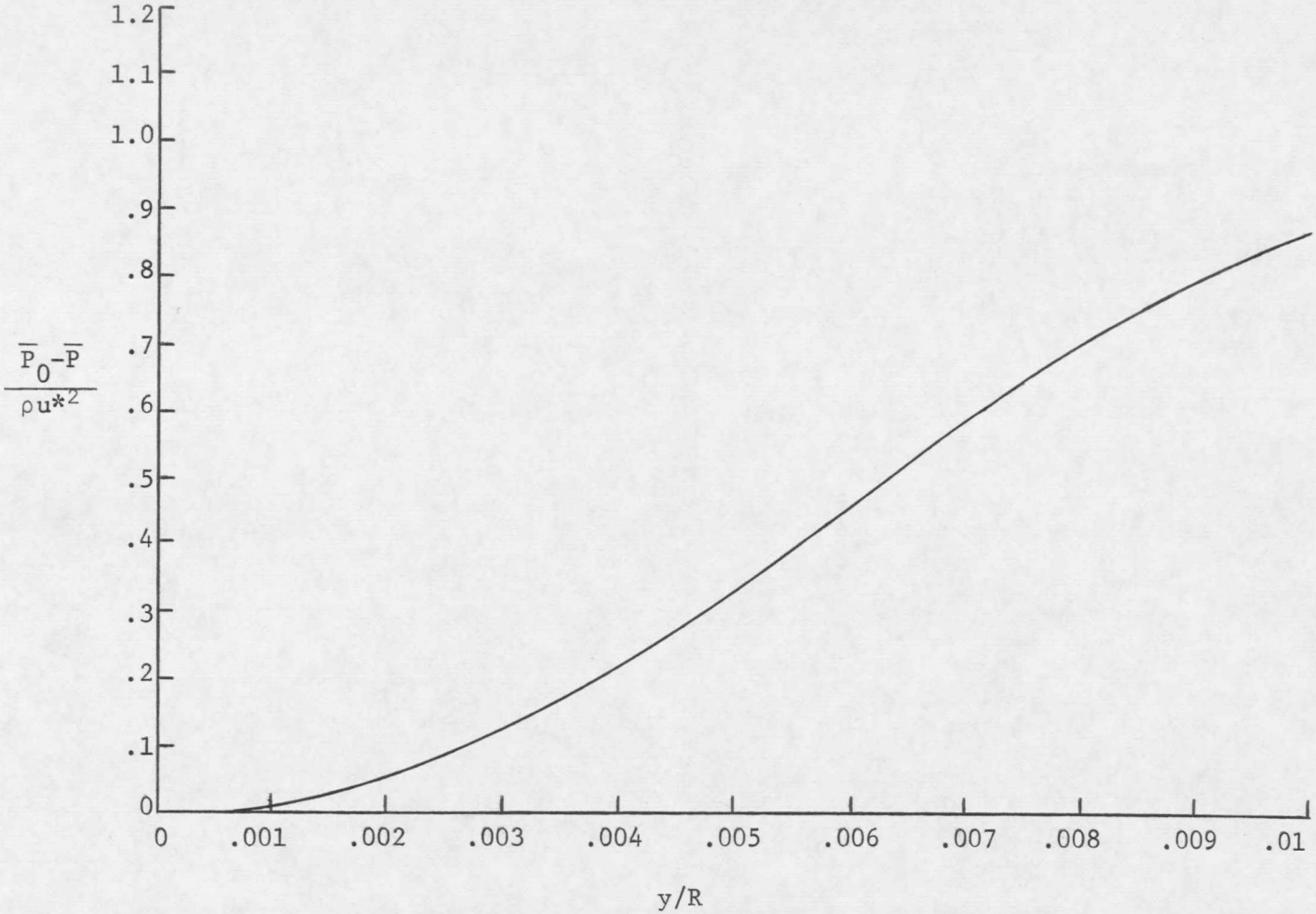

FIGURE 101. Radial Pressure Variation Near Wall of Pipe With Small Roughness Elements

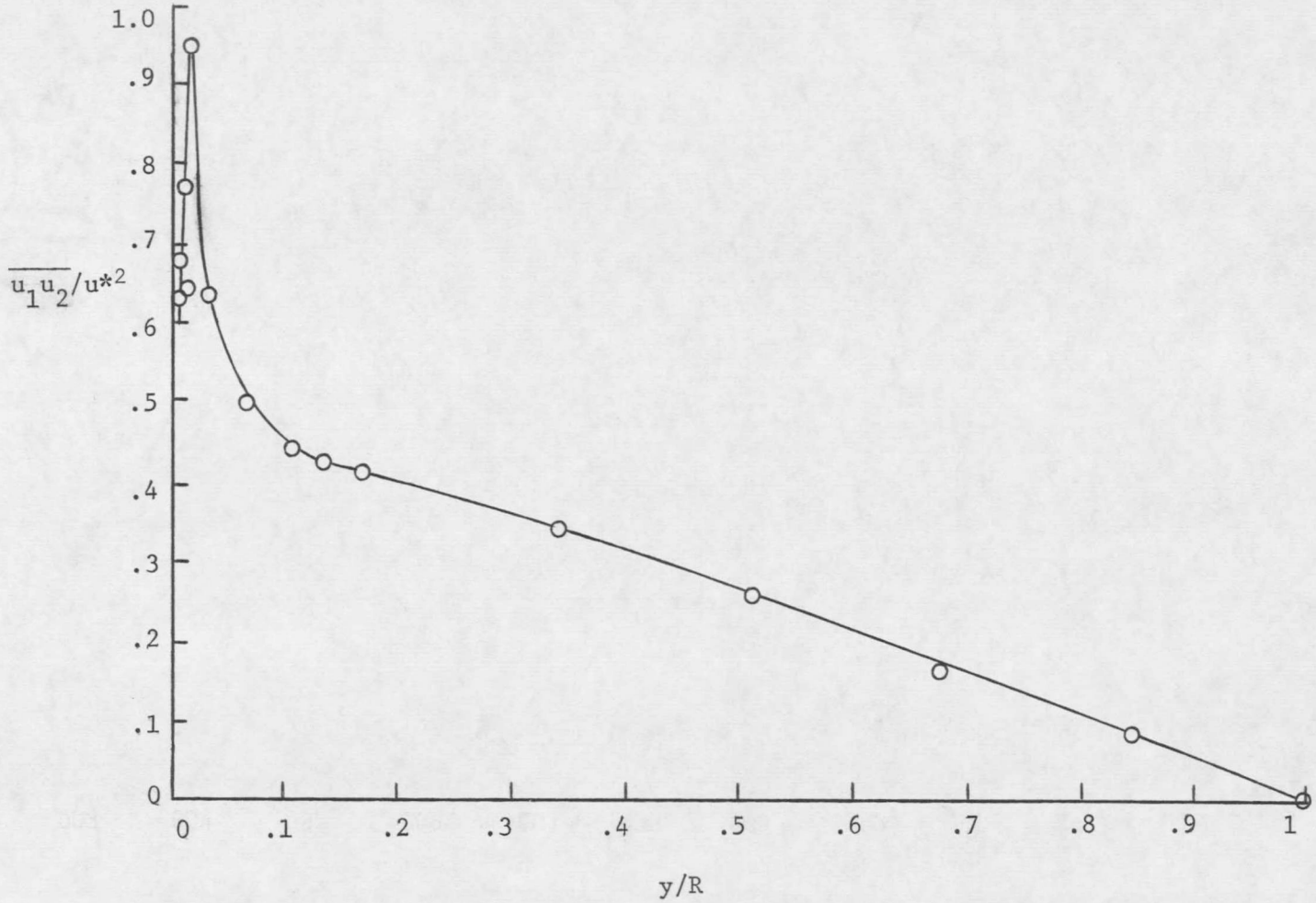

FIGURE 102. Second Order $\overline{u_1u_2}$ Cross Correlation for Flow in Pipe With Small Roughness Elements

correlation is seen to be approximately linear from a null value at the center line to about 0.45 at $y/R \approx 0.1$. At this point the $\overline{u_1 u_2}$ correlation begins to rise rapidly, and a sharp maximum occurs near $y/R = 0.02$. The correlation then decreases toward zero. These results are in good agreement with both those of Gow [15] and those of Robertson et al [47], if their data are adjusted for the failure to account for the vanishing of $\overline{u_1 u_2}$ at the pipe center line. Values of the $\overline{u_1 u_2}$ correlation obtained by Goma and Gelhar [30] are somewhat larger then those obtained in the present investigation, as well as the investigations of Gow [15] and Robertson et al [47], but this is probably accounted for by a difference in roughness type since they used spherical beads whereas sand grains were utilized in the other investigations.

The correlation coefficient corresponding to $\overline{u_1 u_2}$ in Figure 103 shows a nearly constant value of about 0.28 over the major portion of the pipe, $0.1 < y/R < 0.6$. For y/R greater than 0.6 this correlation coefficient tends toward zero, while for $y/R < 0.1$ a peak in the curve is noted. It should be recalled that both Prandtl's mixing length theory and von Karman's similarity hypothesis result in a constant value of the ratio of the $\overline{u_1 u_2}$ shear stress and the turbulence kinetic energy, and this ratio is seen, in Figure 104, to remain constant at about 0.16 over a large portion of the pipe .

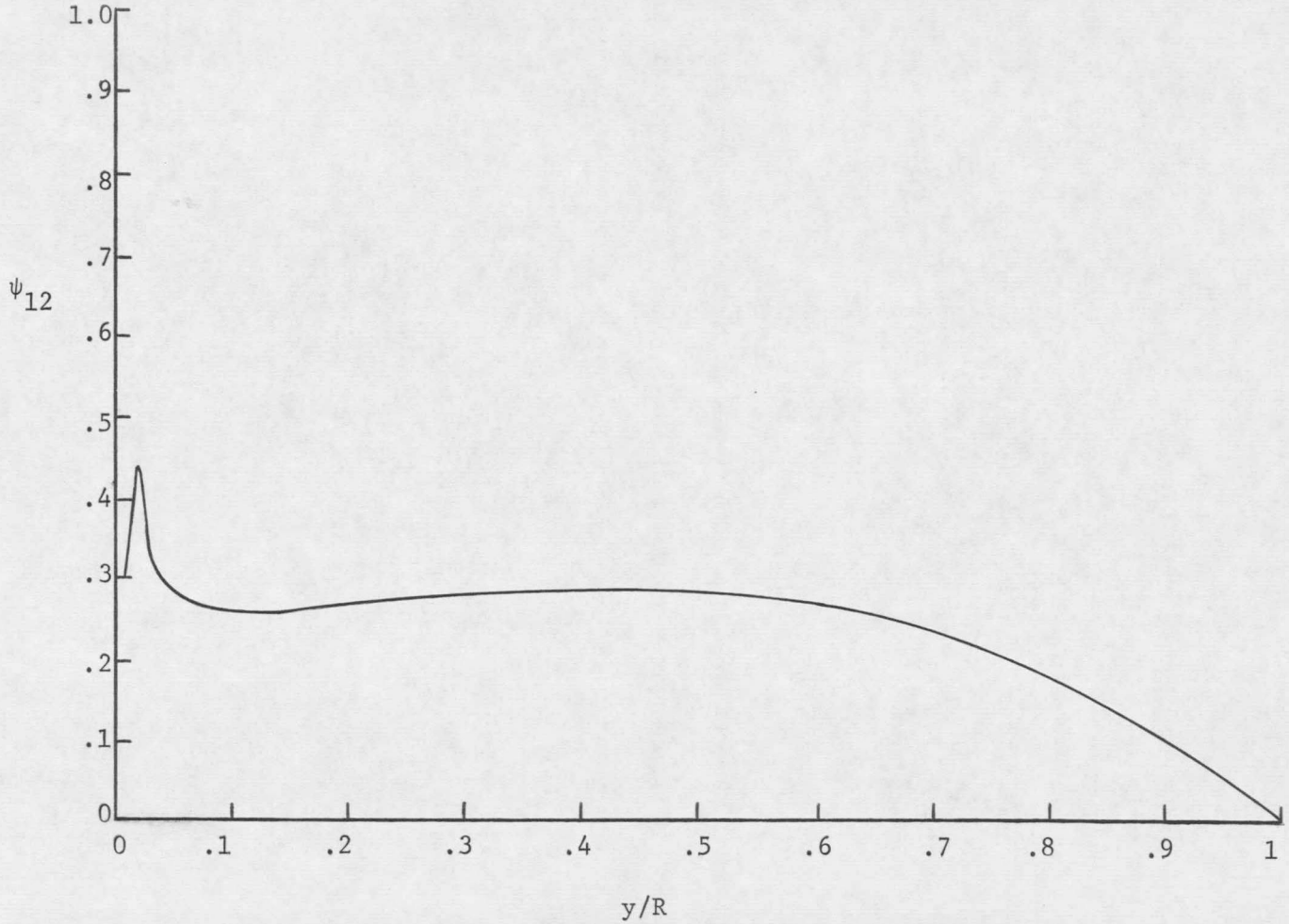

FIGURE 103. Variation of ψ_{12} Correlation Coefficient for Pipe With Small Roughness Elements

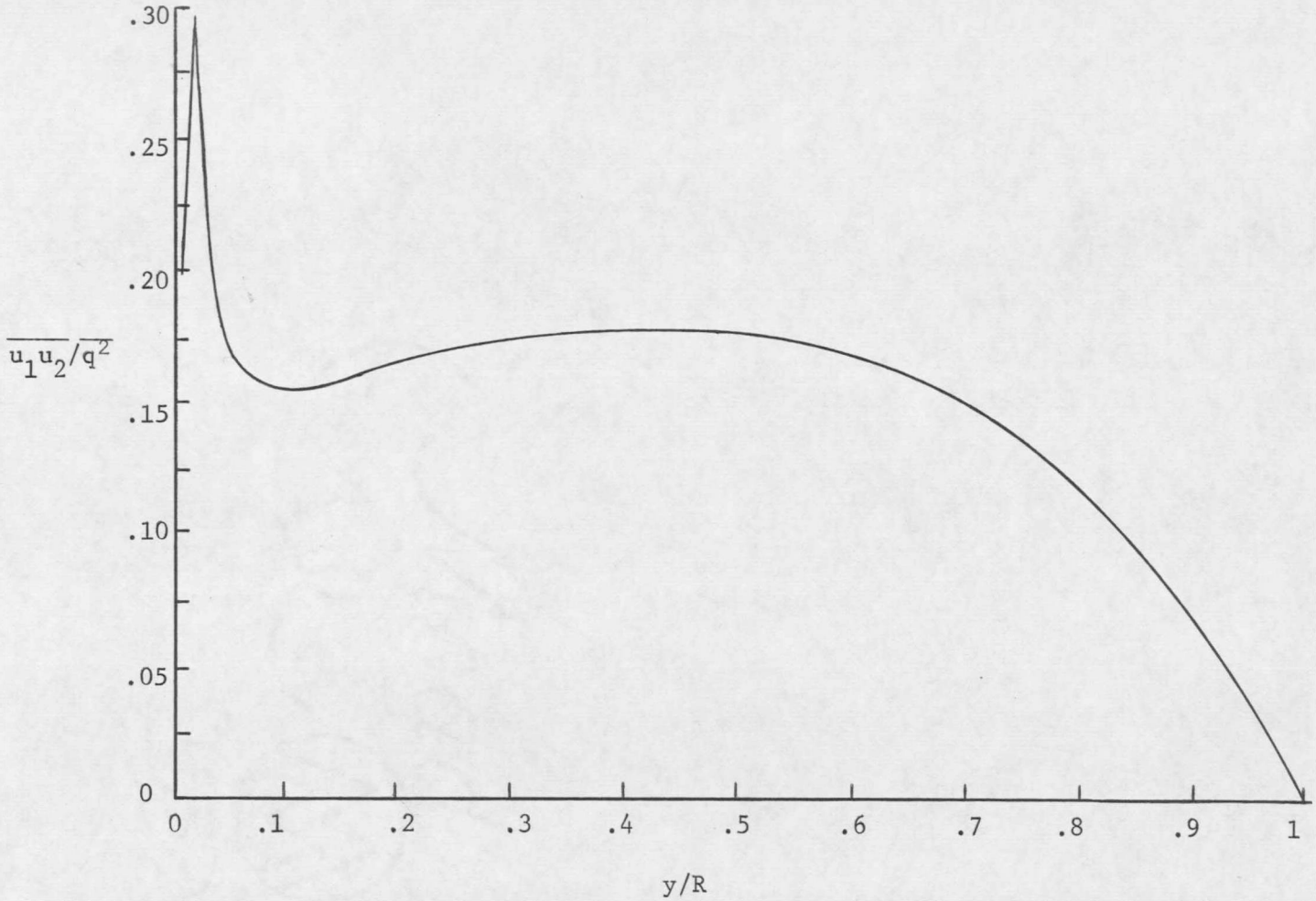

FIGURE 104. Turbulence Shear Stress to Kinetic Energy Ratio for Pipe With Small Roughness Elements

However, as in the case of ψ_{12}, it tends to zero at the pipe center line and exhibits a peak near the wall.

In contrast with flow in a smooth pipe, the $\overline{u_1 u_2}$ correlation cannot be estimated from the mean velocity measurements since the applicable momentum equation, equation (4.13) contains, in this case, the spatial $\overline{U}_1\hat{\overline{U}}_2$ correlation. However, if it is assumed that the experimental measurements of the mean velocity and the $\overline{u_1 u_2}$ correlation are actually spatially averaged quantities, then the $\overline{U}_1\hat{\overline{U}}_2$ spatial correlation can be estimated from equation (4.13). The results of this calculation are presented in Figure 105 where $\overline{U}_1\hat{\overline{U}}_2/u^{*2}$ is seen to vary in a linear fashion from zero at the pipe center line to about 0.45 near y/R = 0.1. A sharp decrease, corresponding to the peak in the $\overline{u_1 u_2}$ correlation, is then observed. The spatial correlation vanishes at y/R = 0.02 and then again begins to increase. The foregoing variation in this spatial correlation thus enables satisfaction of the momentum equation, whereas the momentum equation could not have been satisfied if the radial mean velocity term had not been included as shown by Gow [15].

For flow in a rough pipe, the eddy diffusivity for momentum, which is of immense interest in practical applications, can no longer be determined from equation (2.68) since the turbulent shear stress given by equation (2.66) is not necessarily valid. However, equation (2.66) is not used in the development of equation (2.71),

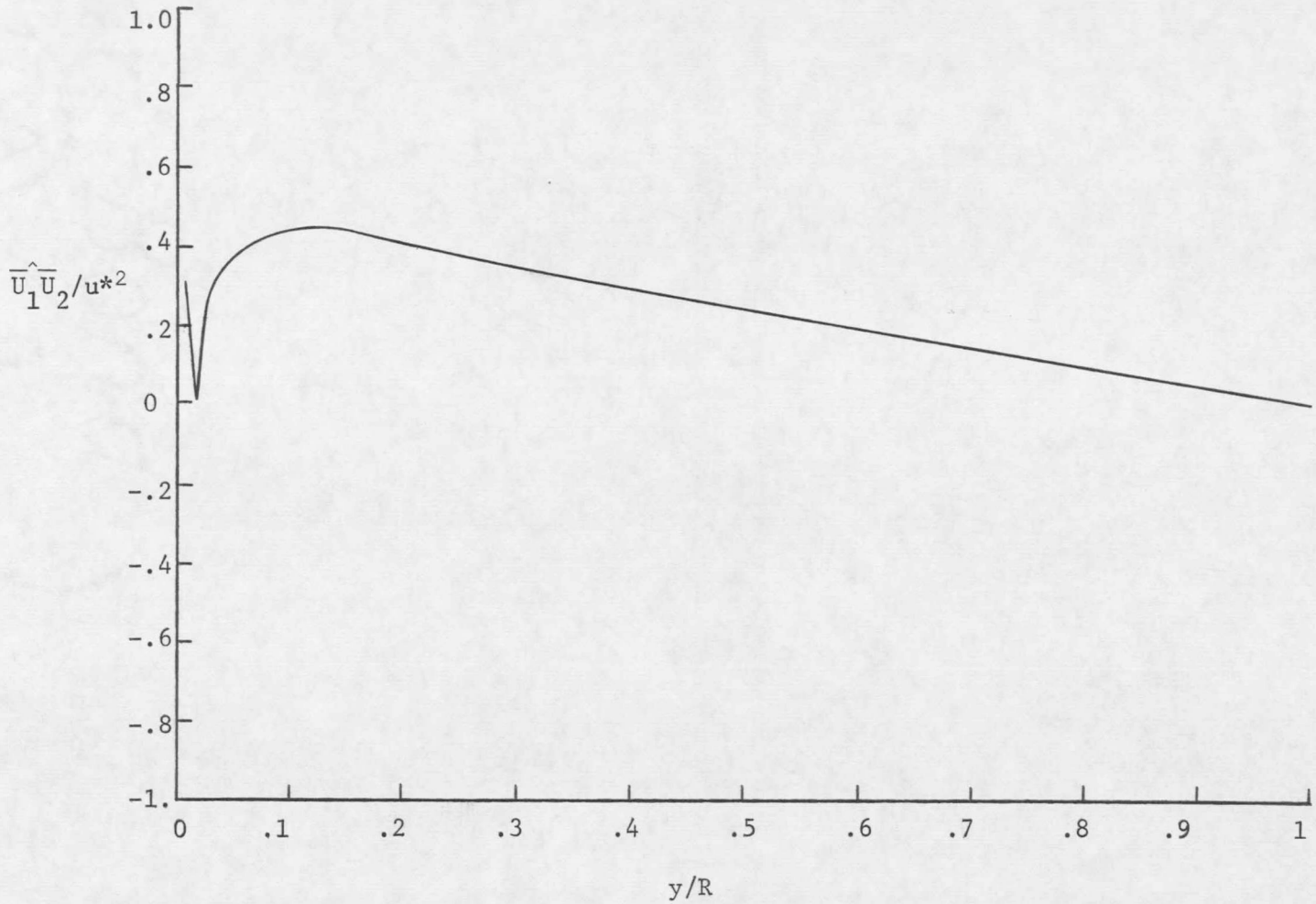

FIGURE 105. Spatial $\overline{U}_1\hat{\overline{U}}_2$ Correlation For Pipe With Small Roughness Elements

so this expression can still be utilized for calculation of the eddy diffusivity. The results of such calculations for the pipe containing the small roughness elements are given in Figures 106 and 107. These figures indicate a constant value of the eddy diffusivity ($\varepsilon_n/Ru^* = 0.08$) for y/R greater than about 0.3. For smaller values of y/R, ε_n tends toward zero, and a very sharp drop immediately adjacent to the wall is indicated by Figure 107.

The second cross correlation term determined experimentally in the current investigation was the cross correlation between longitudinal and angular fluctuating velocities, $\overline{u_1 u_3}$. It should be recalled from the review of the literature that momentum arguments require that this term must vanish for flow in a smooth pipe, and Figures 108 and 109 confirm that this is also the case for flow in the pipe containing the small roughness elements, with one exception. For values of y/R between about 0.04 and 0.1, the $\overline{u_1 u_3}$ correlation is found to have a negative value, reaching an extreme of about -0.1. This indicates the existence of a transfer of longitudinal momentum across planes normal to the x_3 axis in this near wall layer where a peak in the $\overline{u_1 u_2}$ correlation was observed.

The variation of the third order $\overline{u_1^2 u_2}$ correlation with radial position is indicated in Figure 110 for the central region of the pipe and in Figure 111 for the wall region. This correlation is

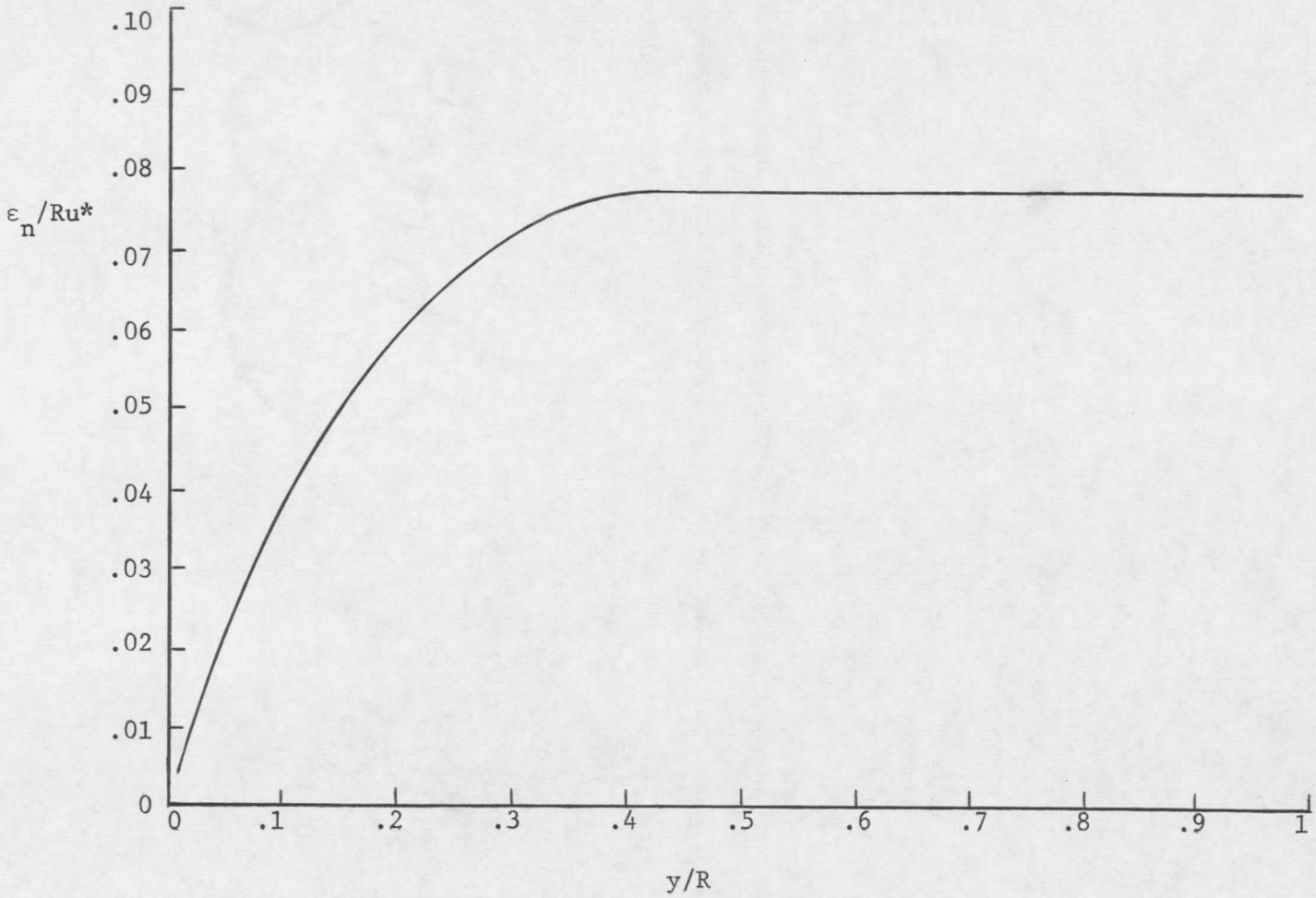

FIGURE 106. Eddy Diffusivity For Momentum in Central Region of Pipe With Small Roughness Elements

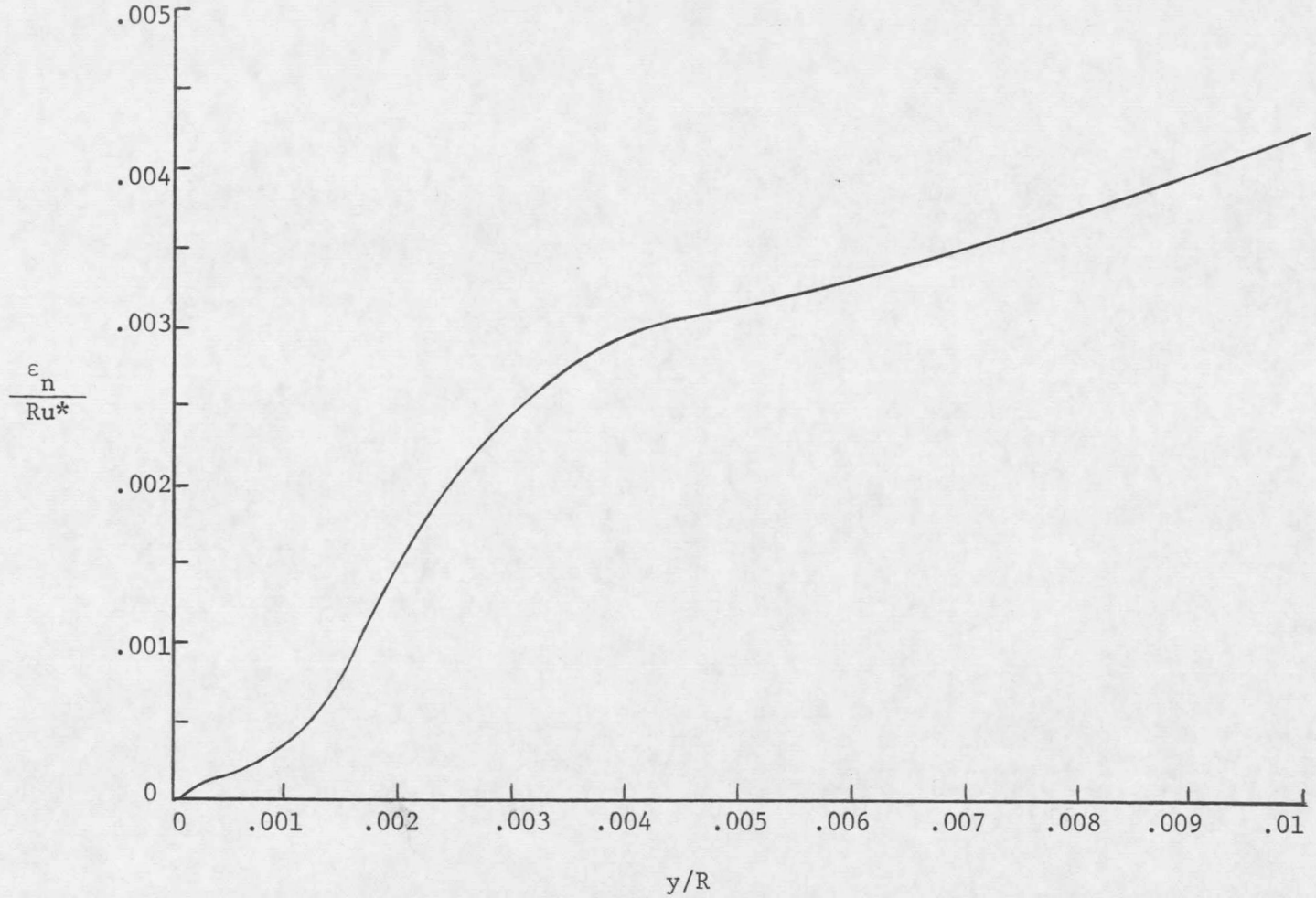

FIGURE 107. Eddy Diffusivity for Momentum in Wall Region of Pipe With Small Roughness Elements

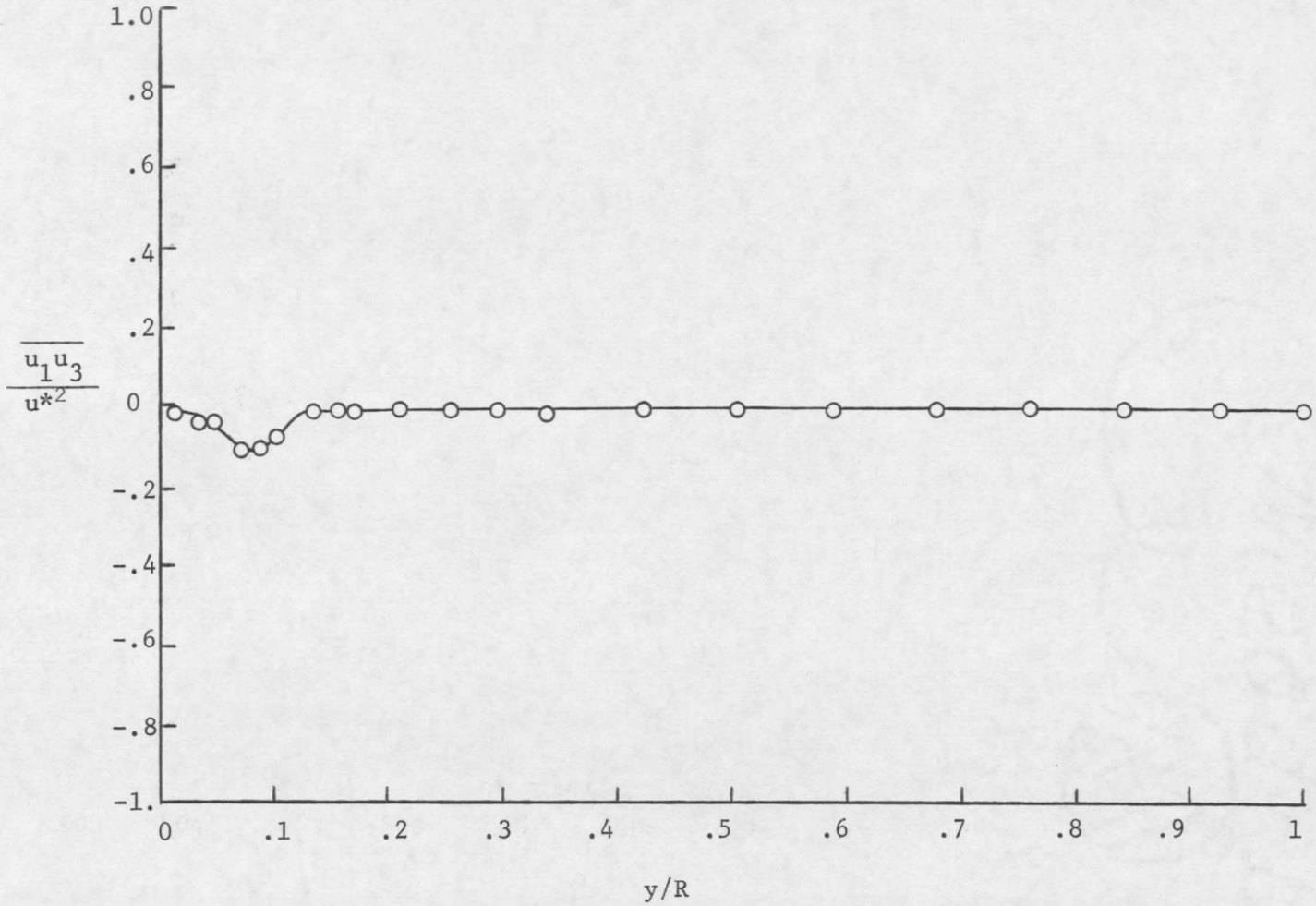

FIGURE 108. Second Order $\overline{u_1 u_3}$ Cross Correlation For Turbulent Core of Pipe With Small Roughness Elements

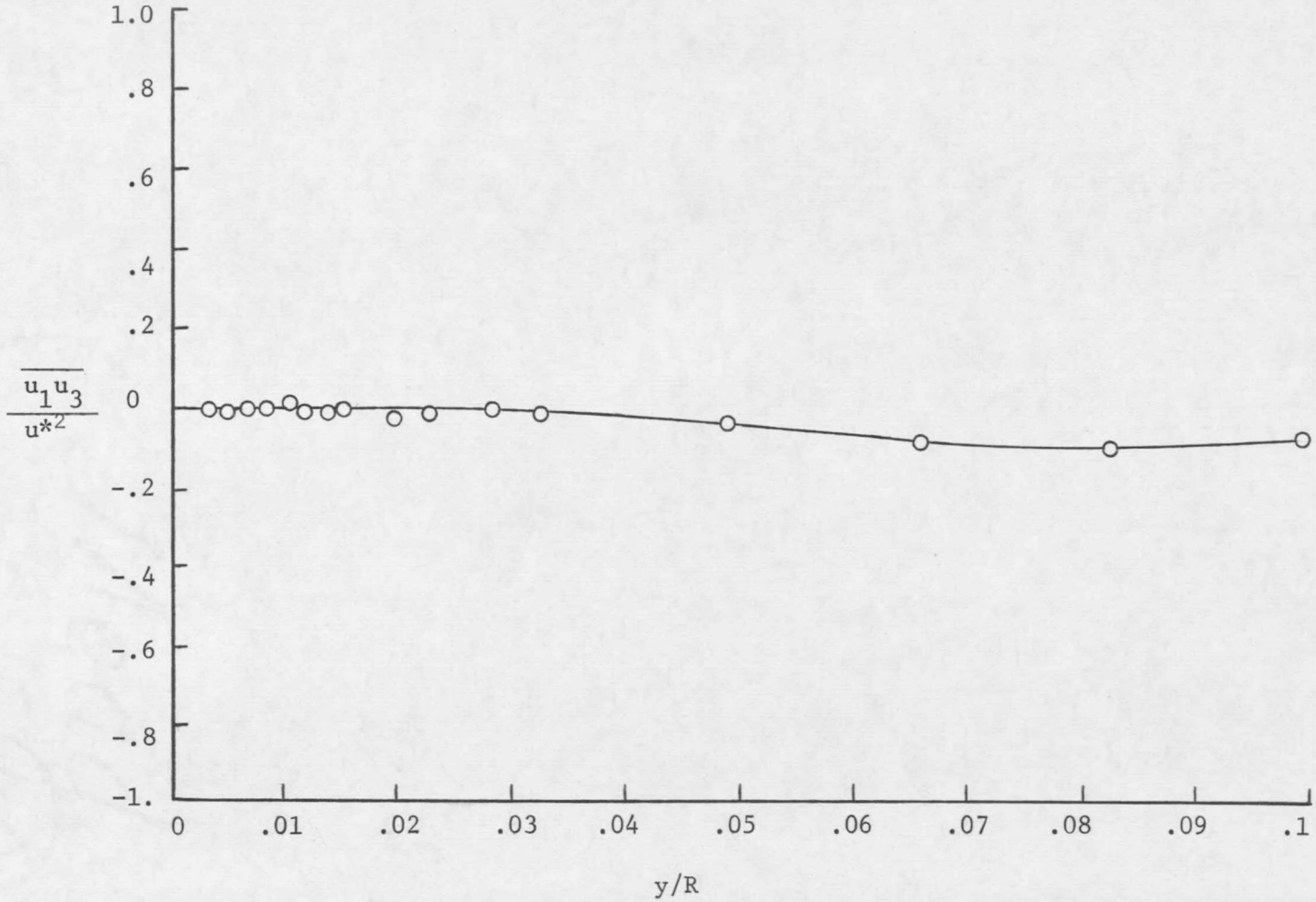

FIGURE 109. Second Order $\overline{u_1 u_3}$ Cross Correlation Near Wall of Pipe With Small Roughness Elements

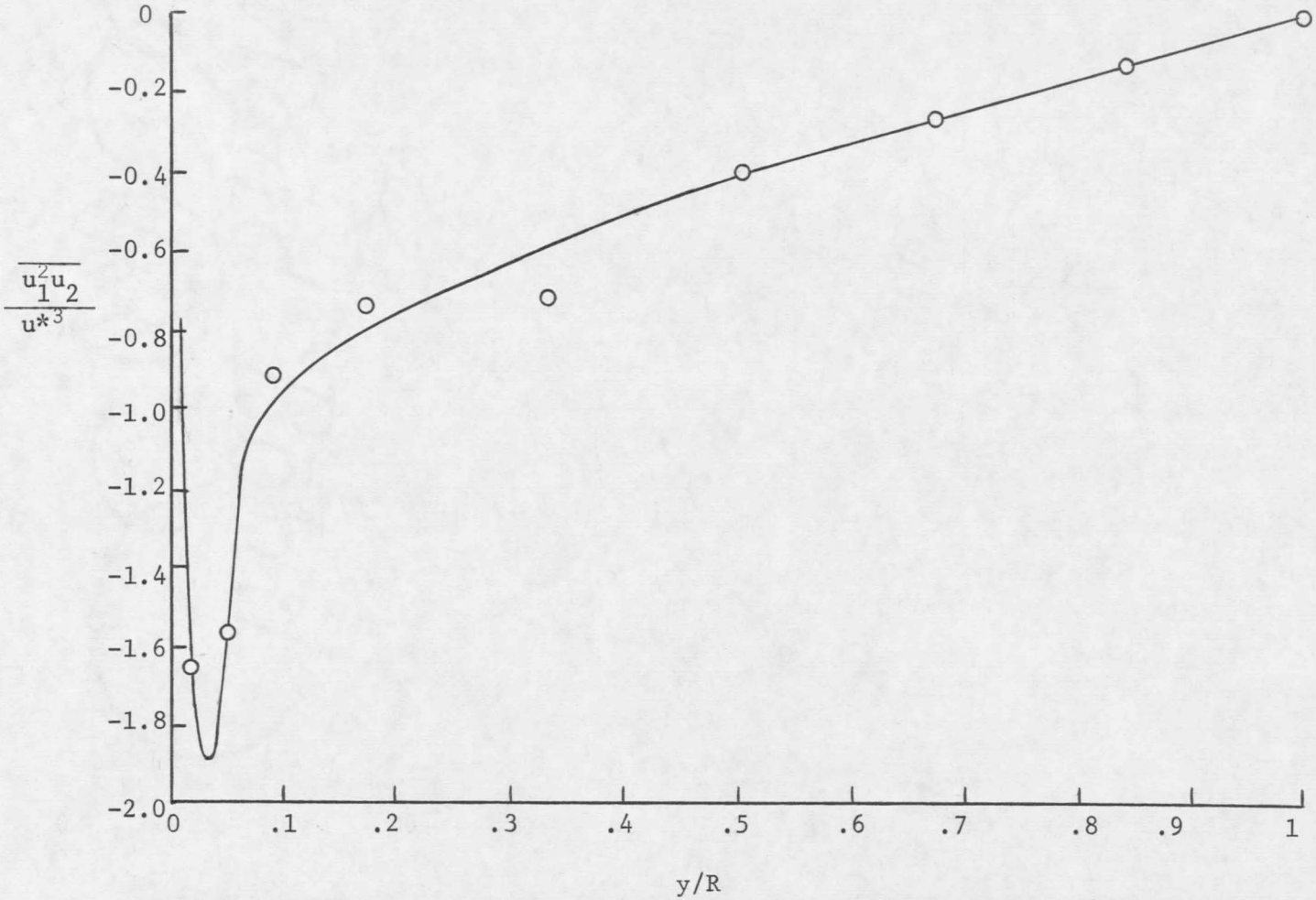

FIGURE 110. Third Order $\overline{u_1^2 u_2}$ Correlation for Central Region of Pipe With Small Roughness Elements

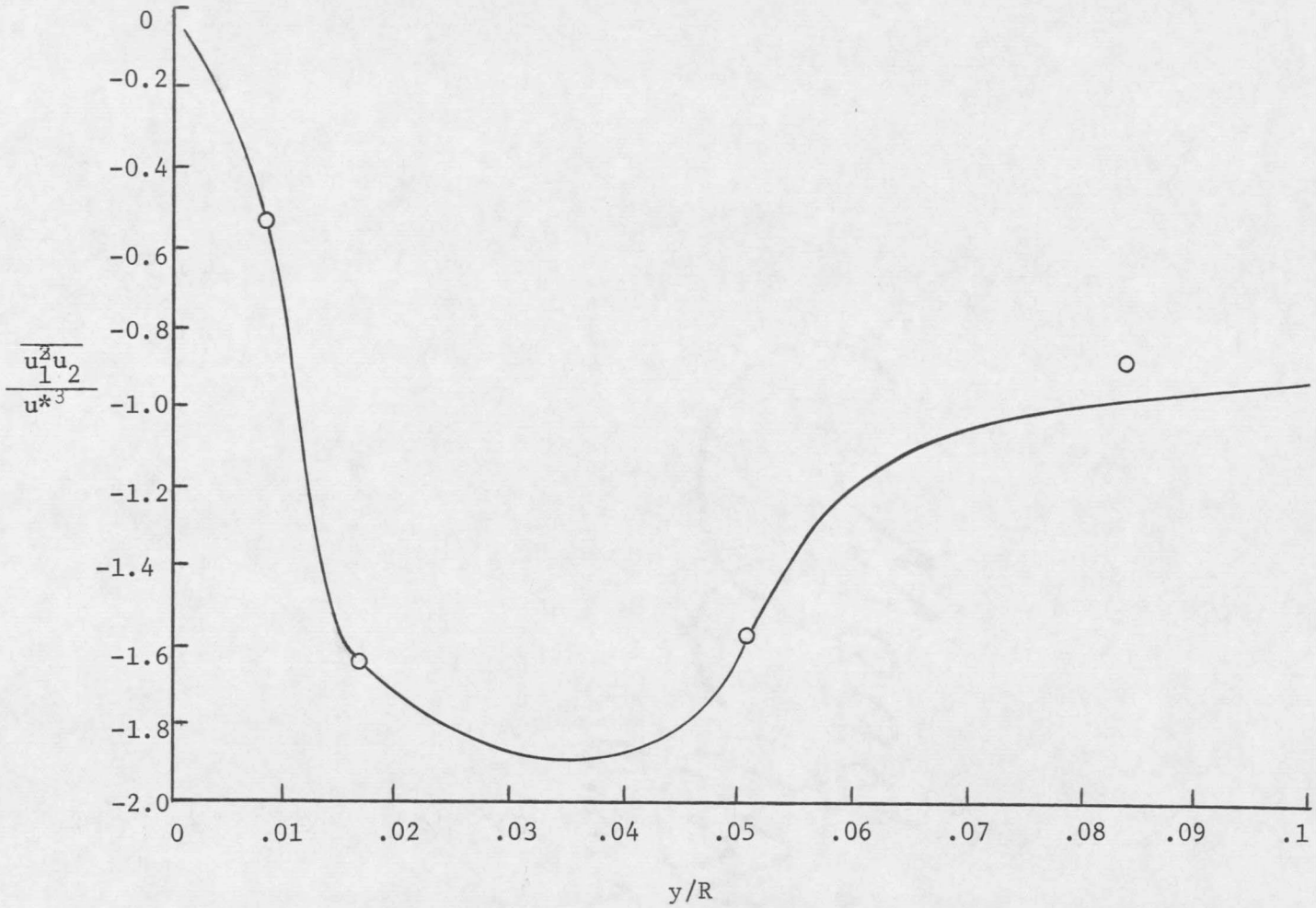

FIGURE 111. Third Order $\overline{u_1^2 u_2}$ Correlation For Wall Region of Pipe With Small Roughness Elements

seen to vary nearly linearly from a null value at the pipe center line to about -0.9 at y/R = 0.1. It then sharply decreases to about -1.9 before vanishing at the solid surface. As with previous correlations, the extreme value occurs not too far above the mean height of the roughness elements. The correlation coefficient corresponding to $\overline{u_1^2 u_2}$ is seen to remain essentially constant over most of the pipe in Figure 112, although it does vanish at the center line and a pronounced extreme value is observed near the wall.

The $\overline{u_2^3}$ correlation, normalized with u^{*3}, is seen in Figures 113 and 114. This dimensionless form of the correlation varies from about 0.5 at the pipe center line to around 1.5 at y/R = 0.04. At this point an increase to a value of about 2.0 is observed until, at the mean height of the roughness elements, the correlation decreases to zero. In contrast with the $\overline{u_1^2 u_2}$ third order correlation, $\overline{u_2^3}$ is seen to be positive over the entire cross section. Figure 115 shows that the correlation coefficient corresponding to $\overline{u_2^3}$ remains nearly constant at a value of 3.0 over the entire cross section, except for a slight dip near the wall.

Dissipation Function

Components of the turbulence dissipation function determined experimentally for the turbulent core are presented in Figures 116

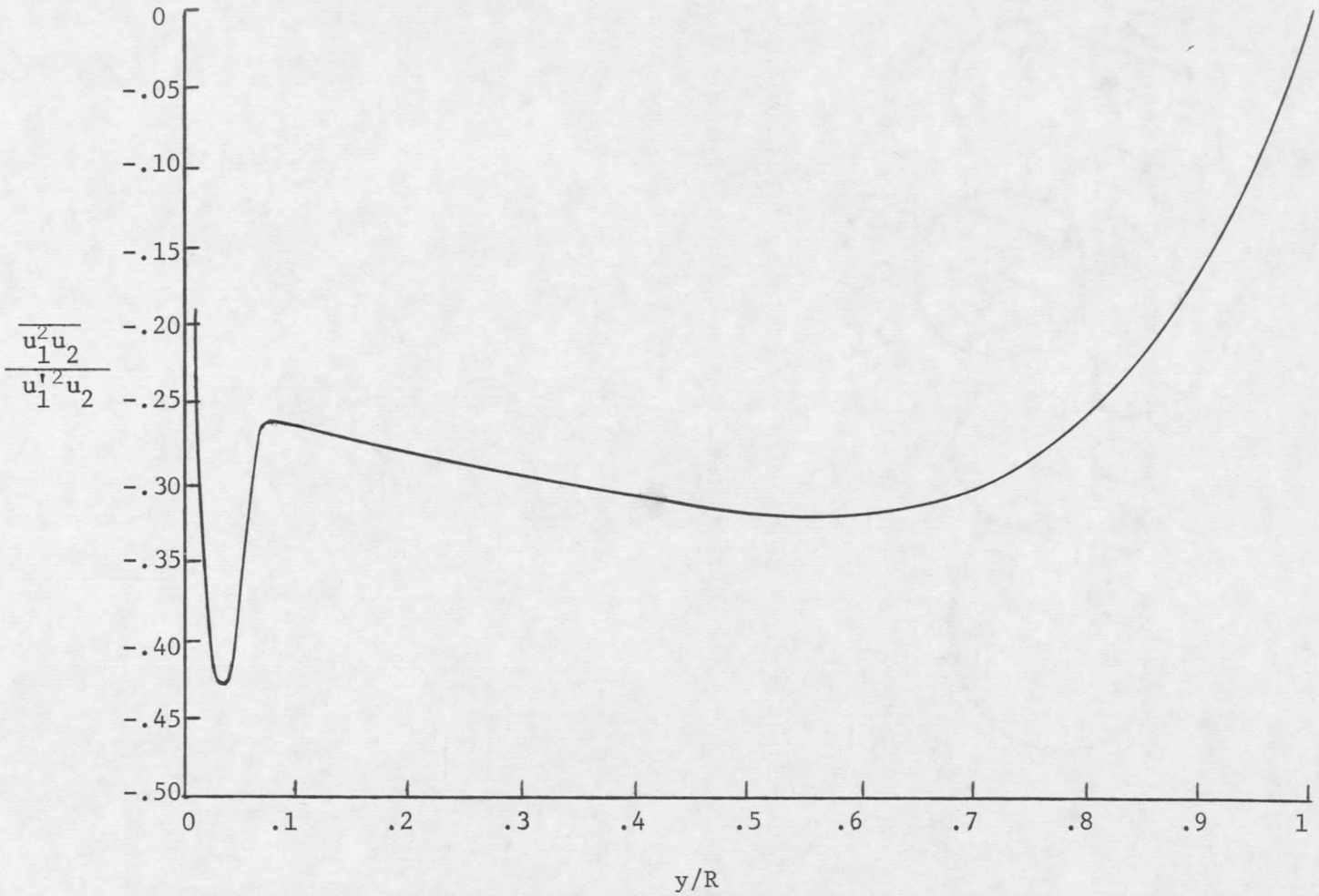

FIGURE 112. Correlation Coefficient For $\overline{u_1^2 u_2}$ in Pipe With Small Roughness Elements

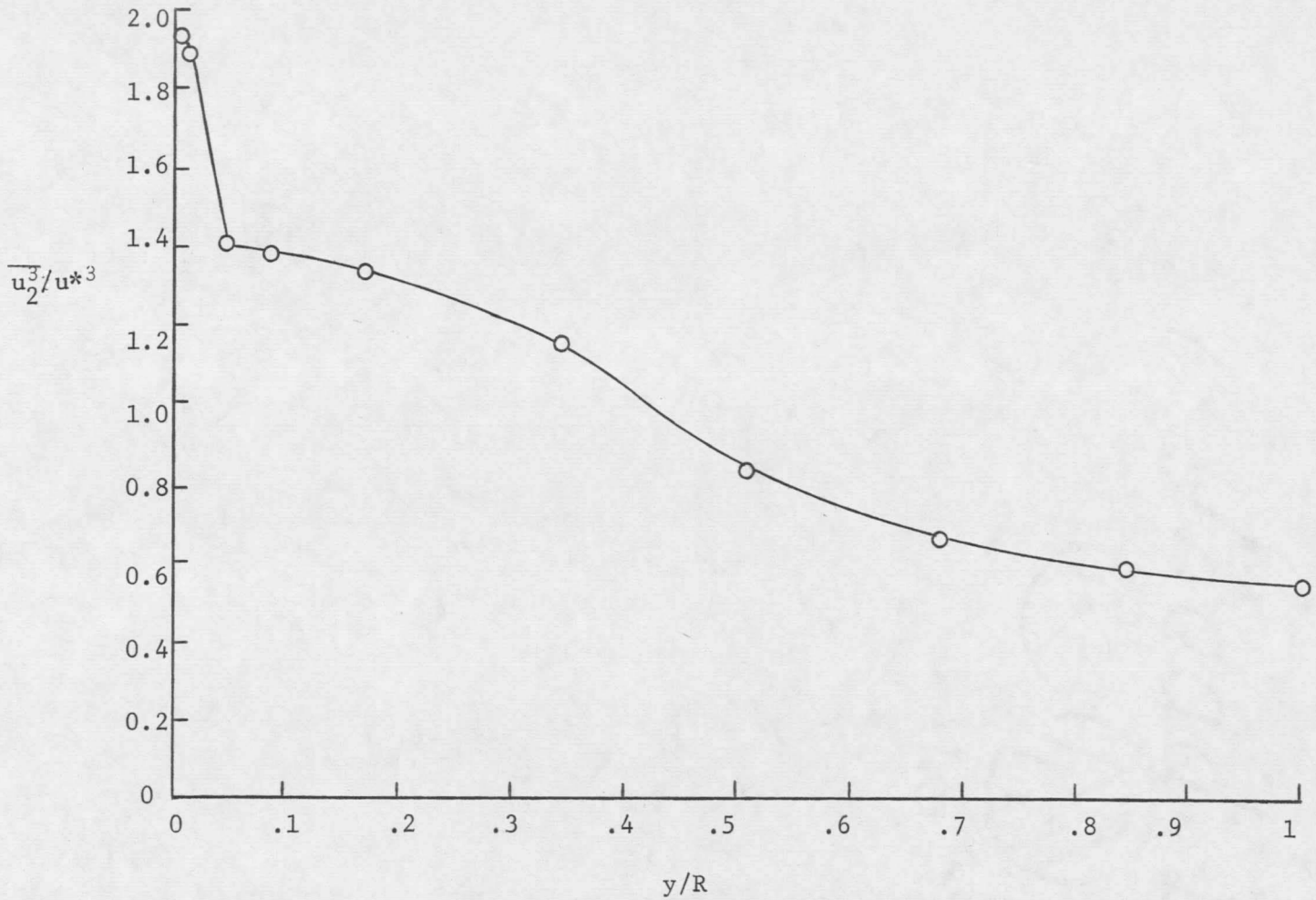

FIGURE 113. Third Order $\overline{u_2^3}$ Correlation For Central Portion of Pipe With Small Roughness Elements

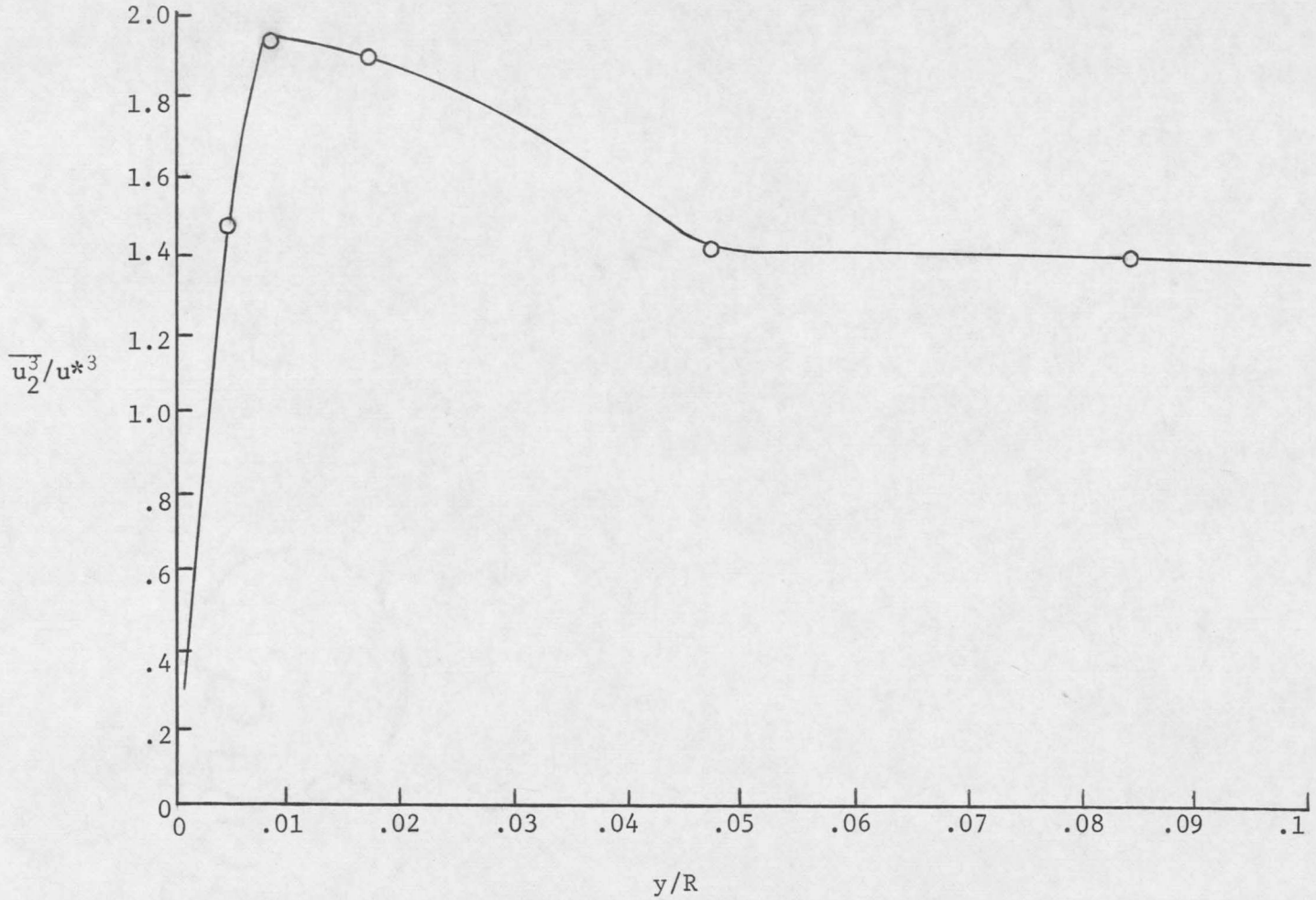

FIGURE 114. Third Order $\overline{u_2^3}$ Correlation Near Wall of Pipe With Small Roughness Elements

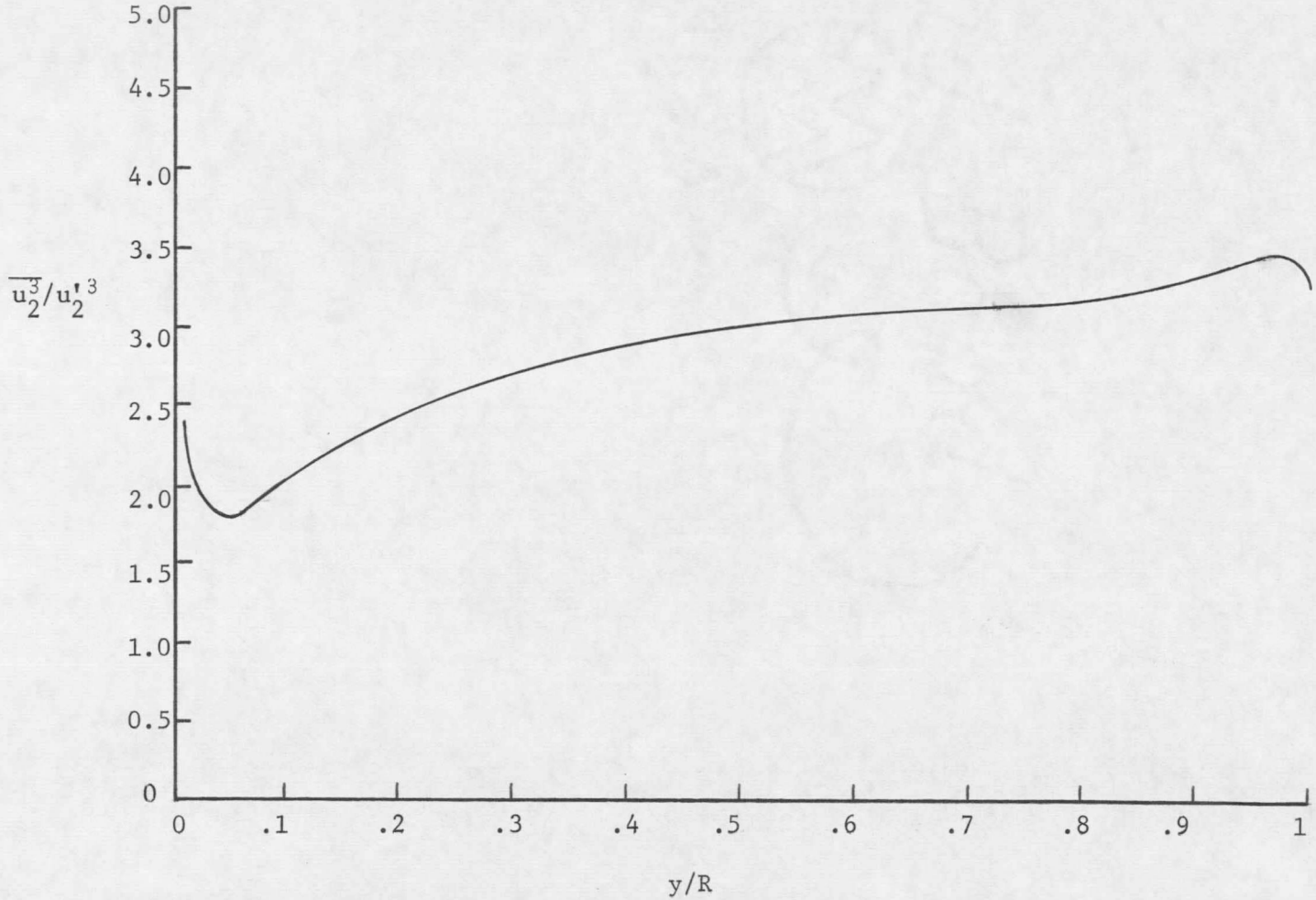

FIGURE 115. Correlation Coefficient for $\overline{u_2^3}$ in Tube With Small Roughness Elements

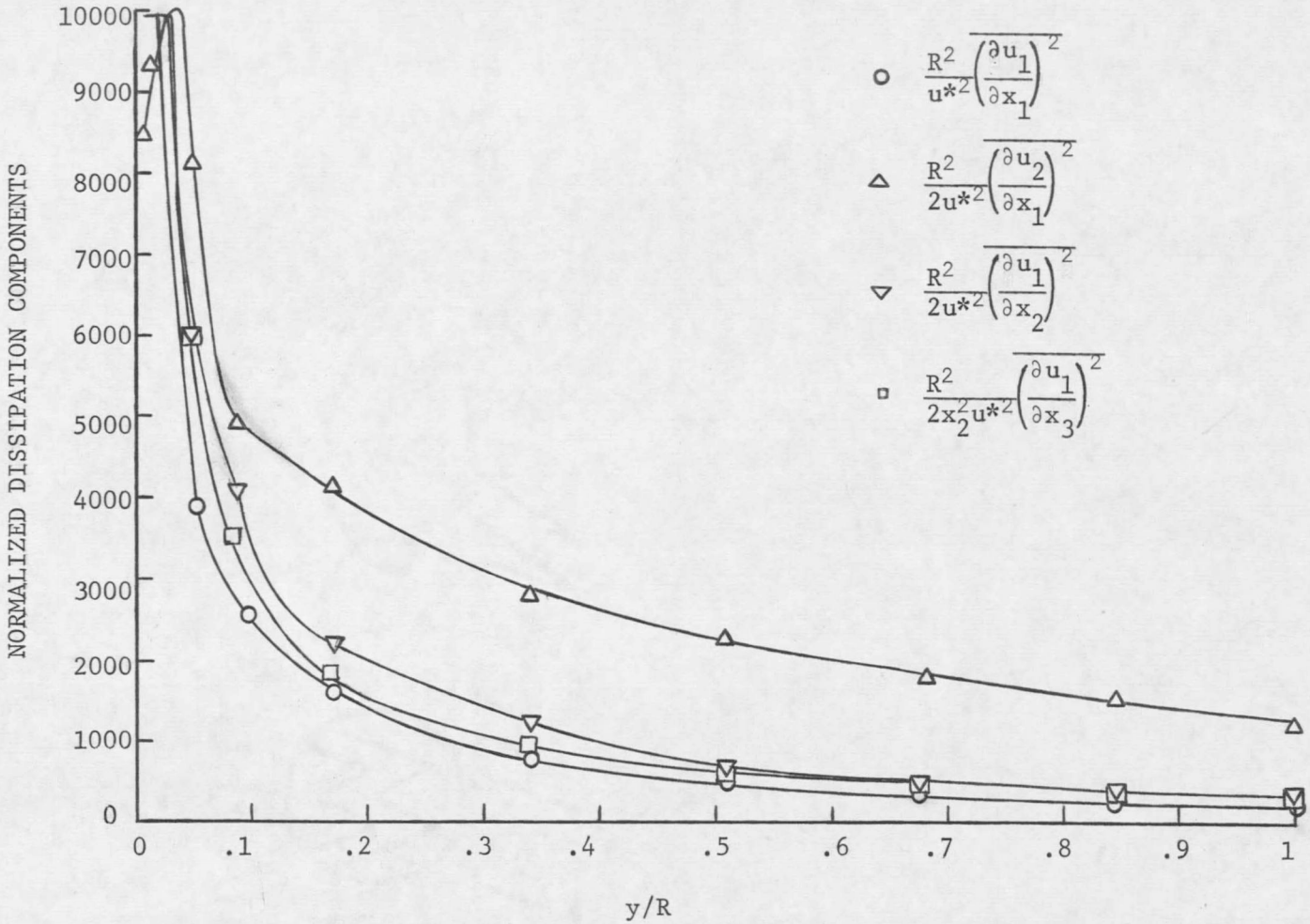

FIGURE 116. Dissipation Terms for Central Region of Tube With Small Roughness Elements

and 117, and values in the wall region of the pipe are presented in Figures 118 and 119. The behavior of all these components is somewhat similar, i.e., they all are relatively small at the pipe center line and have a small rate of magnitude change at this point. As the wall is approached, a sharp increase to a maximum value is noted, after which zero is approached rather rapidly. Some differences should be noted, however. All magnitudes are nearly equal at the pipe center line, $\frac{R^2}{2u^{*2}}\overline{\left(\frac{\partial u_2}{\partial x_1}\right)^2}$ being slightly larger and $\frac{R^2}{2u^{*2}}\overline{\left(\frac{\partial u_3}{\partial x_1}\right)^2}$ being slightly smaller, and all of the components reach a maximum value near $y/R = 0.01$, just above the mean height of the roughness elements, but the magnitudes of these maxima differ considerably as indicated by the difference in scale between Figures 118 and 119. The term $\frac{R^2}{2x_2^2u^{*2}}\overline{\left(\frac{\partial u_1}{\partial x_3}\right)^2}$ has the largest magnitude of about 25,000 while $\frac{R^2}{u^{*2}}\overline{\left(\frac{\partial u_1}{\partial x_1}\right)^2}$ and $\frac{R^2}{2u^{*2}}\overline{\left(\frac{\partial u_1}{\partial x_2}\right)^2}$ are only slightly lower at around 20,000. A significant decrease to about 10,000 occurs for $\frac{R^2}{2u^{*2}}\overline{\left(\frac{\partial u_2}{\partial x_1}\right)^2}$,

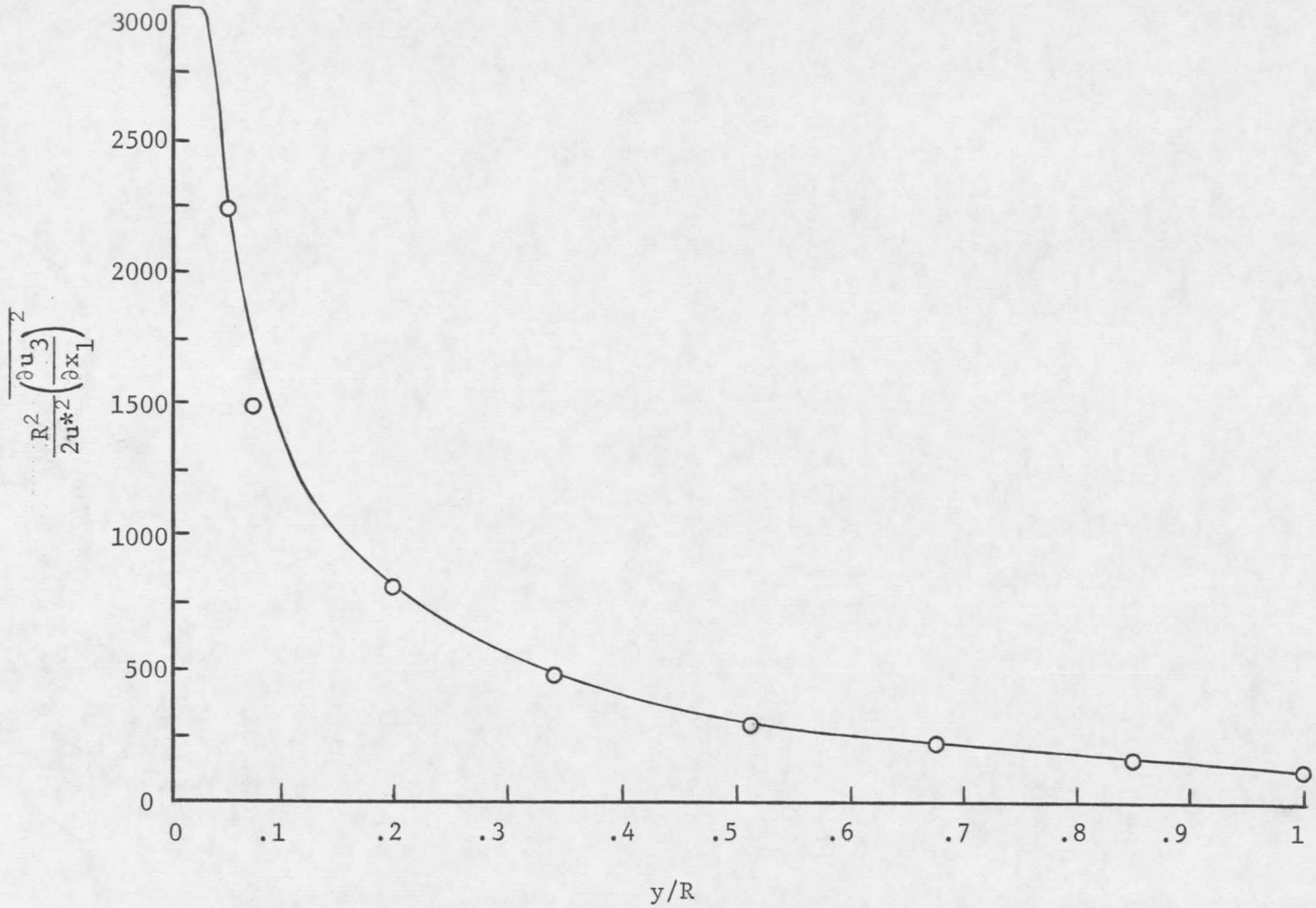

FIGURE 117. Dissipation Terms for Central Region of Tube With Small Roughness Elements

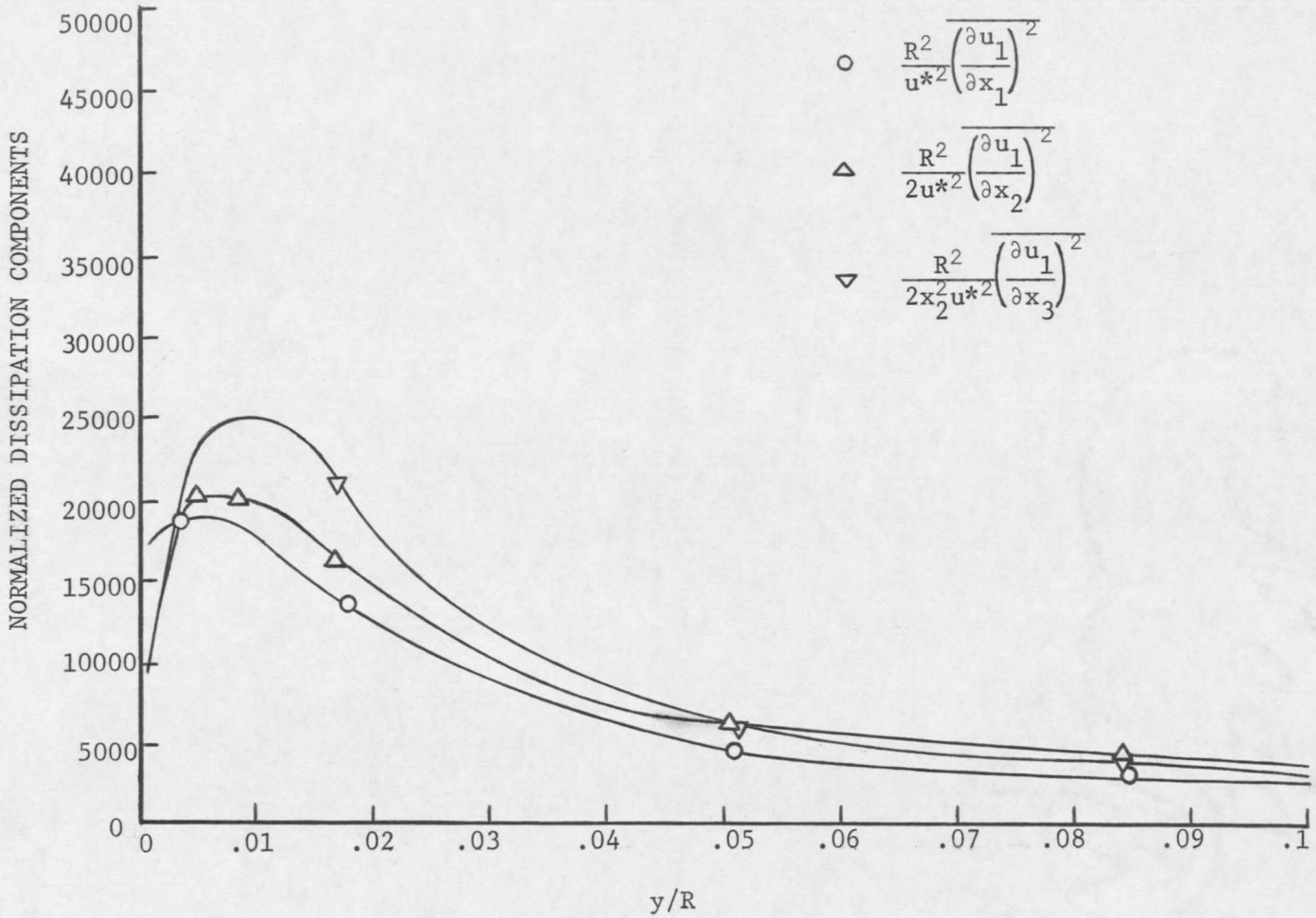

FIGURE 118. Dissipation Terms for Wall Region of Tube With Small Roughness Elements

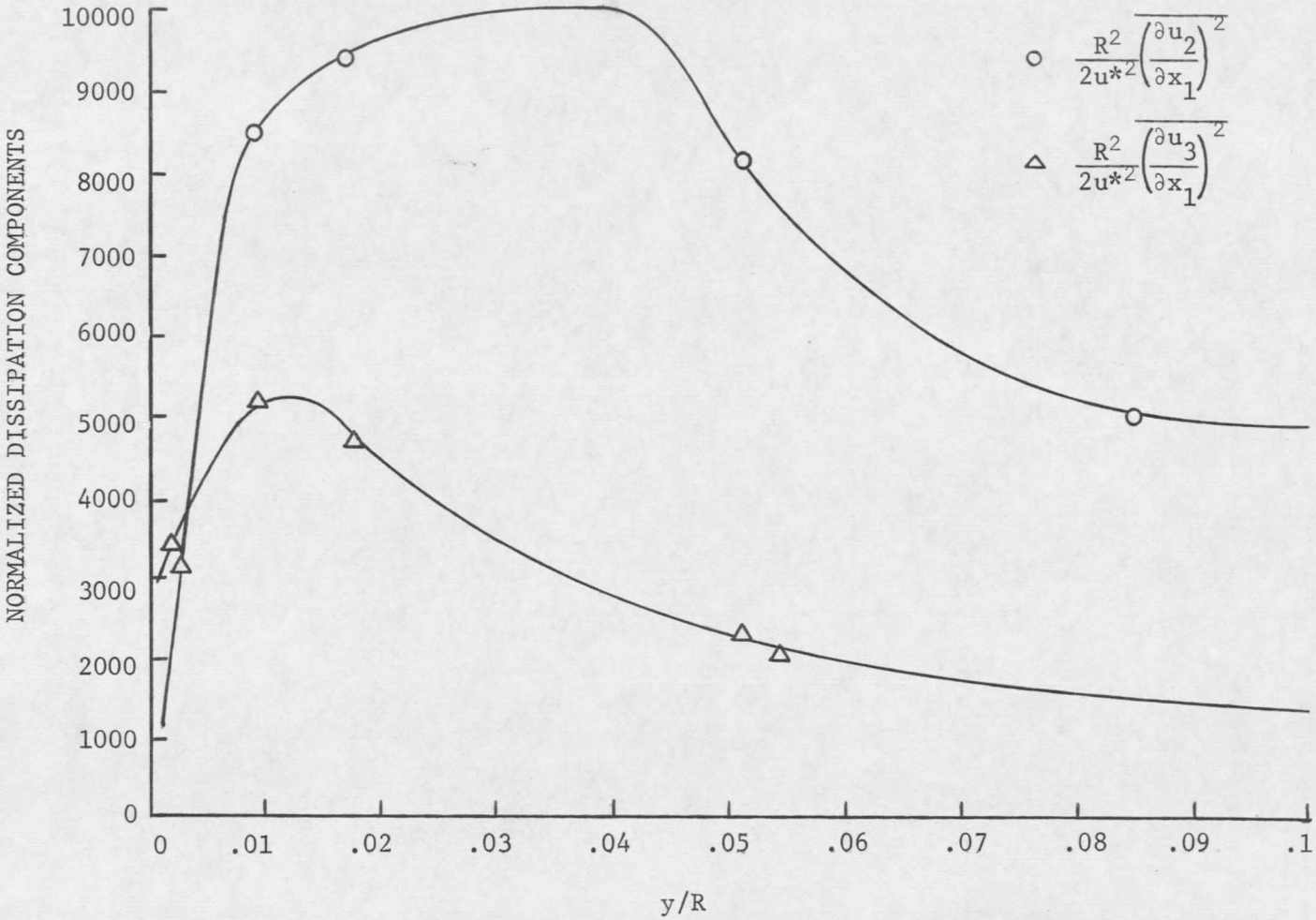

FIGURE 119. Dissipation Terms For Wall Region of Tube With Small Roughness Elements

and $\frac{R^2}{2u^{*2}} \overline{\left(\frac{\partial u_3}{\partial x_1}\right)^2}$ decreases to an even larger extent to approximately 5,500. There appears to be no data available in the literature for comparison with these results.

The foregoing experimental data can now be combined with the isotropic relations given by equation (5.20) for determination of the dissipation function itself, and a dimensionless form of this function is given in Figures 120 and 121 as the solid lines. In similarity with the terms comprising W, the dimensionless dissipation function is very small at the pipe center line and reveals a slow rate of increase at this point. This rate of increase grows in a rather gradual fashion until a maximum value of the dimensionless dissipation function near 0.015 is attained at $y/R \simeq 0.008$. The dissipation function then diminishes rapidly to zero. Thus, as in the case of other turbulence quantities, the dissipation reaches a maximum value just beyond the mean height of the roughness elements.

The dashed line in Figures 120 and 121 is representative of the dissipation function calculated from equation (5.21) where complete isotropy between all terms is assumed. The dissipation calculated in this manner is seen to be slightly less than that obtained experimentally in this investigation, except near the maximum value.

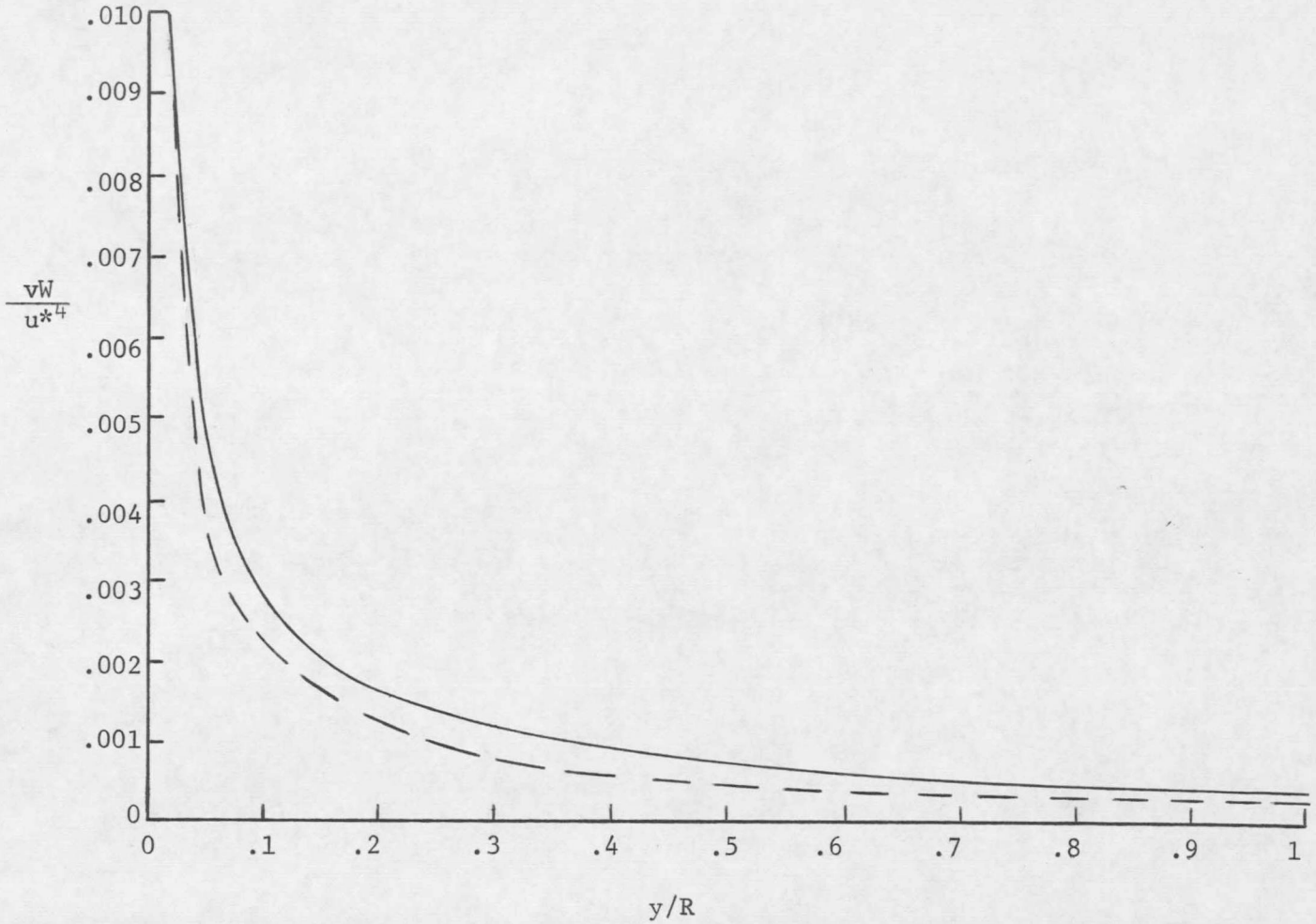

FIGURE 120. Dissipation Function in Central Region of Tube With Small Roughness Elements

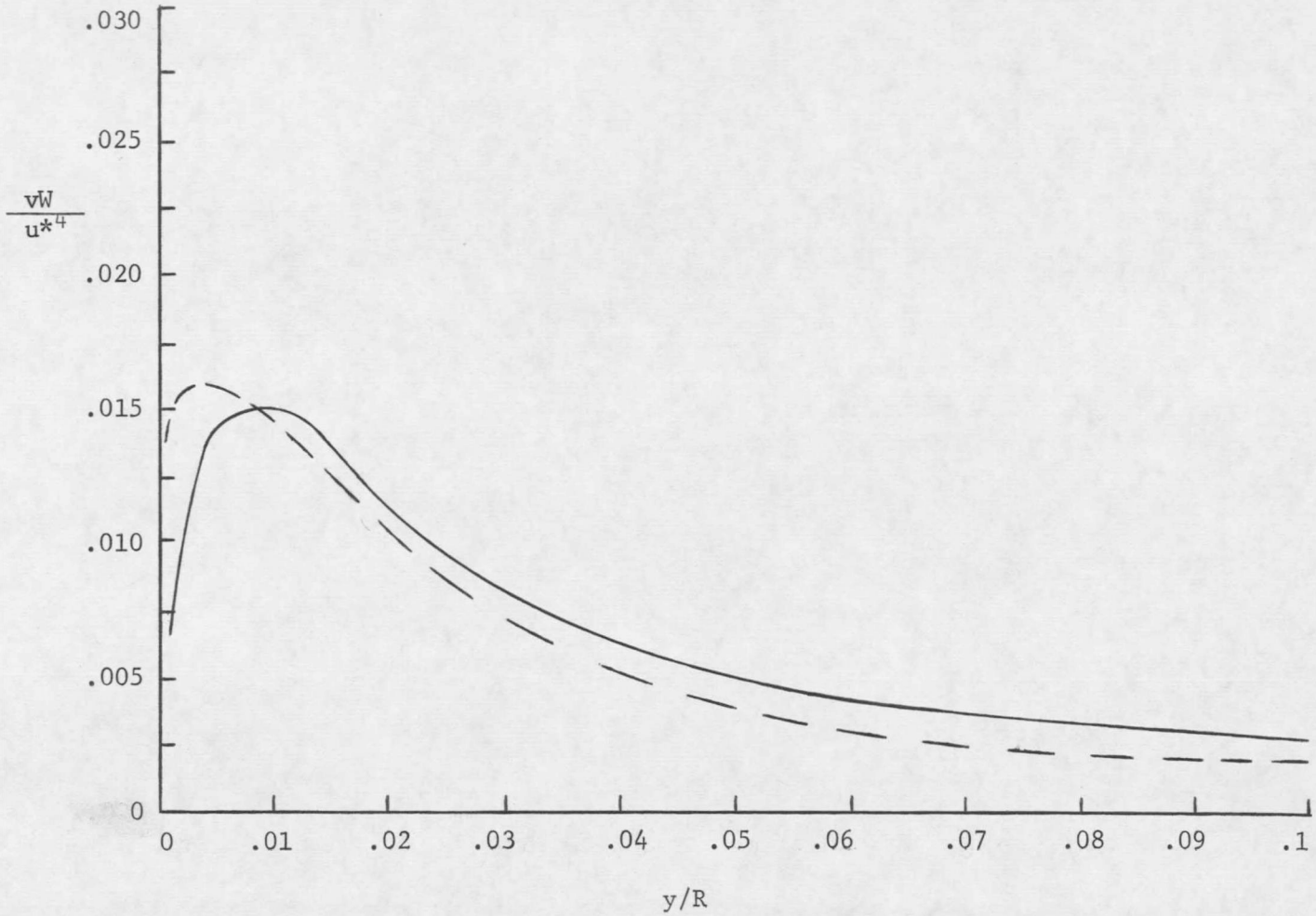

FIGURE 121. Dissipation Function Near Wall of Tube With Small Roughness Elements

The isotropic dissipation becomes slightly larger in this region due to the fact that the maximum occurs at a lower value of y/R. Nevertheless, it would appear that the assumption of complete isotropy in dissipation calculations yields reasonable results for this rough pipe. This fact, combined with the previously determined anisotropy ratios, indicates a tendency toward isotropic flow for the pipe currently under consideration.

A check on the validity of applying Taylor's hypothesis for the shear flow currently under investigation may be obtained by inspection of Figure 122 for the central region of the pipe and Figure 123 for the wall region. In these figures, Lin's [79] condition, equation (2.78b), is investigated. This condition is seen to be satisfied to a high degree of accuracy throughout the flow field, except possibly for points well below the tops of the roughness elements. Therefore, in view of the turbulence intensity results as well as the current result, Taylor's hypothesis is expected to be valid throughout the flow field, except possibly for points much nearer the wall than the mean roughness height.

Energy Relations

Consider first the mean energy balance given by equation (4.30). For a rough pipe, this equation indicates that the energy available

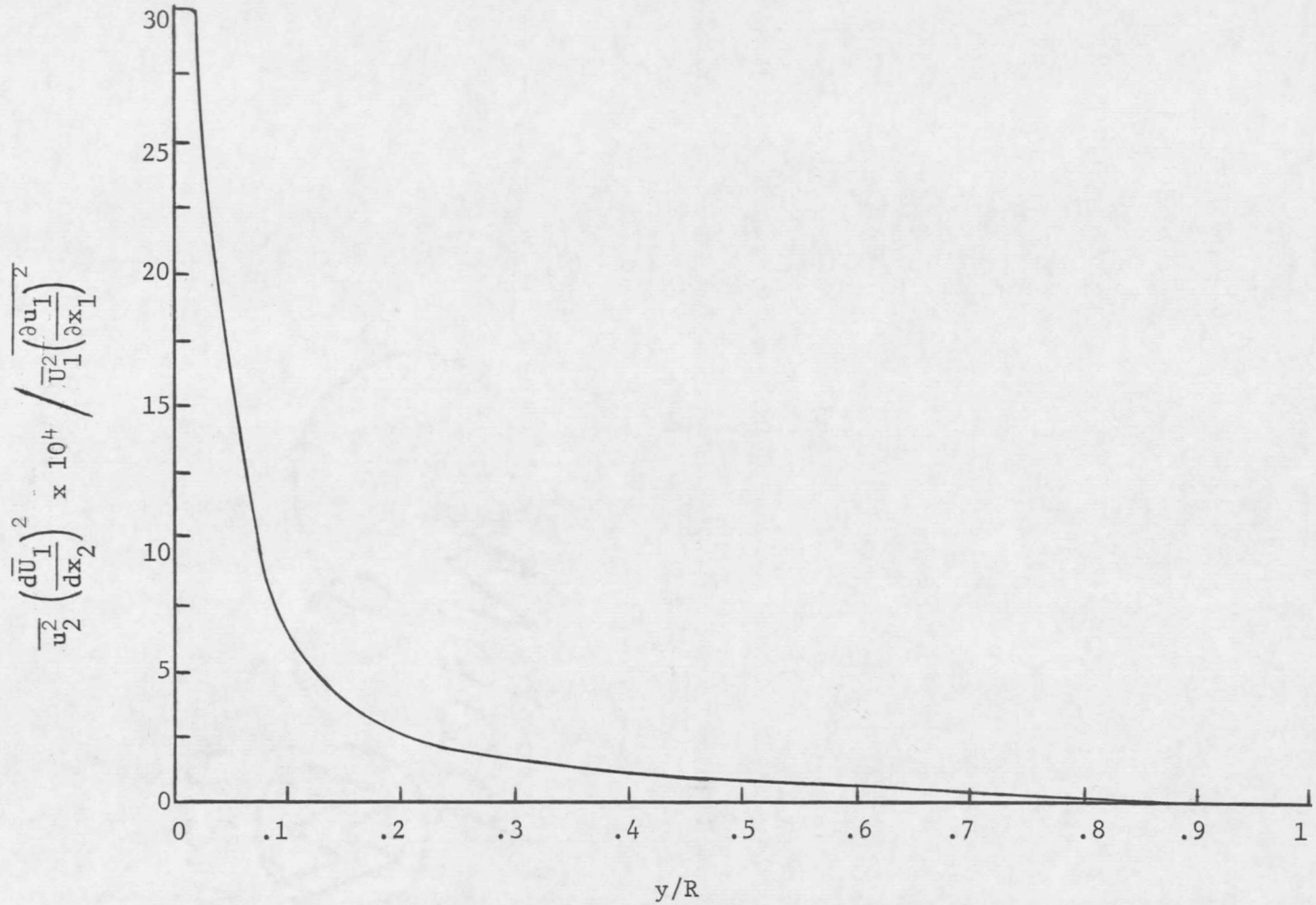

FIGURE 122. Lin's Condition For Applicability of Taylor's Hypothesis in Turbulent Core of Tube With Small Roughness Elements

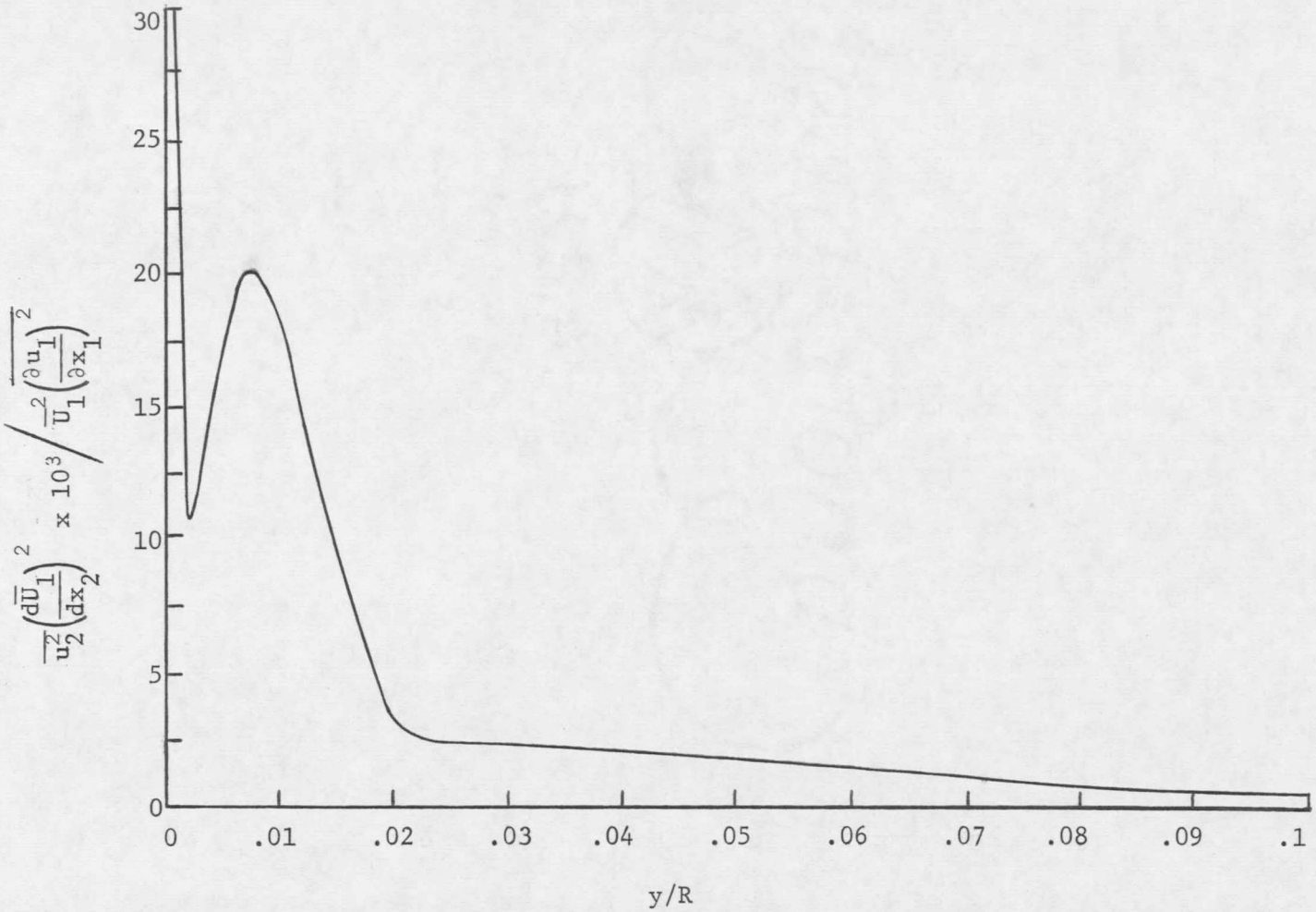

FIGURE 123. Lin's Condition for Applicability of Taylor's Hypothesis Near Wall of Tube With Small Roughness Elements

due to the pressure drop along the pipe is partly converted into turbulence energy by action of the $\overline{u_1 u_2}$ shearing stress, partly converted into an energy associated with the presence of the roughness elements, and partly dissipated directly by viscous action. The mean energy balance determined experimentally for the turbulent core of the pipe is indicated by Figures 124 and 125. Figure 124 shows that only a relatively small amount of energy is available throughout the central portion of the pipe. This quantity vanishes at the center line and decreases to a value of -0.01 at $y/R \approx 0.05$. The curves representing the conversion of mean energy to turbulence energy and to an energy associated with the presence of the roughness elements, termed a roughness energy, are also shown in Figure 124. These curves are seen to be essentially equal to each other and to about one half the available energy for y/R greater than about 0.05. For smaller values of y/R, the turbulence energy production surpasses the roughness energy production. The foregoing results dictate that the direct viscous dissipation of mean energy should be negligibly small in the central portion of the pipe, and this statement is confirmed by Figure 125. Although the dissipation is extremely small throughout this region, a very large gradient is observed to occur for y/R less than about 0.1.

The mean energy balance for that portion of the flow field

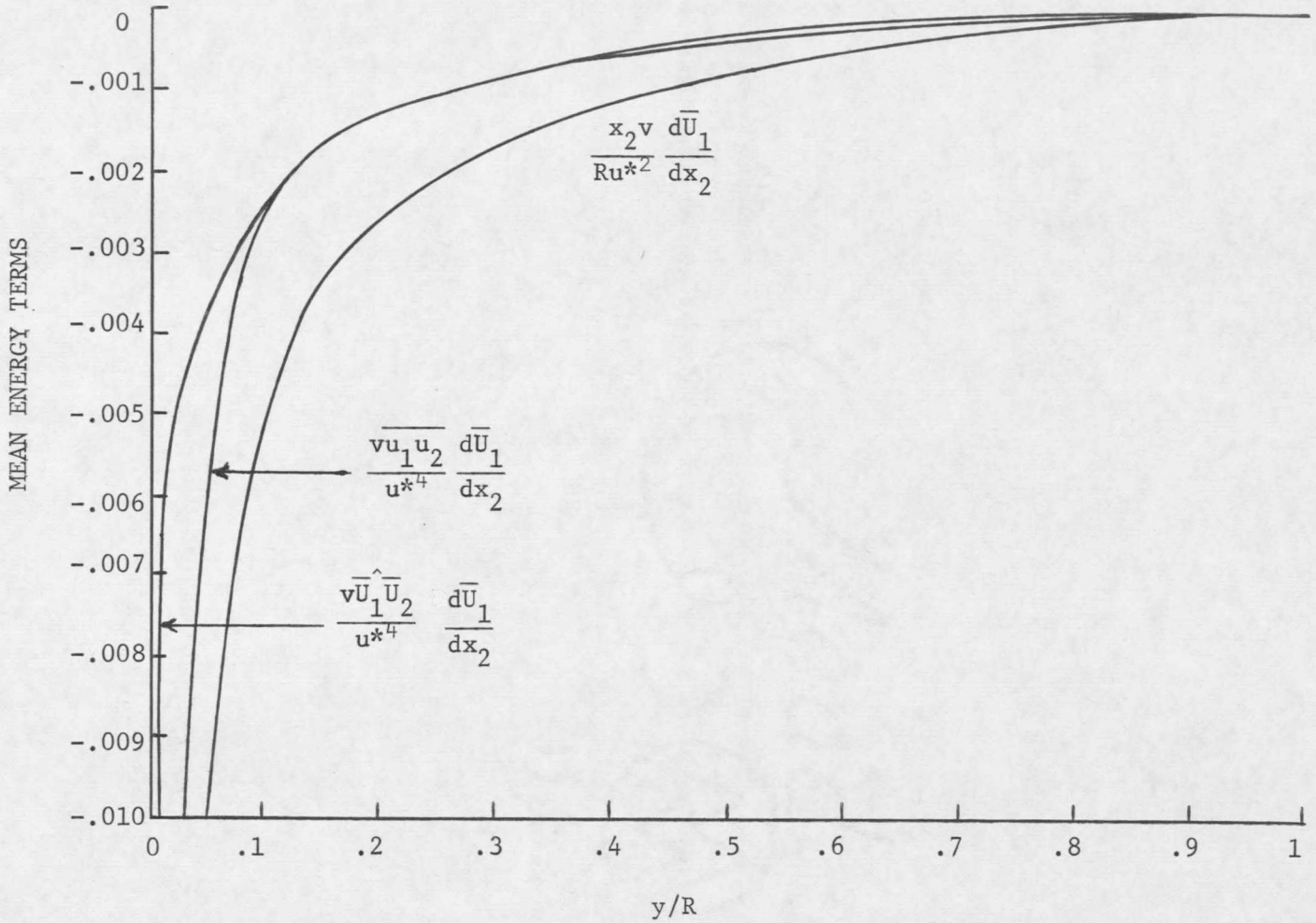

FIGURE 124. Mean Energy Terms for Central Region of Tube With Small Roughness Elements

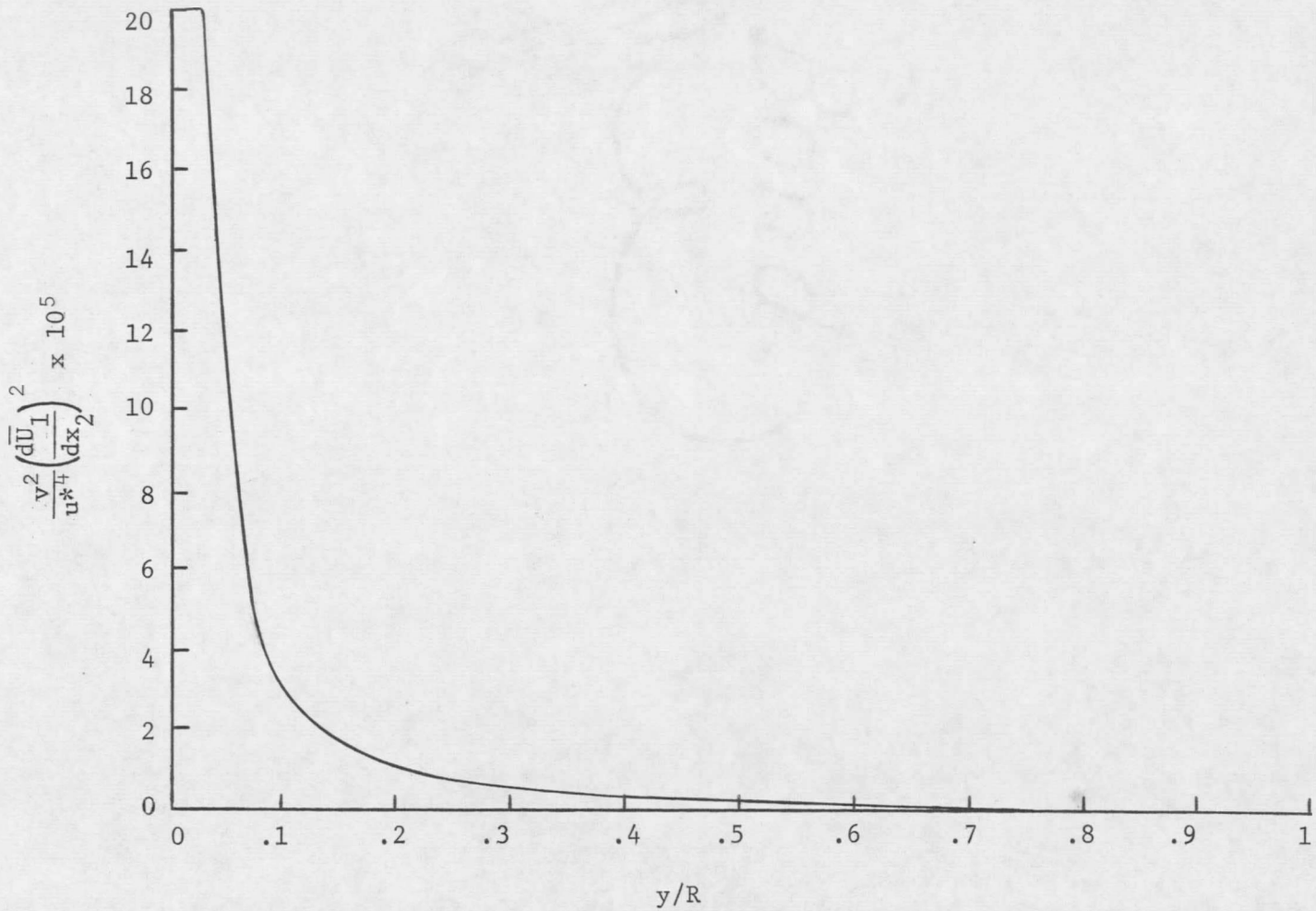

FIGURE 125. Direct Viscous Dissipation of Mean Energy in Turbulent Core of Tube With Small Roughness Elements

immediately adjacent to the pipe wall is presented in Figures 126, 127, and 128. The availability of mean energy is shown by Figure 127 to remain relatively small until the top of the roughness elements is reached, and a marked ascent then occurs. Figure 128 reveals that the dissipation remains small throughout the cross section, and although it does show a marked increase at the mean roughness height, it still does not completely balance the available energy at this point. This difference may be accounted for, however, by examination of the production terms in Figure 126. These terms remain equal until a value of y/R of about 0.03 is reached, at which point they begin to diverge. The turbulence energy production increases in magnitude from this point to a maximum of about 0.03 and then decreases to zero. On the other hand, the roughness energy production decreases in magnitude until a null value is attained, and then a significant increase in magnitude is noted. This increase in magnitude then accounts for the difference between the availability and dissipation of mean energy in the near wall layers.

To summarize these results it should be noted that the bulk of the available energy is taken from the mean flow in a narrow region above the roughness elements. Although a portion is directly dissipated by viscous action, a significant portion is also converted into roughness and turbulence energies. Except for this small region,

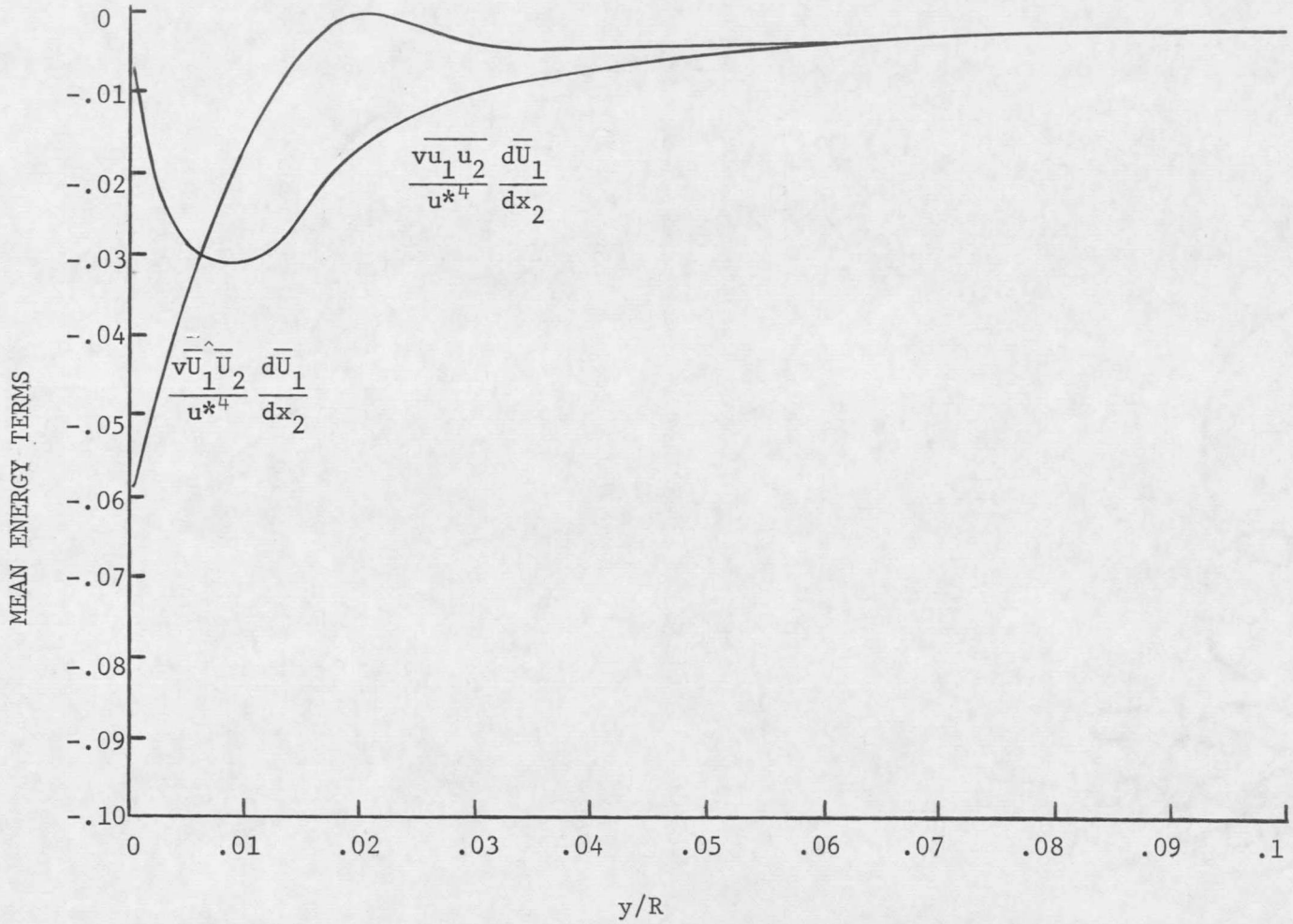

FIGURE 126. Roughness and Turbulence Energy Production Near Wall of Tube With Small Roughness Elements

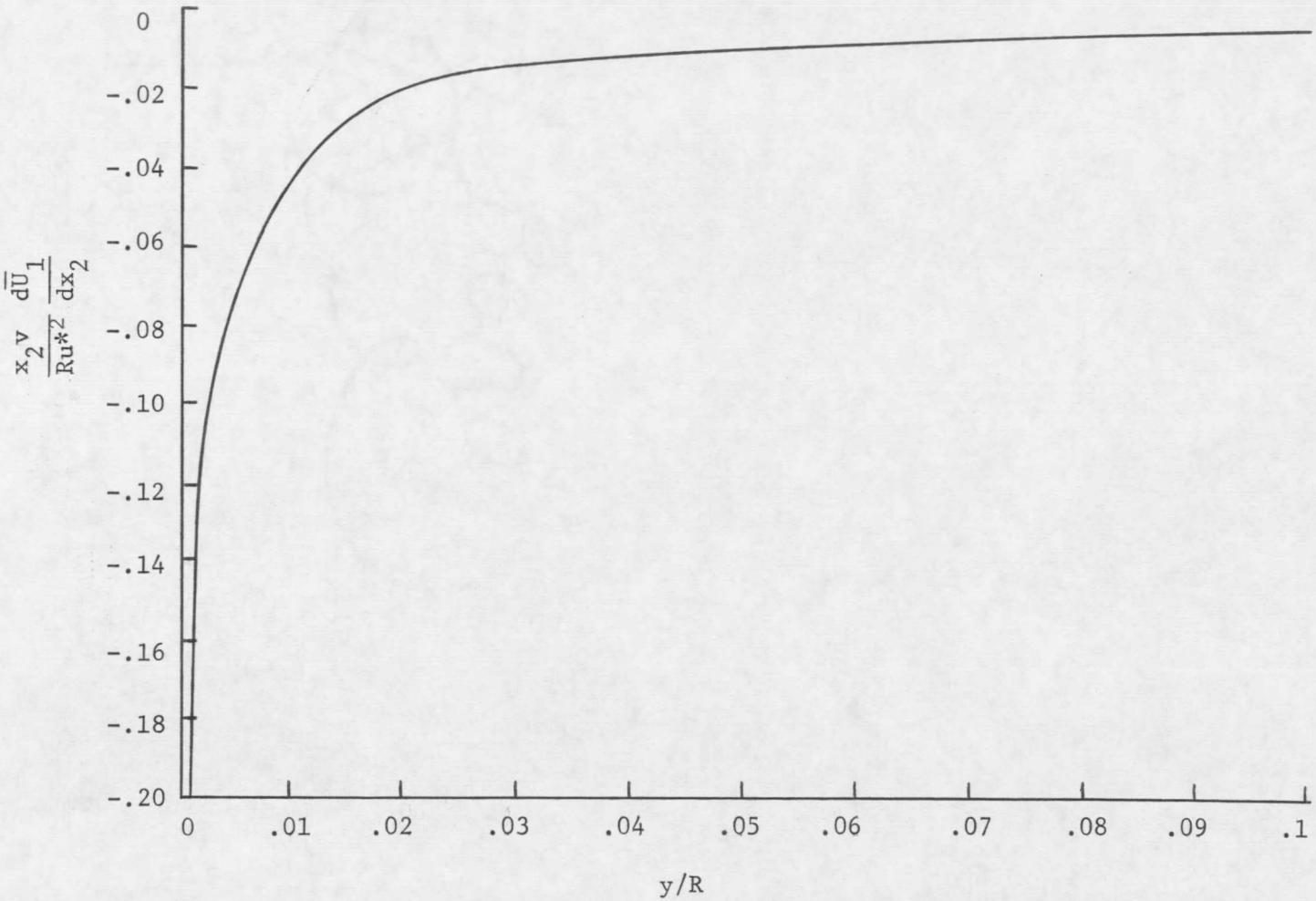

FIGURE 127. Availability of Mean Energy Near Wall of Tube With Small Roughness Elements

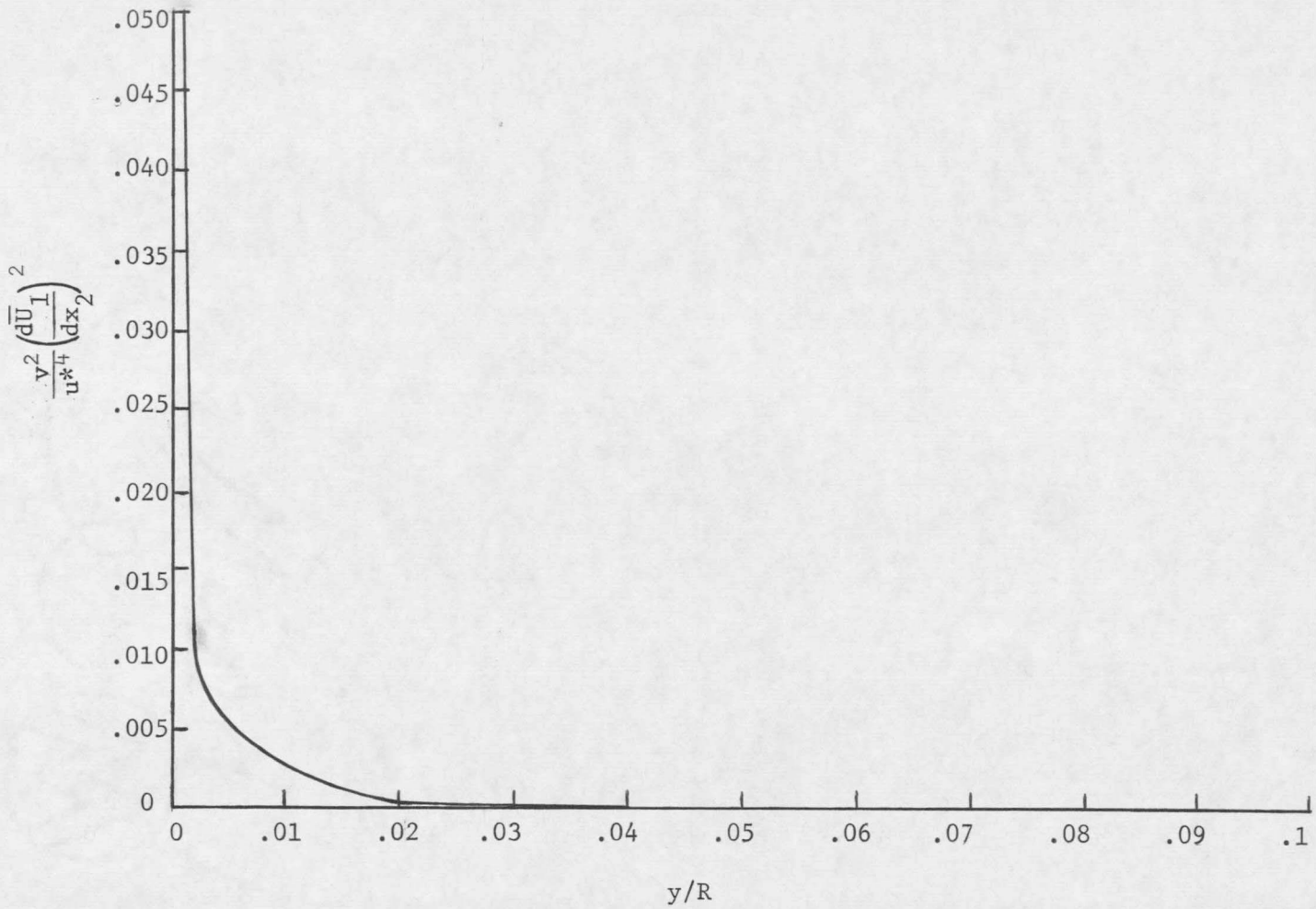

FIGURE 128. Direct Viscous Dissipation of Mean Energy Near Wall of Tube With Small Roughness Elements

the roughness and turbulence energy production terms are nearly equal throughout the pipe.

Having established the amount of energy converted from the mean motion to turbulence energy, the expression for the turbulence energy balance, equation (4.29), will now be examined in order to determine the fate of this converted energy. The portion of this energy which is dissipated by viscous effects was considered in the previous section, and the experimental results are indicated by the solid lines in Figures 120 and 121. A comparison of the production and dissipation produces the result that these two quantities nearly balance each other over the entire cross section, with two exceptions. Near the center of the pipe, the turbulence production vanishes while the dissipation maintains a nonzero value. This fact will have to be accounted for by a diffusion of turbulence energy into this region. Another difference occurs just above the roughness elements where the maximum magnitude of the production is seen to be about twice that of the dissipation. This demands the diffusion of a large amount of energy from this area in order for the energy balance to be satisfied.

Experimentally determined values of the gradient type diffusion of turbulence kinetic energy are indicated in dimensionless form in Figure 129 for the central region of the pipe and in Figure 130 for

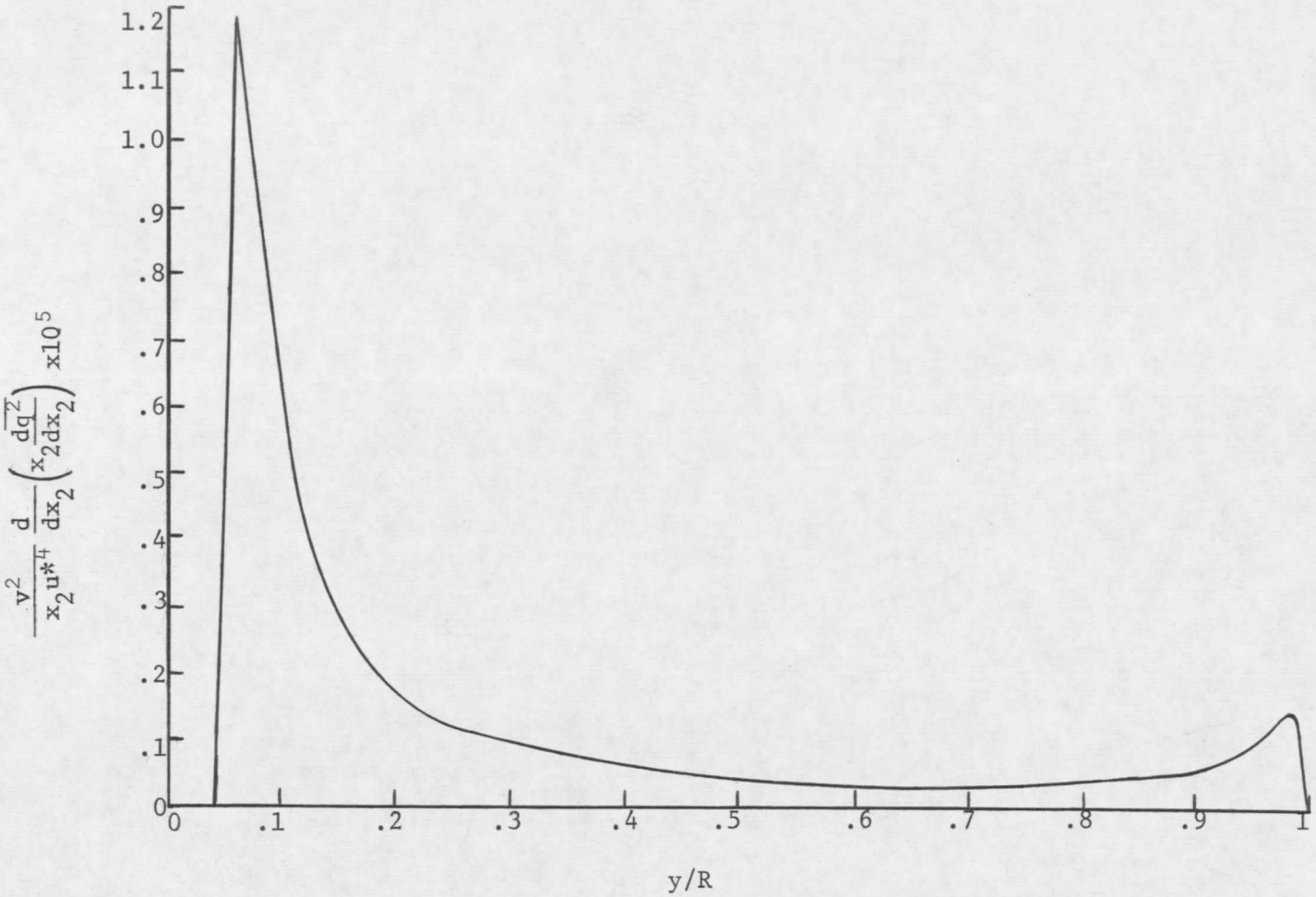

FIGURE 129. Gradient Diffusion of Turbulence Kinetic Energy in Central Region of Tube With Small Roughness Elements

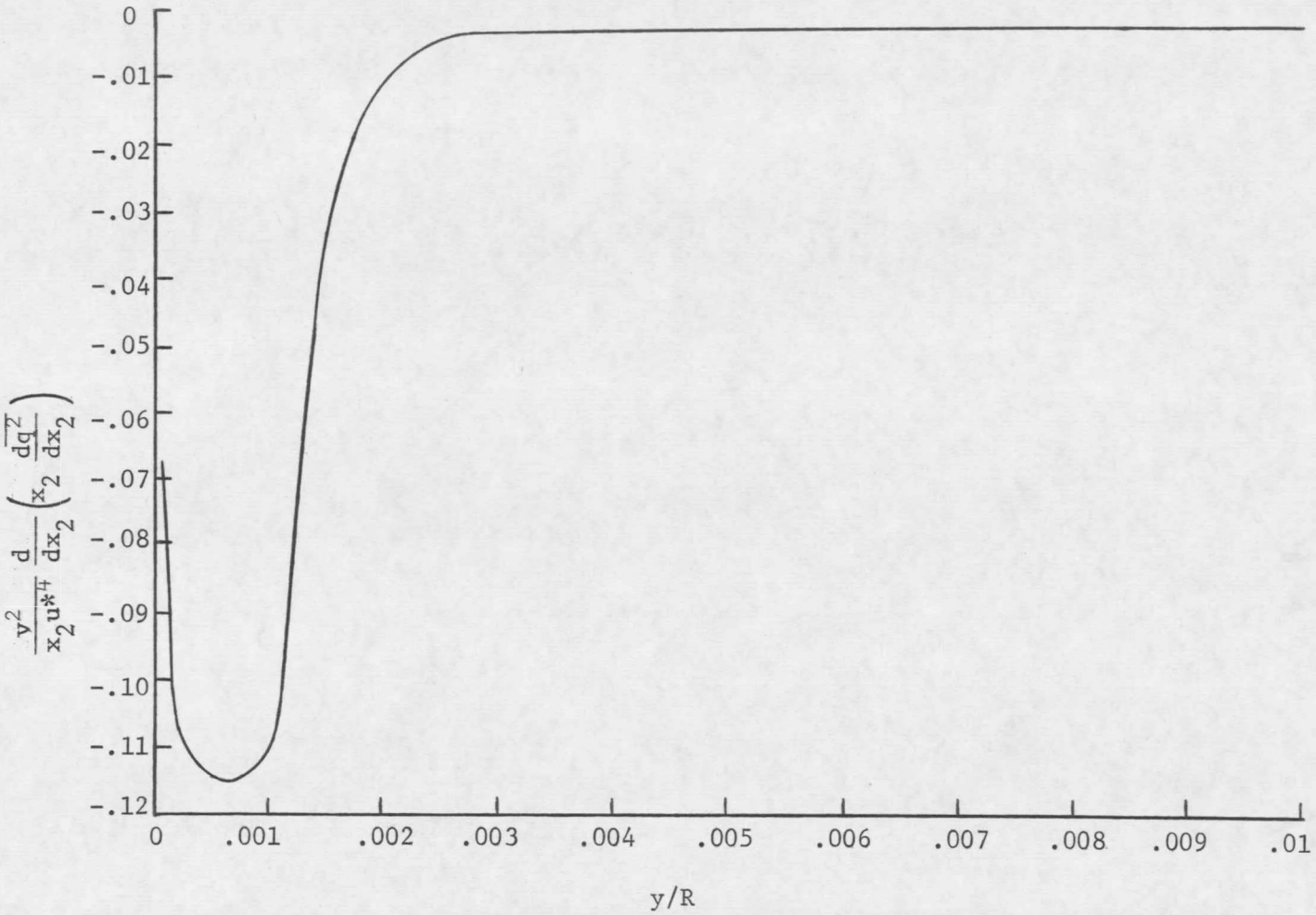

FIGURE 130. Gradient Diffusion of Turbulence Kinetic Energy in Wall Region of Tube With Small Roughness Elements

the wall region. This term is seen to be rather small over the entire cross section, although a small magnitude maximum value is observed near $y/R = 0.1$, and a rather large magnitude minimum value is acquired just below the mean height of the roughness elements. It is surprising to note that even though this diffusion term is small throughout the central portion of the pipe, it remains positive in this region thereby indicating a loss of energy. Thus, the transfer of kinetic energy by gradient diffusion is in a direction from the center line toward the wall resulting in the large gain in energy in the wall region exemplified by Figure 130. Also, this means that there is a loss of energy near the center line, both by viscous dissipation and by gradient diffusion, which will have to be taken into account by a convective diffusion of energy into this area.

All terms appearing in the turbulence energy balance have now been determined experimentally except the convective diffusion term χ, and this term may now be calculated as the closing entry in equation (4.29). For the case of a rough pipe it should be remembered, however, that this term will also contain any possible interactions between turbulence and roughness energy terms. The results of this calculation for χ are presented in Figures 131 and 132. This term is observed to be somewhat larger than the gradient diffusion everywhere except in the near wall region. A decisive maximum value occurs

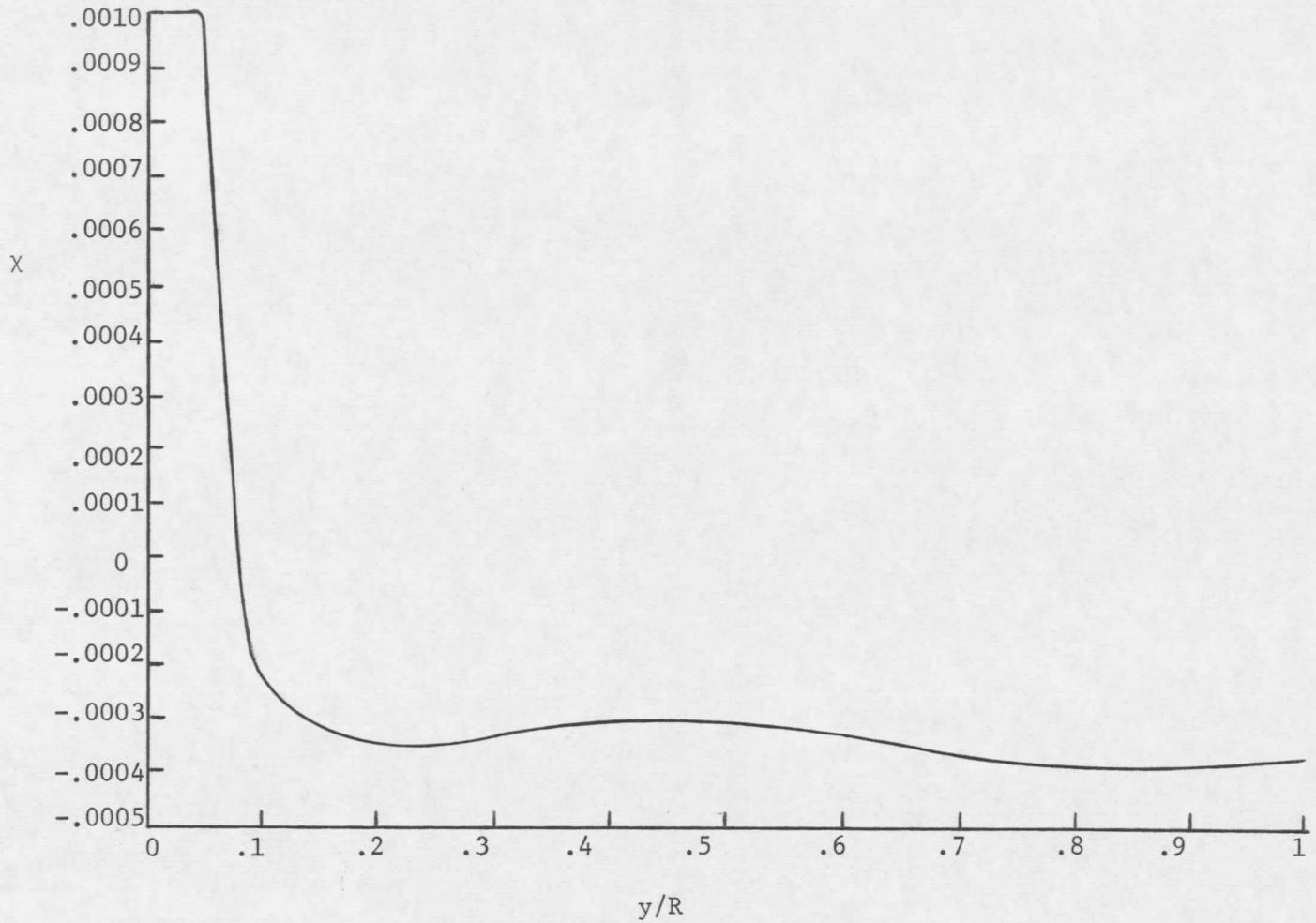

FIGURE 131. Convective Diffusion of Turbulence Energy in Central Region of Tube With Small Roughness Elements

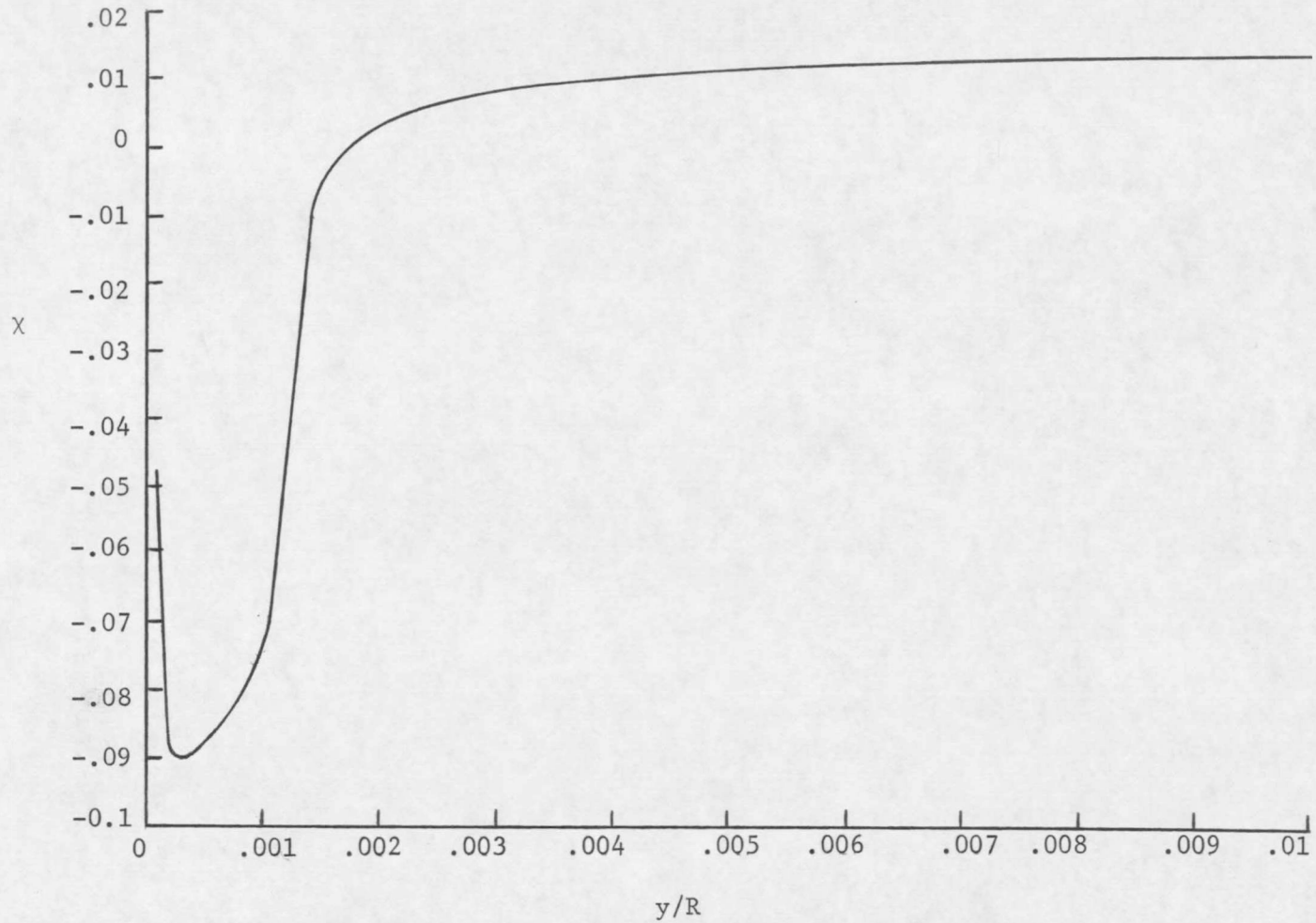

FIGURE 132. Convective Diffusion of Turbulence Energy Near Wall of Tube With Small Roughness Elements

for y/R slightly less than 0.1, and the convective diffusion is negative throughout the remainder of the pipe. This indicates a transfer of energy, from the point where this maximum occurs, both toward the wall and toward the center line. A gain in energy is thereby observed in each of these locations. The energy at the center line compensates for the losses by dissipation and gradient type diffusion, while the gain near the wall must be matched by a dissipative loss.

Energy Spectra

A contour map of the energy spectra of the u_1 fluctuating velocities is presented in Figure 133 for the frequency domain, and transformation to the wave number space is indicated by Figure 134. These figures indicate, for any given value of y/R, that E_1 has a relatively large magnitude at small frequencies and rapidly decreases as higher frequencies are approached. Figure 134 indicates that for a given wave number there is a decrease in energy content of the dissipation eddies in moving from the wall to the center line of the pipe in agreement with the previous examination of the turbulence energy equation. Again for a constant wave number, the energy content of the eddies associated with production and diffusion is seen to indicate a rapid decline, at both the wall and the center line, from

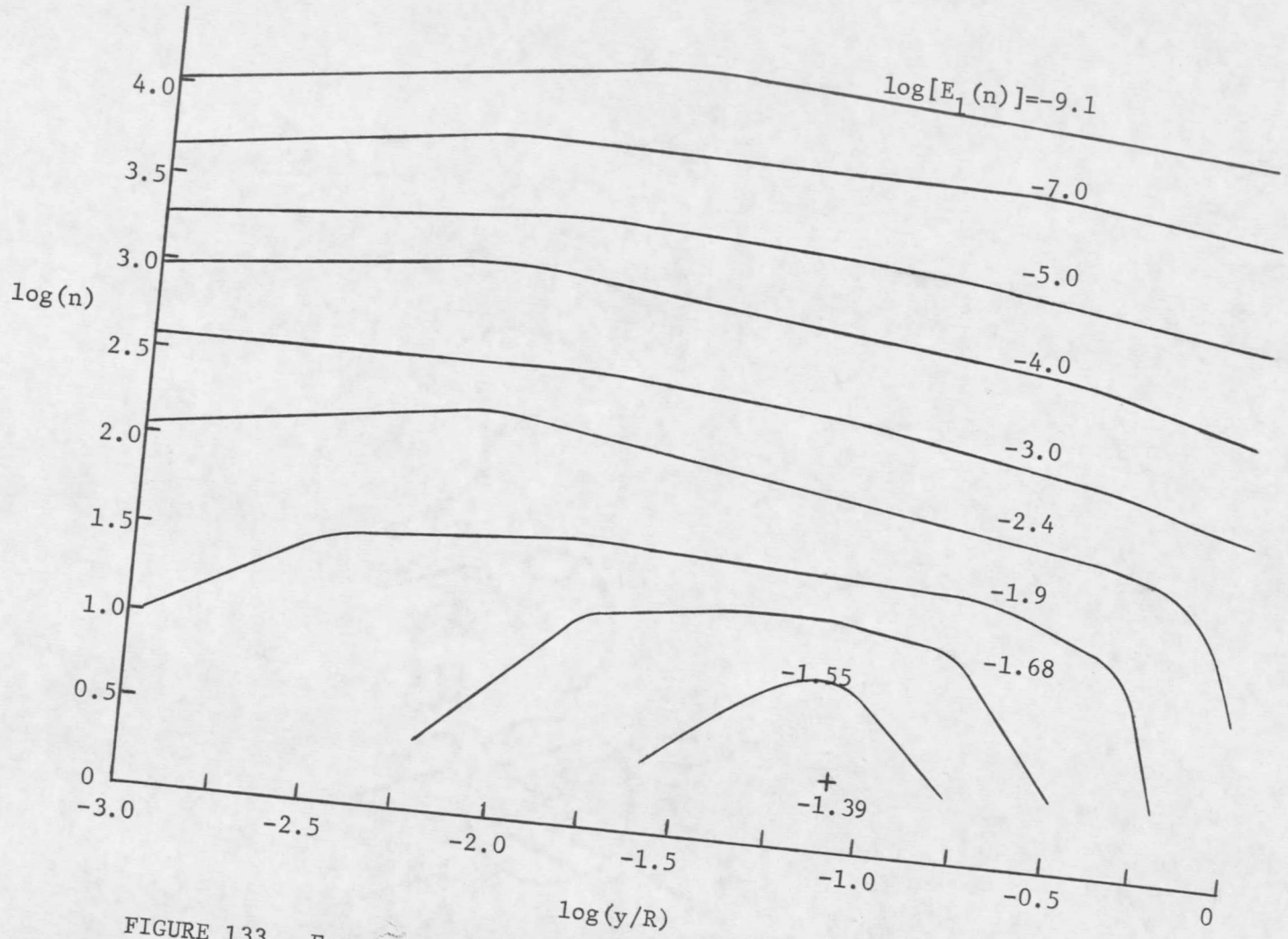

FIGURE 133. Frequency Domain Energy Spectra for u_1 Fluctuations in Tube With Small Roughness Elements

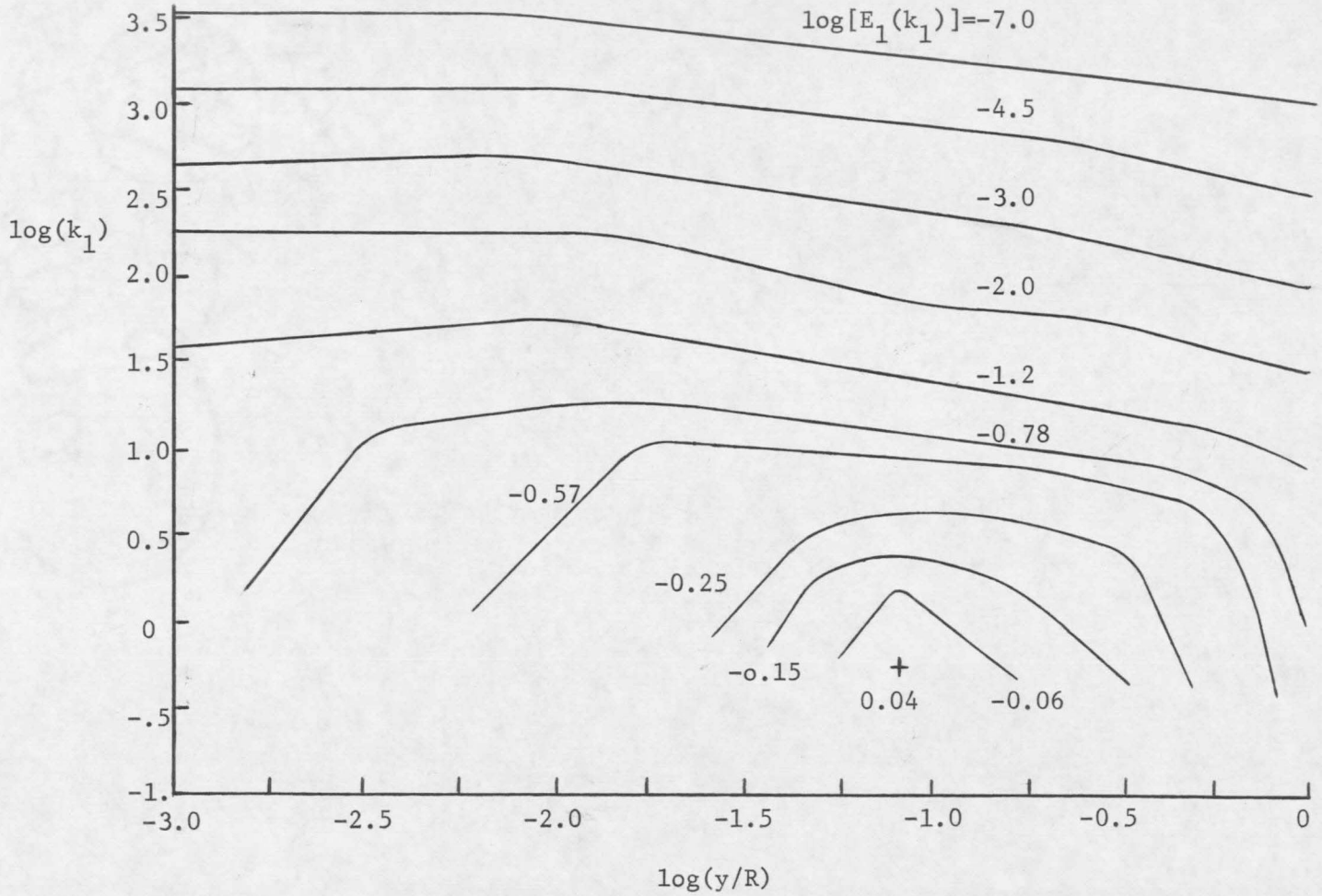

FIGURE 134. Wave Number Space Energy Spectra for u_1 Fluctuations in Tube With Small Roughness Elements

a maximum value at an intermediate radial position. The value of y/R where this maximum occurs is slightly less than 0.1 for the lower wave numbers, and such behavior would be expected since a majority of the turbulence is produced in this region, and diffusion is also relatively large in this vicinity.

The possible existence of the various subranges of eddy sizes can be established by an examination of Figures 135, 136, and 137. Figure 136 shows the inertial subrange where the dominant process is the transfer of energy from smaller to larger wave numbers without significant production or dissipation. Such a subrange appears to be exhibited over a rather wide range of wave numbers over the entire pipe cross-section, and the wave numbers where this law applies decrease in moving from the wall to the center line. The production subrange is shown to indicate a similar behavior in Figure 136. A comparison of these two figures reveals that the production subrange does occur for slightly larger eddies than the inertial subrange, and this is exactly the behavior predicted by Tchen [84]. Within the range of variables examined experimentally in this investigation, an absence of any viscous subrange of eddy sizes is noted in Figure 137 for all values of y/R. The shape of the contours in this figure does indicate, however, that such a subrange will probably occur at extremely large wave numbers.

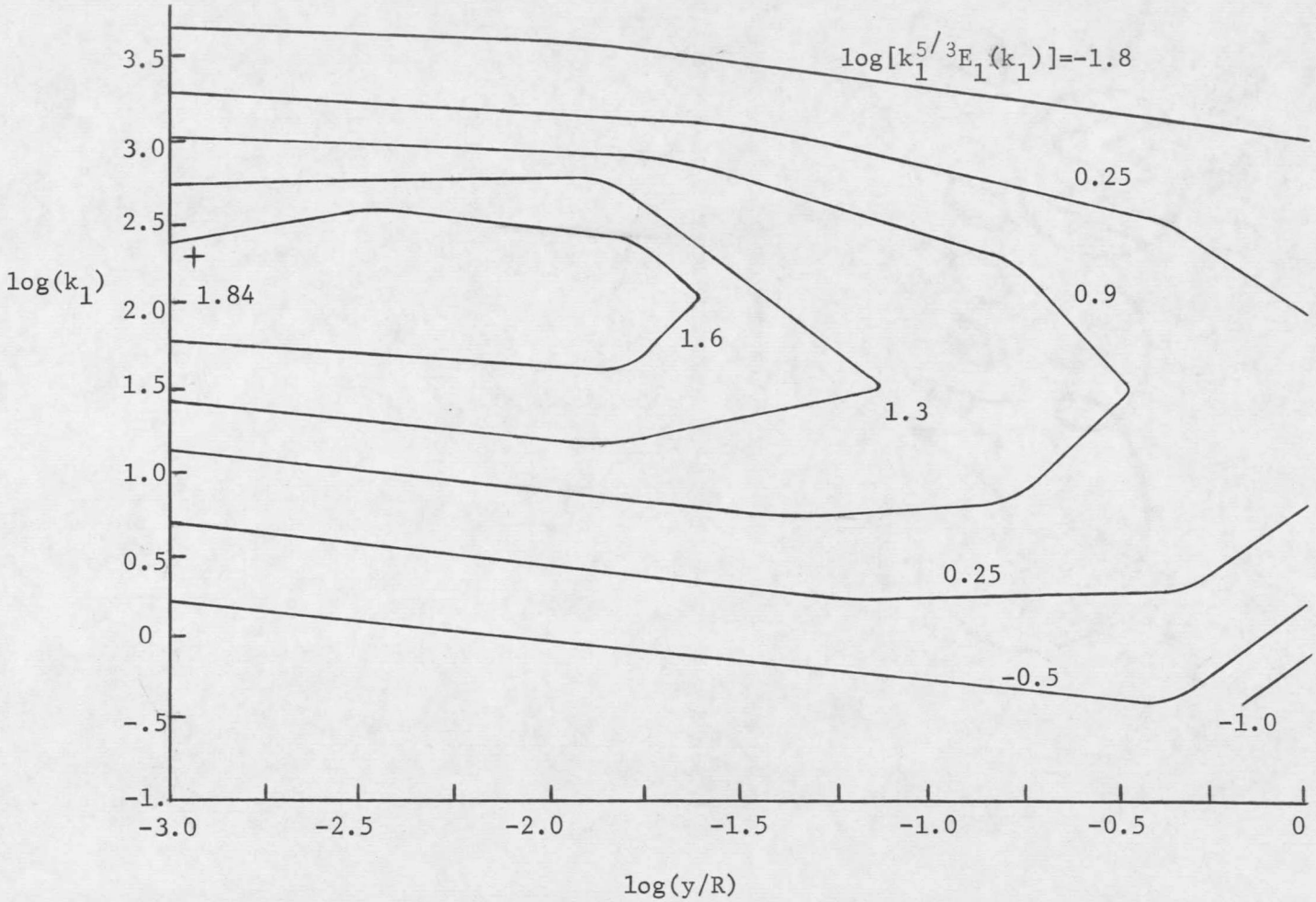

FIGURE 135. Inertial Subrange of Eddy Sizes for u_1 Fluctuations in Tube With Small Roughness Elements

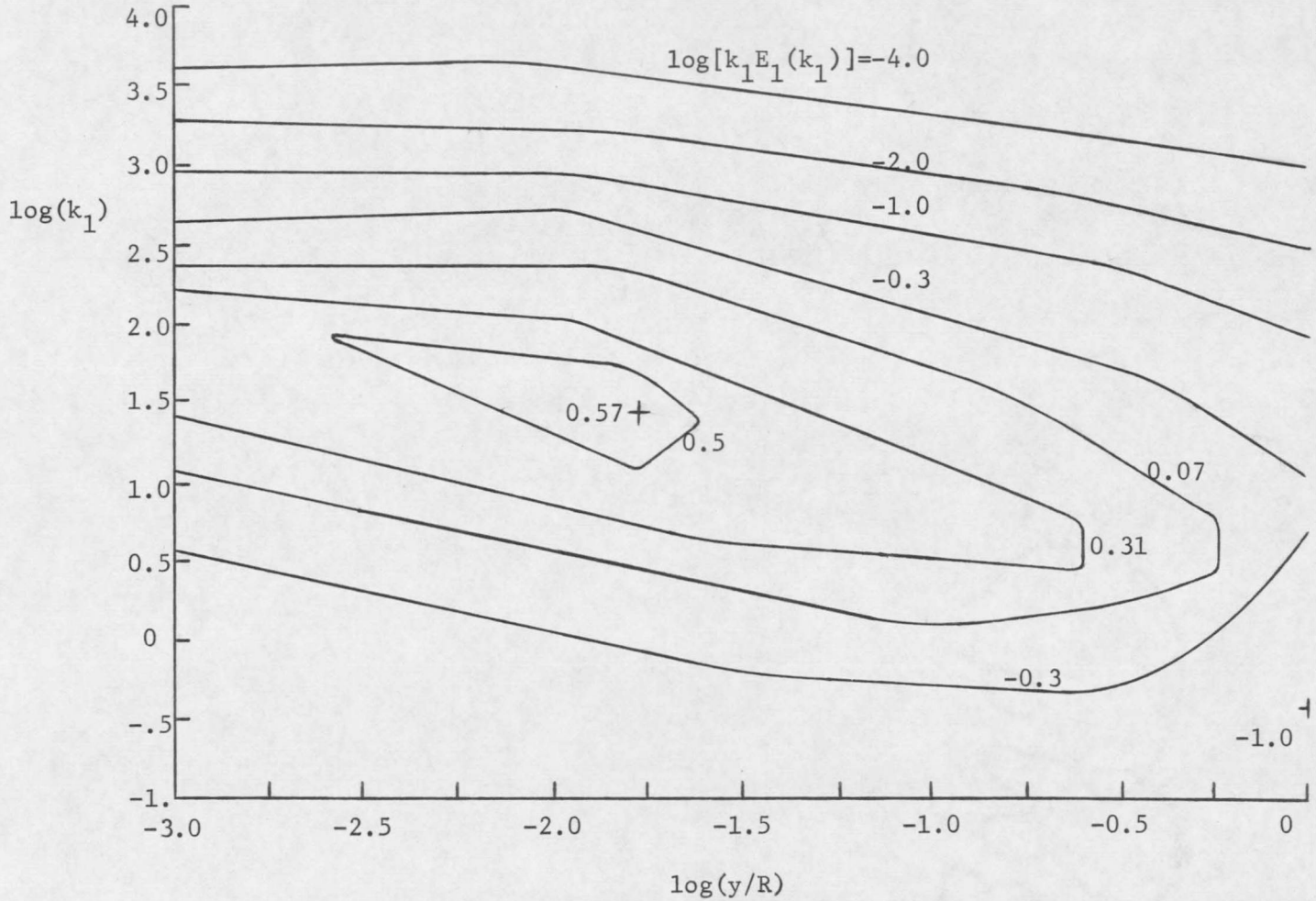

FIGURE 136. Production Subrange of Eddy Sizes for u_1 Fluctuations in Tube With Small Roughness Elements

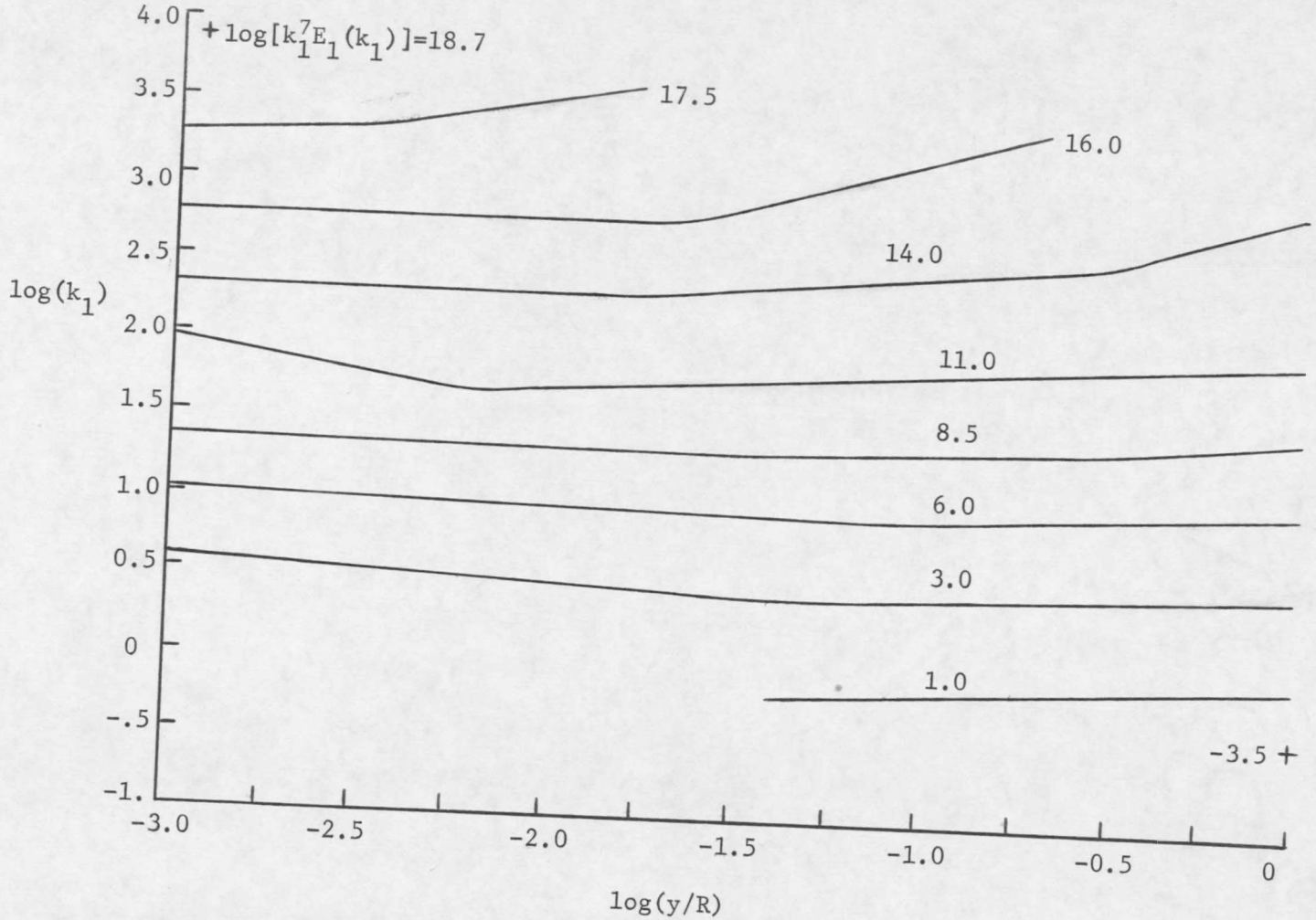

FIGURE 137. Viscous Subrange of Eddy Sizes for u_1 Fluctuations in Tube With Small Roughness Elements

The dimensionless coordinate systems proposed by Robertson et al [47] and Goma and Gelhar [30] for yielding the spectrum function independent of radial position are evaluated in Figures 138 and 139. Figure 139 shows that the coordinates proposed by Goma and Gelhar [30] yield good results for large values of $2nR/\overline{U}_1$ while substantial deviations occur for low values, especially near the wall. Excellent results are obtained through most values of $n\Lambda_1/\overline{U}_1$ by utilizing the system specified by Robertson et al [47]. Slight deviations do occur, however, for large values of $n\Lambda_1/\overline{U}_1$.

Energy spectra in the frequency domain and the wave number space for the velocity fluctuations in the x_2 coordinate direction are shown in Figures 140 and 141 respectively. As in the case of the E_1 spectra, a slight decrease in the energy content of the dissipation eddies may be observed in moving from the wall to the center line of the pipe at a constant frequency or wave number. A significantly different behavior of the E_2 and E_1 spectra are observed for low wave numbers, however. The E_2 spectra immediately adjacent to the wall and those in the vicinity of the pipe center line both show a slight energy deficiency for this wave number range, but no such deficiency is observed for intermediate radial positions. As explained in the previous chapter, this type of energy deficiency is thought to be due to the convective diffusion of pressure energy which

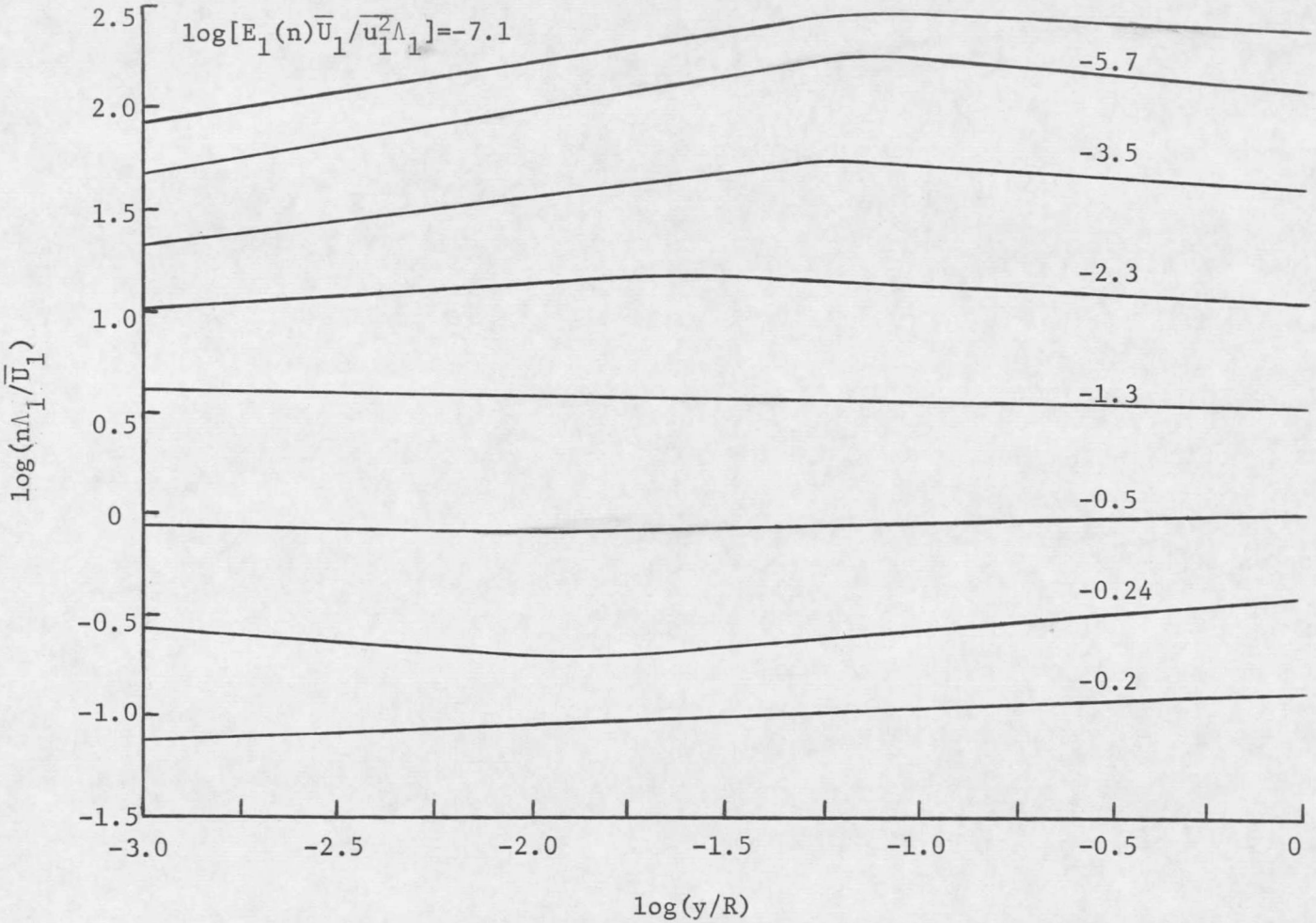

FIGURE 138. u_1 Spectra for Pipe With Small Roughness Elements Normalized as Suggested by Robertson et al [47]

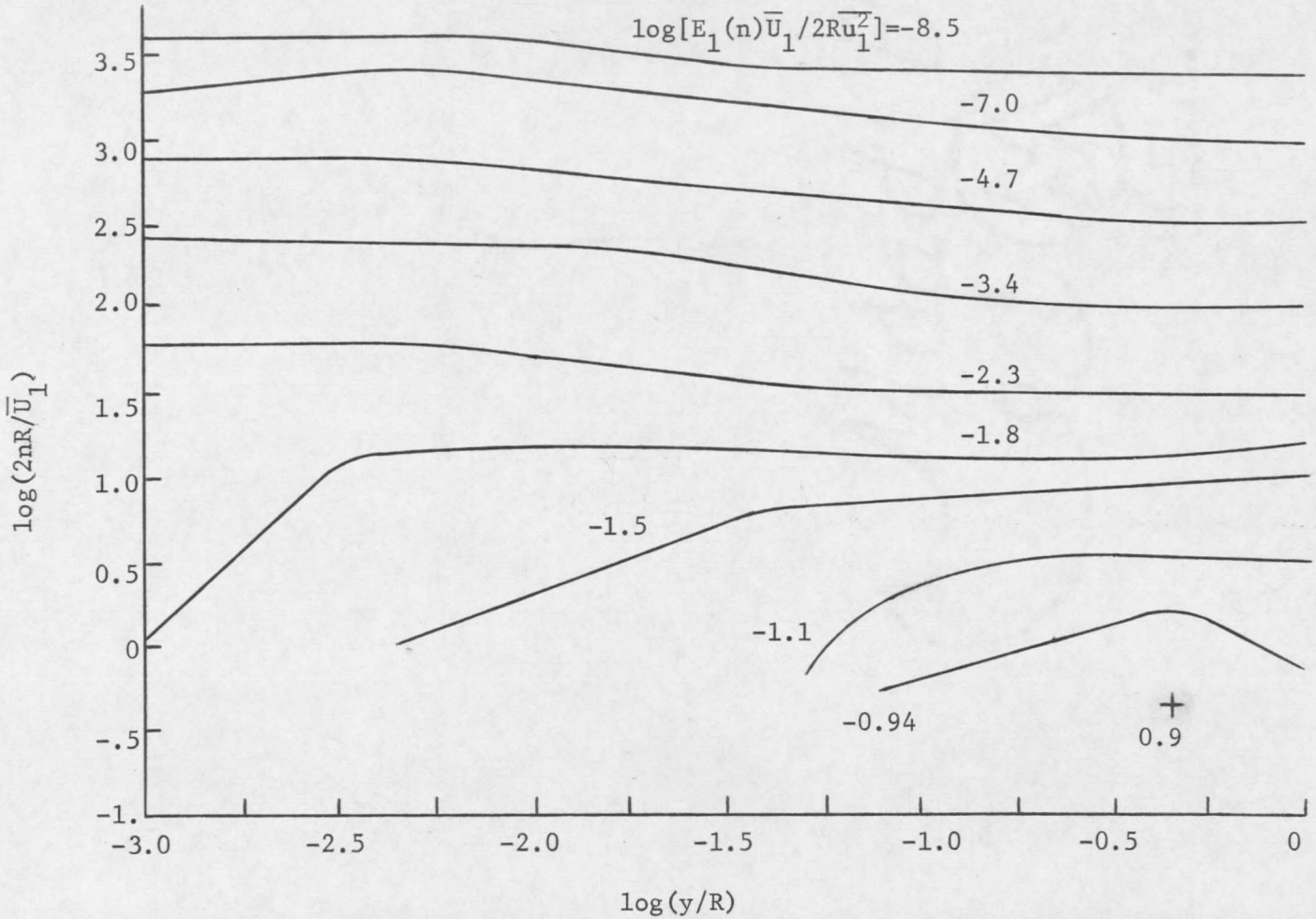

FIGURE 139. u_1 Spectra for Pipe With Small Roughness Elements Normalized as Suggested by Goma and Gelhar [30]

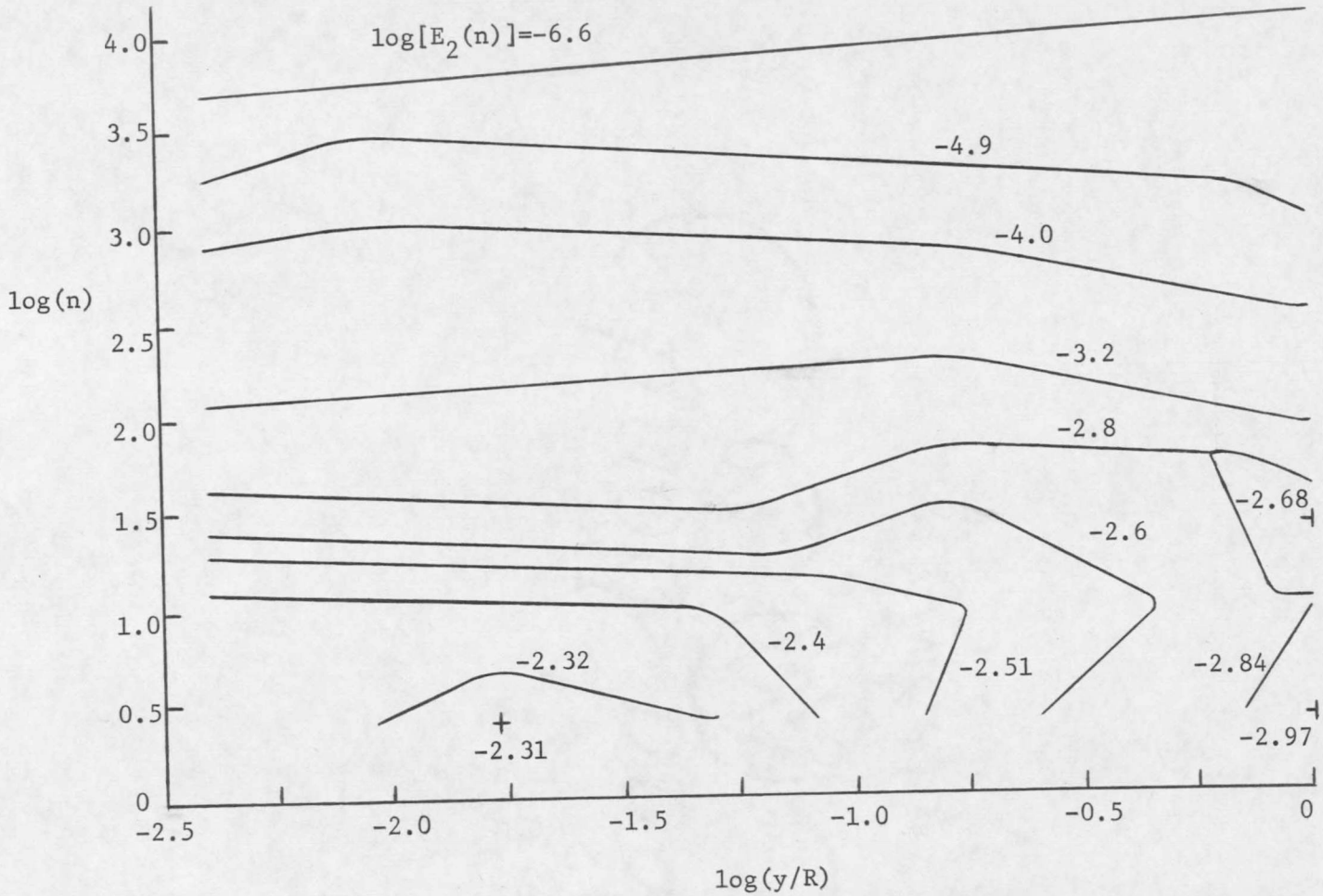

FIGURE 140. Frequency Domain Energy Spectra of u_2 Fluctuating Velocity in Pipe With Small Roughness Elements

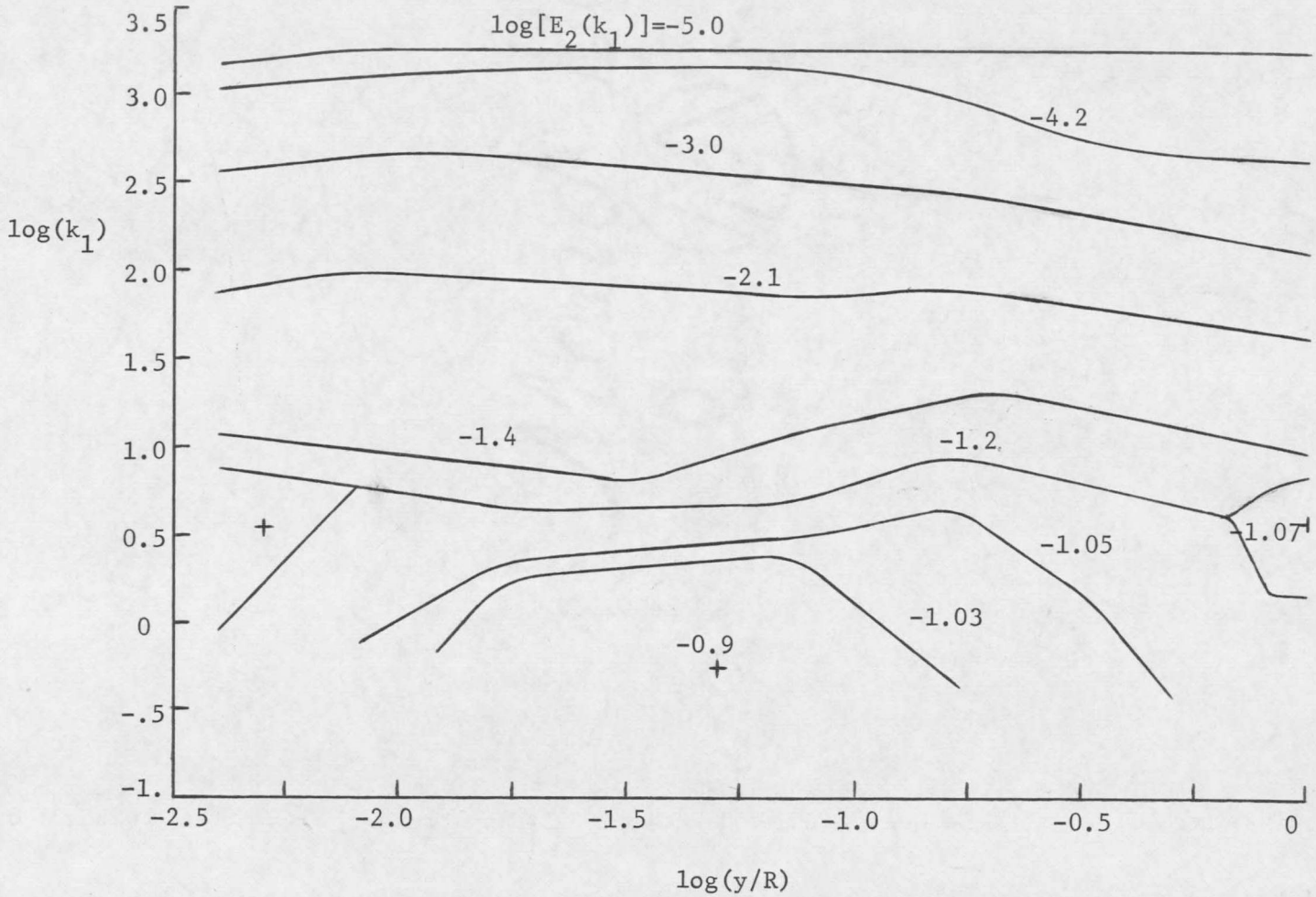

FIGURE 141. Wave Number Space Energy Spectra of u_2 Fluctuating Velocity in Pipe With Small Roughness Elements

is an intermediate wave number phenomena. Care must be utilized, however, in presuming that this interpretation automatically applies for a rough pipe since the convective diffusion term contains, in addition to pressure and kinetic energy, interactions between turbulence and roughness energy. The lack of an energy deficiency at the intermediate radial positions indicates that the commonly accepted process of energy transfer from lower to higher wave numbers occurs in this region. The generally smaller magnitude of the E_2 spectra than the E_1 spectra at a given wave number and a given value of y/R, as indicated by a comparison of Figures 134 and 141, would be expected due to the smaller magnitude of $\overline{u_2^2}$ at any radial position.

The various subranges of eddy sizes for the E_2 spectra are examined by means of Figures 142, 143, and 144. As in the case of the E_1 spectra, the inertial and production subranges are seen to be exhibited over a fairly wide range of wave numbers throughout the pipe, and an increase in magnitude of the wave numbers where these subranges appear is observed as the wall is approached. Also, the production subrange again occurs for slightly larger eddies than does the inertial subrange. The viscous subrange does not appear in Figure 144, but its possible existence at very large wave numbers is indicated.

The dimensionless forms of the energy spectra suggested by

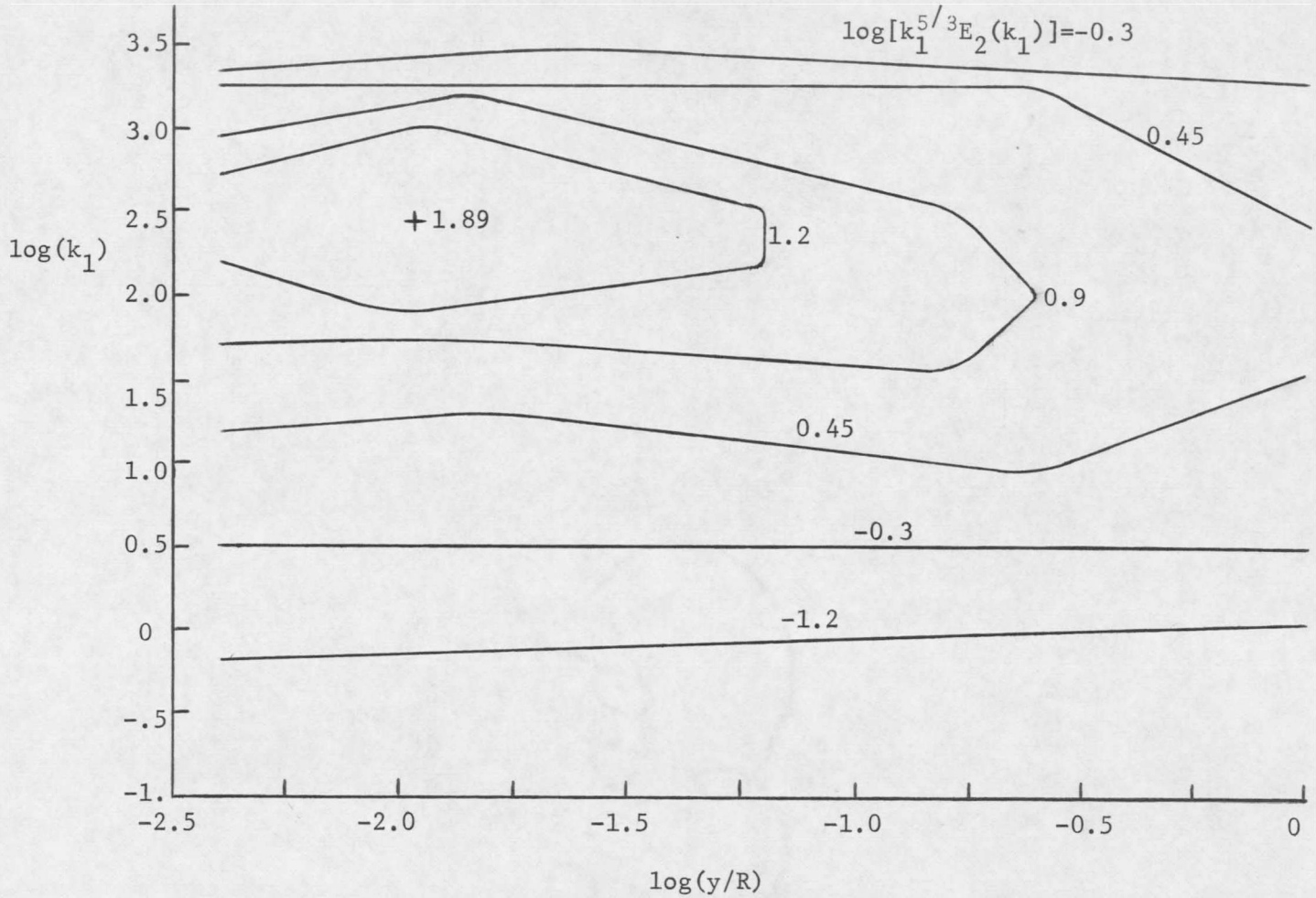

FIGURE 142. Inertial Subrange of Eddy Sizes for u_2 Velocity Fluctuations in Pipe With Small Roughness Elements

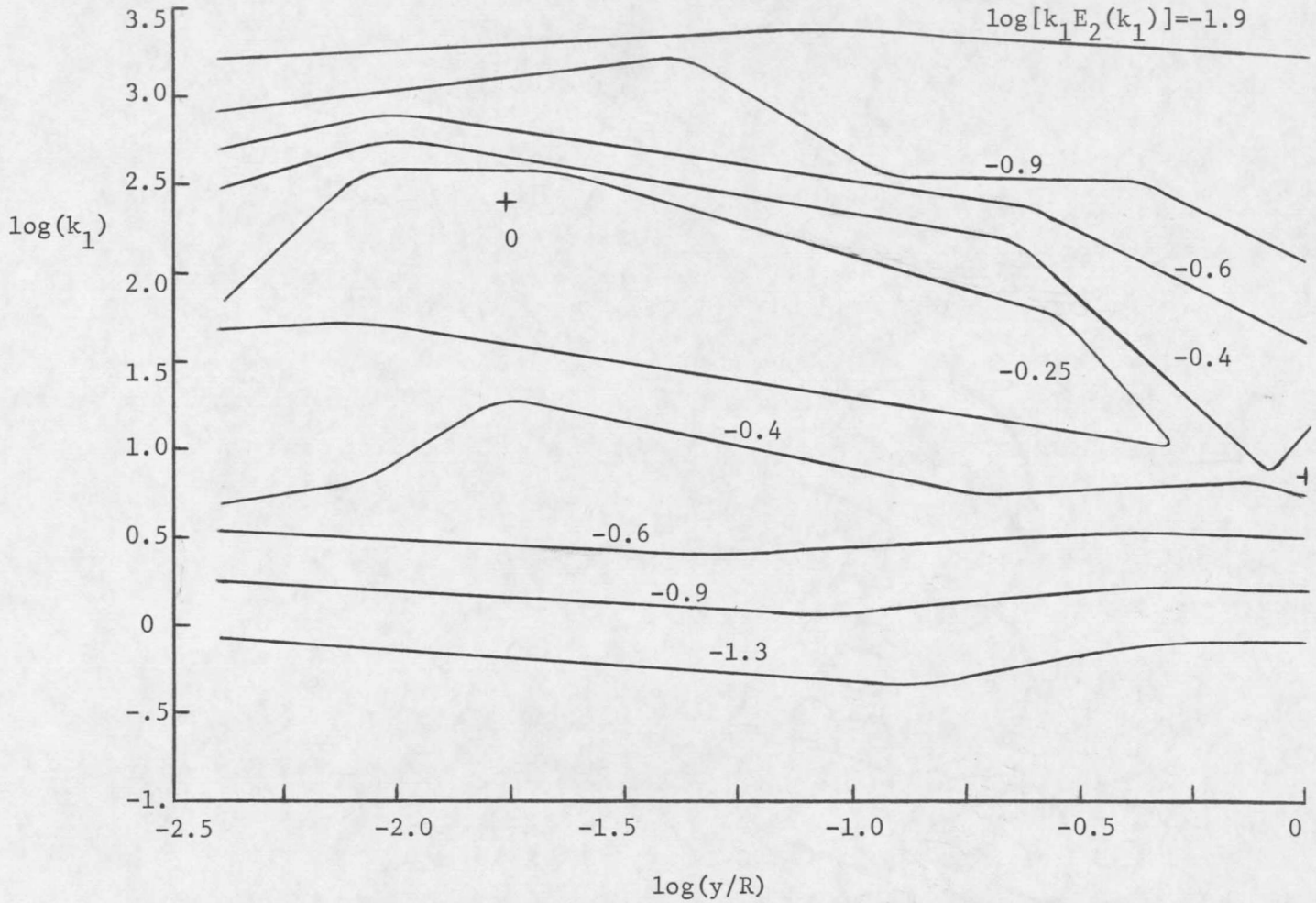

FIGURE 143. Production Subrange of Eddy Sizes for u_2 Velocity Fluctuations in Pipe With Small Roughness Elements

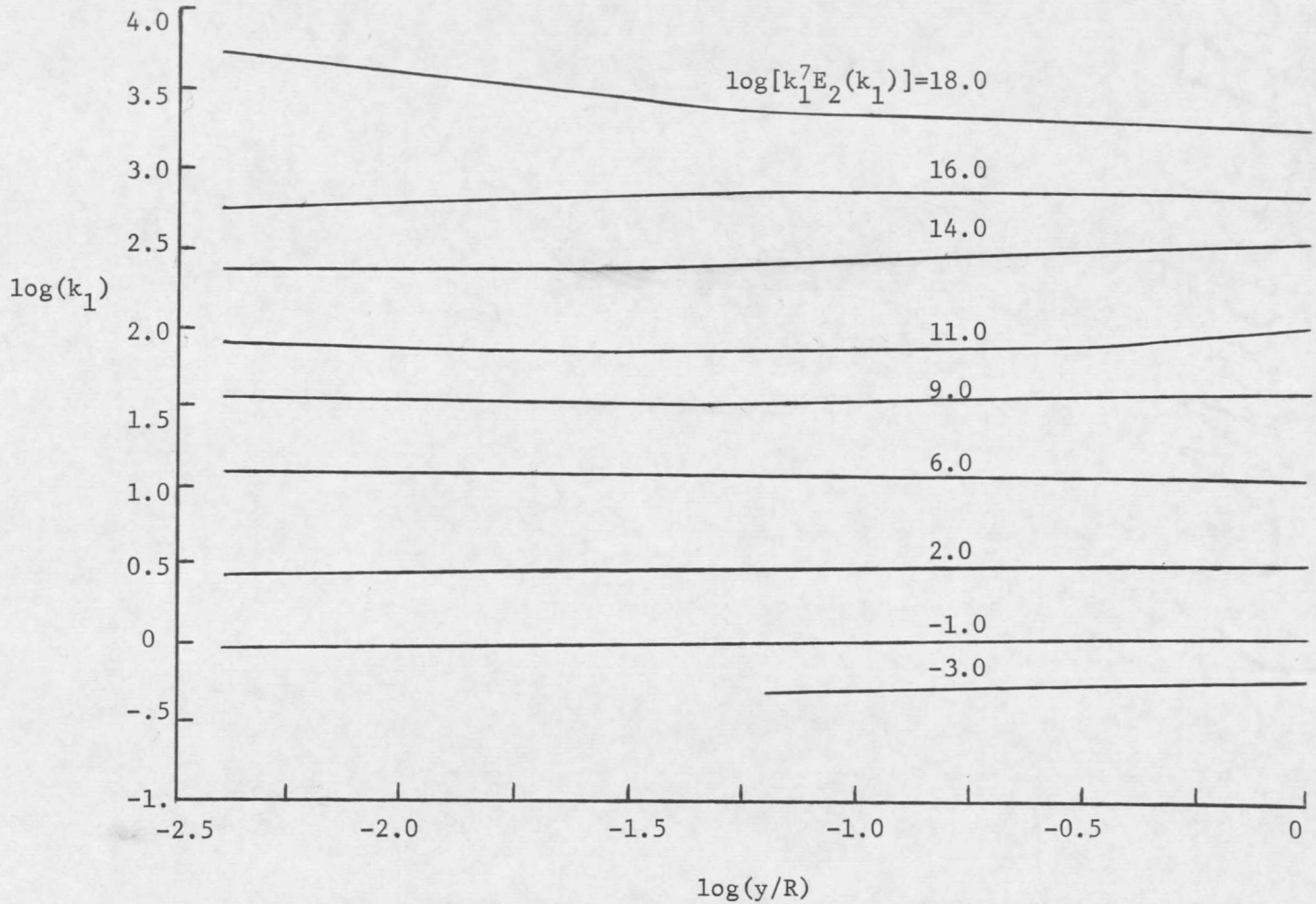

FIGURE 144. Viscous Subrange of Eddy Sizes for u_2 Velocity Fluctuations in Pipe With Small Roughness Elements

Robertson et al [47] and Goma and Gelhar [30] are shown plotted in Figures 145 and 146, respectively, for the u_2 velocity fluctuations. Both of these coordinate systems yield reasonable results except for low wave numbers, especially near the center of the pipe. The failure to exhibit a universal behavior in this region is due to the energy defect observed in the wave number space, Figure 141.

The variation of the E_3 spectrum function for the wave number space and for the frequency domain is indicated in Figures 147 and 148. The behavior of this function is seen to resemble that of the E_2 spectra in most aspects. A very slight decrease in energy content of the viscous dissipation eddies may be observed in moving from the pipe wall to its center line at a constant value of the wave number in Figure 148. An energy deficiency is again observed both at the pipe center line and near the wall, but no such defect is present for intermediate radial positions. This indicates a possible transfer of energy from the u_1 fluctuating velocity to the u_3 fluctuating velocity by action of the fluctuating pressure, although it is conceivable that it might also be indicative of a transfer of energy in favor of u_3 due to interactions between turbulence and roughness energy. A comparison of the magnitudes of the E_3 spectrum function in Figure 148 with those of E_2 in Figure 141 indicates near equality of these two functions. This supports the notion of a

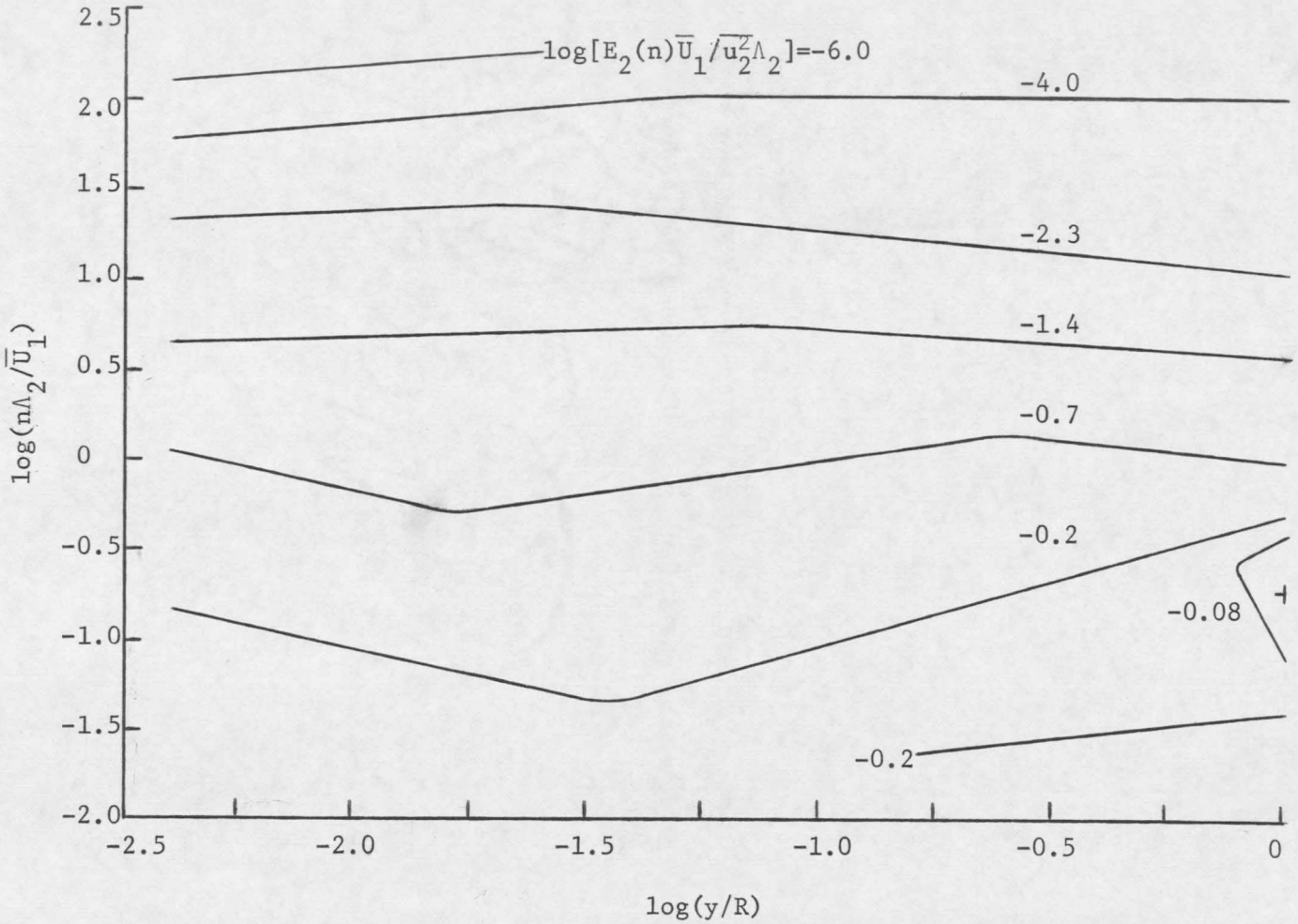

FIGURE 145. u_2 Spectra for Pipe With Small Roughness Elements Normalized as Proposed by Robertson *et al* [47]

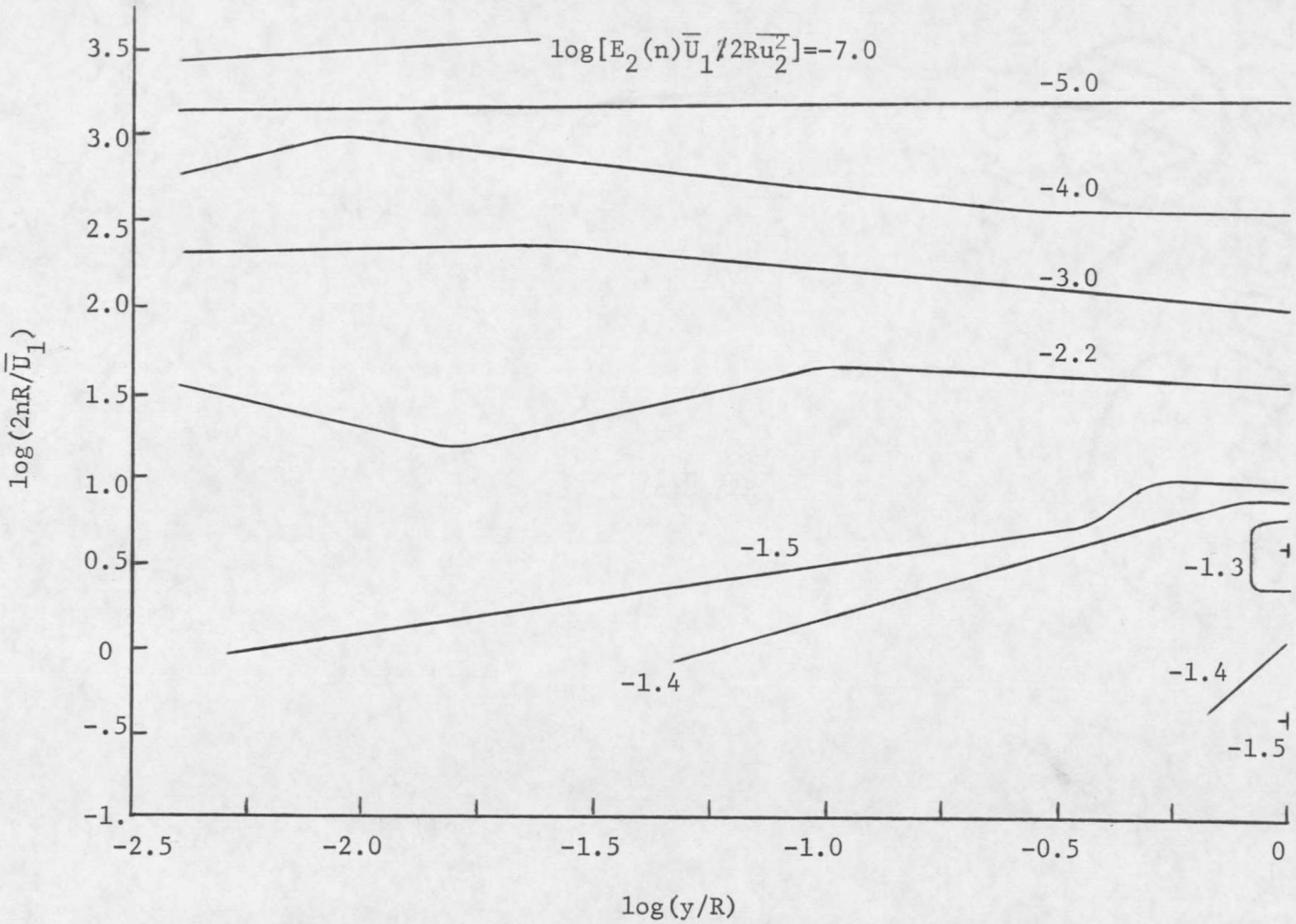

FIGURE 146. u_2 Spectra For Pipe With Small Roughness Elements Normalized as Proposed by Goma and Gelhar [30]

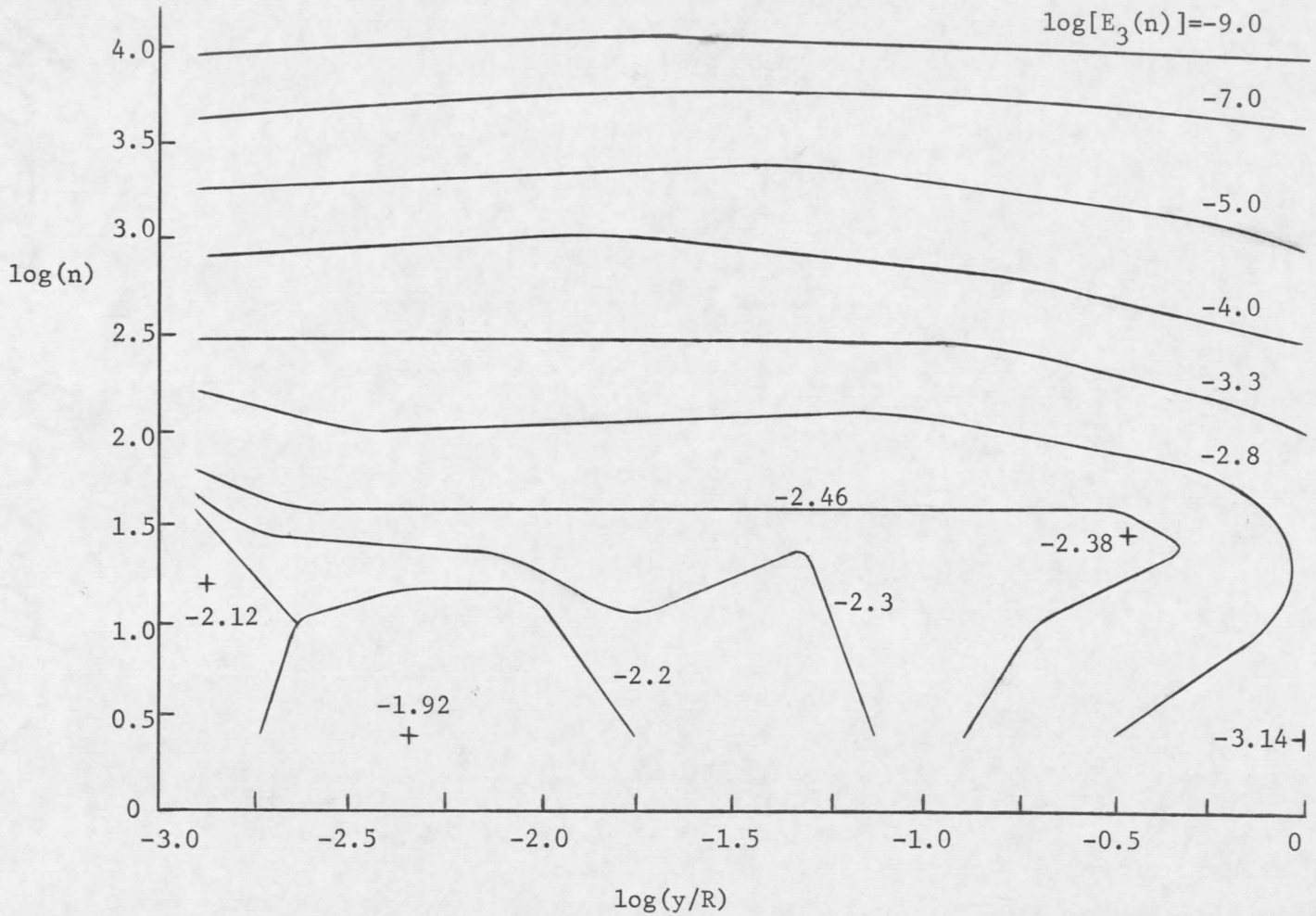

FIGURE 147. Frequency Domain Energy Spectra for u_3 Fluctuating Velocity in Pipe With Small Roughness Elements

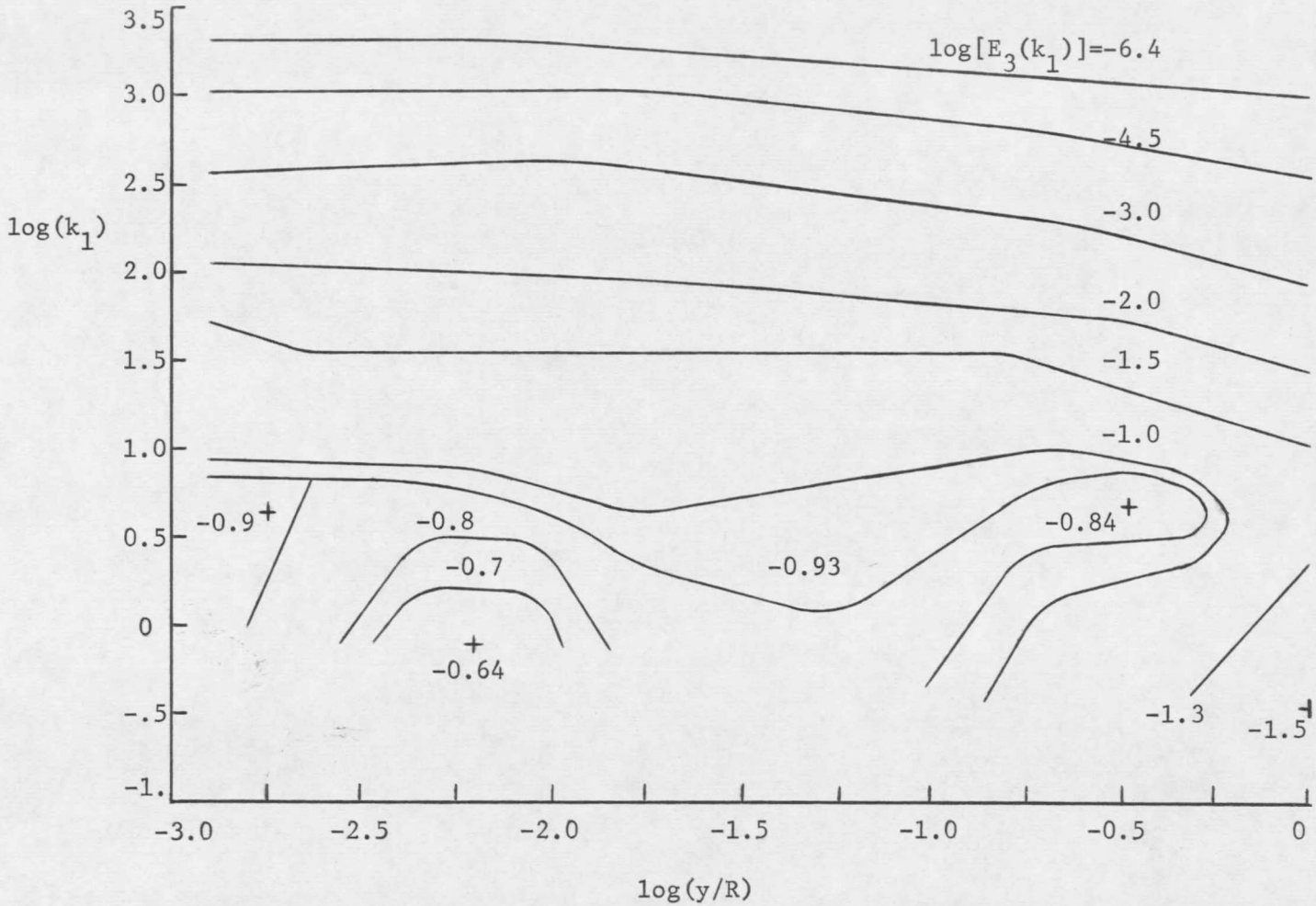

FIGURE 148. Wave Number Space Energy Spectra For u_3 Fluctuating Velocity in Pipe With Small Roughness Elements

tendency toward isotropy by u_2 and u_3 as was concluded by examination of the anisotropy ratios.

The possibility of occurrence of the inertial, production, and viscous subranges of eddy sizes is examined in Figures 149, 150, and 151 respectively. As in the two previous cases, the inertial and production subranges occur throughout the pipe, and the wave numbers where they exist increase as the wall is approached. The production eddies are again larger than the inertial eddies. Figure 151 indicates the apparent occurence of the viscous subrange at very large wave numbers, as was the case with the E_1 and E_2 spectra.

The normalized forms of the E_3 spectra proposed by Robertson et al [47] and Goma and Gelhar [30] are presented in Figures 152 and 153, respectively. Both sets of coordinates indicate a fairly universal behavior for large values of the ordinate, but substantial deviations occur for small values. Thus, although both sets of coordinates yield reasonable results for the E_1 spectra, neither the E_2 or the E_3 functions are correlated in the desired manner.

Autocorrelation Functions

Autocorrelation functions obtained by taking the Fourier cosine transform of the energy spectra are presented in Figures 154, 155, and 156 for the fluctuating velocities in the x_1, x_2 and x_3 coordinate

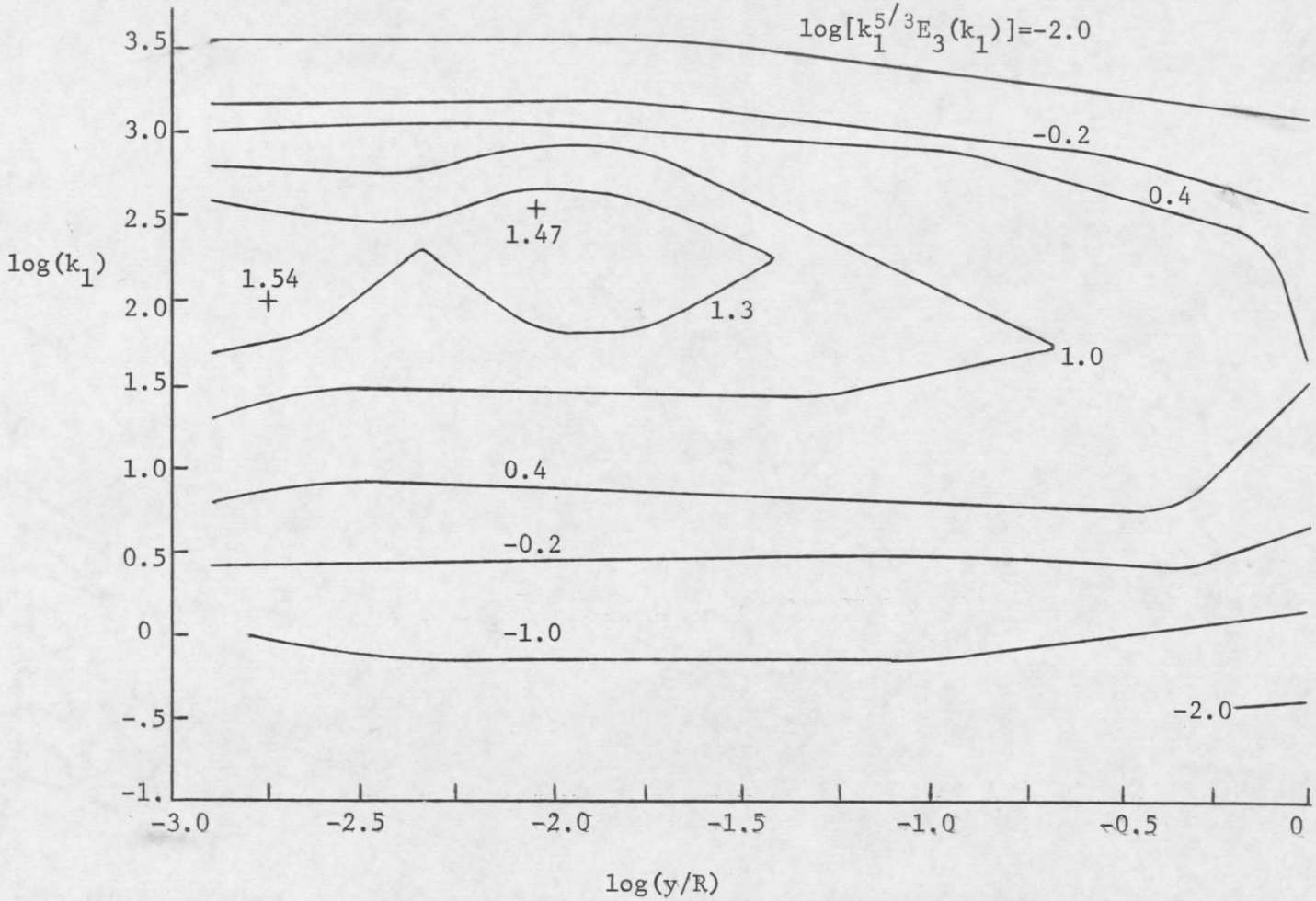

FIGURE 149. Inertial Subrange of Eddy Sizes For u_3 Velocity Fluctuations in Pipe With Small Roughness Elements

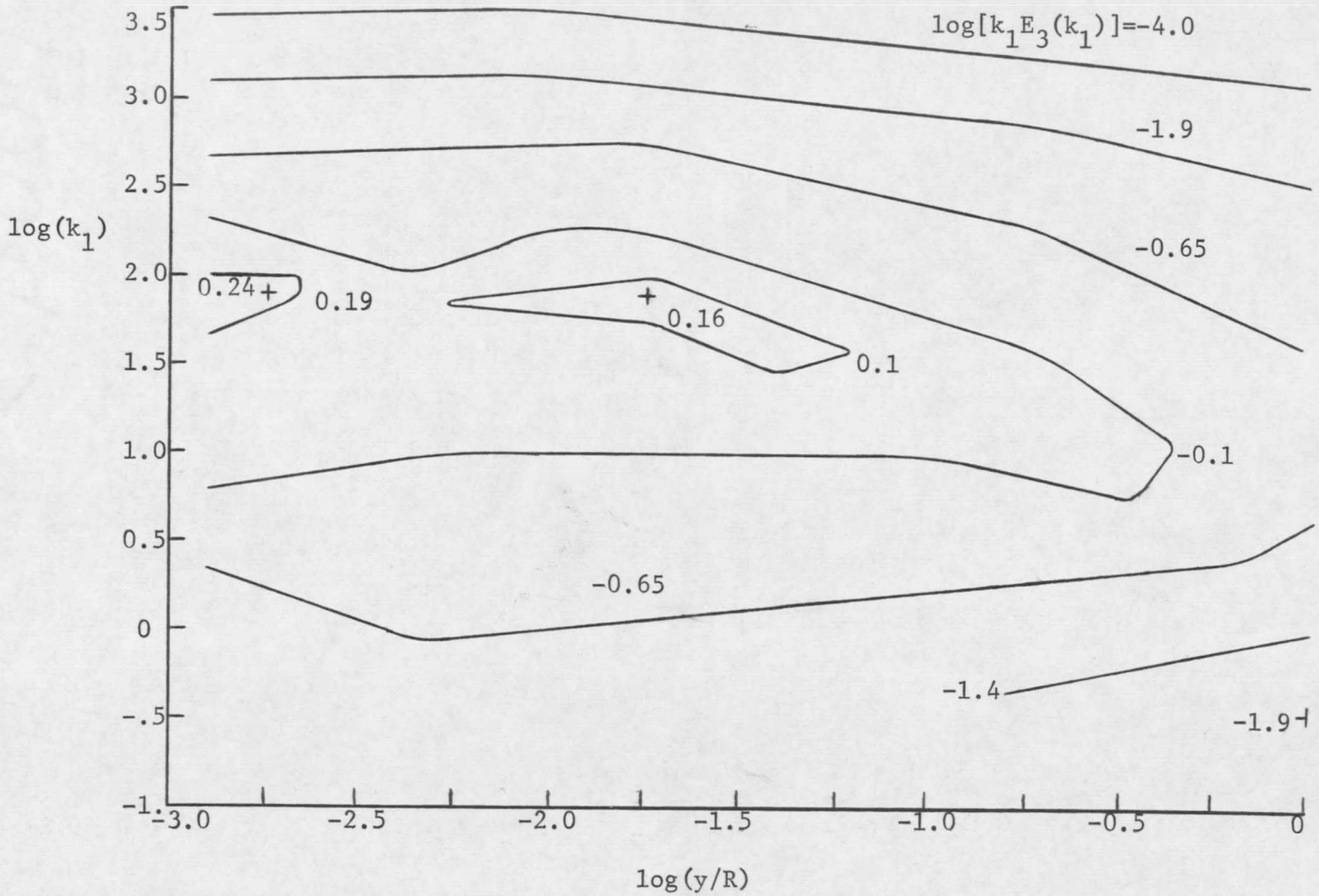

FIGURE 150. Production Subrange of Eddy Sizes for u_3 Velocity Fluctuations in Pipe With Small Roughness Elements

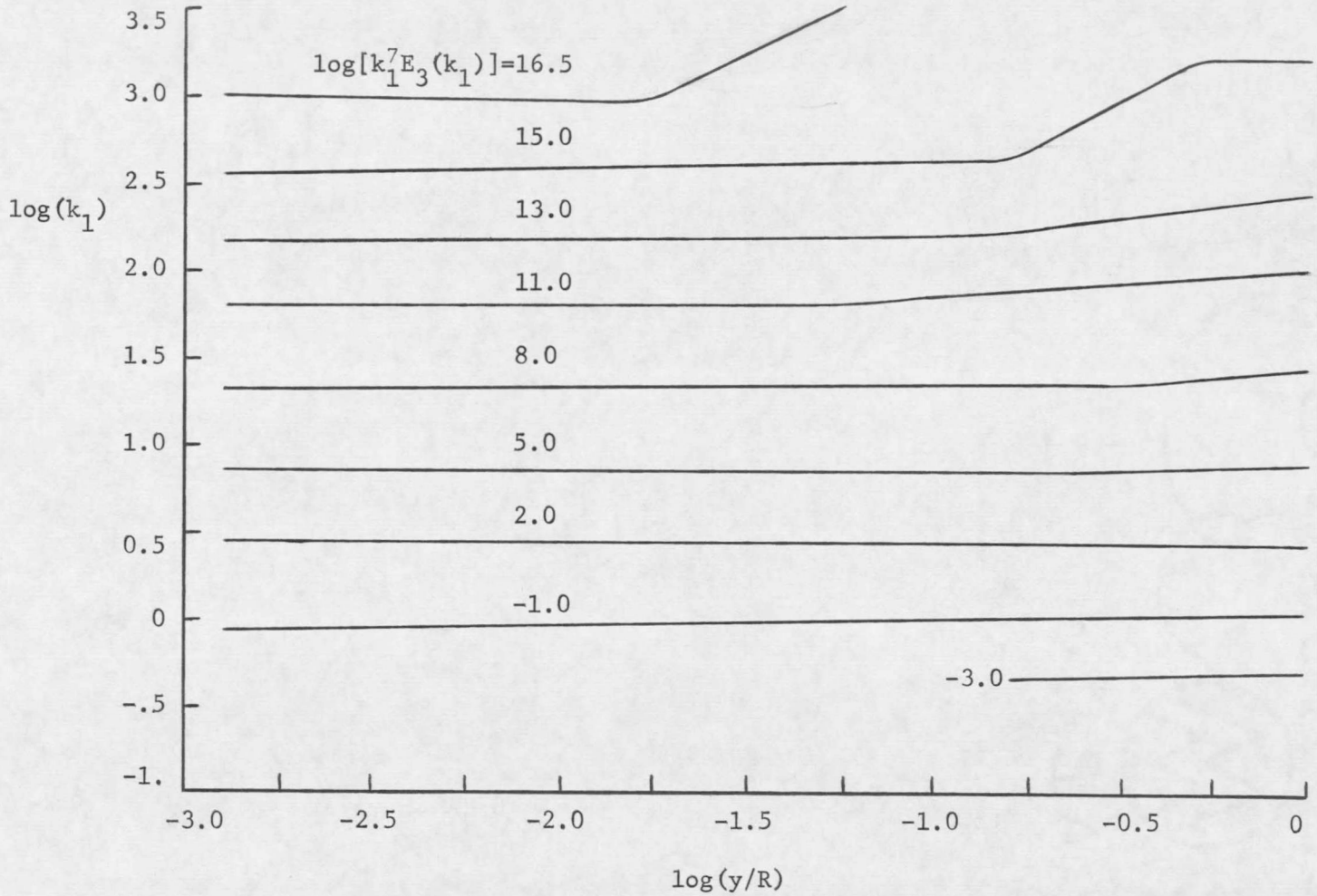

FIGURE 151. Viscous Subrange of Eddy Sizes for u_3 Velocity Fluctuations in Pipe With Small Roughness Elements

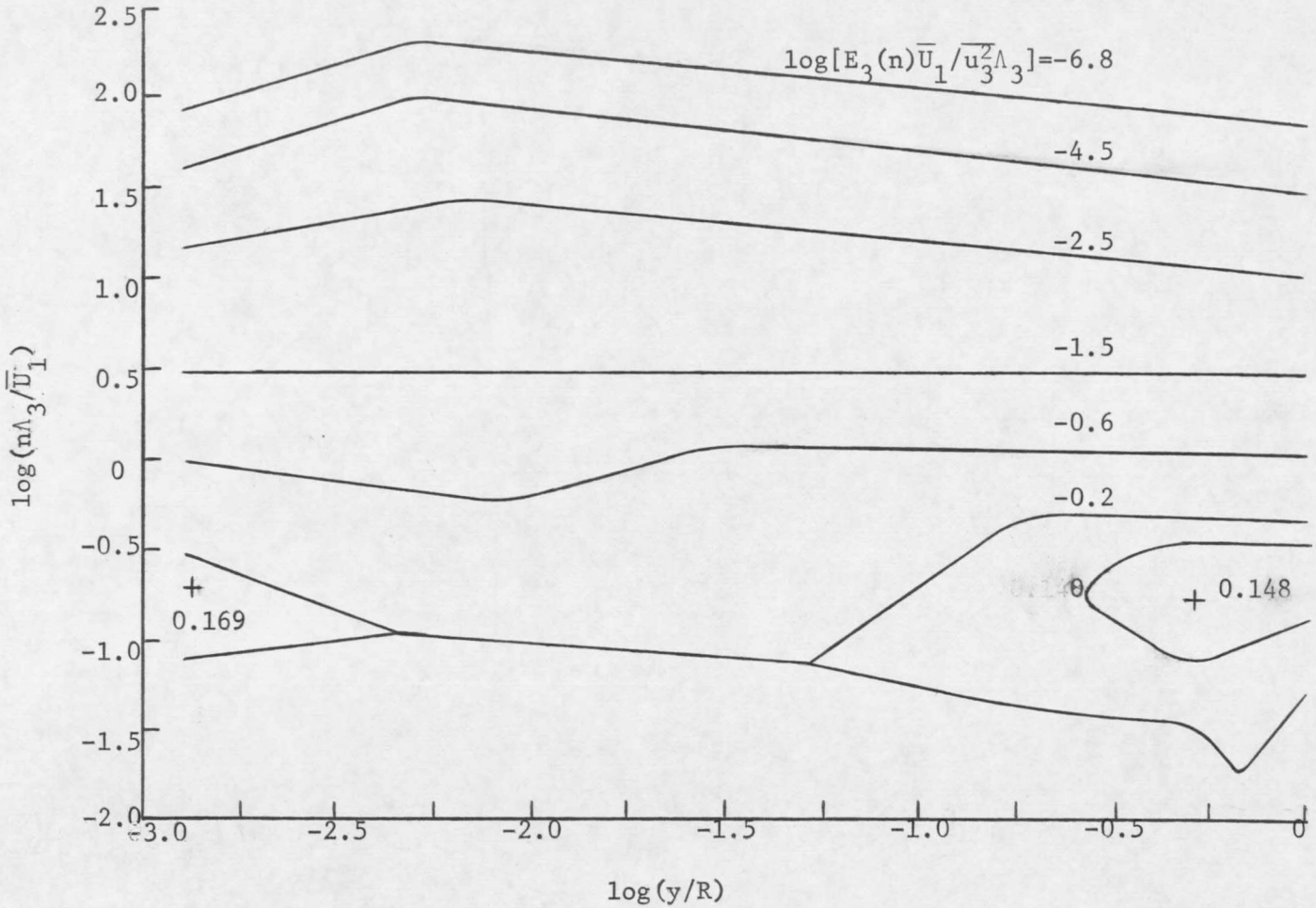

FIGURE 152. u_3 Spectra for Flow in Pipe With Small Roughness Elements Normalized as Suggested by Robertson et al [47]

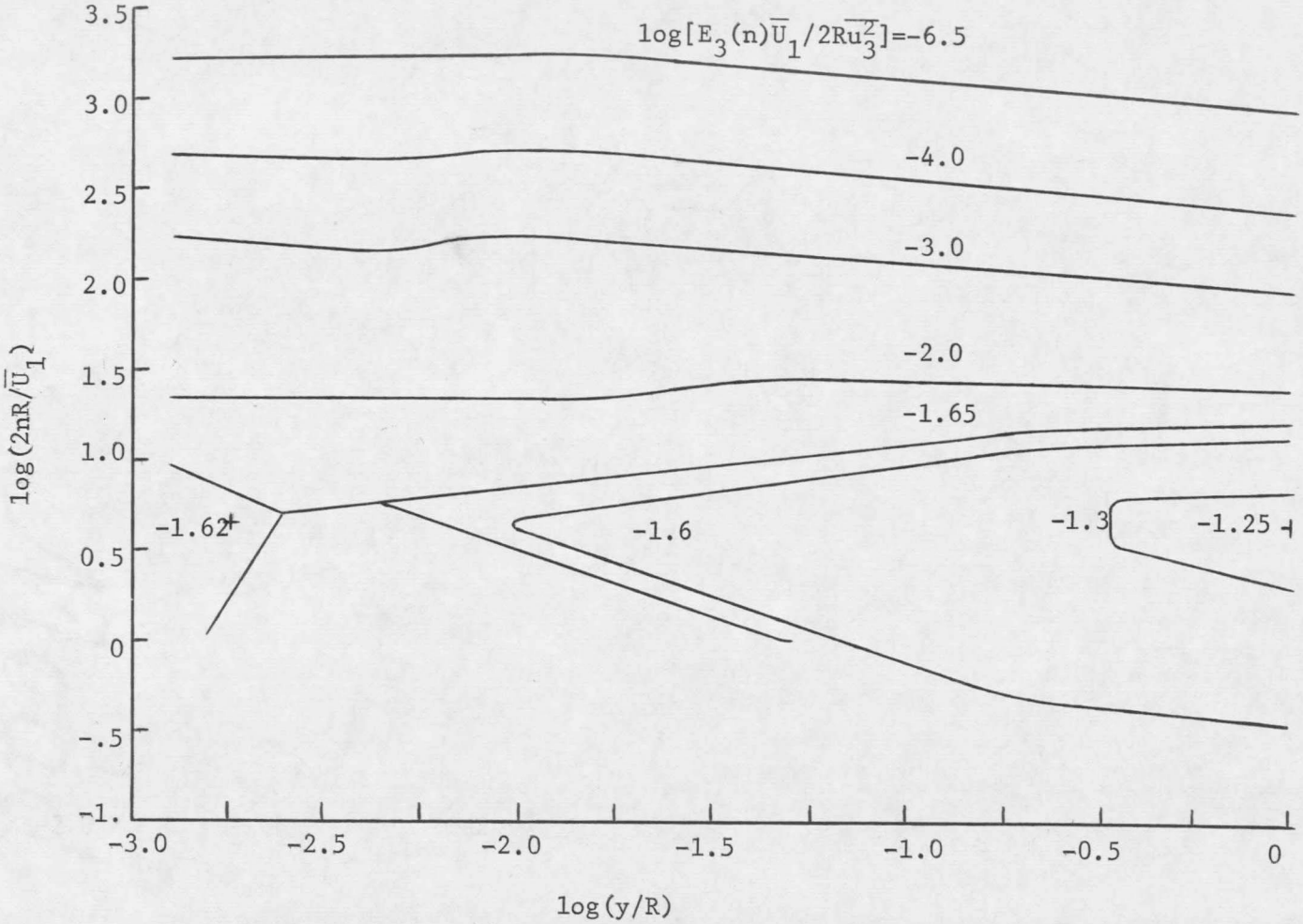

FIGURE 153. u_3 Spectra for Flow in Pipe With Small Roughness Elements Normalized as Suggested by Goma and Gelhar[30]

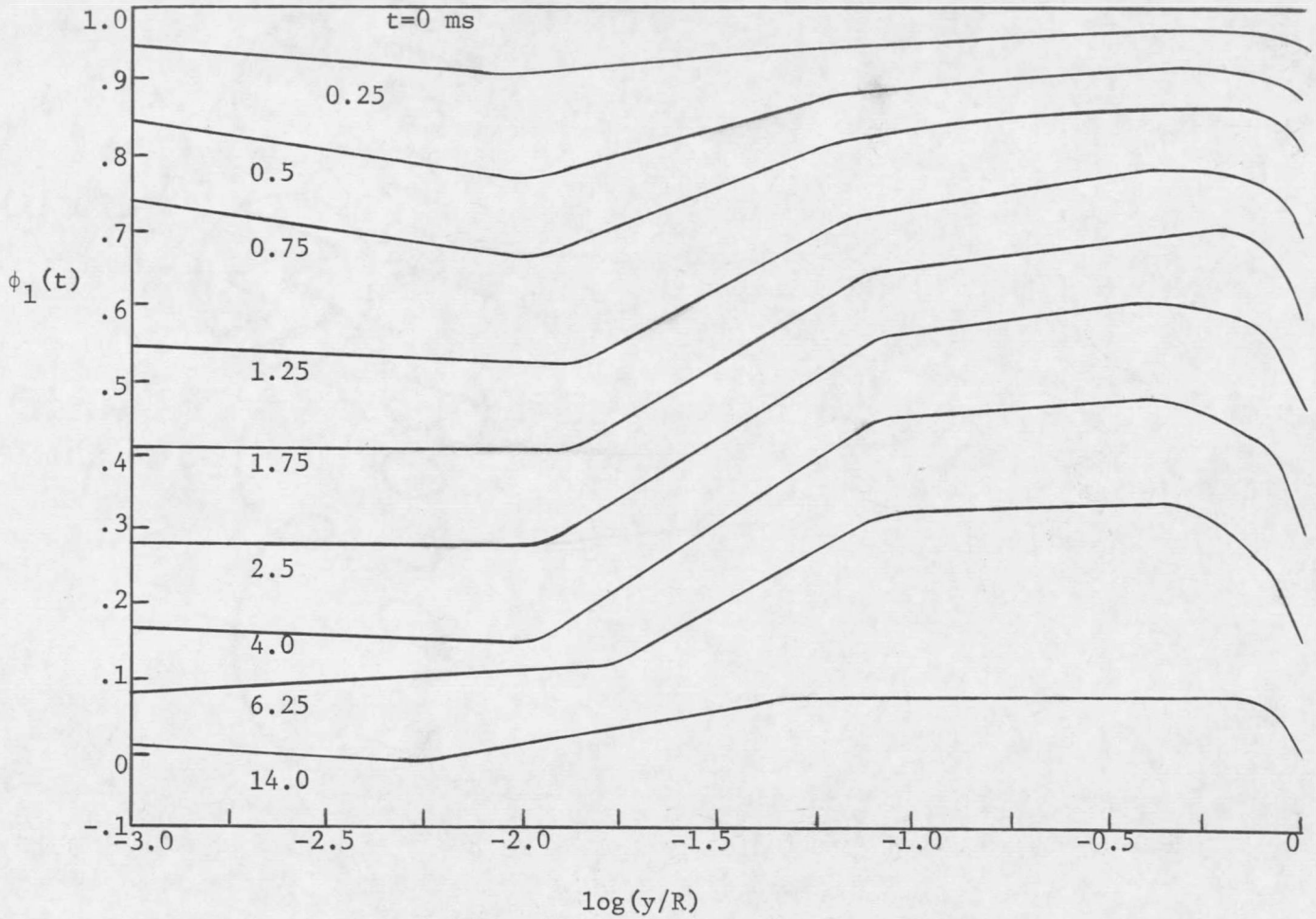

FIGURE 154. Autocorrelation Function for u_1 Velocity Fluctuations in Pipe With Small Roughness Elements

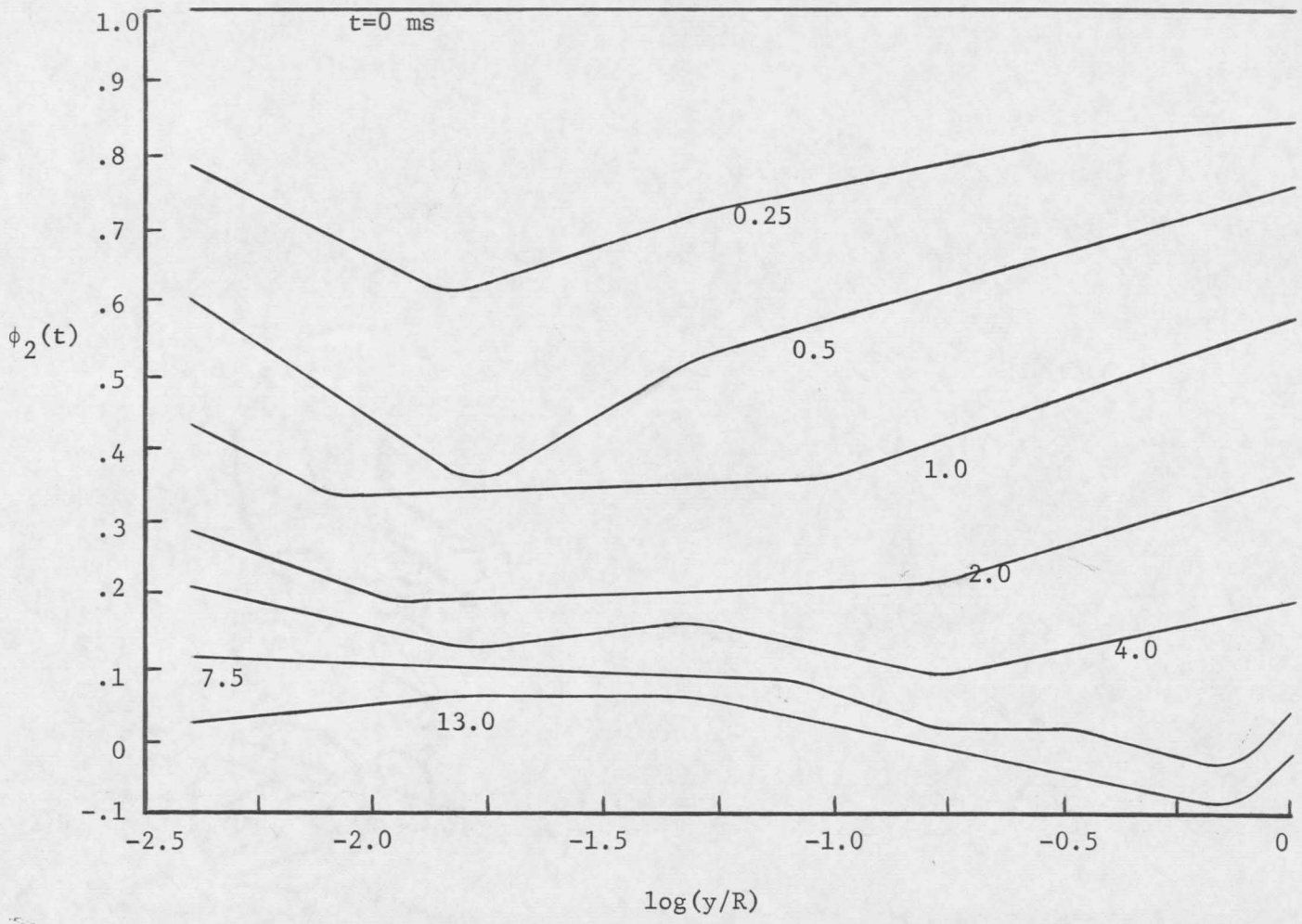

FIGURE 155. Autocorrelation Function for u_2 Velocity Fluctuations in Pipe With Small Roughness Elements

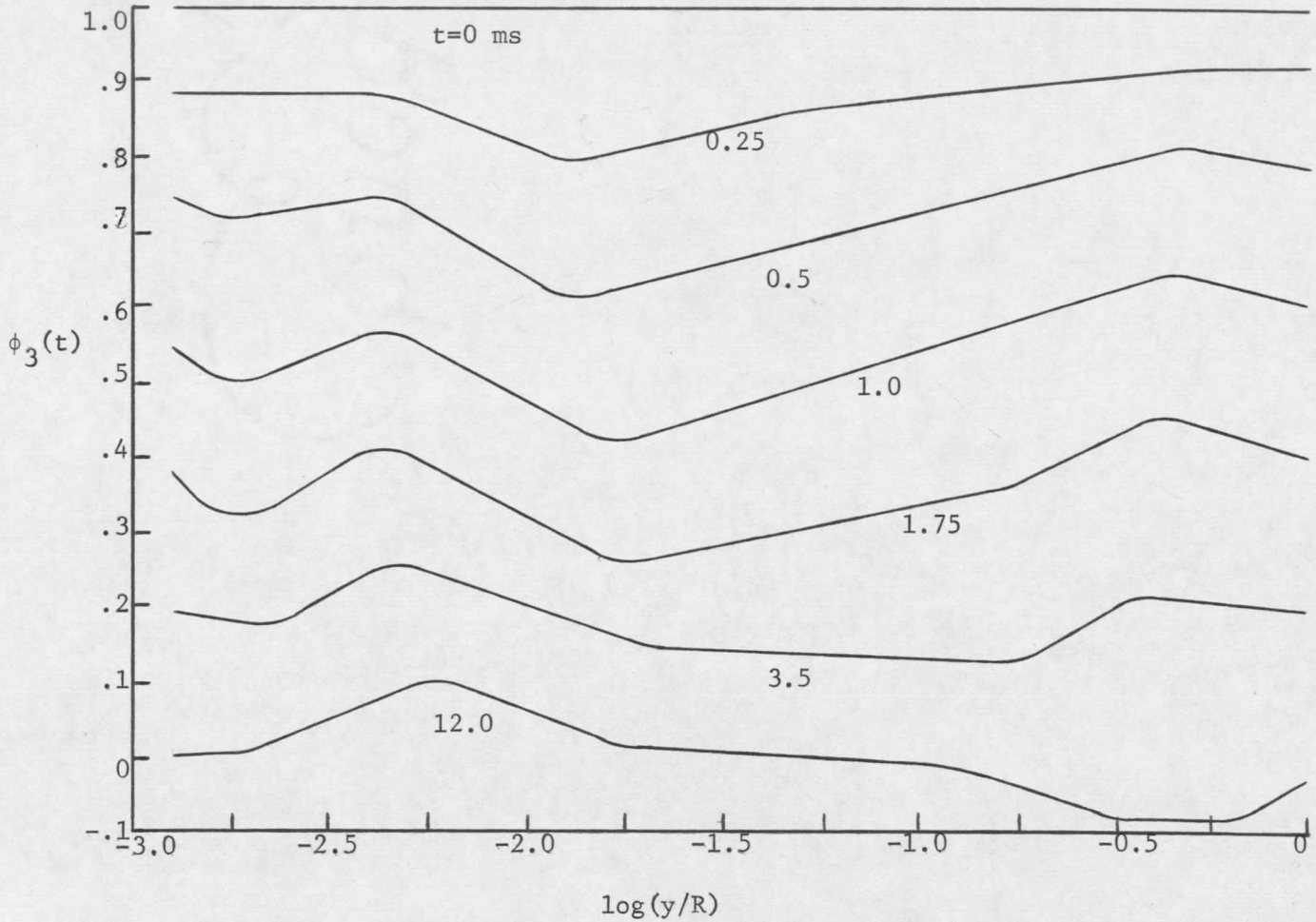

FIGURE 156. Autocorrelation Function for u_3 Fluctuating Velocity in Pipe With Small Roughness Elements

directions respectively. These figures indicate a generally similar behavior for ϕ_1, ϕ_2, and ϕ_3 in that, for a particular value of time, they all acquire a minimum value just beyond the mean height of the roughness elements and then increase as either the wall or the center line is approached. This indicates that the curvature of ϕ_i with respect to time at t = 0 is smaller at this radial position than for other values of y/R. The resultant increasing curvature as the wall is approached is indicative of the increasingly dominant role of the low frequencies in this region. It may be recalled that Bakewell [68] has pointed out that this type of variation is consistent with the intuitive notion that the depth of penetration of the viscous sublayer by high frequency velocity fluctuations should be much lower than that for low frequency fluctuations. On the other hand, the increase in curvature of the autocorrelation functions in moving from the top of the roughness elements toward the center line is compatible with the spectral analysis where very large eddies were found to exist near the center of the pipe.

The behavior described in the preceding paragraph applies to all three autocorrelation functions with only minor modifications. The increase in curvature of the ϕ_1 function at t = 0 in the wall region is not quite as predominant as that of the other two functions. It may be inferred from this occurrence that high frequency u_1 velocity

fluctuations penetrate further into the wall region than do those of u_2 or u_3, as might be anticipated. Also, very near the axis of symmetry of the pipe, the curvature of ϕ_1 and ϕ_3 appears to decrease slightly while that of ϕ_2 continues to increase. This is suggestive of a slight reduction in eddy size in the x_1 and x_3 directions, while they continue to elongate in the x_2 direction. Throughout the majority of the pipe all three functions appear to approach zero asymptotically for a given value of y/R. However, near the center line, significant oscillations of ϕ_2 and ϕ_3 are observed in their approach to zero.

Turbulence Scales

Experimentally determined values of the Eulerian micro scale γ_i, which is a measure of the most rapid changes which occur in the u_i fluctuations, are presented in Figure 157 for the central core of the pipe and in Figure 158 for the wall region. The curves for all three micro scales have a somewhat similar shape, i.e., they all increase slightly, in moving from the center line toward the wall, until a maximum value is attained. This maximum occurs in the vicinity of y/R = 0.4 for γ_1 and γ_3 but is delayed until y/R ≈ 0.09 for γ_2. These micro scales then decrease until a minimum value occurs just above the roughness elements, and the values again show

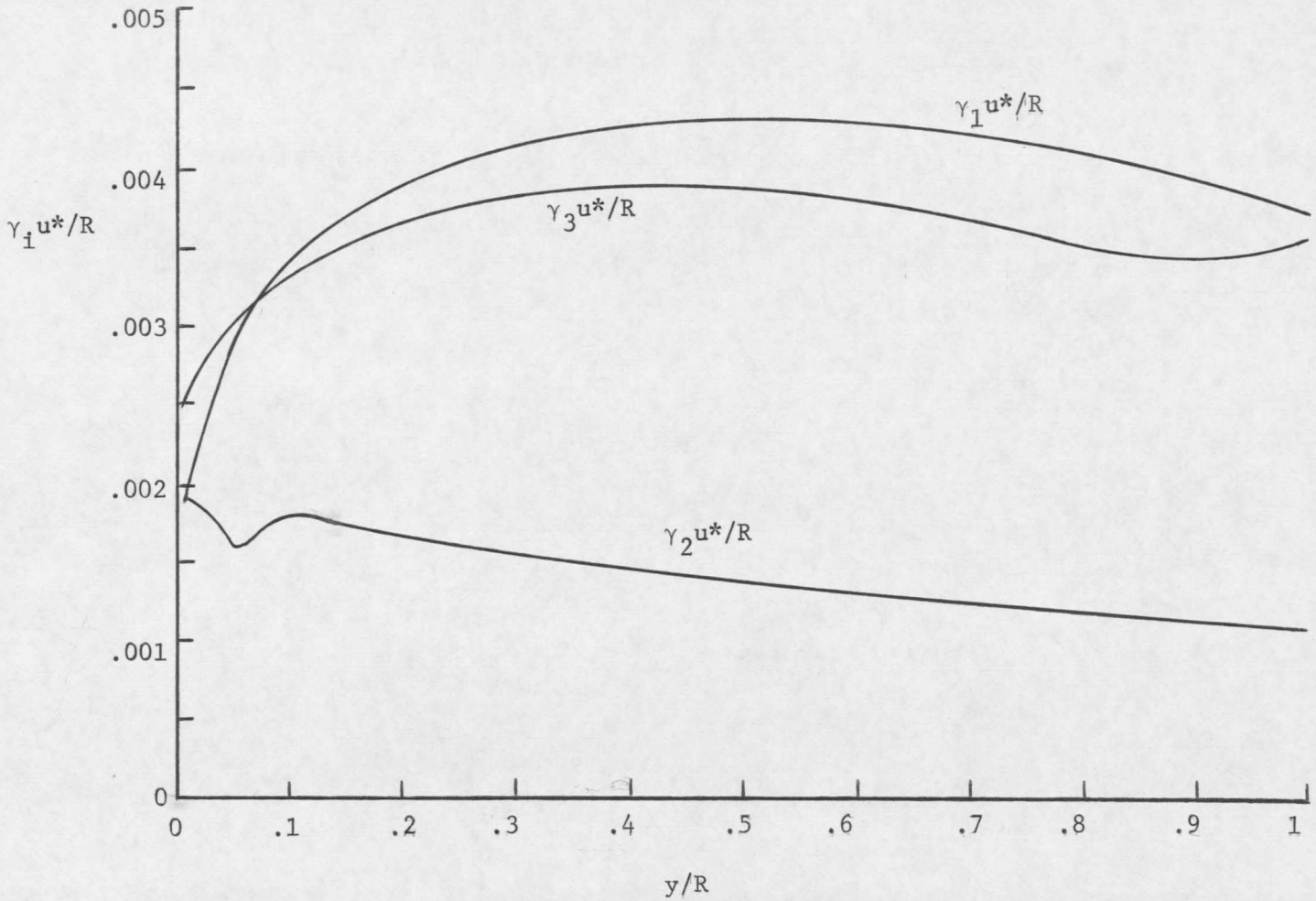

FIGURE 157. Eulerian Micro Scales in Central Region of Pipe With Small Roughness Elements

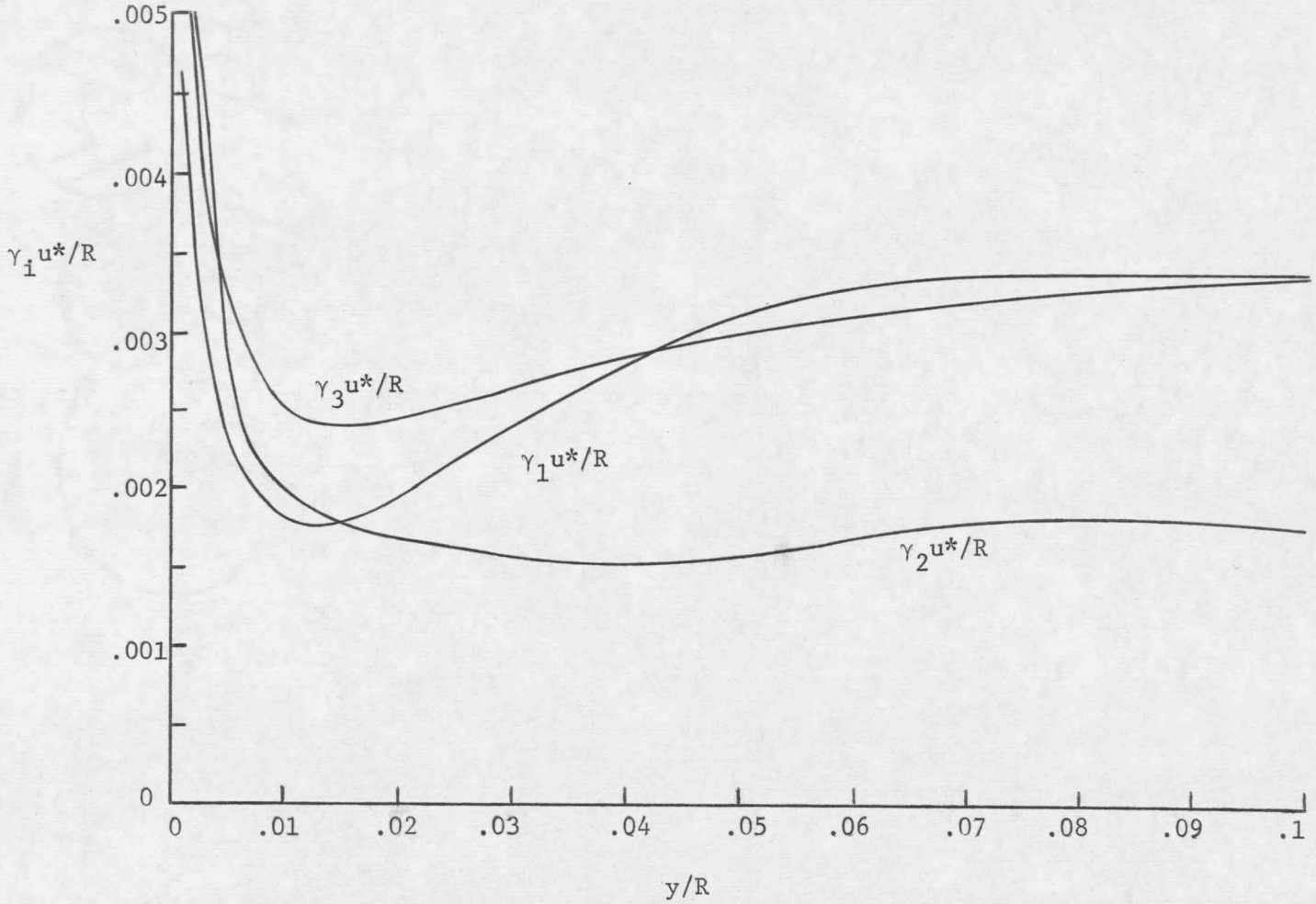

FIGURE 158. Eulerian Micro Scales in Wall Region of Pipe With Small Roughness Elements

an increase. This increase is in accord with the autocorrelation results where it was observed that the high frequency eddies could not penetrate deeply into the viscous sublayer. Except for points near the wall, γ_1 is seen to be larger than γ_3, which, in turn, is larger than γ_2. This indicates the presence of higher frequency fluctuations in the u_2 velocity than in either u_1 or u_3. However, just above the top of the roughness elements, γ_1 becomes smaller than either γ_2 or γ_3, thereby indicating the emergence of very high frequency components in the u_1 fluctuations.

A rough measure of the longest connection time in the behavior of the fluctuating velocities is the Eulerian macro scale, and values of this parameter for the core of the current pipe are presented in Figures 159, 160, and 161. Likewise, this same information for the wall region of the pipe is presented in Figures 162, 163, and 164. These figures indicate that the Eulerian macro scale is fairly constant in the central region of the pipe for all three coordinate directions. Near the wall T_2 shows a slight peak and then remains relatively constant, while T_1 decreases slightly and T_3 decreases very abruptly after reaching a peak value. The peaks in this curve are indicative of very low frequency components, and decreases in T_i denote the disappearance of such components. As in the case of the Eulerian micro scales, T_1 is observed to be largest

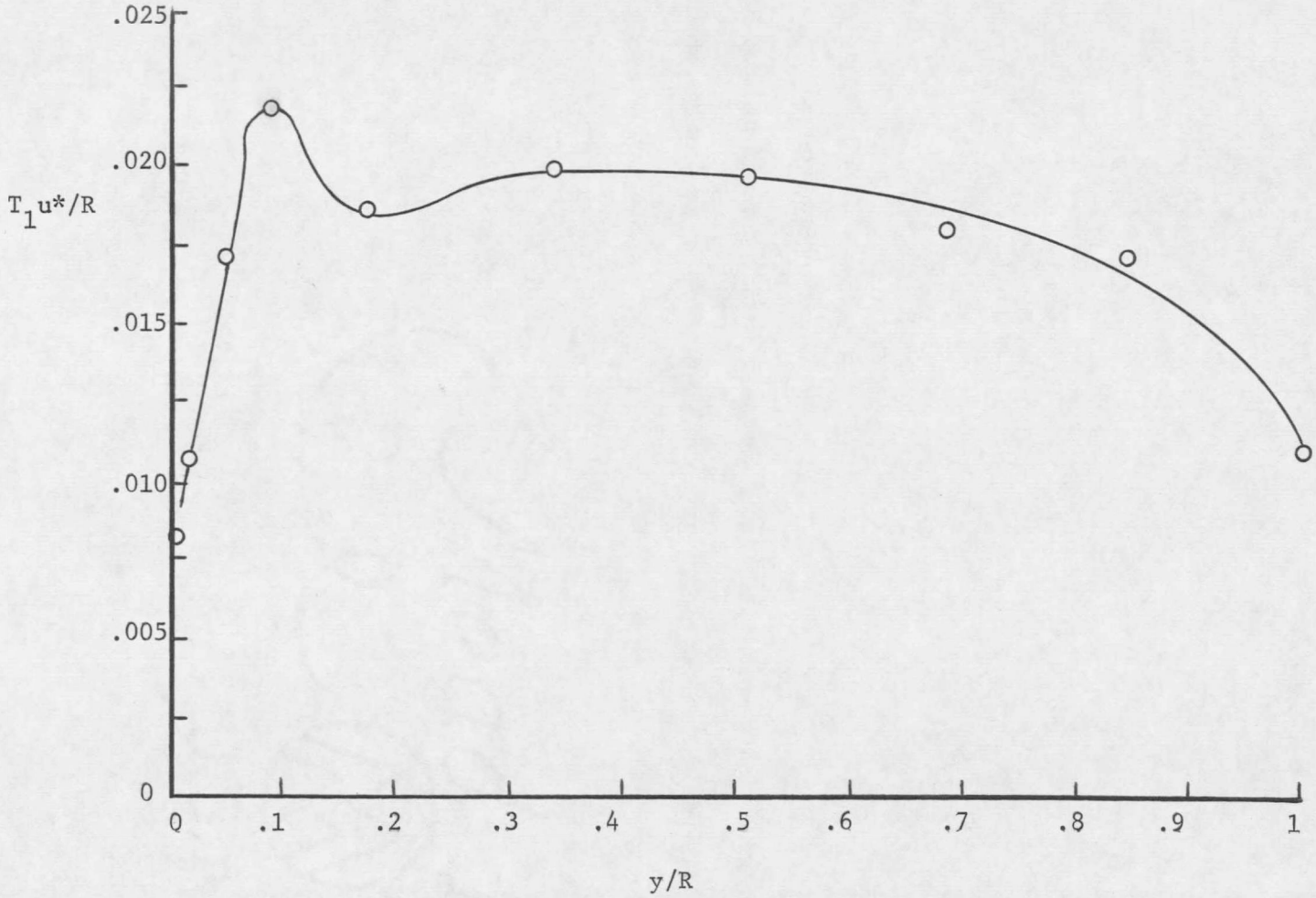

FIGURE 159. Eulerian Macro Scale in x_1 Direction for Central Region of Pipe With Small Roughness Elements

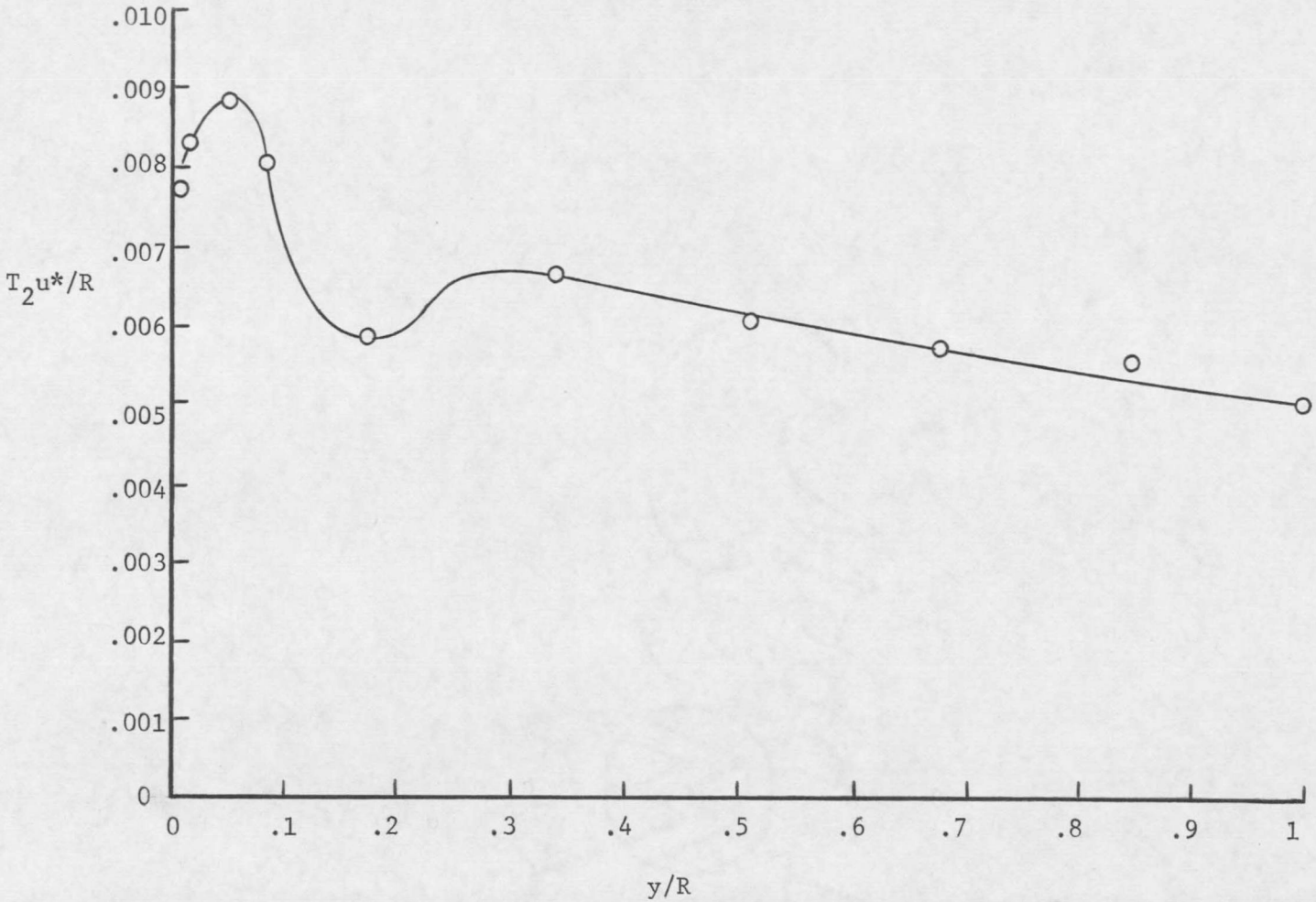

FIGURE 160. Eulerian Macro Scale in x_2 Direction for Central Region of Pipe With Small Roughness Elements

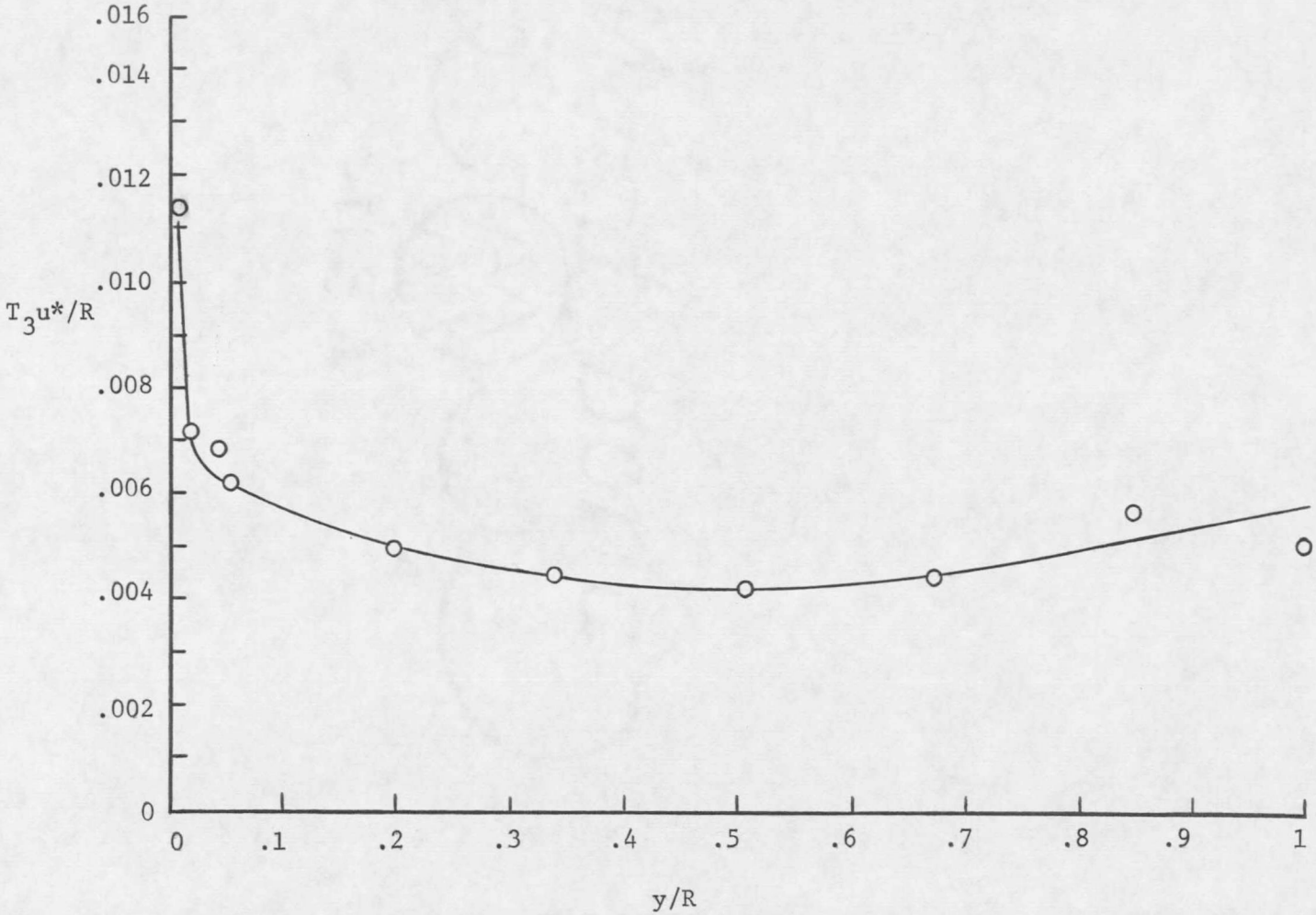

FIGURE 161. Eulerian Macro Scale in x_3 Direction for Central Region of Pipe With Small Roughness Elements

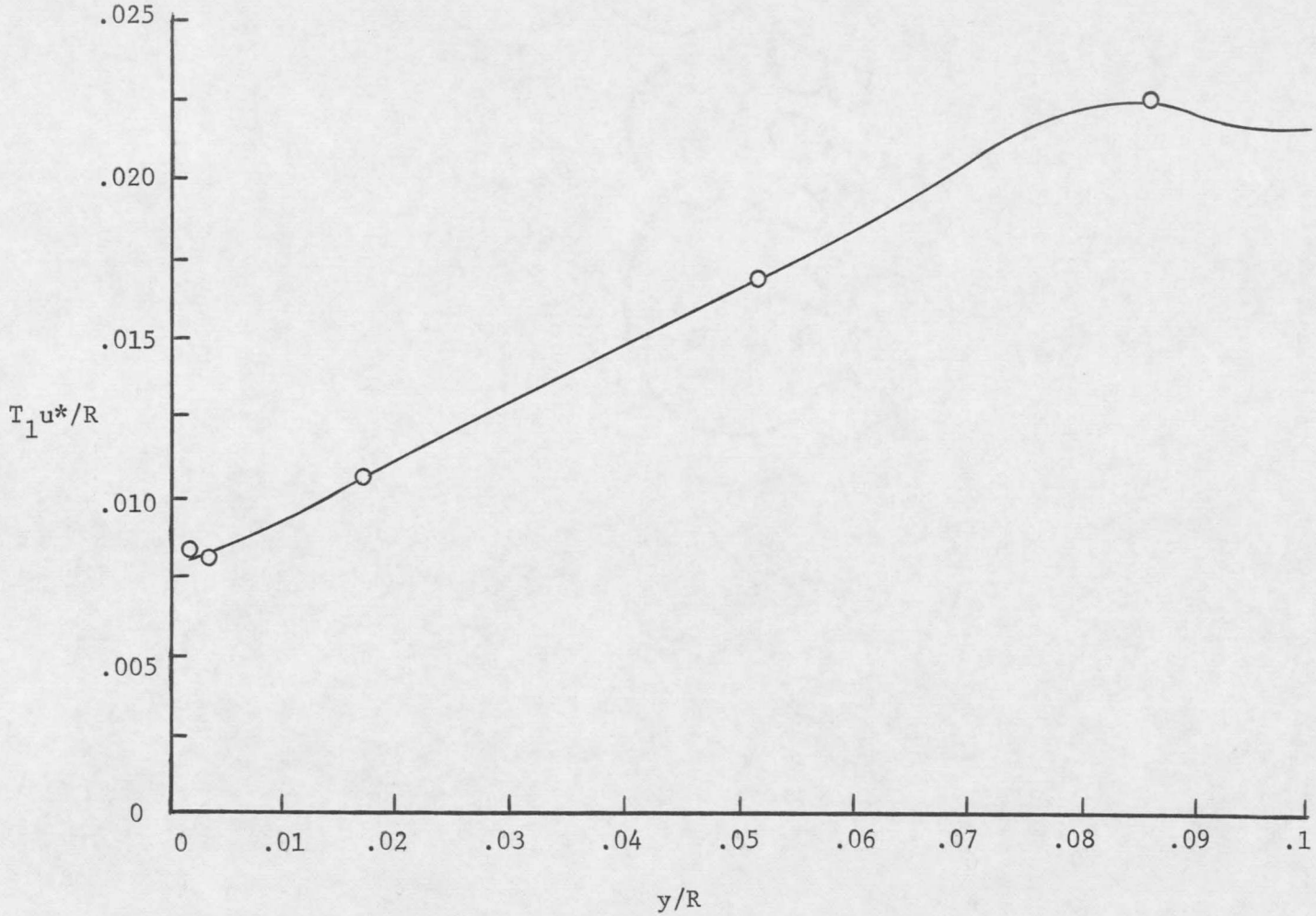

FIGURE 162. Eulerian Macro Scale in x_1 Direction for Wall Region of Pipe With Small Roughness Elements

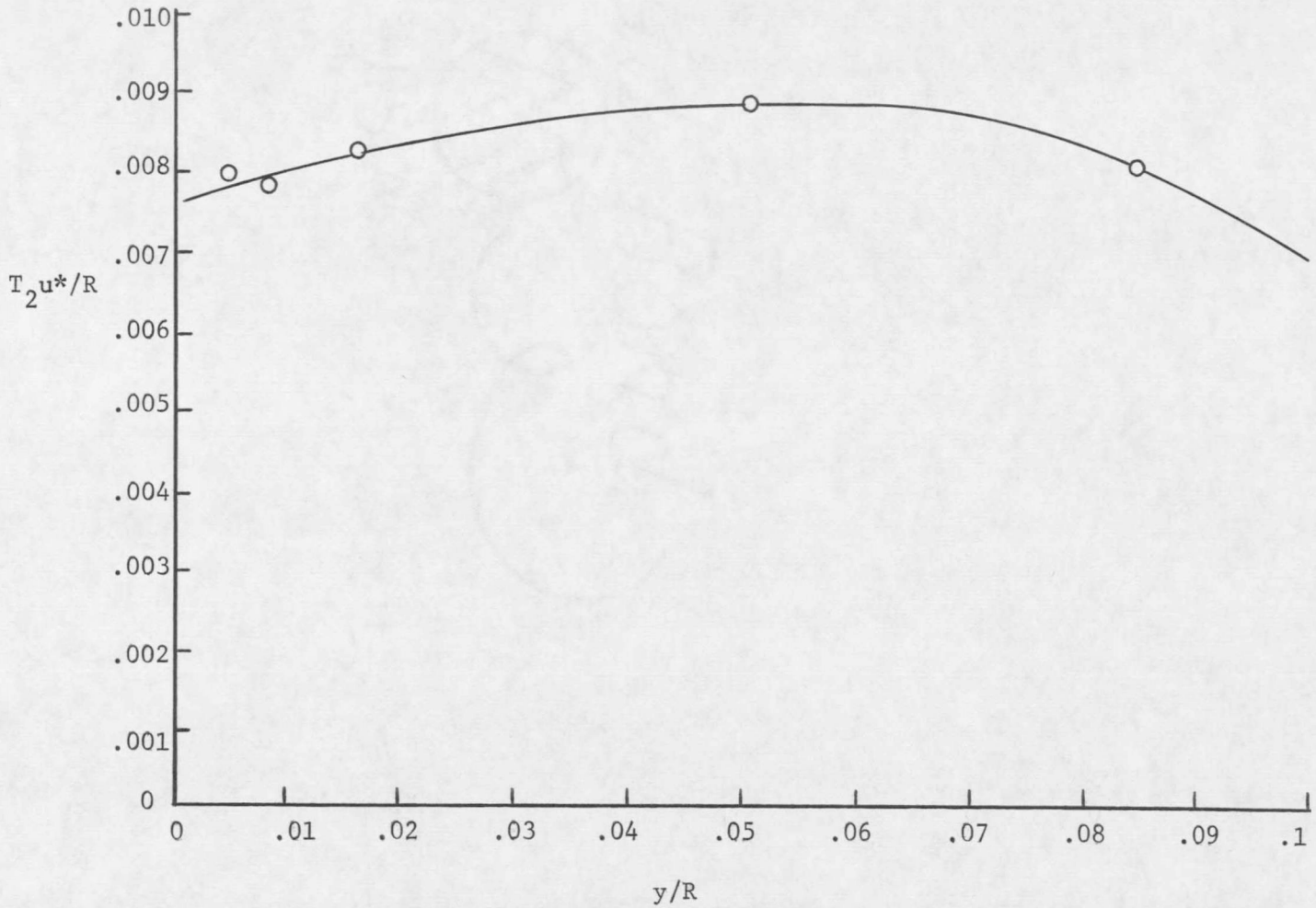

FIGURE 163. Eulerian Macro Scale in x_2 Direction for Wall Region of Pipe With Small Roughness Elements

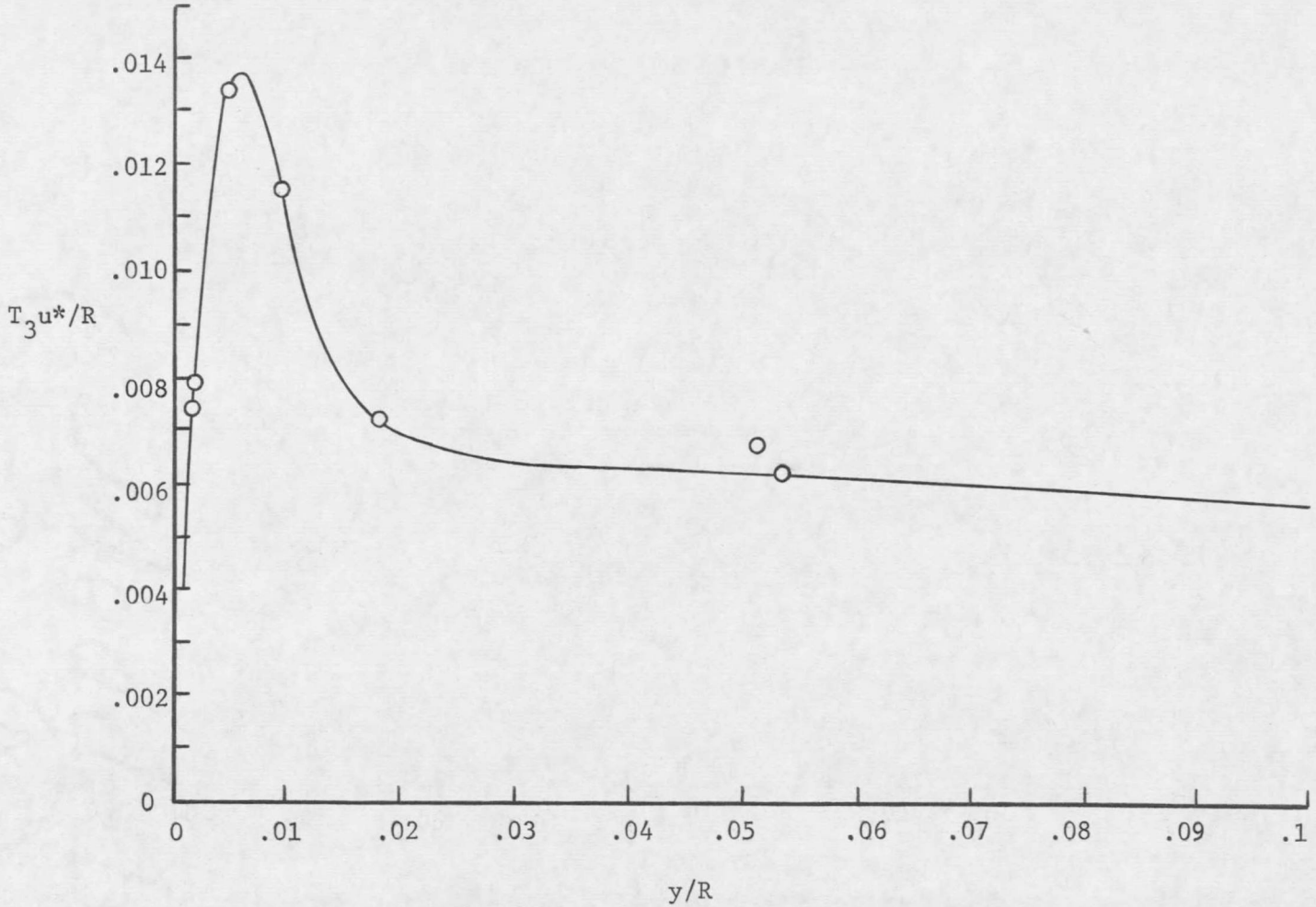

FIGURE 164. Eulerian Macro Scale in x_3 Direction in Wall Region of Pipe With Small Roughness Elements

through the central region of the pipe while T_2 is smallest, though only slightly smaller than T_3.

Transformation of the Eulerian micro scales into the spatial micro scales is indicated by Figures 165 and 166. The spatial micro scales, which reveal the average dimensions of the smallest eddies in the flow field, are seen to generally increase with distance from the wall to a maximum value near the mid radial position. A slight decrease then occurs in proceeding to the center line. This behavior is indicative of a decrease in the size of the viscous dissipation eddies as the wall is approached. Throughout the central region of the pipe, it is seen that these eddies are longest in the x_1 direction and shortest in the x_2 direction. Near the roughness elements, however, there is a decrease in elongation in the x_1 direction and an increase in the x_2 direction. This may be due to the breakup of long eddies in the longitudinal direction by the roughness elements at the same time that cells become interwoven with these elements, thereby causing a stretching action in the x_2 direction.

The variation of the spatial macro scale in the x_1 direction is shown in Figure 167, while variations of the Λ_2 and Λ_3 macro scales are shown in Figure 168. These macro scales, which are indicative of the size of the largest eddies in the flow field, are seen to be relatively constant over the central and major portion of the flow

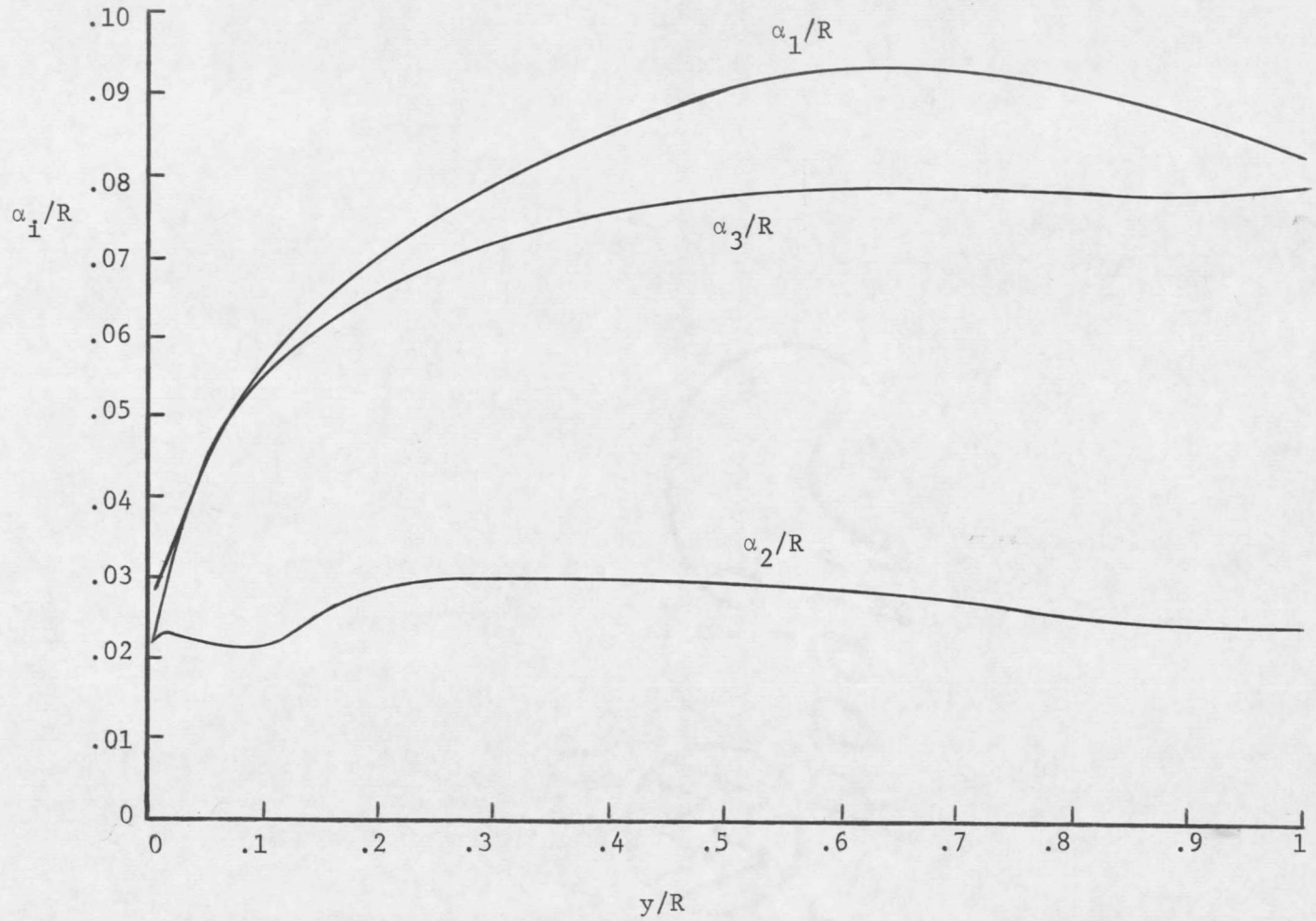

FIGURE 165. Spatial Micro Scales for Central Region of Tube With Small Roughness Elements

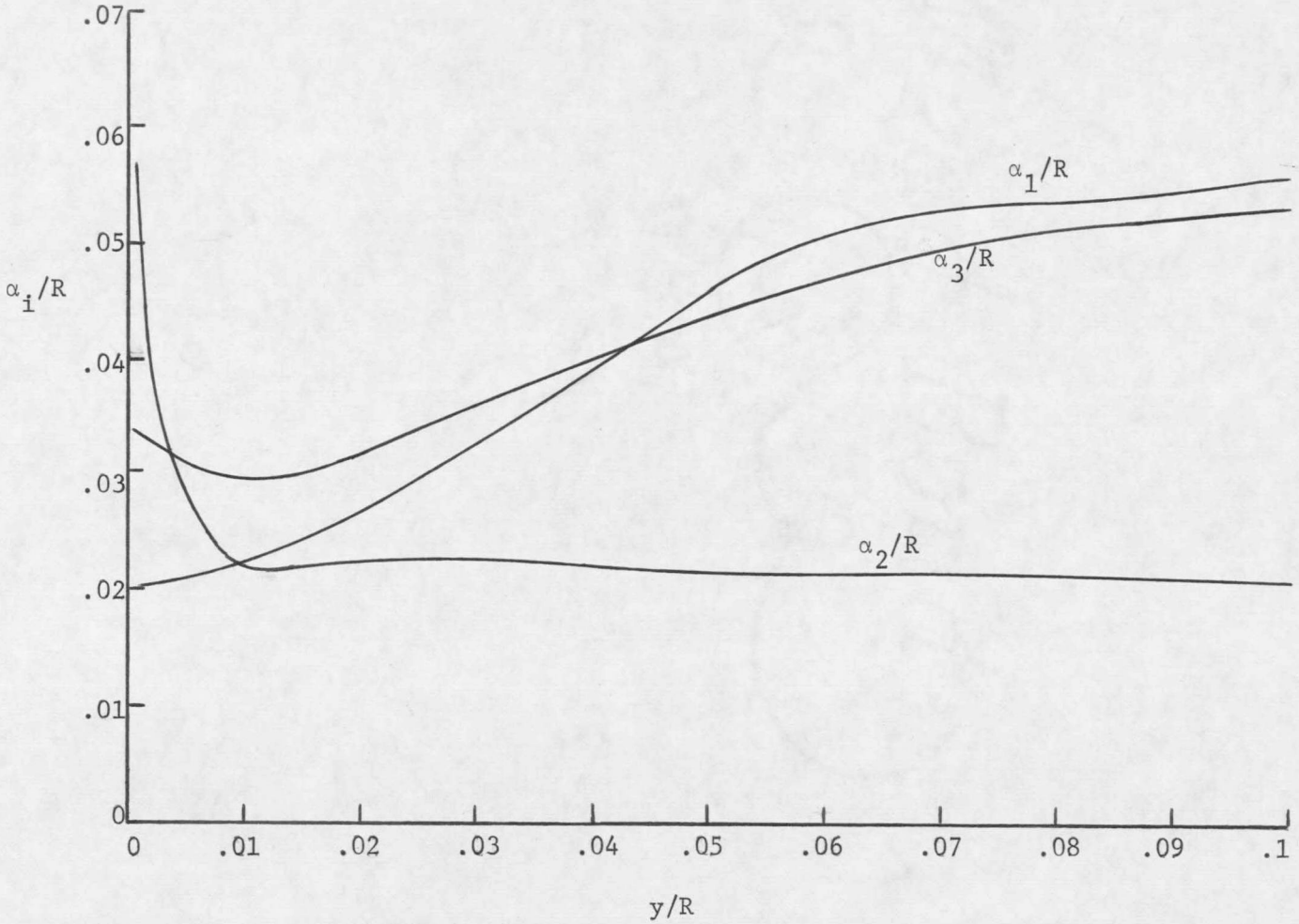

FIGURE 166. Spatial Micro Scales for Wall Region of Pipe With Small Roughness Elements

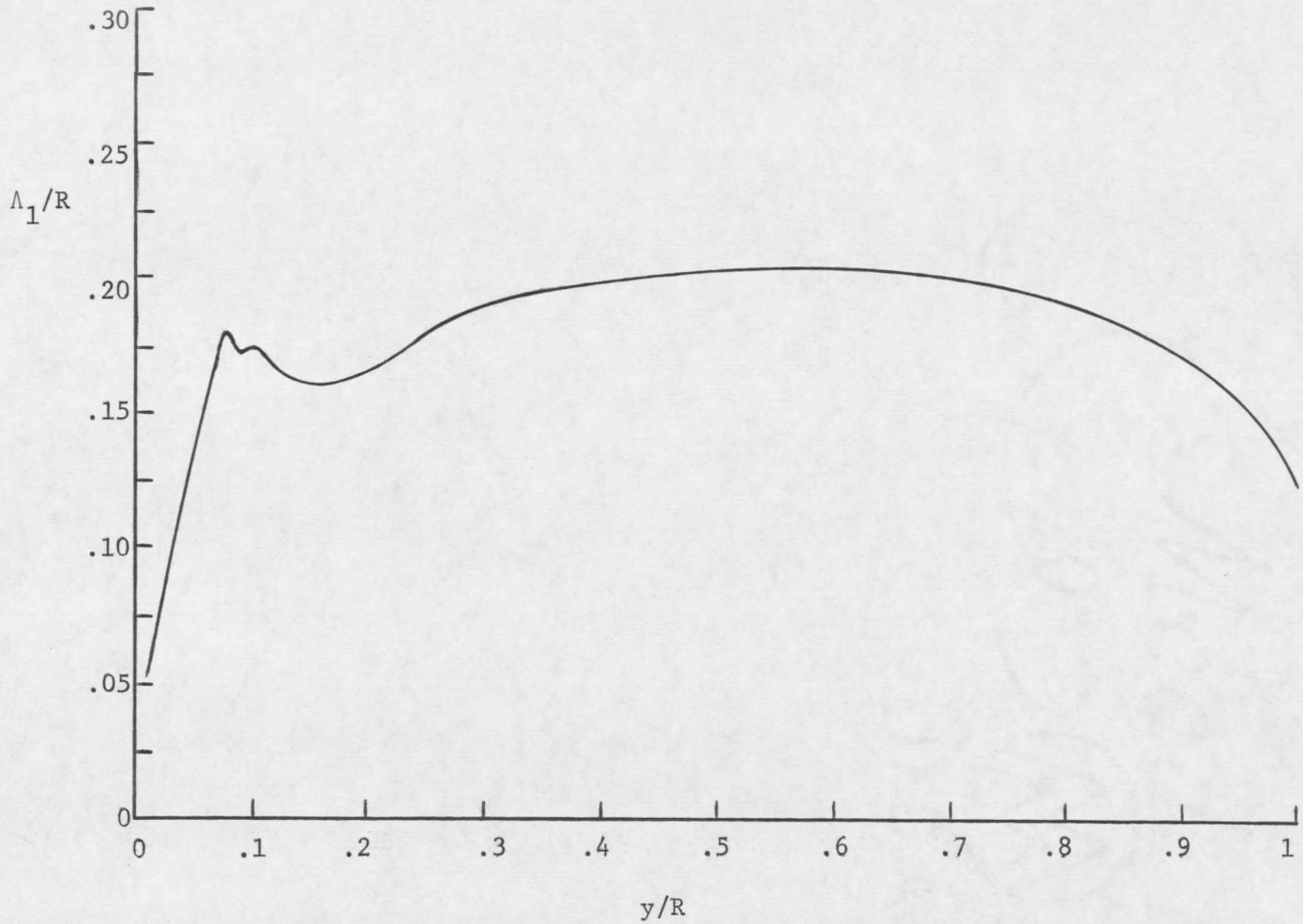

FIGURE 167. Spatial Macro Scale in x_1 Direction for Pipe With Small Roughness Elements

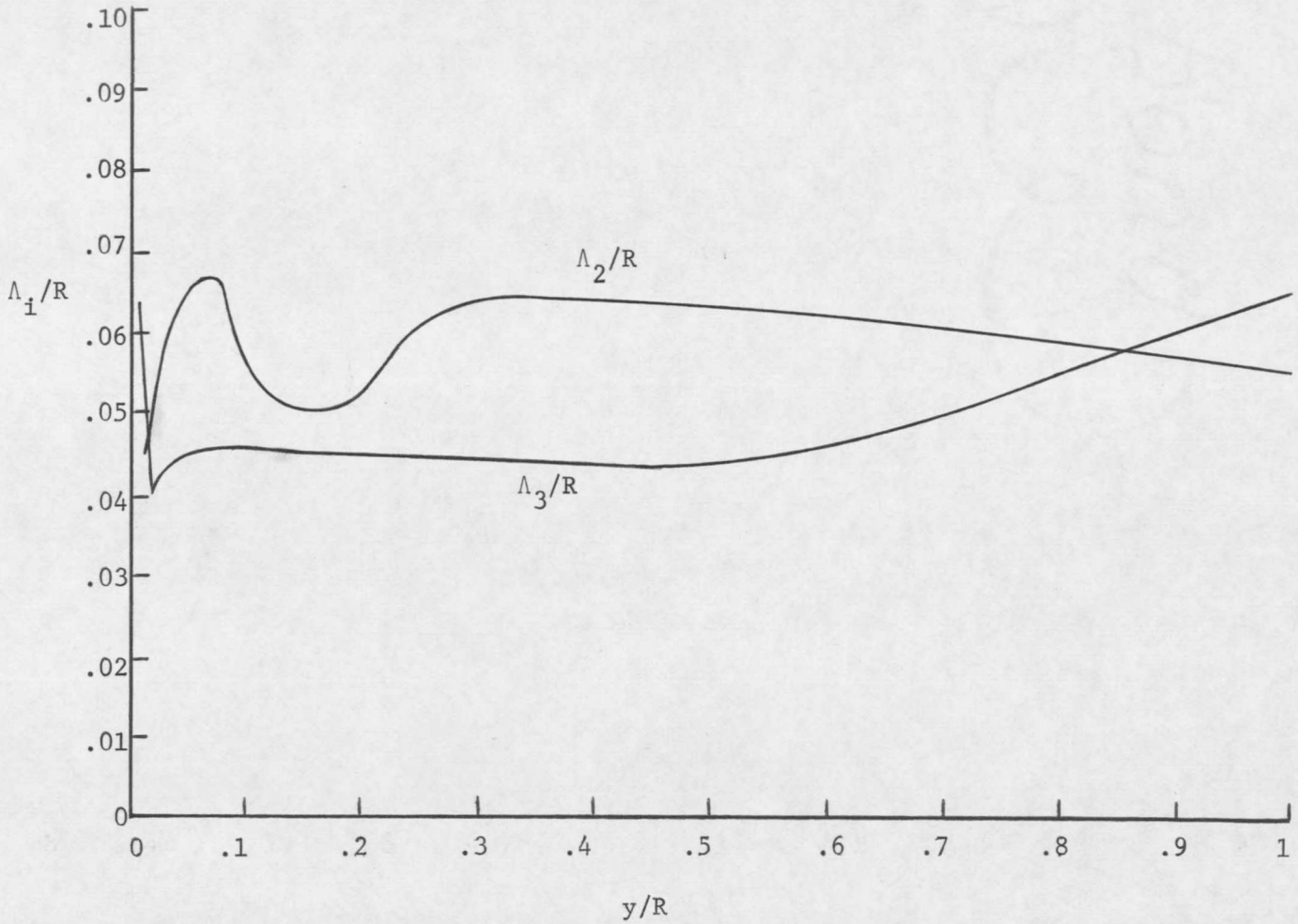

FIGURE 168. Spatial Macro Scales in x_2 and x_3 Directions For Tube With Small Roughness Elements

field. The magnitudes of these macro scales reveal the existence of large eddies which are very elongated in the axial direction. Near the roughness particles, a sharp decrease of elongation in the x_1 direction of the large cells occurs, just as was the case with the small cells. It should be noted that the magnitude of the spatial macro scale in the longitudinal direction determined in this investigation for flow in a rough pipe is in excellent agreement with the value of about 0.15R found by McQuivey and Richardson [69] for flow near a rough surface in an open channel.

CHAPTER VIII

RESULTS FOR LARGE ROUGHNESS

Mean Velocity and Flow Resistance

In utilizing the pipe containing the large roughness elements, measurements were first made of friction factor versus Reynolds number over a wide range of Reynolds numbers in order to establish the equivalent sand diameter. As in previous cases, Gow's [15] data indicated that K was independent of Reynolds number and equal to about 0.312. Thus, pressure measurements employed in conjunction with equation (6.1) yielded the λ-Re data shown in Figure 169, where the solid line is Prandtl's universal friction factor relationship for turbulent flow in a smooth tube, equation (2.35). The experimental measurements presented in Figure 169 indicate that flow in the pipe containing the large roughness elements does follow the type of behavior shown by Nikuradse [2] with his larger sand grains, i.e., there is an abrupt rise from the smooth pipe line without the dip characteristic of smaller roughnesses for the transition regime. The friction factor then becomes independent of Reynolds number in the fully rough flow regime.

Utilization of the data from the fully rough flow regime, together with equation (2.44), allowed the determination of the equivalent sand diameter, k_s, as 0.52 inches. Although this value of k_s is about

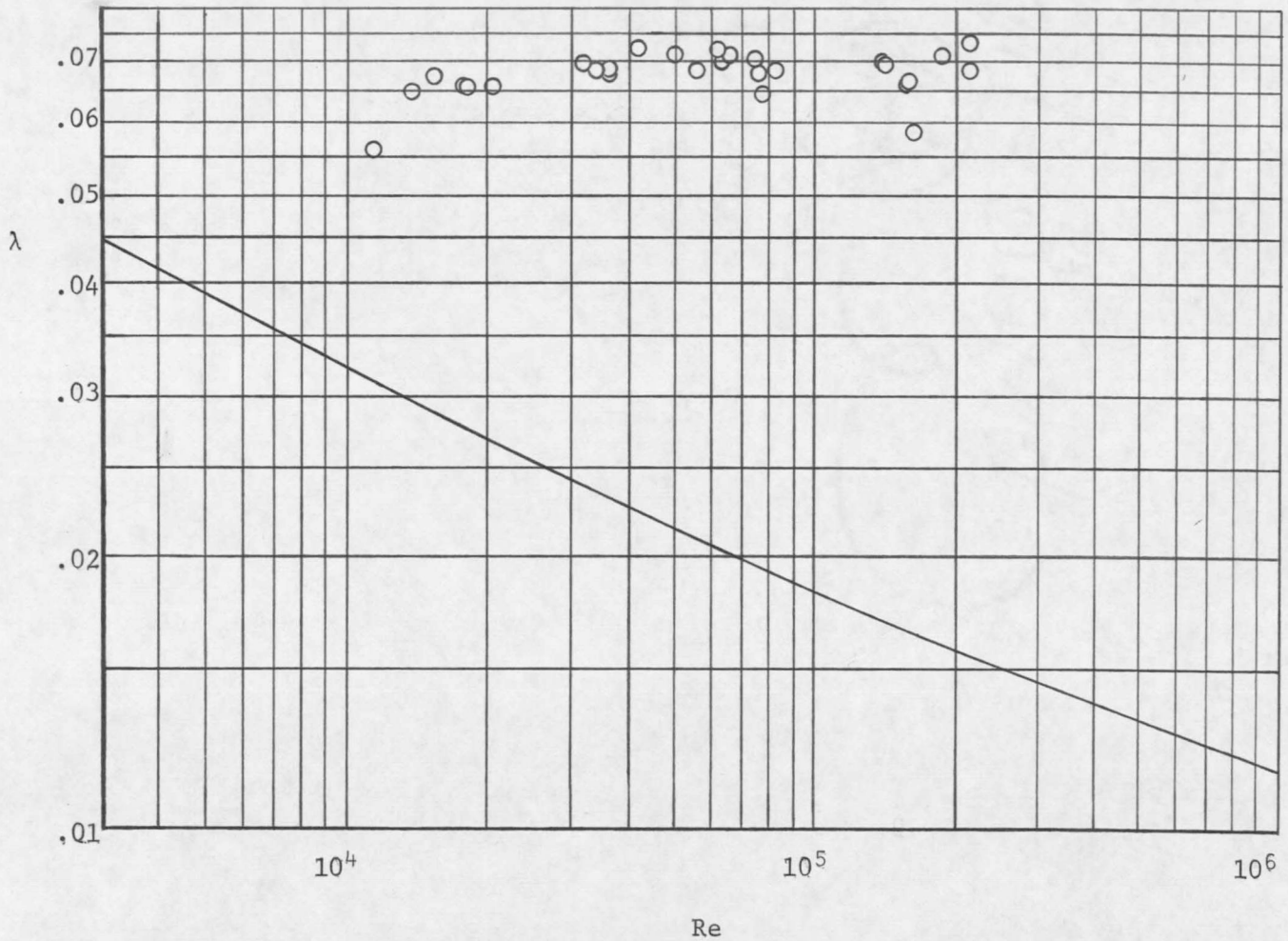

FIGURE 169. Flow Resistance Characterization for Large Roughness

2.3 times as large as the actual mean height of the roughness elements, this result is consistent with the findings of many previous investigators, as pointed out in the literature review. All experimental data obtained for this pipe were at a Reynolds number of 165,000 yielding a value of y^+ at the center line of 7050, and it may be observed from Figure 169 that this Reynolds number yields flow which is well into the fully rough flow regime.

Experimental measurements of the longitudinal mean velocity profile in the turbulent core of this pipe are presented in Figure 170, and such measurements for the wall region are shown in Figure 171. As in the case of the pipe containing the small roughness elements, a slight rise is noted in the mean velocity profile below the tops of the roughness elements, and thus linear interpolation of the experimental data would indicate a nonzero velocity at the wall. This is consistent with the supposition made in the previous chapter that there is an increased heat loss to the solid surface due to the presence of the roughness elements. However, no adverse effect on the experimental data is anticipated since this phenomenon occurs below the top of the sand grains.

Fluctuating Velocities

The rms values of the fluctuating velocities in the three

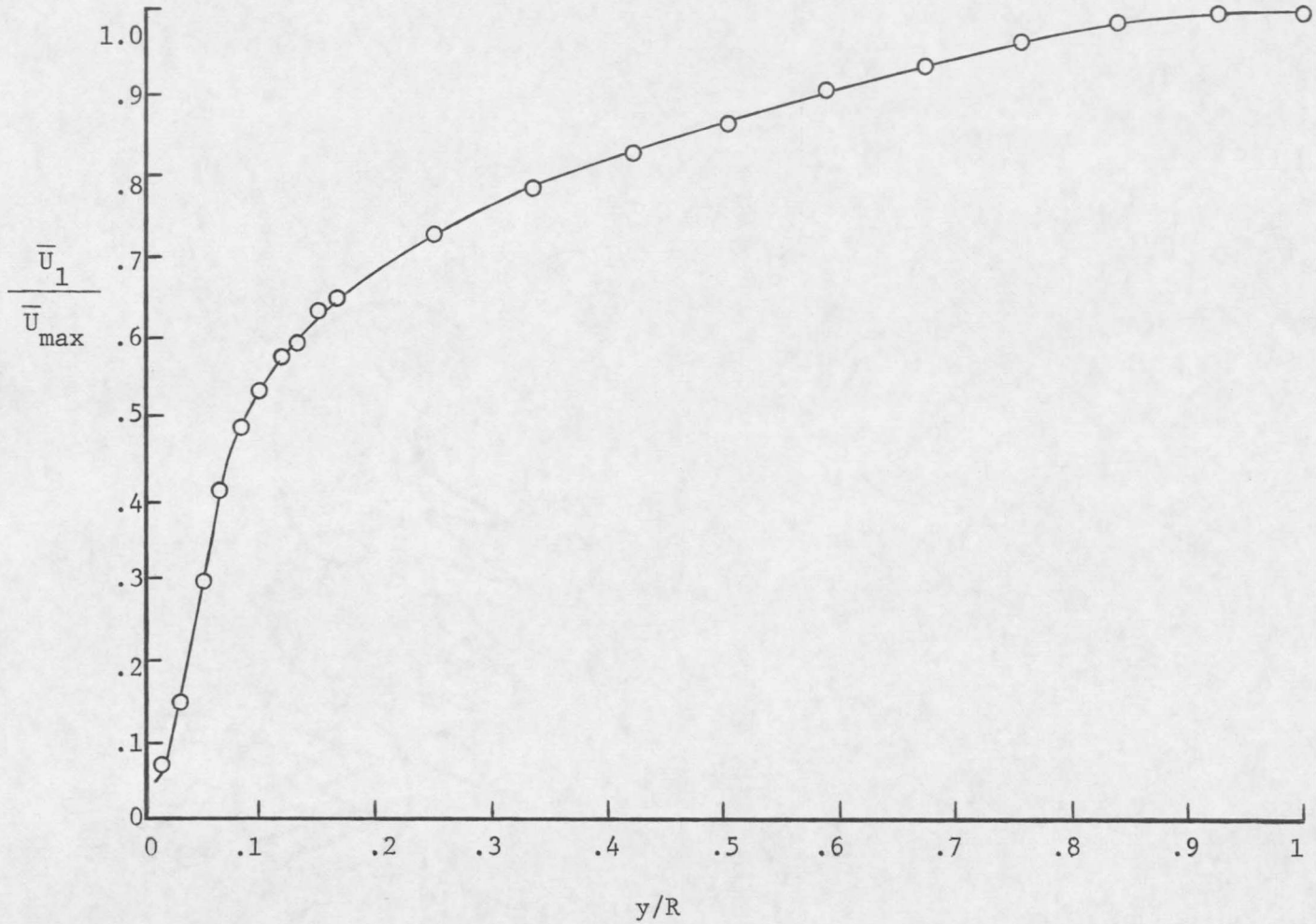

FIGURE 170. Longitudinal Mean Velocity Progile in Central Region of Pipe With Large Roughness Elements

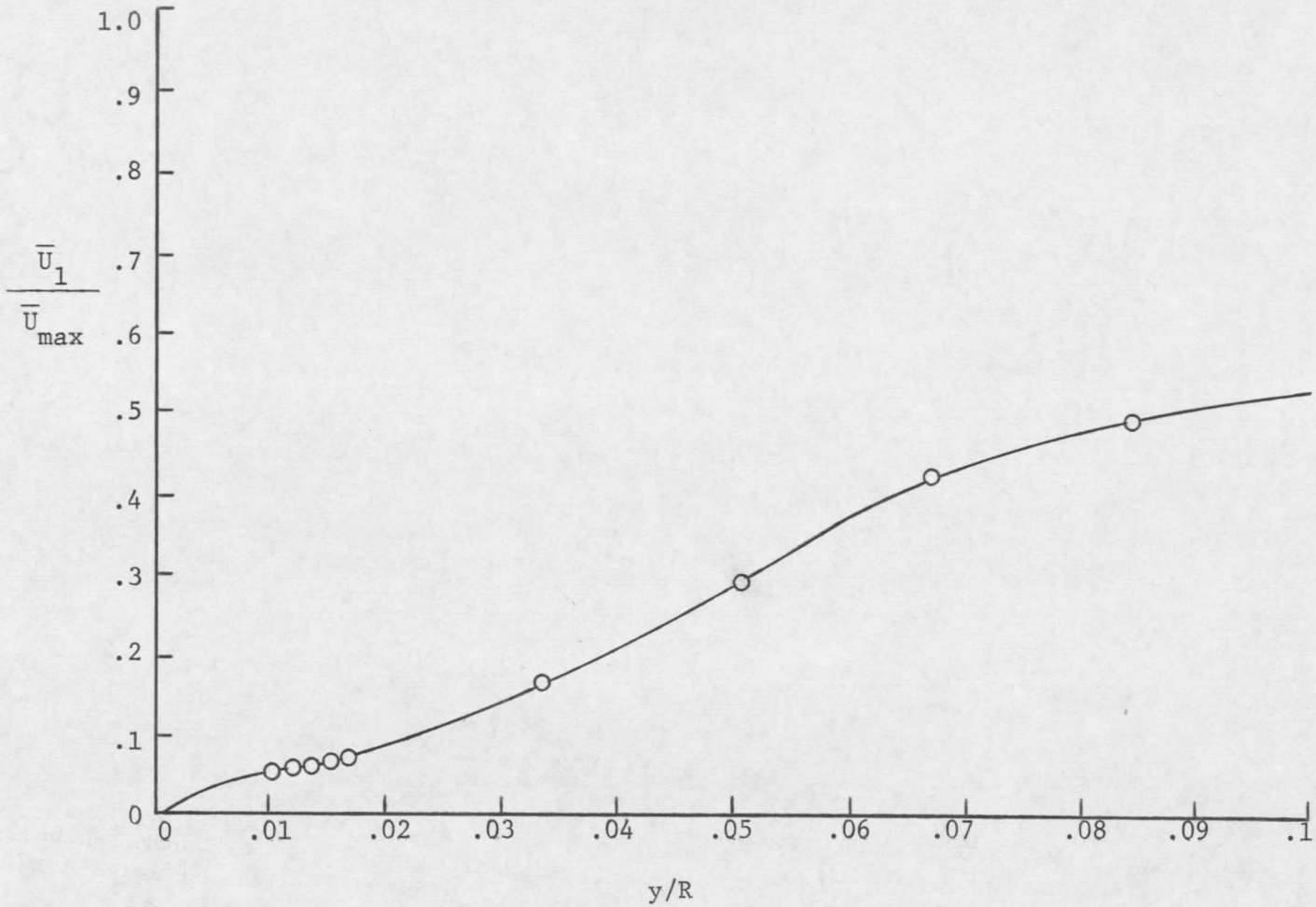

FIGURE 171. Longitudinal Mean Velocity Profile in Wall Region of Pipe With Large Roughness Elements

coordinate directions for the pipe currently under consideration are presented in Figure 172. As required by the momentum relation, equation (4.11), u_2' and u_3' are seen to be approximately equal at the pipe center line, and u_1' has a somewhat larger magnitude. In moving from the center line toward the wall, all three components are observed to increase, u_1' at the fastest rate and u_2' at the slowest. This statement remains valid until just beyond the tops of the roughness elements where pronounced peaks are observed in u_1' and u_2', but no such peak is observed in u_3'. Thus, for a small distance adjacent to the sand grains, u_2' becomes larger than u_3'. When the roughness particles are reached, all three velocity components decrease rapidly to zero. It should also be observed that the magnitudes of u_2' and u_3' do not differ greatly throughout the flow field, thereby indicating a tendency toward isotropy by these two components.

As a check on the assumption of small turbulence intensities, the intensities of all three fluctuating velocity components are presented in Figure 173 for the central region of the pipe and in Figure 174 for the wall region. These curves indicate the presence of small intensities in the central region of the pipe, but as the wall is approached all three intensities increase. None of these exceed about 50%, however, until the tops of the roughness particles are reached, and in view of the discussion in reference [97], the

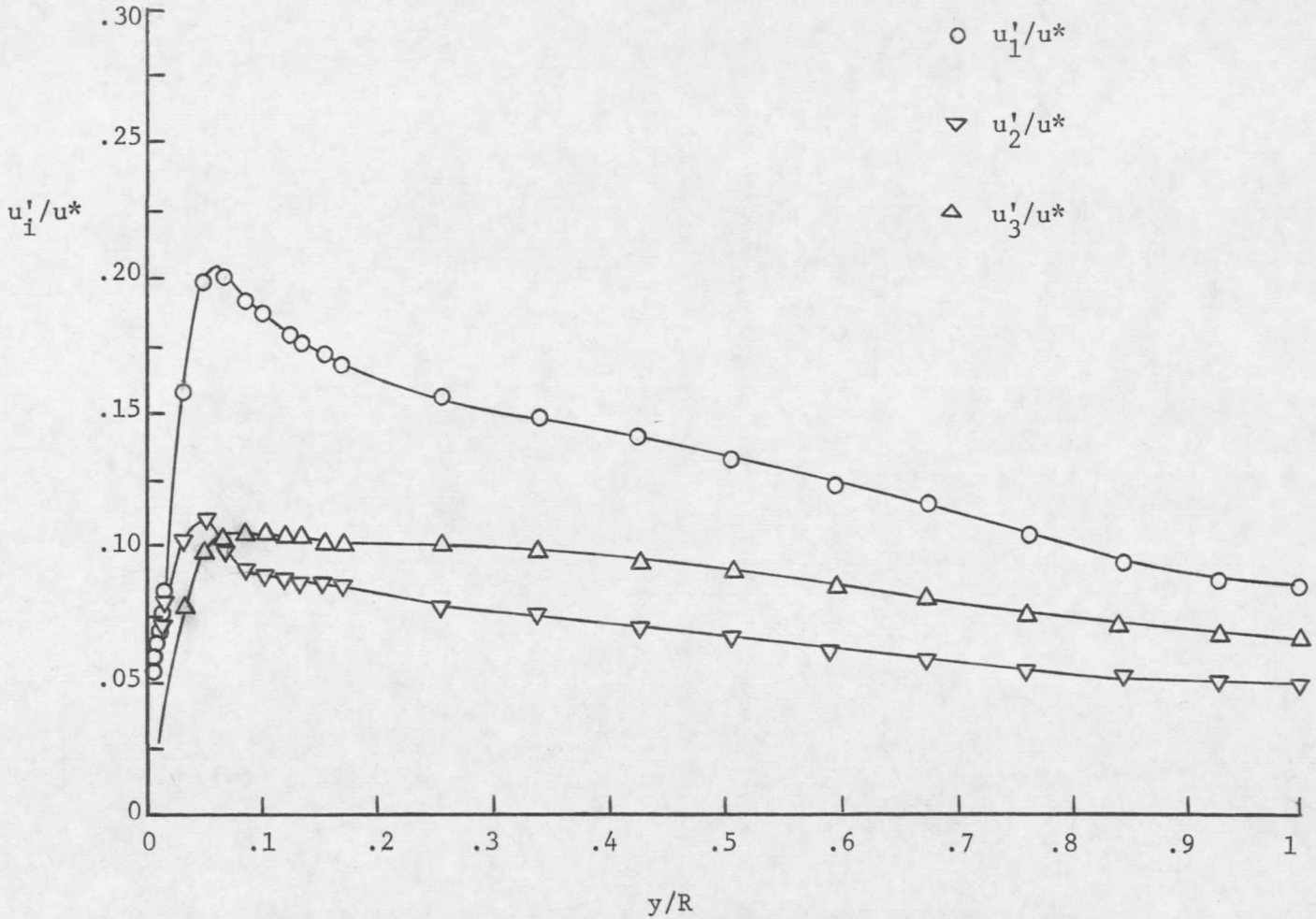

FIGURE 172. RMS Values of Fluctuating Velocities in Pipe With Large Roughness Elements

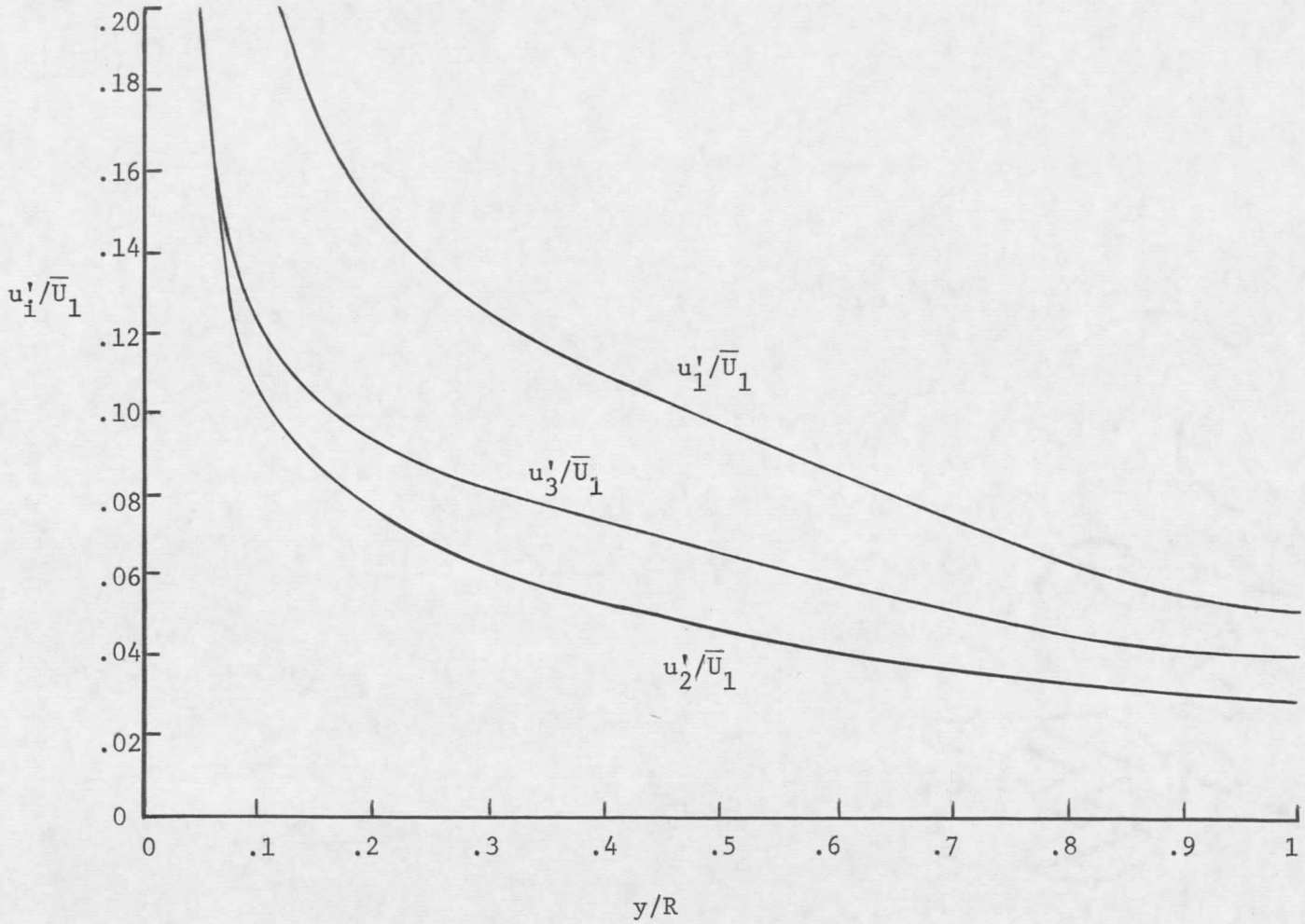

FIGURE 173. Turbulence Intensities in Central Region of Pipe With Large Roughness Elements

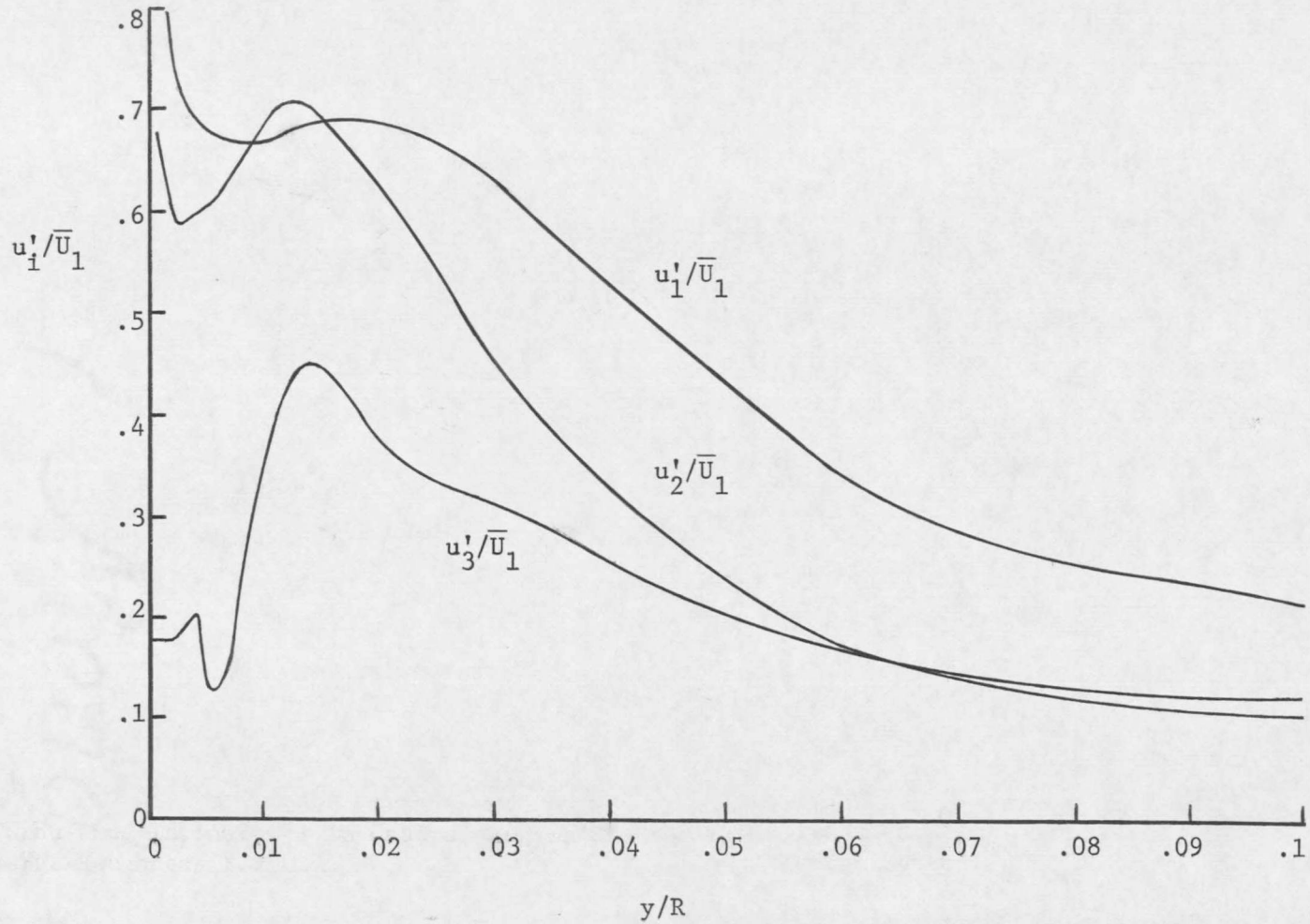

FIGURE 174. Turbulence Intensities in Wall Region of Pipe With Large Roughness Elements

errors involved, though probably significant, are not expected to be prohibitive. Beneath the roughness elements the intensities become exceedingly large, and reliable results are not expected in this region.

The degree of anisotropy prevailing in the pipe currently under consideration may be investigated by means of Figure 175 which shows the variation of the three anisotropy ratios over the pipe cross section. Over most of the central portion of the pipe, u_2'/u_1' and u_2'/u_3' are seen to be essentially constant, the former at about 0.5 and the latter near 0.85. Both increase to a value near unity at the solid surface. On the other hand, u_3'/u_1' decreases in an approximately linear fashion from 0.8 at the pipe center line to 0.6 near $y/R = 0.1$. This term then indicates a decrease as the wall is approached.

Having determined values of the fluctuating velocities in the three coordinate directions, the turbulence kinetic energy can now be calculated. This quantity is shown normalized with the square of the shear velocity in Figure 176. It can be seen that this dimensionless kinetic energy has a value slightly less than unity at the center line and then increases in moving toward the wall. This rate of increase is small near the center line but increases with increasing radius. A pronounced maximum value of about 3.2

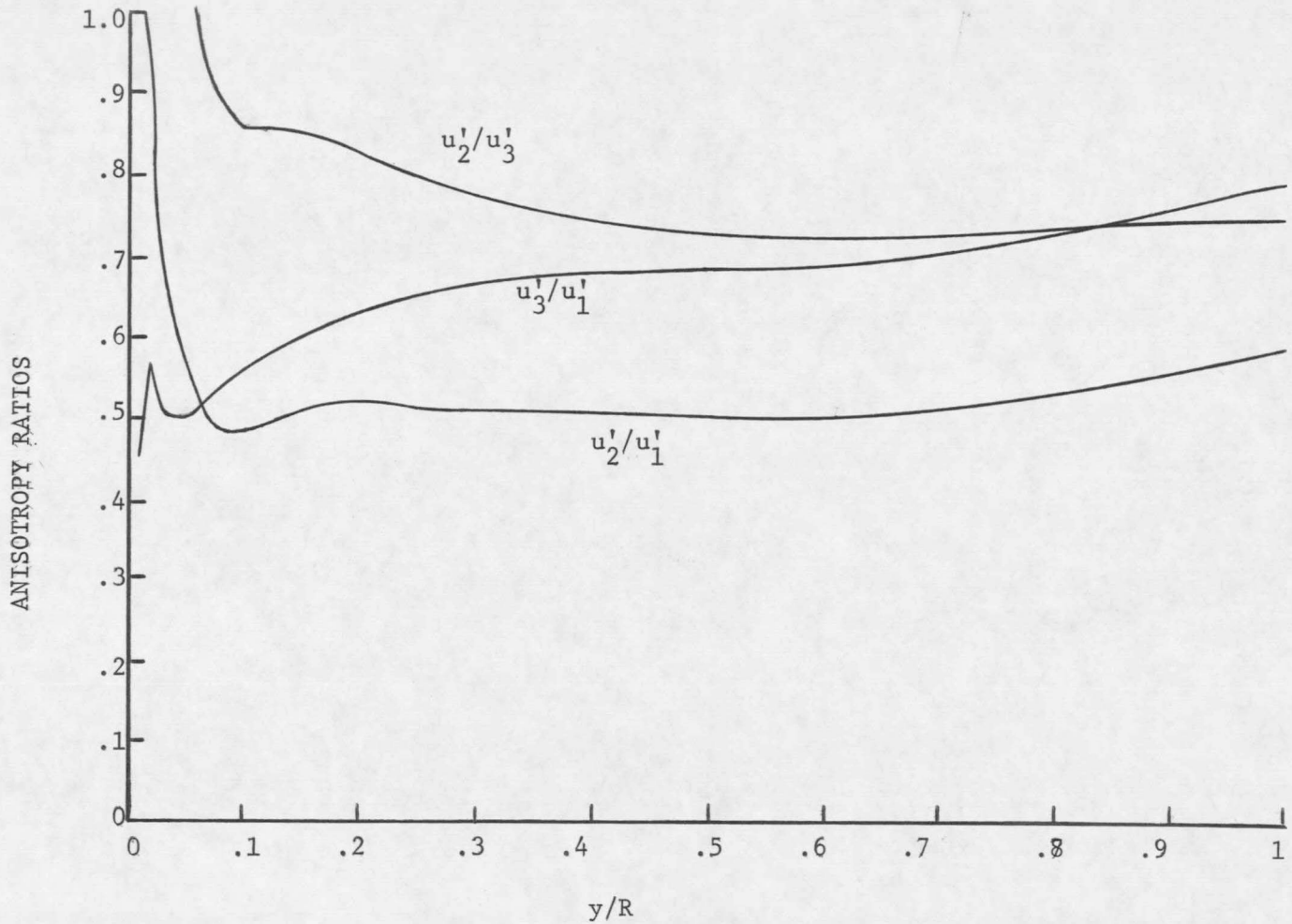

FIGURE 175. Anisotropy Ratios for Pipe With Large Roughness Elements

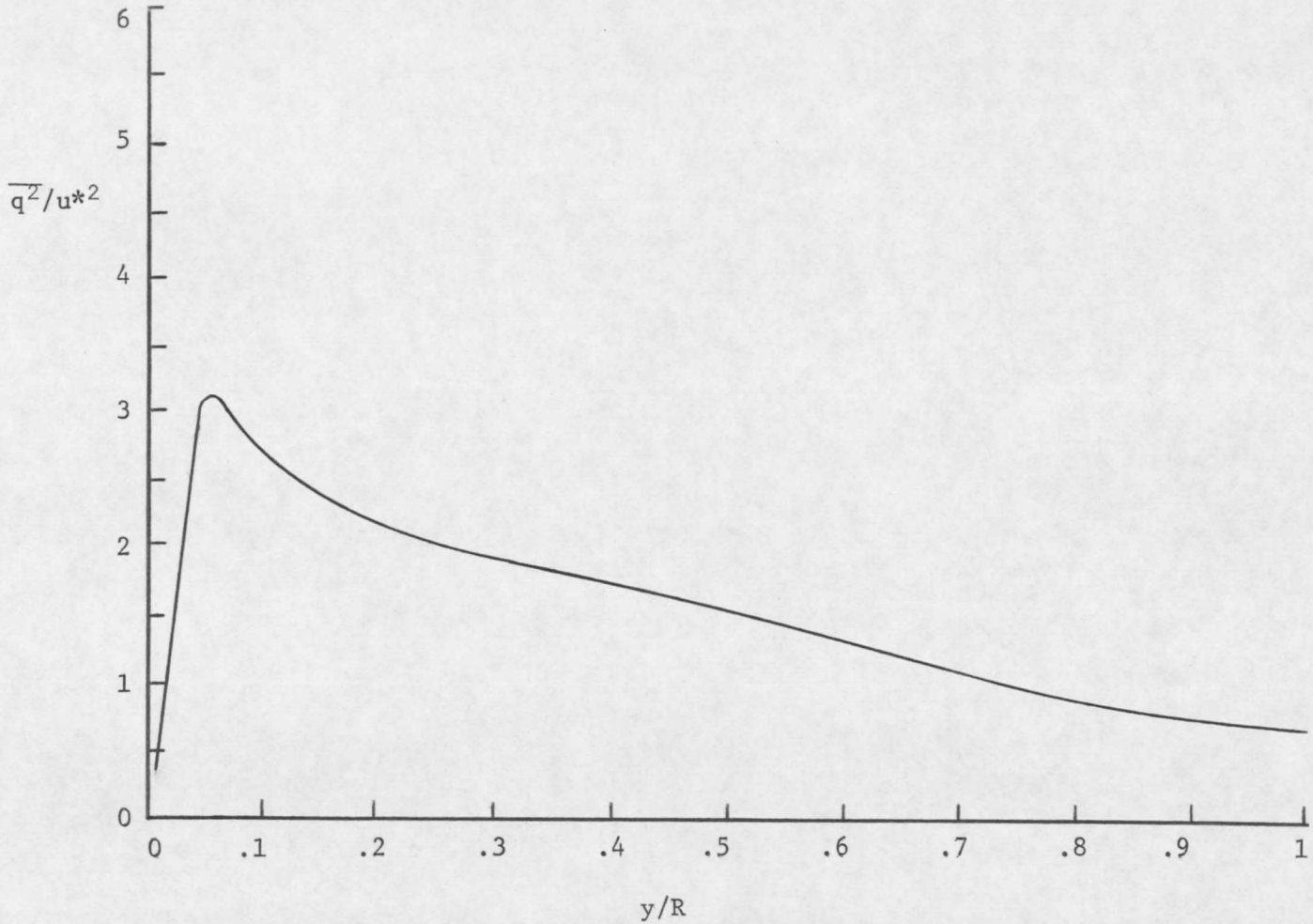

FIGURE 176. Turbulence Kinetic Energy in Pipe With Large Roughness Elements

is acquired near $y/R = 0.06$, and the kinetic energy then decreases to zero as the wall is approached.

It may be recalled that information regarding the pressure variation in the radial direction is required to ascertain the validity of the dynamic head determined from static pressure measurements at the solid boundary. In the previous chapter it was indicated that this pressure variation cannot be rigorously caluclated for flow in a rough pipe because of the spatially averaged mean velocities which appear in equation (4.12). However, if it is assumed that these mean velocity terms yield only a negligible contribution to the pressure term, its radial variation can still be estimated from equation (4.12). In the event that this assumption is not valid, the ordinate in Figure 177 will simply be a combination of the pressure and the spatially averaged mean velocities. With the foregoing discussion in mind, this figure indicates a minimum in the pressure at about the mid radial position. At both the center line and just above the roughness elements, $(\overline{P}_0 - \overline{P})/\rho u^{*2}$ attains a value of about 1.2, and a decrease to a null value is observed very near the wall. By the method utilized for the two previous pipes, the error involved in calculating dynamic head from static pressure measurements at the wall is estimated to be of the order of $2(u^*/\overline{U}_{max})^2$, which in this case amounts to about 0.4%. Therefore, it

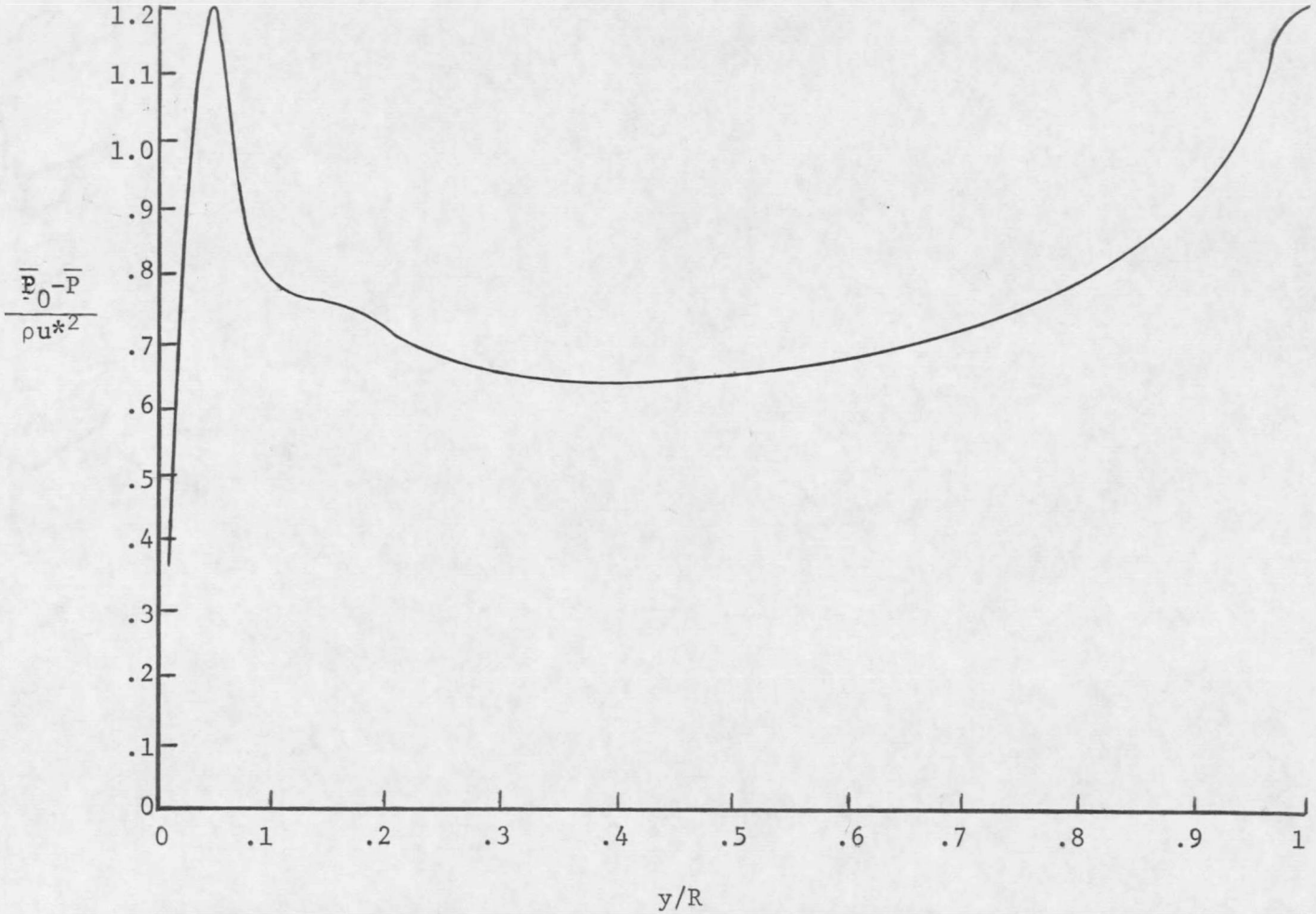

FIGURE 177. Radial Pressure Variation in Pipe With Large Roughness Elements

is believed that measurement of the static pressure at the solid surface is justifiable.

Fluctuating Velocity Correlations

The second order $\overline{u_1 u_2}$ cross correlation, normalized with the square of the shear velocity, is presented in Figure 178 for the pipe containing the large roughness elements. The variation in this correlation is seen to be approximately linear from a null value at the center line to about 0.2 at the mid radial position. The correlation then remains essentially constant near 0.25 for values of y/R between 0.1 and 0.5. A sharp peak in $\overline{u_1 u_2}$ is noted just above the roughness elements, and the correlation then decreases to zero as the wall is approached. As noted in the previous chapter, such behavior is typical of that found by Gow [15] and Robertson *et al* [47].

The correlation coefficient corresponding to $\overline{u_1 u_2}$ in Figure 179 shows a nearly constant value of about 0.2 over the major portion of the pipe, although it does vanish at the wall and the pipe center line. A peak corresponding to that in the $\overline{u_1 u_2}$ correlation is observed near the roughness elements. A very similar behavior is exhibited by the turbulence kinetic energy in Figure 180. It should be recalled that a constant value of this ratio in the central portion of the pipe,

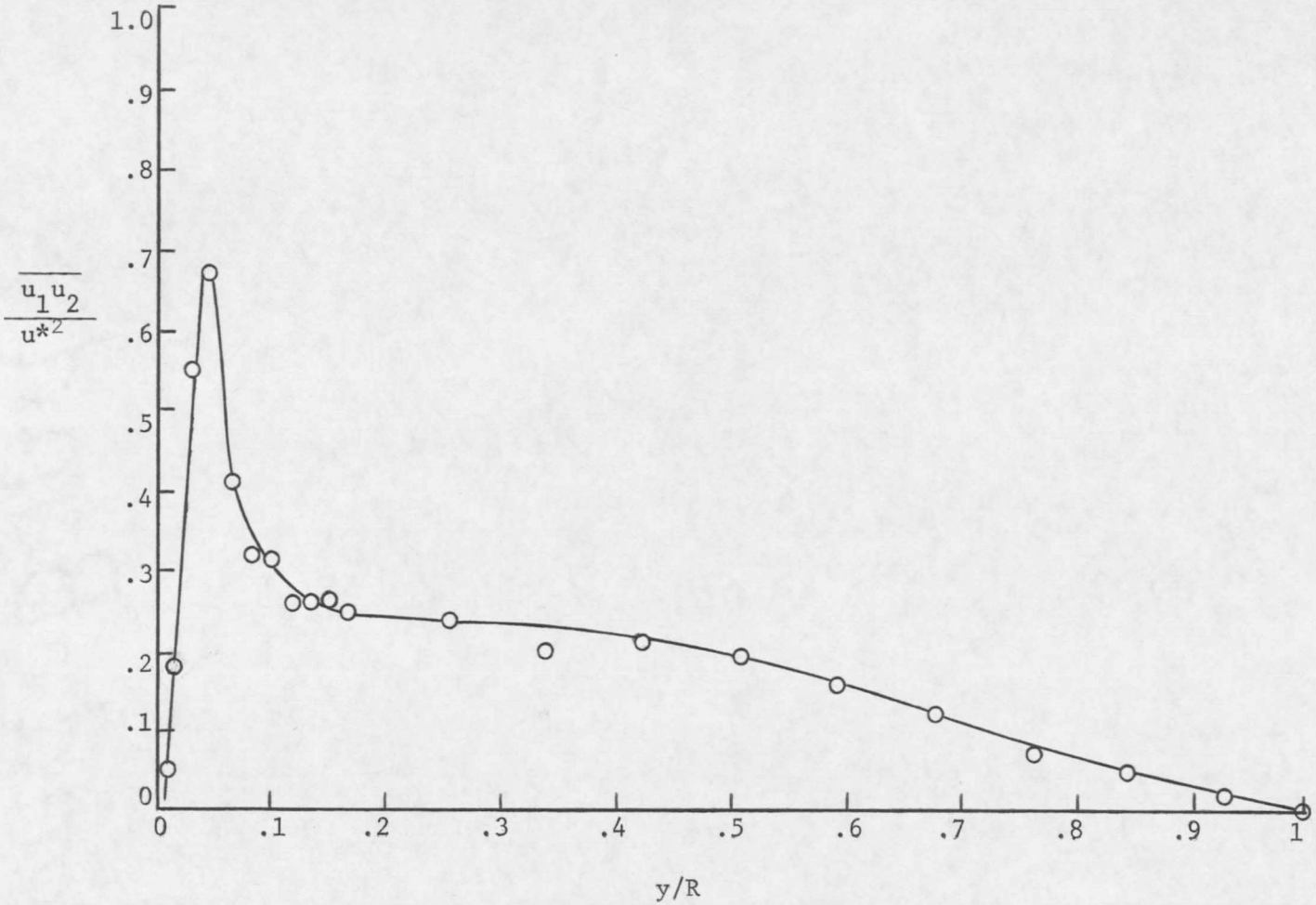

FIGURE 178. Second Order $\overline{u_1 u_2}$ Cross Correlation in Pipe With Large Roughness Elements

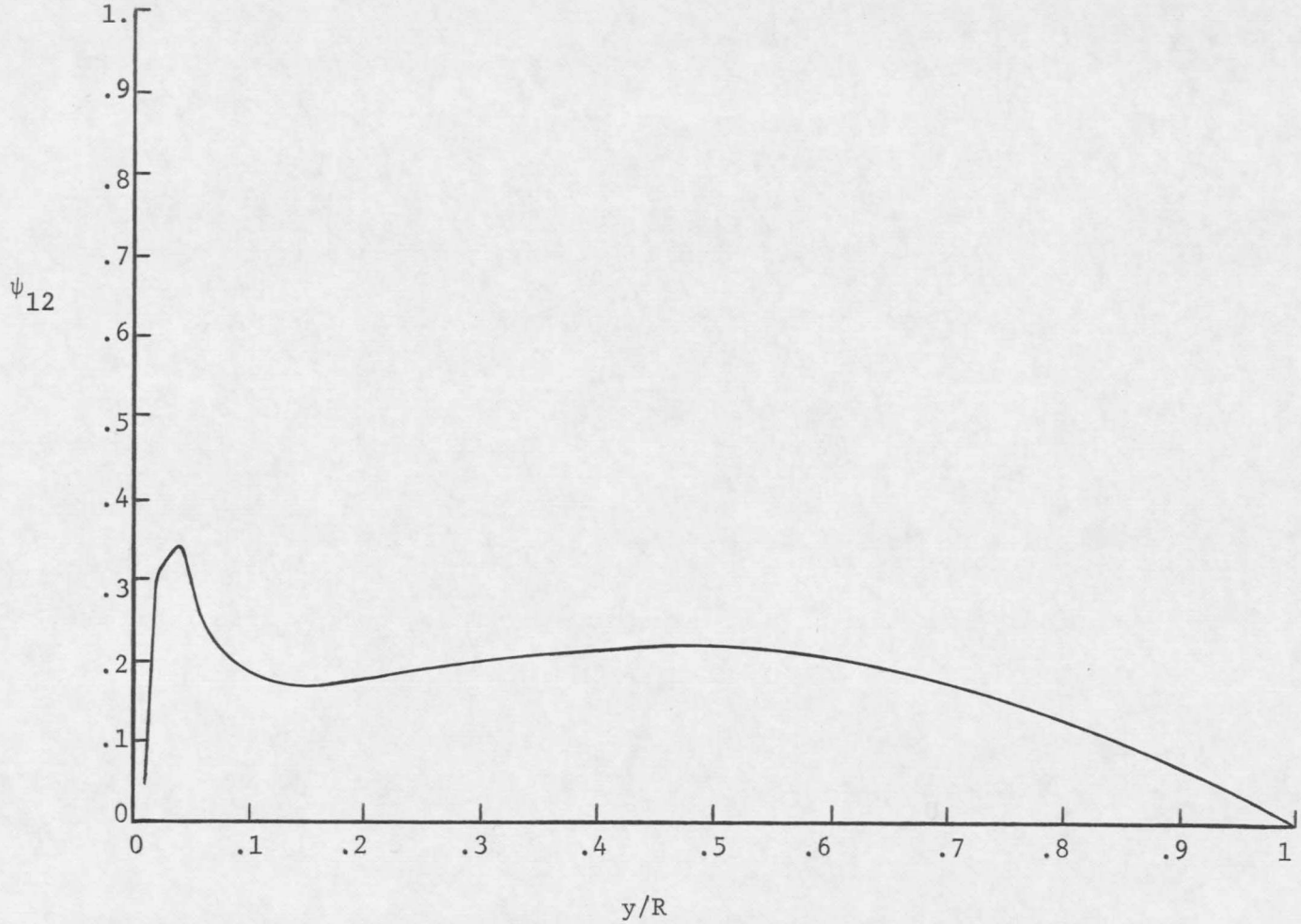

FIGURE 179. Variation of ψ_{12} Correlation Coefficient for Pipe With Large Roughness Elements

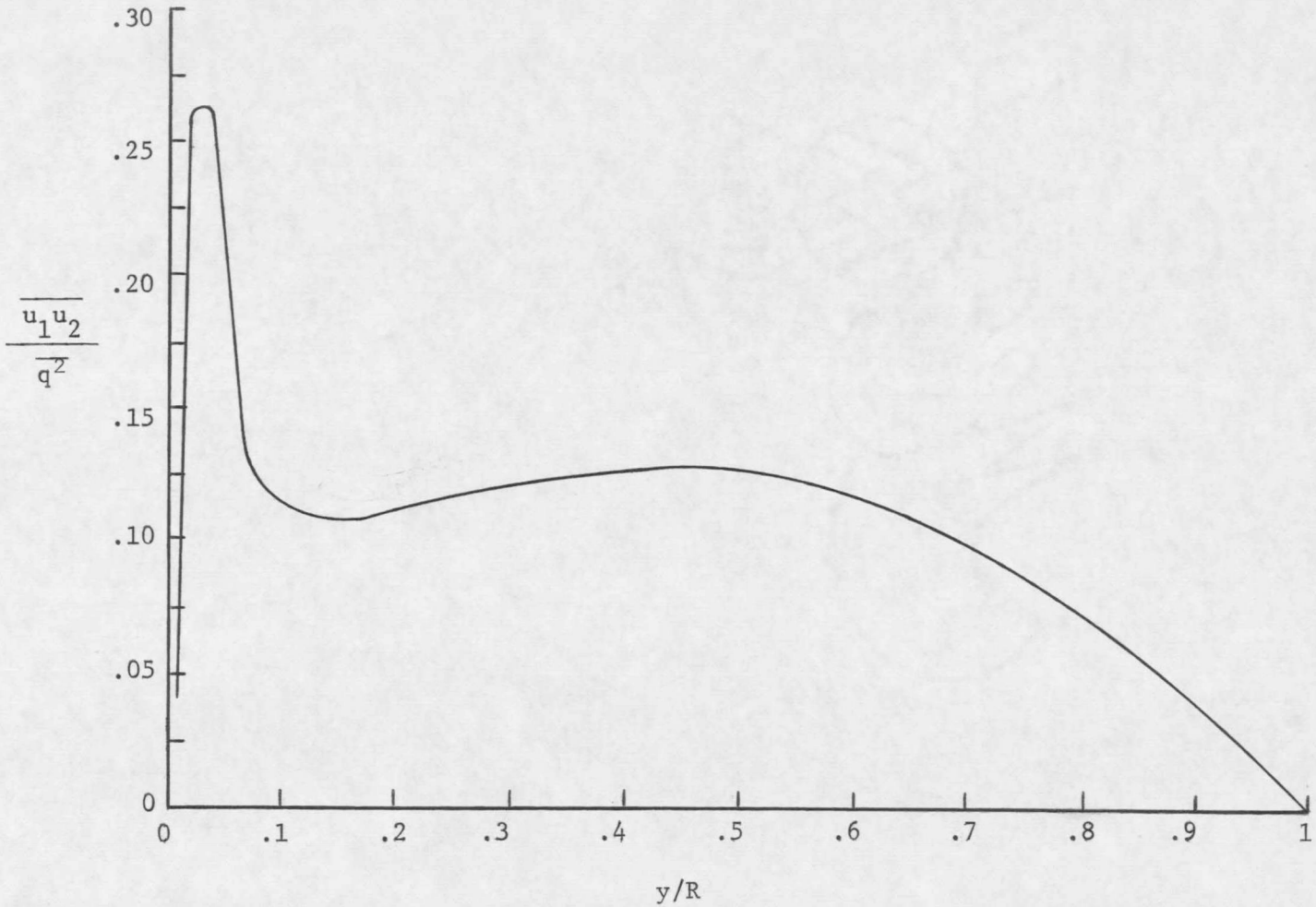

FIGURE 180. Turbulence Shear Stress to Kinetic Energy Ratio for Pipe With Large Roughness Elements

such as indicated by Figure 180, would be obtained if either von Karman's similarity hypothesis or Prandtl's mixing length theory were valid.

It was indicated in the previous chapter that measurements of the $\overline{u_1 u_2}$ correlation and the mean velocity permit calculation of the spatial correlation between mean velocity components in the longitudinal and radial directions. The results of such a calculation for the pipe containing the large roughness particles are indicated in Figure 181. Here, the spatial correlation, normalized with the square of the shear velocity, is seen to increase almost linearly from a null value at the center line to about 0.6 at $y/R = 0.1$. Then, just above the roughness elements a distinct minimum, corresponding to the maximum in $\overline{u_1 u_2}$, is observed

The eddy diffusivity for momentum, determined with the aid of equation (2.71), is presented for flow in the pipe containing the large roughness size in Figures 182 and 183. Figure 182 establishes the fact that this quantity attains a nearly constant value of 0.05 near the center line and crests at a value of about 0.075 near $y/R = 0.4$. A decrease to a minimum value of about 0.005 near the top of the roughness elements is then noted. A second peak is noted well below the top of the roughness elements at $y/R \simeq 0.01$, and the eddy diffusivity then vanishes. A phenomenon such as this second

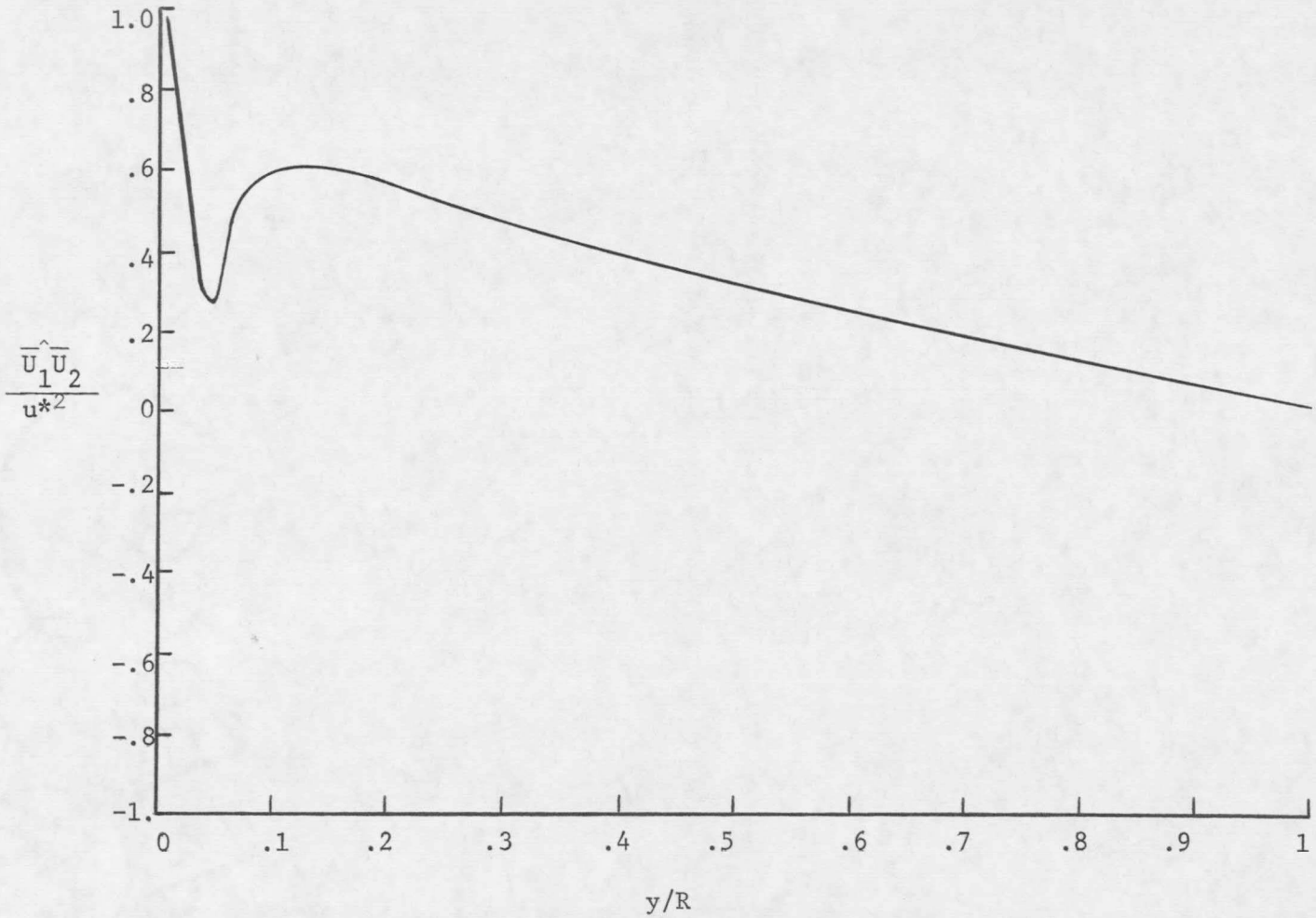

FIGURE 181. Spatial $\overline{U_1}\hat{\overline{U}}_2$ Correlation for Pipe With Large Roughness Elements

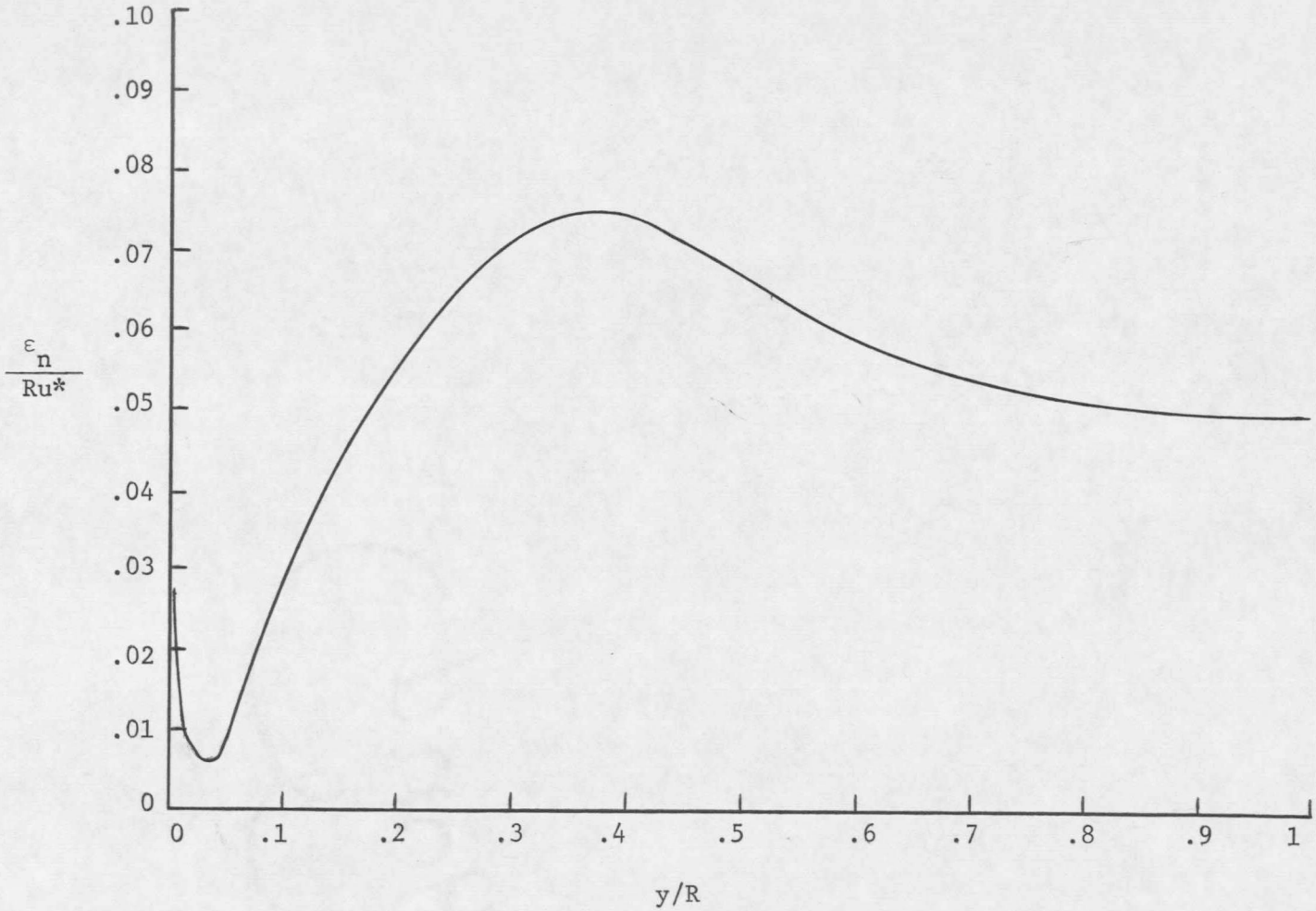

FIGURE 182. Eddy Diffusivity for Momentum in Central Region of Pipe With Large Roughness Elements

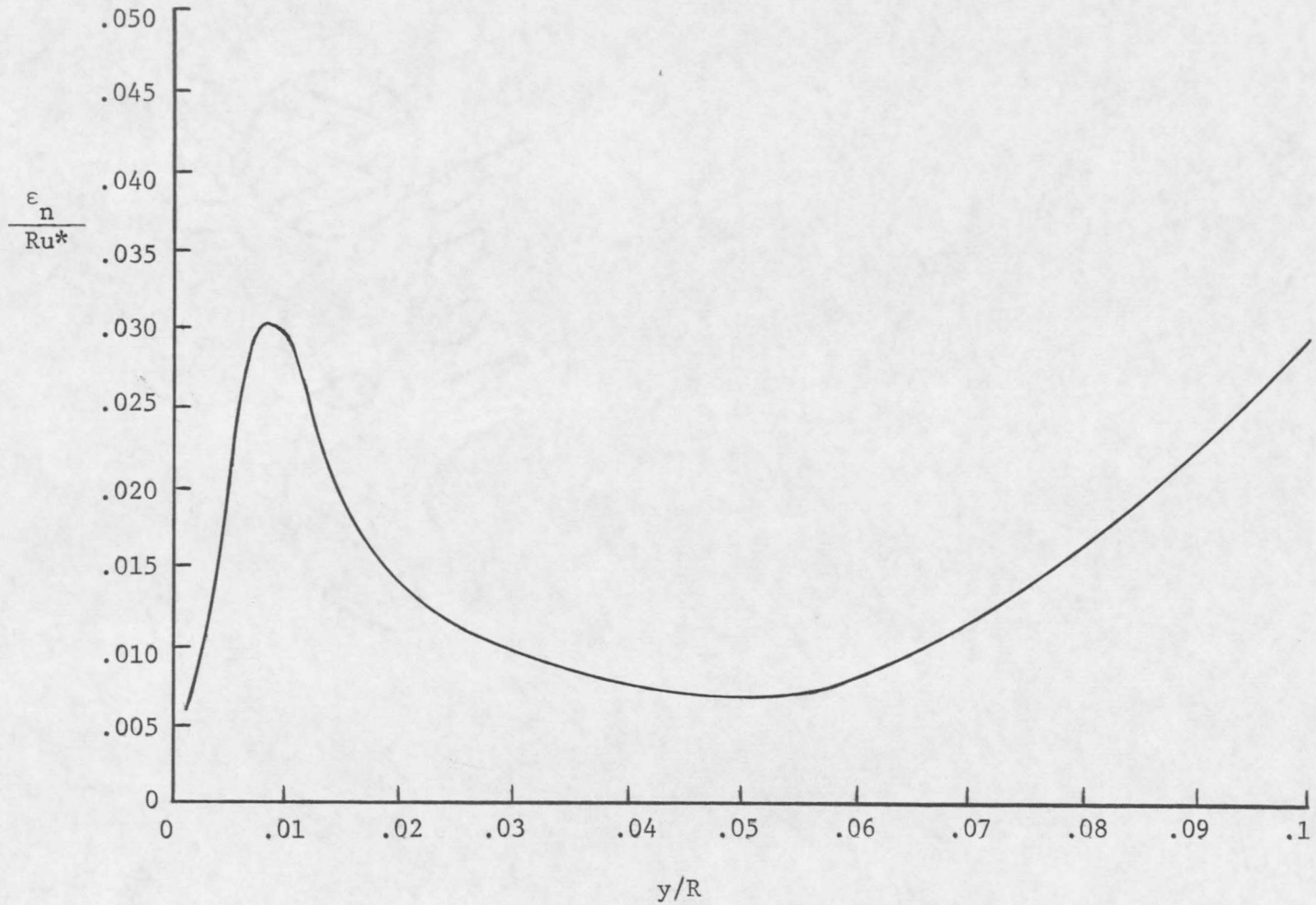

FIGURE 183. Eddy Diffusivity for Momentum in Wall Region of Pipe With Large Roughness Elements

peak is not expected but could have important consequences in many rough pipe considerations, e.g. heat transfer.

The second cross correlation term measured experimentally in the current investigation was the cross correlation between longitudinal and angular fluctuating velocities, $\overline{u_1 u_3}$. Although momentum considerations require this term to be zero for flow in a smooth pipe, nonzero values, except near the center line and at the wall, are indicated in Figure 184. An extreme value of about -0.25 is indicated at a value of y/R approximately equal to the mean roughness height. Such behavior is indicative of a transfer of longitudinal momentum across planes normal to the x_3 axis, and this, in turn, indicates mean velocity variations in the x_3 direction as postulated in the analytical considerations.

The variation of the third order $\overline{u_1^2 u_2}$ correlation with radial position is shown in Figure 185 for the central region of the pipe and in Figure 186 for the wall region. This correlation varies linearly from zero at the pipe center line to about -0.9 at y/R ≈ 0.15. A sharp increase to a maximum value of about 0.5 at the top of the roughness particles is then noted, and afterwards this correlation tends toward zero again. The correlation coefficient corresponding to $\overline{u_1^2 u_2}$ is seen, in Figure 187, to be constant at about -0.5 over most of the pipe, although it does increase to a

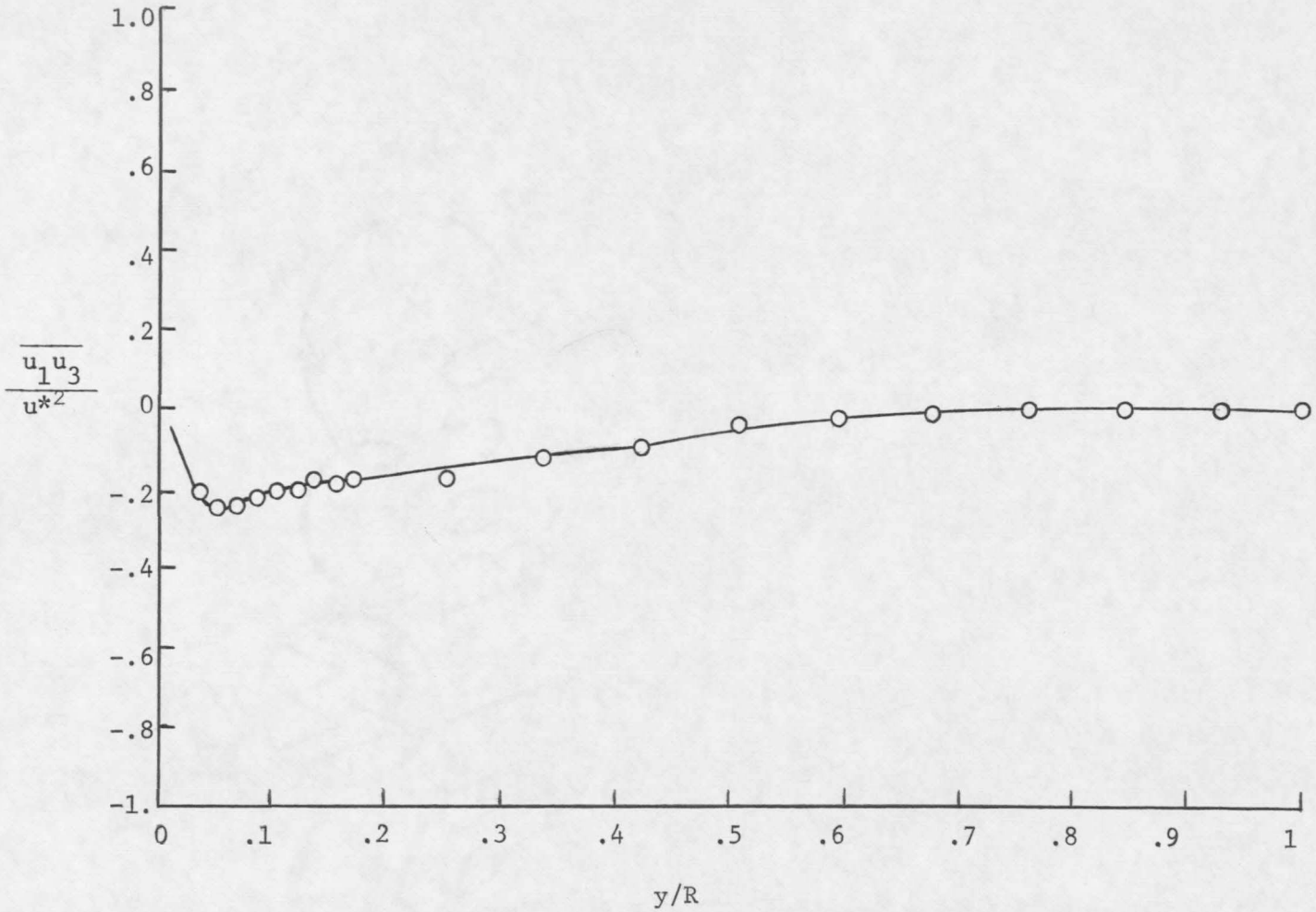

FIGURE 184. Second Order $\overline{u_1 u_3}$ Cross Correlation for Pipe With Large Roughness Elements

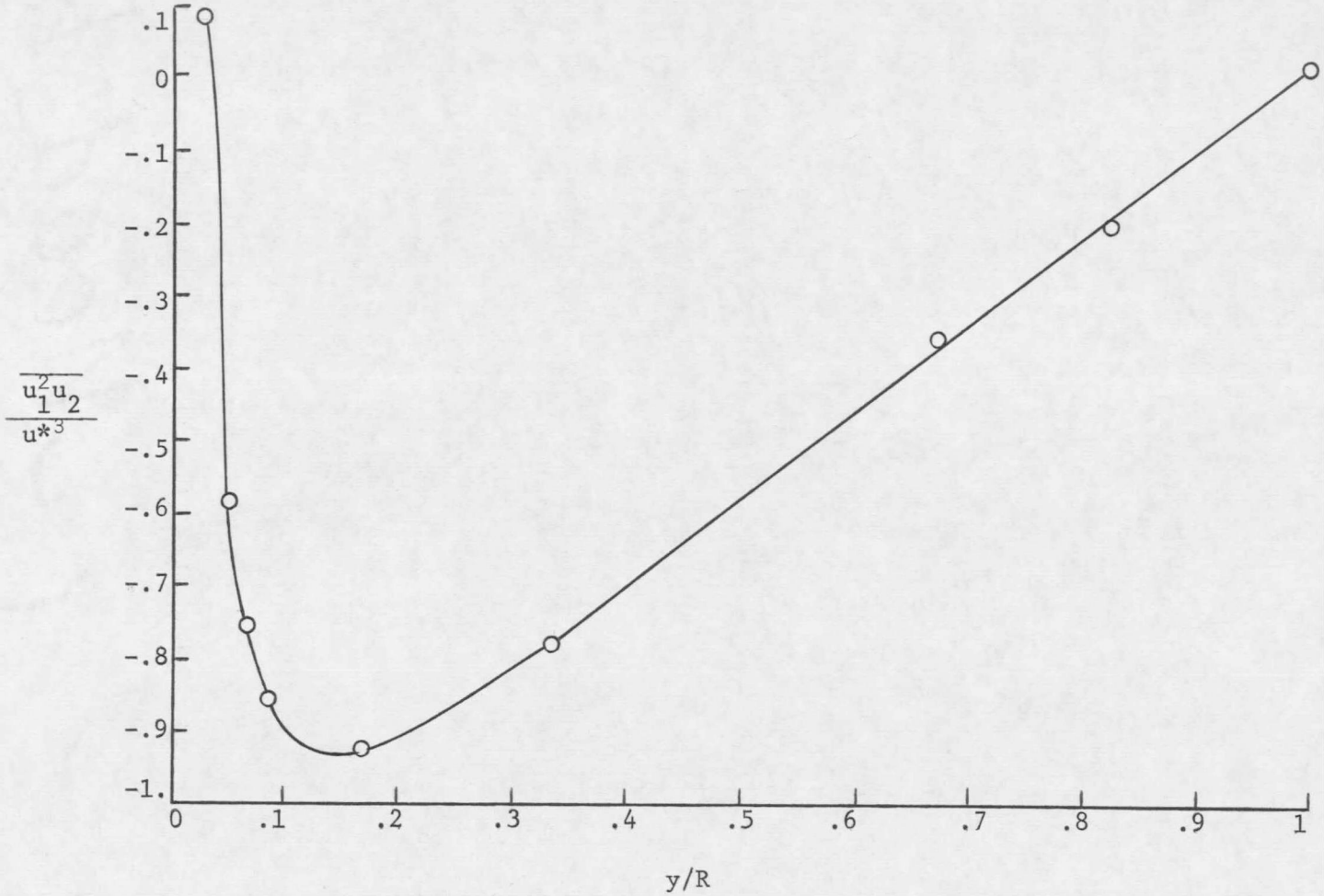

FIGURE 185. Third Order $\overline{u_1^2 u_2}$ Correlation for Central Region of Pipe With Large Roughness Elements

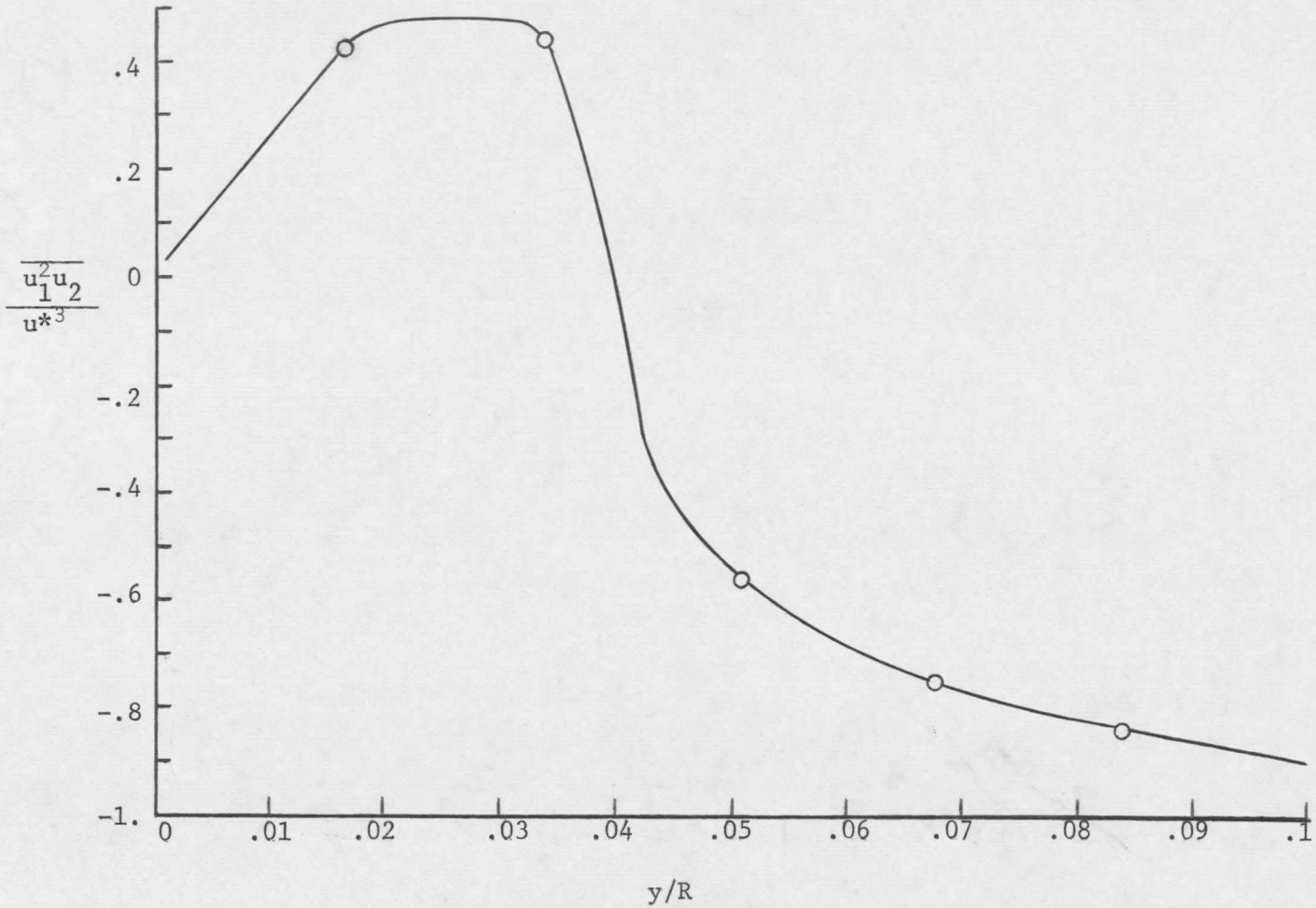

FIGURE 186. Third Order $\overline{u_1^2 u_2}$ Correlation for Wall Region of Pipe With Large Roughness Elements

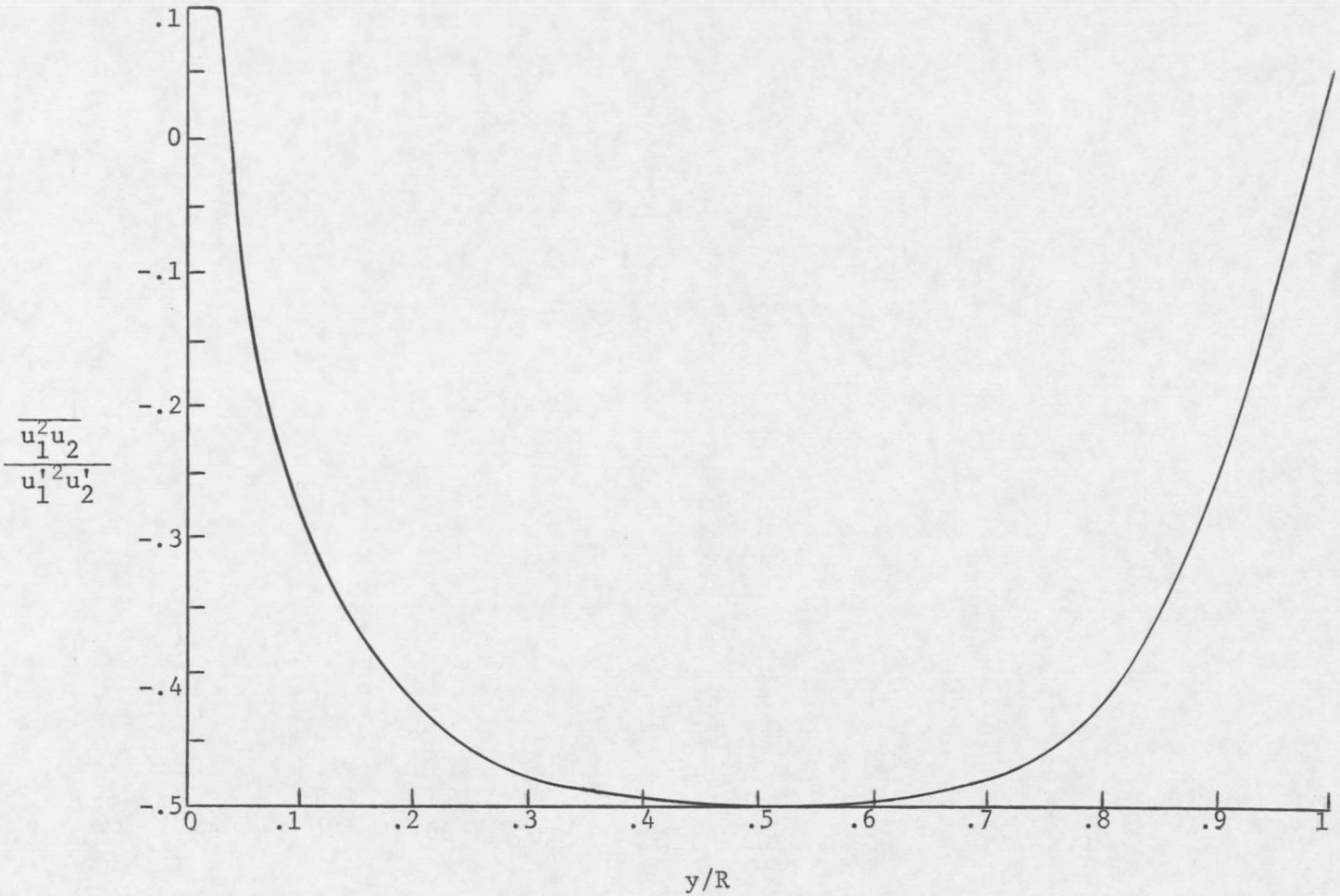

FIGURE 187. Correlation Coefficient for $\overline{u_1^2 u_2}$ in Pipe With Large Roughness Elements

slightly positive value at both the center line and the roughness particles.

The $\overline{u_2^3}$ correlation, normalized with the cube of the shear velocity, is shown in Figures 188 and 189. This dimensionless form of the correlation, though vanishing at the pipe center line, is slightly negative over about the central half of the pipe, and then increases to a peak almost identically at the top of the roughness particles. The correlation coefficient corresponding to $\overline{u_2^3}$ in Figure 190 vanishes at the pipe center line, but is approximately constant at -1.3 over the remainder of the central half of the pipe. From the roughness elements to the mid radial position the coefficient again remains nearly constant, this time near 1.7.

Dissipation Function

Components of the turbulence energy dissipation function determined experimentally for the central region of the pipe are presented in Figures 191, 192, and 193, and values near the wall are presented in Figures 194 and 195. The behavior of all these components is somewhat similar, i.e., they are all relatively small at the pipe center line and have a small rate of magnitude change at this point. As the wall is approached, a sharp increase to a maximum value is noted, after which zero is approached rather rapidly. Some differences

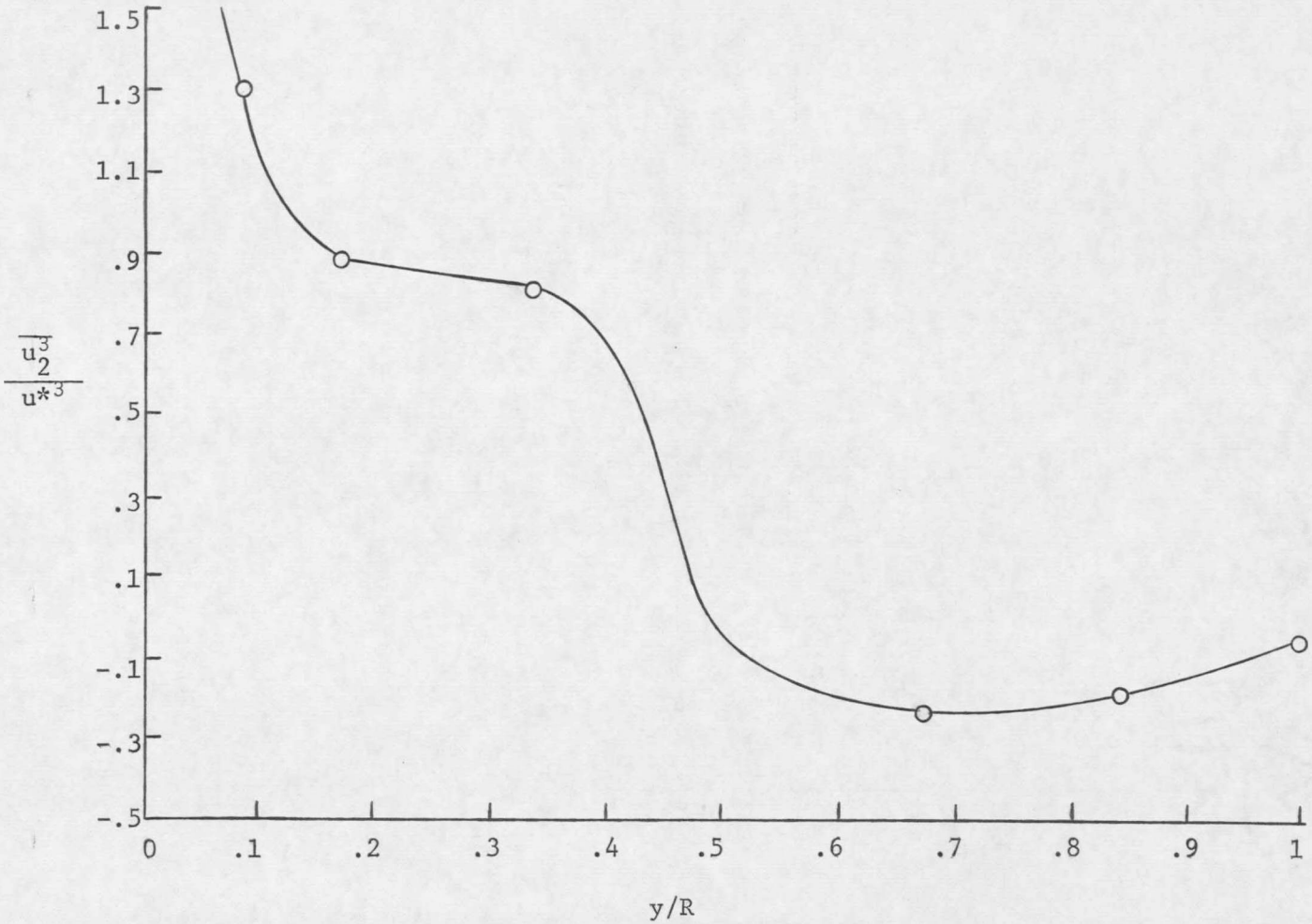

FIGURE 188. Third Order $\overline{u_2^3}$ Correlation For Central Region of Pipe With Large Roughness Elements

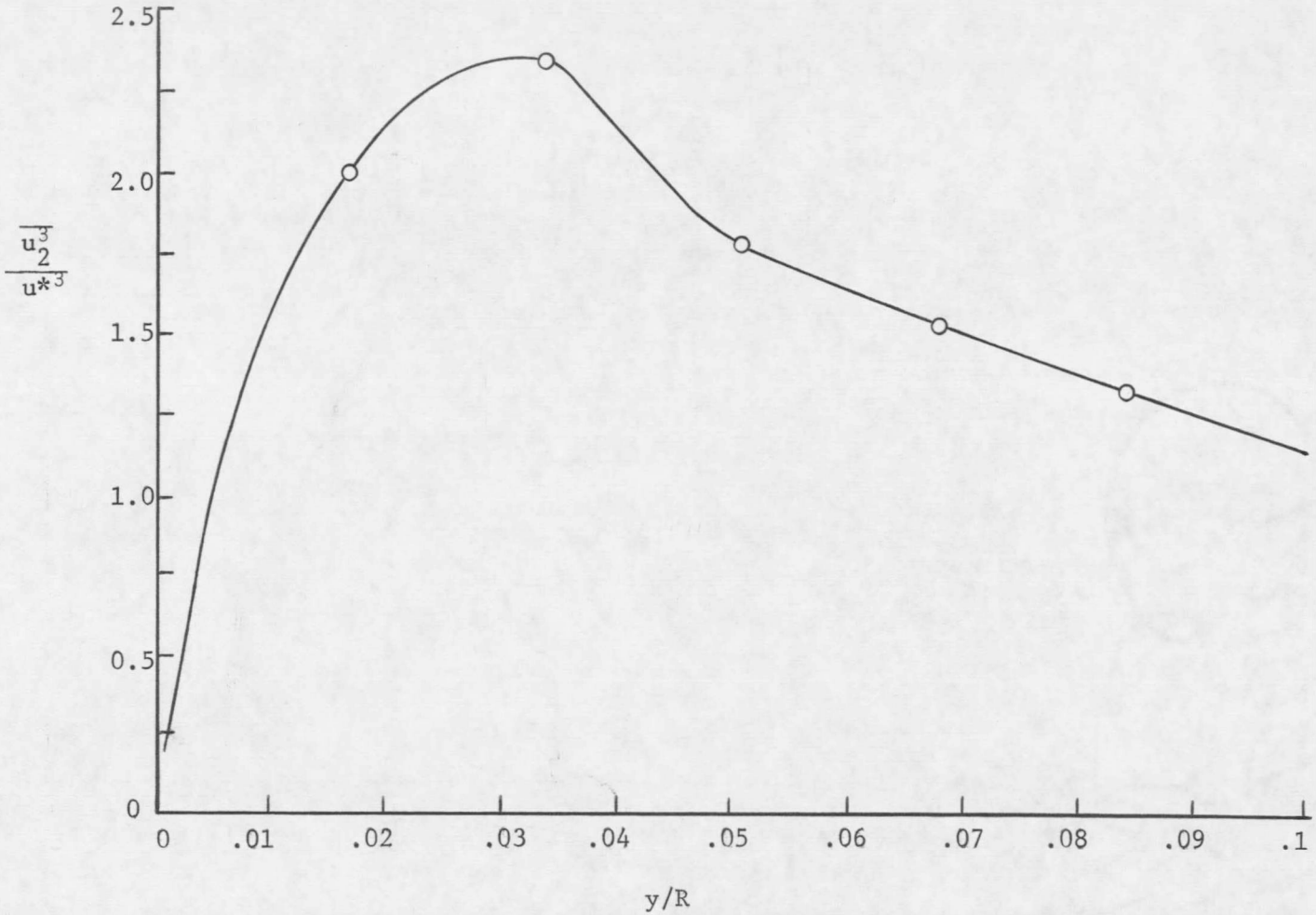

FIGURE 189. Third Order $\overline{u_2^3}$ Correlation Near Wall of Pipe With Large Roughness Elements

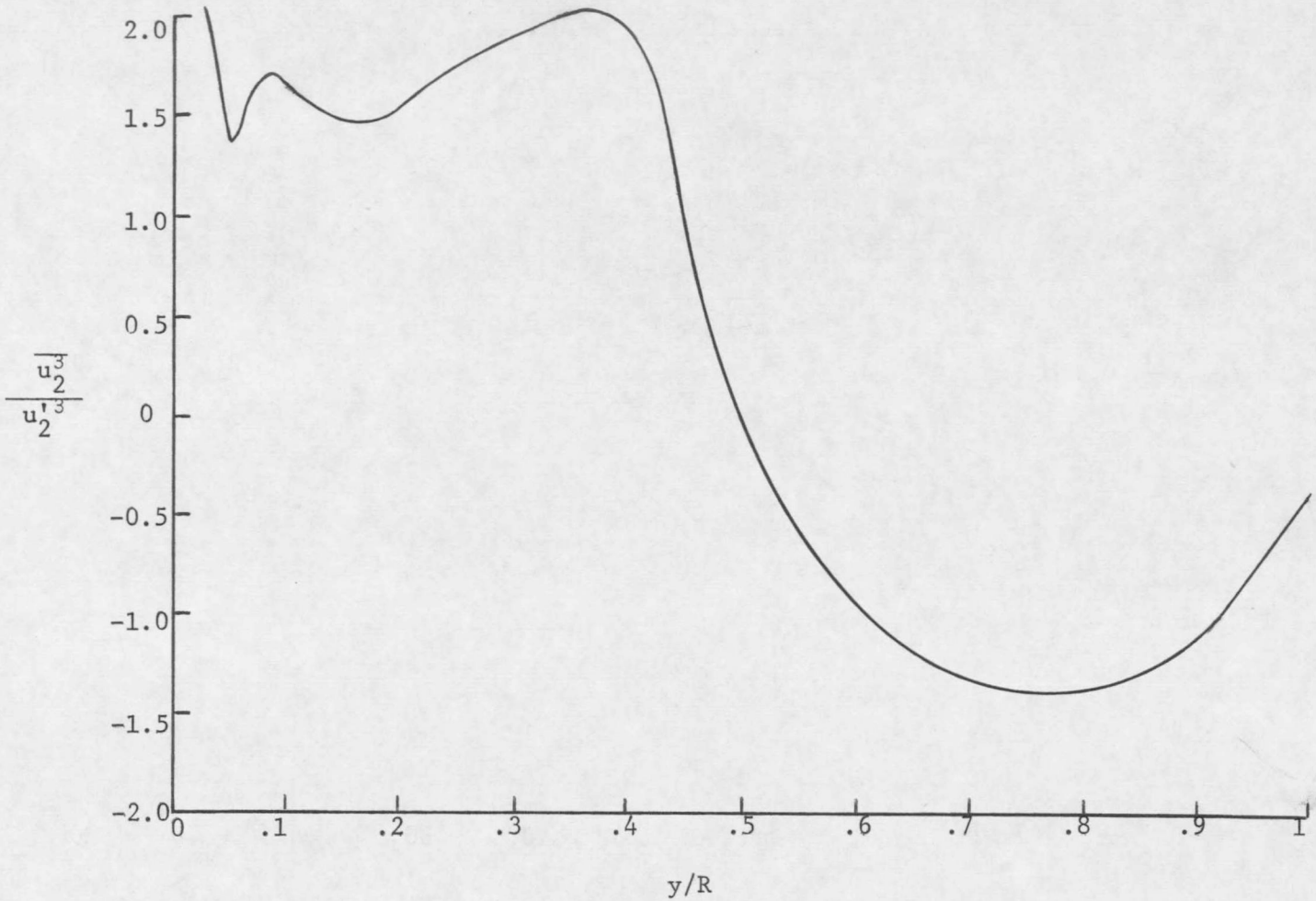

FIGURE 190. Correlation Coefficient for $\overline{u_2^3}$ in Pipe With Large Roughness Elements

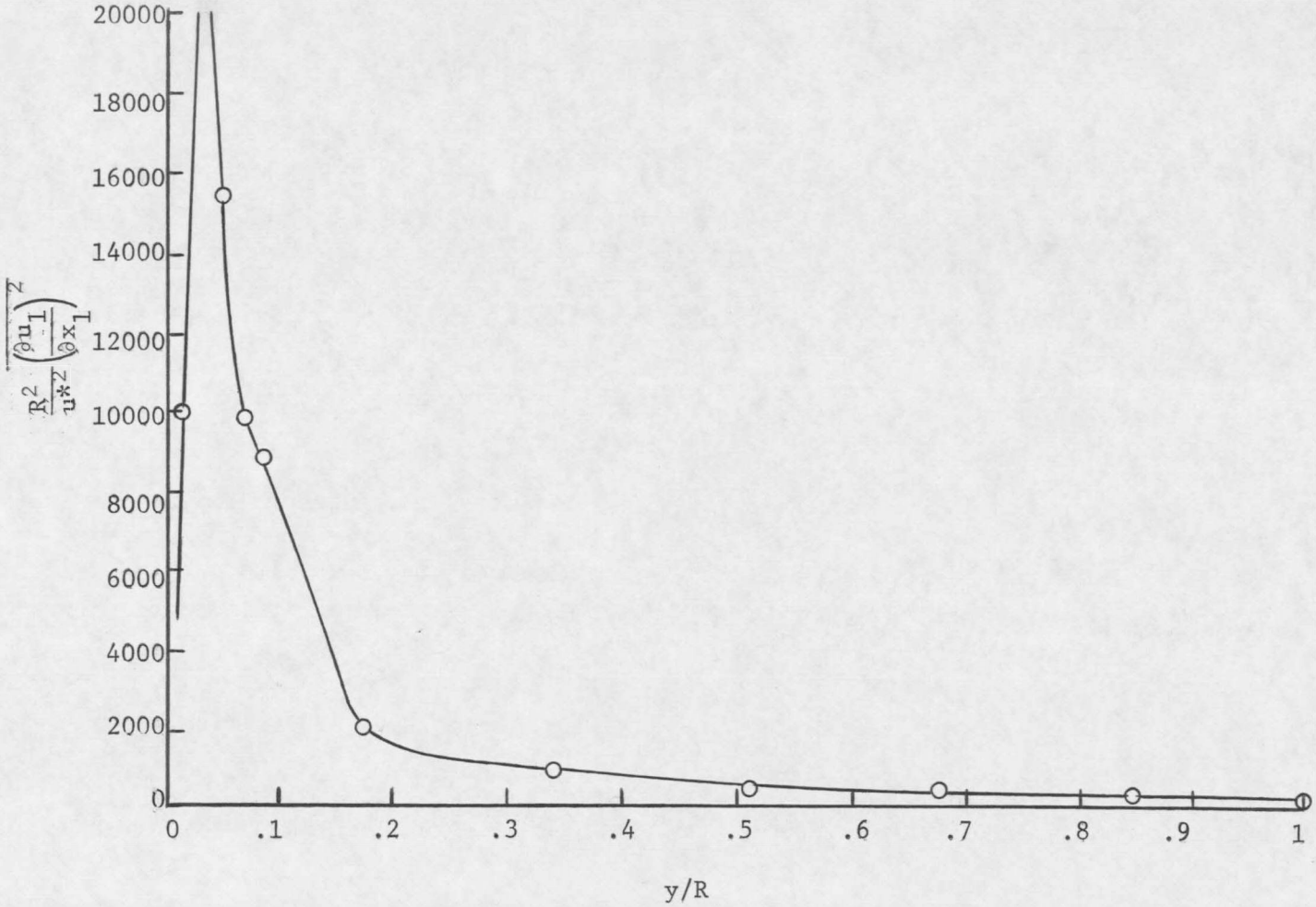

FIGURE 191. Dissipation Terms for Central Region of Pipe With Large Roughness Elements

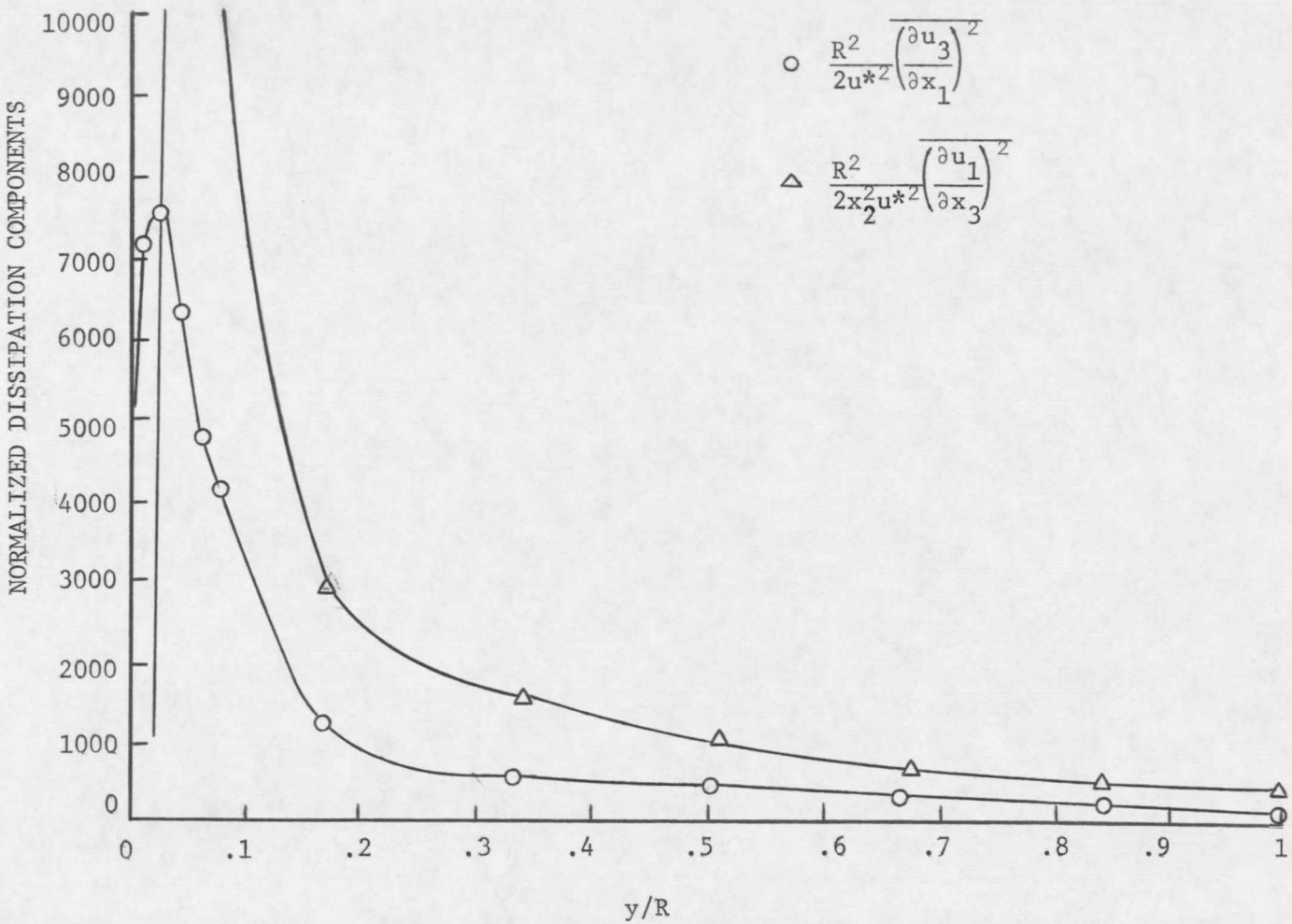

FIGURE 192. Dissipation Terms for Central Region of Pipe With Large Roughness Elements

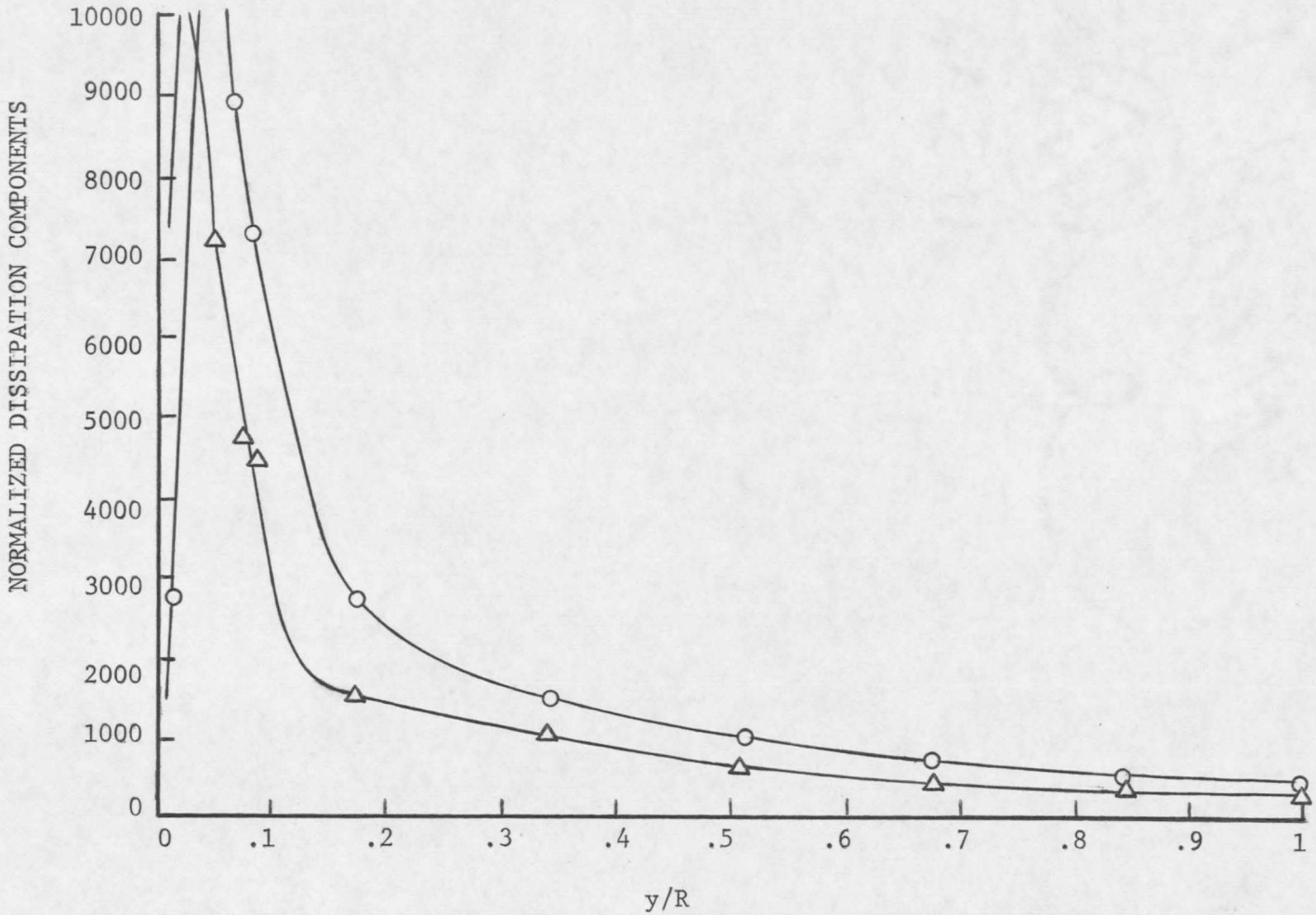

FIGURE 193. Dissipation Terms for Central Region of Pipe With Large Roughness Elements

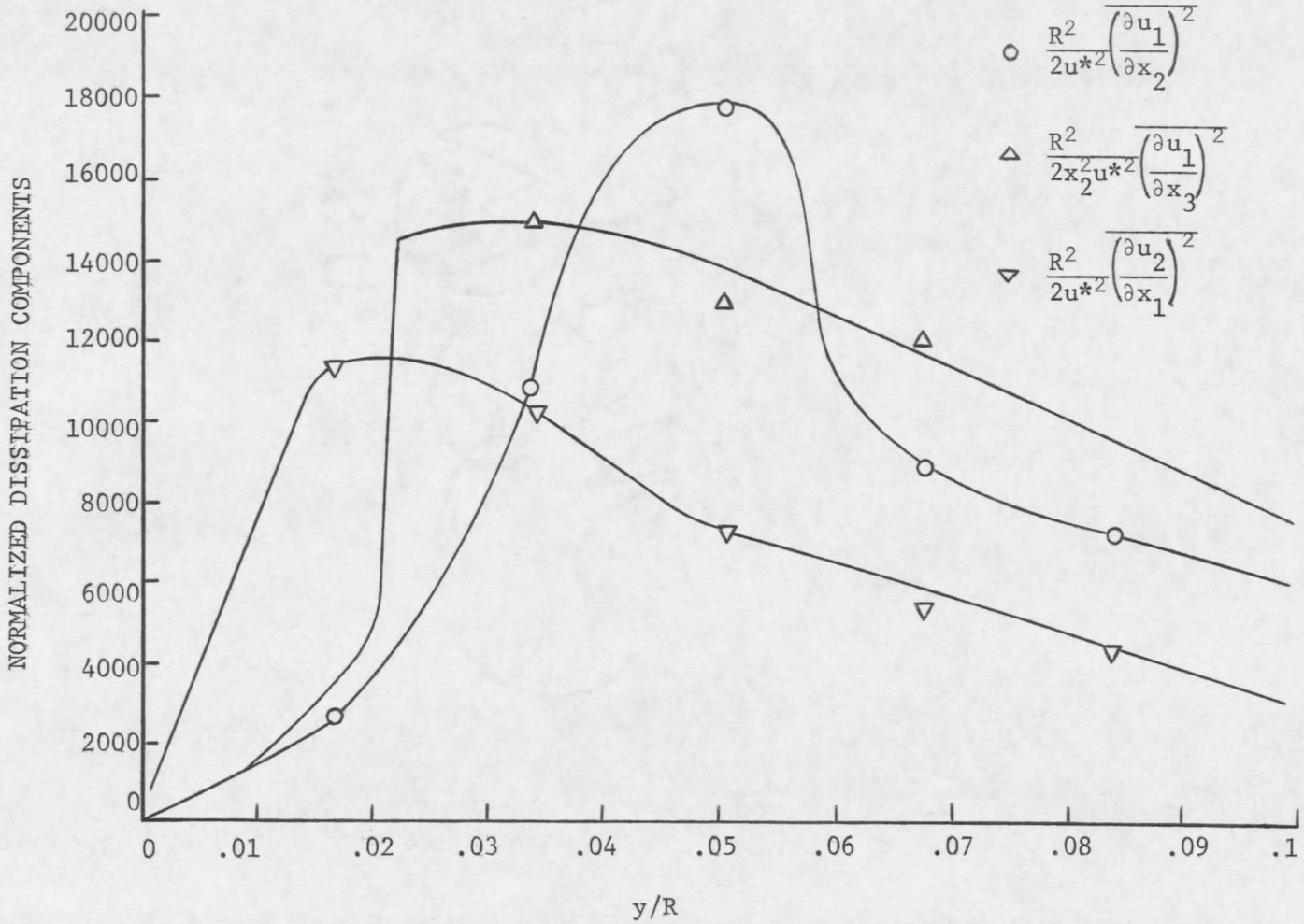

FIGURE 194. Dissipation Terms for Wall Region of Pipe With Large Roughness Elements

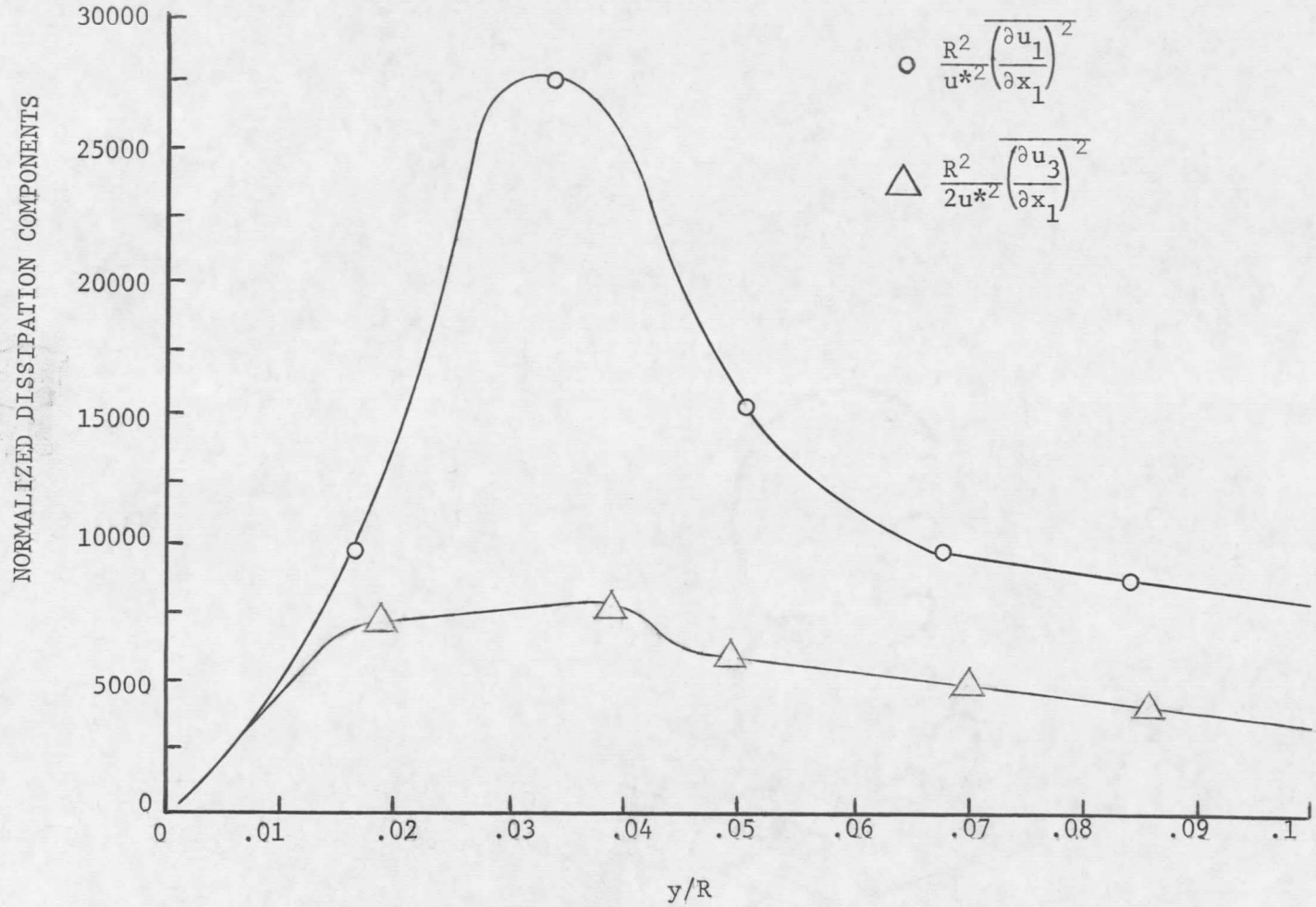

FIGURE 195. Dissipation Terms for Wall Region of Pipe With Large Roughness Elements

should be noted, however. Although all terms are nearly equal at the pipe center line, the maximum values are significantly different as indicated by the differences in scale in Figures 194 and 195.

The maximum value of $\frac{R^2}{2u^{*2}}\overline{\left(\frac{\partial u_3}{\partial x_1}\right)^2}$ is smallest at about 8,000 while $\frac{R^2}{u^{*2}}\overline{\left(\frac{\partial u_1}{\partial x_1}\right)^2}$ is largest near 30,000. Both $\frac{R^2}{2u^{*2}}\overline{\left(\frac{\partial u_1}{\partial x_2}\right)^2}$ and $\frac{R^2}{2x_2^2u^{*2}}\overline{\left(\frac{\partial u_1}{\partial x_3}\right)^2}$ indicate maximum values of 16,000, and $\frac{R^2}{2u^{*2}}\overline{\left(\frac{\partial u_2}{\partial x_1}\right)^2}$ is slightly lower at 12,000. All these maxima occur just above the roughness elements at y/R near 0.03 to 0.04.

The foregoing experimental data can now be combined with the istoropic relations given by equation (5.20) for determination of the dissipation function itself, and a dimensionless form of this function is given as the solid line in Figure 196. In similarity with the terms comprising W, the dimensionless dissipation function is very small at the pipe center line, though not zero, and reveals a slow rate of increase at this point. This rate of increase grows in a rather gradual fashion until a maximum value of the dimensionless dissipation function near 0.0043 is attained at the top of the roughness elements. The dissipation function then diminishes rapidly to

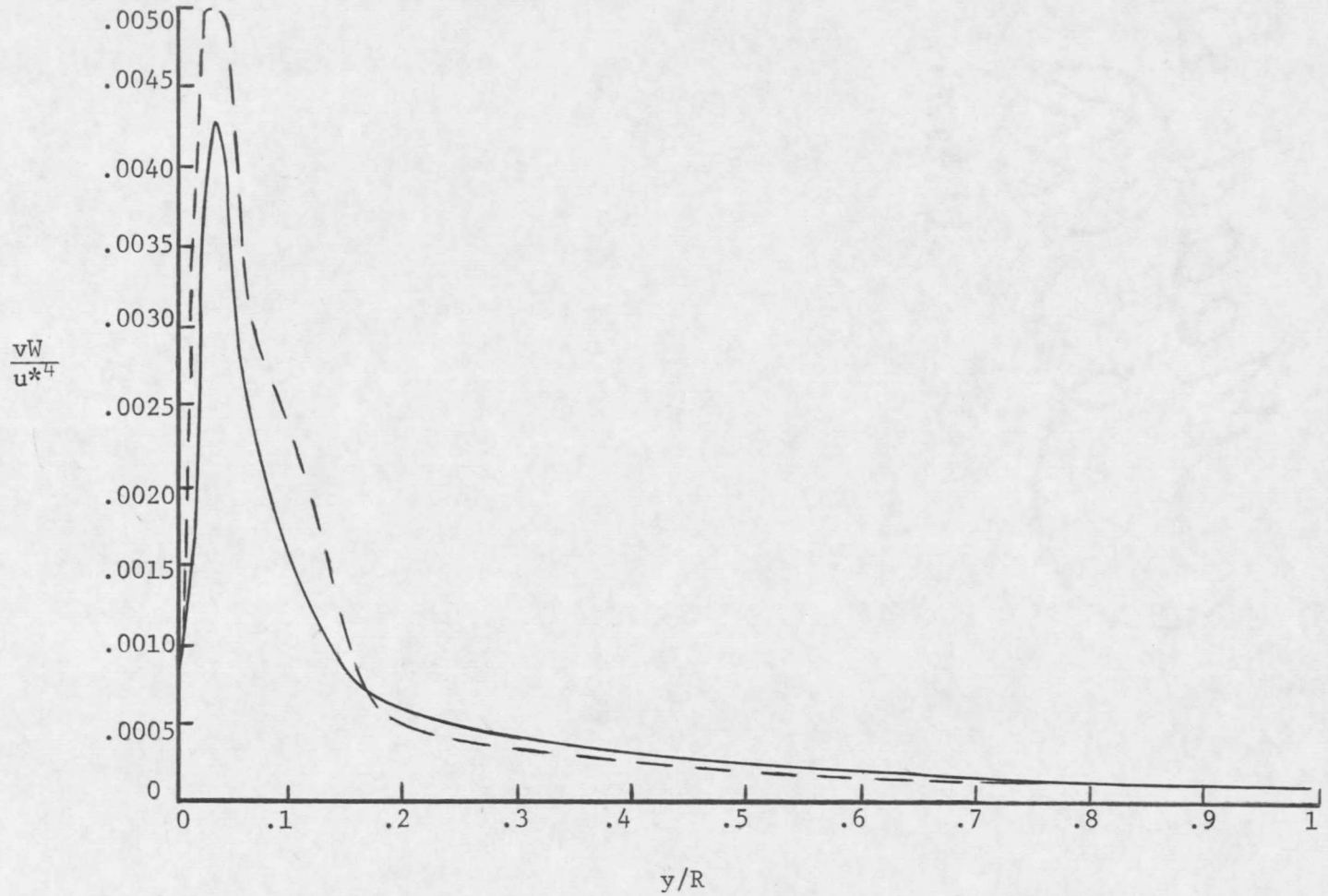

FIGURE 196. Dissipation Function for Pipe With Large Roughness Elements

zero.

The dashed line shown in Figure 196 is representative of the dissipation function calculated from equation (5.21) where complete isotropy between all terms is assumed. The dissipation calculated in this manner is seen to be a very good approximation to that obtained experimentally except just beyond the roughness elements where the maximum dissipation occurs. Here the dissipation calculated by assuming complete isotropy differs at most by about 17% from that determined experimentally.

A check on the validity of applying Taylor's hypothesis for the shear flow currently under investigation may be obtained by inspection of Figure 197. In this figure, Lin's [79] condition, equation (2.78b), is investigated. This condition is seen to be satisfied to an extremely high degree of accuracy for y/R greater than about 0.1, and then the ordinate does not exceed about 7% until below the mean height of the roughness elements. Thus, Lin's condition regarding the applicability of Taylor's hypothesis is satisfied with a reasonable degree of accuracy throughout the entire flow field above the sand grains.

Energy Relations

Consider first the mean energy balance given by equation (4.30).

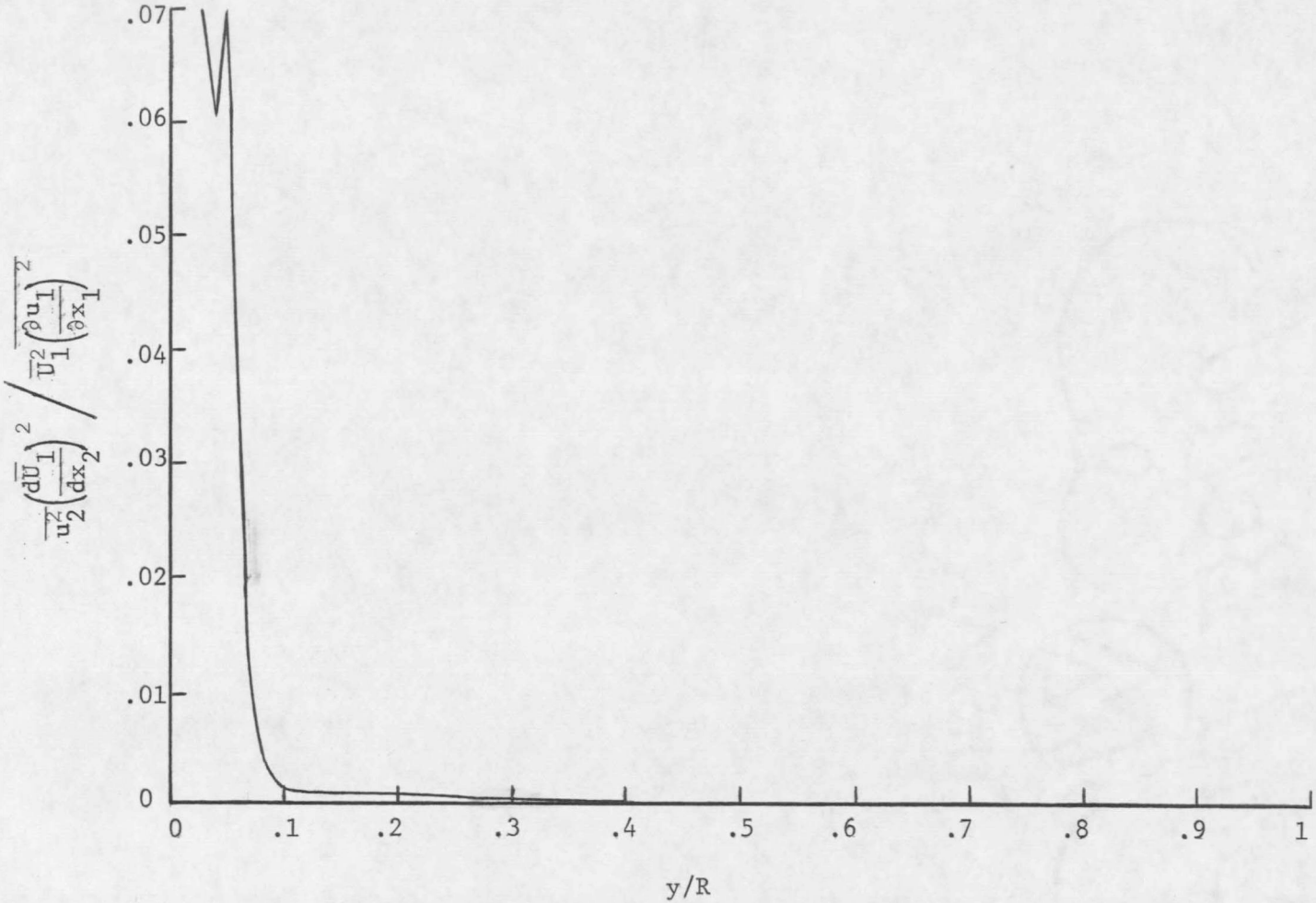

FIGURE 197. Lin's Condition for Applicability of Taylor's Hypothesis in Pipe With Large Roughness Elements

Experimentally determined values of the terms appearing in this energy equation are shown in Figures 198, 199, and 200 for the central region of the pipe and in Figures 200, 201, and 202 for the wall region. The mean energy available due to the pressure drop along the pipe is seen, from Figures 198 and 201, to be relatively small over the central region of the pipe. The availability then peaks to a maximum magnitude slightly above the top of the roughness elements and begins to decrease as the elements themselves are approached. A minimum magnitude occurs at about one half the average roughness height, and the availability then shows a sharp increase in magnitude. The portion of the mean energy which is directly dissipated by viscous effects, shown in Figures 199 and 202, is seen to follow a behavior essentially identical to that described for the availability of mean energy. However, the magnitude of the dissipation is observed to be much smaller than the availability throughout the pipe indicating that a significant portion of the mean energy available must be converted to some other form. This statement is confirmed by Figure 200 which represents the mean energy converted to turbulence energy and that converted to an energy associated with the presence of the roughness elements. Over the central portion of the pipe, these two conversion terms are seen to be approximately equal, but at about the point where availability

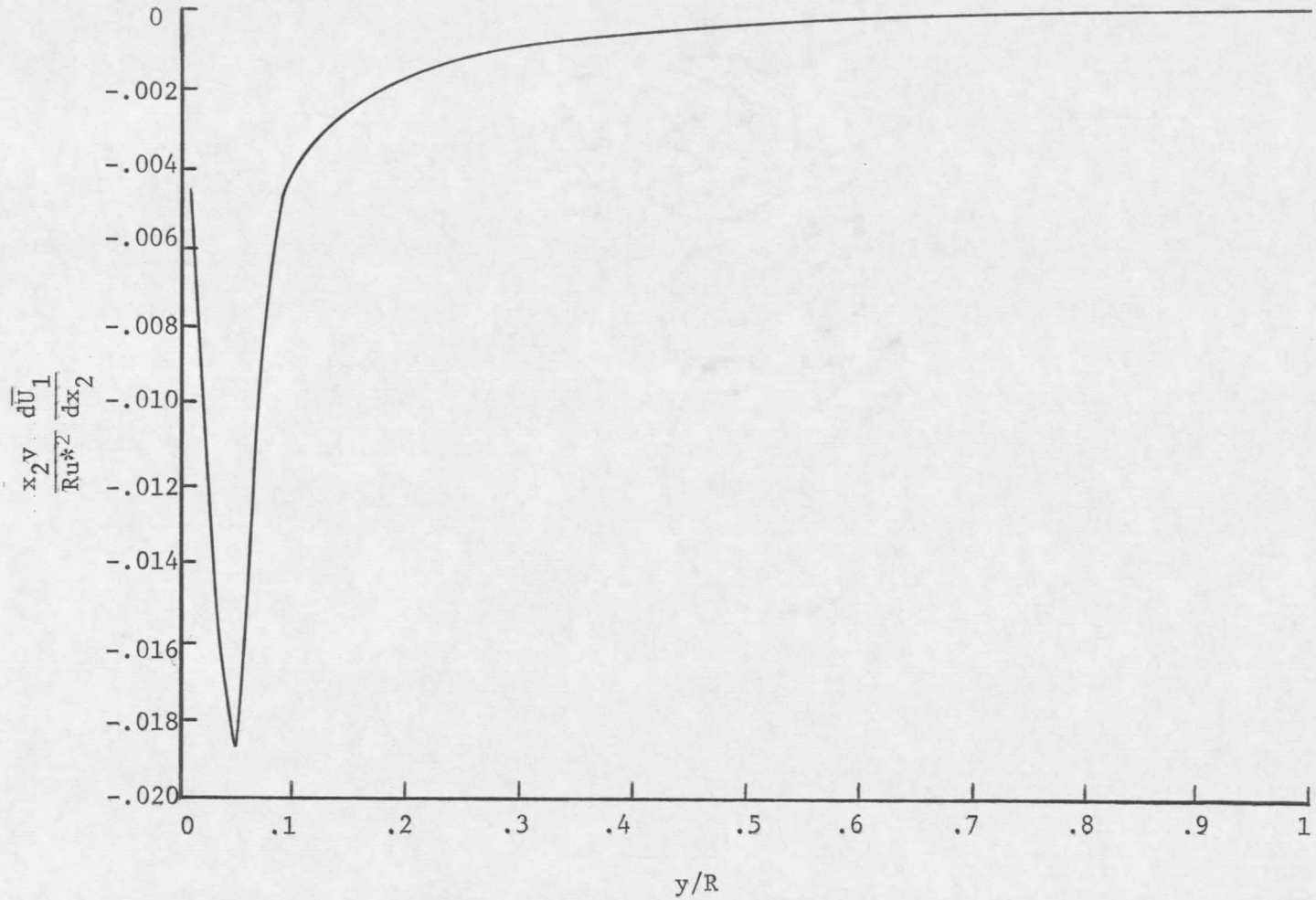

FIGURE 198. Availability of Mean Energy in Central Region of Pipe With Large Roughness Elements

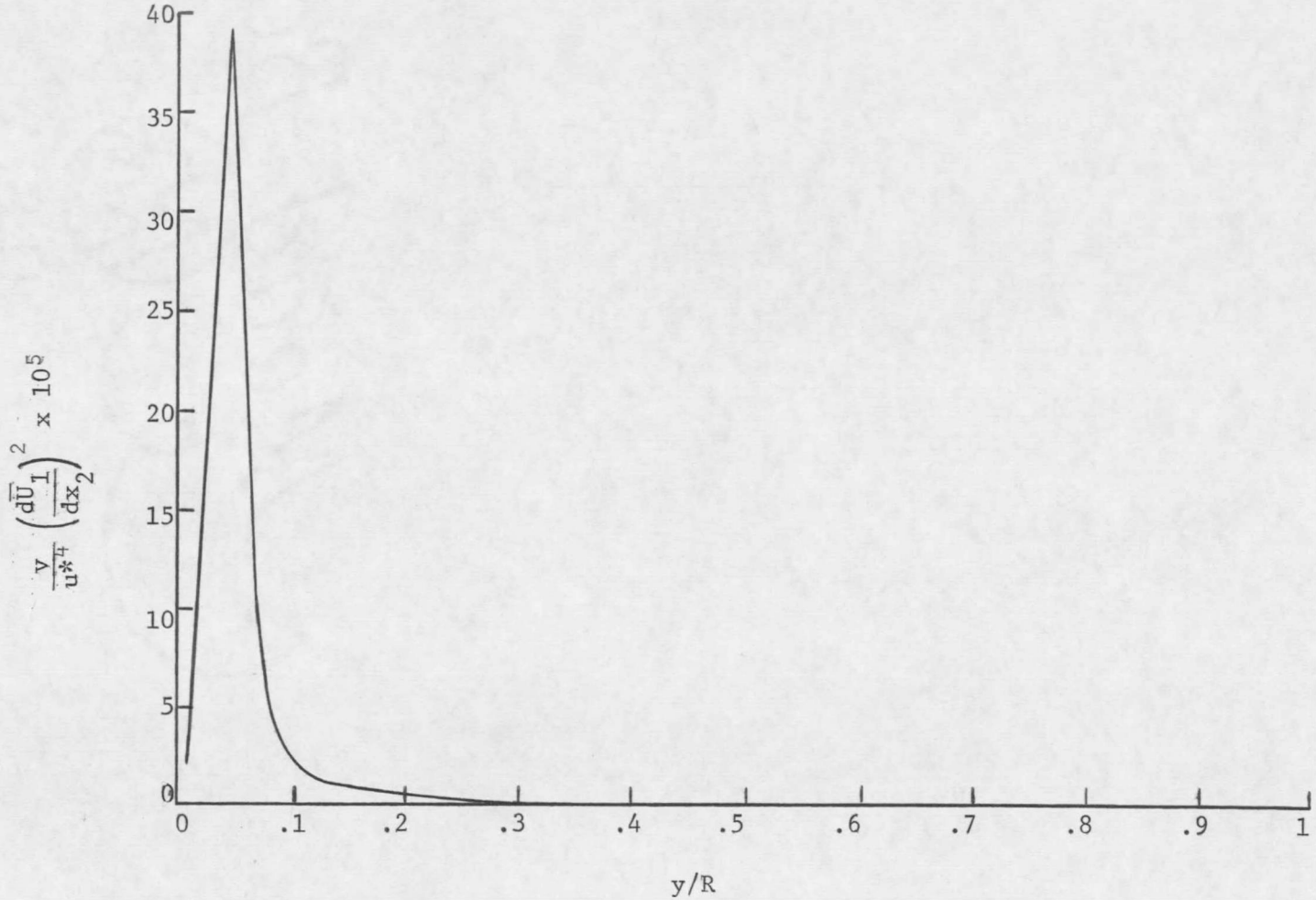

FIGURE 199. Viscous Dissipation of Mean Energy in Central Region of Pipe With Large Roughness Elements

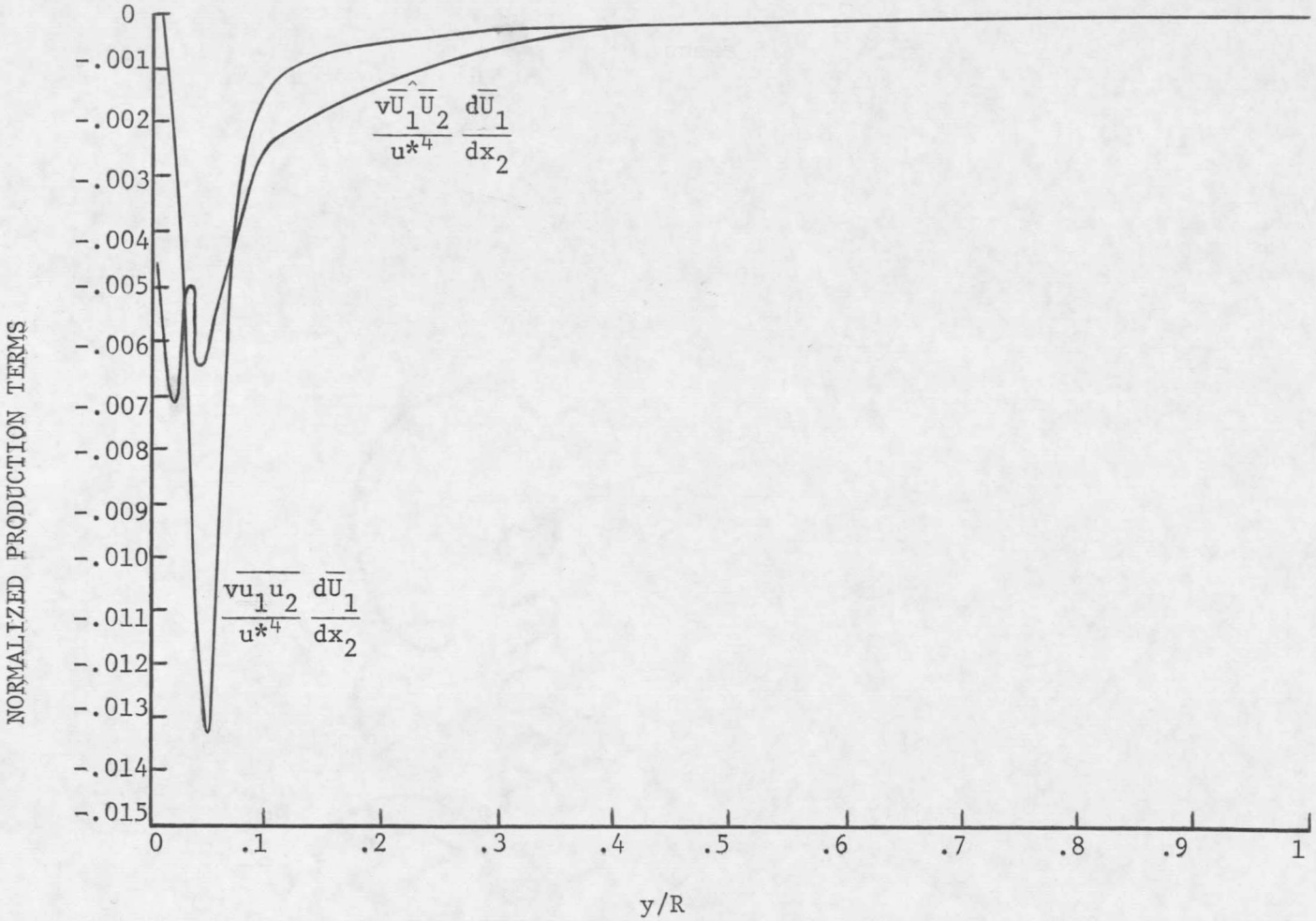

FIGURE 200. Mean Energy Conversion Terms for Pipe With Large Roughness Elements

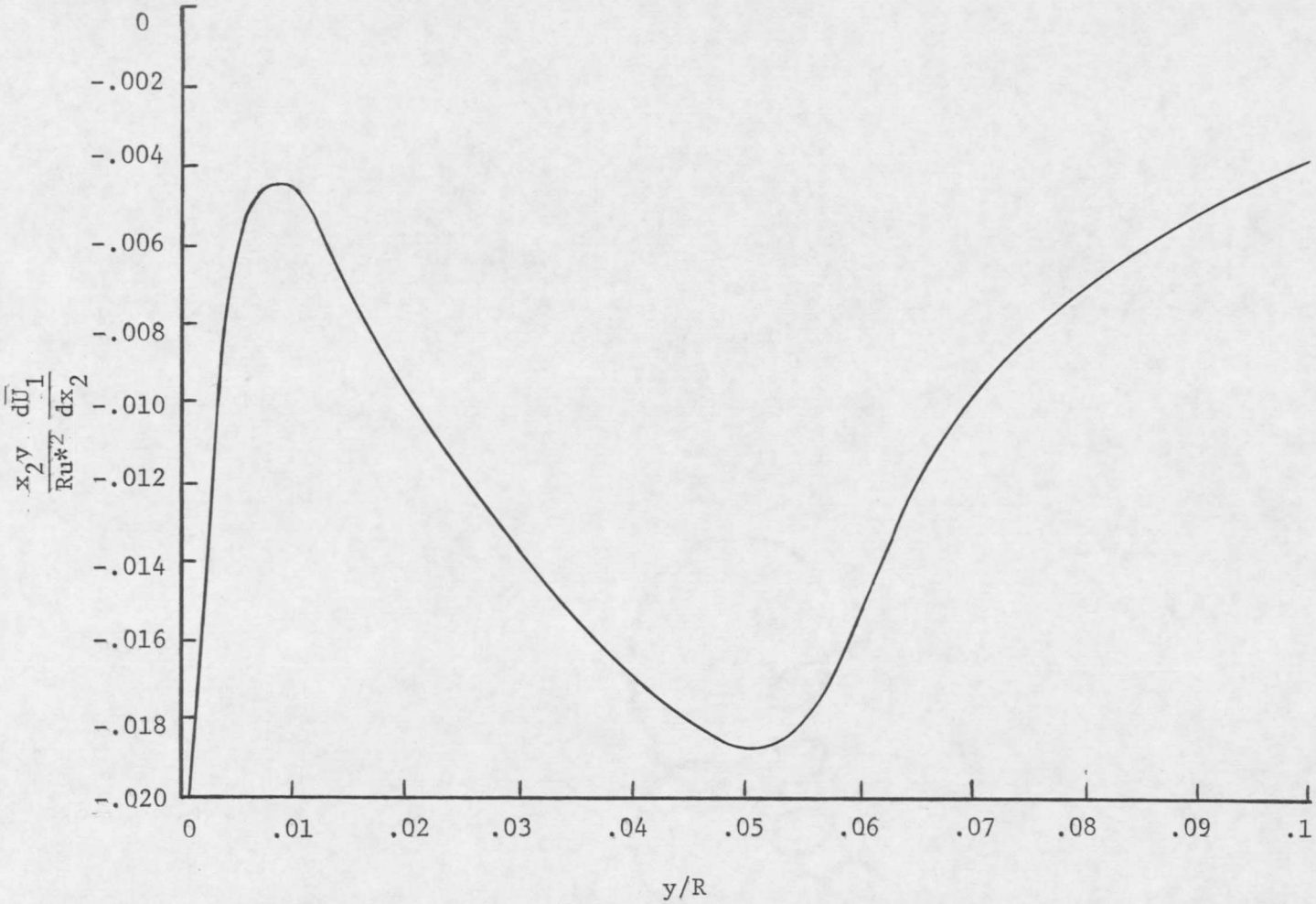

FIGURE 201. Availability of Mean Energy Near Wall of Pipe With Large Roughness Elements

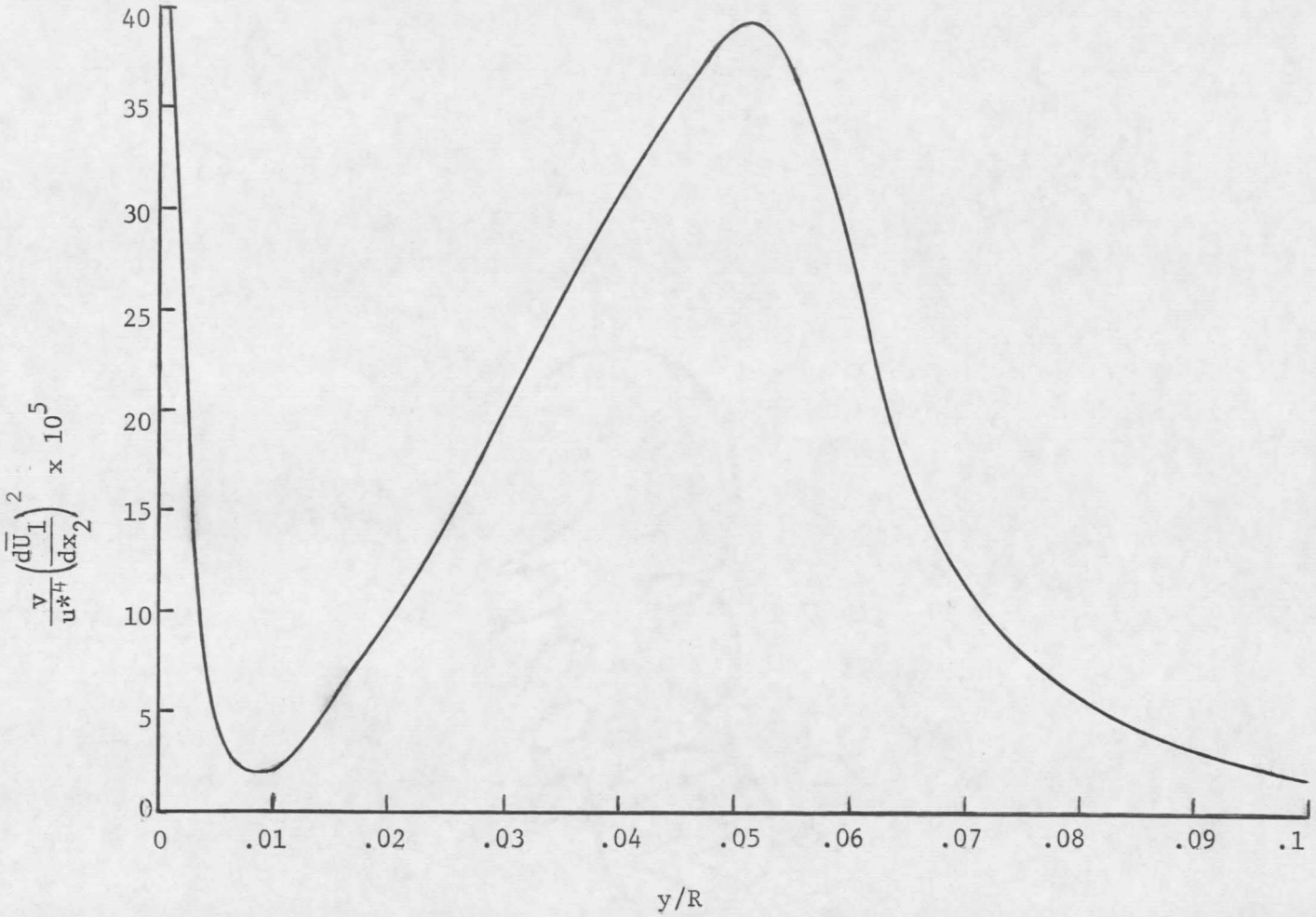

FIGURE 202. Viscous Dissipation of Mean Energy Near Wall of Pipe With Large Roughness Elements

and dissipation possessed maximum magnitudes, the production of turbulence energy far exceeds the production of roughness energy. The turbulence energy production then decreases much more rapidly than does the roughness energy production. Thus, for values of y/R less than ε/R, the roughness energy production exceeds the turbulence energy production.

To summarize these results it should be noted that the bulk of the available energy is taken from the mean flow in a narrow region above the roughness elements. Although a part of this energy is directly dissipated, a large portion is converted into turbulence and roughness energies. Except for the small region near the roughness elements, these two energy production terms are nearly equal throughout the pipe.

Having established the amount of energy converted from the mean motion to turbulence energy, the expression for the turbulence energy balance, equation (4.29), will now be examined in order to determine the fate of this converted energy. The portion of this energy which is dissipated by viscous effects was considered in the previous section, and the experimental results are indicated by the solid line in Figure 196. A comparison of the production and dissipation produces the result that these two quantities nearly balance each other over the central and major portion of the cross-section. However, at the

pipe center line the turbulence production vanishes while the dissipation does not, and the magnitude of the production is seen to be significantly larger than that of the dissipation just beyond the roughness elements. This demands the diffusion of a large amount of energy from this area in order for the energy balance to be satisfied.

Experimentally determined values of the gradient type diffusion of turbulence kinetic energy are indicated in Figure 203 for the central region of the pipe and in Figure 204 for the wall region. This term is observed to be nearly zero over the entire central portion of the pipe. For y/R near 0.1 a very small magnitude maximum is observed, and just above the roughness elements a much larger magnitude minimum value is encountered. The gradient diffusion remains positive for values of y/R less than the mean height of the roughness elements. These results indicate that the gradient diffusion, although small, represents a gain of energy at a radial position just beyond the top of the roughness elements and a loss in energy at other radii. Thus, the gradient diffusion of turbulence energy is toward the tops of the roughness elements from both the wall and the center line.

All terms appearing in the turbulence energy balance have now been determined experimentally except the convective diffusion term

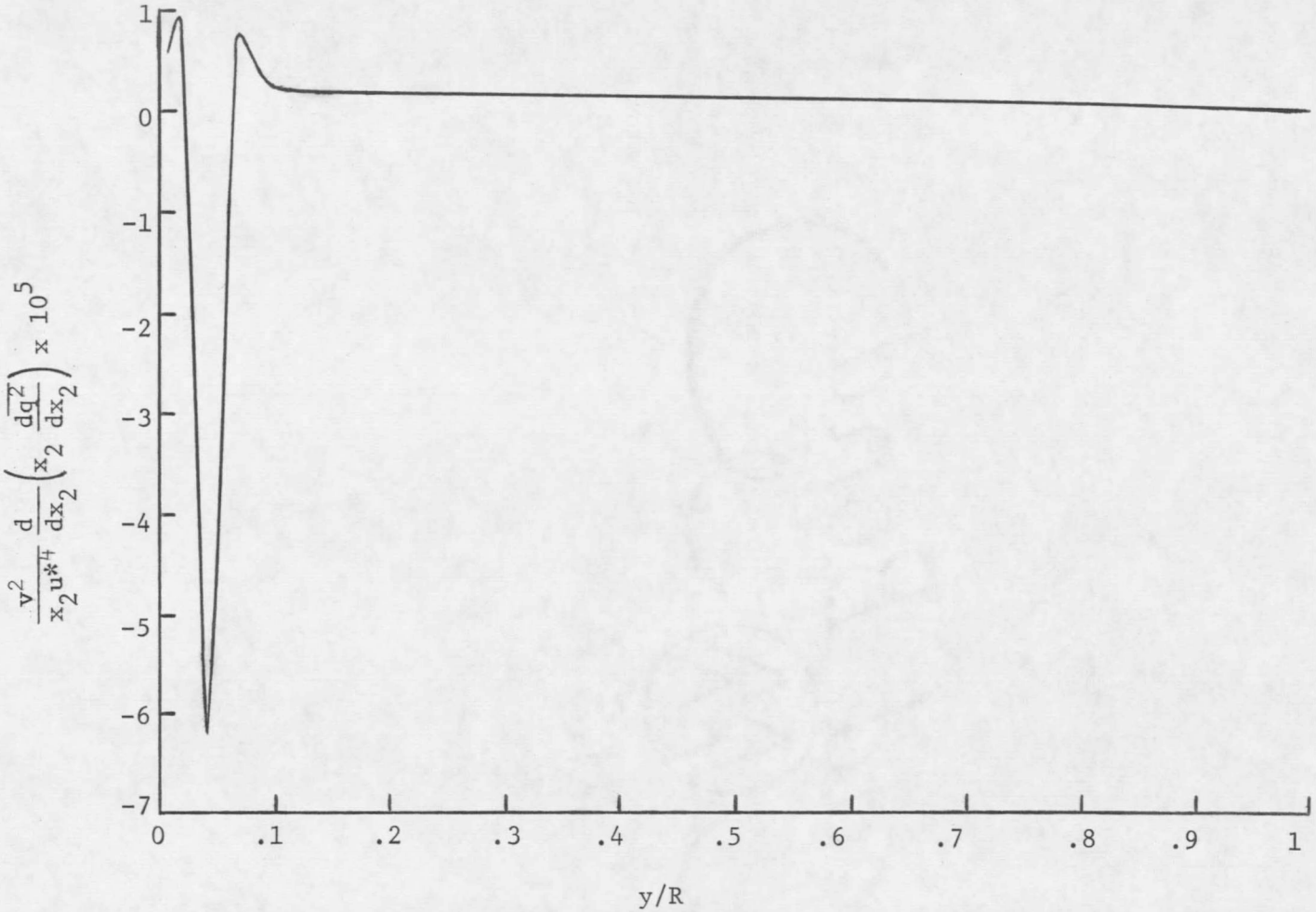

FIGURE 203. Gradient Diffusion of Turbulence Kinetic Energy in Central Region of Pipe With Large Roughness Elements

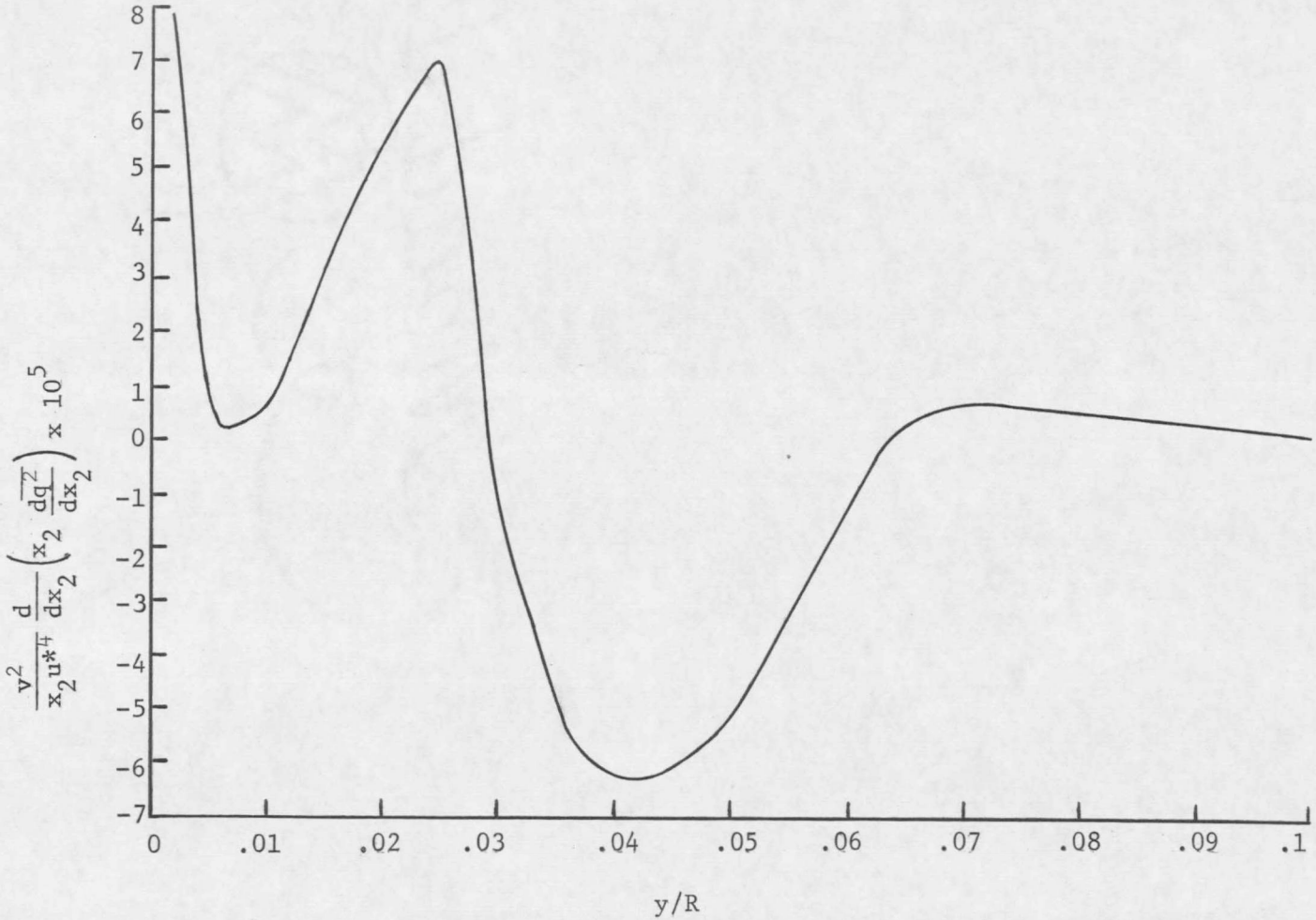

FIGURE 204. Gradient Diffusion of Turbulence Kinetic Energy Near Wall Of Pipe With Large Roughness Elements

χ, and this term may now be calculated as the closing entry in equation (4.29). As pointed out in the previous chapter, it should be remembered that this term also contains, in addition to the convective diffusion, any interactions between turbulence and roughness energy terms. The results of this calculation for χ are presented in Figures 205 and 206. This term is observed to be somewhat larger than the gradient diffusion of kinetic energy for almost all radial positions. Negative values are indicated for values of y/R greater than about twice the mean roughness height, but a pronounced maximum occurs just above the top of the sand grains. This indicates a substantial loss in energy from this region and a corresponding energy gain in the turbulent core of the pipe. Thus, the production and diffusion terms are accounted for in the fluid layers immediately above the sand grains, and dissipation without production at the center line is justified.

Energy Spectra

A contour map of the energy spectra of the u_1 fluctuating velocities is presented in Figure 207 for the frequency domain, and transformation to the wave number space is indicated by Figure 208. These figures show that, for any given value of y/R, E_1 has a relatively large magnitude at small frequencies and rapidly

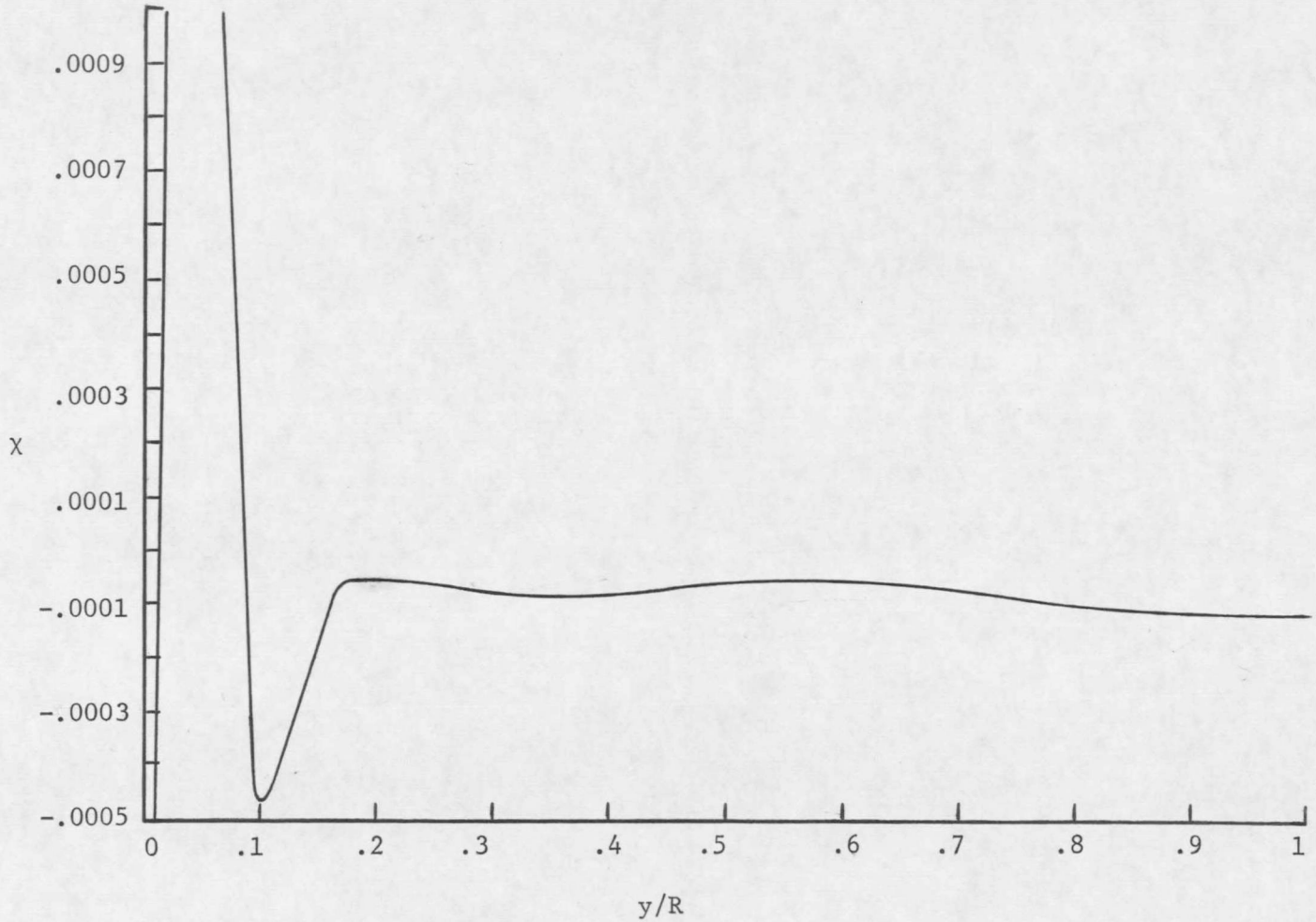

FIGURE 205. Convective Diffusion of Turbulence Energy in Central Region of Pipe With Large Roughness Elements

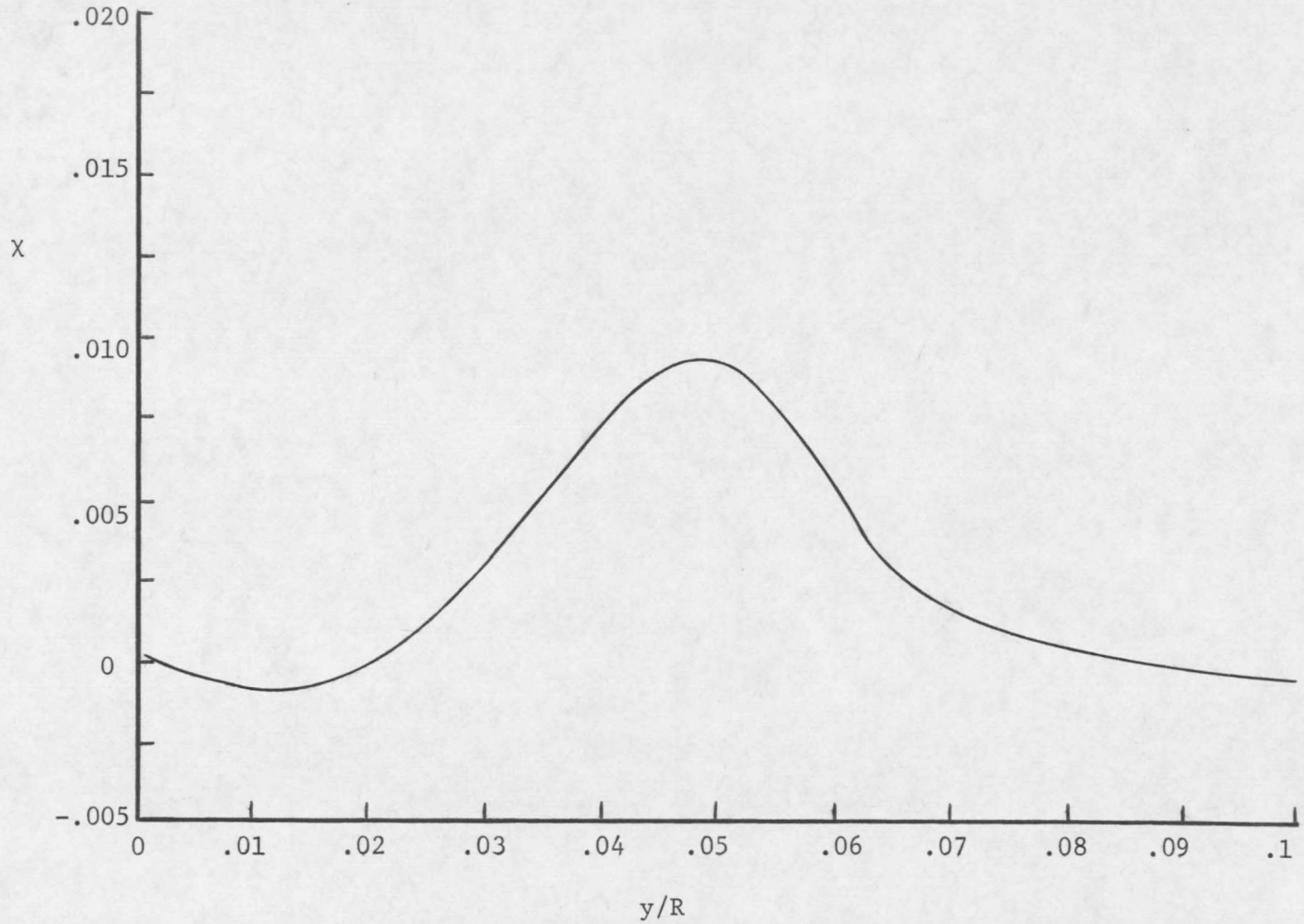

FIGURE 206. Convective Diffusion of Turbulence Energy in Wall Region of Pipe With Large Roughness Elements

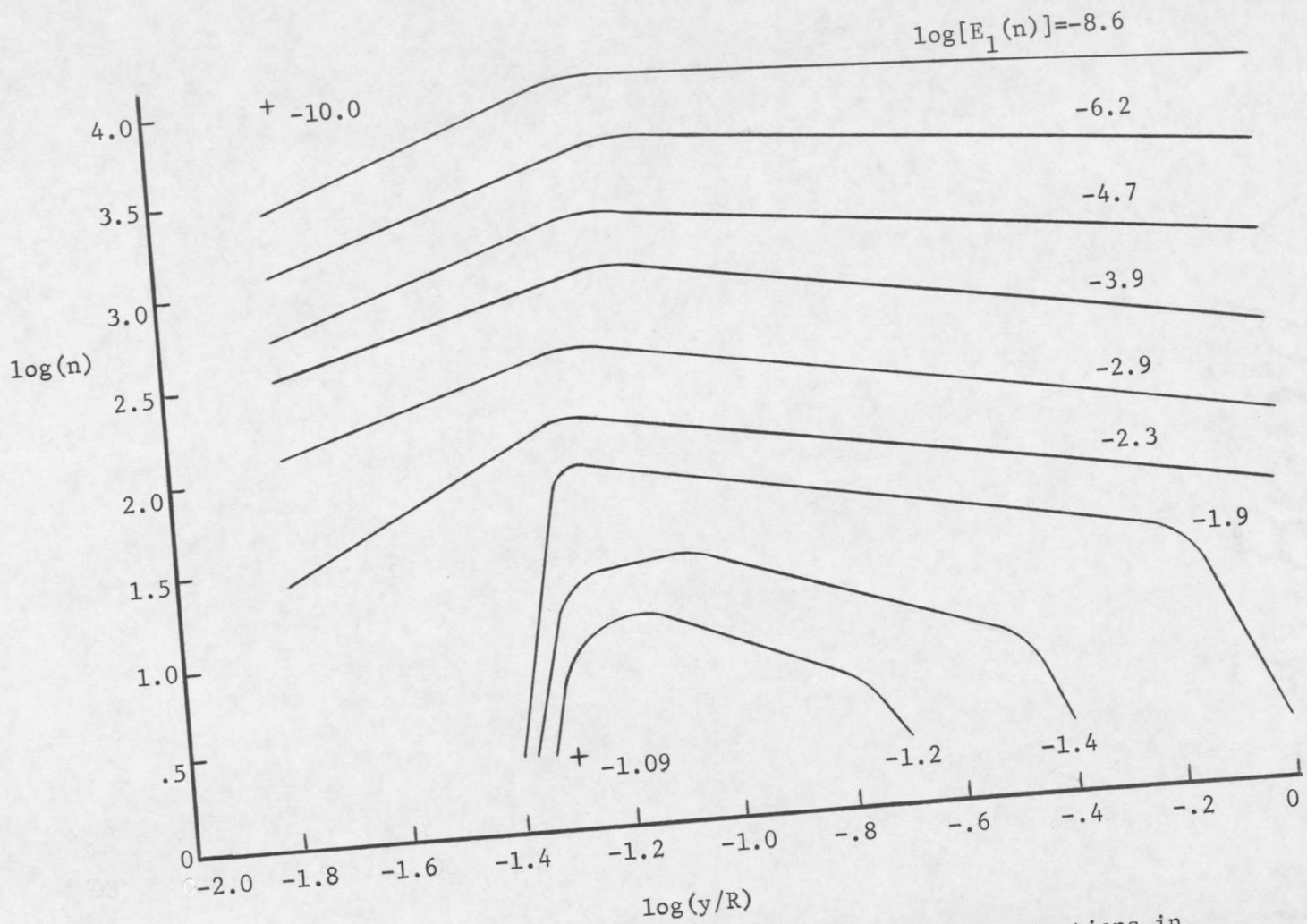

FIGURE 207. Frequency Domain Energy Spectra for u_1 Fluctuations in Pipe With Large Roughness Elements

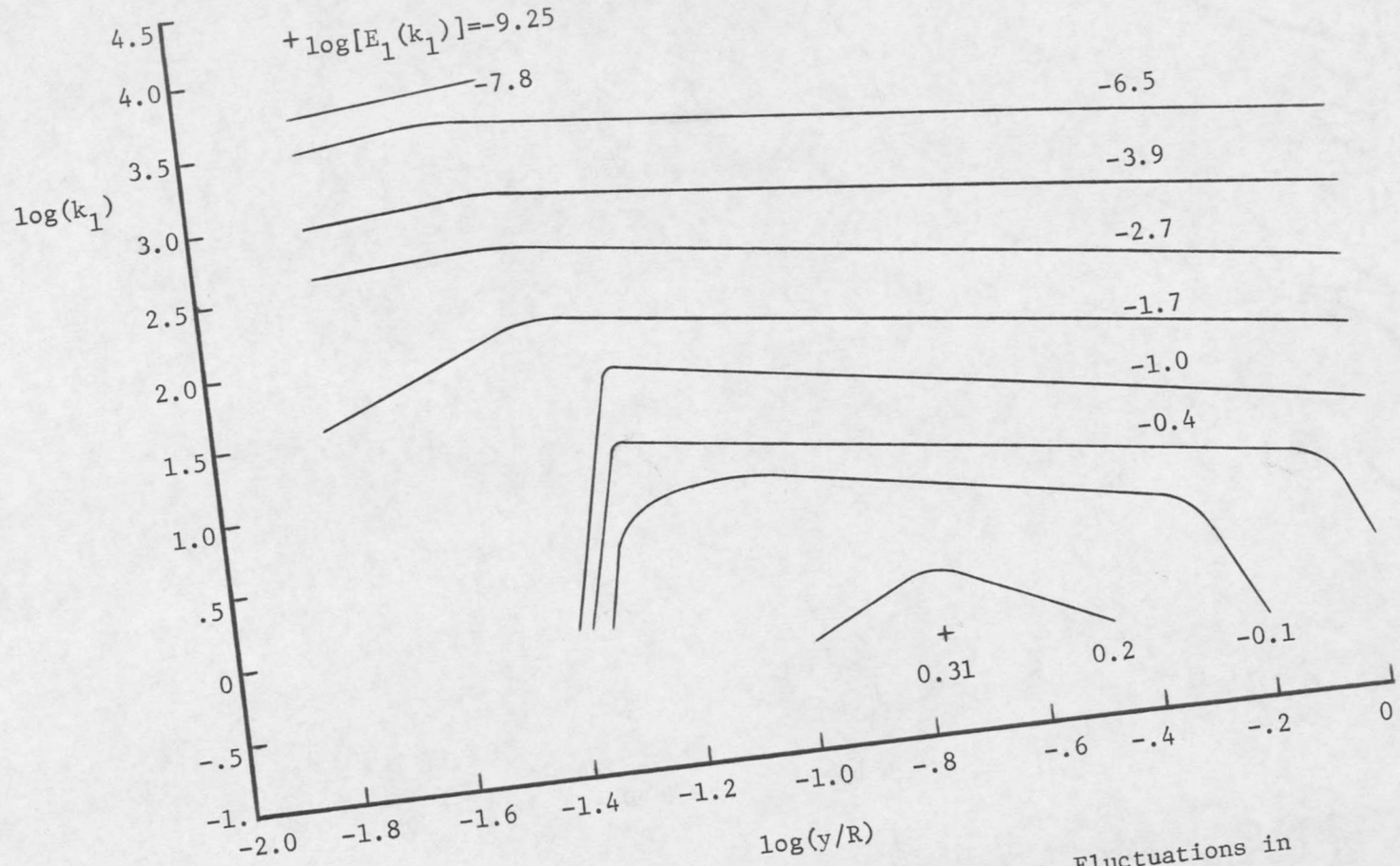

FIGURE 208. Wave Number Space Energy Spectra for u_1 Fluctuations in Pipe With Large Roughness Elements

decreases as higher frequencies are approached. Figure 208 indicates that for a given wave number there is a decrease in energy content of the dissipation eddies in moving from the top of the roughness elements to the center line of the pipe in agreement with the previous examination of the turbulence energy equation. Again for a constant wave number, the energy content of the eddies associated with production and diffusion is seen to exhibit a rapid decline, at both the wall and the center line, from a maximum value at an intermediate radial position. The value of y/R where this maximum occurs is slightly greater than 0.1 for the lower wave numbers, and this value of y/R decreases toward the roughness elements as the wave number is increased.

The possible existence of the various subranges of eddy sizes can be established by an examination of Figures 209, 210, and 211. Figure 209 shows the inertial subrange where the dominant process is the transfer of energy from smaller to larger wave numbers without significant production or dissipation. Such a subrange appears over a substantial range of wave numbers over the entire pipe cross-section and the wave numbers where this law applies decrease slightly in moving from the top of the roughness elements to $y/R \simeq 0.1$ but remain essentially constant from this point to the pipe center line. The production subrange is shown to indicate a similar behavior in

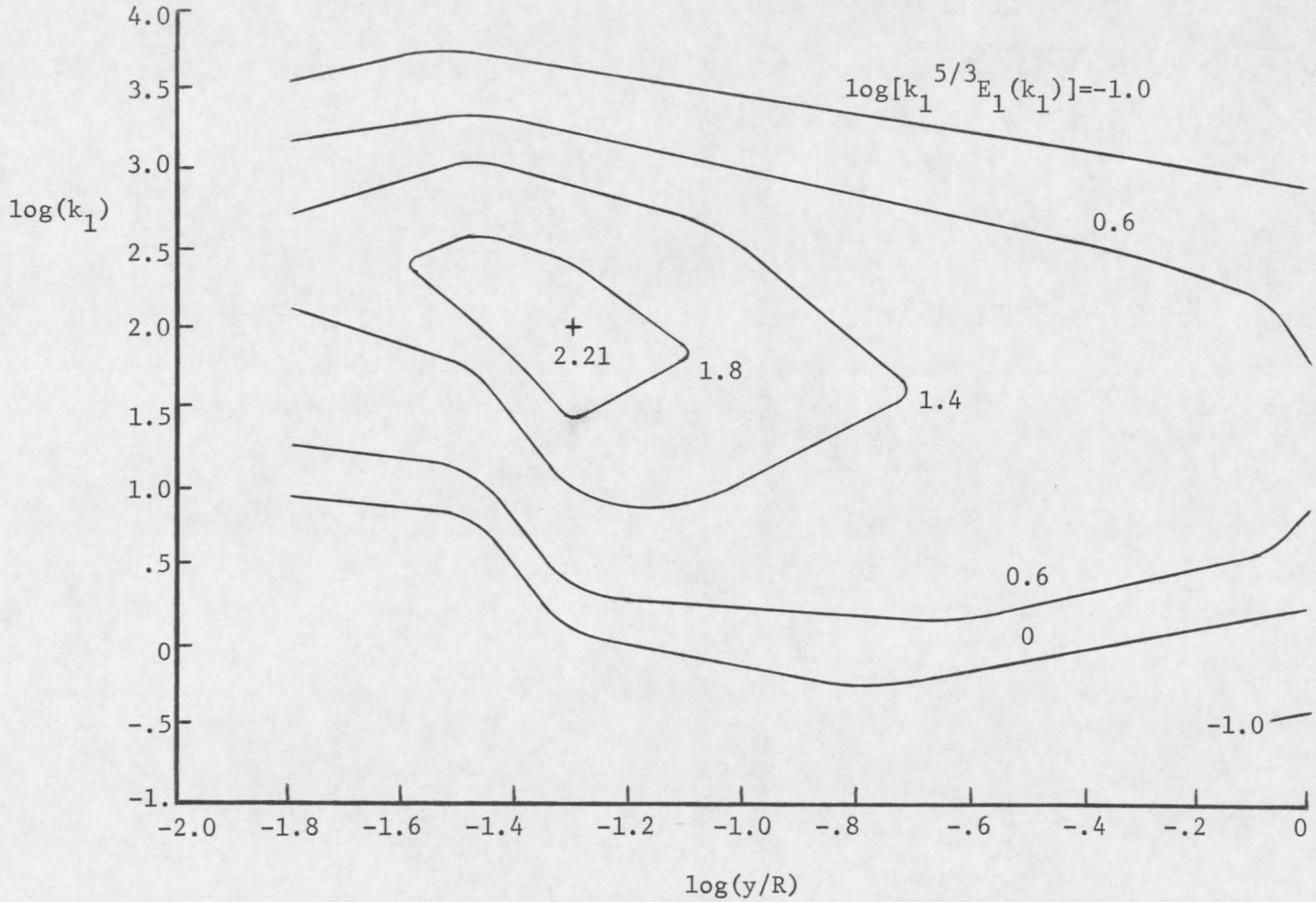

FIGURE 209. Inertial Subrange of Eddy Sizes for u_1 Fluctuations in Pipe With Large Roughness Elements

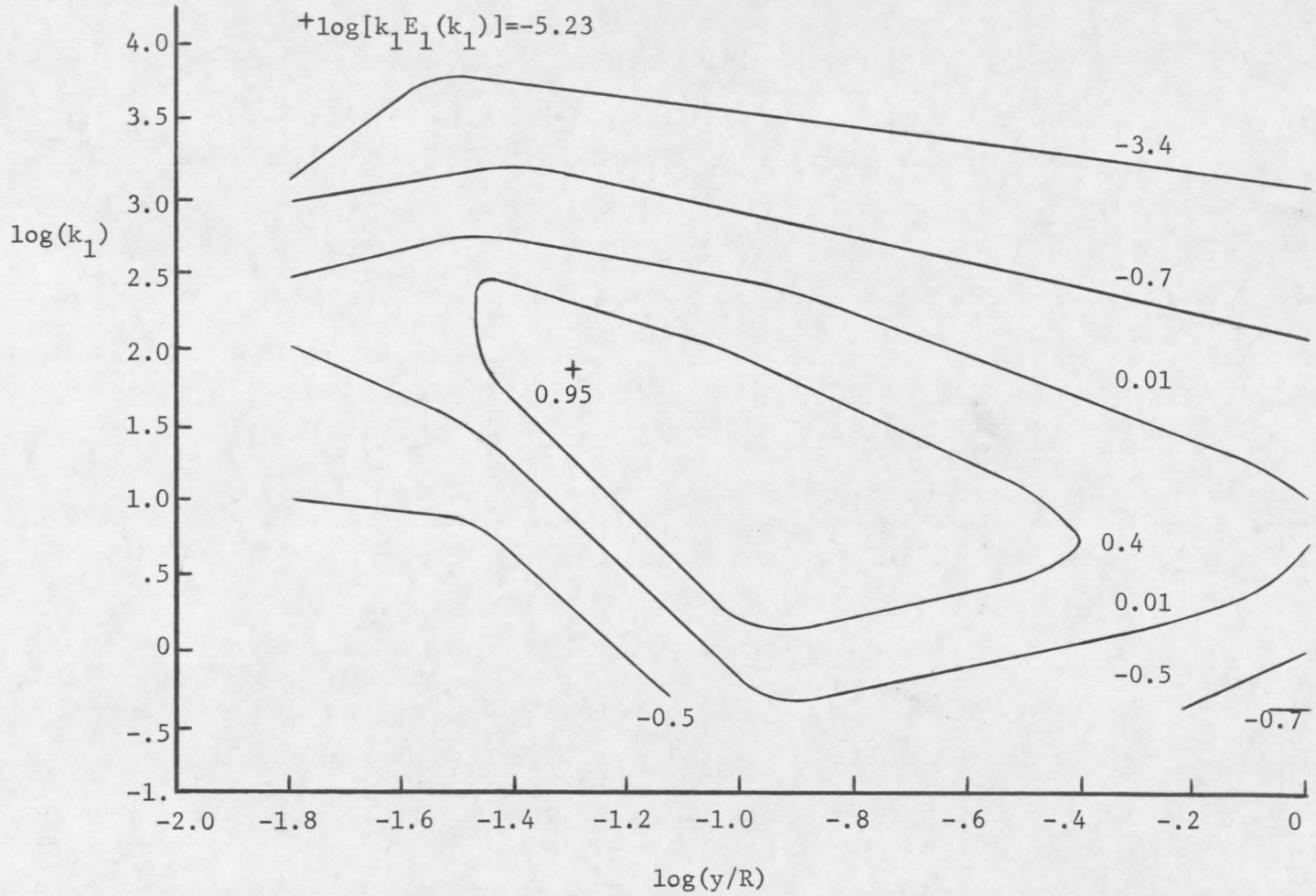

FIGURE 210. Production Subrange of Eddy Sizes for u_1 Fluctuations in Pipe With Large Roughness Elements

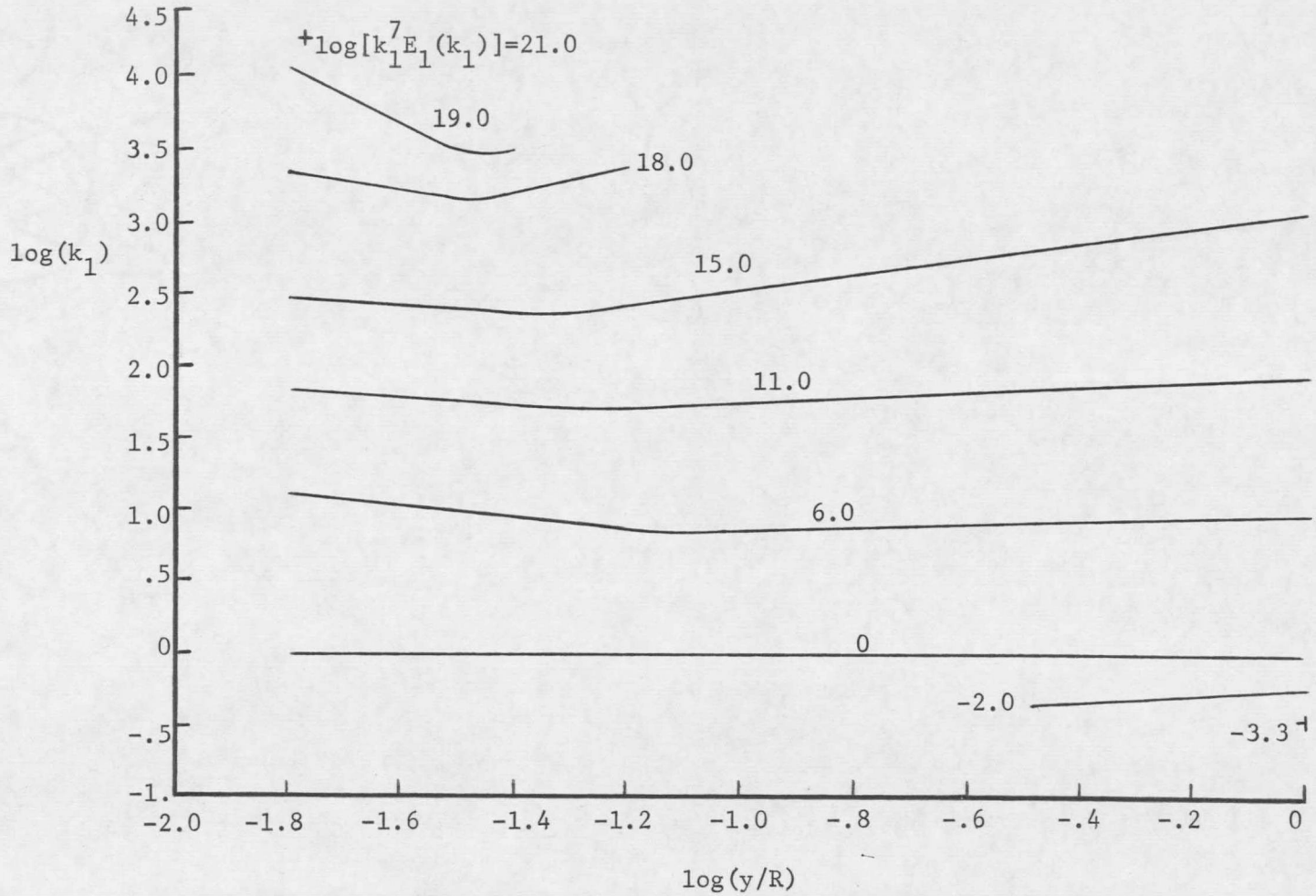

FIGURE 211. Viscous Subrange of Eddy Sizes for u_1 Fluctuations in Pipe With Large Roughness Elements

Figure 210. A comparison of these two figures reveals that the production subrange does occur for slightly larger eddies than does the inertial subrange, and this is exactly the behavior predicted by Tchen [84]. Within the range of variables examined experimentally in this investigation, an absence of any viscous subrange of eddy sizes is noted in Figure 211 for all values of y/R. The shape of the contours in this figure does indicate, however, that such a subrange will probably occur for wave numbers slightly larger than those obtained experimentally.

The dimensionless coordinate systems proposed by Robertson et al [47] and Goma and Gelhar [30] for yielding the spectrum function independent of radial position are evaluated in Figures 212 and 213. Figure 213 shows that the coordinates proposed by Goma and Gelhar [30] yield good results at all values of y/R only for large values of $2nR/\overline{U}_1$. However, the coordinates proposed by Robertson et al [47] appear to yield excellent results over the entire range of experimental variables, although a slight deviation does occur near the wall for large values of $n\Lambda_1/\overline{U}_1$.

Energy spectra in the frequency domain and the wave number space for the velocity fluctuations in the x_2 coordinate direction are shown in Figures 214 and 215 respectively. As in the case of the E_1 spectra, a slight decrease in the energy content of the dissipation eddies may be observed in moving from the wall to the center line of

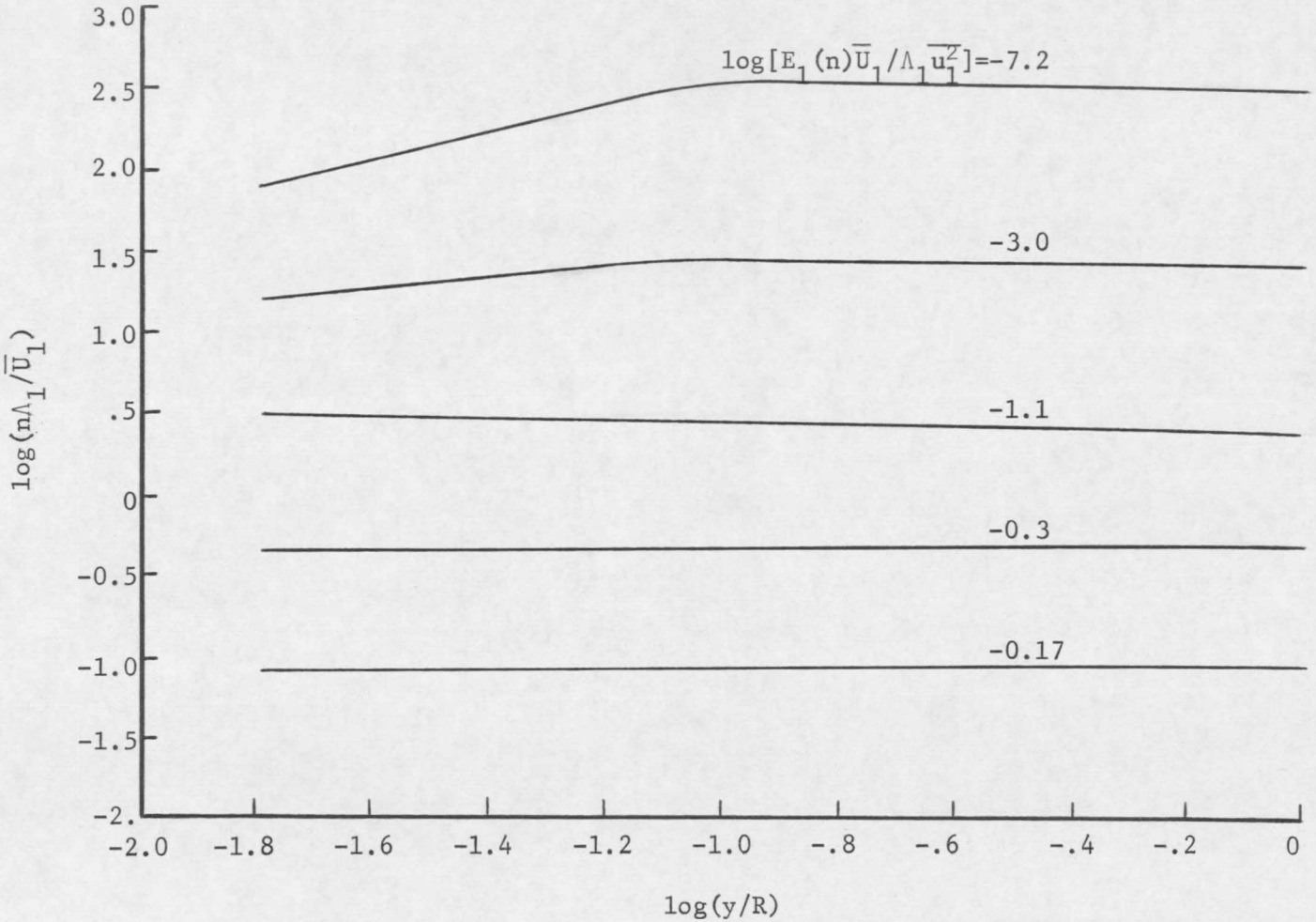

FIGURE 212. u_1 Spectra for Pipe With Large Roughness Elements Normalized as Proposed by Robertson et al [47]

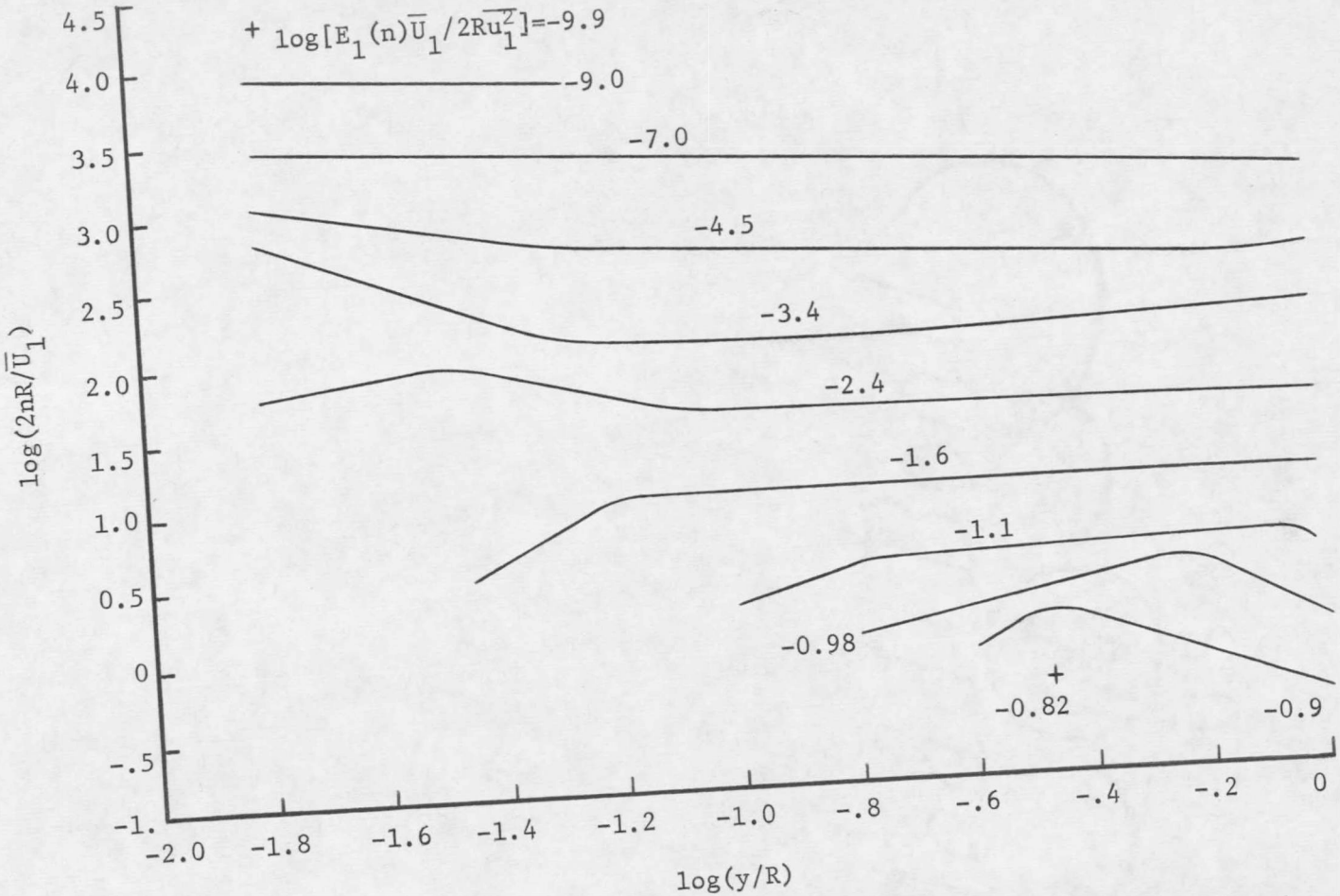

FIGURE 213. u_1 Spectra for Pipe With Large Roughness Elements Normalized as Proposed by Goma and Gelhar [30]

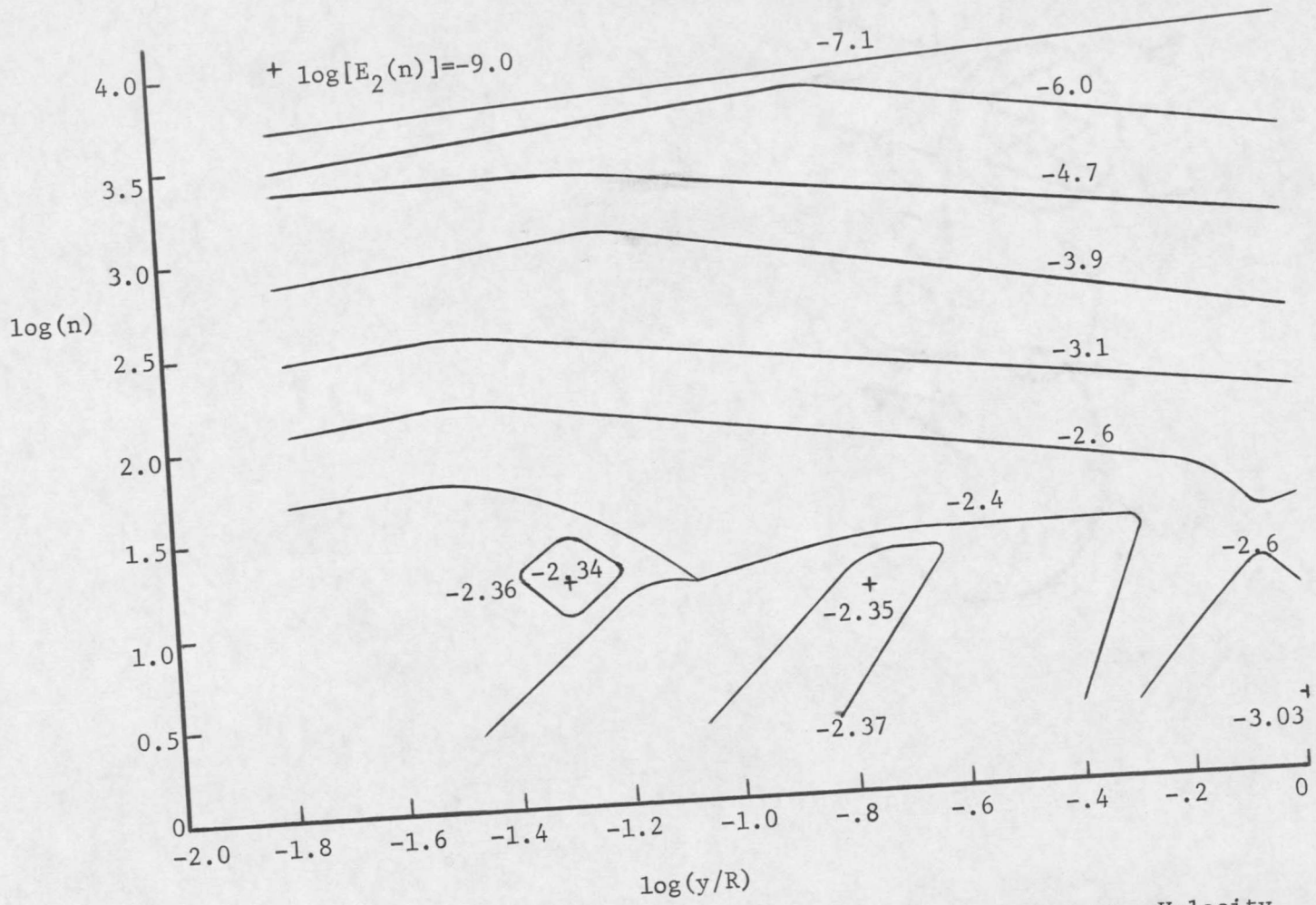

FIGURE 214. Frequency Domain Energy Spectra for u_2 Fluctuating Velocity in Pipe With Large Roughness Elements

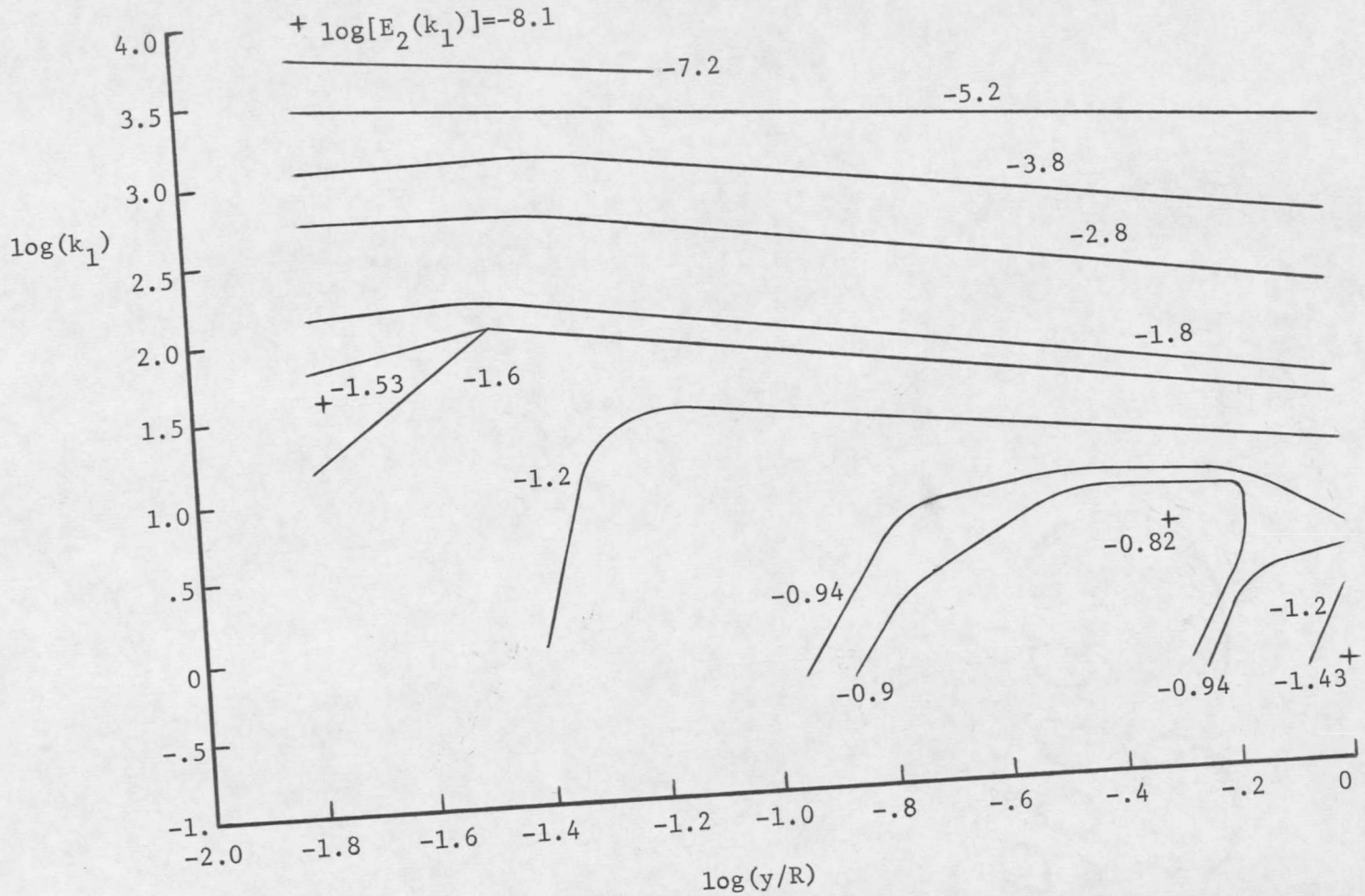

FIGURE 215. Wave Number Space Energy Spectra for u_2 Fluctuations in Pipe With Large Roughness Elements

the pipe at a constant frequency or wave number. As was the case for the smooth pipe and the pipe containing the small roughness elements, a significantly different behavior of the E_2 and E_1 spectra are observed for low wave numbers where an energy deficiency occurs in the E_2 spectra for all values of y/R. This type of energy defect is thought to be due to the convective diffusion of pressure energy which is an intermediate wave number phenomena, but care must be utilized in applying this interpretation for rough pipes, as pointed out in the previous chapter, since the convective diffusion term also represents interactions between roughness and turbulence energy. The generally smaller magnitude of the E_2 spectra than the E_1 spectra at a given wave number and a given value of y/R, as indicated by a comparison of Figure 208 and 215, would be expected due to the smaller magnitude of $\overline{u_2^2}$ at any radial position.

The various subranges of eddy sizes for the E_2 spectra are examined by means of Figures 216, 217, and 218. As in the case of the E_1 spectra, the inertial and production subranges are seen to be exhibited over a fairly wide range of wave numbers throughout the pipe, and an increase in magnitude of the wave numbers where these subranges appear is observed in moving from the center line toward the wall. Also, the production subrange again occurs for slightly larger eddies than does the inertial subrange, and the existence of the viscous

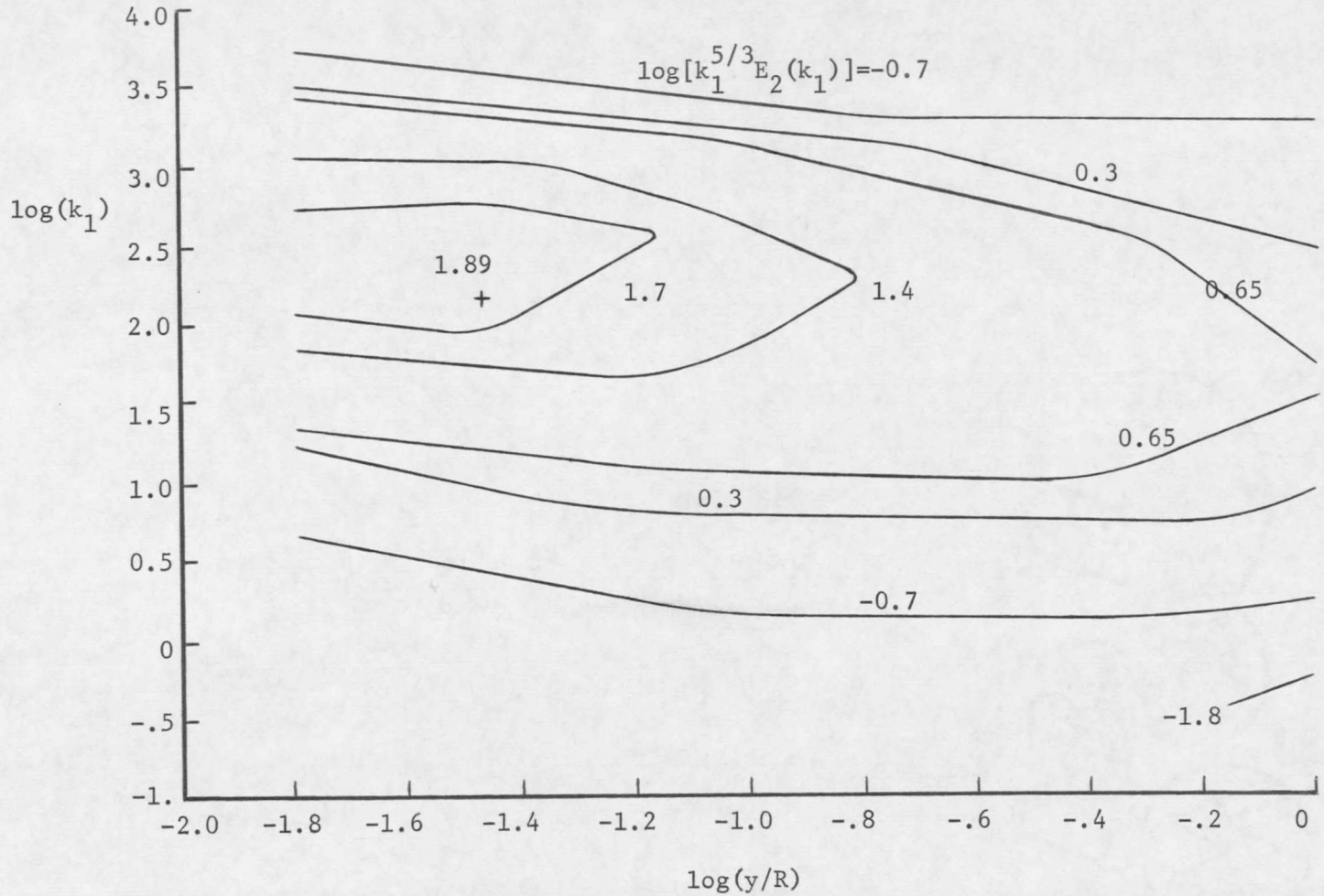

FIGURE 216. Inertial Subrange of Eddy Sizes for u_2 Fluctuations in Pipe With Large Roughness Elements

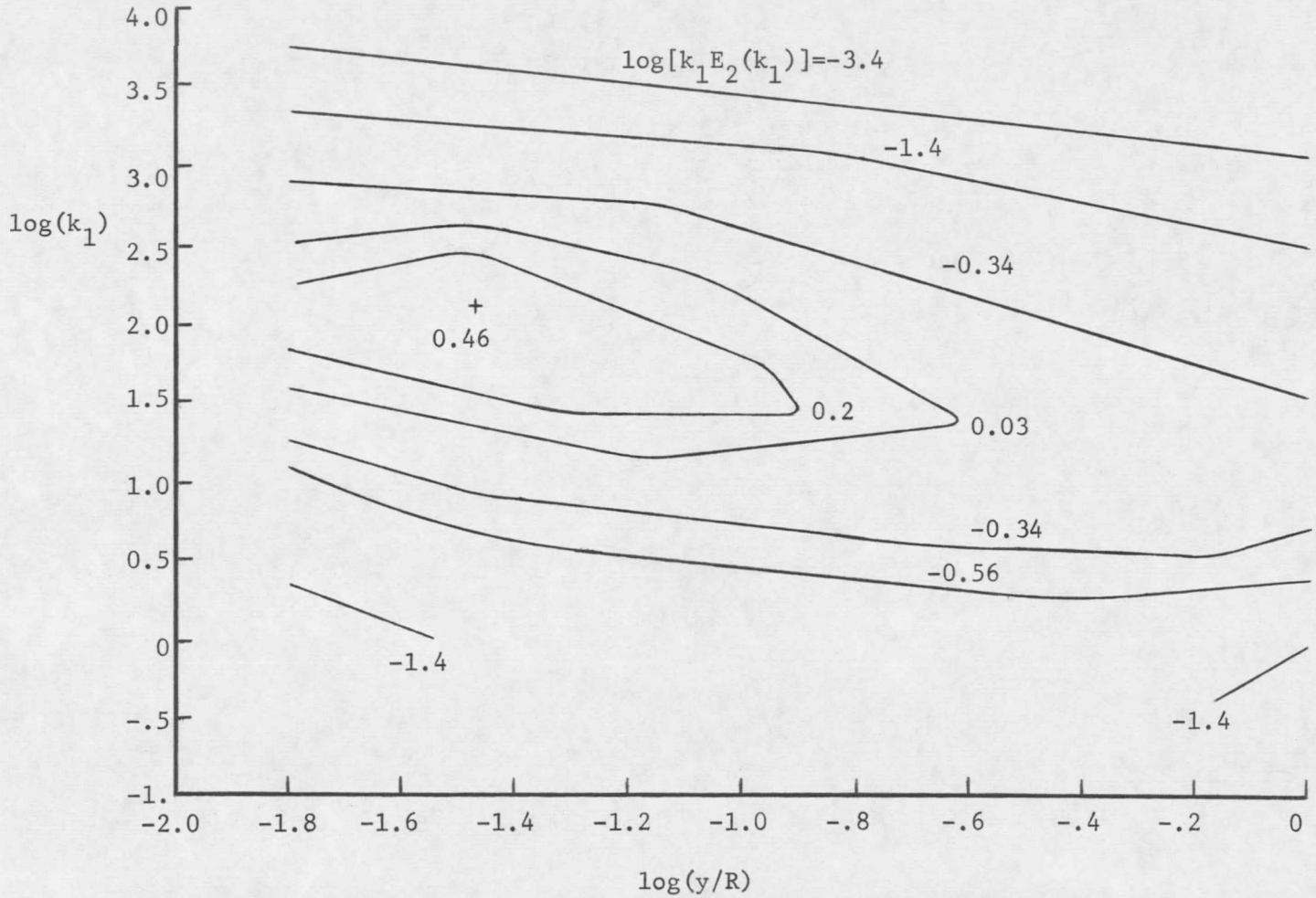

FIGURE 217. Production Subrange of Eddy Sizes for u_2 Fluctuations in Pipe With Large Roughness Elements

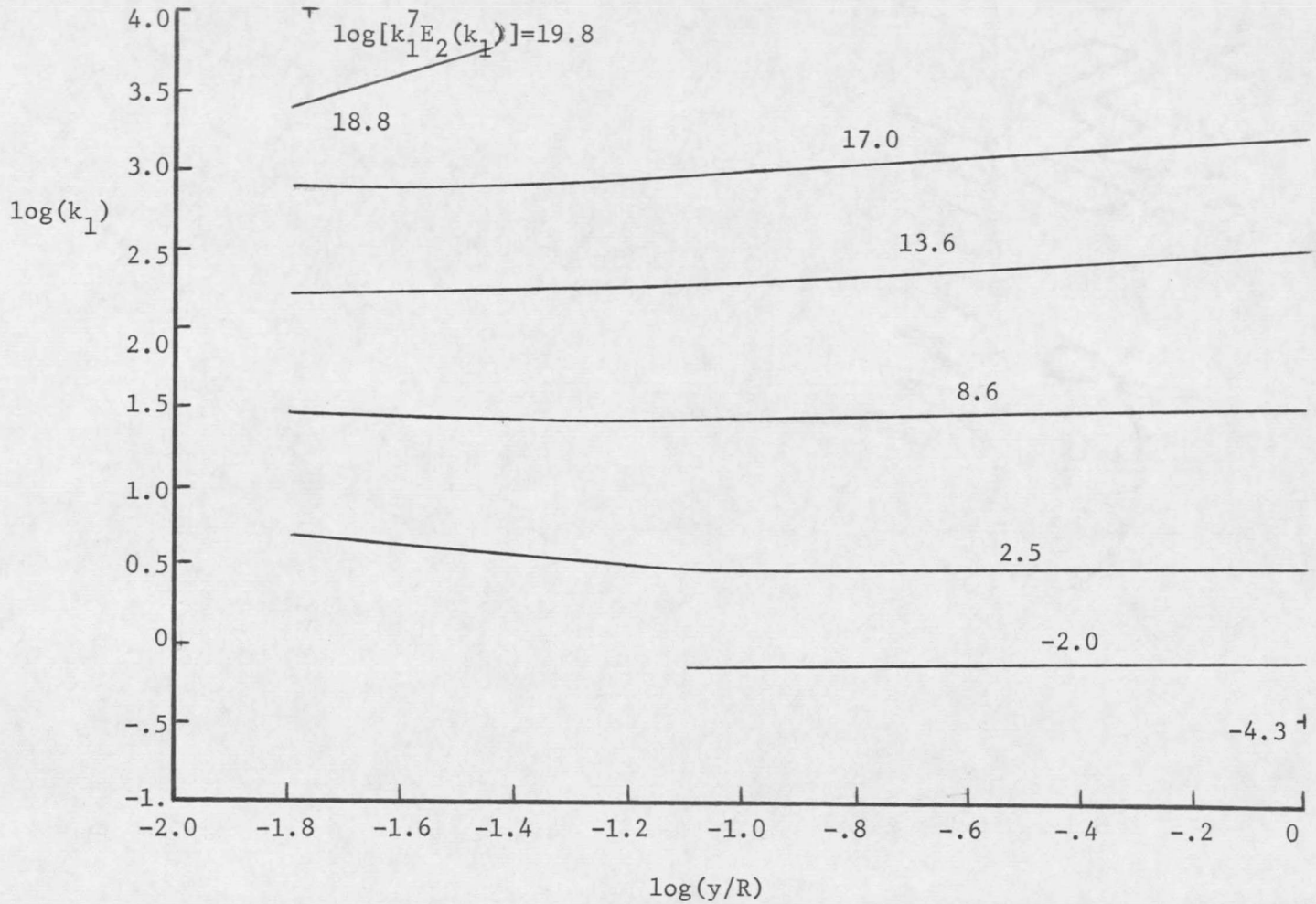

FIGURE 218. Viscous Subrange of Eddy Sizes for u_2 Fluctuations in Pipe With Large Roughness Elements

subrange, Figure 218, is anticipated at very large wave numbers.

Neither the dimensionless coordinate system proposed by Robertson et al [47], Figure 219, nor that proposed by Goma and Gelhar [30], Figure 220, appears to render the E_2 spectra independent of radial position for the pipe containing the large roughness elements. This failure is apparently due to the energy defect observed in the wave number space.

The variation of the E_3 spectrum function for the wave number space and for the frequency domain is indicated in Figures 221 and 222. In similarity with the E_2 spectra, an energy deficiency is noted at low wave numbers for all radial positions except those immediately above the sand grains. As in previous cases, this energy defect is probably due to a transfer of energy from the u_1 fluctuating velocity to the u_3 fluctuating velocity by action of the fluctuating pressure. A comparison of the magnitudes of the E_2 and E_3 spectrum functions, Figures 215 and 222, indicates nearly identically values at a given wave number and a given radial position. Such behavior would be expected due to the tendency toward isotropy by the u_2 and u_3 fluctuating velocities.

The possibility of occurrence of the inertial, production, and viscous subranges of eddy sizes is examined in Figures 223, 224, and 225 respectively. As in the two previous cases, the inertial and

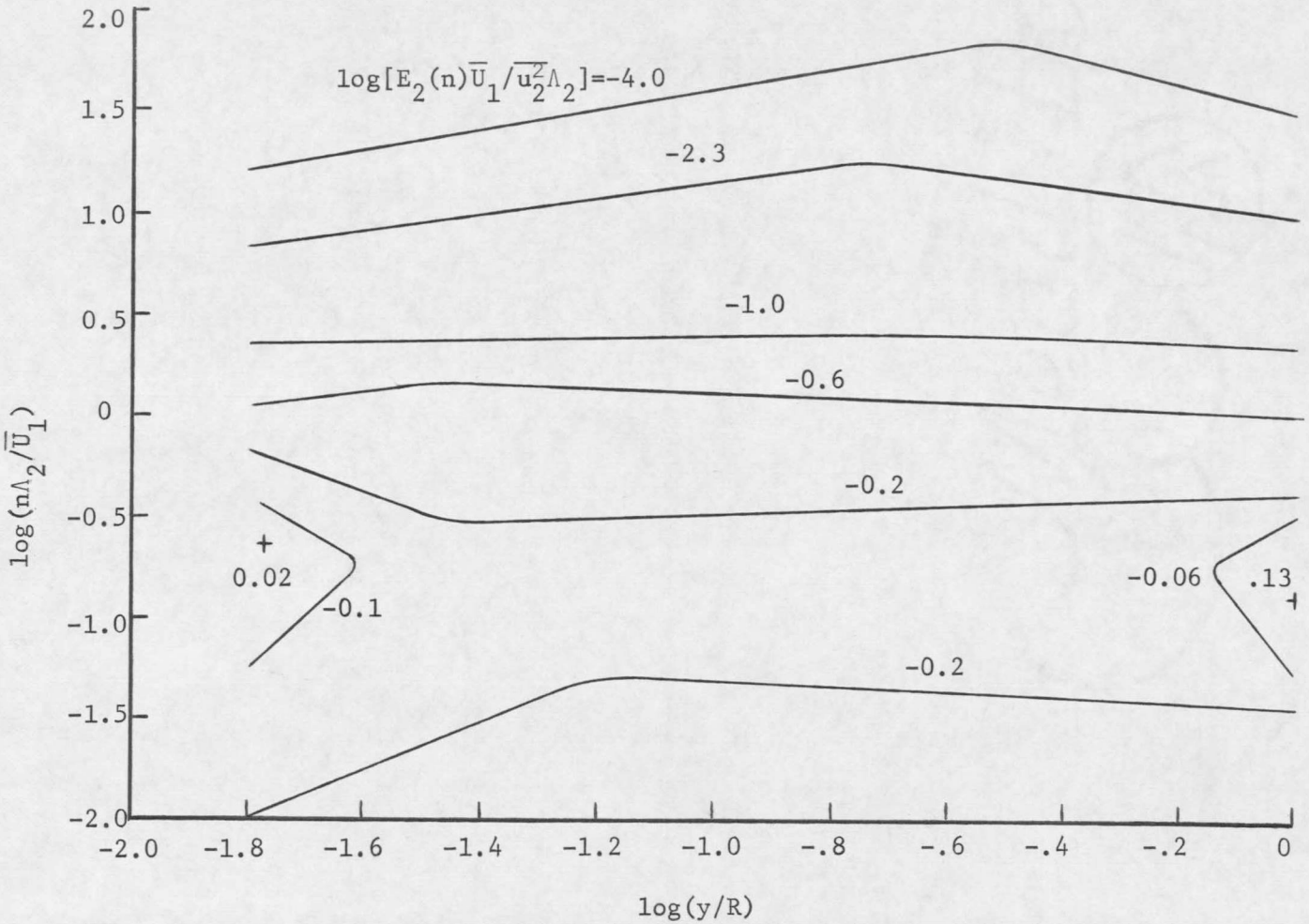

FIGURE 219. u_2 Spectra for Pipe With Large Roughness Elements Normalized as Proposed by Robertson et al [47]

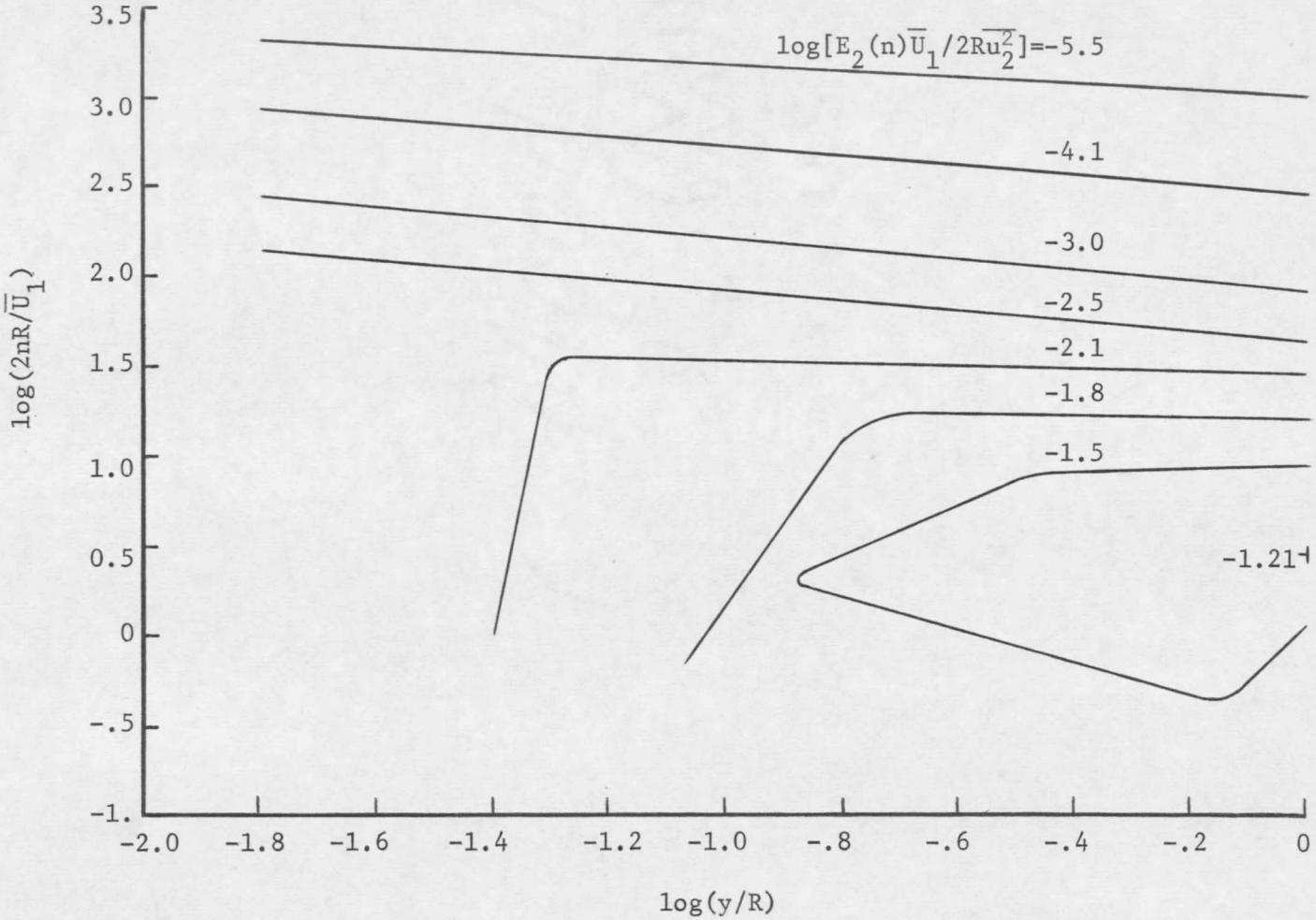

FIGURE 220. u_2 Spectra for Pipe With Large Roughness Elements Normalized as Proposed by Goma and Gelhar [30]

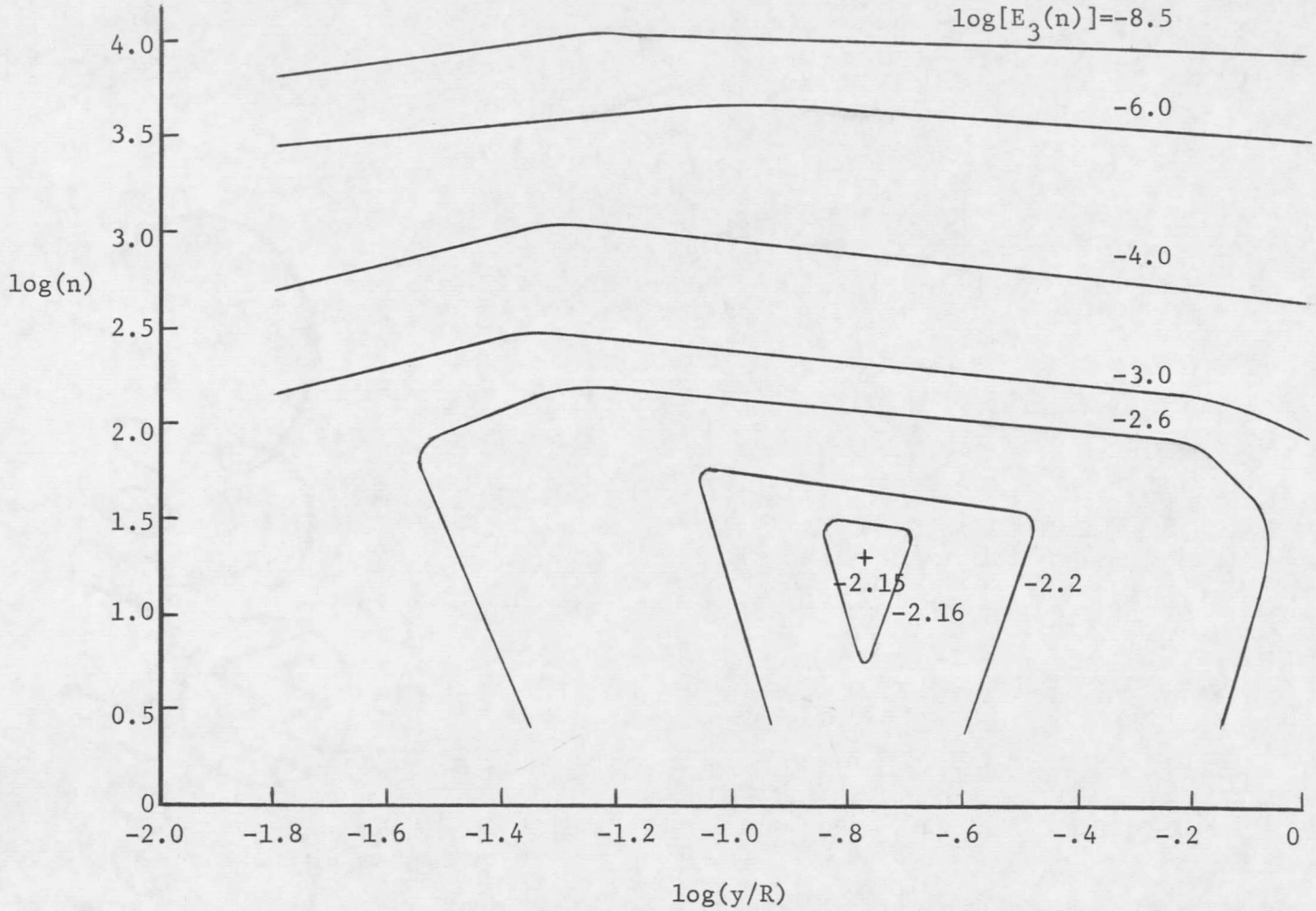

FIGURE 221. Frequency Domain Energy Spectra for u_3 Fluctuating Velocity in Pipe With Large Roughness Elements

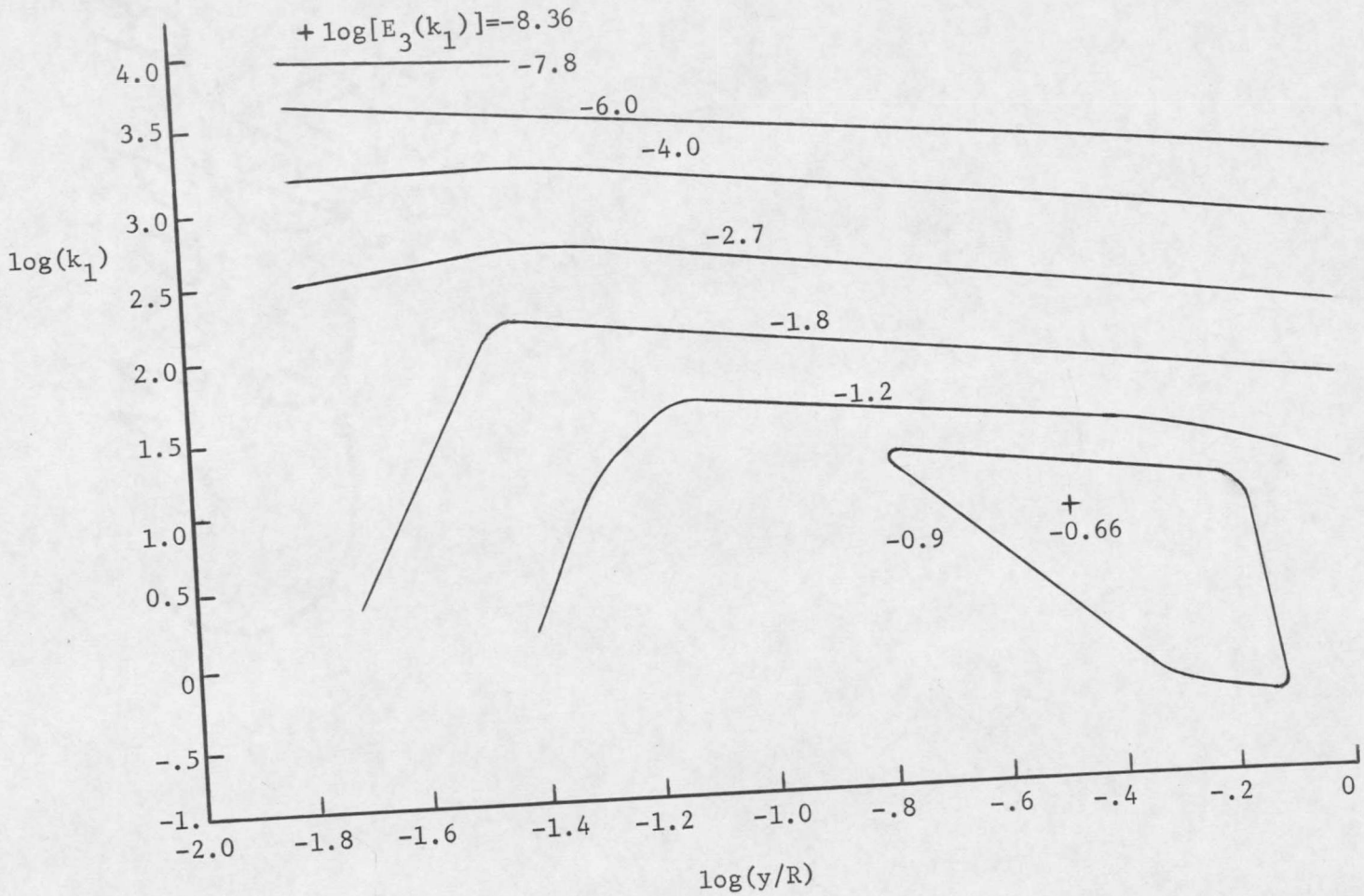

FIGURE 222. Wave Number Space Energy Spectra for u_3 Fluctuating Velocity in Pipe With Large Roughness Elements

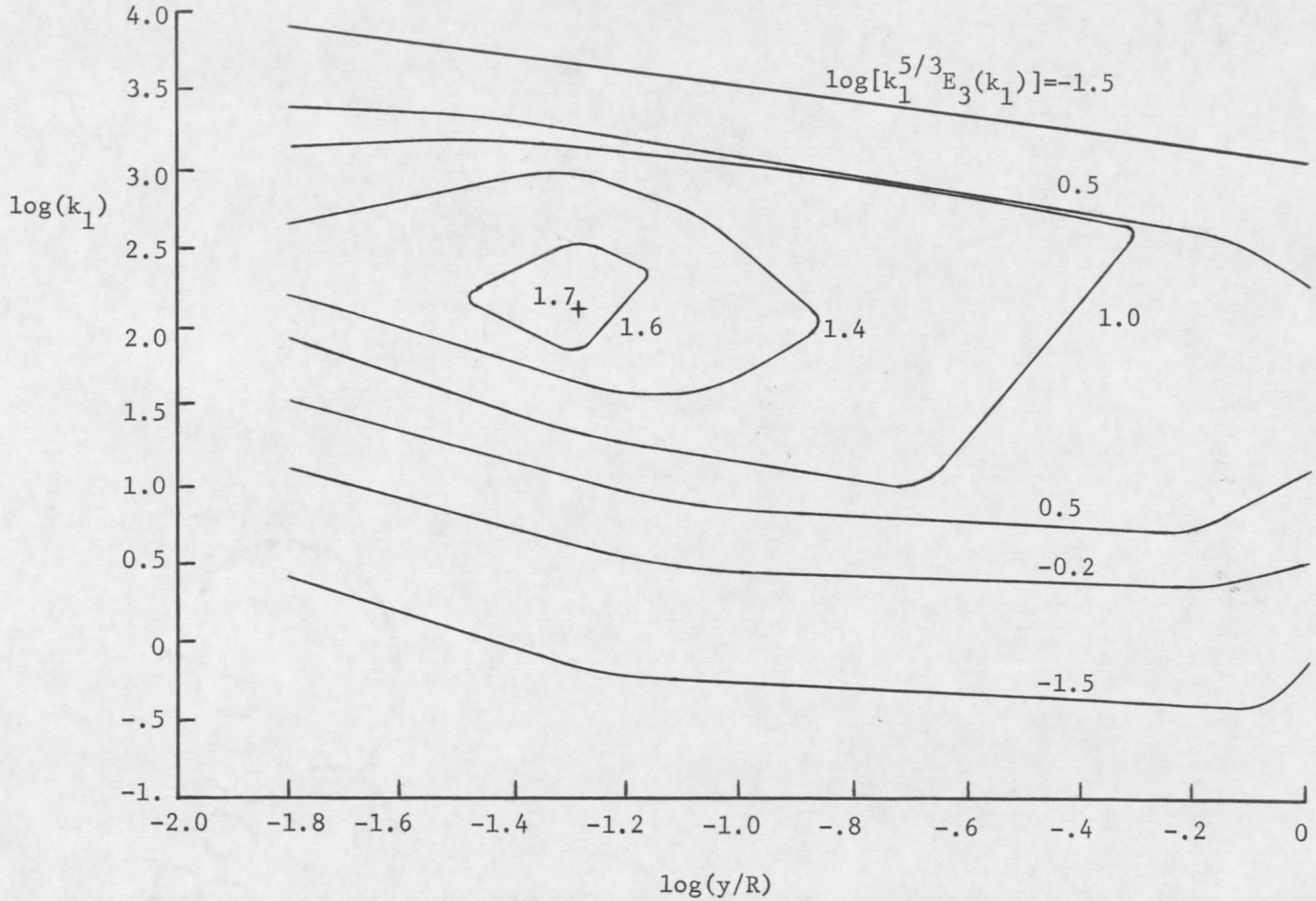

FIGURE 223. Inertial Subrange of Eddy Sizes for u_3 Velocity Fluctuations in Pipe With Large Roughness Elements

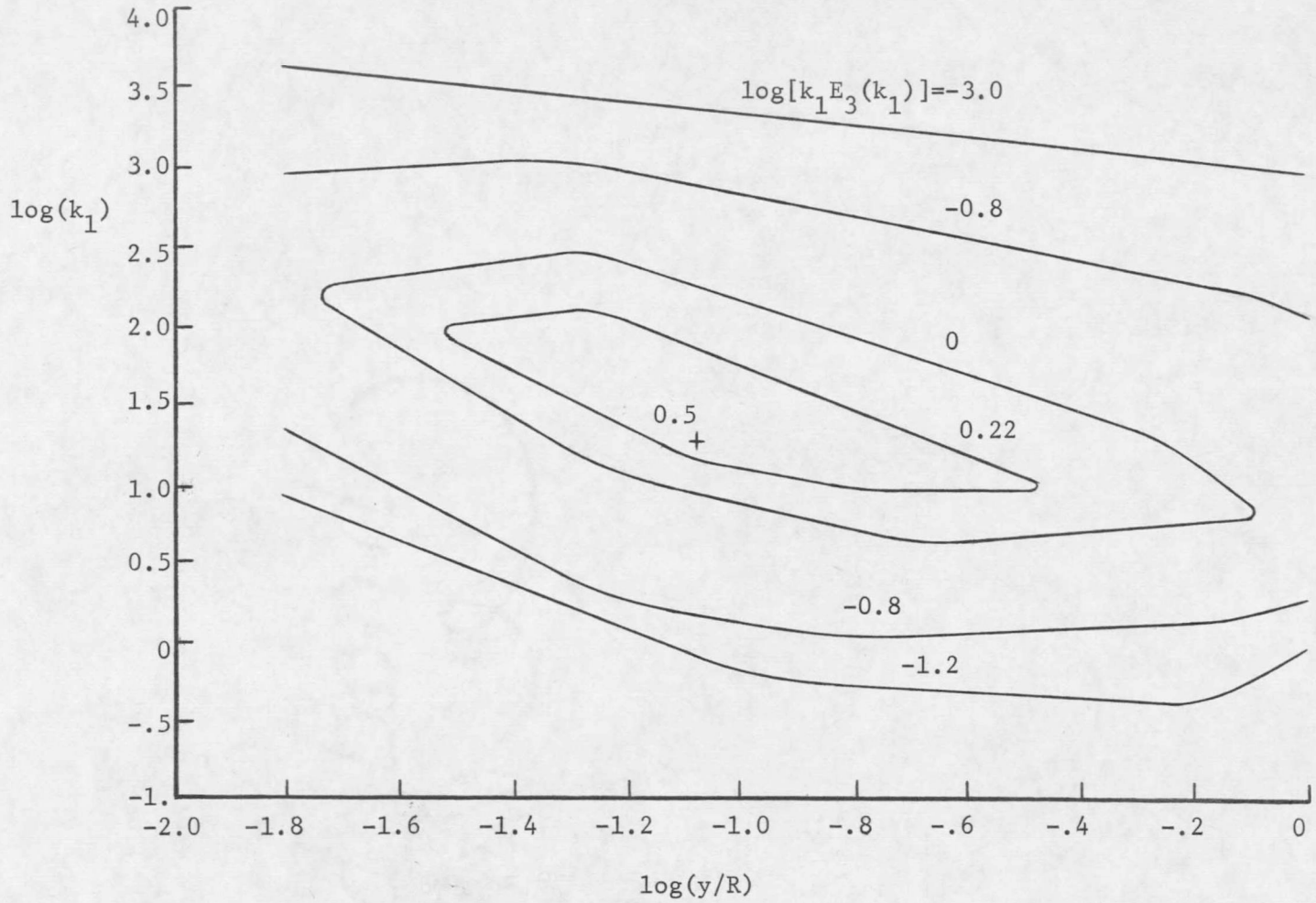

FIGURE 224. Production Subrange of Eddy Sizes for u_3 Velocity Fluctuations in Pipe With Large Roughness Elements

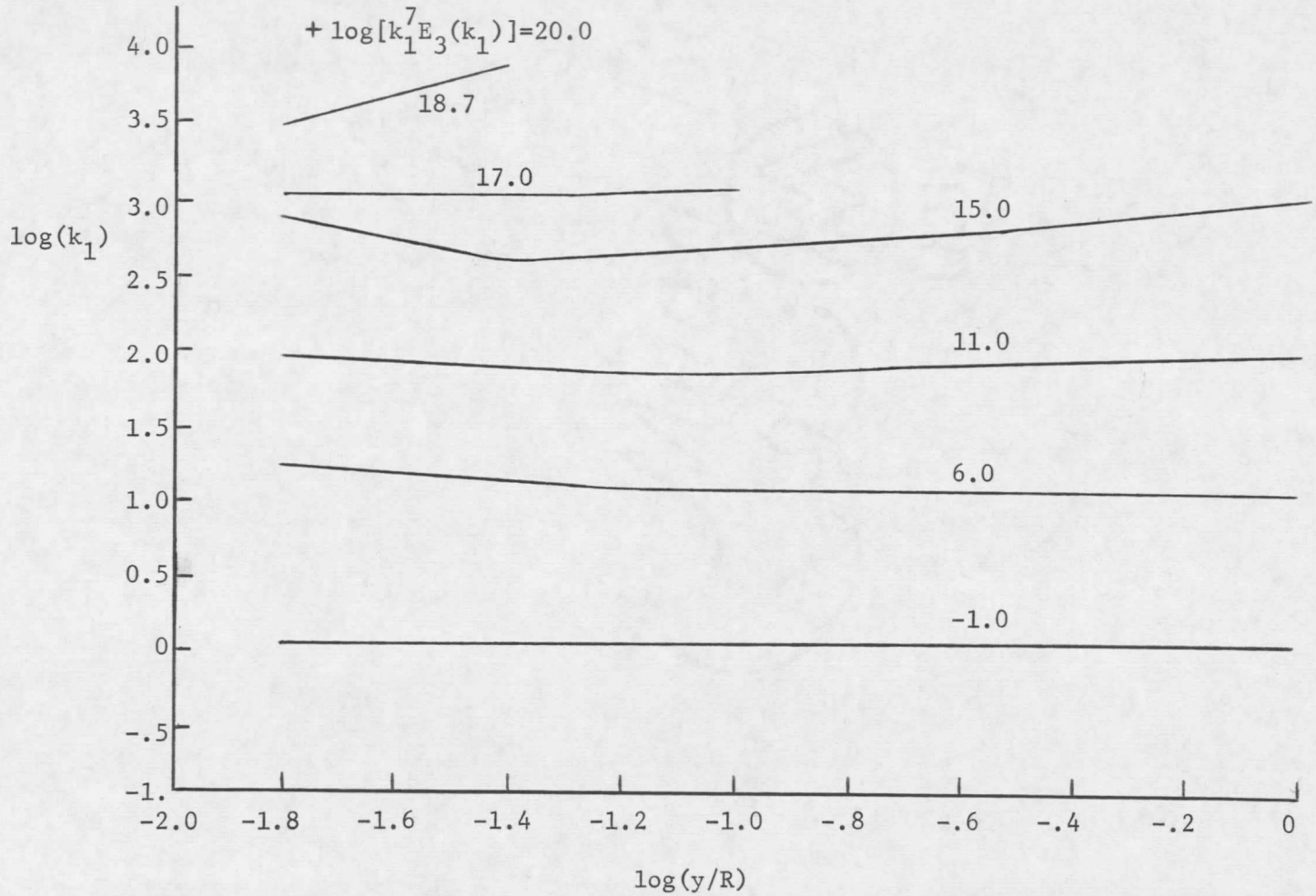

FIGURE 225. Viscous Subrange of Eddy Sizes for u_3 Velocity Fluctuations in Pipe With Large Roughness Elements

production subranges occur throughout the pipe, and the wave numbers where they exist increase as the wall is approached. The production eddies are again larger than the inertial eddies, and Figure 225 indicates the apparent occurrence of the viscous subrange at large wave numbers.

The dimensionless coordinates suggested by Robertson et al [47] tend to impress a fairly universal behavior on the E_3 spectra, as indicated by Figure 226. On the other hand, Figure 227 shows that the coordinate system proposed by Goma and Gelhar yields acceptable results only for large wave numbers.

Autocorrelation Functions

Autocorrelation functions obtained by taking the Fourier cosine transform of the energy spectra are presented in Figures 228, 229, and 230 for the velocity fluctuations in the x_1, x_2 and x_3 coordinate directions respectively. These figures indicate a generally similar behavior for ϕ_1, ϕ_2, and ϕ_3 in that for a particular value of time, they all acquire a minimum value near the mean height of the roughness elements and then increase as either the wall or the center line is approached. This indicates that the curvature of ϕ_i with respect to time at $t = 0$ is smaller at the top of the roughness elements than at other radial positions. The resultant increasing

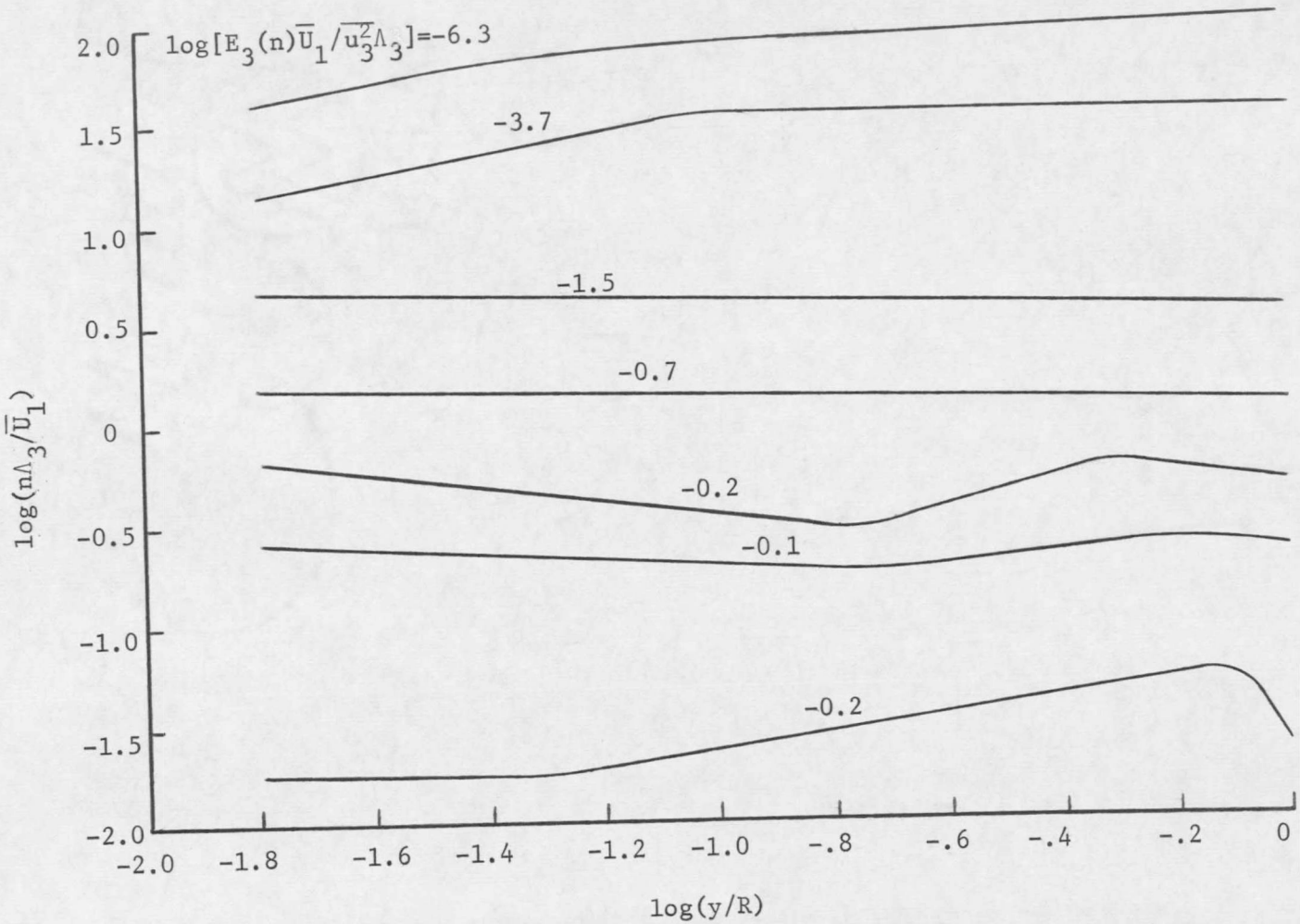

FIGURE 226. u_3 Spectra for Flow in Pipe With Large Roughness Elements Normalized as Suggested by Robertson et al [47]

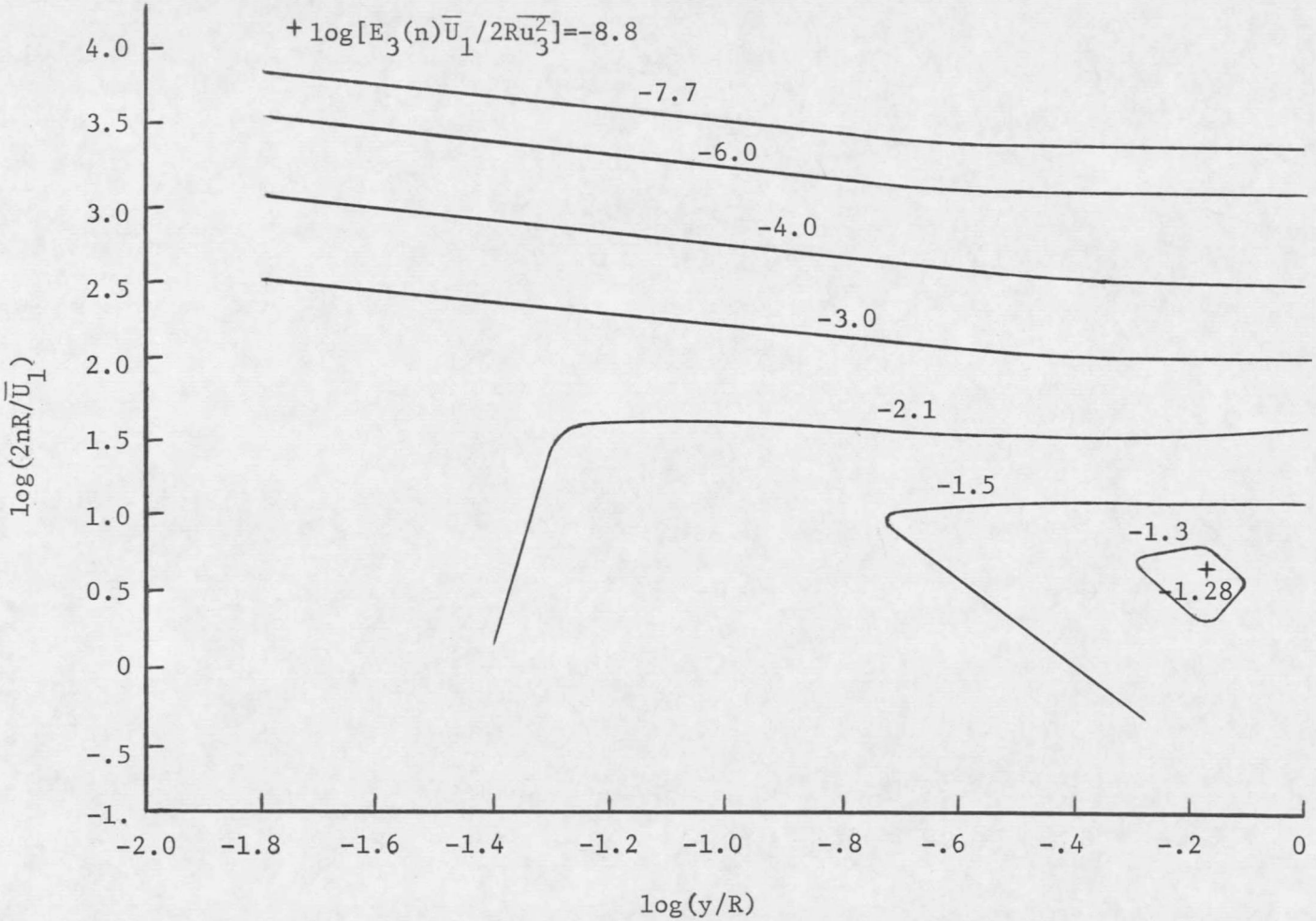

FIGURE 227. u_3 Spectra for Flow in Pipe With Large Roughness Elements Normalized as Suggested by Goma and Gelhar [30]

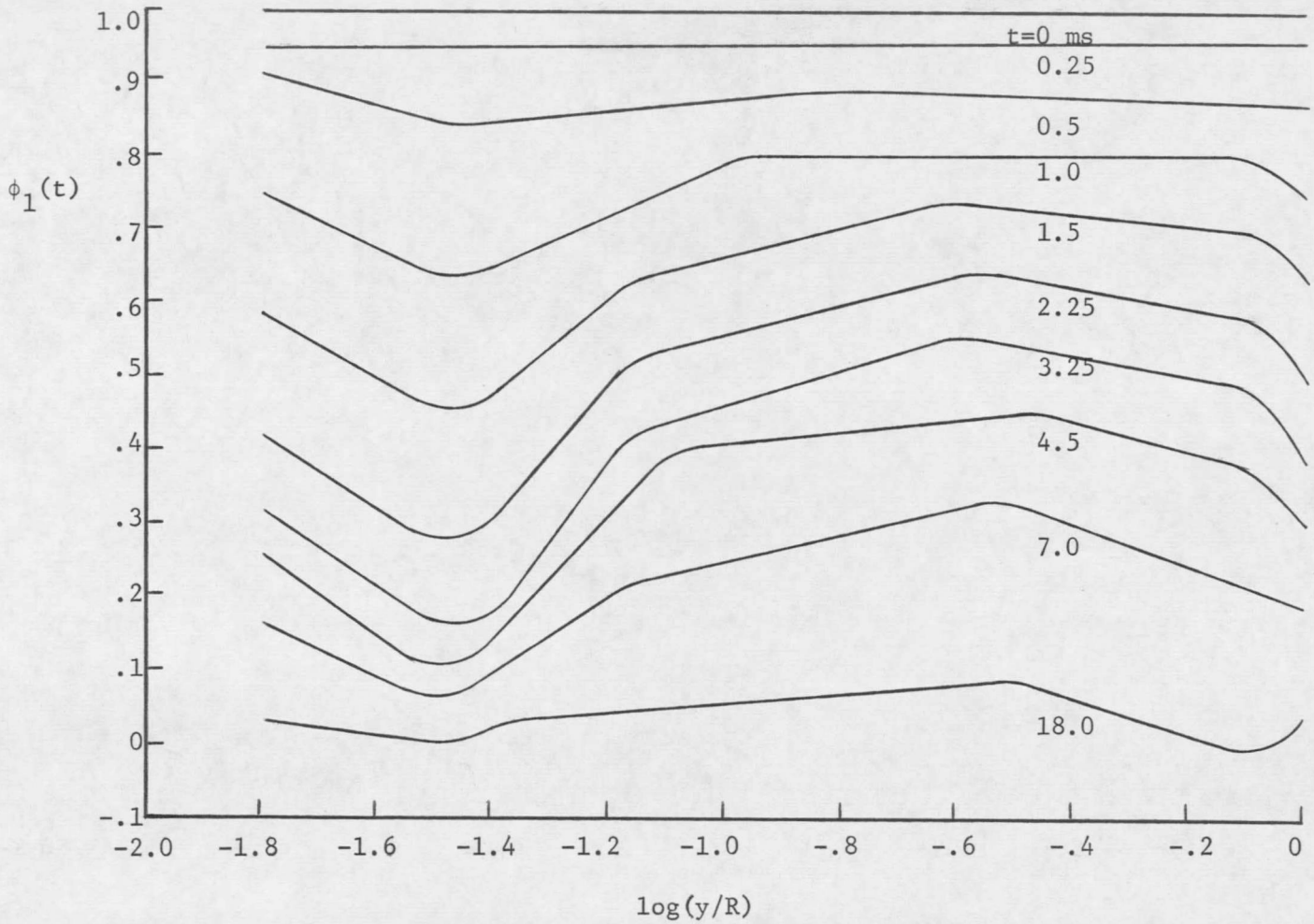

FIGURE 228. Autocorrelation Function for u_1 Velocity Fluctuations in Pipe With Large Roughness Elements

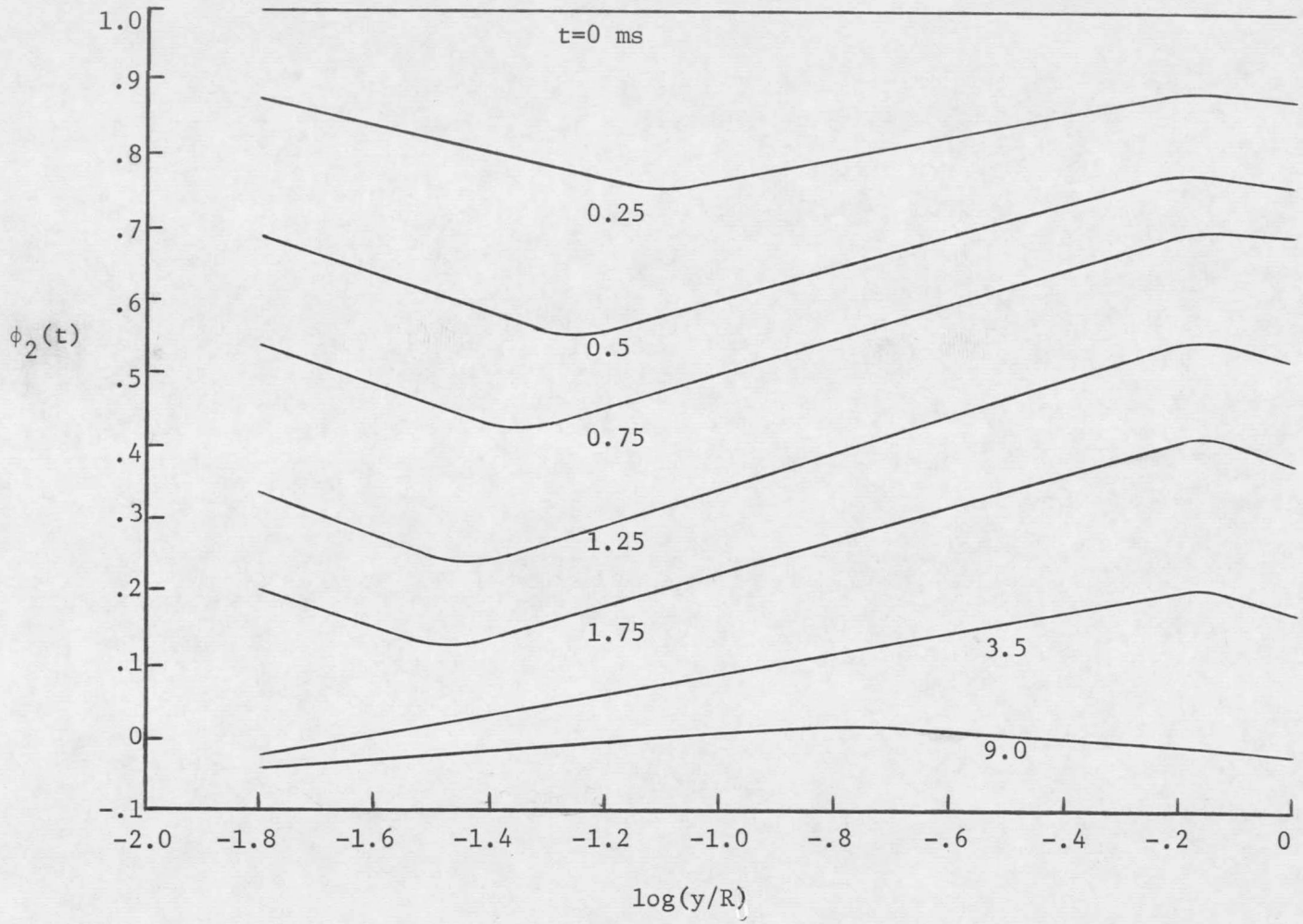

FIGURE 229. Autocorrelation Function for u_2 Velocity Fluctuations in Pipe With Large Roughness Elements

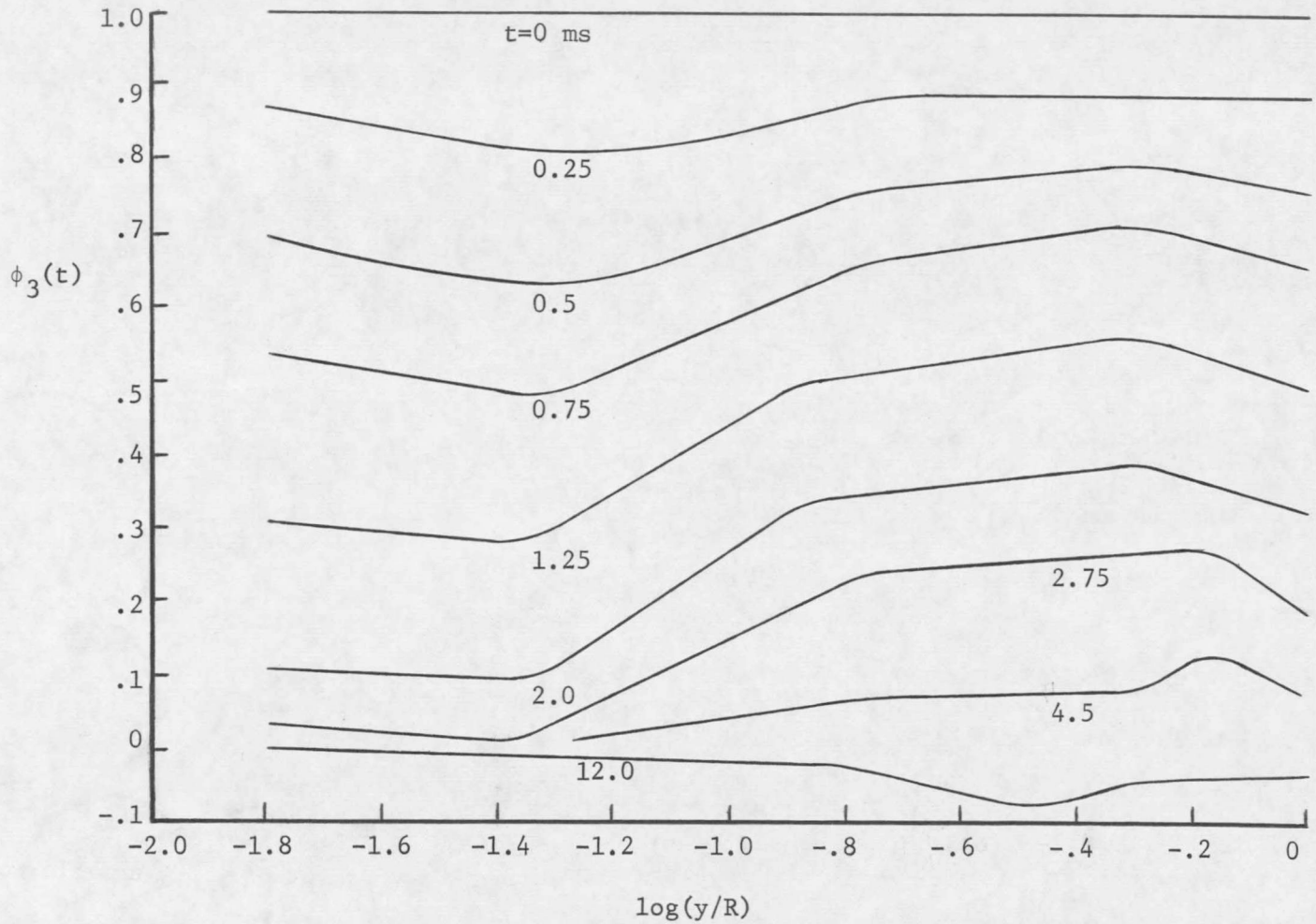

FIGURE 230. Autocorrelation Function for u_3 Velocity Fluctuations in Pipe With Large Roughness Elements

curvature as the wall is approached is indicative of the increasingly dominant role of low frequencies in this region, and also signifies the inability of high frequency velocity fluctuations to penetrate the area containing the roughness elements. On the other hand, the increase in curvature of the autocorrelation functions in proceeding from the roughness elements toward the center line is compatible with the spectral analysis where very large eddies were found to exist near the center of the pipe. The slight decrease in all three autocorrelation functions near the center line of the pipe is suggestive of a slight reduction in eddy size in the three coordinate directions in this region.

Turbulence Scales

Experimentally determined values of the Eulerian micro scale γ_i, which is a measure of the most rapid changes which occur in the u_i fluctuations, are presented in Figure 231. The curves for all three micro scales have a somewhat similar shape, i.e., they are all relatively constant near the center line but increase slightly in moving toward the wall. A pronounced minimum then occurs a short distance above the roughness elements, and the micro scales again increase. This increase is in accord with the autocorrelation results where it was observed that the high frequency eddies could

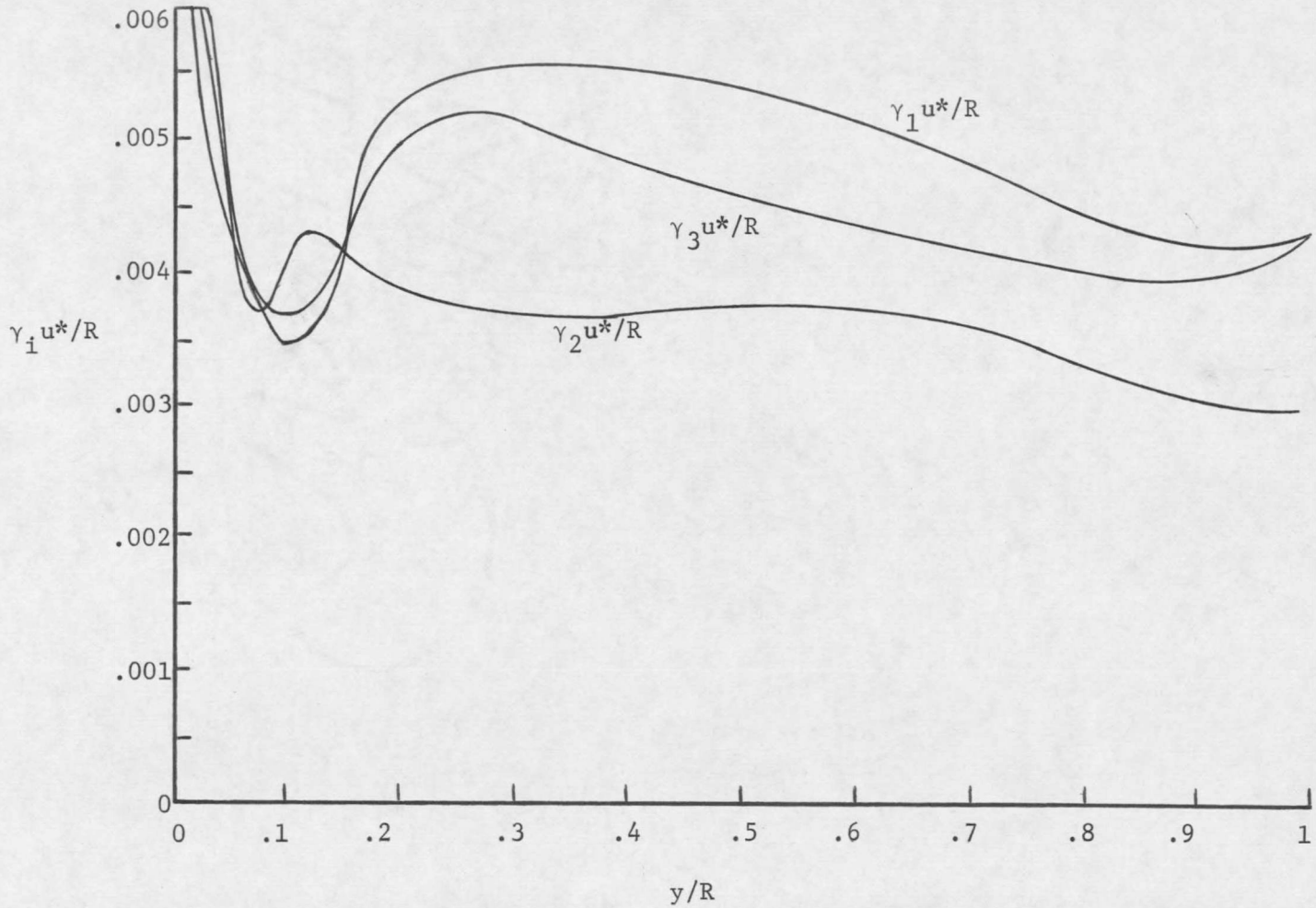

FIGURE 231. Eulerian Micro Scales in Pipe With Large Roughness Elements

not penetrate beneath the roughness elements. Except for points near the wall, γ_1 is seen to be larger than γ_3 which, in turn, is larger than γ_2. This indicates the presence of higher frequency fluctuations in the u_2 velocity than in either u_1 or u_3.

A rough measure of the longest connection time in the behavior of the fluctuating velocities is the Eulerian macro scale, and values of this parameter for the pipe containing the large roughness elements are presented in Figures 232 and 233. These figures indicate that T_3 is relatively constant in the central region of the pipe while T_1 and T_2 decrease slightly in this region. Near the roughness elements all three Eulerian macro scales decrease, indicating that very low frequency fluctuations cannot penetrate into the region occupied by the sand grains. The Eulerian macro scale in the x_1 direction is observed to be larger than the other two throughout the pipe.

Transformation of the Eulerian micro scales into the spatial micro scales is indicated by Figures 234 and 235. The spatial micro scales, which reveal the average dimensions of the smallest eddies in the flow field are seen to generally increase with distance from the wall to a maximum value near $y/R = 0.6$. This behavior is indicative of a decrease in the size of the viscous dissipation eddies as the wall is approached. Throughout the central region of the pipe,

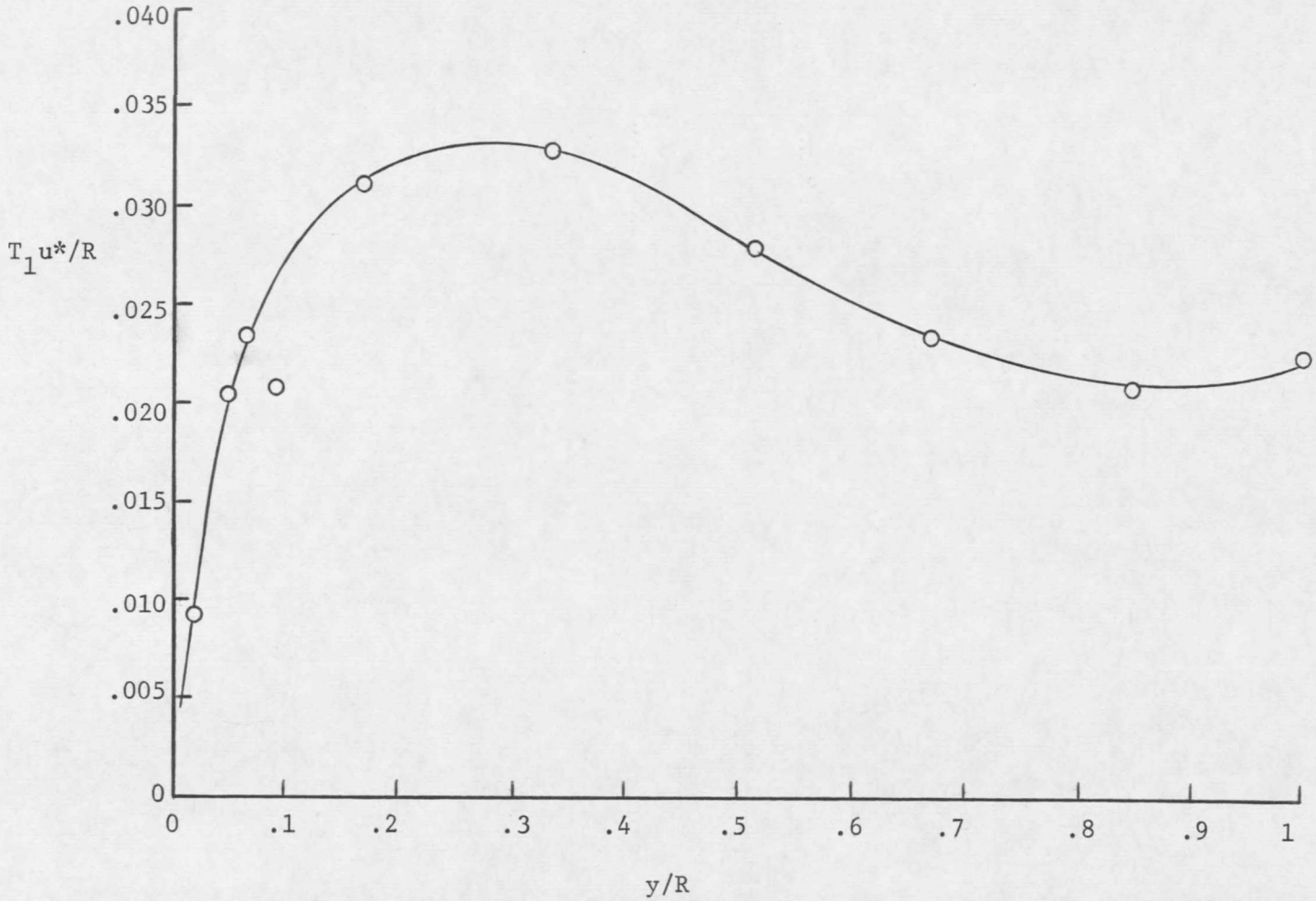

FIGURE 232. Eulerian Macro Scale in x_1 Direction for Pipe With Large Roughness Elements

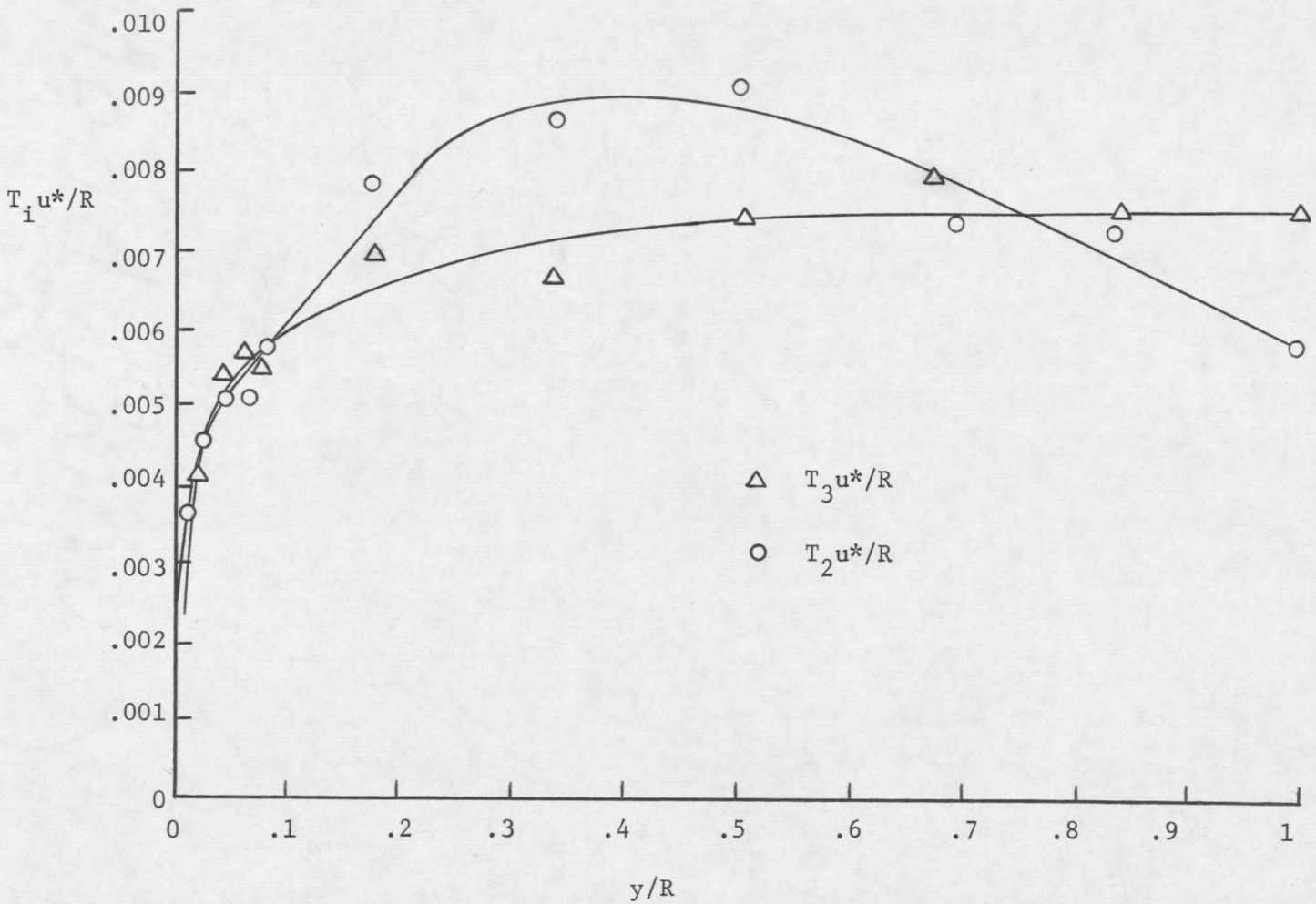

FIGURE 233. Eulerian Macro Scales in x_2 and x_3 Directions for Pipe With Large Roughness Elements

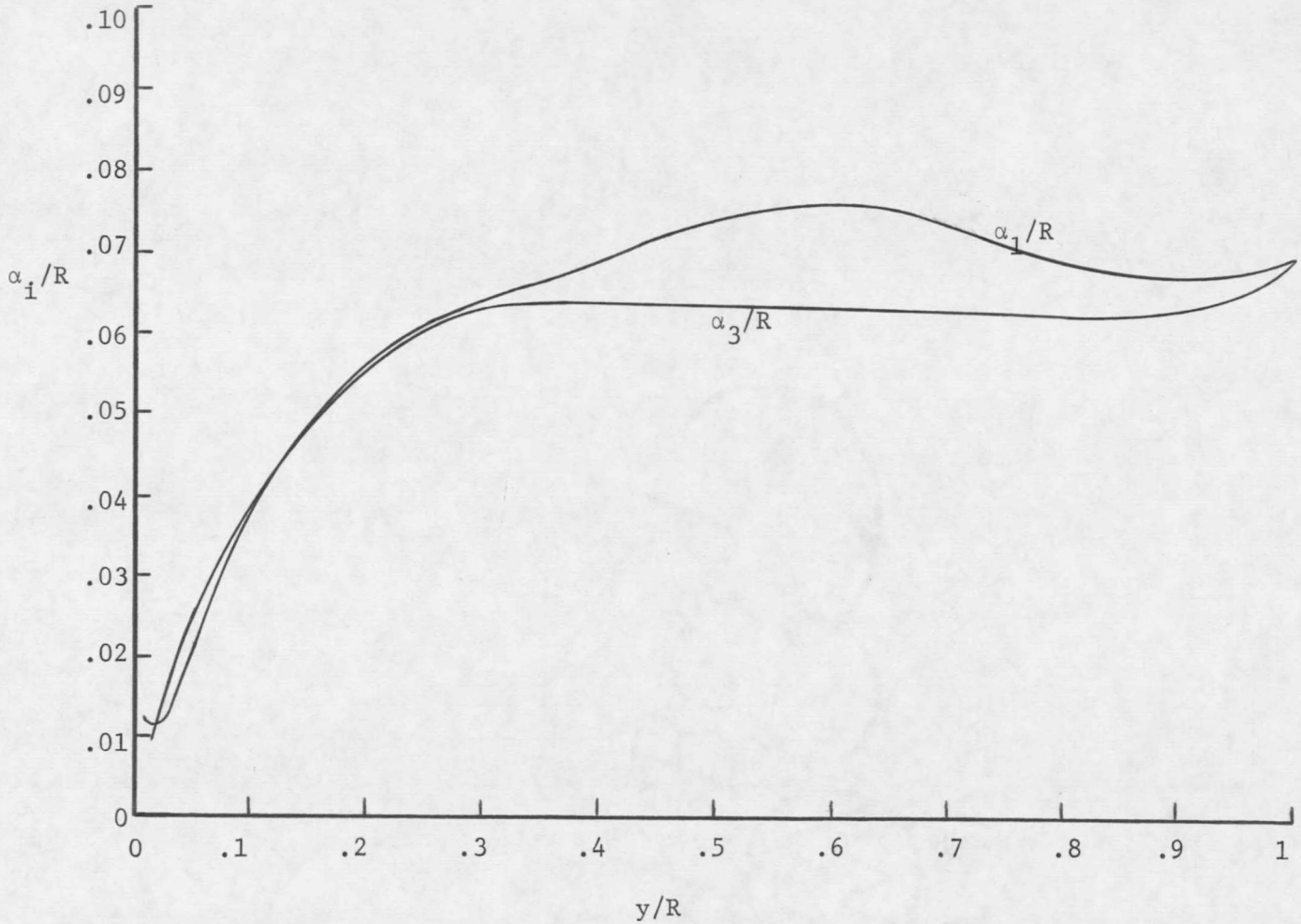

FIGURE 234. Spatial Micro Scales in x_1 and x_3 Directions for Pipe With Large Roughness Elements

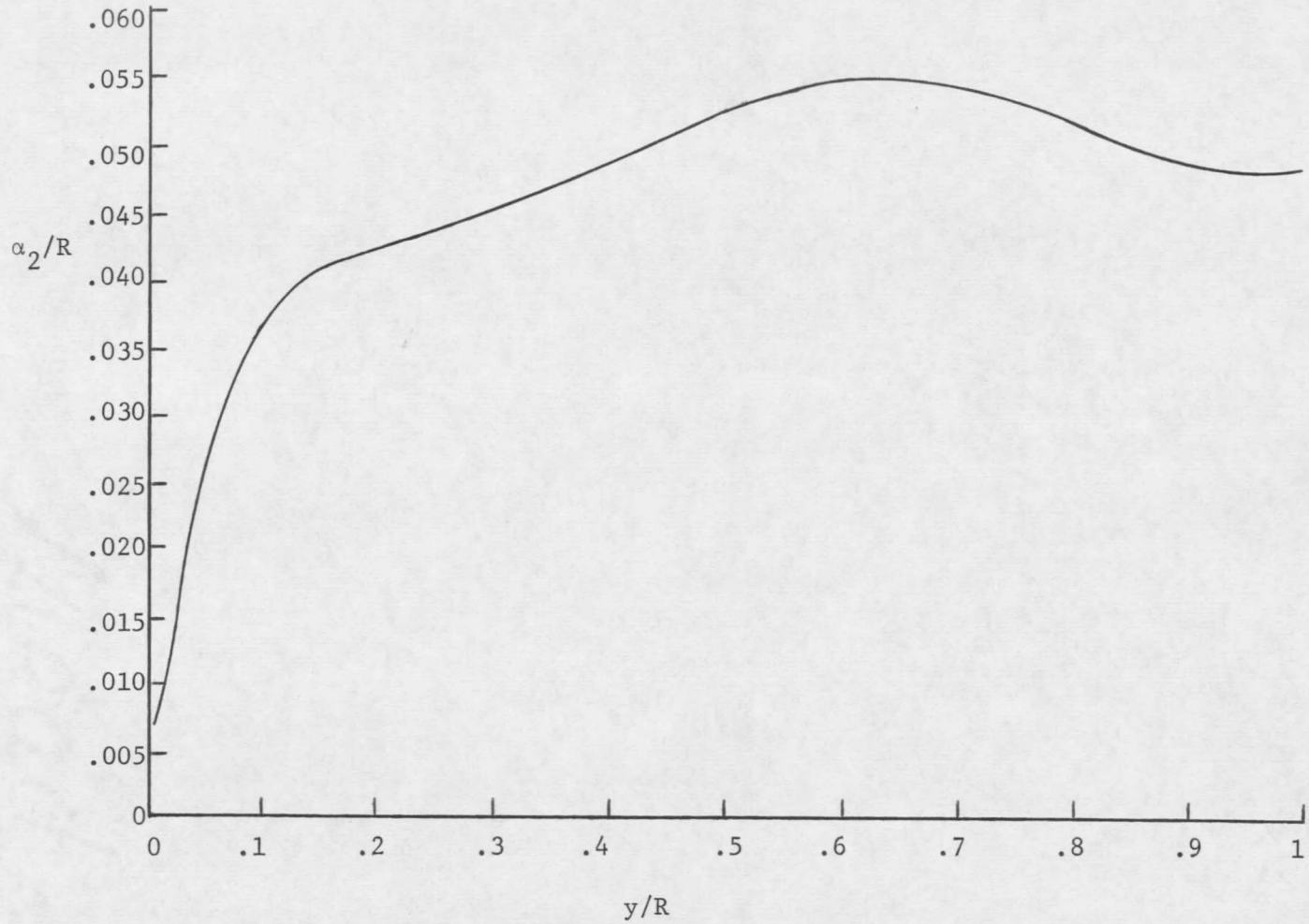

FIGURE 235. Spatial Micro Scale in x_2 Direction for Pipe With Large Roughness Elements

it is seen that these eddies are longest in the x_1 direction and shortest in the x_2 direction.

The variations of the spatial macro scales in the three coordinate directions are shown in Figures 236, 237, and 238. These macro scales, which are indicative of the size of the largest eddies in the flow field, are seen to be essentially constant over the central portion of the flow field. The magnitudes of these macro scales reveal the existence of large eddies which are extremely elongated in the axial direction. Near the roughness elements, all of the macro scales show sharp decreases indicating the breakup of the large eddies by the sand grains. As with the pipe containing the small roughness elements, the longitudinal macro scale Λ_1 in the central region of the pipe shows excellent agreement with the value of 0.15R found by McQuivey and Richardson [69] for flow in an open channel with rough surfaces.

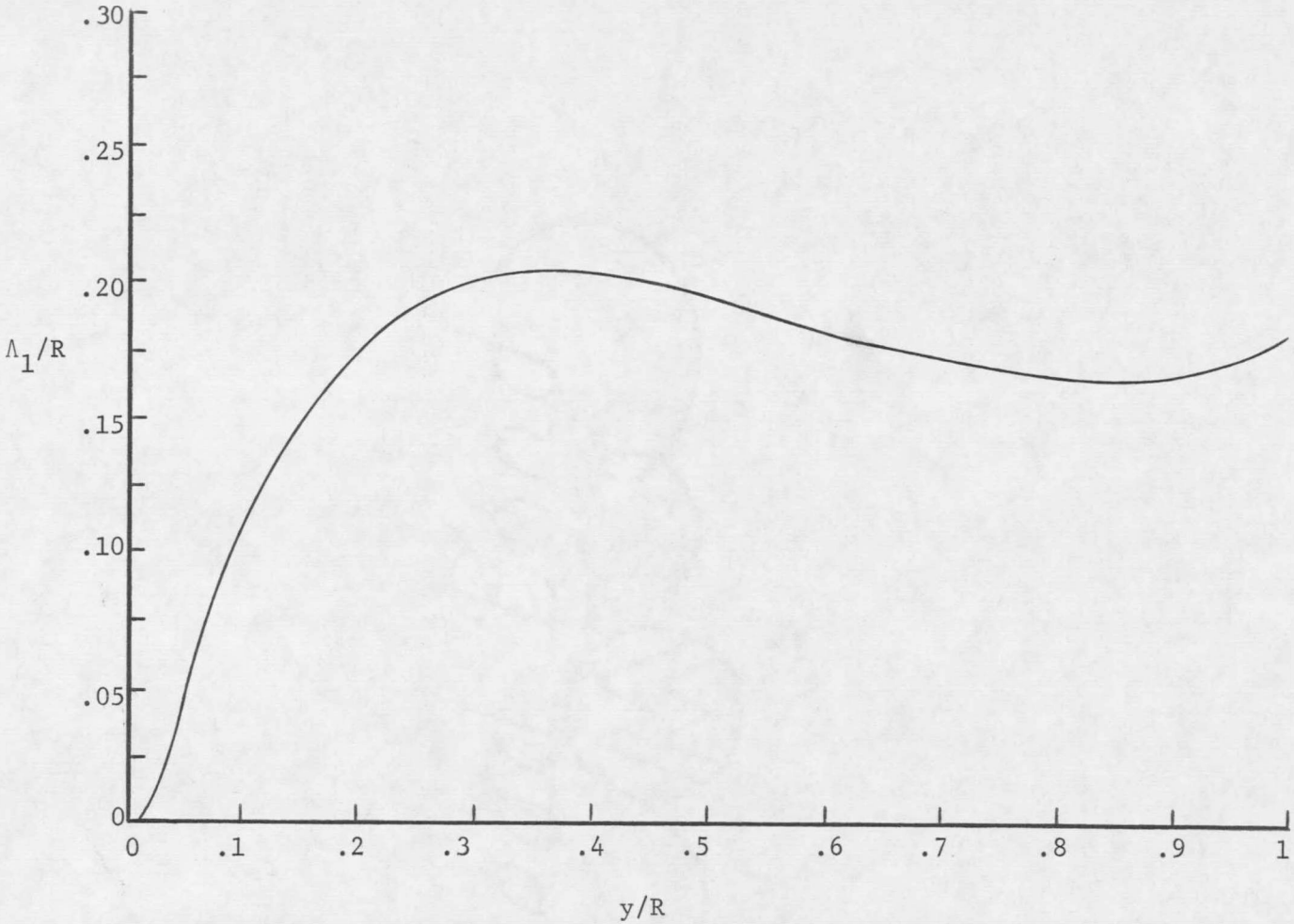

FIGURE 236. Spatial Macro Scale in x_1 Direction for Pipe With Large Roughness Elements

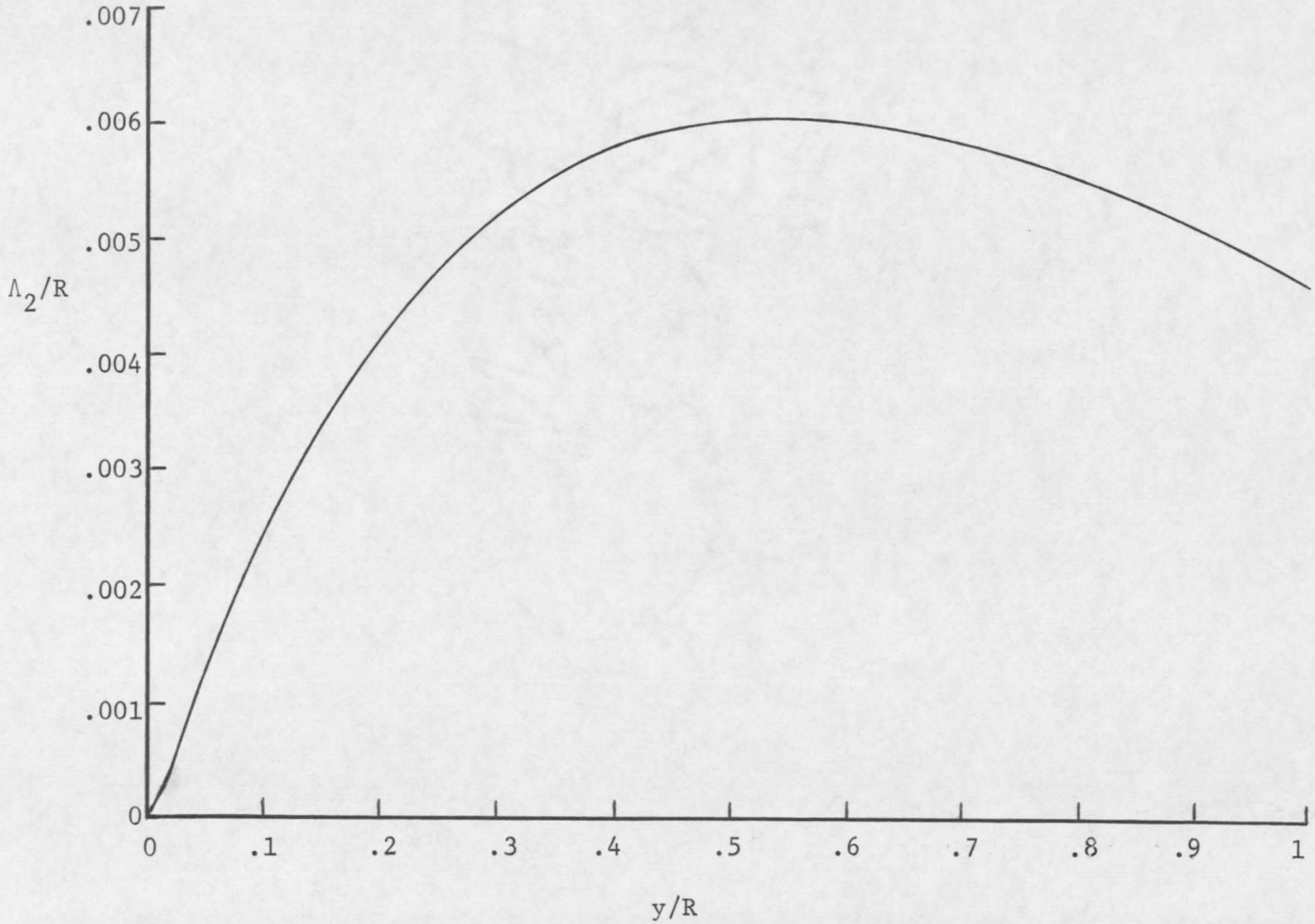

FIGURE 237. Spatial Macro Scale in x_2 Direction for Pipe With Large Roughness Elements

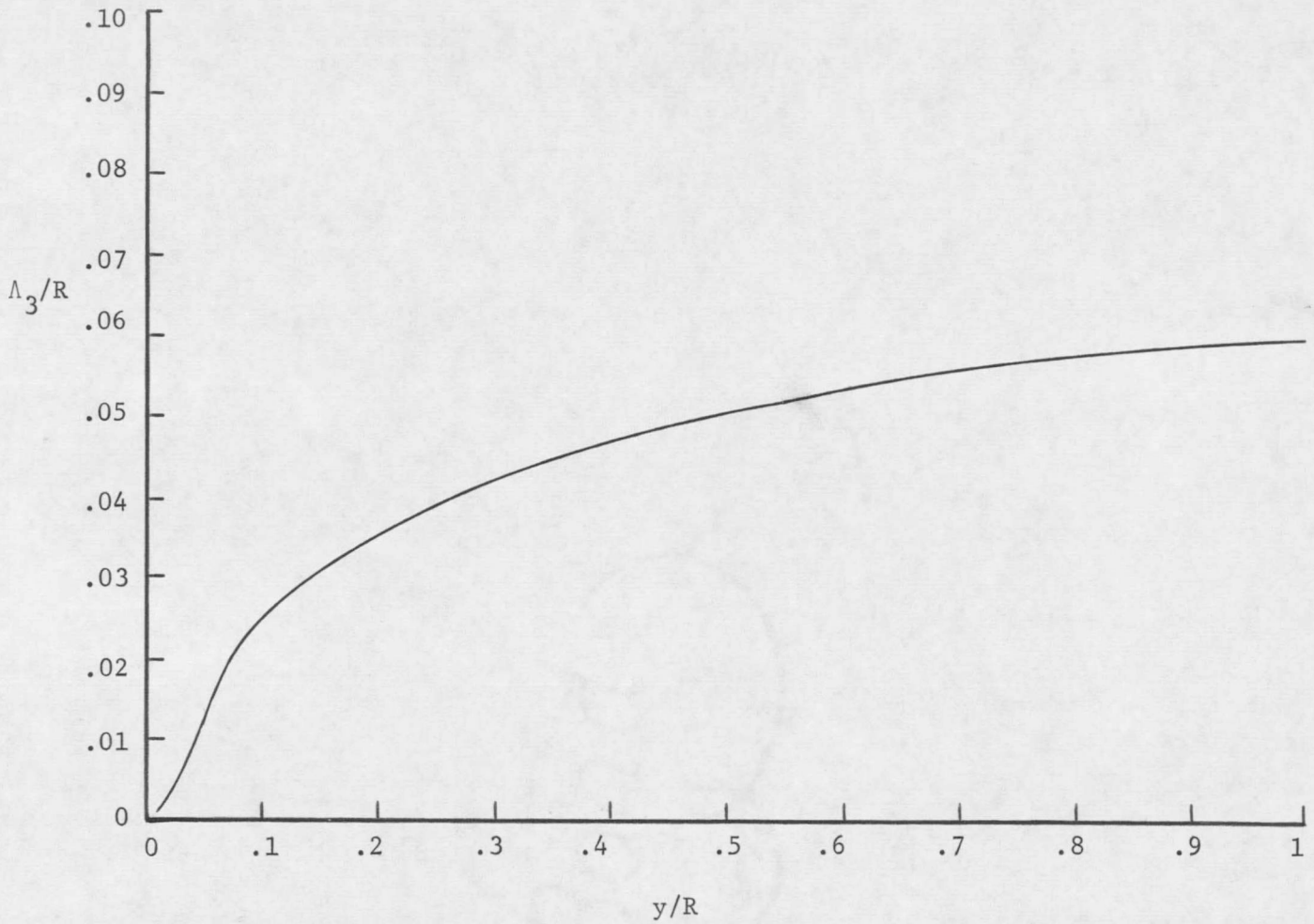

FIGURE 238. Spatial Macro Scale in x_3 Direction for Pipe With Large Roughness Elements

CHAPTER IX

COMPARISON OF SMOOTH AND ROUGH PIPE RESULTS

Mean Velocity and Flow Resistance

A fixed value of the Reynolds number, approximately 165,000, was utilized for the experimental measurements in all three pipes. It has been shown that this Reynolds number yielded flow in the hydraulically smooth, transition, and fully rough flow regimes for the smooth pipe, that containing the small roughness elements, and that containing the large roughness elements respectively. This enabled a study of the changes in flow characteristics in passing from one regime to another at a constant Reynolds number.

A comparison of the mean velocity profiles in these three pipes indicates that the effect of an increase in roughness is to steepen the velocity gradient throughout the central portion of the pipe. Thus, the mean velocity profile in a rough pipe tends to more closely resemble the well known laminar flow profile than does the mean velocity profile in a smooth tube. This behavior also indicates that a much higher center line velocity is required in a rough tube to obtain a given Reynolds number than would be necessary in a smooth tube to acquire the same Reynolds number. The roughness elements tend to create a large drop in the mean velocity at their outer edge so that the velocity gradient near the wall is much steeper

for a smooth than for a rough tube.

Fluctuating Velocities

A comparison of the fluctuating velocities, when normalized with the shear velocity, obtained for flow in the three pipes indicates a similarity in behavior. In all cases u_2' and u_3' are nearly equal at the pipe center line while u_1' has a somewhat larger value. In proceeding toward the wall, all three fluctuating velocities increase to a maximum value before vanishing at the pipe wall. Some effects of roughness are evident, however. Of course, the peaks in the curves for the rough pipes occur at larger values of y/R than do those for the smooth pipe simply due to the presence of the roughness elements. Also, as roughness is increased, u_2' and u_3' tend to become more nearly equal throughout the pipe, indicating a trend toward isotropic flow by these two velocity components. This trend is verified by an examination of the anisotropy ratios, although in each case u_1' prevents the flow from becoming completely isotropic. Of special interest is the fact that u_2' exceeds u_3' in magnitude near the large roughness elements, in contrast to smooth pipe observations.

One of the assumptions implied in the direct application of hot-wire anemometry equipment is that of small turbulence intensities, and the validity of this assumption was investigated for each of the

three pipes. For the smooth pipe and that containing the small roughness elements, it was found that none of the intensities exceeded about 20%, and this is considered to be an acceptable level. For the large roughness the intensities were also found to be less than 20% over the major portion of the cross-section, but a rapid increase was observed just above the roughness particles. At the mean roughness height the intensities had become as large as 50%, and much larger values occurred closer to the wall. Although errors incurred with a 50% turbulence intensity are expected to be large, they are not expected to be prohibitive in view of the discussion in reference [97]. Reliable results are not expected beneath the roughness elements due to the intensities in this region, however.

The turbulence kinetic energy, which is of considerable importance in further considerations, does not vary substantially as roughness is changed if normalization with respect to the square of the shear velocity is utilized. Minor differences include a slight decrease in the magnitude of the dimensionless kinetic energy and an increase in the value of y/R where the maximum magnitude occurs as roughness size is increased.

A knowledge of the fluctuating velocities in the x_2 and x_3 coordinate directions enabled the estimation of the radial pressure variation from equation (4.12). For all three pipes, the magnitude

of this radial pressure drop was found to be small enough that an error of less than 0.4% was incurred by utilizing static pressure measurements at the solid surface for center line dynamic head calculations.

Fluctuating Velocity Correlations

One of the major differences between smooth and rough pipe data is observed in the second order cross correlation terms. In the central region of the pipe, the $\overline{u_1 u_2}$ correlation, normalized with the square of the shear velocity, is observed to become progressively smaller as the roughness size is increased. This occurrence is consistent with the results of Gow [15] and those of Robertson et al [47]. It should also be noted that Goma and Gelhar [30] found identical magnitudes of this normalized correlation for flow in a smooth pipe and one roughened by spherical beads. This indicates a definite effect of the type of roughness elements as well as their size. The reason for the decrease in the second order correlation for flow in rough pipes may be deduced from the analytical considerations where it is seen that mean velocity components in the radial and angular directions, corresponding to flow around the roughness elements, must propagate into the turbulent core. Slightly above the roughness elements, large peaks are observed in $\overline{u_1 u_2}/u^{*2}$ so that

this quantity approaches values obtained in the smooth pipe for a very short distance.

Some basis for both Prandtl's mixing length theory and von Karman's similarity hypothesis was obtained by observing that the ratio of the $\overline{u_1 u_2}$ correlation to the turbulence kinetic energy was nearly constant over the central regions of all three pipes. However, it has been pointed out by Hinze [9] that such an observation does not constitute a rigorous proof of these theories.

Calculations of the eddy diffusivity for momentum, which is of considerable importance in many practical applications, indicate a slightly larger value of this quantity, when normalized with Ru^*, for flow in the transition regime than for flow in either the hydraulically smooth or the fully rough regimes. This may aid in explaining the higher heat transfer efficiency found by Dipprey [1] in the transition regime.

The second cross correlation term measured experimentally in this investigation was the $\overline{u_1 u_3}$ correlation, and the presence of a rough boundary was also found to have significant effects on this quantity. For flow in a smooth pipe there can be no transfer of longitudinal momentum across planes normal to the x_3 axis, so $\overline{u_1 u_3}$ must be zero, and this statement was confirmed experimentally. However, experimental measurements of the $\overline{u_1 u_3}$ correlation for flow

in rough pipes indicated nonzero values of this quantity, and these values increased in magnitude as the roughness size increased. As in the case of the $\overline{u_1 u_2}$ correlation, the reason for such behavior may be deduced from the analytical considerations where mean radial and angular velocity components are allowed.

The effects of roughness on the third order correlation terms are not observed to be as pronounced as those on the second order correlation terms, but definite effects are present. The results obtained for the smooth pipe and that containing the small roughness elements indicate a high degree of similarity with only minor differences occurring in extreme values and radial positions where these extreme values occur. In each case the $\overline{u_1^2 u_2}$ correlation, normalized with the cube of the shear velocity, is seen to be negative over the entire cross section and to vary from zero at the center line to an extreme value in the vicinity of $y/R = 0.15$ before returning to zero at the solid boundary. In contrast $\overline{u_2^3}/u^{*3}$ is positive over the entire cross section and varies from about 0.6 at the center line to an extreme value very near the wall before returning to zero. On the other hand, $\overline{u_1^2 u_2}/u^{*3}$ for the large roughness elements is seen to acquire a positive value just above the sand grains, although it does remain negative for other radial positions. Also, in this case $\overline{u_2^3}/u^{*3}$ is found to be negative over

most of the cross-section, acquiring a positive value only near the top of the roughness elements. This indicates that, while the convective diffusion of turbulence kinetic energy may be similar in the smooth pipe and that containing the small roughness elements, a significant change may occur for flow in the fully rough regime.

Dissipation Function

A comparison of dissipation function measurements for the three pipes indicates that the presence of a rough boundary significantly affects this term. An increase in the size of the roughness elements produces a substantial decrease in the magnitude of vW/u^{*4}, and although a major portion of the dissipation occurs near the solid boundary for all three pipes, the value of y/R where this peak in the dissipation occurs is seen to increase with roughness size. In each case, experimentally determined values of the dissipation function were compared with values calculated from the assumption of complete isotropy between components of the dissipation function. Such calculated values were found to be in much better agreement with experimental values for the two rough pipes than for the smooth pipe. This tends to confirm the trend toward isotropy indicated by the anisotropy ratios.

Some insight as to the reason for the changes which occur in the

dissipation function can be obtained by an examination of the components of this function. Significant decreases in the maximum magnitudes of $\frac{R^2}{2u^{*2}}\overline{\left(\frac{\partial u_1}{\partial x_2}\right)^2}$ and $\frac{R^2}{2x_2^2u^{*2}}\overline{\left(\frac{\partial u_1}{\partial x_3}\right)^2}$ as roughness size is increased seem to explain the smaller values of the dissipation function in the rough pipes. A tentative explanation for the decrease in magnitude of these two quantities can be obtained by observation of the values of y/R where the maxima occur. This value is extremely near the wall for the smooth pipe and is slightly beyond the top of the roughness elements for the other two pipes. Thus, it is possible that the occupancy of the area very near the wall by the roughness elements prevents the maximum from occurring in this region and thereby yields a change in the basic flow structure.

It should also be noted that measurement of the dissipation terms allowed the evaluation of Lin's [79] condition regarding the applicability of Taylor's hypothesis in a shear flow. This condition was found to be satisfied to a reasonable degree of accuracy for all three pipes.

Energy Relations

Two types of energy balances were investigated in the current

study. A mean energy balance indicated that the energy available due to the pressure drop along the pipe in the longitudinal direction was partly directly dissipated, partly converted into a roughness energy, and partly converted to turbulence energy. A turbulence energy balance then revealed that the portion of the mean energy which was converted to turbulence energy was partly directly dissipated and partly diffused to other regions of the pipe by either gradient type diffusion or convective diffusion.

Experimental measurements of the quantities appearing in the mean energy balance indicated that the bulk of the available energy is taken from the mean flow in a narrow region adjacent to the wall for all three pipes. In the central region of these pipes the availability was found to approximately equal the conversion to other forms of energy. Near the wall sharp increases in all energy terms; availability, dissipation, and conversion; occurred. Direct viscous dissipation was seen to represent the fate of a considerable portion of the available mean energy in the smooth pipe, and proportionately less energy was dissipated directly as the roughness was increased. Instead, a part of the available energy was converted into an energy associated with the presence of the roughness elements, and the majority of this production occurred below the tops of the sand grains. Since these sand grains occupied the region where the

maximum turbulence production occurred in the smooth pipe, the majority of the turbulence energy in the rough pipes was produced just above the mean roughness height.

Consider now the turbulence energy balance. The direct viscous dissipation of turbulence energy, as described in the previous section, is seen to be nearly identical to the turbulence production over the majority of the flow field so that the turbulence is in energy equilibrium. Exceptions to these statements are evident for all three pipes at two radial positions, the pipe center line and the point where a maximum turbulence production occurs. Near the center line the production vanishes in all cases while the dissipation does not. This requires a diffusion of energy into this area in order to satisfy the energy balance. Also, at the point where the production is a maximum, the production is significantly larger than the dissipation, thereby necessitating an energy diffusion from this region.

Examination of the experimentally determined values of the gradient diffusion of turbulence kinetic energy indicates a significant effect of the roughness elements. For the smooth pipe there is seen to be a transfer of energy by gradient diffusion, both toward the wall and the center line, from the point where production is a maximum. This results in a loss of energy in the region where

production exceeds dissipation and a gain of energy at the center line where production vanishes but dissipation remains nonzero. A completely different phenomenon occurs in the rough pipes. In this case the transfer of energy is from the center line toward the wall, resulting in a loss of energy at the center line and a gain of energy near the top of the roughness elements where most of the turbulence is produced. This, of course, will have to be balanced by a convective diffusion of turbulence energy. It should be noted that the gradient type diffusion is relatively small over the entire cross section for all three pipes and decreases as roughness is increased.

The convective diffusion term, calculated as the closing entry in the turbulence energy balance, was found to exhibit a somewhat similar behavior for all three pipes. A maximum value was observed near the point where the production was a maximum, and the convective diffusion was negative in the central region of the pipe. Thus a loss of energy occurred near the top of the roughness elements, or near the edge of the viscous sublayer, and an energy gain was observed in the turbulent core. This then represented complete satisfaction of the turbulence energy balance.

Energy Spectra

For all three pipes, a very similar behavior was found for the energy spectra of the u_1 fluctuating velocity. The commonly accepted

picture of energy transfer from smaller to larger wave numbers was verified by the fact that E_1 is relatively large at small wave numbers and rapidly decreases as higher frequencies are approached. A decrease in energy content of the dissipation eddies occurs in moving from the wall to the center line of the pipe, and the eddies associated with production and diffusion of kinetic energy indicate a maximum energy content at an intermediate radial position. Such behavior is consistent with examination of the energy equation in the previous section. In all cases the inertial and production subranges were observed throughout the pipe for a significant range of wave numbers, and the existence of the viscous subrange at large wave numbers was hypothesized. Several means of normalizing these spectra were attempted, and the coordinate systems suggested by Robertson et al [47] and Goma and Gelhar [30] appeared to yield the best results.

A similarity was also found to exist among the E_2 spectra for the three pipes investigated experimentally. A decrease in the energy content of the viscous dissipation eddies was observed in proceeding from the wall to the center line, and an energy deficiency, postulated as being due to a transfer of u_1 energy in favor of u_2 by the fluctuating pressure, was observed for small wave numbers. This energy deficiency occurred at significantly different values of y/R for the three pipes, however. For the smooth pipe it was observed

only at an intermediate radial position, while for the pipe containing the small roughness elements an energy defect occurred everywhere except at intermediate radial positions. In the pipe containing the large roughness elements such a deficiency was noted at all radial positions. For all three pipes, E_2 was found to be generally smaller than E_1 at a given radial position and a given wave number as would be expected due to the smaller magnitude of $\overline{u_2^2}$. As in the case of E_1, both the inertial and the production subranges were observed, and the existence of the viscous subrange of eddy sizes was postulated to occur at large wave numbers.

All the remarks in the preceding paragraph regarding the E_2 spectra also apply to the E_3 spectra. In addition, comparison of the magnitudes of E_1 and E_2 with those of E_3 for each pipe are in agreement with results expected from mean squared values of the fluctuating velocities.

Autocorrelation Functions

The autocorrelation functions in the x_1, x_2, and x_3 coordinate directions were obtained in this investigation by taking the Fourier cosine transform of the energy spectrum function in the respective coordinate direction. None of these autocorrelation functions appear to be influenced significantly by the presence of the roughness

elements. For all three correlation functions, and all degrees of roughness, a minimum value is obtained near the edge of the roughness elements or the viscous sublayer for a particular value of time. The functions then increase in proceeding toward either the wall or the center line. The increase near the wall was interpreted as being indicative of the increasingly dominant role of low frequencies in this area, while that in the central region of the pipe was taken to be representative of the large eddies occurring in this region. However, immediately adjacent to the center line a slight reduction in eddy size occurred. For the large roughness, this reduction took place in all three coordinate directions, but for the smooth pipe, and that containing the small roughness, reduction occurred only in the x_1 and x_3 coordinate directions.

Turbulence Scales

The behavior of the Eulerian micro scales, which are a measure of the most rapid changes in the velocity fluctiations, in the three coordinate directions is somewhat similar for all three pipes. In every case these turbulence scales were found to increase slightly in moving from the center line toward the wall, and a pronounced minimum value occurred just beyond either the viscous sublayer or the top of the roughness elements. An increase was then observed

in proceeding toward the wall. This increase was interpreted as an indication of the inability of the very high frequency fluctuations to penetrate the wall region. For the smooth pipe γ_1 was always found to be larger than γ_3, which was larger than γ_2. This indicated the presence of higher frequencies in the u_2 velocity fluctuations than in either u_1 or u_3. The same observation was also valid for the rough pipes except for the region immediately above the roughness elements where γ_1 became smaller than γ_2 or γ_3. This indication of higher frequencies in the u_1 fluctuations above the roughness elements may be due to vortex shedding from the sand grains.

The Eulerian macro scales of turbulence, which are a rough measure of the longest connection time in the behavior of the fluctuating velocities, also are found to exhibit a somewhat similar behavior for the three pipes in that T_1, T_2, and T_3 remain relatively constant through the central region of the pipe with $T_1 > T_3 > T_2$. Near the wall, however, some deviation does occur. In the smooth pipe, T_1 decreases while T_2 and T_3 increase. This is indicative of the disappearance of some of the very low frequency components of u_1 at the same time that u_2 and u_3 are extended to lower frequencies. For the pipe containing the small roughness elements T_2 exhibits a slight peak just above the top of the sand grains and then remains relatively constant in moving toward the wall. On the other hand,

T_1 decreases slightly and T_3 decreases abruptly after reaching a slight peak. This indicates that low frequency fluctuations parallel to the wall tend to be disrupted by the presence of the roughness elements, while low frequency fluctuations normal to the wall tend to intermesh with the roughness particles. For the pipe containing the large particles, all three Eulerian macro scales decrease near the top of the sand grains. Thus, these particles are large enough that the low frequency fluctuations in the x_2 direction cannot penetrate below them.

The average dimensions of the smallest (viscous dissipation) eddies in the flow field are represented by the spatial micro scales of turbulence. For all three pipes studied experimentally, the spatial micro scales in the three coordinate directions generally reached a maximum value near the mid radial position and then decreased in moving toward either the wall or the center line. The decrease in proceeding toward the center line represents a slight decrease in the size of the viscous dissipation eddies in this region, and a more substantial reduction in size occurs in moving toward the wall. Throughout the flow field the dissipation eddies are observed to be elongated most in the x_1 direction and least in the x_2 direction. The addition of roughness particles to the solid boundary appears to affect the spatial micro scales only in the

region immediately above the roughness elements. For the pipe containing the small roughness elements, the sand particles tend to disrupt the eddies in the longitudinal direction causing a decrease in elongation. At the same time, the eddies are stretched slightly in the x_2 direction as they are interwoven with the roughness particles. For the pipe containing the large roughness elements, however, all of the spatial micro scales become nearly identically near the crests of the particles.

For turbulent flow in the central region of a pipe, the spatial macro scales, which are indicative of the size of the largest eddies in the flow field, appear to be qualitatively independent of the nature of the pipe wall. In all cases in the current investigation these macro scales were found to be relatively constant through this region with $\Lambda_1 > \Lambda_2 > \Lambda_3$. This indicates the existence of large eddies which are very elongated in the axial direction and somewhat suppressed in the angular direction. As in the case of the spatial micro scales, a slight dependency on roughness size is observed near the solid boundary. For the smooth boundary, the elongation of these cells in the radial direction was seen to be suppressed by the presence of the wall so that Λ_3 became larger than Λ_2. The small roughness elements were observed to disrupt the cells in the longitudinal direction so that a decrease in Λ_1 occurred. The large

eddies appeared to be completely disrupted by the presence of the large roughness elements since all three macro scales were observed to decrease near the tops of these elements.

CHAPTER X

CONCLUSION AND RECOMMENDATIONS

This study was undertaken in an attempt to gain an increased understanding of the nature of turbulent flow in pipes having both smooth and rough boundaries. A review of the available literature indicated that a great deal of information was available regarding turbulent flow in smooth pipes, but little was known regarding the structure of turbulent flow near rough boundaries. The available information did indicate definite changes in the flow structure, but the nature of these changes had not been determined. Several methods of analysis were employed in the present investigation in an attempt to determine these changes in structure.

First, applicable forms of the governing differential equations expressing the conservation of mass, momentum, and energy were developed in order to determine the controlling parameters. This development was effected in the following manner. The governing momentum equations are the well known Navier-Stokes equations, but in this form, the equations are not generally useful for turbulent flow because of the random fluctuations which appear in the pressure and velocity components. However, this random nature suggests the possibility of a statistical analysis, and this is effected by

writing the pressure and the velocity components as the sum of mean and fluctuating quantities. In the previous analytical investigations for smooth pipes, the mean velocity components in the radial and angular directions have been considered to vanish by continuity arguments, but for flow in rough pipes, mean velocity components in both radial and angular directions must exist as the fluid passes over the roughness elements thereby dictating their inclusion in the momentum equations. Also, for rough pipes velocity gradients may exist in both angular and longitudinal directions, in contrast to smooth pipes, due to the presence of the roughness elements. Thus, introduction of mean and fluctuating quantities into the Navier-Stokes equations, and time averaging these expressions, still results in a set of relationships which are rather difficult to apply for flow in rough pipes. However, in analogy with the statistical time average, the random shape of sand grain type roughness elements suggests the possibility of a statistical averaging process in the angular direction. Such an average was defined, and the momentum equations were spatially averaged according to this definition. This yielded a set of momentum equations very similar to those normally obtained for flow in smooth pipes, and as the roughness size went to zero the two groups of expressions became identical. The only terms included in the rough pipe equations which do not appear

in smooth pipe equations are spatial correlations between radial and angular mean velocities. All terms appearing in the resulting equations, except the spatial correlations, could be measured experimentally, and the spatial correlations were calculated as the closing entry.

A relationship expressing the distribution of the mean energy was obtained simply by multiplying the momentum equation in the longitudinal direction by the longitudinal mean velocity gradient in the radial direction. This equation indicated that the energy available due to the pressure drop along the pipe was partly dissipated directly by viscous action, partly converted into turbulence energy by action of the $\overline{u_1 u_2}$ shear stress, and partly converted into an energy associated with the presence of the roughness elements by the $\overline{\hat{U}_1 \hat{U}_2}$ shear stress. For flow in smooth pipes this expression reduced directly to the mean energy balance previously obtained by Laufer [41].

The fate of that portion of the mean energy converted to turbulence energy was then investigated through the development of a turbulence energy balance. The spatial averaging concept was again employed in this derivation. It was found that the resulting equation could be written in a form identical to that obtained by Laufer [41] for flow in smooth pipes. This equation showed that the portion of

the mean energy converted to the turbulence energy was partly directly dissipated by viscous effects and partly diffused to other radial positions by either gradient diffusion or convective diffusion. However, in the rough pipe equation, the convective diffusion term was also found to be indicative of any interactions between turbulence and roughness energy.

Having established the controlling parameters for turbulent flow in rough pipes, an experimental investigation was devised to determined the effects of wall roughness on these parameters. The aparatus utilized in this investigation consisted of a one foot diameter, closed circuit wind tunnel. All velocity measurements were obtained by hot-wire anemometry techniques. Basically, two types of analysis were utilized in this experimental study. The first consisted of the direct measurement of the controlling parameters found from the analytical results. These parameters were measured in pipes containing three degrees of roughness which yielded flow in all three regimes, hydraulically smooth, transition, and fully rough. These data were then supplemented by experimental measurements of the distributions of the fluctuating velocities in the frequency domain and conversion of these measurements to the wave number space. Such measurements also permitted calculation of autocorrelation functions and the various turbulence scales.

The results of this experimental study may be briefly summarized in the following manner. Experimental measurements of the longitudinal mean velocity and rms values of fluctuating velocities did not show a substantial roughness dependency, in agreement with previous investigations. Minor differences in smooth and rough pipe results include the fact that the mean velocity profile in the central region of the pipe becomes flatter as the roughness size is reduced, and the value of y/R where the fluctuating velocities reach an extreme value is shifted outward from the wall as roughness size is increased. The anisotropy ratios indicate a slight trend toward isotropy with increasing roughness, and this tendency is confirmed by comparing experimentally determined values of the dissipation function with values obtained assuming complete isotropy between components of the dissipation function.

Although the measurements described in the foregoing paragraph indicated somewhat similar results for smooth and rough pipes, other types of measurements indicated a wide divergence in the results. This tendency was especially predominate in both cross correlation and energy equation measurements. The second order $\overline{u_1 u_2}$ correlation, normalized with u^{*2}, showed a significant decrease as roughness size was increased, and the analytical results show that this indicates an increase in the spatial $\overline{\hat{U}_1 \hat{U}_2}$ correlation as roughness increases.

Also, the $\overline{u_1 u_3}$ correlation became nonzero for the rough pipes indicating a transfer of longitudinal momentum in the angular direction, and such a phenomenon cannot occur for smooth pipes. A relatively high degree of similarity was found to exist between the third order $\overline{u_1^2 u_2}$ and $\overline{u_2^3}$ correlations for flow in the smooth tube and that containing the small roughness elements; but large differences occurred for the tube containing the large roughness elements. This indicates that any changes in the convective diffusion for the pipe containing the large roughness elements may be due to the diffusion of kinetic rather than pressure energy.

Significant changes with roughness were also observed for the terms appearing in the energy equations. In both the mean and the turbulence energy balance, the major effects appeared to be due to the fact that the roughness elements occupied the region where most of the energy exchanges occurred in the smooth pipe. Also, for the rough pipes a portion of the available mean energy was converted to a roughness energy, but this appeared to be taken from the portion which was directly dissipated in the smooth pipe rather than from the portion which was converted to turbulence energy. One of the most distinct effects of roughness on the turbulence energy balance was to substantially suppress both the gradient diffusion of kinetic energy and the direct viscous dissipation of the turbulence

energy. In addition the direction of the gradient diffusion of kinetic energy showed a complete reversal from the smooth pipe behavior where it resulted in an energy gain at the center line of the pipe. However, since both the gradient diffusion and the dissipation were of smaller magnitudes than in the smooth pipe, significant changes were not observed in the convective diffusion of total turbulence energy. On the other hand, the measurements of the third order correlations, at least for the large roughness, indicate changes in the convective diffusion of kinetic energy, so a change in the convective diffusion of pressure energy is demanded. Such a change is indicated by the spectral analysis where significant differences in radial positions where energy defects in $E_2(k_1)$ and $E_3(k_1)$ occur are observed.

A great deal of similarity for energy spectra in a given coordinate direction was observed for the smooth and rough pipes. Except for the energy defects noted in the previous paragraph, energy transfer was found to be from smaller to larger wave numbers in all cases. Both production and inertial subranges existed for fairly wide wave number ranges, and the production subrange was observed for slightly larger eddies than the inertial subrange. The experimental results indicated the probable existence of the viscous subrange at very high wave numbers. As would be expected in view of the

foregoing statements, roughness was also found to have little effect on the autocorrelation functions.

A large amount of insight regarding the structural turbulence changes with roughness was also gained by an examination of the various scales of turbulence. This examination was highly complimentary to the previously described examination of the turbulence energy balance. In the central region of the pipe, variations in eddy size were observed to be relatively independent of the nature of the solid boundary. The flow in this area consisted of large eddies which were very elongated in the axial direction, while their extent in the angular direction was somewhat suppressed. The small eddies contained by these large eddies were also elongated in the axial direction but were more suppressed in the radial than the angular direction. The size of both the large and the small eddies was seen to reach a maximum near the mid radial position and to decrease only slightly at the center line. In contrast, the eddies near the wall were very much dependent on the nature of the solid boundary. About the only effect of the smooth pipe in this region was the retardation of the extent of the larger eddies in the direction normal to the surface. Addition of the small roughness elements tends to disrupt the longitudinal extent of both the large and small eddies. At the same time, the small eddies tend to be stretched in the radial

direction as they are interwoven with the roughness particles. On the other hand, the large roughness elements appeared to almost completely obliterate the large eddies, which are considered to be responsible for turbulence production and the diffusion of turbulence kinetic energy. In addition, a tendency toward isotropy by the viscous dissipation eddies is noted since their extent in all directions becomes nearly the same.

In summary, turbulent flow in smooth and rough pipes has been investigated both analytically and experimentally in this study. Applicable forms of the governing differential equations expressing the conservation of mass, momentum, and energy were derived in order to determine the controlling parameters, and an experimental investigation was devised to determine these, as well as other, parameters of interest. Although much of this desired information is currently available for flow in smooth pipes, all of the measurements were first performed for flow in a smooth pipe in order to verify the apparatus and experimental techniques. These results were found to be in excellent agreement with previously obtained data, and in addition, much more comprehensive data than were previously available have been provided. The same techniques were then utilized for the rough pipe measurements.

This experimental study indicated very definite changes in the

basic flow structure as the wall roughness is varied. Probably the most important reason for this is the fact that the roughness elements occupy the region where turbulence is produced in the smooth pipe by the three-dimensional streaky structure observed by Kline et al [80]. Moreover, the possibility of structural changes in going from the transition regime to the fully rough flow regime has been indicated. Tentative descriptions of all these various changes in flow structure, as determined from hot-wire data, have been given.

Before a complete and definite determination of the flow structure near rough surfaces can be made, flow visualization data are needed in addition to the hot-wire results obtained from the present study. Also, additional hot-wire data, possibly regarding the distribution of the $\overline{u_1u_2}$ and $\overline{u_1u_3}$ shear stresses in the frequency domain and the variation of the spatial correlations with radial position, would be helpful. In addition, the results of Goma and Gelhar [30] regarding the $\overline{u_1u_2}$ shear stress for flow in a pipe roughened with spherical beads indicate the possibility of an effect of roughness type on the flow structure, so the entire investigation described here should be repeated for other types of roughness elements. In conducting such an analysis, it is felt that digital, rather than analog, signal handling would be profitable. This could be accomplished by feeding the linearized hot-wire signals directly into an analog to digital

converter and recording the output, e.g., on magnetic tape. Mean squared values of the fluctuating velocities and the various correlations could then be obtained by processing these data on a digital computer, and a Fourier integral analysis could be applied to obtain the energy spectra, autocorrelations, and turbulence scales.

APPENDICES

APPENDIX I

HOT-WIRE SENSITIVITY FOR AN ARBITRARY ORIENTATION

Consider a hot-wire oriented at an arbitrary position in a flow field as shown in Figure 239. The size of this probe is taken to be sufficiently small so that the cylindrical velocity components can be represented in a cartesian coordinate system. The velocity component sensed by the hot-wire will be that portion of the instantaneous velocity which acts in a direction normal to the wire, and an expression for this velocity in terms of the angles σ and ζ is now sought. The total vector velocity can be expressed as

$$\vec{U} = (\overline{U}_1 + u_1)\,\vec{i}_1 + u_3\vec{i}_2 - u_2\vec{i}_3 \quad , \tag{I.1}$$

and a unit vector parallel to the wire can be written as

$$\vec{i}_P = -\cos\sigma\cos\zeta\,\vec{i}_1 + \sin\sigma\cos\zeta\,\vec{i}_2 + \sin\zeta\vec{i}_3 \quad . \tag{I.2}$$

The velocity component normal to the wire can then be expressed as

$$\vec{V} = \vec{U} - (\vec{U}\cdot\vec{i}_P)\,\vec{i}_P \quad , \tag{I.3}$$

or

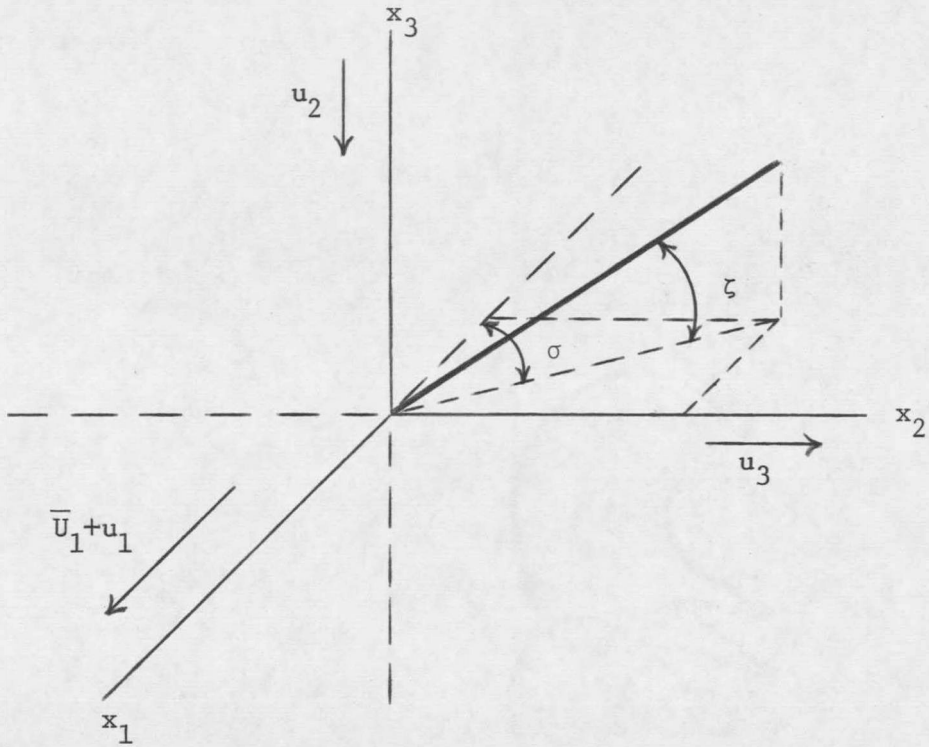

FIGURE 239. Sketch of Hot-Wire at an Arbitrary Orientation with Respect to the Mean Velocity

$$\vec{V} = [\ (\overline{U}_1 + u_1)\ (1 - \cos^2\sigma\ \cos^2\zeta) + \frac{1}{2}\ u_3\ \sin 2\sigma\ \cos^2\zeta$$

$$- \frac{1}{2}\ u_2\ \cos\sigma\ \sin 2\zeta]\ \vec{i}_1 + [\frac{1}{2}(\overline{U}_1 + u_1)\ \sin 2\sigma\ \cos^2\zeta$$

$$+ u_3(1 - \sin^2\sigma\ \cos^2\zeta) + \frac{1}{2}\ u_2\ \sin\sigma\ \sin 2\zeta]\vec{i}_2$$

$$+ [\frac{1}{2}(\overline{U}_1 + u_1)\ \cos\sigma\ \sin 2\zeta - \frac{1}{2}\ u_3\ \sin\sigma\ \sin 2\zeta$$

$$- u_2\ \cos^2\zeta]\vec{i}_3 \quad . \qquad \text{(I.4)}$$

Assuming small turbulence intensities, $u_i/\overline{U}_1$, so that such terms to powers greater than the first may be neglected, the magnitude of the normal velocity may be written as

$$V = \Big\{(\overline{U}_1^2 + 2\overline{U}_1 u_1)\ \Big[(1 - \cos^2\sigma\ \cos^2\zeta)^2 + \frac{\sin^2 2\sigma \cos^4\zeta}{4}$$

$$+ \frac{\cos^2\sigma \sin^2 2\zeta}{4}\Big] + \overline{U}_1 u_3\ \Big[\sin 2\sigma\ \cos^3\zeta\ (1 - \cos^2\sigma\ \cos^2\zeta)$$

$$+ \sin 2\sigma\ \cos^2\zeta(1 - \sin^2\sigma \cos^2\zeta) - \frac{\sin\sigma\ \cos\sigma \sin^2 2\zeta}{2}\Big]$$

$$+ \overline{U}_1 u_2\ \Big[\cos\sigma \sin 2\zeta(\cos^2\sigma \cos^2\zeta - 1) + \frac{\sin\sigma \sin 2\sigma \sin 2\zeta \cos^2\zeta}{2}$$

$$- \cos\sigma \sin 2\zeta \cos^2\zeta \Big] \Big\}^{1/2} \quad . \tag{I.5}$$

Expanding the radical on the right hand side of equation (I.5) by the binomial series finally results in

$$V = \kappa \, (\bar{U}_1 + u_1 + \Omega u_3 + \Gamma u_2) \quad , \tag{I.6}$$

where κ, Ω, and Γ are functions of σ and ζ given by

$$\kappa = [(1 - \cos^2\sigma\cos^2\zeta)^2 + \frac{1}{4}(\sin^2 2\sigma\cos^4\zeta$$

$$+ \cos^2\sigma\sin^2 2\zeta)]^{1/2} \quad , \tag{I.7a}$$

$$\Omega = \frac{1}{8K^2} [4 \sin 2\sigma \cos^3\zeta (1 - \cos^2\sigma\cos^2\zeta)$$

$$+ 4 \sin 2\sigma \cos^2\zeta \, (1 - \sin^2\sigma \cos^2\zeta)$$

$$- \sin 2\sigma \sin^2 2\zeta] \quad , \tag{I.7b}$$

$$\Gamma = \frac{1}{4K^2} [2 \cos\sigma \sin 2\zeta \, (\cos^2\sigma \cos^2\zeta - 1 - \cos^2\zeta)$$

$$+ \sin\sigma \sin 2\sigma \sin 2\zeta \cos^2\zeta] \quad . \tag{I.7c}$$

Thus, the velocity sensed by a hot-wire for a given orientation with respect to the mean velocity can be determined from equations (I.6) and (I.7). Some specific results from these equations are given in Table 3.

σ	ζ	κ	Ω	Γ
$\pm 90°$	---	1.0	0	0
--	$\pm 90°$	1.0	0	0
45°	0	0.707	0	1.0
-45°	0	0.707	0	-1.0
0	45°	0.707	-1.0	0
0	-45°	0.707	1.0	0

Table 3. Hot-Wire Sensitivity For Specific Orientations

APPENDIX II

EQUIPMENT LIST

A complete list of the equipment utilized in the experimental portion of this investigation is given below. The abbreviations in this list refer to those used in the schematic diagrams of the electrical systems in Chapter V.

Abbreviation	Equipment Type
Blower	Aerovent Type CBD Centrifugal Blower
Pressure Transducer	MKS Baratron Type 77-H Pressure Head
Pressure Indicator	MKS Baratron Type 77-MXR Indicator
Manometer	Meriam Instrument Co. Model 347B2 Micromanometer
Anemometer	Thermo Systems Inc. Model 1010A Constant Temperature Anemometer
Linearizer	Thermo Systems Inc. Model 1005B Linearizing Circuit
Scope	Tektronix Type 549 Storage Oscilloscope with Dual Trace Plug in Unit
Cor #1	Thermo Systems Inc. Model 1015B Correlator
Cor #2	Thermo Systems Inc. Model 1015C Correlator
RMSVM #1	Hewlett Packard Model 3400A rms voltmeter

Abbreviation	Equipment Type
	modified for increased averaging time
RMSVM #2	Thermo Systems Inc. Model 1060 rms voltmeter
DCVM #1	Hewlett Packard Model 3440A Mainframe with Model 3444A DC Multi-function Unit Plug in
DCVM #2	Hickock Model DMS-3200 DC Digital Voltmeter
DCVM #3	Honeywell Type VT100 DC Digital Voltmeter
DCVM #4	Honeywell Digitest Model 333
PS #1	Harrison Laboratories Inc. Model 855B DC Power Supply
PS #2	Burr Brown Research Corp. Model 527 DC Power Supply
SQ	Burr Brown Research Corp. Model 4098/25 Differential Input Multiplier/Divider Wired as Squaring Circuit
Wave Analyzer	Hewlett Packard Model 3590A Wave Analyzer with Model 3594A Sweeping Local Oscillator Plug in
X-Y Plotter	Hewlett Packard Model 7004A X-Y Recorder with Model 17175A Filter and Model 17171A DC Preamplifier on each axis

Abbreviation	Equipment Type
A/D	Hewlett Packard Model 5610A 16 Channel analog to digital converter and multiplexer
Computer	Hewlett Packard Model 2115A Digital Computer
Pulse Generator	Electronic Research Laboratories, Montana State University, Model 921A Digital Controller
TTY	Teletype Corporation Model 33
Gen #1	Hewlett Packard Model 3300A Function Generator with Model 3304A Sweeps/Offset Plug in
Gen #2	Wavetek Model 110 Function Generator
Gen #3	General Radio Type 1390-A Random Noise Generator
Filter	Spectrum Corp. Variable Band Pass Filter

APPENDIX III

DETERMINATION OF WAVE ANALYZER EFFECTIVE BANDWIDTHS

In the derivation of the equations tranforming the wave analyzer outputs to energy spectra, it was assumed that the high and low pass filters in the instrument were ideal so that the wave analyzer was totally sensitive to any signal within the set bandwidth and completely insensitive to any signal outside this bandwidth. This behavior will certainly not be characteristic of any real filter, but instead a more gradual roll off will be exhibited. This fact may be accounted for, however, by determining the total amount of energy sensed by the instrument at a given bandwidth setting and then calculating an effective bandwidth which an ideal filter would have to possess in order to pass the same amount of energy.

The determination of this effective bandwidth was accomplished in the following manner. A sine wave was input to the wave analyzer from a function generator, and the amplitude of this sine wave was adjusted until a zero dB reading was obtained from the wave analyzer with the bandwidth centered on the frequency of the sine wave. The wave analyzer was then allowed to sweep through the sine wave frequency and the output was recorded on an X-Y plotter. The resultant plot completely defined the characterics of the high and low pass filters in the wave analyzer, and since the height of this

curve had been set to unity (zero dB), the effective bandwidth of an ideal filter was simply equal to the total area under the curve, which could be determined by numerical integration.

The procedure outlined in the foregoing paragraph was repeated for sine waves of numerous frequencies, and for each of these sine waves the various bandwidth and sweep rate settings available on the wave analyzer were utilized. As might be expected, it was found that the effective bandwidth did not depend on either frequency or sweep rate but was only a function of the bandwidth indicated on the instrument. Numerous tests showed that for indicated bandwidths of 10 Hz, 100 Hz, and 1000 Hz the effective values of the bandwidth were 6.20 Hz, 93.3 Hz, and 954 Hz respectively. This information then permits usage of equations developed assuming ideal filters.

APPENDIX IV

CALIBRATION OF ANALOG TO DIGITAL CONVERSION SYSTEM

As stated in Chapter V, the wave analyzer outputs were recorded with the aid of a Hewlett Packard 2115A digital computer, through an analog to digital converter, for frequencies above 300 Hz. For frequencies below 300 Hz, electronic noise dictated that the signals be recorded directly on an X-Y plotter, and DC preamplifiers on this plotter allowed scale adjustment so that frequency and dB could be read directly. Since voltage attenuation was utilized in the analog to digital conversion system, however, calibration of this system was necessary. This was accomplished in the following manner. First, since only slowly varying DC signals were being read, sampling rate was not a critical consideration in signal handling. Thus, the sampling rate was determined so that the electronic noise was effectively averaged to zero. Preliminary tests indicated this to be accomplished by a sampling rate near 2500 readings per second, and this value was then utilized for the entire investigation.

Determination of scale factors between voltages read by the computer and frequency and dB was effected by using a sine wave input to the wave analyzer and reading frequency and dB directly from the panel meters. Comparison of these values with voltage printed out from the computer allowed the plotting of curves of

voltage versus frequency and voltage vs dB. An extremely large number of such calibration points indicated a linear relationship in each case. The coefficients in these relationships were obtained by utilizing least squares techniques to curve fit the calibration data. This curve fitting procedure indicated that all the experimental calibration data lay within $\pm 1\%$ of the straight line relationships. These relationships were then incorporated directly into the programs used for controlling the computer during experimental runs so that frequency and dB was obtained directly as the output of the computer program.

APPENDIX V

COMPUTER PROGRAMS FOR DATA REDUCTION

As stated in Chapter V all of the initial data reduction was carried out in a single computer program. Output from this program was in the form of both printed output and punched cards, and these punched cards were used as input to numerous additional programs for arranging the data in desired forms and for plotting the data. Only this basic data reduction program will be reproduced here, and this program is arranged in the following form. The main program is used for conversion of voltages to longitudinal mean and fluctuating velocities since this type of data was obtained in every experimental run. Gross turbulence parameters, such as Reynolds number and friction factor are also obtained from this program, and corrections for heat loss to the wall are applied to the data. A subroutine, entitled AUX, is then used for analysis of any secondary data, such as cross correlation data. The complete program follows.

```
C         BASIC DATA REDUCTION PROGRAM FOR TURBULENT PIPE FLOW
C         THIS PROGRAM REQUIRES SUBROUTINES WRNRE,AUX
      DIMENSION DL(10,10),Y(50),UM(50),ECC(50),UR(50),ALP(80)
C         FIX CONSTANT VALUES
      R=53.36
      RAD=5.9415
      GC=32.174
      C1=16.34*5.0/(9.0*10.0**5)
      C2=18.18*5.0/(9.0*10.0**5)
      C3=12.7/13.596
      C4=25.6/(10.0**5)
      C5=1440.0/517.149
      WRITE (106,300)
  300 FORMAT (' ')
C         INPUT HEADER CARD GIVING TYPE OF RUN
  170 READ (105,501) (ALP(I),I=1,80)
  501 FORMAT (80A1)
C         PRINT RUN TYPE
      WRITE (108,502) (ALP(I),I=1,80)
  502 FORMAT ('1',9X,80A1)
C         INPUT DISTANCES BETWEEN STATIC TAPS IN FEET
      READ (105,400) DL(1,2),DL(2,3),DL(3,4),DL(4,5),DL(5,6),DL(6,7),
     1DL(7,8),DL(8,9)
  400 FORMAT (8F10.4)
      DO 401 I=1,7
      IP=I+2
      DO 401 J=IP,9
  401 DL(I,J)=DL(I,J-1)+DL(J-1,J)
C         INPUT RUN NO, INITIAL ATM TEMP (F) AND PRESS (IN. HG),
C         INITIAL MEAN CENTERLINE VOLTAGE, FINAL TEMP PRESS AND VOLTAGE,
C         WIRE DIA (IN.)
      READ (105,1) NR,TB1,PB1,EMC1,TB2,PB2,EMC2,DW
    1 FORMAT (I5,F15.4,6F10.4)
      IF (NR) 626,626,927
  927 READ (105,2) PD1,TW1,P6B1,PD2,TW2,P6B2,DS,EDS
C         INPUT INITIAL DYNAMIC HEAD (IN. H2O), H2O TEMP (C), AND STATIC
C         -ATM PRESS (IN. H2O) THEN FINAL VALUES AND SAND DIA (IN.) AND
C         EQUIVALENT SAND DIA (IN.)
    2 FORMAT (8F10.4)
C         INPUT PRESSURE DROPS (MM HG) AND CALCULATE AVG PRESS DROP
      APD1=0.0
      APD2=0.0
      K=0
    6 READ (105,3) I,J,DP1,DP2
```

```
    3 FORMAT (2I5,2F10.4)
      IF (I) 4,4,5
    5 APD1=APD1+DP1/DL(I,J)
      APD2=APD2+DP2/DL(I,J)
      K=K+1
      GO TO 6
    4 AK=K
      APD1=APD1*C5/AK
      APD2=APD2*C5/AK
      APD=(APD1+APD2)/2.0
      EC=EMC1
      T=0.0
      K=1
      L=1
      M=1
C        INPUT DIST FROM WALL (IN.), MEAN AND RMS VOLTAGE, AIR TEMP
C        (C),AND MEAN CENTERLINE VOLTAGE IF AVAILABLE
   12 READ (105,7) Y(K),UM(K),UR(K),TP,EC1
    7 FORMAT (5F10.4)
      IF (Y(K)) 8,8,9
    9 T=TP
      GO TO 10
    8 K=K-1
      EC1=EMC2
      M=0
   10 IF (EC1) 11,200,11
  200 K=K+1
      GO TO 12
   11 DO 13 I=L,K
      AI=I-L+1
      AL=K-L+2
   13 ECC(I)=EC+AI*(EC1-EC)/AL
      L=K+1
      EC=EC1
      K=K+1
      IF (M) 14,14,12
   14 K=K-1
      AK=K
C        CALCULATE FLUID PROPERTIES AND FLOW PARAMETERS
      T=T/AK
      IF (NR-58) 402,402,403
  403 T=1.8*T+32.0
  402 WS=RAD*APD/24.0
      TB1=TB1-32.0
```

```
      TB2=TB2-32.0
      DEN=(C5*(12.7*(PB1*(1.0-C1*TB1)/(1.0+C2*TB1)+PB2*(1.0-C1*TB2)/(
     11.0+C2*TB2))+C3*(P6B1*(1.00335-C4*TW1)+P6B2*(1.00335-C4*TW2))))
      TWR=1.25*T
      DENW=DEN/(R*(TWR+459.69))
      DEN=DEN/(R*(T+459.69))
      XNU=(1.134+0.001396*T)/(DEN*10.0**5)
      XNUW=(1.134+0.001396*TWR)/(DENW*10.0**5)
      US=(GC*WS/DEN)**0.5
      UMX=(2.0*GC*(0.5*C5*(2.0*C3*(PD1*(1.00335-C4*TW1)+PD2*(
     11.00335-C4*TW2))))/DEN)**0.5
C        CORRECT VELOCITIES FOR HEAT LOSS TO WALL
      DO 15 I=1,K
      UM(I)=UM(I)*UMX/ECC(I)
      UR(I)=UR(I)*UMX/ECC(I)
      XKC=0.5*(12.0*XNUW/DW)**0.45
      XKCC=Y(I)/DW*2.0
      XK=0.0417/XKCC
      IF (UM(I)**0.45-XK*XKC) 27,27,28
   27 UM(I)=0.0
      GO TO 15
   28 UM(I)=(UM(I)**0.45-XK*XKC)**(1.0/0.45)
   15 CONTINUE
C        CALCULATE AVERAGE VELOCITY
      UAVG=0.0
      DO 30 I=1,K
   30 UAVG=UAVG+(UM(I)+UM(I+1))*((RAD-Y(I+1))**2-(RAD-Y(I))**2)
      UAVG=UAVG/(2.0*RAD*RAD)
      RE=2.0*RAD*UAVG/(12.0*XNU)
      F=8.0*GC*WS/(DEN*UAVG*UAVG)
      SRPA=US*DS/(12.0*XNU)
      SRPE=US*EDS/(12.0*XNU)
      ARR=DS/RAD
      ERR=EDS/RAD
      WRITE (108,601) NR,K
  601 FORMAT ('0RUN NUMBER'I5,39X,'NO OBSERVATIONS='I3)
      WRITE (108,602) RE,F
  602 FORMAT (' REYNOLDS NO='E15.8,27X,'FRICTION FACTOR='E15.8)
      WRITE (108,603) UMX,UAVG
  603 FORMAT (' MAXIMUM VELOCITY (FPS)='E15.8,16X,'AVERAGE VELOCITY (F
     1PS)='E15.8)
      WRITE (108,604) XNU,DEN
  604 FORMAT (' KINEMATIC VISCOSITY (FT2/SEC)='E15.8,9X,'DENSITY (LBM/
     1FT3)='E15.8)
      WRITE (108,605) WS,US
```

```
605 FORMAT (' WALL SHEAR (PSF)='E15.8,22X,'SHEAR VELOCITY (FPS)='
   1E15.8)
    WRITE (108,606) APD,T
606 FORMAT (' AVERAGE PRESSURE DROP (PSF/FT)='E15.8,8X,'TEMPERATURE
   1(F)='E15.8)
    WRITE (108,607) DS,EDS
607 FORMAT (' ACTUAL SAND DIAMETER (IN.)='E15.8,12X,'EQUIVALENT SAND
   1DIAMETER (IN.)='E15.8)
    WRITE (108,608) SRPA,SRPE
608 FORMAT (' ACTUAL ROUGHNESS PARAMETER='E15.8,12X,'EQUIVALENT ROUG
   1HNESS PARAMETER='E15.8)
    WRITE (108,609) ARR,ERR
609 FORMAT (' ACTUAL RELATIVE ROUGHNESS='E15.8,13X,'EQUIVALENT RELAT
   1IVE ROUGHNESS='E15.8)
    BETA=UAVG/UMX
    XKAP=1.5*US/(UMX-UAVG)
    WRITE (108,610) BETA,XKAP
610 FORMAT (' PIPE FACTOR='E15.8,27X,'KAPPA='E15.8,//)
    WRITE (108,611)
611 FORMAT (22X,'PREDICTED FRICTION FACTOR FOR HYDRAULICALLY SMOOTH
   1FLOW')
    FB=0.3164/(RE**0.25)
    FE=0.0056+0.5/(RE**0.32)
    FP=F
    DO 93 I=1,1000
    IF (FP) 94,94,100
100 FUN=1.0/FP**0.5-2.0*ALOG10(RE*FP**0.5)+0.8
    FUNP=-(1.0+1.0/(2.0*FP**0.5))/FP
    DIF=FUN/FUNP
    FP=FP-DIF
    IF (ABS(DIF)-0.0001) 92,92,93
 93 CONTINUE
 94 FP=0.0
 92 WRITE (108,612) FB,FP,FE
612 FORMAT (' BLASIUS='E15.8,14X,'PRANDTL='E15.8,14X,'EMPIRICAL='
   1E15.8)
    IF (EDS) 613,613,614
614 FR=1.0/(1.74-2.0*ALOG10(ERR))**2
    WRITE (108,615) FR
615 FORMAT ('0'17X,'PREDICTED FRICTION FACTOR FOR FULLY ROUGH FLOW='
   1E15.8)
613 DO 616 I=1,2
    WRITE (106,617) NR,RE,F,UMX,UAVG,XNU,EDS
617 FORMAT (I8,6E12.5)
    GO TO (618,616),I
```

```
  618 WRITE (106,726)
  726 FORMAT ('13'78X)
  616 CONTINUE
      CALL WRNRE(NR,RE,ERR)
      WRITE (108,620)
  620 FORMAT (15X,'YPLUS'17X,'Y/R'14X,'UM/UMX'10X,'URMS (FPS)'13X,'URM
     1S/US')
      DO 621 I=1,K
      YREL=Y(I)/RAD
      UREL=UR(I)/US
      URELL=UM(I)/UMX
      YRELL=Y(I)*US/(12.0*XNU)
      WRITE (108,622) YRELL,YREL,URELL,UR(I),UREL
  622 FORMAT (5E20.8)
  621 WRITE (106,623) YREL,UR(I),UM(I),UREL
  623 FORMAT (F8.4,F7.2,2F7.3)
      CALL AUX(Y,UR,UM,K,RE,F,UMX,UAVG,XNU,DEN,WS,US,DS,EDS,NR,DW,T)
      GO TO 170
  626 CALL EXIT
      END


      SUBROUTINE WRNRE(N,R,E)
C        OUTPUT HEADER FOR PRINTER
C        N=RUN NUMBER   R=REYNOLDS NUMBER
C        E=EQUIVALENT RELATIVE ROUGHNESS
      WRITE (108,1)
    1 FORMAT ('1'23X,'*************************************************
     1***')
      WRITE (108,2)
    2 FORMAT (24X,'****************************************************
     1')
      WRITE (108,3) N,R
    3 FORMAT (24X,'***RUN NO'I5,7X,'REYNOLDS NO='E15.8,'***')
      WRITE (108,4) E
    4 FORMAT (24X,'***EQUIVALENT RELATIVE ROUGHNESS='E15.8,'***')
      WRITE (108,2)
      WRITE (108,5)
    5 FORMAT (24X,'****************************************************
     1'//)
      RETURN
      END
```

```
      SUBROUTINE AUX(Y,UR,UM,K,RE,F,UX,UG,XU,SN,WS,US,DS,ED,NR,DW,T)
C        AUXILIARY SUBROUTINE TO BE USED WITH BASIC DATA REDUCTION
C             PROGRAM FOR SECONDARY DATA
      DIMENSION Y(50),UR(50),UM(50),DIN(8,50),DOUT(9,50),XN(100)
     1,DB(100)
      READ (105,1) ICODE
    1 FORMAT (I2)
C        ICODE=0  NO AUXILIARY DATA
C        ICODE=1  UV CROSS CORRELATION DATA
C        ICODE=2  UW CROSS CORRELATION DATA
C        ICODE=3  VW CROSS CORRELATION DATA
C        ICODE=4  U-U(R) CORRELATION DATA
C        ICODE=5  U-U(THETA) CORRELATION DATA
C        ICODE=6  UV ENERGY SPECTRUM DATA
C        ICODE=7  UW ENERGY SPECTRUM DATA
C        ICODE=8  U-V TIME DERIVATIVE DATA
C        ICODE=9  U-W TIME DERIVATIVE DATA
C        ICODE=10 THIRD ORDER UV CORRELATION DATA
C        ICODE=11 THIRD ORDER VW CORRELATION DATA
C        ICODE=12 MEAN VELOCITY ENERGY SPECTRUM DATA
C        ICODE=13 MEAN VELOCITY DATA
C        ICODE=14 RADIAL PRESSURE VARIATION DATA
C        ICODE=15 U TIME DERIVATIVE DATA
      IF (ICODE) 2,2,3
    3 IF (ICODE-15) 110,6,6
  110 IF (ICODE-12) 6,7,7
    6 DO 4 I=1,K
    4 READ (105,5) (DIN(J,I)J=1,8)
    5 FORMAT (8F10.4)
      DIST=.005
      RAD=5.9415
      XXX=ED/RAD
      IF (ICODE-2) 102,101,100
  100 IF (ICODE-7) 102,101,103
  103 IF (ICODE-9) 102,101,102
  101 DOUT(1,1)=Y(1)
      DOUT(2,1)=UR(1)
      DOUT(3,1)=UM(1)
      DO 104 I=2,K
      DOUT(1,I)=Y(I)+0.007
      DOUT(2,I)=UR(I)+0.007*(UR(I-1)-UR(I))/(Y(I-1)-Y(I))
  104 DOUT(3,I)=UM(I)+0.007*(UM(I-1)-UM(I))/(Y(I-1)-Y(I))
      DO 105 I=1,K
      Y(I)=DOUT(1,I)
      UR(I)=DOUT(2,I)
```

```
105 UM(I)=DOUT(3,I)
    DO 106 I=1,K
    C=UR(I)/DIN(3,I)
    DOUT(1,I)=C*DIN(1,I)
106 DOUT(2,I)=C*DIN(1,I)
    DO 107 I=2,K
    DOUT(3,I)=DOUT(1,I)+0.007*(DOUT(1,I-1)-DOUT(1,I))/(Y(I-1)-Y(I))
107 DOUT(4,I)=DOUT(2,I)-0.007*(DOUT(2,I-1)-DOUT(2,I))/(Y(I-1)-Y(I))
    DOUT(3,1)=DOUT(1,1)
    DOUT(4,1)=DOUT(2,1)
    DO 108 I=1,K
    C=UR(I)/DIN(3,I)
    DIN(1,I)=DOUT(3,I)/C
108 DIN(2,I)=DOUT(4,I)/C
102 DO 8 I=1,K
    DOUT(1,I)=Y(I)/RAD
    DOUT(2,I)=UR(I)
    DOUT(3,I)=UM(I)
    IF (ICODE-15) 111,112,112
112 C=UR(I)/DIN(1,I)
    DOUT(6,I)=(C*1000.*DIN(3,I)/DIN(2,I))**2
    DOUT(8,I)=DOUT(6,I)/(UM(I)*UM(I))
    DOUT(4,I)=0.0
    DOUT(5,I)=0.0
    DOUT(7,I)=0.0
    GO TO 8
111 GO TO (11,11,13,14,14,11,11,18,18,20,21),ICODE
 11 C=UR(I)/DIN(3,I)
    DOUT(4,I)=C*DIN(4,I)/US
    DOUT(5,I)=C*C*(DIN(1,I)**2-DIN(2,I)**2)/(US*US)
    GO TO 8
 13 C=UR(I)/DIN(1,I)
    DOUT(4,I)=C*DIN(4,I)
    DOUT(5,I)=C*DIN(3,I)
    DOUT(6,I)=C*C*(DIN(1,I)**2-DIN(2,I)**2)
    GO TO 8
 14 C=2.0*UR(I)/(DIN(1,I)+DIN(2,I))
    DOUT(4,I)=C*DIN(1,I)
    DOUT(5,I)=C*DIN(2,I)
    DOUT(6,I)=C*C*0.25*(DIN(3,I)**2-DIN(4,I)**2)
    DOUT(7,I)=(C*DIN(4,I)*RAD/(US*DIST))**2/288.
    GO TO 8
 18 C=UR(I)/DIN(3,I)
    DOUT(4,I)=C*DIN(4,I)
```

```
      DOUT(5,I)=C*C*(DIN(1,I)**2-DIN(2,I)**2)
      DOUT(6,I)=(C*1000.0*DIN(7,I)/DIN(5,I))**2
      DOUT(7,I)=(C*1000.0*DIN(8,I)/DIN(6,I))**2
      DOUT(8,I)=DOUT(6,I)/(UM(I)*UM(I))
      DOUT(9,I)=DOUT(7,I)/(UM(I)*UM(I))
      GO TO 8
   20 C=UR(I)/DIN(3,I)
      DOUT(4,I)=C*DIN(4,I)
      DOUT(5,I)=C*C*(DIN(1,I)**2-DIN(2,I)**2)
      DOUT(6,I)=0.25*C*C*C*(DIN(5,I)**2-DIN(6,I)**2)/(US**3)
      DOUT(7,I)=0.25*C*C*C*(DIN(7,I)**2-DIN(8,I)**2)/(US**3)
      GO TO 8
   21 C=UR(I)/DIN(1,I)
      DOUT(4,I)=C*DIN(4,I)
      DOUT(5,I)=C*DIN(3,I)
      DOUT(6,I)=C*C*(DIN(1,I)**2-DIN(2,I)**2)
      DOUT(7,I)=0.25*C*C*C*(DIN(5,I)**2-DIN(6,I)**2)
      DOUT(8,I)=0.25*C*C*C*(DIN(7,I)**2-DIN(8,I)**2)
    8 CONTINUE
      I1=5
      I2=0
      IF (ICODE-15) 115,116,116
  116 IP1=15
      I1=8
      GO TO 50
  115 GO TO (31,32,33,34,35,36,37,38,39,40,41),ICODE
   31 IP1=1
      GO TO 50
   32 IP1=2
      GO TO 50
   33 I1=6
      IP1=3
      GO TO 50
   34 I1=7
      IP1=4
      GO TO 50
   35 I1=7
      IP1=5
      GO TO 50
   36 I2=-1
      IP1=1
      IP2=6
      GO TO 50
   37 I2=-1
```

```
      IP1=2
      IP2=7
      GO TO 50
   38 I2=9
      IP1=1
      IP2=8
      GO TO 50
   39 I2=9
      IP1=2
      IP2=9
      GO TO 50
   40 I2=7
      IP1=1
      IP2=10
      GO TO 50
   41 I1=6
      I2=8
      IP1=3
      IP2=11
   50 WRITE (106,51) IP1
   51 FORMAT (I2,78X)
      CALL WRNRE(NR,RE,XXX)
      WRITE (108,52) IP1
   52 FORMAT (30X,'DATA TYPE'I3,//)
      WRITE (108,53)
   53 FORMAT (9X,'D-1'9X,'D-2'9X,'D-3'9X,'D-4'9X,'D-5'9X,'D-6'9X,'D-7'
     19X,'D-8'9X,'D-9')
      WRITE (106,61) NR,RE,F,UX,UG,XU,ED
   61 FORMAT (I8,6E12.5)
      WRITE (106,61) K,DN,WS,DW,US,T,DS
      DO 54 I=1,K
      WRITE (108,55) (DOUT(J,I),J=1,I1)
   55 FORMAT (9E12.4)
   54 WRITE (106,56) (DOUT(J,I),J=1,I1)
   56 FORMAT (F8.4,F7.2,3F7.3,4E11.4)
      IF (I2) 7,2,57
   57 CALL WRNRE(NR,RE,XXX)
      WRITE (106,51) IP2
      WRITE (108,52) IP2
      WRITE (108,53)
      WRITE (106,61) NR,RE,F,UX,UG,XU,ED
      WRITE (106,61) K,DN,WS,DW,US,T,DS
      DO 58 I=1,K
      WRITE (108,55) (DOUT(J,I),J=1,I2)
```

```
 58 WRITE (106,56) (DOUT(J,I),J=1,I2)
    GO TO 2
  7 READ (105,1) N
    IF (N) 2,2,60
 60 WRITE (106,51) ICODE
    CALL WRNRE(NR,RE,XXX)
    WRITE (108,52) ICODE
    WRITE (106,61) NR,RE,F,UX,UG,XU,ED
    WRITE (106,61) K,DN,WS,DW,US,T,DS
    IF (ICODE-7) 70,70,71
 70 RMS=DOUT(4,N)
    GO TO 72
 71 RMS=UR(N)
 72 YR=Y(N)/RAD
    L=0
 66 L=L+1
    READ (105,63) XN(L),DB(L)
 63 FORMAT (2F10.4)
    IF (XN(L)) 65,66,66
 65 L=L-1
    C=XN(1)*10.0**(DB(1)/10.0)*2.0*3.1415927/6.2
    LM=L-1
    DO 67 I=1,LM
    IF (XN(I+1)-300.) 981,981,982
981 XYZU=6.2
    GO TO 67
982 XYZU=93.3
 67 C=C+(XN(I+1)-XN(I))*(10.0**(DB(I+1)/10.0)+10.0**(DB(I)/10.0))*
   13.1415927/XYZU
    WRITE (108,73) YR,RMS,UM(N),L
 73 FORMAT (2X,'Y/R='E15.8,5X,'RMS VELOCITY='E15.8,1X,'FPS'5X,'UMEAN=
   1'E15.8,1X,'FPS'5X,'NO OBS='I3)
    WRITE (106,74) YR,RMS,UM(N),L
 74 FORMAT (3E26.8,I2)
    WRITE (108,75)
 75 FORMAT (10X,'FREQ (CPS)'8X,'FREQ (1/SEC)'6X,'WAVE NO (1/FT)'1X,'E
   1I(FREQ) (FT2/SEC)'3X,'EI(K1) (FT3/SEC2)')
    DO 80 I=1,L
    IF (XN(I)-300.) 983,984,984
983 XYZU=6.2
    GO TO 985
984 XYZU=93.3
985 XNR=XN(I)*2.0*3.1415927
    WN=XNR/UM(N)
    EN=RMS*RMS*10.0**(DB(I)/10.0)/(C*XYZU)
```

```
      EK=UM(N)*EN
      WRITE (108,81) XN(I),XNR,WN,EN,EK
   81 FORMAT (5E20.8)
   80 WRITE (106,82) XN(I),XNR,WN,EN,EK
   82 FORMAT (5E16.8)
      GO TO 7
    2 RETURN
      END
```

SELECTED BIBLIOGRAPHY

1. Dipprey, D. F., An Experimental Investigation of Heat and Momentum Transfer in Smooth and Rough Tubes at Various Prandtl Numbers, Ph.D. Thesis, California Institute of Technology, Pasadena, 1961.

2. Nikuradse, J., Laws of Flow in Rough Pipes, NACA TM 1292, 1950.

3. Kline, S. J., Discussion of ASME paper no. 68-FE-26, Transactions of ASME, D, Journal of Basic Engineering, 90, 4, 467-468, 1968.

4. Kline, S. J., Observed Structure Features in Turbulent and Transitional Boundary Layers, Fluid Mechanics of Internal Flow, ed. by G. Sovran, Elsevier Publishing Co., New York, 27-79, 1967.

5. Shepherd, D. G., Elements of Fluid Mechanics, Harcourt, Brace, and World, New York, 1965.

6. Bakhmeteff, B. A., The Mechanics of Turbulent Flow, Princeton University Press, Princeton, New Jersey, 1936.

7. Goldstein, S., Fluid Mechanics in the First Half of This Century, Annual Review of Fluid Mechanics, 1, ed. by W. R. Sears and M. van Dyke, Annual Reviews Inc., Palo Alto, California, 1-28, 1969.

8. Goldstein, S., Modern Developments in Fluid Dynamics, vols. I and II, Clarendon Press, Oxford, 1938.

9. Hinze, J. O., Turbulence, McGraw Hill Book Co., New York, 1959.

10. Kuethe, A. M., Review of Transport Processes in Turbulent Shear Flows, Proceedings of the Third Midwestern Conference on Fluid Mechanics, University of Minnesota, Minneapolis, 85-102, 1953.

11. Schlichting, H., Boundary Layer Theory, trans. by J. Kestin, McGraw Hill Book Co., New York, 1968.

12. Townsend, A. A., The Structure of Turbulent Shear Flow, Cambridge University Press, Cambridge, 1956.

13. Kays, W. M., Convective Heat and Mass Transfer, McGraw Hill Book

Co., New York, 1966.

14. Deissler, R. G., Analytical and Experimental Investigation of Adiabatic Flow in Smooth Tubes, NACA TN2138, 1950.

15. Gow, J. L., Fully-Developed Turbulent Flow in Smooth and Rough Walled Pipe, M.S. Thesis, Mechanical Engineering Department, Montana State University, Bozeman, 1969.

16. Hughes, W. F. and J. A. Brighton, Theory and Problems of Fluid Dynamics, Schaum Publishing Co., New York, 1967.

17. Corcoran, W. H., F. Page, W. G. Schlinger, and B. H. Sage, Temperature Gradients in Turbulent Gas Streams, Industrial and Engineering Chemistry Fundamentals, 44, 2, 410-419, 1952.

18. Longwell, P. A., Mechanics of Fluid Flow, McGraw Hill Book Co., New York, 1966.

19. Mower, M. G., Velocity Profile Measurements of Laminar, Turbulent, and Laminar Pulsating Flow, M.S. Thesis, Mechanical Engineering Department, Montana State University, Bozeman, 1967.

20. Ross, D., A new Analysis of Nikuradse's Experiments on Turbulent Flow in Smooth Pipes, Proceedings of the Third Midwestern Conference on Fluid Mechanics, University of Minnesota, Minneapolis, 651-668, 1953.

21. Coantic, M., Evolution, en fonction du nomber de Reynolds, de la distribution des vitesses moyennes et turbulentes dans une conduite, Compte Rendus Académie Science, A, 264, 849-852, 1967.

22. Corcoran, W. H., J. B. Opfell, and B. H. Sage, Momentum Transport in Fluids, Academic Press, New York, 1956.

23. Page, F., W. G. Schlinger, D. K. Breaux, and B. H. Sage, Point Values of Eddy Conductivity and Viscosity in Uniform Flow Between Parallel Plates, Industrial and Engineering Chemistry Fundamentals, 44, 2, 424-430, 1952.

24. Quarmby, A., Fully Developed Turbulent Flow in the Circular Tube and Parallel Plate Channel, Transactions of ASME, E, Journal of Applied Mechanics, 36, 1, 124-127, 1969.

25. Rothfus, R. R. and C. C. Monrad, Correlation of Turbulent Velocities For Tubes and Parallel Plates, Industrial and Engineering Chemistry Fundamentals, 47, 6, 1144-1148, 1955.

26. Tennekes, H., Outline of a Second Order Theory of Turbulent Pipe Flow, AIAA Journal, 6, 9, 1735-1740, 1968.

27. Taylor, G. I., Statistical Theory of Turbulence, Parts I-IV, Turbulence, Classic Papers on Statistical Theory, ed. by S. K. Friedlander and L. Topper, Interscience Publishers, New York, 18-75, 1961.

28. Wang, Chi-tek, On the Velocity Distribution of Turbulent Flow in Pipes and Channels of Constant Cross-Section, Transactions of ASME, A, Journal of Applied Mechanics, 85, 1946.

29. Williamson, J. W., An Extension of Prandtl's Mixing Length Theory, ASME paper no. 69-FE-48 presented at Applied Mechanics and Fluids Engineering Conference, Evanston, Illinois, June, 1969.

30. Goma, R. J. and L. W. Gelhar, Turbulent Pipe Flow with Rough and Porous Walls, Department of Civil Engineering, Massachusetts Institute of Technology, Hydrodynamics Laboratory Report no. 109, Cambridge, 1968.

31. Brand, R. S. and L. N. Persen, Implications of the "Law of the Wall" for Turbulent Boundary Layers, ACTA Polytechnica Scandiavica, Physics Including Nucleonics Series, no. 30, 1964.

32. Pai, S. I., On Turbulent Flow Between Parallel Plates, Transactions of ASME, E, Journal of Applied Mechanics, 20, 1, 109-114, 1953.

33. Pai, S. I., On Turbulent Flow in Circular Pipe, Journal of Franklin Institute, 256, 4, 337-352, 1953.

34. Knudsen, J. G. and D. L. Katz, Fluid Dynamics and Heat Transfer, McGraw Hill Book Co., New York, 1958.

35. Brodkey, R. S., The Phenomena of Fluid Motions, Addison-Wesley, Reading, Massachusetts, 1967.

36. Dorfman, A. S., Application of the Prandtl-Mises Tranformation

in the Solution of a Boundary Value Problem, High Temperature, 5, 761-769, 1967.

37. Okabe, Jun-ichi, Some Features of Velocity Distributions of Turbulent Flows of an Incompressible Fluid in Boundary Layers and in Channels, Kyushu University, Research Institute for Applied Mechanics Reports, 12, 44, 71-107, 1964.

38. Bakewell, H. P. Jr., An Experimental Investigation of the Viscous Sublayer in Turbulent Pipe Flow, report to U. S. Naval Ordnance Systems Command, Hydro-propulsion Section under contract Nonr(G)-00043-65, Department of Aerospace Engineering, Pennsylvania State University, University Park, 1966.

39. Clark, J. A., A Study of Incompressible Turbulent Boundary Layers in Channel Flow, Transactions of ASME, D, Journal of Basic Engineering, 90, 4, 455-467, 1968.

40. Laufer, J., Investigation of Turbulent Flow in a Two-Dimensional Channel, NACA Report 1053, 1951.

41. Laufer, J., Structure of Turbulence in Fully Developed Pipe Flow, NACA Report 1174, 1954.

42. Reynolds, H. C., D. M. McEligot, and M. E. Davenport, Velocity Profiles and Eddy Diffusivities for Fully Developed, Turbulent, Low Reynolds Number Pipe Flow, ASME paper no. 68-WA/FE-34 presented at Winter Annual Meeting, New York, December, 1968.

43. Schraub, F. A., A Study of the Structure of the Turbulent Boundary Layer With and Without Longitudinal Pressure Gradients, Ph.D. Thesis, Engineering Mechanics Department, Stanford University, 1965.

44. Rothfus, R. R., C. C. Monrad, and V. E. Senecal, Velocity Distribution and Fluid Friction in Smooth Concentric Annuli, Industrial and Engineering Chemistry Fundamentals, 42, 12, 2511-2520, 1950.

45. Dipprey, D. F. and R. H. Sabersky, Heat and Momentum Transfer in Smooth and Rough Tubes at Various Prandtl Numbers, Technical Report no. 32-269, Jet Propulsion Laboratory, California Institute of Technology, Pasadena, 1962.

46. Robertson, J. M., J. D. Martin, and T. H. Burkhart, Turbulent Flow in Rough Pipes, Industrial and Engineering Chemistry Fundamentals, 7, 2, 253-265, 1963.

47. Robertson, J. M., T. H. Burkhart, and J. D. Martin, Study of Turbulent Flow in Rough Pipes, University of Illinois, Theoretical and Applied Mechanics report no. 279, Urbana, 1965.

48. Moody, L. F., Friction Factors for Pipe Flow, Transactions of ASME, 66, 671, 1944.

49. Brown, B. J. and Y. H. Chu, Boundary Effects of Uniform Size Roughness Elements in Two-Dimensional Flow in Open Channels, Misc. Paper H-68-5, U. S. Army Corps of Engineers, Waterways Experiment Station, Vicksburg, Mississippi, 1968.

50. Wallach, J., Surface Topography Description and Measurement, Surface Mechanics, ASME, 1-23, 1969.

51. Whitehouse, D. J. and J. F. Archard, The Properties of Random Surfaces in Contact, Surface Mechanics, ASME, 36-57, 1969.

52. Williamson, J. B. P., J. Pullen, and R. T. Hunt, the Shape of Solid Surfaces, Surface Mechanics, ASME, 24-35, 1969.

53. Morris, H. N., Flows in Rough Conduits, Transactions of ASCE, 120, 373-398, 1955.

54. Rand, W., Discussion of ASCE paper no. 2745, Transactions of ASCE, 120, 400-402, 1955.

55. Scottron, V. E. and J. L. Power, The Influence of Pressure Gradient on the Turbulent Boundary Layer over a Rough Surface, Department of the Navy, David Taylor Model Basin, Hydromechanics Laboratory, Report no. 2115, Washington, D.C., 1965.

56. Perry, A. E. and P. N. Joubert, Rough-Wall Boundary Layers in Adverse Pressure Gradients, Journal of Fluid Mechanics, 17, 2, 193-211, 1963.

57. Townes, H. W., Flow Over a Rough Surface, Ph.D. Thesis, California Institute of Technology, Pasadena, 1965.

58. Townes, H. W. and R. H. Sabersky, Experiments on the Flow Over a Rough Surface, International Journal of Heat and Mass Transfer, 9, 5, 1966.

59. Seban, R. A. and G. L. Caldwell, The Effect of a Spherical Protuberance on the Local Heat Transfer to a Turbulent Boundary Layer, Transactions of ASME, C, Journal of Heat Transfer, 90, 4, 408-412, 1968.

60. Roberson, J. A., Surface Resistance of Plane Boundaries Roughened With Discrete Geometric Shapes, Washington State University, College of Engineering, Research Division, Bulletin no. 308, Pullman, 1968.

61. Roberson, J. A. and C. K. Chen, Flow in Conduits With Low Roughness Concentration, presented at the ASCE Hydraulics Division Specialty Conference, Massachusetts Institute of Technology, Cambridge, August, 1968.

62. Larras, J., Répartition des vitesses au sein d'un ecoulement turbulent rectiligne uniforme à surface libre, Compte Rendus Académie Science Paris, A, 265, 441-444, 1967.

63. Migay, V. K., Heat Transfer in Rough Pipes, Heat Transfer - Soviet Research, 1, 2, 69-79, 1969.

64. Logan, E. Jr. and J. B. Jones, Flow in a Pipe Following an Abrupt Increase in Surface Roughness, Transactions of ASME, D, Journal of Basic Engineering, 85, 1, 35-38, 1963.

65. Marris, A. W., Discussion of ASME paper no. 62-Hyd-5, Transactions of ASME, D, Journal of Basic Engineering, 85, 1, 39, 1963.

66. Robertson, J. M. and J. D. Martin, Turbulence Structure Near Rough Surfaces, AIAA Journal, 4, 12, 2242-2245, 1966.

67. Smutek, R., Discussion of ASCE paper no. 5855, Journal of the Hydraulics Division, Proceedings of ASCE, 95, no. HY1, 519-523, 1969.

68. Bakewell, H. P. Jr., An Experimental Investigation of the Viscous Sublayer in Turbulent Pipe Flow, Ph.D. Thesis, Aeronautical Engineering Department, Pennsylvania State University, University

Park, 1966.

69. McQuivey, R. S. and E. V. Richardson, Some Turbulence Measurements in Open Channel Flow, Journal of the Hydraulics Division, Proceedings of ASCE, 95, no. HY1, 209-223, 1969.

70. Thinh, N. van, On Some Measurements Made by Means of a Hot-Wire in a Turbulent Flow Near a Wall, DISA Information, no. 7, 13-18, 1969.

71. Thinh, N. van, Sur la mesure de la vitesse dans un écoulement turbulent par anéométrie à fil chaud, du voisinage, d'une paroi lisse, Compte Rendus Académie Science, A, 264, 1150-1152, 1967.

72. Lin, C. C., Statistical Theories of Turbulence, Princeton Aeronautical Series no. 10, Princeton University Press, Princeton, New Jersey, 1961.

73. Ohji, M., Statistical Theory of Wall Turbulence, Physics of Fluids, 10, 2, S153-S154, 1967.

74. Phillips, O. M., Shear Flow Turbulence, Annual Review of Fluid Mechanics, 1, ed. by W. R. Sears and M. van Dyke, Annual Reviews, Inc., Palo Alto, California, 245-264, 1969.

75. Biot, M. A., Simplified Variational and Physical Analysis of Heat Transfer in Laminar and Turbulent Flow, Physics of Fluids, 10, 7, 1424-1437, 1967.

76. Spalding, D. B., A Theory of the Turbulent Boundary Layer, Proceedings of the Canadian Congress of Applied Mechanics, 3, ed. by H. Karnopp, Laval University, Quebec, 117-143, 1967.

77. Dryden, H. L., A Review of the Statistical Theory of Turbulence, Turbulence, Classic Papers on Statistical Theory, ed. by S. K. Friedlander and L. Topper, Interscience Publishers, New York, 115-150, 1961.

78. Taylor, G. I., The Spectrum of Turbulence, Turbulence, Classic Papers on Statistical Theory, ed. by S. K. Friedlander and L. Topper, Interscience Publishers, New York, 100-114, 1961.

79. Lin, C. C., On Taylor's Hypothesis and the Acceleration Terms in the Navier-Stokes Equations, Quarterly of Applied Mathematics, 10, 4, 295-306, 1953.

80. Kline, S. J., W. C. Reynolds, F. A. Schraub, and P. W. Runstadler, The Structure of Turbulent Boundary Layers, Journal of Fluid Mechanics, 30, 4, 741-773, 1967.

81. Pao, Yih-Ho, Structure of Turbulent Velocity and Scalar Fields at Large Wavenumbers, Physics of Fluids, 8, 6, 1063-1075, 1965.

82. Kolmogoroff, A. N., The Local Structure of Turbulence in Incompressible Viscous Fluid for Very Large Reynolds Numbers, Turbulence, Classic Papers on Statistical Theory, ed. by S. K. Friedlander and L. Topper, Interscience Publishers, New York, 151-155, 1961.

83. Karman, Th. von and C. C. Lin, On the Concept of Similarity in the Theory of Isotropic Turbulence, Turbulence, Classic Papers on Statistical Theory, ed. by S. K. Friedlander and L. Topper, Interscience Publishers, New York, 179-186, 1961.

84. Tchen, C. M., The Spectrum of Energy in Turbulent Shear Flow, Journal of Research, National Bureau of Standards, 50, 1, 51-62, 1953.

85. Lumley, J. L., Interpretation of Time Spectra Measured in High Intensity Shear Flows, Physics of Fluids, 8, 6, 1056-1062, 1965.

86. Coantic, M., Quelques résultants nouveaux sur la structure de la turbulence dans la sous-couche visqueuse, Compte Rendus Académie Science, A, 264, 967-970, 1967.

87. Wills, J. A. B., Convection Velocities in a Viscous Sublayer, National Physical Laboratory, Aerodynamics Division Report 1251, Teddington, England, 1967.

88. Corcos, G. M., The Structure of the Turbulent Pressure Field in Boundary Layer Flows, Journal of Fluid Mechanics, 18, 353-378, 1964.

89. Willmarth, W. W. and C. E. Wooldridge, Measurements of the Fluctuating Pressure at the Wall Beneath a Thick Turbulent

Boundary Layer, Technical Report, Department of Aeronautical and Astronautical Engineering, University of Michigan, Aerodynamics Laboratory, 1962.

90. Wills, J. A. B., On Pressure Fluctuations Under Turbulent Boundary Layers, Proceedings of the 11th International Congress of Applied Mechanics, ed. by Henry Görtler, Springer-Verlag, Berlin, 889-895, 1966.

91. Reynolds, A. J., Wall Layers With Non-Uniform Shear Stress, Journal of Fluid Mechanics, 22, 3, 443-448, 1965.

92. Einstein, H. A. and H. Li, The Viscous Sublayer Along a Smooth Boundary, ASCE Proceedings, 82, no. EM2, 945-1--945-27, 1956.

93. Townes, H. W., J. L. Gow, R. E. Powe, and N. Weber, Flow Rates From Pressure Drop Measurements, Instruments and Control Systems, 42, 6, 120-121, 1969.

94. Bendat, J. S. and A. G. Piersol, Measurement and Analysis of Random Data, John Wiley and Sons, New York, 1966.

95. Blackman, R. B. and J. W. Tukey, The Measurement of Power Spectra, Dover Publications, Inc., New York, 1959.

96. Kozin, F., A Brief Introduction to Some Basic Ideas on the Topic of Random Functions, Stochastic Processes in Dynamical Problems, ASME, 1-16, 1969.

97. Thermo Systems, Inc., Hot-Wire and Hot-Film Measurements and Applications, Technical Bulletin no. 4, Minneapolis, Minnesota.

98. Melnik, W. L. and J. R. Weske, eds., Advances in Hot-Wire Anemometry, Department of Aerospace Engineering, University of Maryland, College Park (AFOSR no. 68-1492), 1967.

99. King, L. V., On the Convection of Heat From Small Cylinders in a Stream of Fluid, Philosophical Transactions of the Royal Society, Series A, 214, 373-432, 1914.

100. Thermo Systems, Inc., Heat Flux System Model 1010A Instruction Manual, Minneapolis, Minnesota.

101. Wills, J. A. B., The Correction of Hot-Wire Readings for Proximity to a Solid Boundary, Journal of Fluid Mechanics, 12, 3, 388, 1962.

102. Champagne, F. H., Turbulence Measurements With Inclined Hot-Wires, Ph.D. Thesis, Department of Chemical Engineering, University of Washington, 1966.

103. Champagne, F. H. and C. S. Sleicher, Turbulence Measurements With Inclined Hot-wires, Part 2. Hot-wire Response Equation, Journal of Fluid Mechanics, 28, 177-182, 1967.

104. Champagne, F. H., C. A. Sleicher, and O. H. Wehrmann, Turbulence Measurements With Inclined Hot-wires, Part 1. Heat Transfer Experiments With Inclined Hot-Wires, Journal of Fluid Mechanics, 28, 153-175, 1967.

105. Friehe, C. A. and W. H. Schwarz, Deviations From the Cosine Law for Yawed Cylindrical Anemometer Sensors, ASME paper no. 68-WA/APM-16, to appear in Transactions of ASME, E, Journal of Applied Mechanics.

106. Uberoi, M. S. and S. G. Kovasznay, On Mapping and Measurement of Random Fields, Quarterly of Applied Mathematics, 10, 4, 375-393, 1953.

107. Klebanoff, P. S., Characteristics of Turbulence in a Boundary Layer With Zero Pressure Gradient, NACA TN3187, 1954.

108. Enochson, L. D., Data Acquisition and Processing, Stochastic Processes in Dynamical Problems, ASME, 17-28, 1969.

109. Powe, R. E. and G. V. Smith, Curve Fitting With Several Independent Variables, Journal of the Mississippi Academy of Sciences, XIV, 32-37, 1968.

MONTANA STATE UNIVERSITY LIBRARIES
3 1762 10011160 6

[redacted]

[redacted]
D378
P872 Powe, Ralph
cop.2 Turbulence structure
in smooth and rough pipes

	NAME AND ADDRESS
10-13-72	E.R. GARNER ME
	CK SANDE ME
	CK SANDE ME
R	
R	
R	
2	
R	

[redacted]

D378
P872
cop. 2